Wave-seabed interaction and mechanisms of freak wave formation in coastal zones

Jie Zhang

ÉCOLE DOCTORALE ED353 – SCIENCES POUR L'INGÉNIEUR

THÈSE

pour obtenir le grade de

DOCTEUR de L'ÉCOLE CENTRALE de MARSEILLE

Spécialité : Mécanique et Physique des Fluides

Ecole doctorale : Sciences pour l'Ingénieur : Mécanique, Physique, Micro et Nanoélectronique

Préparée à l'**I**nstitut de **R**echerche sur les **P**hénomènes **H**ors-**E**quilibre (IRPHÉ) (UMR 7342 - Aix Marseille Univ., CNRS, Centrale Marseille), Marseille, France

Présentée par

Jie ZHANG

Interactions vagues-fond marin et mécanismes de formation des vagues scélérates en zone côtière

Dirigée par

Michel BENOIT et Olivier KIMMOUN

Soutenue publiquement le 21 septembre 2020 devant le Jury composé de :

Rapporteur	Pr. Kostas	BELIBASSAKIS	NTUA,	
Rapporteur	Pr. Vincent	REY	MIO	& Univ. Toulon,
Examinateur	Dr. Agnès	MAUREL	ESPCI	& Inst. Langevin,
Examinateur	Pr. Yuxiang	MA	SLCOE	& DUT,
Examinateur	Dr. Félicien	BONNEFOY	LHEEA	& ECN,
Examinateur	Pr. Christian	KHARIF	IRPHÉ	& ECM,
Directeur	Pr. Michel	BENOIT	IRPHÉ	& ECM,
Co-directeur	Dr. Olivier	KIMMOUN	IRPHÉ	& ECM.

A DISSERTATION

Submitted in total fulfilment of the requirements of the degree of

Doctorate of Philosophy of ECOLE CENTRALE DE MARSEILLE

Spciality: Mechanics and Physics of Fluids

Doctoral School: Engineering Sciences: Mechanics, Physics, Micro and Nano-electronics

Prepared at the **I**nstitut de **R**echerche sur les **P**hénomènes **H**ors-**E**quilibre (IRPHÉ) (UMR 7342 - Aix Marseille Univ., CNRS, Centrale Marseille), Marseille, France

Presented by

Jie ZHANG

Wave-seabed interaction and mechanisms of freak wave formation in coastal zones

Supervisors

Michel BENOIT and Olivier KIMMOUN

Publicly defended on September 21, 2020 - Ph.D. Examination Committee:

Reviewer	Pr. Kostas	BELIBASSAKIS	NTUA,	
Reviewer	Pr. Vincent	REY	MIO	& Univ. Toulon,
Examiner	Dr. Agnès	MAUREL	ESPCI	& Inst. Langevin,
Examiner	Pr. Yuxiang	MA	SLCOE	& DUT,
Examiner	Dr. Félicien	BONNEFOY	LHEEA	& ECN,
Examiner	Pr. Christian	KHARIF	IRPHE	& ECM,
Supervisor	Pr. Michel	BENOIT	IRPHE	& ECM,
Co-supervisor	Dr. Olivier	KIMMOUN	IRPHE	& ECM.

In memory of my forever beloved grandfathers
À la mémoire de mes grands-pères
ZeJiu ZHANG (1933.02-1999.12)
BingKe SUN (1944.08-2019.02)

Interactions vagues-fond marin et mécanismes de formation des vagues scélérates en zone côtière

Résumé

Dans la communauté maritime, le terme de 'vague scélérate' est utilisé pour les vagues dont la hauteur dépasse le double de la hauteur significative de l'état de mer ambiant, et qui apparaissent plus fréquemment que prédit par la distribution de Rayleigh pour les hauteurs de vagues, fondée sur une hypothèse d'état de mer gaussien. En domaine océanique, des vagues scélérates ayant causé des pertes de vies humaines et de graves dommages ont été massivement signalées au cours des dernières décennies. Dans les zones côtières, une bathymétrie irrégulière peut également provoquer des vagues extrêmes du fait des interactions entre le fond marin et les vagues.

Dans cette thèse, nous nous concentrons sur trois mécanismes d'interactions vagues-fond pouvant entraîner la formation de vagues extrêmes. Le premier scénario est un phénomène de résonance, connu sous le nom de résonance de Fabry-Perot, qui peut se développer lorsque des vagues monochromatiques se propagent sur une bathymétrie comportant deux zones d'ondulations sinusoïdales sur un fond par ailleurs plat. Dans la zone du résonateur située entre les deux zones de rides, une augmentation significative de la hauteur de l'onde incidente peut être obtenue si la condition de résonance est satisfaite. En comparant des simulations numériques avec une condition limite de fond exacte ou approchée et une solution analytique linéaire asymptotique, nous observons un décalage de fréquence de résonance pour la condition de résonance dans les cas où le rapport entre l'amplitude des ondulations et la profondeur de l'eau est grand : la résonance se produit pour un nombre d'onde plus petit que celui prévu par la théorie analytique approchée. Cet effet de décalage de fréquence de résonance joue un rôle secondaire pour la résonance de Bragg, mais il s'avère très important pour la résonance de Fabry-Perot.

Le second scénario correspond aux instabilités des trains de houle modulés en amplitude, appelés communément 'breathers', qui se propagent sur des fonds irréguliers. Trois types de profils bathymétriques sont étudiés expérimentalement et numériquement avec un modèle entièrement non-linéaire et avec l'équation non-linéaire (cubique) de Schrödinger. Cette étude a permis de montrer que, pour de faibles profondeurs et pour certaines conditions, l'amplitude de la modulation peut atteindre deux fois l'amplitude du train initial. Cette amplification en faible profondeur résulte de mécanismes qui n'existent pas en profondeur constante. Les influences des paramètres pouvant affecter la dynamique des breathers, y compris le paramètre du breather d'Akhmediev, la profondeur d'eau, la cambrure de l'onde porteuse, la période de la vague et les pentes du fond sont analysées.

Le troisième scénario correspond à des trains de vagues irrégulières unidirectionnelles se propageant sur des profils de fond côtier variables. Lorsqu'un état de mer incident

en condition d'équilibre passe sur une barre ou une marche submergée, une dynamique de non-équilibre apparaît et force l'état de mer à un nouvel équilibre compatible avec la profondeur finie, caractérisé par des statistiques fortement non-gaussiennes et une probabilité accrue d'occurrence de vagues extrêmes. La combinaison d'expériences à grande échelle et de simulations complètement non-linéaires permet de mieux comprendre la réponse dynamique du train de vagues. Les données obtenues ont été analysées en profondeur en utilisant une combinaison d'approches spectrales, bispectrales et statistiques.

Mots-clés:

vagues côtières extrêmes, vagues scélérates, interactions vagues-fond marin, résonance de Fabry-Perot, focalisation modulationnelle, vagues non-linéaires.

Wave-seabed interaction and mechanisms of freak wave formation in coastal zones

Abstract

In the maritime community, the term "rogue wave" or "freak wave" is used for waves whose wave height exceeds twice the significant wave height of the ambient sea state, and which appear more frequently than predicted by the Rayleigh distribution for wave height based on a Gaussian sea state hypothesis. In the oceanic domain, rogue waves that have caused loss of lives and severe damage have been widely reported in recent decades. In coastal areas, irregular bathymetry can also trigger such high extreme waves due to seabed-wave interactions.

In this thesis, we focus on three mechanisms or scenarios of wave-bottom interactions that can lead to the formation of high waves. The first scenario is a resonance phenomenon, known as Fabry-Perot resonance, which can develop when monochromatic waves propagate over a bathymetry with two areas of sinusoidal undulations on an otherwise flat bottom. In the resonator zone located between the two areas of ripples, a significant increase in the height of the incident wave can be obtained if the resonance condition is met. By comparing numerical simulations with either exact or approximated bottom boundary condition and an asymptotic linear analytical solution, we observe a shift of the resonance frequency at the resonance condition for cases where the ratio between the amplitude of the ripples and the water depth is large: resonance occurs for a smaller wave number than predicted by the approximate analytical theory. This downshift effect of resonance frequency plays a secondary role for Bragg resonance, but it is very important and sensitive for Fabry-Perot resonance.

The second scenario corresponds to the instabilities of the amplitude modulated wave trains, commonly called "breathers", which propagate over irregular bottoms. Three types of bathymetric profiles are studied experimentally and numerically with a fully nonlinear model and with nonlinear (cubic) Schrödinger equation. This study has shown that for shallow depths and for certain conditions, the amplitude of the modulation can reach twice the amplitude than that of the initial train. This shallow depth amplification results from mechanisms that do not exist at constant depth. The influences of parameters that can affect the dynamics of breathers, including the Akhmediev breather parameter, water depth, steepness of the carrier wave, wave period and bottom slopes are analysed.

The third scenario corresponds to unidirectional irregular wave trains propagating on variable coastal bottom profiles. When an incident sea state in equilibrium condition passes over a submerged bar or step, non-equilibrium dynamics appear and force the sea state to a new equilibrium compatible with the finite depth. This sea state adaptation process is characterized by highly non-Gaussian statistics and an increased probability of extreme wave occurrence. The combination of large-scale experiments and fully nonlinear

simulations allows a better understanding of the dynamic response of the wave train. The resulting data were analysed in depth using a combination of spectral, bispectral and statistical approaches.

Key words:

extreme coastal waves, freak waves, wave-bottom interaction, Fabry-Perot resonance, modulational focusing, nonlinear waves.

Remerciements

Pendant mes études de doctorat, de nombreuses personnes m'ont soutenu sur différents aspects. Je n'aurais pas pu aller aussi loin sans leur accompagnement physique ou spirituel. Ce chapitre leur est consacré.

Tout d'abord, je voudrais exprimer mon immense gratitude et ma profonde admiration à mes directeurs de thèse, le Pr. Michel Benoit et le Dr. Olivier Kimmoun. Ce sont eux qui m'ont porté dans ce merveilleux champ de vagues et qui ont partagé avec moi leurs connaissances de manière désintéressée et patiente. Je leur dois une fière chandelle pour leurs conseils. Je n'oublierai jamais les jours et les nuits où nous avons travaillé ensemble. Je remercierai en particulier Michel pour avoir toujours été prêt à m'aider, non seulement dans le domaine scientifique, mais aussi dans la vie quotidienne. Face à un problème, la curiosité et l'enthousiasme dans la recherche d'explications possibles, l'attitude critique et rigoureuse dans l'examen des idées, et l'esprit de coopération dans le partage des résultats sont des leçons de vie que j'ai apprises de lui au cours des quatre dernières années.

Ma gratitude va aux Dr. Agnès Maurel, Pr. Yuxiang Ma, Dr. Félicien Bonnefoy, et Pr. Christian Kharif pour le temps qu'ils ont consacré à leur fonction de membres du jury de thèse et les avis et réflexions précieuses qu'ils ont partagés pendant la soutenance. Je tiens à remercier le Pr. Kostas Belibassakis pour ses commentaires sur ma thèse et je remercie le Pr. Vincent Rey pour avoir soigneusement révisé ma thèse et présidé la soutenance.

Ensuite, je voudrais exprimer ma gratitude à mes collègues de l'équipe Structures-Atmosphère-Océan (SAO) de l'Irphé : quelle famille chaleureuse ! Paul Pergler, le Dr. Christos Papoutsellis et Romain Pinguet m'ont beaucoup soutenu. Je garderai tous les souvenirs joyeux du temps que nous avons partagé dans le même bureau. Et je tiens à remercier les collègues du laboratoire d'hydraulique de Tainan pour leur aide, en particulier Li Meng-Syue pour son soutien technique pendant la campagne expérimentale.

Enfin et surtout, je tiens à remercier mes parents bien-aimés. C'est leur encouragement constant et leur amour sans limite qui font de moi ce que je suis. Ils ont toujours été ma force d'affronter ce monde. Mais pour décrire à quel point je les apprécie, toutes les langues sont bien pâles.

Contents

List of Figures

List of Tables

Part I
General introduction

Le terme "vague scélérate" est souvent utilisé dans la communauté maritime pour désigner une vague dont la hauteur dépasse le double de la hauteur significative de l'état de mer, et qui apparaît plus fréquemment que prévu pour l'état de mer considéré. Récemment, ces vagues extrêmes ont suscité l'intérêt de la communauté scientifique, car de plus en plus de preuves montrent qu'elles se produisent avec une fréquence étonnante. Les observations faites dans le monde indiquent que des vagues extrêmes peuvent se produire dans n'importe quelle condition d'état de la mer. Dans les zones côtières, où l'activité humaine est intense, l'étude des vagues extrêmes est d'une grande importance pour la protection de la vie et la sécurité des biens. Diverses hypothèses et mécanismes ont été introduits pour expliquer la probabilité d'occurrence inattendue des vagues scélérates. La formation de vagues scélérates dans les zones côtières pourrait être intensifiée par l'interaction entre les vagues et le fond marin lorsque les ondes de gravité de surface se propagent dans un milieu non-homogène. Dans ce contexte, cette étude de doctorat est consacrée à la recherche sur la formation de vagues scélérates du fait de la bathymétrie variable des zones côtières. La partie I décrit en détail les motivations et le contexte de cette étude. Le modèle mathématique de la théorie potentielle et deux approches de modélisation numérique sont présentés. Dans la partie II, nous abordons le problème de la diffusion de Bragg, considérant la combinaison de vagues linéaires et de fond ondulé monochromatique. Les résonances de Bragg et de Fabry-Pérot sont étudiées en utilisant une solution analytique linéaire asymptotique et des modèles d'ondes linéaires. Dans la partie III, la focalisation de la modulation est examinée en condition côtière. Dans ce cas, les vagues faiblement non-linéaires se propagent sur des fonds fortement variables. Les "breathers" générés en grande profondeur d'eau entraînent la formation de vagues scélérates en zone de faible profondeur en raison des instabilités induites par les variations de profondeur. Ce phénomène est étudié à l'aide d'expériences à grande échelle et de simulations avec un modèle entièrement non-linéaire et l'équation de Schrödinger cubique non-linéaire. Dans la partie IV, nous discutons du comportement non-Gaussien dû aux changements de profondeur d'eau, lorsque des trains d'ondes irréguliers avec forte non-linéarité se propagent sur des fonds très variables. Ce sujet est également étudié expérimentalement à grande échelle et numériquement avec un modèle entièrement non-linéaire. Les expériences étudiées proviennent de deux groupes universitaires, dont certaines réalisées durant cette thèse.

Le temps coule comme la rivière, rien ne l'arrête, ni jour ni nuit.
Les Entretiens de Confucius
Confucius (IVe siècle av. J.-C.)

Chapter 1

Introduction

1.1 Research background

1.1.1 Definition of freak waves in oceanic and coastal zones

During my Ph.D. study, I devoted myself to research activities dealing with extreme and freak waves in coastal areas. The motivation lies in the fact that these waves are rather dangerous since freak waves may attack marine or coastal structures, and then disappear at once. In the background of global warming and elevation of mean sea level, the conditions of coastal areas are believed to change and evolve faster than before. Human has to gradually retreat from previous coastlines and deal with new ones, some cities are facing the increasing pressure of being submerged by water flooding during the last decades. For example, due to the huge environmental burden (mainly due to the rising sea-level and city sinking), the government of Indonesia has to migrate its capital from Jakarta to East Kalimantan. This is a sign of enormous impacts on human life due to environmental change. As was put in the *Special Report on the Ocean and Cryosphere in a Changing Climate* (SROCC) of the United Nations' *Intergovernmental Panel on Climate Change* (IPCC), cities and megacities (including New York City, Tokyo, Jakarta, Mumbai, Shanghai, Lagos, and Cairo) are "at serious risk from climate-related ocean changes". It is also believed that climate changes will result in more frequent and stronger storms, posing an increasingly large threat to our coastal coastlines and maritime structures. People are facing more and more severe challenges from nature. There are clear necessity and urgency for scientists to better understand the extreme events in coastal areas and to seek for new paths to live in harmony with nature.

The term rogue or freak wave is used in the maritime community for waves whose crest-to-trough height H exceeds a certain threshold of the background sea-state (usually characterized by its significant wave height H_s), and that appear more frequently than expected for the sea state. The significant wave height H_s is defined as four times the standard deviation of the surface elevation. Hereafter, the ratio H/H_s will be referred to as *Abnormal Index* (AI). For instance, Dysthe et al. (2008) refer to a freak wave when

$AI > 2$, while Fedele (2016) considers the threshold as 2.2. To study waves with more practical meaning in storm conditions, some authors additionally constrain H_s to be larger than a certain threshold. Oceanographers have made significant efforts to record and analyze freak waves. More and more emerging evidence shows that freak waves seem to be more common than expected. Over the past decade, records of freak waves were massively reported, like in Europe (Didenkulova and Anderson, 2010; O'Brien et al., 2017; Godoi et al., 2017) and Asia (Glejin et al., 2014; Li et al., 2016). Hundreds of freak waves under various conditions (deep or shallow water, with or without ambient currents, different spreading angles, different meteorological conditions) have been reported. Particular attention has been paid to freak waves in coastal areas (Didenkulova and Anderson, 2010; Nikolkina and Didenkulova, 2011; Didenkulova and Pelinovsky, 2011). These pieces of evidence also imply that freak waves may potentially occur under a large variety of sea-state conditions.

However, the concept of a freak wave is somewhat ill-defined due to the complexity and variety of freak wave mechanisms. By using Monte Carlo simulations of ocean surface waves, based on the simple superposition of second order corrected random phase sinusoidal making up typical wave spectra, Gemmrich and Garrett (2008) argued that the reported freak waves are not necessarily freakish, possibly they are merely consequences of linear superposition. However, current freak wave definition does not distinguish the "classical" extreme waves which are described by conventional physics and statistics from the "freak" extreme waves, in which new mechanisms should be taken into account (Hansom et al., 2015). In stormy sea states, it is just a matter of probability to encounter waves with $AI > 2$, but should all these waves be considered as freak waves? In general, the answer is no since it is in our expectation to meet large waves in energetic sea states. One of the key characteristics of a freak wave is its abnormality. The abnormality refers to the significant differences in height between the large waves and their neighbors which make them (i.e. the freak wave events) hard to be foreseen by casual observers. For instance, strongly localized high waves happening in relatively calm sea states ('walls of water'), waves with moderate crests but very deep troughs (so-called 'holes in the sea'), or even wave packets with three adjacent large waves (known as 'three sisters') are commonly considered as freak waves (Kharif and Pelinovsky, 2003). These waves accord better to the meanings of terminologies of "freak" and "rogue". Such waves, which usually appear very locally in space and time, are tricky to track and predict. This is because spatial wave information is at least as important as temporal information. However, in-situ measurements (arrays of buoys) provide very limited information regarding the spatial variation of the wave field. Sometimes they are more troublesome to us compared to "classical" extreme waves since we have no idea whether or to what extent we should reinforce our marine structures and ships. The necessity of distinguishing "classical" and "freak" extreme waves in practice has been discussed in Haver (2004). Since it is our intention to study mechanisms leading to high wave formation instead of redefining freak waves, in this thesis we stick to the definition $AI > 2$ for freak waves, and we no longer make a clear distinction for "classical" and "freak" extreme waves.

1.1.2 Possible physical mechanisms leading to freak waves

Various possible mechanisms at the origin of freak waves have been put forward based on different conditions and assumptions (Onorato et al., 2013; Adcock and Taylor, 2014). Chien et al. (2002) summarized previous hypotheses on freak wave formation and categorized them into internal and external causes. The outer factors include i. continuous wave energy accumulation obtained from the storms; ii. wave energy concentration due to refraction, reflection, and diffraction which are caused by the change of bathymetry; iii. interaction with currents or surges caused by different storms. The inner evolution mechanisms include i. linear/nonlinear energy superposition due to dispersion; ii. nonlinear wave-wave interaction; iii. self-focusing due to modulational instability.

In Kharif et al. (2009), the freak wave mechanisms are reorganized according to nonlinearity and dispersion:

1) quasi-linear mechanisms, including (spatial) geometrical focusing in finite water depth, (spatial-temporal) focusing due to dispersion, wave-current interaction, crossing sea-states;

2) nonlinear mechanisms in infinite and finite water depths, mainly referring to the so-called modulational instability;

3) nonlinear mechanisms in shallow water depth where modulational instability is absent or non-dominant, wave-bottom interaction, and focusing due to nonlinear dispersion could also result in freak waves.

As indicated above, extreme waves may happen regardless of the water depth condition. Obviously, the extreme events occurring in coastal areas are more likely to result in disastrous consequences for structures, navigation and crew safety compared to the ones happen offshore in the open ocean. In the coastal areas, the wave-bottom interaction is more and more involved as the water depth decreases. It is natural for researchers to consider the role of wave-bottom interaction, and how significant this interaction is in the process of extreme wave formation. The author is aware of external factors like meteorological conditions which are also important for freak wave formation (see the concept of "dynamical swell" in Cavaleri et al. (2016), for instance), but they are left for future studies and this Ph.D. thesis focuses on water-bottom interaction mechanisms.

1.2 Outline of content of the Ph.D. manuscript

In this study, we focused on three scenarios of wave-bottom interactions that may result in the formation of extreme waves. Regarding the interaction of waves with variable bottom profiles, the Bragg scattering (interaction between monochromatically undulated bottom and linear sinusoidal waves) and modulational focusing (interaction between sloping bottoms and weakly nonlinear side-band modulated waves) are studied. Then, water depth transition effects are discussed for nonlinear irregular waves propagating over

step or bar bottom profiles. These topics are investigated by using a combination of large-scale experiments and fully nonlinear simulations, except for Bragg scattering where we focus on linear simulations. Three-dimensional nonlinear processes are significantly different from uni-directional (long-crested) ones, the dimensionality also plays a very important role in the formation of high waves. Here, with the primary aim to investigate the effects related to uneven bottom profiles, we restrict ourselves solely to uni-directional cases. Considering the effect of wave directionality (e.g. short-crested seas) is a topic left for future research.

Part I introduces the background and motivation of this Ph.D. study. The nonlinear water wave problem is briefly reviewed, together with the boundary limitations and the corresponding assumptions. The so-called Zakharov formulation of the problem using the free surface potential is also introduced. The Zakharov formulation retains the full nonlinearity of surface waves. Two numerical models that solve the water wave problem in a highly accurate manner are then introduced. One modeling approach to incorporate breaking effects within the framework of potential wave theory is also presented.

In part II we discuss the wave resonance mechanisms between incident waves and backward-scattered waves due to periodic variations of the bottom. The Fabry-Perot resonance is considered in the linear wave framework. First, the asymptotic theory is compared with the simulation results of the linear version of the Whispers3D models with both exact and first-order approximated bottom boundary conditions (BBC). It is found that the frequency (wave-number) downshift dominates the Fabry-Perot resonance condition when the relative ripple amplitude is large. Then the wave-number downshift effects are further discussed under different approximated BBCs. The exact, first-order, and second-order approximation of bottom boundary conditions are implemented in Whispers3D and solved in a semi-analytical manner to simulate a large number of runs. For comparison, different variants of the mild-slope equation family are also used and compared, including the classical mild-slope equation (MSE), the extended MSE (EMSE), and modified MSE (MMSE). The sensitivity of the Fabry-Perot resonance to various aspects and assumptions related to wave modeling is discussed through a comparison of seven models in total.

In part III, the instabilities of breather-type solutions that appear as the wave trains propagate in a dissipative media over strongly non-uniform bottoms are studied. This topic has been investigated through several experimental campaigns in a large wave flume in Taiwan, with a broad range of wave conditions. In this part, we report several representative experimental cases conducted in the 'mid-size tank'. These cases permit to discuss the effects of numerous factors, including the bottom slope, gradient transition, breather type, incident wave nonlinearity and relative water depth, during the adaptation of incident breathers to the solutions that meet the actual experimental conditions. A numerical simulation study is also included, considering both a fully nonlinear model and a non-conservative cubic nonlinear Schrödinger equation with variable coefficients. The capabilities of the two models in describing the evolution and instability characteristics of breathers are discussed.

Part IV presents the depth transition effects on irregular sea-states. As an incident

equilibrium or near-equilibrium sea state passes over a submerged step or bar, non-equilibrium dynamics appears and forces the sea state to a new, finite-depth equilibrium along with strong non-Gaussian statistics and intensified occurrence probability of large wave events. The non-equilibrium dynamics is studied by the powerful combination of large-scale experiments and fully nonlinear numerical simulations. Two sets of experiments are studied in this part: the experimental campaign in the 'mid-size' tank of Tainan Hydraulics Laboratory and the experiments reported in Trulsen et al. (2020). The data analysis approaches are thoroughly reviewed, including spectral, bispectral, statistical and grouping analyzes of the recorded free surface time series. These approaches are adopted to characterize the sea state adaptation process. The deviation of the characteristic properties from Gaussian expectation is discussed, in particular the statistical distributions of the free surface elevation and the wave heights are included.

Chapter 2

Mathematical modeling of water wave problem

Waves surround us in forms of sound, radio, light and so on. Among them, water waves are good representative examples of waves since they are very common and can be observed with bare eyes. But from the scientific point of view, water waves are intricate manifestations of mechanical waves. Ocean waves vary from mild oscillations of the surface to powerful, roaring, and wild billows. Water waves are complex because, on one hand, they are characterized as dispersive and nonlinear. On the other hand, the boundaries of the water body can be very different, being permeable or solid, fixed or mobile. Let alone the water waves interact with other media of factors, like winds, ambient currents or solid obstacles.

The *Navier-Stokes* (N-S) equations are the most celebrated tool for describing water waves in a deterministic way under the assumption that water is a Newtonian and incompressible homogeneous fluid. However, the analytical properties of the N-S equations are not yet fully clear. The difficulties in fully understanding the N-S equations do not prevent researchers and engineers from applying it for practical issues. Via reasonable assumptions for particular situations, the original N-S equations can be reduced to simpler forms or approximate models, which can be solved analytically or numerically. For instance, the small-amplitude assumption (linear wave theory) and long-wave assumption (shallow water theory) are commonly used in practice. For a historical review of wave theories, see for example (Craik, 2004). With a growing need for more sophisticated wave models, more nonlinear and dispersive properties of waves should be taken into consideration. For gravity waves in open seas or in laboratory wave facilities, the viscosity can be typically ignored except for particular topics or applications (e.g. in the vicinity of a body in water). With an additional assumption of irrotational flow, the potential wave theory, with which high accuracy for nonlinearity and dispersion can be reached, is applicable. The three topics in this Ph.D. thesis will be studied based on the potential wave theory.

2.1 The potential wave theory and the corresponding assumptions

We will consider the two-dimensional water wave problem in the vertical plane (x, z) of a Cartesian coordinate system with z-axis positive upward and having its origin at the undisturbed free surface. As is indicated in Figure (I.2.1), the fluid domain is labeled as Ω, the free surface elevation is $\eta(x, t)$ forming a time-dependent movable boundary $\Gamma_1 : z = \eta(x, t)$. The still water depth is a time-independent function denoted as $h(x)$, and the fixed bottom boundary is $\Gamma_2 : z = -h(x)$.

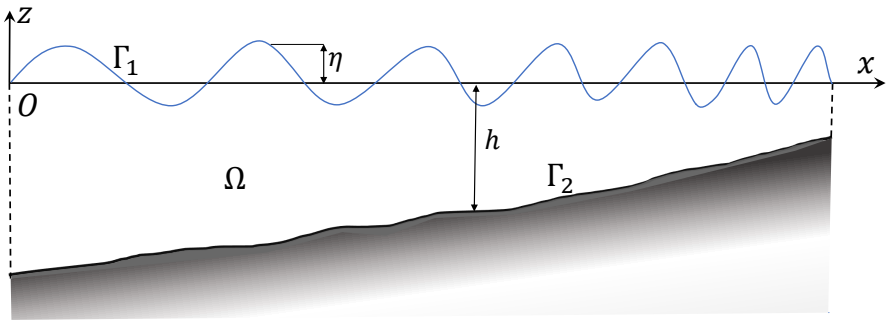

Figure I.2.1: Sketch of the fluid domain and definitions of main notations.

Considering that the flow is irrotational, the water wave problem can be formulated in terms of the velocity potential $\phi(x, z, t)$. Then, assuming the fluid is incompressible and homogeneous, with constant density ρ in space and time, the continuity equation in the fluid domain Ω results in a Laplace equation on $\phi(x, z, t)$:

$$\phi_{xx} + \phi_{zz} = 0, \quad \text{in}\,\Omega, \tag{I.2.1}$$

where the subscripts denote partial derivatives.

The assumption of an inviscid fluid ensures that, at the free surface boundary Γ_1, the pressure equals the atmospheric pressure which is here regarded as constant on the water-air interface (ignoring also the surface tension). Without loss of generality, the atmospheric pressure is chosen as zero for convenience. The *Dynamic Free Surface Boundary Condition* (DFSBC), resulting from the Bernoulli condition written on the free surface, is:

$$\phi_t + \frac{1}{2}\left((\phi_x)^2 + (\phi_z)^2\right) + g\eta = 0, \quad \text{on}\,\Gamma_1. \tag{I.2.2}$$

where g is the acceleration of gravity.

The *Kinematic Free Surface Boundary Condition* (KFSBC) expresses the impermeable condition of the free surface (particles of the fluid cannot "jump" out of the free surface), and is expressed as:

$$\eta_t + \phi_x\eta_x - \phi_z = 0, \quad \text{on}\,\Gamma_1. \tag{I.2.3}$$

At the bottom, an impermeability condition is also satisfied, implying that the component of the velocity normal to the bottom is zero. The *Bottom Boundary Condition* (BBC) for the fixed bottom is:

$$\phi_x h_x + \phi_z = 0, \quad \text{on}\,\Gamma_2. \tag{I.2.4}$$

Finally, lateral boundary conditions (applied at the dash lines in Figure (I.2.1)) also need to be specified as, for example, periodicity, Dirichlet or Neumann boundary conditions depending on the situation to be modeled. Eq. (I.2.1) to (I.2.4) constitute the nonlinear potential water wave problem. The main difficulties in solving this problem are that, on one hand, the two FSBCs are nonlinear and coupled. On the other hand, the FSBCs are applied at the free surface η which evolves as a function of time and is one of the unknowns of the problem.

2.2 The formulations of Zakharov equations

It was shown (e.g. Zakharov, 1968; Craig and Sulem, 1993) that the potential wave problem can be reformulated as a conservative Hamiltonian system (it is also referred to as *Zakharov/Craig-Sulem* formulation, ZCS). The Hamiltonian (total energy of the fluid) is expressed as a functional of the free surface elevation $\eta(x,t)$ and the free surface potential $\tilde{\phi}(x,t) \equiv \phi(x, z=\eta(x,t), t)$.

The FSBCs Eq. (I.2.2) and Eq. (I.2.3) on Γ_1 are then formulated using only free surface variables:

$$\begin{cases} \eta_t = -\tilde{\phi}_x \eta_x + \tilde{w}\left(1+\eta_x^2\right) + 2\nu_v \eta_{xx} & \text{(I.2.5)} \\ \tilde{\phi}_t = -g\eta - \dfrac{1}{2}\tilde{\phi}_x^2 + \dfrac{1}{2}\tilde{w}^2\left(1+\eta_x^2\right) - 2\nu_v \tilde{\phi}_{zz} + \dfrac{P_{surf}}{\rho} & \text{(I.2.6)} \end{cases}$$

where $\tilde{w} \equiv \phi_z(x, z=\eta(x,t), t)$ represents the vertical velocity at the free surface. The derivatives of $\tilde{\phi}(x,t)$ are deduced using the chain rule.

Note that two kinds of dissipative terms are included in Eq. (I.2.5) and Eq. (I.2.6), which could be activated when necessary. Following the work of Dias et al. (2008), two terms associated with kinematic viscosity ν_v are included to model the general dissipation in a numerical wave tank. The term P_{surf}/ρ in Eq. (I.2.6) represents an additional source of dissipation for modeling depth-induced breaking, its formulation will be introduced in Section (3.3).

Now, the two coupled equations describe the evolution of η and $\tilde{\phi}$ in time, once $\tilde{w}$ is determined from $(\eta, \tilde{\phi})$. Solving the vertical velocity at the free surface from a *Boundary Value Problem* (BVP) on the fluid domain is known as a *Dirichlet-to-Neumann* (DtN) problem, or DtN operator. The DtN problem is of fundamental importance for the Zakharov formulation and has been extensively studied. One approach is to use spectral representations in the horizontal direction(s), known as *Higher Order Spectral* (HOS) method. This method was derived independently by West et al. (1987) and by Dommermuth and Yue (1987) for the flat bottom condition. The variable bottom case

is studied by Liu and Yue (1998) accounting for arbitrary order for both free surface and bottom. A recent study by Gouin et al. (2016) shows that it is possible to consider the orders of nonlinearity differently for the free surface and the bottom boundary conditions. But inevitably, the implementation of these methods is in conjunction with truncation of DtN operator. The truncation of the DtN is not amiable for very short waves since simulations could be prone to numerical instabilities (Ambrose et al., 2014).

Direct numerical methods solving the complete formulation of water waves exist, for example, the *Boundary Integral Equations Method* (BIEM). It projects the problem on the boundary surface of the fluid domain using Green's function (see e.g. Grilli et al., 1989; Wang et al., 1995; Fochesato et al., 2007). The BIEM is accurate in the description of nonlinear waves including overturning waves when a Lagrangian approach is used to track the free surface. It is mainly used for local-scale wave-structure interaction, but for a large-scale domain, such a method is computationally expensive.

Another approach is represented by Boussinesq-type models, where the potential is approximated by a power series of the vertical coordinate, for mild bottom variation case (Madsen et al., 2002), arbitrary bottom profile with improved dispersion property (Madsen et al., 2006) with the velocity formulation. Later, the potential formulation version of Madsen et al. (2006)'s work was put forward by Bingham et al. (2009). These models are popular since both the accuracy and efficiency are acceptable. The restriction of these models is also clear: with high-order spatial derivatives involved, the numerical schemes play an important role and the practical application to real uneven bathymetry cases in two horizontal dimensions remains challenging.

Recently, new approaches were introduced to retain the full nonlinearity of the problem by adopting a spectral method to represent the vertical structure of the potential. One option is to represent the vertical velocity potential by using a series of local modes (known as *Hamiltonian Coupled-Mode System*, HCMS), as done by Athanassoulis and Belibassakis (2007) for arbitrary but uniform water depth, and by Belibassakis and Athanassoulis (2011) for arbitrary bottom profiles. Recently Papoutsellis et al. (2018) numerically implemented the work of Belibassakis and Athanassoulis (2011), therein, they showed that the evolution and propagation of nonlinear waves are well described. In another approach, the velocity potential is projected on a polynomial basis, using the set of orthogonal Chebyshev polynomials of the first kind, following the work of Tian and Sato (2008). It has been shown in Yates and Benoit (2015) that using a spectral method in the vertical direction is more efficient than using finite difference schemes. This model can be regarded as fully nonlinear and fully dispersive (if the maximum order of polynomials adopted is high enough) and is applicable for arbitrary bottom profiles without restriction on the magnitude of the bottom slope. This code has been validated for different cases (Raoult et al., 2016; Zhang and Benoit, 2019; Simon et al., 2019), showing very good performance regarding the accurate prediction of wave propagation and acceptable computational burden. It should be noticed that these approaches manage to keep all nonlinear properties of the potential wave problem just as the direct numerical methods, in the meantime, the computational effort is considerably reduced.

Two highly accurate numerical codes are adopted in this Ph.D. study of simulation

the nonlinear water wave problem in the form of Eq. (I.2.5) and Eq. (I.2.6). One is the numerical realization of the Boussinesq-type model introduced by Bingham et al. (2009), the other is the fully nonlinear numerical model introduced by Yates and Benoit (2015); Raoult et al. (2016). The latter is called Whispers3D (for *Wave and Hydrodynamics Integrated SPectral Element Research Software*). Both numerical models are briefly presented in the next chapter.

Chapter 3

Description of two nonlinear numerical wave models

In this chapter, a short presentation of the two nonlinear phase resolving models used in the course of this Ph.D. are given. These models were available at the beginning at the Ph.D. thesis. They have been used for the simulations presented in the following parts of the manuscript, with some developments and adaptations from my side for the presented applications.

3.1 Boussinesq-type model

In the Boussinesq-type model for highly nonlinear and dispersive water waves using potential formulation (Bingham et al., 2009), the velocity potential ϕ is expanded around a certain elevation $\hat{z}(x)$ in the water column using a power series of the vertical coordinate z:

$$\phi(x,z,t) \approx \sum_{n=0}^{4N_B+1} \frac{1}{n!}\,(z-\hat{z})^n\,\hat{\phi}^{(n)}, \tag{I.3.1}$$

where N_B is related to the order of the model, with possible values $N_B = 1$ or 2. We use the notation $\hat{\phi}^{(n)} \equiv \partial^n\phi/\partial z^n|_{z=\hat{z}}$ for $n = 0,\ 1,\ 2,\ 3,\ ...,\ \infty$, with $\hat{z}$ being usually fixed at the middle of the water column to optimize the dispersion properties. We define $\hat{w} \equiv \hat{\phi}^{(1)}$ as the vertical velocity at the chosen elevation.

This model has been intensively studied in the literature (Madsen et al., 2006; Bingham et al., 2009), the basic ideas are briefly recalled here. Introducing Eq. (I.3.1) into the Laplace equation in Eq. (I.2.1) and assuming $\hat{z}$ is a function of a slow variable δx (with $\delta \ll 1$), the velocity potential ϕ can be formulated as an expression of $\hat{\phi}^{(0)}$ and $\hat{w}$. In the $N_B = 2$ version of the model, the expression of ϕ is truncated at order $O(\delta^2)$ and the highest order derivatives involved is $4N_B + 1 = 9$. The accuracy of the truncation can be significantly improved by adopting the enhancement technique with which new expansion variables $(\phi^*, \hat{w}^*)$ are obtained by applying the L-operators:

$$\hat{\phi}^{(0)} = L_p\,(\hat{z}\nabla)\,\hat{\phi}^*, \quad \hat{w} = L_w\,(\hat{z}\nabla)\,\hat{w}^*, \tag{I.3.2}$$

where $L_p\left(\hat{z}\nabla\right) = L_0 + \nabla\hat{z}\cdot L_1\nabla$ and $L_w\left(\hat{z}\nabla\right) = L_0 + \nabla\hat{z}\cdot L_2\nabla$. The coefficients of a linear operator $L_0\left(\hat{z}\nabla\right)$ are computed to let the high-order derivatives from $2N_B+2$ to $4N_B+1$ vanish. The shoaling enhancement operators $L_1\left(\hat{z}\nabla\right)$ and $L_2\left(\hat{z}\nabla\right)$ are used to optimize the linearized shoaling behavior of the model. The expressions of these L-operators can be found in Bingham et al. (2009).

Now the velocity potential ϕ is expressed as a function of $\hat{\phi}^*$ and $\hat{w}^*$ via Eq. (I.3.2). The expressions of the potential at the free surface and at the bottom can be derived using the chain rule. With the Dirichlet boundary condition at the free surface $\phi|_{z=\eta} = \tilde{\phi}$ and the BBC Eq. (I.2.4) expressed in terms of $\hat{\phi}^*$ and $\hat{w}^*$, a linear system is established. The potential ϕ can be obtained from the solutions of the linear system, $\hat{\phi}^*$ and $\hat{w}^*$. Finally, the vertical velocity at the free surface $\tilde{w}$ is computed to advance the model in time.

The numerical solution procedure is based on the finite difference method for the spatial derivative and the explicit fourth-order Runge-Kutta scheme for the time integration. In the horizontal direction, a stencil of seven points is used in order to apply up to fifth-order derivative operators. In practice, the model is coded with MATLAB.

In the linearized $N_B = 2$ model and considering uniform water depth, the dispersion relationship is given explicitly by:

$$\frac{C_{N_B}^2}{gh} = \frac{1 + \sum_{n=0}^{2N_B} D_{2n}\left(kh\right)^{2n}}{1 + \sum_{n=0}^{2N_B+1} E_{2n}\left(kh\right)^{2n}}, \tag{I.3.3}$$

where C_{N_B} denotes the phase velocity. The coefficients D_{2n} and E_{2n} depend on the expansion level $\hat{z}(x)/h(x)$, they are given in Madsen et al. (2006) (their Eq. (25)). In order to evaluate the dispersion property of this model, Eq. (I.3.3) has to be compared to the exact Airy phase velocity in flat bottom condition, namely:

$$\frac{C_{Airy}^2}{gh} = \frac{\tanh kh}{kh}. \tag{I.3.4}$$

3.2 Whispers3D model

The modeling approach of Whispers3D is presented in previous works (Yates and Benoit, 2015; Raoult et al., 2016) and summarized hereafter. First, a change of the vertical coordinate from $z \in [-h(x), \eta(x,t)]$ to $s \in [-1, 1]$ is applied, transforming the varying domain to a rectangular one:

$$s(x,z,t) = \frac{2z + h(x) - \eta(x,t)}{h(x) + \eta(x,t)}. \tag{I.3.5}$$

The nonlinear potential water wave problem is then reformulated in the new (x,s,t)-space with $\varphi(x, s(x,z,t), t) \equiv \phi(x,z,t)$. Using the set of Chebyshev polynomials $T_n(s), n = 0, 1, ..., N_T$, as an expansion basis for $s \in [-1, 1]$, the potential $\phi(x,z,t)$ is approximated

in the transformed (x, s) domain as:

$$\varphi(x, s(x, z, t), t) \approx \varphi_{N_T}(x, s(x, z, t), t) = \sum_{n=0}^{N_T} a_n(x, t) T_n(s), \tag{I.3.6}$$

where the $a_n(x, t), n = 0, 1, ..., N_T$ coefficients are now the main unknowns of the problem.

Then, the approximation Eq. (I.3.6) of φ is inserted into the governing equations composed of the Laplace equation, a new Dirichlet FSBC with $\varphi_{N_T}|_{s=1} = \tilde{\phi}$ on the free surface, and the BBC expressed in the (x, s) coordinate system. The so-called Chebyshev-tau method, a variant of the Galerkin method, is used to project the Laplace equation onto the T_n polynomials for $n = 0, 1, ..., N_T - 2$ eliminating the s coordinate and resulting in a set of $N_T - 1$ equations on the a_n coefficients at each location x. These $N_T - 1$ equations are supplemented with the Dirichlet FSBC and the BBC, so that a system of $N_T + 1$ linear equations with $N_T + 1$ unknowns $(a_n, n = 0, ..., N_T)$ at each abscissa is formed.

In this model the order of horizontal spatial derivatives does not exceed 2, which is highly beneficial for numerical implementation. These spatial derivatives are evaluated using high order finite difference formulas, using stencils composed typically of $N_{sten} = 5$ to 9 nodes.

The solutions of the linear system are the a_n coefficients from which the free surface vertical velocity $\tilde{w}$ can be computed:

$$\tilde{w}(x) = \frac{2}{h(x) + \eta(x)} \sum_{n=0}^{N_T} a_n(x) n^2. \tag{I.3.7}$$

An explicit third-order Runge-Kutta scheme (SSP-RK3) is used for time marching of Eq. (I.2.5) and Eq. (I.2.6). In the Whispers3D code, one can balance the accuracy of results and efficiency of simulation via the choice of the parameters N_T, N_{sten}, and discretization in space and time. The implementation of the code is done in Fortran.

The dispersion relation of the linear model in constant water depth was derived analytically in Benoit et al. (2017):

$$\frac{C_{N_T}^2}{gh} = \frac{1 + \sum_{n=1}^{N_T-2} \alpha_n (kh)^{2n}}{1 + \sum_{n=1}^{N_T-1} \beta_n (kh)^{2n}}, \tag{I.3.8}$$

where the coefficients α_n and β_n for different values of N_T can be found in Tab. 1 of Benoit et al. (2017).

The dispersion properties of Boussinesq-type model and Whispers3D are plotted in Figure (I.3.1), showing the relative error on wave phase celerity with respect to the Airy dispersion relation for linear waves over a flat bottom (Eq. (I.3.4)). Is is observed that, as expected, the dispersion properties of both models improve with increasing approximation order, i.e. N_B for the Boussinesq model, and N_T for Whispers3D. Dispersion errors of both models remain low for $kh < \pi$ if a value of N_T greater than 5 to 6 is used

in Whispers3D. For larger values of kh (above, say, 30), using larger values of N_T in Whispers3D (e.g. $N_T > 7$) allows to get a better representation of the celerity of deep water waves in comparison with the Boussinesq-type model. For instance, with $N_T = 10$ the relative error on wave celerity from Whispers3D remains below 2.5% for kh up to 100.

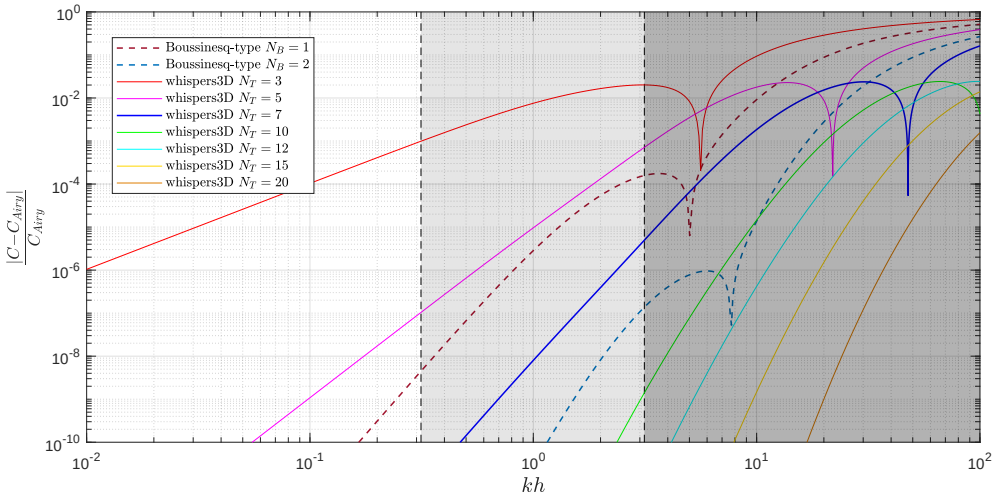

Figure I.3.1: Comparison of the dispersive property between the Boussinesq-type model (with $N_B = 1, 2$), the Whispers3D model (with $N_T \in [3, 20]$) and exact Airy solution. The two vertical dash lines divide the relative water depth kh into shallow water region ($kh < \pi/10$), intermediate water depth region, and deep water region ($kh > \pi$).

3.3 Inclusion of wave breaking effect in Whispers3D

Due to the limitation of potential theory, it is not possible to model the breaking events in the same manner as in nature. Instead, it is achieved in Whispers3D by adding an artificial pressure-like term P_{surf}/ρ in Eq. (I.2.6) to dissipate the energy of breaking wave events. The breaking wave dissipation is activated only for waves that exceed a breaking criterion. There are a variety of approaches to detect breaking inception, and three of them are implemented in Whispers3D (Simon et al., 2019).

Here a relatively simple detection method, called the geometric method, is adopted based on the local slope of the free surface. In 2D simulation cases, individual waves are separated using the zero-crossing method. The angle of the wave slope with respect to the horizontal axis is defined as $\beta = \eta_x$, as shown in Figure (I.3.2). A wave starts to break when $\beta > \beta_b$ and the breaking process of this wave stops when $\beta < \beta_f$. The breaking thresholds $[\beta_b, \beta_f]$ depend on the type of breaking waves. Following the calibration of Cienfuegos et al. (2010) for a Boussinesq-type model, β_b takes a value between 28° and 32° for spilling breakers and between 35° and 36° for plunging breakers. The angle of

termination of breaking is suggested to be set β_f to approximately 10°.

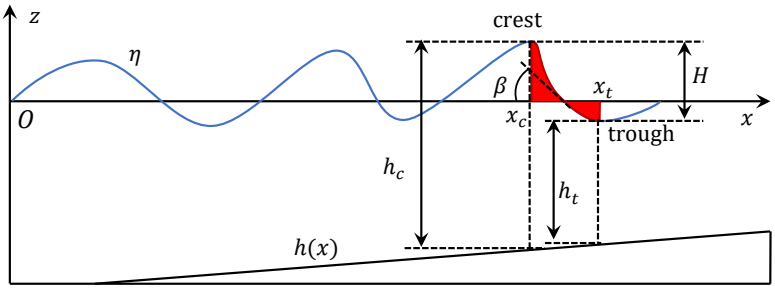

Figure I.3.2: Sketch of the geometric parameters for the wave breaking model

Guignard and Grilli (2001) introduced a dissipation method in analogy to a hydraulic jump propagating over a flat bottom. The dissipation method adopted here is a variation of this method, which was proposed by Papoutsellis et al. (2019). The difference is that the dissipation is applied on the wave front only, i.e. $x \in [x_c, x_t]$ (red zone in Figure (I.3.2)), instead of the whole wavelength as in Guignard and Grilli (2001). The pressure P_{surf} consists of three terms:

$$P_{surf} = \nu_b(t) S(x) \eta_t(x,t), \tag{I.3.9}$$

where $S(x)$ is a spatial smoothing function of sinusoidal shape. $\nu_b(t)$ is evaluated from the following expression:

$$\nu_b(t) = \mu_b \left(\rho g C \frac{h H^3}{4 h_c h_t} \right) \left[\int_{x_c}^{x_t} S(x) \left(\eta_t(x,t) \right)^2 \mathrm{d}x \right]^{-1}, \tag{I.3.10}$$

where μ_b is a calibration constant reflecting the intensity of breaking waves with subscript 'b' for breaking, C denotes the local phase velocity, $H = h_c - h_t$ is the breaking wave height, as indicated in Figure (I.3.2). In practice, Svendsen et al. (1978) recommended selecting μ_b around 1.5. Simon et al. (2019) have chosen μ_b varying in $[0.9, 1.2]$, as properly calibrated values in reproducing different breaking wave experiments. In addition, the breaking dissipation is gradually activated in time (over a few time steps) in order to avoid numerical instability caused by an abrupt activation of the dissipative term.

The detailed breaking modeling strategy in Whispers3D is presented in Simon et al. (2019), together with comparisons of several combinations of breaking criteria and dissipation methods against a set of four experiments in wave flume (one with regular waves and three with irregular waves) considering various shapes of coastal bottom profile.

Part II
Bragg scattering due to undulated bottoms

Dans cette partie, on étudie la résonance de Bragg de vagues monochromatiques se propageant dans un domaine comportant deux zones d'ondulations sinusoïdales sur un fond par ailleurs plat. Elle est connue sous le nom de résonance de Fabry-Pérot (F-P) et appartient à la classe I_2 de résonance de Bragg. Dans le domaine situé entre les deux zones d'ondulations (appelé résonateur), une augmentation significative des amplitudes de vague aura lieu si les conditions de résonance sont remplies. La solution analytique linéaire asymptotique (ALAS) du problème des ondes linéaires avec la condition limite au fond (BBC) approximative du premier ordre a été fournie par Couston et al. (2015). La condition de résonance F-P est double: (1) le nombre d'onde des ondulations du fond est deux fois supérieur à celui des ondes sinusoïdales incidentes (condition de résonance de Bragg); (2) le résonateur est d'une longueur particulière. L'ALAS prévoit que, pour une bathymétrie avec les longueurs de deux zones d'ondulations et la distance entre eux prescrites, les amplitudes de vague dans le résonateur augmentent de manière exponentielle avec $\epsilon = \delta/h$ (δ étant l'amplitude des ondulations du fond, et h la profondeur d'eau moyenne). Les effets de l'approximation du premier ordre de la BBC ont été discutés sur la base des simulations utilisant Whispers3D (intégré en temps) avec soit la BBC exacte, soit la BBC approchée de premier ordre. Il a été démontré que, pour des valeurs importantes de ϵ, le nombre d'onde de résonance est réduit et influence de manière significative la manifestation de la résonance. Cette partie du travail a été publiée dans l'article Zhang and Benoit (2019), reproduit dans le chapitre 2. Comme étape supplémentaire dans l'étude des effets de diminution du nombre d'onde de résonance, le modèle Whispers3D avec BBC exacte, de premier ordre ou de second ordre a été résolu de manière semi-analytique. Trois versions des équations de pente douce introduites par Berkhoff (1972); Kirby (1986a); Chamberlain and Porter (1995) sont également incluses pour comparaison. Ces modèles se distinguent principalement par leurs hypothèses faites pour la BBC. En effectuant un grand nombre de tests avec différents ϵ et nombres d'onde incidents, le nombre d'onde de résonance F-P et le facteur d'amplification des amplitudes sont comparés entre différents modèles dans le chapitre 3. Enfin, les principales conclusions sont résumées dans le chapitre 4.

L'homme d'une vertu supérieure est comme l'eau. L'eau excelle à faire du bien aux êtres et ne lutte point. Elle habite les lieux que déteste la foule. C'est pourquoi il (le sage) approche du Tao.

Tao Te King - Le Livre de la voie et de la vertu

Lao Tseu (IVe siècle av. J.-C.)

List of the symbols of Part II

a_I	separated 1^{st}-order incident wave amplitude
$a^{(n)}_{I,B}, a^{(n)}_{I,F}$	n^{th}-order incident bound and free wave amplitudes
a_n	coefficient of Chebyshev polynomials in Whispers3D
a_R	separated 1^{st}-order reflected wave amplitude
$a^{(n)}_{R,B}, a^{(n)}_{R,F}$	n^{th}-order reflected bound and free wave amplitudes
A	general coefficient in Premise
$\mathcal{A}$	complex incident wave amplitude function
B	general coefficient in Premise
$\mathcal{B}$	complex reflected wave amplitude function
C	phase velocity of wave in actual water depth
$\bar{C}$	phase velocity of wave for the mean water depth
C_g	group velocity of wave in actual water depth
$\bar{C}_g$	group velocity of wave for the mean water depth
d	bottom ripple amplitude
D	general coefficient in Premise
E^{FP}	normalized wave amplitude within the resonator
f	vertical structure of potential for constant water depth
F	vertical structure of potential for variable water depth
g	acceleration due to gravity
h	mean water depth in F-P bathymetry case
h_{hump}	height of a parabolic hump
$\tilde{h}$	actual water depth in F-P bathymetry case
k_b	bottom ripple wave-number
k_B	theoretical Bragg resonance wave-number
k_I	separated incident wave-number
k_R	separated reflected wave-number
k^n	wave-number of n^{th} order free mode
$\bar{k}$	wave-number for the mean water depth
L_1, L_2	length of patch 1 and 2
L_b	bottom ripple wavelength
L_{hump}	parabolic hump length
L_r	resonator length in F-P bathymetry case
N_1, N_2	number of ripples in patch 1 and 2
N_{sten}	stencil size in Whispers3D
N_T	maximum order of Chebyshev polynomial used in Whispers3D
R^B_j	Bragg reflection coefficient of patch j
R^{FP}	reflection coefficient of F-P case
$\mathcal{R}^B_j$	complex Bragg reflection coefficient of patch j
T^B_j	Bragg transmission coefficient of patch j
$\mathcal{T}^B_j$	complex Bragg transmission coefficient of patch j
T^{FP}	transmission coefficient of F-P case
u_0	coefficient in MSE model
u_1, u_2	coefficients in MMSE model
W_s	normalized parabolic hump length

δ	bottom ripple function
ϵ	relative ripple amplitude
η	free surface elevation
θ_I	phase of the separated 1^{st}-order incident wave
$\theta_{I,B}^{(n)}, \theta_{I,F}^{(n)}$	phase of the separated nth-order incident bound and free wave
θ_R	phase of the separated reflected 1^{st}-order wave
$\theta_{R,B}^{(n)}, \theta_{R,F}^{(n)}$	phase of the separated nth-order reflected bound and free wave
κ	detune wave-number parameter of k_B
$\phi(x,z,t)$	velocity potential
$\Phi(x)$	velocity potential on the free surface, prescribed solution of mild-slope equation family
$\hat{\phi}(z,t)$	time-independent velocity potential, prescribed solution of Whispers3D
$\hat{\phi}_I(z,t)$	time-independent velocity potential imposed on lateral boundary
$\varphi(x,s)$	velocity potential in transformed domain
$\varphi_{N_T}(x,s)$	approximation of velocity potential in transformed domain
ω	angular wave frequency
ω_B	Bragg resonance frequency corresponding to k_B
Ω	detune wave frequency parameter of ω_B
Ω_c	cut-off frequency in ALAS

Chapter 1

Introduction

1.1 Bibliography survey of Bragg scattering problem

The problem of wave reflection by periodic seabed topography has been extensively studied since it was discovered. This phenomenon, firstly experimentally demonstrated by Davies (1982), is called Bragg scattering due to its close analogy in crystallography. In the attempts of explaining water wave Bragg scattering theoretically, Davies and Heathershaw (1984) adopted a regular perturbation method to expand the problem in powers of a small parameter ϵ (ratio of ripple amplitude d and mean water depth h) and solved the problem at the lowest order. The reflected waves appear at second-order as forced solutions, so this model is only capable of predicting infinitesimal reflection coefficients. However in cases near the resonance condition (i.e. when the incident wavelength is twice that of the bottom ripples) where reflected waves are of the same order as that of incident waves, the model is no longer valid. In the work of Davies and Heathershaw (1984), this is solved by considering an artificial correction that ensures energy conservation law. The experiments reported in Davies and Heathershaw (1984) covered different number of ripples (1, 2, 4, 10) and relative ripple amplitudes (d/h = 0.08 to 0.32, with d being the dimensional ripple amplitude, and h the mean water depth). This experimental data have frequently been used to validate theoretical and numerical models since published.

Mei (1985) used a multiple-scale perturbation method to achieve a better prediction of the reflected and transmitted waves near resonance condition cases. His analytical solution is still at the lowest order, but includes the reflected wave effect, thus it is applicable for strong reflection cases. The theory of Mei showed good agreement with the experimental data of Davies and Heathershaw (1984). Then Kirby (1986a) provided a relatively more general model by extending the usual *Mild-Slope Equation* (MSE) (Berkhoff, 1972, 1976). This model, known as *Extended Mild-Slope Equation* (EMSE), considers not only the slowly varying mean water depth as in mild-slope equations, but also the rapidly varying, arbitrary,

small-amplitude deviation from the mean water depth. It is generally applicable for both resonant and non-resonant scattering cases with undulated bottoms. In the cases where the resonant scattering is weak, the slow, non-resonant scattering effects due to slow change of average water depth become important. The EMSE reduces to the theory of Mei (1985) when considering constant mean water depth. The BBC in Kirby (1986a)'s formulation is still of first-order approximation, the corrugation amplitude is assumed to remain small compared to their wavelength. The cases with oblique incidence were studied theoretically by Mei et al. (1988), and numerically by Dalrymple and Kirby (1986). Yu and Mei (2000) pointed out the unreliability of using Bragg scattering mechanism for shore protection: it might indeed result in attenuation or suppression of waves after the sandbars, but amplification is also possible when considering reflection from the shoreline.

The high-order effects of Bragg scattering mechanics have been discussed by several authors. First, according to the number of components in the wave-bottom interaction, Liu and Yue (1998) suggested classifying triad interaction of two surface waves and one bottom wave as Class I Bragg resonance. The quartet interactions containing two surface waves and two bottom waves (Class II) or three surface waves and one bottom wave (Class III) are classified as *High-Order Bragg* (HOB) resonances. For doubly sinusoidal beds, both Class I and Class II resonance could manifest. Belzons et al. (1991) and Guazzelli et al. (1992) showed experimental evidence of significant higher-order Bragg resonant interactions between linear waves and doubly sinusoidal beds. Sub-harmonic reflection is significant even for small bottom undulation amplitudes. In these experiments, the relative ripple amplitudes of the doubly sinusoidal beds were relatively large, varying from $d/h = 0.13$ to 0.4 for three bottom setups. A clear trend was observed for the Class I resonance peaks, as the relative ripple amplitude increases, the resonance peak shifts towards lower wave-number. This downshift of wave-number is also observed in the 10-ripple and $d/h = 0.16$ case of Davies and Heathershaw (1984). Guazzelli et al. (1992) conducted numerical computations based on a full potential theory of linear waves by decomposing the smooth wavy bottom into a number of steps. Including evanescent modes in conjunction with step-wise approximation of the bed, the computation of Guazzelli et al. (1992) showed good agreement with the experimental data. For the Class II Bragg, the super-harmonic wave could also result in HOB resonance, but it is relatively less appealing since high-frequency waves are less sensitive to bottom profile. A three-scale asymptotic analytical theory for Class II Bragg resonance was provided by Rey et al. (1996) showing good agreement with the experimental data of Guazzelli et al. (1992). The Class III Bragg resonance is predicted by Liu and Yue (1998). It is different from Class I and II because in Class III resonance the frequency of the resonant wave, which can be either reflected or transmitted, is a sum or difference of the incident wave frequencies. It should be mentioned that this Class III HOB resonance could result in significant spectral evolution, generation infragravity waves and affect-

ing the bottom profile. The corresponding asymptotic theory was put forward by Alam et al. (2010) in a general three-dimensional context (waves are oblique with respect to the bottom undulations). Recently Class III resonance has been confirmed in a laboratory wave tank (Peng et al., 2019). Bragg resonance could also develop due wave-flow interaction. The wave-current Bragg resonance was studied by Kirby (1988). Using also multiple-scale expansion, he found that the presence of a current shifts the resonant frequency by possibly significant amounts and enhances the reflection effect by bar fields due to the additional effect of the perturbed current field. The effect of current on Bragg resonance for both regular waves and irregular waves have been investigated experimentally by, for example, Magne et al. (2005). More recently, Bragg scattering effects on irregular wave trains by small-amplitude topography in the presence of an irrotational (almost uniform) current was studied by Ardhuin and Magne (2007). Bragg resonance of surface and interfacial waves has also been studied (Elandt et al., 2015), its cloaking effect is discussed since it can potentially protect offshore floating structures (Couston et al., 2017).

Meanwhile, researchers are also interested in the nonlinear effects associated with the finite amplitude of surface waves and bottom bars. Hara and Mei (1987) conducted experiments to verify the existence of cut-off detuning frequency and provided an extended linear theory with second-order effects (of the bottom bars and of the free surface waves) included. They found that even for low-steepness surface waves, the inclusion of second-order effects of bottom bars improves the agreement with experimental measurements (for $d/h \approx 0.2$). Kirby (1986b) put forward a theory of weakly nonlinear Stokes waves at third order of wave amplitude on the basis of the works of Kirby and Dalrymple (1983) and Kirby (1986a). But the application of this theory is limited by the validity range of Stokes theory. For relatively deep water, the bottom effect is insignificant; however, for relatively shallow water depth, Stokes theory is no longer valid. O'Hare and Davies (1993) adopted a successive-application-matrix model, and compared it with the EMSE model. Two models showed similar behavior, while the former is slightly closer to experimental data of Guazzelli et al. (1992) (EMSE model underestimated the sub-harmonic resonance). Especially for large bottom ripple amplitude case (with d/h up to 0.4), the simulated resonance peaks shift towards lower wave-numbers.

Chamberlain and Porter (1995) presented a new form of the mild-slope equation, the so-called *Modified Mild-Slope Equation* (MMSE), which retains the second-order terms of bottom variations $\mathrm{O}(h_{xx},\ |h_x|^2)$ on the basis of the mild-slope assumption $|h_x| \ll kh$ (h is the water depth and k the corresponding wave-number). Thus, the MMSE model is applicable to larger ripple amplitude cases. Good agreement was achieved when the MMSE model was adopted to simulate the 4-ripple and $d/h = 0.32$ case of Davies and Heathershaw (1984). The wave-number k in the EMSE of Kirby (1986a) corresponds to the mean water depth; however, the wave-number in the MMSE model follows the actual bathymetry. The approximated

version of the mild-slope equation and the extended mild-slope equation can be derived from the MMSE if the corresponding assumptions are made. Porter and Staziker (1995) improved the MMSE model to include the evanescent modes and discontinuity of bottom slope by adding an interfacial matching condition, known as the 'mass-conserving matching condition' or the 'jump condition'. Porter and Porter (2001) extended the MMSE model to three-dimensional case. L. Zhang and Edge (1999) presented a *Hybrid Method* (HM) for the cases with steep undulation bars consisting of two or more slow and rapid oscillations. In the HM, the rapidly varying components are expanded with respect to the slow varying components and the higher-order terms neglected in Kirby (1986a) are retained for steep undulations. The HM reduces to MMSE of Chamberlain and Porter (1995) when the rapidly-varying components are removed. Liu et al. (2012) studied the MMSE analytically by adopting recursive formulae for calculating arbitrary order derivatives of the terms which are proportional to the bottom curvature and to the square of the slope. Analytical Taylor series solutions of the MMSE for different piece-wise smooth bathymetries can be constructed. Liu et al. (2019) showed that the MMSE model can be solved analytically as waves propagate over singly periodic sinusoidal ripples by separating the sinusoidal ripples into four monotonic subintervals and transforming into an explicit MMSE. The solutions in the form of Frobenius series have been constructed. Very recently, Liu et al. (2020) studied the Bragg scattering phenomenon as linear waves propagate over a finite array of trapezoidal bars with significant depth transitions and showed analytical solutions in terms of Taylor series to the MMSE.

The Bragg scattering problem has been investigated with more accurate and computationally expensive numerical models. Liu and Yue (1998) adopted the HOS method based on Dommermuth and Yue (1987), which is accurate up to fourth order for both free-surface and bottom steepness. Dalrymple and Kirby (1986) and L. Zhang and Edge (1999) adopted the BIEM for linear wave problem, and considered the exact BBC. A very significant improvement of the method has been put forward in Athanassoulis and Belibassakis (1999) by including an additional sloping-bottom mode in the standard representation. This enhanced coupled-mode theory, being equivalent to the complete linearized problem, is very efficient. Madsen et al. (2006) used a Boussinesq-type model to consider the exact BBC to study all three classes of Bragg resonances. They used linear wave model for Class I and Class II resonances, and fully nonlinear model for Class III resonance. To conclude, the bottom nonlinearity can be multi-fold: (1) the downward shift of Bragg resonance condition, so-called wave-number (frequency) downshift (for Class I Bragg resonance); (2) the relatively significant second-order sub-harmonic resonance (for Class II Bragg resonance); (3) a more involved role of evanescent modes in the interference process, which also results in changes of Bragg condition (for all classes of Bragg resonance).

The full nonlinearity of the bottom ripple can be studied by using Floquet the-

ory which has no small-amplitude assumption on the bottom ripples. In the work of Howard and Yu (2007), the normal mode problem of basins with specially corrugated bottoms has been studied and compared with an asymptotic solution. The effects of evanescent modes are also discussed. In their work, a special shape of the bottom corrugation is chosen for the convenience of the mathematical derivation. Higher-order Bragg resonances of water waves was discussed in Yu and Howard (2010), where the wave-number of the surface wave is an integer multiple of half of the bottom corrugation wave-number. In their work, the terms second- and high-order resonances are in the sense described by Guazzelli et al. (1992). Then, Yu and Zheng (2012) presented the way of imposing a Robin boundary condition to study a more realistic case where the bottom is of a three-part flat-corrugated-flat profile for Class I Bragg resonance study. They did not only show results of the Bragg scattering in the vicinity of the first-order resonance tongue but also higher-order ones. In the latter cases, non-trivial wave reflection due to bottom ripples is also possible. Then Yu and Howard (2012) showed that for an arbitrary periodic bottom profile, the Floquet theory is applicable by representing the bottom profile with a Fourier series. With such a method it is made possible to consider more general bottom profiles, the sinusoidal shape being of course included. Recently this theory has been confirmed experimentally (Weidman et al., 2015).

In this part of the thesis, a variation of Class I Bragg resonance (classified as Class I_2 Bragg resonance), the *Fabry-Perot* (F-P) resonance case is studied. An optical Fabry-Perot cavity consists of two partially reflecting mirrors surrounding a dielectric medium. The F-P resonance was discussed for water waves only recently in Couston et al. (2015) within the framework of linear potential flow theory. In such a case, both surface waves and bottom ripples are sinusoidal. Two separated patches of singly-sinusoidal ripples are set in analogy to the partially reflecting mirrors. Four wave components (two bottom waves and two surface waves) exist in F-P resonance, but unlike Class II Bragg resonance, the two bottom waves are uncorrelated. The study of Couston et al. (2015) was based on linear wave and small-amplitude ripple assumption, as in Mei (1985). When the F-P resonance condition is met, significant enhancement of incident wave is achieved within the flat region between two patches of ripples, called the 'resonator'. As one of the two subjects of this part, the effects associated with the finite-amplitude bottom ripples on the F-P resonance are studied in detail while the assumption of linear surface wave remains. The main findings are presented in a journal paper in *Physical Review E* entitled *Effect of finite amplitude of bottom ripples on F-P resonance of water waves* by Zhang and Benoit (2019). In this paper, it is shown that the frequency (wave-number) downshift which is induced by the finite-amplitude bottom ripples plays an important role in the F-P resonance condition. This downshift dominates the enhancement rate of incident waves achieved within the resonator. This journal paper is included in Chapter 2 as it is. Then the second objective of this part of work is to further investigate the significance of different BBC as-

sumptions on the wave-number downshift. The study of the effects associated with BBC will be investigated by using a full potential theory of linear waves (using the linearized version of Whispers3D) as a benchmark. Various approximated models with different degrees of assumptions on the BBC are considered, including the asymptotic linear analytical theory, Whispers3D with first- or second-order approximated BBC, MSE, EMSE and MMSE. In Chapter 3, this investigation is given as supplementary materials to the PRE paper (Zhang and Benoit, 2019). In Chapter 4, the main findings of this part of work are summarized.

1.2 Bibliography survey of wave separation technique

The separation of incident waves and reflected ones is of great importance for many practical purposes, such as the evaluation of the efficiency of breakwaters, the calibration of wave-absorption zones, or the design of active wave absorption paddle movements, etc. In the study of Bragg or F-P resonance, the wave separation technique is necessary for evaluating the reflection and transmission coefficients from the time series measured in experiments or simulations. The first study is provided by Goda and Suzuki (1976), who estimated the incident and reflected wave amplitudes via Fourier analysis of two time series recorded simultaneously at two different locations. This method is valid for unidirectional linear regular as well as irregular waves, but the distance between the two wave gauges should not be even integer of half (spectral-peak) wavelength. This 2-gauges method was then extended to 3-gauges (Mansard and Funke, 1980) and N-gauges (Zelt and Skjelbreia, 1993) for increased accuracy. For some purposes like the generation of signals for active absorption devices, it is more convenient to do the separation directly in the time domain. Frigaard and Brorsen (1995) put forward a 2-gauges approach, the *Separating the Incident and the Reflected Waves* (SIRW) method, by using a relatively small digital filter. Then, Baldock and Simmonds (1999) extended this method for cases with sloping bottom by considering linear shoaling of waves to determine wave amplitudes and phase changes. This approach could be useful for other linear separation methods. Based on Morlet wavelet transformation, Ma et al. (2010) proposed another time-domain separation approach, valid for linear regular or irregular waves over either flat or sloping bottoms. This approach was extended to the three-dimensional case in Ma et al. (2011).

For nonlinear waves, in general, both bound modes (travelling with carrier wave's celerity) and free modes (travelling with their own celerities) are present in time series. They are separable due to different phase velocities. Lin and Huang (2004) considered this property and put forward an N-gauges (at least 4-gauges, and more reliable for 5-gauges or even more) method for separating high-order regular incident and reflected waves. Liu and Li (2016) improved the method of Lin and Huang (2004) with a least-square method for better resolution of the incident and reflected strongly nonlinear regular waves in shallow waters, and extended it

to obliquely-incidence conditions. As was noticed by Andersen et al. (2017), the work of Lin and Huang (2004) adopted Stokes linear dispersion which makes their work only reliable for second-order. For higher-order cases possible errors may come from amplitude dispersion. In Andersen et al. (2017), this limitation has been largely released by choosing the dispersion relationship of Stokes V theory or stream function theory according to their applicability. With the consideration of wave-wave interactions, the irregular waves are more tricky to be incorporated. Recently the nonlinear separation method has been extended to bichromatic waves (Andersen et al., 2019) and narrow-banded irregular waves (Eldrup and Andersen, 2019).

First, the basic technique of Goda and Suzuki (1976) for reflection evaluation is reviewed here, which has been widely used for wave flume tests. Consider the synthesized profiles of the incident and reflected waves for a specific angular frequency ω:

$$\eta(x_m, t) = a_I \cos(\epsilon_I - \omega t) + a_R \cos(\epsilon_R + \omega t), \tag{II.1.1}$$

where a_I and a_I denotes the incident and reflected amplitudes, $\epsilon_I = kx_m + \theta_I$, $\epsilon_R = kx_m + \theta_R$, θ_I denotes initial phase of incident wave, and θ_R for reflected wave. The wave-number k as a function of water depth and angular frequency is identical for both two components, and is computed from dispersion relationship. The unknown parameters a_I, a_R, ϵ_I, and ϵ_R are computed in frequency domain. This method is applicable for irregular wave analysis when this technique is applied for all frequency components of the spectrum.

By the time this dissertation was written, the state-of-art separation technique for regular nonlinear wave is provided by Andersen et al. (2017). This is introduced for our study of Class I Bragg resonance and F-P resonance (sometimes considered as Class I_2 Bragg resonance). This approach perfectly covers our study purpose at the present stage. But it should be noticed that for Class III Bragg resonances, the bichromatic separation approach (Andersen et al., 2019) should be adopted rather than regular nonlinear wave separation. Here the essentials of the approach for regular waves separation is briefly reviewed. In the time domain the free surface elevation η measured at probe m is written as:

$$\begin{aligned}\eta(x_m, t) = {} & err(t) + a_I^{(1)} \cos\left(k_I x_m - \omega t + \theta_I^{(1)}\right) + a_R^{(1)} \cos\left(k_R x_m + \omega t + \theta_R^{(1)}\right) \\ & + \sum_{n=2}^{N} \left\{ a_{I,B}^{(n)} \cos\left[n\left(k_I x_m - \omega t\right) + \theta_{I,B}^{(n)}\right] + a_{R,B}^{(n)} \cos\left[n\left(k_R x_m + \omega t\right) + \theta_{R,B}^{(n)}\right] \right\} \\ & + \sum_{n=2}^{N} \left[a_{I,F}^{(n)} \cos\left(k^{(n)} x_m - n\omega t + \theta_{I,F}^{(n)}\right) + a_{R,F}^{(n)} \cos\left(k^{(n)} x_m + n\omega t + \theta_{R,F}^{(n)}\right) \right],\end{aligned} \tag{II.1.2}$$

where $err(t)$ denotes the time evolution of all modes higher than the chosen order

N as well as noise, $a_I^{(1)}$, $a_R^{(1)}$ are the first-order amplitudes for incident and reflected waves, $a_{I,B}^{(n)}$, $a_{R,B}^{(n)}$ are the nth-order amplitudes for incident and reflected bound waves, and $a_{I,F}^{(n)}$, $a_{R,F}^{(n)}$ are the nth-order amplitudes for incident and reflected free waves, respectively. In analogy with wave-number, the phases $\theta_I^{(1)}$, $\theta_R^{(1)}$, $\theta_{I,B}^{(n)}$, $\theta_{R,B}^{(n)}$, $\theta_{I,F}^{(n)}$, $\theta_{R,F}^{(n)}$ are defined in the same way. k_I and k_R are the to-be-determined wave-numbers as functions of the water depth h, angular frequency ω and also the corresponding amplitudes, using Stokes V or stream function theory. Assuming that free components are of much smaller energy compared to other components, the linear theory is adopted for high-order free waves, thus $k^{(n)}$ is the wave-number determined by Stokes linear dispersion relationship:

$$(n\omega)^2 = gk^{(n)} \tanh(k^{(n)}h). \tag{II.1.3}$$

Since the incident and reflected wave amplitudes are unknown, this method starts with an initial guess from linear dispersion, then computes wave amplitudes for all components with latest computed wave-number in an iterative manner in the Fourier space. The computation stops when the convergence of wave-number is reached. The advantage of this method is that the incident and reflected wave-numbers are computed separately and could take different values: this is more realistic for finite wave amplitude cases. More detailed description of the to-be-solved matrix and the accuracy of this method can be found in Andersen et al. (2017). This method has been implemented independently using Matlab during this PhD work.

Chapter 2

Finite-amplitude bottom ripple effects on Bragg/Fabry-Perot resonance conditions

This chapter contains the article *Effect of finite amplitude of bottom ripples on F-P resonance of water waves*, published in *Physical Review E* in 2019.

In this paper, we present a study regarding the effect of finite amplitude of bottom ripples on the F-P resonance mechanism in the linear wave theory framework, by testing a wide range of ripple amplitude with a highly accurate numerical model. Three systems are considered, called A, B and C. In system A, the linear water wave problem is solved with the exact BBC applied on the real bottom profile, while in system B we consider the linear water wave problem with the first-order approximation of the BBC applied at the mean level of bottom profile. Both systems A and B are implemented and numerically simulated with the linearized version of Whispers3D. System C starts from the same problem as system B, but it is solved analytically using additional assumptions and a multiple-scale expansion method. The leading order solution, which will be referred to as Asymptotic Linear Analytical Solution (ALAS), was presented recently by Couston et al. (2015).

The simulation results showed that, for finite amplitude bottom ripples, the F-P resonance does not manifest according to the resonance condition predicted by ALAS. However, for a slightly decreased incident wave-number, the resonance was recovered with good correspondence with ALAS in terms of maximum amplification of waves in the resonator, even for the largest ripple amplitude considered in our tests. This so-called wave-number downshift appears to play a non-trivial role in the formation of resonance because the resonance condition becomes increasingly strict as ripple amplitude increases. In particular, we demonstrate that the effect of finite amplitude of bottom ripples is related to the form of the dispersion relation of water waves, which is a nonlinear function of the local water depth.

Effect of finite amplitude of bottom corrugations on Fabry-Perot resonance of water waves

Jie Zhang and Michel Benoit*
Aix Marseille Univ, CNRS, Centrale Marseille, IRPHE (UMR 7342), Marseille, France

(Received 11 February 2019; published 15 May 2019)

Recently, the mechanism of Fabry-Perot (F-P) resonance in optics was extended to monochromatic water waves propagating in a domain with two patches of sinusoidal corrugations on an otherwise flat bottom. Assuming small-amplitude surface waves, an asymptotic linear analytical solution (ALAS) was derived by L. A. Couston *et al.* Phys. Rev. E **92**, 043015 (2015). When resonance conditions are met, the ALAS predicts large amplification of the incident waves in the resonator area between the two patches of corrugations. Based on the ALAS, the amplitude of these standing waves is expected to increase exponentially with the relative amplitude of bottom corrugations ($\delta = d/h$, where d is the corrugation amplitude and h the still water depth). In the present work, we examine the effects associated with the assumptions made in deriving the ALAS regarding the effect of a finite amplitude of bottom corrugation (i.e., finite value of δ), still in the linear wave framework. F-P resonance is studied by means of highly accurate numerical simulations, considering either the exact linear water wave problem (system A) or an approximate problem with a first-order expansion of the bottom boundary condition (system B). The numerical model is first validated on a Bragg resonance case, through comparisons with the ALAS, experimental measurements, and existing numerical simulations, showing its ability to represent well the so-called wave-number downshift of Bragg resonance (i.e., the slight decrease in the incident wave number where maximum resonance is reached in comparison with the value predicted by the ALAS). We then analyze how this downshift affects the F-P resonance, especially when the corrugations are of finite amplitude, i.e., δ varying from 0.05 to 0.4. The wave-number downshift appears to have a strong effect on the F-P resonance for $\delta > 0.1$: very low wave amplification manifests for the wave number predicted by the ALAS. However, when the incident wave number is slightly decreased (by an amount increasing with δ) the F-P resonance case can be recovered, and the maximum amplification values are found to be close to the predictions from the ALAS (e.g., up to a factor of about 27 for $\delta = 0.4$). The variations of the reflection coefficient and enhancement factor obtained from systems A and B as a function of the incident wave number are discussed and compared to ALAS predictions. In particular, it is found that the resonance peak is extremely narrow when $\delta = 0.2$ and 0.4.

DOI: 10.1103/PhysRevE.99.053109

I. INTRODUCTION AND OBJECTIVES

In optics, a Fabry-Perot (F-P) etalon is an interference device first described by two young French physicists at the University of Marseille (France) at the end of the 19th century [1]. Typically it consists of two parallel highly reflecting mirrors with a small interval; the incident light waves passing through will form interference fringes after a series of reflections. In the past century, the F-P resonance mechanism has been comprehensively studied and applied to different fields of physics [2,3].

In analogy to light waves, water waves can constructively interfere when propagating over a region with a constant water depth superimposed on two sets of small periodic bottom corrugations or bars. Recently, Couston *et al.* [4] studied water wave F-P resonance within the framework of linear potential wave theory. Based on the asymptotic linear theory, they found that significant amplification of incident regular waves with particular wave numbers can be expected over the flat-bottom area between two sets of bottom corrugations.

The mechanism behind this resonance is the well-known Bragg scattering (or resonance), which has been extensively studied. By applying linear perturbation method, Davies [5] and Davies and Heathershaw [6] have shown theoretically that simple harmonic waves will be scattered due to wave-bottom interactions when passing through a finite number of sinusoidal rigid bars on an otherwise flat bottom. Experimental demonstrations confirming the effects of sandbars [6,7] were available soon after the theory was introduced. When the incident wavelength is twice that of the sandbars, Bragg resonance takes place. However, Davies and Heathershaw's regular perturbation method [6] fails when it is close to the resonance condition (i.e., the reflection coefficient becomes unbounded for resonance condition for a large number of bars). By considering two wave components with opposite propagation directions on the surface and introducing a cut-off frequency, Mei [8] developed an analytical approximate theory via multiple-scale perturbation method. This theory is able to predict the resonance. The leading order of Mei's theory agrees reasonably well with Heathershaw's experiments with the same linearization assumptions adopted by Davies [7]. Yu and Mei [9] also pointed out the unreliability for shore protection using Bragg resonance: it may result in suppression of waves after the sandbars, but amplification is also possible when considering reflection from the shoreline.

*benoit@irphe.univ-mrs.fr

Higher-order Bragg resonance can be defined by the number of components participating in the interactions. The aforementioned case is denoted class I Bragg resonance, which is second-order triad interactions (one bottom and two surface waves). In class II Bragg resonance, doubly sinusoidal corrugations on the bottom and two surface wave components interact [10,11]. Note that the F-P resonance, which includes two corrugation modes on the bottom, involves only second-order interactions. Such resonances are classified as I_2 Bragg resonance (see [12]). In class III, monochromatic sinusoidal corrugations and three surface wave components are included [13]. The aforementioned high-order Bragg resonances are third-order quartet wave-bottom interactions. Higher-order nonlinearities of incident waves and bottom corrugations can be included by keeping more terms in the perturbation methods [10,14]. However, the increase in accuracy comes at the expense of simplicity of formulations.

With a family of special shapes of bottom corrugations, the constraints on the bottom steepness and/or amplitude can be released by using Floquet theory for linear wave motion [15–17]. Recently an experimental demonstration of this theory was realized [18]. However, in this case the bottom corrugations are no longer sinusoidal perturbations.

Alternatively, the nonlinearities associated with surface waves and bottom corrugations were also studied by using different numerical models solving the water wave problem to different target orders. For instance, using a boundary integral equation method, Dalrymple and Kirby [19] placed the bottom elements directly on the bars, keeping an exact bottom elevation in a linear wave framework. Kirby [20] extended the mild-slope equation of Berkhoff to the Bragg resonance case considering not only the bars on the seabed, but also the variable mean elevation of the bottom. Porter [21] extended the equation to the three-dimensional (3D) case. The high-order spectral (HOS) method developed by Dommermuth and Yue [22] was used to study the high-order Bragg resonance with the fourth-order (for both bottom and free surface) model [13].

The present work mainly focuses on a better understanding of the effects associated with the modeling of the bottom boundary condition on Bragg and F-P resonances within the linear wave theory framework, by taking advantage of an accurate and efficient numerical model. The linearized water wave problem as well as the assumptions associated with Bragg resonance, the F-P resonance condition, and the asymptotic linear analytical solution (ALAS) of the problem are recalled in Sec. II. The numerical model is introduced and validated against Bragg resonance experiments in Sec. III. Then the model is applied to study the F-P resonance in Sec. IV, considering various relative corrugation amplitudes, with most attention paid to the influence of the bottom boundary condition. The main conclusions and outlook for future work are summarized in Sec. V.

II. PROBLEM DESCRIPTION AND MATHEMATICAL MODELING

A. Bathymetry for Bragg and Fabry-Perot cases

Considering long-crested plane waves, the problem is formulated in a two-dimensional (2D) Cartesian coordinate system (x, z), with the x axis coinciding with the still water level and the z axis pointing upwards. The elevation of the impermeable bottom is expressed as

$$z = -\tilde{h}(x) = -h + \zeta(x), \tag{1}$$

where $h > 0$ is a constant water depth and $\zeta(x)$ describes the elevation of the bottom corrugations. These corrugations are assumed to have a sinusoidal shape over one zone (Bragg case) or two distinct zones (Fabry-Perot case) of finite length. In the latter case, these zones are labeled 1 and 2, respectively, and we assume that the bars have the same wavelength L_b (and wave number $k_b = 2\pi/L_b$) and the same amplitude d. Each patch is composed of an integer number of bars N_j, thus covering a distance $L_j = N_j L_b$ between the abscissa x_j^s and $x_j^e = x_j^s + N_j L_b$. The perturbation of the bottom elevation for each patch j ($j = 1, 2$) thus reads

$$\zeta(x) = d \sin\left[k_b\left(x - x_j^s\right) - \theta_j\right], \quad x \in \left[x_j^s, x_j^e\right], \tag{2}$$

where θ_j is the phase of the corrugation patch j, chosen here to be either 0 or π in order to have a continuous bottom profile. The distance between the two patches, denoted L_r, is called the *resonator length*. Without loss of generality, we set $x_1^s = 0$ for the first patch (the second one then starting at $x_2^s = N_1 L_b + L_r$). A representation of the F-P resonator configuration is shown in Fig. 1.

We consider monochromatic incident waves coming from $x = -\infty$ with amplitude a and wave number k in the region of uniform water depth h, associated with a wave period T and an angular frequency $\omega = 2\pi/T$. The nondimensional parameter $\mu = kh$ is used as a measure of the relative water depth (or dispersive effects), and ka measures the steepness of water waves (or nonlinear effects). The slope of the bottom corrugations is characterized by $k_b d$, and the nondimensional corrugation amplitude is defined as $\delta = d/h$.

B. Linear mathematical modeling approaches

1. Exact linear model: System A

The fluid is assumed inviscid and homogeneous with a constant density. The flow is assumed irrotational, so that a velocity potential ϕ can be introduced. The velocity field is then $\vec{u} = \nabla\phi$. The surface tension is neglected and the atmospheric pressure at the free surface is assumed uniform and constant in time (set here to 0 without loss of generality).

We further assume that surface waves are of small amplitude compared to both the wavelength and the mean water depth, i.e., $ka \ll 1$ and $a/h \ll 1$. In this case, the free surface boundary conditions can be linearized and applied at the still water level $z = 0$. The governing equations for ϕ thus simplify to

$$\phi_{xx} + \phi_{zz} = 0, \quad -\tilde{h}(x) \leqslant z \leqslant 0, \tag{3a}$$

$$-\omega^2\phi + g\phi_z = 0, \quad z = 0, \tag{3b}$$

$$-\zeta_x\phi_x + \phi_z = 0, \quad z = -\tilde{h}(x), \tag{3c}$$

where g is the acceleration due to gravity, and subscripts denote partial derivatives (e.g., $\phi_x = \frac{\partial\phi}{\partial x}$). The free surface elevation η is obtained via $\eta(x,t) = -\phi_t(x, z = 0, t)/g$. In this system, no assumption is made regarding the amplitude of

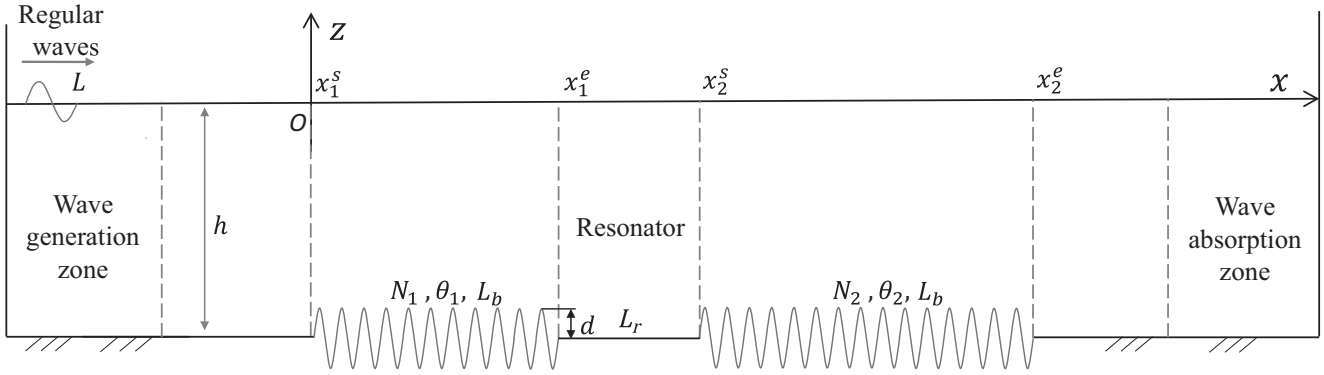

FIG. 1. Sketch of the problem setup for F-P resonance.

the bars, implying that the bottom boundary condition (BBC), Eq. (3c), is applicable for arbitrary δ and hereafter referred to as the *exact BBC*. System (3) is called "system A" in the following.

2. Linear model with a small bar amplitude: System B

As marine sandbars are usually of small amplitude with a stabilized pattern provided the sea state is steady, it is often reasonable to assume that the nonlinearity of the bars is small, i.e., $\delta \ll 1$. With this assumption, the exact BBC, Eq. (3c), can be approximated, using a truncated Taylor expansion of the potential around the mean elevation $z = -h$ and omitting second- and higher-order terms in δ, as

$$-(\zeta\phi_x)_x + \phi_z = 0, \quad z = -h. \tag{4}$$

Hereafter, Eq. (4), now applied at the uniform elevation $z = -h$, is referred to as the *approximate BBC*, and the system composed of Eqs. (3a), (3b), and (4) is called "system B." Note that with this approximate system, the Laplace equation, Eq. (3a), has to be solved over a rectangular domain of constant height h.

3. Asymptotic linear model: System C

To obtain an analytical solution of system B, Mei [8] adopted a multiple-scale expansion method and solved the leading-order problem. By introducing fast variables (x, t) and slow variables $(x' = \varepsilon x,\ t' = \varepsilon t)$, assuming that ε is a small parameter, the multiple-scale expansion of the velocity potential $\phi(x, x', z, t, t')$ reads

$$\phi = \varepsilon\phi^{(1)} + \varepsilon^2\phi^{(2)} + O(\varepsilon^3), \tag{5}$$

where the terms at order $O(\varepsilon^3)$ and higher have been neglected. Assuming that the second-order term $\phi^{(2)}$ is small compared to $\phi^{(1)}$, the first-order potential $\phi^{(1)}$ can be expressed over the jth patch as

$$\phi^{(1)} = f(z)[\mathcal{A}_j(x', t')e^{-ikx} + \mathcal{B}_j(x', t')e^{ikx}]e^{i\omega t} + \text{c.c.}, \tag{6}$$

where c.c. denotes the complex conjugate. $\mathcal{A}_j$ and $\mathcal{B}_j$ are the slowly varying complex amplitudes of the incident and reflected waves over patch j, and

$$f(z) = -\frac{ig}{2\omega}\frac{\cosh k(h+z)}{\cosh kh} \tag{7}$$

gives the vertical dependence of the potential for the (assumed uniform) water depth h.

Applying Eqs. (5)–(7) to system B and enforcing the solvability and compatibility conditions (see [12] for details) for $\phi^{(2)}$, the following system is obtained, governing the evolution of amplitudes $\mathcal{A}_j$ and $\mathcal{B}_j$ over patch j (hereafter referred to as "system C"),

$$\frac{\partial\mathcal{A}_j}{\partial t'} + C_{gB}\frac{\partial\mathcal{A}_j}{\partial x'} = -\Omega_c e^{i\theta_j}\mathcal{B}_j, \tag{8a}$$

$$\frac{\partial\mathcal{B}_j}{\partial t'} - C_{gB}\frac{\partial\mathcal{B}_j}{\partial x'} = \Omega_c e^{-i\theta_j}\mathcal{A}_j, \tag{8b}$$

where the angular frequency $\omega_B = \omega(k_B)$ and the group celerity $C_{gB} = C_g(k_B)$ of incident waves at resonant Bragg wave number $k_B = k_b/2$ (with corresponding wavelength $L_B = 2L_b$) are computed from linear wave theory for the water depth h (note that subscript B is used for the "Bragg resonant" case as predicted by the ALAS). Ω_c denotes the so-called "cutoff frequency"

$$\Omega_c = \frac{\omega_B}{4}\frac{k_b d}{\sinh k_b d}. \tag{9}$$

The wave number k and frequency ω of incident waves are assumed to vary in the vicinity of the Bragg resonance values, i.e., $k = k_B + \kappa$ with $\kappa \ll k_B$, and $\omega = \omega_B + \Omega$ with $\Omega = \kappa C_{gB} \ll \omega_B$.

The time variation of complex amplitude can be written explicitly, e.g., $\mathcal{A}_j(x', t') = A_j(x')e^{i\Omega t'}$ and $\partial\mathcal{A}_j/\partial t' = i\Omega\mathcal{A}_j$ for the periodic steady state. Over the flat-bottom sections, the right-hand sides of Eqs. (8a) and (8b) are 0, which means that the incident and reflected waves are no longer coupled and that they propagate at the speed of their own group velocity.

One interesting feature of system C is that it can be solved analytically: its solution (i.e., the ALAS) is the envelopes of the amplitudes of incident and reflected waves, as functions of the slow variable x'. The ALAS provides reasonable results near the resonance condition when applied to the experiments by Heathershaw [7] on Bragg resonance.

This ALAS was recently extended to the case of two patches by Couston *et al.* [4] to study the F-P resonance. The main results are the global reflection and transmission coefficients (for the set of two patches), which are recalled

below:

$$R^{\mathrm{FP}}_{\mathrm{ALAS}}\big|_{x_1^s} = \sqrt{\frac{\left(R_1^B\right)^2 + \left(R_2^B\right)^2 - 2R_1^B R_2^B \cos\gamma}{1 + \left(R_1^B R_2^B\right)^2 - 2R_1^B R_2^B \cos\gamma}}, \quad (10a)$$

$$T^{\mathrm{FP}}_{\mathrm{ALAS}}\big|_{x_2^e} = \sqrt{\frac{\left[1 - \left(R_1^B\right)^2\right]\left[1 - \left(R_2^B\right)^2\right]}{1 + \left(R_1^B R_2^B\right)^2 - 2R_1^B R_2^B \cos\gamma}}, \quad (10b)$$

where $\mathcal{R}_j^B = \mathcal{B}_j(x_j^s)/\mathcal{A}_j(x_j^s) = R_j^B \exp(i\alpha_j^B)$ and $\mathcal{T}_j^B = \mathcal{A}_j(x_j^e)/\mathcal{A}_j(x_j^s) = T_j^B \exp(i\beta_j^B)$ are the (complex) reflection and transmission coefficients for a single patch (Bragg) case, they are functions of Ω/Ω_c (see [4] for more details), evaluated at the beginning x_j^s and the end x_j^e of the jth patch, respectively, and

$$\gamma = \pi - 2\theta_1 + 2kL_r - \alpha_1^B - \alpha_2^B. \quad (11)$$

In addition to Bragg resonance condition (i.e., $k = k_B$), the wave energy will be trapped within the resonator when γ in Eq. (11) is an integer multiple of 2π, which gives a condition on the possible values of the resonator length when $k = k_B$:

$$k_b L_r^{(m)} = (2m+1)\pi + \theta_1 + \theta_2, \quad \text{with} \quad m \in \mathbb{N}. \quad (12)$$

This is denoted the F-P resonance condition, under which the standing waves with the highest achievable amplitude are expected between the two patches. The nondimensional amplitude of the standing waves within the resonator is defined as the enhancement factor E^{FP} in [4]

$$E^{\mathrm{FP}}_{\mathrm{ALAS}} = \frac{\mathcal{A}_1(x_1^e) + \mathcal{B}_1(x_1^e)}{\mathcal{A}_1(x_1^s)} = \left(1 + R_2^B\right)\frac{T^{\mathrm{FP}}_{\mathrm{ALAS}}}{T_2^B}. \quad (13)$$

The aforementioned results indicate that large amplification of the incident waves could take place in the resonator area, with enhancement factors greater than 2 or even larger depending on the incident wave conditions and bottom characteristics. For instance, in the case simulated in [4], the following setup is chosen: $N_1 = 11$, $N_2 = 15$, $\theta_1 = \theta_2 = 0$, $k_b h = 1.64$, $k_b d = 0.164$ (i.e., $\delta = 0.1$), and $k_b L_r = 11\pi$ [i.e., $m = 5$ in the F-P resonance condition, Eq. (12)].

Considering each patch individually, with the Bragg condition satisfied, the reflection and transmission coefficients are $R_1^B \approx 0.597$ and $T_1^B \approx 0.803$ for the first patch and $R_2^B \approx 0.734$ and $T_2^B \approx 0.679$ for the second patch. Relatively strong reflection of incident waves is expected, based on the principle of energy conservation, and waves passing through a single patch are of smaller amplitude. In the F-P case with precisely chosen resonator length $k_b L_r = 11\pi$, the overall reflection and transmission coefficients are $R^{\mathrm{FP}}_{\mathrm{ALAS}} \approx 0.245$ and $T^{\mathrm{FP}}_{\mathrm{ALAS}} \approx 0.970$. The standing waves in the resonator are amplified by a factor of $E^{\mathrm{FP}}_{\mathrm{ALAS}} \approx 2.476$.

In Fig. 2, we show the relationship between $E^{\mathrm{FP}}_{\mathrm{ALAS}}$ and δ (keeping $N_1 = 11$, $N_2 = 15$, $\theta_1 = \theta_2 = 0$, $k_b h = 1.64$, and $k_b L_r = 11\pi$ fixed). It can be observed that within the linear framework, $E^{\mathrm{FP}}_{\mathrm{ALAS}}$ increases exponentially as the amplitude of bars increases. As δ becomes larger, one can anticipate that the results from the ALAS will become unrealistic, mainly for two reasons: on one hand, the standing waves will be of a high amplitude so that nonlinear effects due to the finite wave amplitude will be significant; on the other hand, these waves might become too steep to preserve their shape and wave breaking should occur. Regarding the ALAS, the assumption on the smallness of the bottom slope is violated, and so is the assumption of linearity of the water waves over the resonator area.

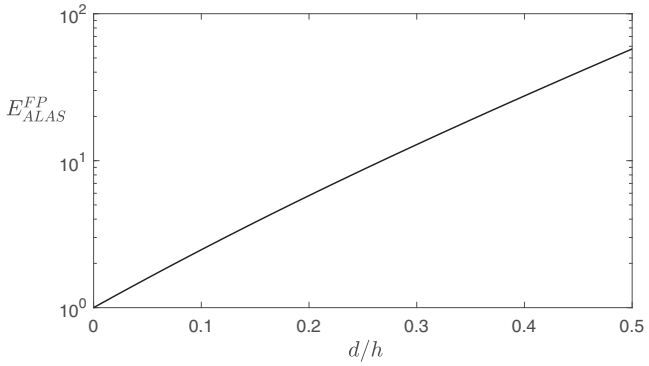

FIG. 2. Enhancement factor $E^{\mathrm{FP}}_{\mathrm{ALAS}}$ as a function of the nondimensional corrugation amplitude $\delta = d/h$. The water depth, setup of two patches, and length of the resonator are the same as those used in [4].

III. NUMERICAL MODELING AND VALIDATION IN THE BRAGG RESONANCE CASE

A. Description of the numerical model

The numerical simulations of systems A and B are performed with a highly accurate code, called WHISPERS-3D. This code is developed to solve the fully nonlinear potential wave problem with variable bottom conditions, in the form of two coupled nonlinear equations, corresponding to the two nonlinear free surface boundary conditions (FSBCs). In dimensional form for the case of a single horizontal dimension [23], they are expressed as

$$\eta_t = -\eta_x \tilde{\Phi}_x + \tilde{w}[1 + (\eta_x)^2], \quad (14a)$$

$$\tilde{\Phi}_t = -g\eta - \tfrac{1}{2}(\tilde{\Phi}_x)^2 + \tfrac{1}{2}\tilde{w}^2[1 + (\eta_x)^2], \quad (14b)$$

where $\tilde{\Phi}(x,t) \equiv \Phi(x, z = \eta(x,t), t)$ is the free surface velocity potential and $\tilde{w}(x,t) \equiv \Phi_z(x, z = \eta(x,t), t)$ is the vertical velocity at the free surface. Note that these equations involve only free surface variables, though a 2D vertical (x,z) situation is modeled.

In order to march Eqs. (14) in time, the vertical velocity $\tilde{w}(x,t)$ has to be determined as a function of $[\eta(x,t), \tilde{\Phi}(x,t)]$, corresponding to a so-called Dirichlet-to-Neumann problem. The modeling approach used is presented in previous works [24,25] and summarized hereafter. Following Tian and Sato [26], a spectral approach is used in the vertical to approximate the velocity potential. Using the set of orthogonal Chebyshev polynomials of the first kind, denoted $T_n(s)$, $n = 0, 1, \ldots, N_T$, with $s \in [-1, 1]$, as an expansion basis, the potential is approximated at any given time t (omitted for

brevity hereafter) as

$$\Phi(x,z)=\varphi(x,s)\approx\sum_{n=0}^{N_T}a_n(x)T_n(s), \tag{15}$$

where $s(x,z,t)$ is the scaled vertical coordinate allowing us to map the water column $z\in[-\tilde{h}(x),\eta(x,t)]$ into the fixed range $s\in[-1,1]$, and the a_n coefficients ($n=0,1,\ldots,N_T$) depend upon the local abscissa x (and time t).

The main steps involved in solving the Dirichlet-to-Neumann problem and integrating Eqs. (14) in time are summarized as follows: (i) first, the system of governing equations composed of the Laplace equation, a Dirichlet FSBC on the potential, and the BBC is expressed in the (x,s) coordinate system; (ii) then the approximation given in Eq. (15) is inserted into these equations; (iii) the so-called Chebyshev-tau method, a variant of the Galerkin method, is used to project the Laplace equation onto the T_n polynomials for $n=0,1,\ldots,N_T-2$, eliminating the s coordinate and giving a set of N_T-1 equations on the a_n coefficients at each location x; (iv) two additional equations are obtained by considering the Dirichlet FSBC and the BBC so that a system of N_T+1 linear equations with N_T+1 unknowns ($a_n, n=0,\ldots,N_T$) at each abscissa is formed; and (v) once this linear system is solved for the a_n coefficients, the vertical velocity at the free surface is obtained as

$$\tilde{w}(x,t)=\frac{2}{\tilde{h}(x)+\eta(x,t)}\sum_{n=1}^{N_T}a_n(x,t)n^2, \tag{16}$$

allowing Eqs. (14) to be integrated in time.

In WHISPERS-3D, horizontal derivatives are approximated using fourth-order finite-difference formulas using stencils of five nodes on a regular grid and an explicit third-order Runge-Rutta scheme (SSP-RK3) is used for time marching. The maximum order N_T of polynomials in Eq. (15) determines the accuracy of the model. With this representation of the potential, the model exhibits a geometric convergence as a function of N_T, so that a high accuracy of the vertical structure of the flow can be obtained with a limited number of terms, usually in the range $N_T\in[5,10]$. This property was carefully verified for a number of cases with regular or irregular waves over flat or variable bottom conditions [24,25].

The linearized version of the numerical model, solving the system of Eqs. (3), was extensively studied in [27], for both flat and variable bottom profiles. The dispersion relation of the linear model was derived analytically [27],

$$\frac{C_{N_T}^2}{gh}=\frac{1+\sum_{p=1}^{N_T-2}\alpha_p\mu^{2p}}{1+\sum_{p=1}^{N_T-1}\beta_p\mu^{2p}}, \tag{17}$$

where C_{N_T} denotes the approximation of the phase celerity of the waves given by the model at order N_T. The computational method for obtaining the analytical expressions of α_p and β_p coefficients can be found in [27].

In order to illustrate the resolving capability of the model for the water depth conditions considered here ($\mu=kh\approx k_Bh=0.82$), the evolution of the relative error $|C_{N_T}-C_{\text{Airy}}|/C_{\text{Airy}}$ on the phase celerity of the linearized version of the model with respect to the exact Airy phase celerity under flat-bottom conditions [given by $C_{\text{Airy}}^2/(gh)=\tanh(\mu)/\mu$] is plotted as a function of N_T in Fig. 3. It is shown that this error decreases exponentially with increasing N_T. For this relative water depth $\mu=0.82$, the difference between C_{N_T} and C_{Airy} drops below the machine precision as N_T exceeds 12. In the simulations performed hereafter, a value of $N_T=7$ will be systematically used. With this value the relative error on phase celerity is about 2×10^{-9}.

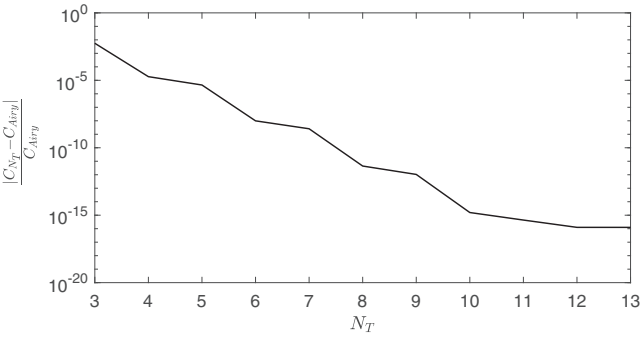

FIG. 3. Relative error on the phase celerity of the linear version of the numerical model (with respect to the exact Airy celerity) for the relative water depth $\mu=0.82$ as a function of the maximum order of polynomials N_T.

We point out that Liu and Yue [13] simulated Bragg resonance cases by solving Eqs. (14) with the (nonlinear) HOS method. In the HOS method [13,22], assuming periodic boundary conditions in the horizontal direction, the velocity potential is represented by a large number of free wave modes whose amplitudes are determined via a pseudospectral method. The problem is solved by combining a perturbation expansion method for the potential and Taylor expansions of the nonlinear FSBCs and the BBC around their mean levels, giving an approximate solution at a given target order in wave steepness. The numerical model adopted here does not assume spatial periodicity of the spatial domain, the BBC is applied at the exact position of the bottom (in system A), and the FSBCs are applied at the exact position of the free surface (in the nonlinear version of the model). The vertical variation of the potential at each horizontal node is instead represented by a series of Chebyshev polynomials given by Eq. (15). By increasing the order N_T of this vertical approximation (and concurrently decreasing the spatial grid size), extremely accurate representations of the potential can be reached over the fluid domain, for both the linearized and the fully nonlinear versions of the code.

B. Simulation results of the Bragg resonance case

The experiments conducted by Davies and Heathershaw [6] on Bragg resonance have been intensively studied since their publication, e.g., in [8,13,19,20,28]. We start by simulating one case of these experiments in order to validate the linearized version of WHISPERS-3D.

In the experiments in [6], patches with $N=2$, 4, and 10 bars were tested. We select the case with the longest patch ($N=10$) because in this case stronger wave-bottom interaction is expected, resulting in significant reflection of incident waves. Besides, this case clearly showed a wave-number downshift effect and is thus considered most challenging for

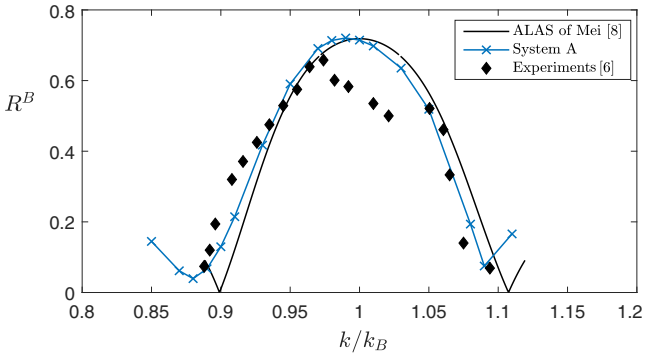

FIG. 4. The simulation results (system A) of Davies and Heathershaw's experiments [6] with 10 bars are compared with the experimental measurements. The ALAS prediction based on Mei's theory [8] is also given as a reference.

the numerical model. In the experiments, the bottom corrugations are fixed at $d = 0.05$ m and $L_b = 1$ m. The relative corrugation amplitude $\delta = 0.16$ is achieved by adjusting the water depth h. The wavelength of incident waves is determined from the Bragg resonance condition $L = L_B$. Regarding the numerical model, sinusoidal waves are generated and absorbed by using relaxation zones with $4L_B$ in length. Before and after the patch of corrugations, two zones with constant water depth h and length $3L_B$ are used. The domain is meshed with a regular grid defined by $\Delta x = L_B/64$. The time step is chosen as $\Delta t = T/64$, giving a Courant-Friedrichs-Lewy number CFL $= 1$ (CFL $= C\Delta t/\Delta x$, with phase velocity $C = L/T$). It should be noted that in the numerical simulations, instead of using the dispersion relationship of Airy wave theory, the wave period T is determined by the analytical dispersion relationship, Eq. (17), of WHISPERS-3D at order N_T.

A series of runs is performed by varying the wave number of incident waves around the value k_B corresponding to expected resonance based on the ALAS. Once a periodic state is reached over the domain, the reflected and transmitted waves are separated by Goda and Suzuki's method [29], and the corresponding reflection coefficient from the ALAS R^B is evaluated following Eq. (6a) in [4]. The reflection coefficients are compared in Fig. 4, from which it can be concluded that the numerical results show good agreement with the experimental results as well as theoretical predictions for the primary resonance tongue.

However, it is also clear that the maximum reflection coefficient is not obtained for the Bragg condition $k_B = k_b/2$, as is predicted by the ALAS, but for a slightly smaller wave number. This effect corresponds to the so-called wave-number downshift (or, equivalently, frequency downshift). Liu and Yue [13] explained this slight detuning by showing that the spatially averaged local wave number over the patch is always larger than the incident wave number, while it was considered uniform over the whole domain during the derivation of the ALAS. In other words, the "effective" wave number over the patch (whose mean water depth is h) is greater than the wave number of a uniform water depth h (this is further discussed in Sec. IV C below). A slightly smaller incident wave number is thus required to compensate this increase due to the presence of bars; then the Bragg condition is met again.

We also note that Liu and Yue [13] obtained results very similar to those for system A in Fig. 4 using the HOS method (see Fig. 6 in [13]), although the nonlinearity of water waves is excluded in the present model. This implies that the wave-number downshift in this configuration is mainly a BBC effect, and not a nonlinear effect. Overall, the good agreement of the present results of system A with the experimental, the ALAS, and the numerical results of [13] validates the current numerical model for the Bragg resonance case.

IV. SIMULATION AND ANALYSIS OF FABRY-PEROT RESONANCE

A. Description of the numerical setup

Now consider the F-P resonance; we aim at investigating whether large enhancement factors (see Fig. 2) for finite-amplitude bars can be realized within the exact linear framework (system A). In other words, we focus on the effects associated with the assumption of smallness of the corrugation amplitude. To this end, the assumption of small-amplitude surface waves is preserved, and the height of standing waves in the resonator should in principle remain small for the linear approach to apply.

Regarding the numerical setup, we again follow the work in [4] as introduced in Sec. II except for the amplitude of corrugations. Here, four kinds of tests with different corrugation amplitudes are studied: $\delta = 0.05$, 0.1, 0.2, and 0.4. Note that, for this bottom configuration, ALAS predicts $E^{\mathrm{FP}}_{\mathrm{ALAS}} \approx 27.579$ when $\delta = 0.4$. With such large amplification, even small to moderate incident waves could lead to very large standing waves, with possible dramatic effects on the local structures. For the numerical settings, the generation and absorption zones are $4L_B$ in length. The domain is uniformly meshed with $\Delta x = L_B/128$. The time step is chosen as $\Delta t = T/256$, giving CFL $= 0.5$. The duration of the simulations depends on the corrugation amplitude δ. Indeed, for F-P resonance, runs with higher bar amplitudes take more time to reach a time-periodic steady state.

B. Simulations with ALAS-tuned incident waves for small to moderate corrugation amplitudes

For the considered setup, the free surface motion consists of left- and right-propagating components with the same frequency, i.e., reflected and transmitted waves. The reflected waves are the comprehensive results of all the bars downstream at any given x. This suggests that no reflected wave is expected after the second patch. Standing waves are expected over the flat-bottom zones before the first patch and within the resonator. Over the patches, not only the phase of the free surface envelope but also its amplitude is slowly modulated because of the change in the total number of downstream bars. By excluding the fast oscillations, the ALAS describes the envelope of the free surface elevation and indicates the slow space modulation of the wave amplitude. Its computation formula can be found in the Appendix in [4].

In this section, we present results of simulations of system A and system B (done with the linearized version of WHISPERS-3D) using an incident wave number as predicted by

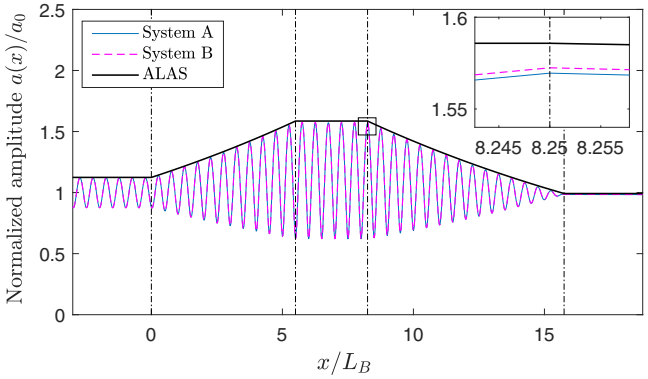

FIG. 5. Computed envelope of the free surface elevation at the end of the simulations of systems A and B ($t = 100T$) for the case $\delta = 0.05$ with the wave number $k = k_B$, compared to the envelope from the ALAS.

the ALAS, namely, $k = k_B$, for different cases with increasing values of δ.

For the case with small bottom corrugation amplitude $\delta = 0.05$, Fig. 5 shows that the simulated results of systems A and B are almost superimposed. For this case, the reflection and enhancement coefficients predicted by the ALAS are both small, namely, $R^{\mathrm{FP}}_{\mathrm{ALAS}} \approx 0.124$ and $E^{\mathrm{FP}}_{\mathrm{ALAS}} \approx 1.586$. Nice agreement with the ALAS is observed throughout the computational domain, and the time required to achieve a quasi–steady state is less than 100 incident wave periods. This case validates the applicability of the current numerical model to the F-P resonance case.

The simulation results with the higher corrugation amplitude $\delta = 0.1$ are shown in Fig. 6. The duration of simulation is now $200T$. For this case, the results of systems A and B are still too close to be distinguished on the global scale, which means that the assumption on the BBC adopted by Davies [5] and Mei [8] remains appropriate. However, simulation results deviate slightly from the ALAS results. The reflection coefficient from system A, $R^{\mathrm{FP}}_A \approx 0.329$ ($R^{\mathrm{FP}}_B \approx 0.336$ from system B), is larger than the $R^{\mathrm{FP}}_{\mathrm{ALAS}} \approx 0.245$ from the ALAS, and the enhancement factor from system A, $E^{\mathrm{FP}}_A \approx 2.385$ ($E^{\mathrm{FP}}_B \approx 2.397$), is smaller than the expected $E^{\mathrm{FP}}_{\mathrm{ALAS}} \approx 2.476$ from the ALAS.

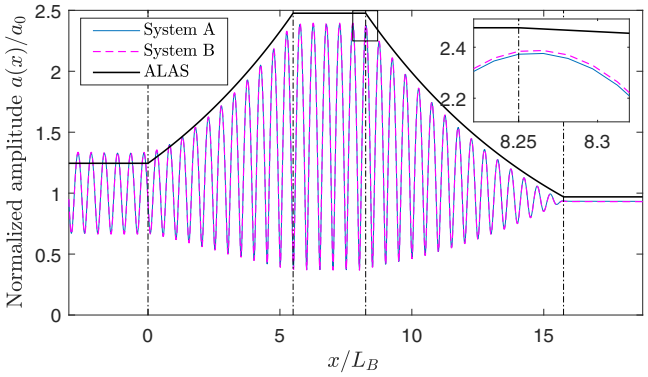

FIG. 6. Same as Fig. 5, for the case $\delta = 0.1$. The simulation duration is $t = 200T$.

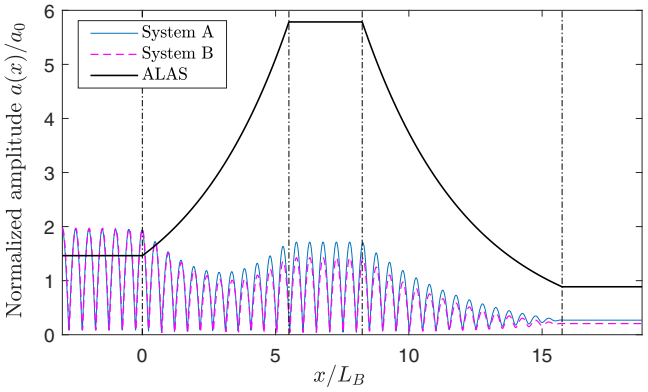

FIG. 7. Same as Fig. 5, for the case $\delta = 0.2$. The simulation duration is $t = 900T$.

The corrugation amplitude is then increased to $\delta = 0.2$. It is clearly shown in Fig. 7 that the results from systems A and B and from ALAS predictions are different. Before the first patch, simulations with systems A and B show that the incident waves are nearly fully reflected with a reflection coefficient $R^{\mathrm{FP}}_A \approx 0.956$ for system A, resulting in little energy being transferred through the second patch of corrugations. Within the resonator, the enhancement factor does not reach the predicted value by the ALAS, $E^{\mathrm{FP}}_{\mathrm{ALAS}} \approx 5.785$: only $E^{\mathrm{FP}}_A \approx 1.711$ is obtained with system A. Clearly, the F-P resonance does not manifest in this case with either system A or system B. In addition, it is also noteworthy that the results of systems A and B are no longer superimposed, implying that the assumption on the smallness of bottom corrugations is less acceptable for $\delta = 0.2$ or larger. Finally, we point out that this case is much more time-consuming compared to the cases with smaller corrugation amplitudes: no less than $900T$ is required to approach the steady state.

C. Simulations with slightly detuned incident waves for a finite corrugation amplitude

As the linearized version of WHISPERS-3D with the exact BBC has been proven valid for the Bragg and F-P resonances (at least for small-amplitude bars), it is interesting to investigate whether large enhancement factors could be achieved in the case where the bottom corrugations are of finite amplitude and to analyze why the F-P resonance could not be realized for $\delta = 0.2$ in the previous subsection. For this purpose, tests with finite corrugation amplitudes are performed here, namely, $\delta = 0.2$ and then 0.4.

1. Slightly detuned simulations with $\delta = 0.2$

The case $\delta = 0.2$ is repeated here, but now the wave number of incident waves is detuned by a small value, so that k/k_B varies in the range [0.92, 1.10]. The numerical parameters and settings for systems A and B remain unchanged. The effect of detuning the wave number k/k_B on the reflection coefficient R^{FP} is plotted in Fig. 8. The ALAS curve is symmetric with respect to the resonance condition $k/k_B = 1$, where a minimum value is reached. However, when departing from this value the reflection coefficient increases very rapidly, meaning

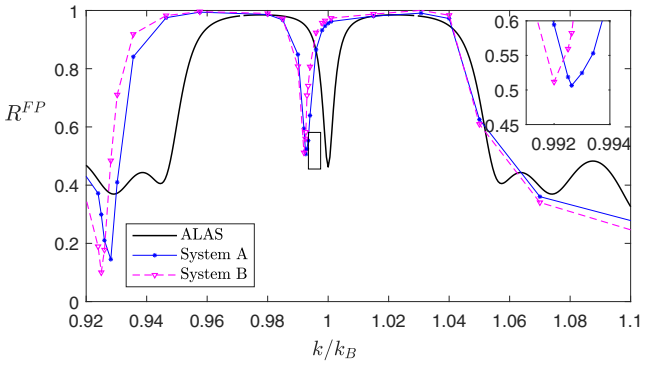

FIG. 8. Effect of the detuned wave number (normalized by k_B) on the reflection coefficient R^{FP} for systems A and B. The ALAS prediction based on Eq. (10a) is also superimposed.

that the F-P resonance is sensitive to the wave number (or, equivalently, the frequency) of incident waves, especially for finite-amplitude bottom corrugations. Regarding the results for systems A and B, there are clear shifts of the symmetry axis from $k/k_B = 1$ toward smaller values. For this value of $\delta = 0.2$, the difference between the exact BBC (system A) and the approximate BBC (system B) remains limited.

For the same set of simulations, the enhancement factor in the resonator is plotted in Fig. 9. Again the detuning effect is clearly visible, with a downshift of the peak of maximum E_A^{FP} towards a lower value, namely, $k \approx 0.992\,63 k_B$, for system A.

It is verified here that E_A^{FP} is quite low for $k = k_B$, as shown in Fig. 7. This can be explained by the sensitivity of the F-P resonance to the incident wave number and by the wave-number downshift for finite corrugation amplitude. Following Liu and Yue [13] for Bragg resonance, we can evaluate a "mean" wave number $\bar{k}_j$ over patch j by a numerical averaging method,

$$\bar{k}_j = \frac{1}{x_j^e - x_j^s} \int_{x_j^s}^{x_j^e} k_j(x) dx, \tag{18}$$

where $k_j(x)$ denotes the local wave number over patch j as computed from the dispersion relation for the actual water depth $\tilde{h}(x) = h - \zeta(x)$. The ratio $\mathcal{D}_j = \bar{k}_j/k(h)$ is a measure

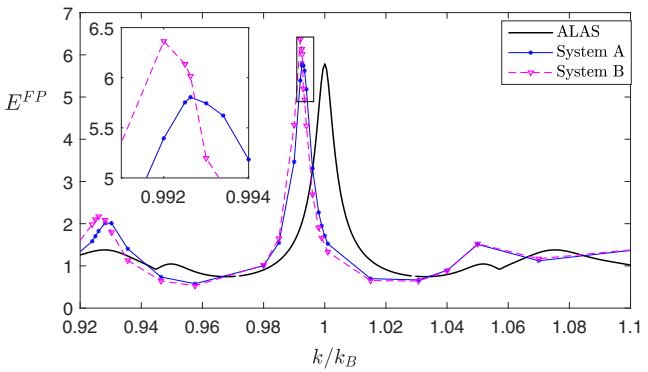

FIG. 9. Effect of the detuned wave number (normalized by k_B) on the enhancement factor E^{FP} for systems A and B. The ALAS prediction based on Eq. (10a) is also superimposed.

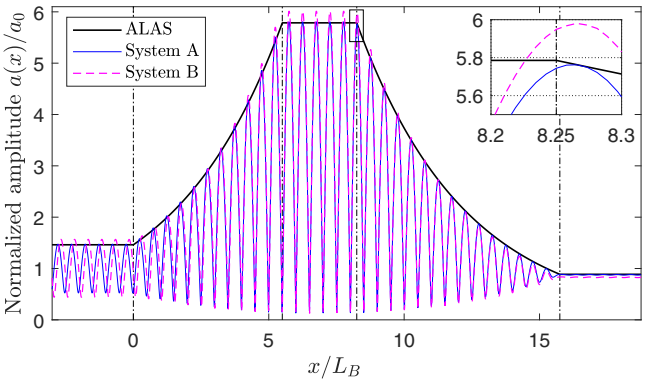

FIG. 10. Computed envelope of the free surface elevation at the end of the simulations of systems A and B ($t = 900T$) for the case $\delta = 0.2$ with the wave number slightly smaller ($k' = 0.992\,63 k_B$) than the F-P condition, compared to the ALAS envelope (calculated for $k = k_B$).

of the effect of the undulated bottom. For the present case (same corrugation amplitude for the two patches), we obtain $\mathcal{D}_1 = \mathcal{D}_2 \approx 1/0.9933$. Based on this result, it is anticipated that the nondimensional incident wave number should be $k/k_B = \mathcal{D}_1^{-1} = 0.9933$ to recover F-P resonance, which indeed is located very close to the shifted resonance condition in Figs. 8 and 9. As shown in these figures, it is speculated that the "real" resonance condition for the incident wave number in the present case falls between 0.992 63 and 0.993.

In Fig. 10, the simulation results for systems A and B using the slightly detuned incident wave number $k/k_B = 0.992\,63$ are plotted, together with the ALAS envelope curve (for $k = k_B$). Good agreement is achieved between the simulated results (in particular, with system A) and the ALAS prediction regarding the maximum wave amplitude over the whole domain. It should be noted that the differences in the results for system A vs system B are due to the difference in the degree of downshift associated with each of the two systems (clearly shown in the inset in Fig. 9). Thus, the wave-number downshift is mainly a leading-order phenomenon but is also influenced by the order of approximation of the BBC.

2. *Slightly detuned simulations with* $\delta = 0.4$

To demonstrate the significance of the wave-number downshift and to show that the F-P resonance can be realized even for high bottom corrugation amplitudes, an additional test for $\delta = 0.4$ is performed and analyzed, with system A only. As shown in Fig. 2, the enhancement factor predicted by the ALAS for this case should be $E_{\mathrm{ALAS}}^{\mathrm{FP}} \approx 27.579$, associated with the reflection coefficient $R_{\mathrm{ALAS}}^{\mathrm{FP}} \approx 0.762$. The assumption on the smallness of bottom corrugations is obviously no longer fulfilled, and it is thus interesting to compare the results for system A (with the exact BBC) and for the ALAS.

Considering that the "exact" condition for F-P resonance is unknown, Eq. (18) is used to provide the first guess of the shifted F-P resonance condition, leading to $k = 0.972 k_B$. Then the proper incident wave number associated with the largest enhancement factor E_A^{FP} is found by exploring a range of wave numbers in the vicinity of this value. The result

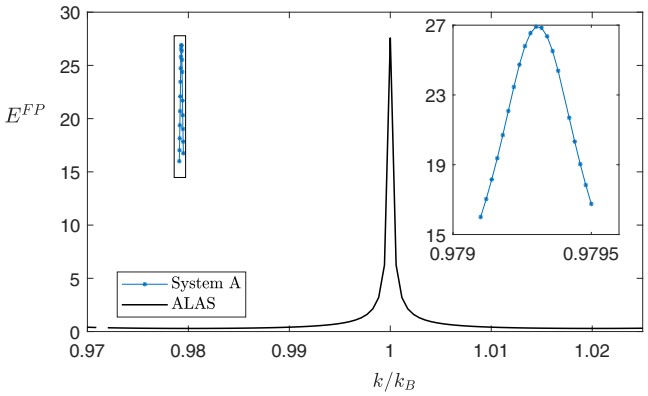

FIG. 11. Effect of the detuned wave number (normalized by k_B) on the enhancement factor E^{FP} for system A. The ALAS prediction based on Eq. (10a) is also superimposed.

regarding the enhancement factor is shown in Fig. 11. The region where the F-P resonance takes place is extremely sharp and narrow, meaning that the resonance condition is very strict. Among the set of discrete values considered in the simulations, the detuned incident wave number corresponding to the maximum enhancement factor is $k = 0.979\,313k_B$. The "exact" resonance condition is found to lie between $0.9793k_B$ and $0.979\,317k_B$. It should be noted that even though the amplitude of bottom corrugations is high, the prediction of the value of the maximum E^{FP} by the ALAS is quite reliable: system A gives $E_A^{\mathrm{FP}} \approx 26.918$ at maximum, which is quite close to $E_{\mathrm{ALAS}}^{\mathrm{FP}} = 27.579$. Such a close match was not guaranteed *a priori*, as the wave number corresponding to the maximum enhancement factor is significantly shifted downwards.

As a confirmation of the realization of F-P resonance, the envelope of the simulation done with system A using the incident wave number $k = 0.979\,313k_B$, corresponding to the maximum enhancement factor in Fig. 11, is shown in Fig. 12. A reasonable agreement is found, confirming the possibility of reaching large enhancement factors in the resonator within

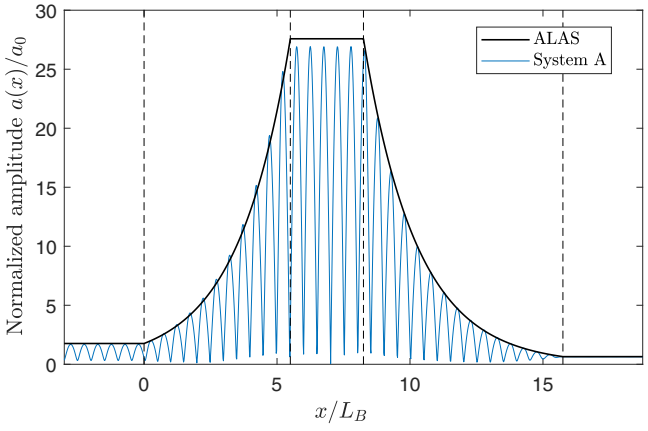

FIG. 12. Computed envelope of the free surface elevation at the end of the simulations with system A ($t = 10\,000T$) for the case $\delta = 0.4$ with the wave number slightly smaller ($k' = 0.979\,313k_B$) than the F-P condition, compared to the ALAS envelope (calculated for $k = k_B$).

the framework of the exact linear wave theory. Note that the simulation duration to reach a steady state for this value of $\delta = 0.4$ needs to be significantly increased: $10\,000T$ was used for this run.

V. CONCLUSIONS

Recently, Couston *et al.* [4] investigated the applicability of the F-P resonance mechanism to water waves by using two patches of corrugations on an otherwise flat bottom. For small bottom corrugation amplitude and linear waves, they built an asymptotic linear approximate system and solved it by adopting the multiple-scale method, obtaining at leading order an asymptotic linear analytical solution (ALAS). The ALAS is the envelope of the wave amplitude as a function of the space coordinate x. The reflection coefficient, transmission coefficient, and enhancement factor are also derived analytically for the F-P resonance. In the linear framework, the enhancement factor increases exponentially as the relative amplitude of the bottom corrugations increases.

The influence of the assumption of small corrugation amplitude adopted in the ALAS derivation was studied here by using an accurate numerical model solving the linear water wave problem with either the exact BBC (system A) or the first-order approximate BBC (system B). A detailed study was performed for the particular case where the ratio of corrugation amplitude to water depth $\delta = d/h$ varies in the range [0.05, 0.4], using the same settings as in Ref. [4] for the other geometrical parameters. When the corrugation amplitude is small, for example $\delta = 0.05$, predictions from the ALAS are in good agreement with the numerical simulations. For larger values, however, we observe that the resonance does not manifest under the F-P resonance condition. Based on further analyses of the cases with finite corrugation amplitudes $\delta = 0.2$ and 0.4, the following conclusions can be drawn.

(1) If the finite amplitude of bottom corrugations is taken into account, F-P resonance does not occur for incident waves with a wave number equal to the target resonant wave number $k_B = k_b/2$. No matter whether the exact BBC or the approximate BBC is considered, the simulation results show that waves are almost fully reflected by the finite-amplitude bottom corrugations ($R^{\mathrm{FP}} \to 1$ before the first patch) and that standing waves are still formed in the resonator but the enhancement factors are not comparable to the values predicted by the ALAS. For example, for the case $\delta = 0.2$, in the ALAS, the reflection coefficient $R_{\mathrm{ALAS}}^{\mathrm{FP}} \approx 0.462$ and the enhancement factor $E_{\mathrm{ALAS}}^{\mathrm{FP}} \approx 5.786$, however, $R_A^{\mathrm{FP}} \approx 0.956$ and $E_A^{\mathrm{FP}} \approx 1.711$ are observed in the simulation with system A. Clearly, F-P resonance is not realized in the simulations of system A or system B at the expected wave number k_B when $\delta > 0.1$.

(2) By slightly decreasing the wave number of incident waves, however, a situation close to the predicted F-P resonance can be reached with systems A and B. Even for the case with the highest corrugation amplitude studied in the present work, $\delta = 0.4$, the resonance can be recovered for the incident wave number $k = 0.979\,313k_B$. In this case, the reflection coefficient and enhancement factor from the numerical simulation with system A are $R_A^{\mathrm{FP}} \approx 0.687$ and $E_A^{\mathrm{FP}} \approx 26.918$, respectively. As shown in Fig. 12, the agreement between the

ALAS prediction and the simulation result is good, with a relative error of enhancement factor of only 2% compared to the ALAS value, $E^{\mathrm{FP}}_{\mathrm{ALAS}} \approx 27.579$. This demonstrates that F-P resonance can be effectively realized for a finite corrugation amplitude within the linear wave theory, but only for specifically detuned incident wave numbers.

(3) In line with the previous conclusion, it appears that the range of incident wave numbers prone to F-P resonance is extremely narrow for high corrugation amplitudes. As illustrated in Fig. 9 for $\delta = 0.2$ and Fig. 11 for $\delta = 0.4$, as soon as the incident wave number departs from the optimal value, even slightly, the resonance can no longer develop. The incident waves are then strongly reflected by the two-patch system. The deviation of the optimal wave number from the F-P resonance condition $k = k_B$ increases with the amplitude of bottom corrugations. This extreme narrowness of the resonance range makes the possibility of realizing such resonance for practical coastal applications questionable, or, at least, attainable for only very particular incident wave conditions, all the more so as the required duration to reach maximum amplification of waves in the resonator area was observed to increase roughly exponentially as a function of δ.

(4) The fact that the resonant wave number cannot be accurately predicted by the ALAS for finite-amplitude bottom corrugations is mainly related to the implied assumption of the ALAS that the wave number maintains a constant value over the patch of corrugations. In fact, when waves propagate over a patch of corrugations, the effective wave number is slightly higher over this area, as highlighted by the analysis in [13] based on a third-order expansion of the linear dispersion relation. In the numerical model used here, which can cope with arbitrary bottom shapes, the variations of local wave properties due to a variable bottom are fully accounted for, even in the linear framework. This explains the difference between the numerical model results and the ALAS for prediction of the wave-number downshift. Equation (18) can be used to provide a primary estimate of the wave-number downshift.

(5) On the other hand, the approximation related to the first-order expansion of the BBC (i.e., considering system B instead of system A) appears to have less influence. At least for the range of bottom corrugation amplitudes $\delta \in [0.05, 0.2]$ considered in the present study, the differences in the results for system A vs system B are quite limited.

In the near-future, the effects associated with the assumption of small-amplitude surface waves will be studied by using the fully nonlinear wave model, (14), and applying the fully nonlinear version of WHISPERS-3D. Finite-amplitude incident waves will introduce higher-order modes due to wave-bottom interactions. Furthermore, the dispersion relation will be affected by the finite amplitude of waves, which will certainly influence the occurrence of F-P resonance, as we have shown in this work that the F-P condition is very sensitive to the effective wave number over the patches of corrugations.

ACKNOWLEDGMENTS

The authors wish to thank Louis-Alexandre Couston for several discussions on various aspects of Bragg and Fabry-Perot resonance and suggestions on a preliminary version of this article. J.Z. gratefully acknowledges the financial support from the China Scholarship Council covering his Ph.D. thesis (Grant No. 201604490045).

[1] C. Fabry and A. Pérot, Ann. Chim. Phys. **12**, 459 (1897).
[2] J. M. Vaughan, *The Fabry Perot Interferometer: History, Theory, Practice and Applications* (Taylor & Francis Group, New York, 1989).
[3] N. Ismail, C. C. Kores, D. Geskus, and M. Pollnau, Opt. Express **24**, 16366 (2016).
[4] L. A. Couston, Q. C. Guo, M. Chamanzar, and M. R. Alam, Phys. Rev. E **92**, 043015 (2015).
[5] A. G. Davies, J. Mar. Res. **40**, 331 (1982).
[6] A. G. Davies and A. D. Heathershaw, J. Fluid Mech. **144**, 419 (1984).
[7] A. D. Heathershaw, Nature **296**, 343 (1982).
[8] C. C. Mei, J. Fluid Mech. **152**, 315 (1985).
[9] J. Yu and C. C. Mei, J. Fluid Mech. **404**, 251 (2000).
[10] V. Rey, É. Guazzelli, and C. C. Mei, Phys. Fluids **8**, 1525 (1996).
[11] É. Guazzelli, V. Rey, and M. Belzons, J. Fluid Mech. **245**, 301 (1992).
[12] L. A. Couston, M. A. Jalali, and M. R. Alam, J. Fluid Mech. **815**, 481 (2017).
[13] Y. M. Liu and D. K. P. Yue, J. Fluid Mech. **356**, 297 (1998).
[14] T. Hara and C. C. Mei, J. Fluid Mech. **178**, 221 (1987).
[15] L. N. Howard and J. Yu, J. Fluid Mech. **593**, 209 (2007).
[16] J. Yu and L. N. Howard, J. Fluid Mech. **659**, 484 (2010).
[17] J. Yu and G. F. Zheng, J. Fluid Mech. **713**, 362 (2012).
[18] P. D. Weidman, A. Herczynski, J. Yu, and L. N. Howard, J. Fluid Mech. **777**, 122 (2015).
[19] R. A. Dalrymple and J. T. Kirby, J. Waterway, Port, Coastal, Ocean Eng. **112**, 309 (1986).
[20] J. T. Kirby, J. Fluid Mech. **162**, 171 (1986).
[21] R. Porter and D. Porter, J. Fluid Mech. **434**, 301 (2001).
[22] D. G. Dommermuth and D. K. P. Yue, J. Fluid Mech. **184**, 267 (1987).
[23] V. E. Zakharov, J. Appl. Mech. Tech. Phys. **9**, 190 (1968).
[24] M. L. Yates and M. Benoit, Int. J. Numer. Methods Fluids **77**, 616 (2015).
[25] C. Raoult, M. Benoit, and M. L. Yates, Coastal Eng. **114**, 194 (2016).
[26] Y. Tian and S. Sato, Coastal Eng. J. **50**, 369 (2008).
[27] M. Benoit, C. Raoult, and M. L. Yates, Wave Motion **74**, 159 (2017).
[28] P. A. Madsen, D. R. Fuhrman, and B. L. Wang, Coastal Eng. **53**, 487 (2006).
[29] Y. Goda and Y. Suzuki, in *15th International Conference on Coastal Engineering* (Honolulu, HI, 1976), pp. 828–845.

Chapter 3

Supplementary materials: further investigation of wave-number downshift phenomenon within seven linear wave models

In Chapter 2, the effect of finite ripple amplitude on the F-P resonance has been discussed. Here, we further analyze the wave-number downshift phenomenon within various linear wave models. In line with the work presented in Chapter 2, the linear wave models of systems A, B and C are included in the present study. But they are solved here in a semi-analytical manner, ensuring both efficiency and convergence of the simulations. Then, an intermediate case between the exact BBC and first-order approximated BBC, called the second-order approximation of BBC, is implemented in the linear version of Whispers3D. This system with the second-order approximated BBC is also solved semi-analytically. Furthermore, three versions of the mild-slope equation family are also included and compared, namely the classical elliptic MSE (Berkhoff, 1972, 1976), the EMSE (Kirby, 1986a) and the MMSE Chamberlain and Porter (1995). As it is discussed in Chapter 1, the three mild-slope equations are valid for different orders of mild bottom slope magnitude. From a theoretical perspective, the ranking order of the model validity range is MMSE > EMSE > MSE. It is believed that the differences among these models mainly result from the BBC approximations. The comparative analysis of the various models considered here allows gaining insight into the bottom effects on the wave-number downshift for the F-P resonance phenomenon.

3.1 Presentation of the seven linear wave models for the study of wave-number downshift

Considering small-amplitude long-crested plane waves, the full potential theory of linear waves is composed of Eqs. (I.2.1) to (I.2.4) with the nonlinear terms in the DFSBC (Eq. (I.2.2)) and the KFSBC (Eq. (I.2.3)) ignored. Within the small-amplitude wave assumption, the FSBCs are applied at the undisturbed water surface $z = 0$ instead of $z = \eta(x, t)$.

For the F-P resonance case, the water depth is considered to be of the form $\tilde{h}(x) = h - \delta(x)$, where h is the (constant) mean water depth and $\delta(x)$ is the shape of ripples superimposed on the flat bottom:

$$\delta(x) = \begin{cases} d\sin\left[k_b(x - x_1^s) - \theta_1\right], & x \in [x_1^s, x_1^e], \\ d\sin\left[k_b(x - x_2^s) - \theta_2\right], & x \in [x_2^s, x_2^e], \\ 0, & \text{elsewhere.} \end{cases} \tag{II.3.1}$$

where x_j^s and x_j^e represent the start and the end of patch of ripples j ($j = 1, 2$). k_b and $L_b = 2\pi/k_b$ denote the wave-number and wavelength of the bottom corrugations, respectively. Each patch j is composed of an integer number $N_j \in \mathbb{N}$ of ripples, so that its length is $L_j = x_j^e - x_j^s = N_j L_b$. θ_j is the initial phase of the j-th patch (consider either $\theta_j = 0$ or π for a continuous bottom shape). The relative ripple amplitude is characterized by the ratio $\epsilon = d/h$. The resonator length is denoted by $L_r = x_2^s - x_1^e$.

With the bottom profile $\tilde{h}(x) = h - \delta(x)$ inserted into the potential linear wave theory in Eqs. (I.2.1) to (I.2.4), we obtain:

$$\begin{cases} \phi_{xx} + \phi_{zz} = 0, & -\tilde{h}(x) \le z \le 0, \quad \text{(II.3.2)} \\ \phi_{tt} + g\phi_z = 0, & \text{on } z = 0, \quad \text{(II.3.3)} \\ \phi_z - \delta_x \phi_x = 0, & \text{on } z = -\tilde{h}(x). \quad \text{(II.3.4)} \end{cases}$$

The free surface elevation $\eta(x, t)$ is related to the velocity potential by:

$$\eta(x, t) = -\frac{1}{g}\phi_t(x, z = 0, t). \tag{II.3.5}$$

In the following, seven linear wave models are introduced. The governing equations for the bulk of domain (Eq. (II.3.2)) and on the free surface (Eq. (II.3.3)) are shared by all models. The models are distinguished according to the assumptions introduced for the BBC (Eq. (II.3.4)).

3.1.1 Linear Whispers3D modeling: Laplace equation with three BBCs at different orders

a/ Model I: Laplace equation with exact BBC

As a reference linear solution, the full potential linear wave problem composed of Eq. (II.3.2) to Eq. (II.3.4) is solved by the linear version of Whispers3D. The properties of the linear version Whispers3D have been detailed in Benoit et al. (2017). We stress that the BBC considered in Model I is Eq. (II.3.4):

$$\phi_z = \delta_x \phi_x, \text{ on } z = -\tilde{h}(x), \tag{II.3.6}$$

which has no limitation on the bottom gradient or curvature. Furthermore, the exact BBC is applied on the 'actual' vertical elevation, i.e. $z = -h + \delta$.

b/ Model II: Laplace equation with first-order approximate BBC

In Model II, an additional assumption on the magnitude of bottom variations is introduced, requiring $\epsilon = |\delta|/h \ll 1$. In such a case, the water depth is formally written as $\tilde{h}(x) = h - \epsilon\delta(x)$. Then, based on a Taylor expansion of the exact BBC Eq. (II.3.4) around the mean water depth $z = -h$, the first-order approximate BBC is obtained, with the terms $O(\epsilon)$ ignored:

$$\phi_z = (\delta\phi_x)_x, \quad z = -h. \tag{II.3.7}$$

Note that the first-order approximated BBC is applied on the constant (undisturbed) elevation $z = -h$. This is the same BBC used by Mei (1985) and Couston et al. (2015) to derive their analytical solutions.

c/ Model III: Laplace equation with second-order BBC

Both the exact and first-order approximated BBC have been tested in Zhang and Benoit (2019) (referred to as system A and system B in that paper), showing different degrees of wave-number downshift. In addition, here we have the second-order approximation of the exact BBC based on Taylor expansion tested:

$$\phi_z = (\delta\phi_x)_x + \frac{1}{2}\left(\delta^2\phi_{xz}\right)_x, \quad z = -h. \tag{II.3.8}$$

This approximate BBC is again applied at the mean bottom depth $z = -h$. This is the BBC adopted in the derivation of analytical theory for Class II Bragg resonance by Rey et al. (1996).

3.1.2 Mild-slope equations: three formulations

a/ Model IV: Classical mild-slope equation by Berkhoff (1972)

Berkhoff (1972, 1976) introduced the classical MSE to describe the combined effects of refraction and diffraction for waves propagating over variable water depth. Smith and Sprinks (1975) obtained the same MSE using a more succinct derivation. As its name suggests, the MSE assumes a small bottom slope $h_x \ll kh$ (if h is slowly varying). The commonly accepted limit of validity of the MSE for the bottom gradient is 1 : 3 (Booij, 1983). The mild-slope approximation also involves applying an averaging procedure to the vertical structure of the wave field and integrating the depth variable out of the solution. To this end, it is assumed that the velocity potential may be expressed as:

$$\phi(x,z,t) = F(\tilde{h},z)\Phi(x)e^{-i\omega t} \tag{II.3.9}$$

in which the vertical dependence of the potential

$$F(\tilde{h},z) = \frac{\cosh k(\tilde{h}+z)}{\cosh k\tilde{h}} \tag{II.3.10}$$

is assumed to be the same as the solution obtained for progressive linear waves in uniform water depth (in which case this expression corresponds to the exact solution of the problem). Here, however, k is the local wave-number obtained from the linear dispersion relation $\omega^2 = gk\tanh(k\tilde{h})$, considering the angular frequency ω and the local water depth $\tilde{h}$.

Although it has already been pointed out that the classical MSE fails in describing Bragg scattering problem with ripple bed profiles, the classical MSE is included here for completeness and comparison purposes. The formulation of the classical MSE reads:

$$(CC_g\Phi_x)_x + k^2CC_g\Phi = 0, \tag{II.3.11}$$

where $C = \omega/k$ and $C_g = \partial\omega/\partial k$ denote the phase celerity and the group celerity, respectively evaluated at the local water depth $\tilde{h}$. We note that Eq. (II.3.11) can be reformulated equivalently as:

$$\Phi_{xx} + \frac{(CC_g)_x}{CC_g}\Phi_x + k^2\Phi = 0, \tag{II.3.12}$$

where it can be shown that:

$$\frac{(CC_g)_x}{CC_g} = G(k\tilde{h})\frac{\tilde{h}_x}{\tilde{h}}. \tag{II.3.13}$$

The function G depends on the relative water depth $k\tilde{h}$ only, and can be calculated analytically as:

$$G(k\tilde{h}) = \frac{k\tilde{h}}{\tau + k\tilde{h}(1-\tau^2)}\left[1 - 3\tau^2 + \frac{2\tau}{\tau + k\tilde{h}(1-\tau^2)}\right], \tag{II.3.14}$$

denoting $\tau = \tanh(k\tilde{h})$. With the formulation (II.3.12-II.3.13), the slope of the bottom $\tilde{h}_x$ appears explicitly in the MSE.

b/ Model V: Extended mild-slope equation by Kirby (1986a)

Kirby (1986a) extended the mild-slope equation by considering a bed consisting of ripples superimposed on an otherwise slowly varying 'mean' depth. To better illustrate this model, here we temporarily assume the bottom profile $\tilde{h}$ can be considered as the sum of slow variations $h(x)$ and rapid undulations $\delta(x)$ about the 'mean' level $h(x)$, i.e. $\tilde{h}(x) = h(x) - \delta(x)$. Note that in the F-P resonance study, h is not a varying but a constant mean water depth. Apart from the assumptions of the classical MSE, further assumptions of EMSE are introduced for ripple amplitude. The wavelengths of ripples are comparable to the order of surface wavelength, but ripple amplitudes are of a smaller scale. Namely, it is assumed $O(h_x/kh) \approx O(k\delta) \ll 1$.

Based on this assumption, the formulation of EMSE for the undulated bottom with slowly varying mean depth $h(x)$ is (Kirby, 1986a):

$$\left(\bar{C}\bar{C}_g\Phi_x\right)_x + \bar{k}^2\bar{C}\bar{C}_g\Phi - g\,\mathrm{sech}^2\left(\bar{k}h\right)\left(\delta\Phi_x\right)_x = 0, \tag{II.3.15}$$

where the terms proportional to h_x^2 and δh_x have been neglected. Note that $\bar{k}$, $\bar{C}$, $\bar{C}_g$ correspond to 'mean' values, computed using the slowly varying mean water depth $h(x)$. The bars on top of k, C and C_g are used to distinguish these variables from the ones computed with local water depth $\tilde{h}$. The trial function of the velocity potential $\phi(x, z, t)$ is also slightly different from Eq. (II.3.9), considering the 'mean' water depth h only:

$$\phi(x, z, t) = \frac{\cosh \bar{k}(h + z)}{\cosh \bar{k}h}\Phi(x)e^{-i\omega t}. \tag{II.3.16}$$

If the last term including δ in Eq. (II.3.15) is neglected, then Eq. (II.3.15) reduces to the classical MSE Eq. (II.3.11) without bottom undulations.

When applying this equation to Bragg and F-P resonance cases where the mean water depth h is constant, the values of $\bar{k}$, $\bar{C}$, $\bar{C}_g$ become uniform in space. In this case, the EMSE Eq. (II.3.15) reduces to:

$$\Phi_{xx} + \bar{k}^2\Phi - \frac{g\,\mathrm{sech}^2\left(\bar{k}h\right)}{\bar{C}\bar{C}_g}\left(\delta\Phi_x\right)_x = 0, \tag{II.3.17}$$

c/ Model VI: Modified mild-slope equation by Chamberlain and Porter (1995)

Chamberlain and Porter (1995) proposed a more general MMSE formulation compared to the classical MSE (Berkhoff, 1972, 1976) and EMSE (Kirby, 1986a). One of the two mild-slope equation assumptions was released: the approximation on

the trial form of velocity potential in Eq. (II.3.10) remains, whereas the assumption on the bottom slope $h_x \ll kh$ is released. The formulation of MMSE reads:

$$\Phi_{xx} + \frac{(CC_g)_x}{CC_g}\Phi_x + \left(k^2 + \frac{gr(\tilde{h})}{CC_g}\right) = 0, \tag{II.3.18}$$

in which

$$u_0(\tilde{h}) = \int_{-\tilde{h}}^{0} F^2(\tilde{h}, z)dz = \frac{1}{2k}\left(1 + \frac{2q}{\sinh 2q}\right)\tanh q = \frac{CC_g}{g}, \tag{II.3.19}$$

where $q = k\tilde{h}$ is used for brevity. The additional term $r(\tilde{h})$ is given by:

$$r(\tilde{h}) = u_1(\tilde{h})\tilde{h}_{xx} + u_2(\tilde{h})\tilde{h}_x^2, \tag{II.3.20}$$

This term could be neglected on the basis of the mild slope approximation $h_x \ll kh$ and then Eq. (II.3.18) reduces to the classical MSE Eq. (II.3.15). Through the term $r(\tilde{h})$ the MMSE permits to consider second-order effects of the bottom variations, involving a term proportional to the curvature of the bottom and a term proportional to the square of the bottom slope. It was derived with different approaches by various authors (see e.g. Massel, 1993; Chamberlain and Porter, 1995; Suh et al., 1997; Chandrasekera and Cheung, 1997). These approaches, resulting in the same formulation as Eq. (II.3.18), have different (but equivalent) expressions of u_1 and u_2. In this work, we follow the formulation of Chamberlain and Porter (1995):

$$\begin{cases} u_1(\tilde{h}) = \dfrac{\operatorname{sech}^2 q}{4\,(2q + \sinh(2q))}\left[\sinh(2q) - 2q\cosh(2q)\right], & \text{(II.3.21)} \\ u_2(\tilde{h}) = \dfrac{k\operatorname{sech}^2 q}{12\,(2q + \sinh(2q))^3}\left[16q^4 + 32q^3\sinh(2q) - 9\sinh(2q)\sinh(4q)\right. \\ \qquad \left. +12q\left(q + \sinh(2q)\left(\cosh^2(2q) - 2\cosh(2q) + 3\right)\right)\right], & \text{(II.3.22)} \end{cases}$$

It is shown that, with the corresponding approximations adopted, Eq. (II.3.18) reduces to Eq. (II.3.11) or Eq. (II.3.15) as special cases. As in the MSE, the coefficients in the MMSE, k, C, C_g, r are evaluated using the local water depth $\tilde{h}$. It has been shown by Chamberlain and Porter (1995) that only the models considering local wave-number at the actual depth (i.e. models I–IV and VI here) could detect significant second-order resonance.

3.1.3 Model VII: Asymptotic linear analytical solution by Couston et al. (2015)

The asymptotic linear theories of both Mei (1985) and Couston et al. (2015) are built on the basis of model II and concentrate on the reflection and transmission processes in the vicinity of the resonance. For the bathymetry defined in

Eq. (II.3.1), the Bragg resonance manifests when the incident wave-number is $k_B = k_b/2$ (to be clear, the subscript 'B' stands for 'Bragg' and 'b' for 'bottom'). The Bragg resonance condition in frequency is $\omega = \omega_B$ with $\omega_B = \sqrt{gk_B \tanh(k_B h)}$.

Assume the monochromatic incident water waves coming from $x = -\infty$ with a detuned wave-number $k = k_B + \kappa$ (assuming $\kappa \ll k_b$), we know the corresponding detuned frequency is $\omega = \omega_B + \Omega$, where $\Omega = C_g\kappa$ and C_g is the group celerity at the Bragg wave-number:

$$C_g = \frac{1}{2}\left(1 + \frac{2k_B h}{\sinh 2k_B h}\right)\frac{\omega_B}{k_B}. \tag{II.3.23}$$

Due to the wave-bottom interaction, the amplitude is modulated in space. The first-order solution of model II over undulated bottom patch j considering slow spatial modulation of the incident and reflected wave amplitudes is expressed as follows:

$$\phi = f(z)[\mathcal{A}_j(x', t')e^{-ikx} + \mathcal{B}_j(x', t')e^{ikx}]e^{i\omega t} + \text{c.c.}, \tag{II.3.24}$$

where c.c. denotes the complex conjugate, $i = \sqrt{-1}$, x' and t' are the slow variables. $\mathcal{A}_j$, $\mathcal{B}_j$ denote the slowly varying complex amplitudes of the incident and reflected waves respectively. The reflected wave amplitude is at the same order as the incident wave amplitude. Then the time variation can be written explicitly $\mathcal{A}_j = A_j(x')e^{i\Omega t'}$, $\mathcal{B}_j = B_j(x')e^{i\Omega t'}$. $f(z)$ is the vertical structure of the velocity potential:

$$f(z) = -\frac{ig}{2\omega}\frac{\cosh k(h+z)}{\cosh kh} = -\frac{ig}{2\omega}F(h, z). \tag{II.3.25}$$

The governing equations over the patch j consist of two coupled parabolic equations for forward and backward-scattered waves:

$$i\Omega\mathcal{A}_j + C_g\frac{\partial\mathcal{A}}{\partial x'} = -\Omega_c e^{i\theta_j}\mathcal{B}_j, \tag{II.3.26a}$$

$$i\Omega\mathcal{B}_j - C_g\frac{\partial\mathcal{B}}{\partial x'} = \Omega_c e^{-i\theta_j}\mathcal{A}_j, \tag{II.3.26b}$$

where

$$\Omega_c = \frac{\omega_B k_B d}{2\sinh 2k_B h}. \tag{II.3.26c}$$

It can be seen that for the flat bottom parts (where $\delta(x) = 0$), $\Omega_c = 0$: the incident and reflected waves propagate at the speed of group velocity without coupling. If only one patch j is considered, the model returns to Mei's theory for Bragg resonance (Mei, 1985). The complex Bragg reflection and transmission coefficients are expressed as functions of the normalized detuning frequency Ω/Ω_c:

$$\mathcal{R}_j^B(\mathcal{P})|_{x_j^s} = \frac{\mathcal{B}(x_j^s, t')}{\mathcal{A}(x_j^s, t')} = \frac{e^{-i\theta_j}\sinh S_j\mathcal{Q}}{\mathcal{Q}\cosh S_j\mathcal{Q} + i\mathcal{P}\sinh S_j\mathcal{Q}}, \tag{II.3.27a}$$

$$\mathcal{T}_j^B(\mathcal{P})|_{x_j^e} = \frac{\mathcal{A}(x_j^e, t')}{\mathcal{A}(x_j^s, t')} = \frac{\mathcal{Q}}{\mathcal{Q}\cosh S_j\mathcal{Q} + i\mathcal{P}\sinh S_j\mathcal{Q}} \tag{II.3.27b}$$

where

$$\mathcal{P} = \Omega/\Omega_c, \quad \mathcal{Q} = \sqrt{1-\mathcal{P}^2}, \quad S_j = \frac{\Omega_c L_j}{C_g}. \tag{II.3.27c}$$

The normalized amplitude and phase shift of reflected waves are $R_j^B = |\mathcal{R}_j|$ and $\alpha_j^B = Arg\,(\mathcal{R}_j)$, the normalized amplitude of the transmitted waves is $T_j^B = |\mathcal{T}_j|$.

If two patches are considered, and the system is solvable thanks to the continuity of the free surface elevation over the resonator area, i.e. the amplitude of the incident waves of the second patch equals that of the transmitted wave of the first patch. Thus, the reflection and transmission coefficients for F-P resonance are expressed as:

$$R^{FP}|_{x_1^s} = \left[\frac{(R_1^B)^2 + (R_2^B)^2 - 2R_1^B R_2^B\cos\gamma}{1 + (R_1^B R_2^B)^2 - 2R_1^B R_2^B\cos\gamma}\right]^{1/2}, \tag{II.3.28a}$$

$$T^{FP}|_{x_2^e} = \left\{\frac{\left[1-(R_1^B)^2\right]\left[1-(R_2^B)^2\right]}{1 + (R_1^B R_2^B)^2 - 2R_1^B R_2^B\cos\gamma}\right\}^{1/2}, \tag{II.3.28b}$$

where

$$\gamma = \pi - 2\theta_1 + 2k_B L_r - \alpha_1^B - \alpha_2^B. \tag{II.3.29}$$

In addition to Bragg resonance condition, the wave energy will be trapped within the resonator when $\gamma = 2m\pi$ ($m \in \mathbb{N}$). Replacing γ in Eq. (II.3.29) results in a condition on the possible values of the resonator length when $k = k_B$

$$k_b L_r^{(m)} = (2m+1)\pi + \theta_1 + \theta_2, \quad \text{with} \quad m \in \mathbb{N}. \tag{II.3.30}$$

This is denoted as F-P resonance condition in which the standing waves with highest achievable amplitude are expected between two patches. The non-dimensional amplitude of the standing waves within the resonator is defined as enhancement factor E^{FP} and can be computed as follows (Couston et al., 2015):

$$E^{FP} = \frac{|\mathcal{A}(x_1^e, t')| + |\mathcal{B}(x_1^e, t')|}{|\mathcal{A}(x_1^s, t')|} = \left(1 + R_2^B\right)\frac{T^{FP}}{T_2^B}. \tag{II.3.31}$$

In the following, we refer to the reflection and transmission coefficients and the enhancement factor R^{FP}, T^{FP} and E^{FP} as *Asymptotic Linear Analytical Solution* (ALAS) of the F-P resonance.

3.2 Numerical implementation of Whispers3D and mild-slope models

3.2.1 Numerical implementation of models I, II and III (in Whispers3D)

In the Zakharov formulation of the water wave problem, we march in time the free-surface elevation and the free-surface potential. For that, we need to solve a Laplace equation on the velocity potential within the fluid domain given the current value of the free surface elevation (which defines the upper boundary of the fluid domain) and the associated value of the free surface potential, used as a Dirichlet condition on the potential on that surface. This is referred to as a Laplace BVP. As it has been outlined in Part I Subsection (3.2), the approach used in Whispers3D involves three steps for solving the Laplace BVP problem:

- a change of variables for the vertical coordinate s defined in Eq. (I.3.5);
- approximation of the velocity potential $\varphi(x,s,t) \approx \varphi_{N_T}(x,s,t)$ using Chebyshev polynomials of the first kind to a given order N_T shown in Equation (I.3.6);
- application of the Chebyshev-Tau method in the vertical.

Once the a_n coefficients at each location in space are solved, the vertical velocity $\tilde{w}$ can be computed, which allows marching the free surface variables (η and $\tilde{\phi}$) in time.

This procedure of solving the DtN problem was used in Zhang and Benoit (2019). We found that, with increasing relative ripple amplitudes ϵ, the physical time to be simulated to reach an established periodic regime increases markedly, which means the duration of the simulations should be extended correspondingly. For example, in the largest ripple amplitude case ($\epsilon = 0.4$) of Zhang and Benoit (2019), it took nearly 10,000 wave periods for the enhancement factor to achieve a (quasi-) steady level. In order to avoid unconverged results and to drastically reduce the computational time, a method to solve the BVP in a semi-analytical manner was developed recently, and is briefly presented hereafter.

a/ Governing equations of the semi-analytical approach

Here, a more detailed description is given to explain the procedure used to obtain the so-called semi-analytical solution in the linearized version of Whispers3D. It is assumed that the wave induced motion of the fluid is purely harmonic in time at the steady state, which allows writing the solution as:

$$\phi(x,z,t) = \hat{\phi}(x,z)e^{-i\omega t}, \tag{II.3.32}$$

where the hat symbol denotes the time-invariant semi-analytical solution, and $\omega = 2\pi/T$ is the angular frequency of wave oscillation in time.

In the linear wave model where the nonlinear terms are ignored, such an ansatz permits to eliminate the time dependence in all the governing equations. The Laplace equation and the FSBC given in Eq. (II.3.2) and Eq. (II.3.3) are now formulated as:

$$\begin{cases} \hat{\phi}_{xx} + \hat{\phi}_{zz} = 0, \quad -\tilde{h}(x) \leq z \leq 0, & \text{(II.3.33)} \\ g\hat{\phi}_z - \omega^2\hat{\phi} = 0, \quad \text{on } z = 0. & \text{(II.3.34)} \end{cases}$$

At the two ends of the computational domain, instead of the relaxation zones adopted in Zhang and Benoit (2019), two time-invariant radiation-type lateral boundary conditions are applied:

$$\begin{cases} \hat{\phi}_x + ik\hat{\phi} = 2ik\hat{\phi}_I, \quad \text{on} \quad x = x_{beg} & \text{(II.3.35)} \\ \hat{\phi}_x - ik\hat{\phi} = 0, \quad \text{on} \quad x = x_{end}, & \text{(II.3.36)} \end{cases}$$

where x_{beg} and x_{end} denote the upwave and downwave limits of the computational domain, respectively. The incident wave potential is taken as

$$\phi_I(x,z,t) = \hat{\phi}_I(x,z)e^{-i\omega t} = a_I F(h,z)e^{ikx}e^{-i\omega t}, \tag{II.3.37}$$

where a_I represents its (complex) amplitude (which can be chosen arbitrary in a linear wave approach).

With the Eqs. (II.3.33) to (II.3.36), supplemented by one of the BBCs introduced in Eqs. (II.3.6) to (II.3.8), the semi-analytical solution of models I, II, III can be obtained solving the linearized DtN problem once far all, and thus avoiding time integration of the Zakharov equations.

The first step of solving this system is to convert the governing equations from the physical (x,z) domain to the (x,s) domain. It should be noticed that the approximated BBCs (in models II and III) differ from the exact BBC (in model I) in the sense that they are applied on the constant mean water depth. Therefore, the transformation of the vertical variable is different. It is thus appropriate to introduce the implementation of model I and model II/III separately.

b/ Numerical implementation of model I

For model I with the exact BBC applied on $z = -\tilde{h}(x)$, the expressions of $s(x,z)$ and its derivatives are:

$$\begin{cases} s = 2z/\tilde{h} + 1, \\ s_x = (1-s)\,\tilde{h}_x/\tilde{h}, \quad s_{xx} = (1-s)\left(\tilde{h}\tilde{h}_{xx} - 2\tilde{h}_x^2\right)/\tilde{h}^2, \\ s_z = 2/\tilde{h}, \qquad\qquad s_{zz} = 0. \end{cases} \tag{II.3.38}$$

With the change of variables, we have $\varphi(x,s) \equiv \hat{\phi}(x,z)$. Using the chain rule, the governing equations are formulated in terms of $\varphi(x,s)$:

$$\varphi_{xx} + 2\varphi_{xs}s_x + \varphi_{ss}\left(s_x^2 + s_z^2\right) + \varphi_s s_{xx} = 0, \qquad -1 \leq s \leq 1, \tag{II.3.39}$$

$$g\varphi_s s_z - \omega^2 \varphi = 0, \qquad \text{on} \quad s = 1, \tag{II.3.40}$$

$$\varphi_x + \varphi_s s_x + ik\varphi = 2ik\varphi_I, \text{at} \quad x = x_{beg},\ -1 \leq s \leq 1, \tag{II.3.41}$$

$$\varphi_x + \varphi_s s_x - ik\varphi = 0, \qquad \text{at} \quad x = x_{end},\ -1 \leq s \leq 1, \tag{II.3.42}$$

$$\varphi_s\left(s_z - \delta_x s_x\right) - \delta_x \varphi_x = 0, \qquad \text{on} \quad s = -1, \tag{II.3.43}$$

It is assumed that the wave bottom is locally flat at both ends of the domain, so that $s_x(x_{beg}) = 0$ in Eq. (II.3.41) and $s_x(x_{end}) = 0$ in Eq. (II.3.42).

Then, the next step is to approximate the vertical velocity potential by using a series of Chebyshev polynomials (denoted as T_n, with $n \in \mathbb{N}$ being the degree of the polynomial). By selecting the $N_T + 1$ first polynomials, the velocity potential in the vertical direction is approximated as:

$$\hat{\phi}(x,z) \equiv \varphi(x,s) \approx \varphi_{N_T}(x,s) = \sum_{n=0}^{N_T} a_n(x) T_n(s). \tag{II.3.44}$$

The expression and the properties of Chebyshev polynomials of the first kind can be easily found in textbooks or on the internet. Here, the following properties will be used:

$$\begin{cases} T_n(\cos\theta) = \cos(n\theta), \\ T_n(\pm 1) = (\pm 1)^n \\ \dfrac{\mathrm{d}^p T_n}{\mathrm{d}s^p}\Big|_{s=\pm 1} = (\pm 1)^{n+p} \displaystyle\prod_{k=0}^{p-1} \frac{n^2 - k^2}{2k+1}. \end{cases} \tag{II.3.45}$$

With the approximation of the potential in Eq. (II.3.44) and the terms related to s in Eq. (II.3.38) inserted, then the known values of T_n given at fixed boundaries Eq. (II.3.45), the governing equations of model I are reformulated.

The Laplace equation (Eq. (II.3.39)) in the fluid domain is:

$$\sum_{n=0}^{N_T} a_{n,xx} + \frac{2(s-1)\delta_x}{h-\delta} \sum_{n=0}^{N_T} a_{n,x} T_{n,s} + \sum_{n=0}^{N_T} a_n T_{n,s} \frac{(s-1)}{h-\delta}\left(\frac{2\delta_x^2}{h-\delta} + \delta_{xx}\right)$$
$$+ \frac{(s-1)^2 \delta_x^2 + 4}{(h-\delta)^2} \sum_{n=0}^{N_T} a_n T_{n,ss} = 0, \ -1 \leq s \leq 1, \tag{II.3.46}$$

The free surface boundary condition (Eq. (II.3.40)) results in:

$$\sum_{n=0}^{N_T} a_n \left(2n^2 - \frac{\omega^2 (h-\delta)}{g} \right) = 0, \tag{II.3.47}$$

The lateral boundary conditions applied at the upwave limit (Eq. (II.3.41)) is:

$$\sum_{n=0}^{N_T} (a_{n,x} + ika_n) T_n(s) = 2ika_I F(h,s) e^{ikx_{beg}}, \text{ at } x = x_{beg}, \ -1 \leq s \leq 1, \tag{II.3.48}$$

Similarly, the radiation condition applied at the downwave limit (Eq. (II.3.42)) is:

$$\sum_{n=0}^{N_T} (a_{n,x} - ika_n) T_n(s) = 0, \text{ at } x = x_{end}, \ -1 \leq s \leq 1, \tag{II.3.49}$$

The exact BBC applied on the bottom (Eq. (II.3.43)) is:

$$\frac{2(1+\delta_x^2)}{h-\delta} \sum_{n=0}^{N_T} (-1)^{n+1} n^2 a_n - \delta_x \sum_{n=0}^{N_T} (-1)^n a_{n,x} = 0. \tag{II.3.50}$$

The last step is to apply the Chebyshev-Tau method to the equations involving a vertical dependence, namely the Laplace equation (Eq. (II.3.46)), and the two lateral boundary conditions (Eq. (II.3.48) and (II.3.49)). To that end, we use the operator

$$< f >_p \equiv \frac{2}{\pi C_p} < f, T_p >, \quad \text{with} \begin{cases} C_0 = 2, \\ C_p = 1 \quad \text{for} \quad p > 0, \end{cases} \tag{II.3.51}$$

basing on the inner product

$$< f, g > \equiv \int_{-1}^{+1} \frac{f(s) g(s)}{\sqrt{1-s^2}} ds, \tag{II.3.52}$$

This operator is applied to Eq. (II.3.46) with p ranging from 0 to $N_T - 2$ at all interior nodes x_j of the domain (i.e. for j ranging from 2 to npx $-$ 1). This results in $N_T - 1$ linear equations on the a_n coefficients at each node x_j, supplemented with the FSBC (Eq. II.3.47) and the BBC (Eq. II.3.50), leading thus to $N_T + 1$ equations. This operator is also applied to Eqs. (II.3.48) and (II.3.49) with p ranging from 0 to N_T, leading to $N_T + 1$ equations on the a_n coefficients at $x_1 = x_{beg}$ and $x_{npx} = x_{end}$. Note that the terms $< F(h,s) >_p$ at $x = x_{beg}$ can be computed analytically, as explained in Benoit et al. (2017) (see Eq. (71)).

c/ Numerical implementation of model II/III

For models II and III, the approximate BBCs are applied on the constant elevation $z = -h$, so the expressions of $s(x, z)$ and its derivatives are different from exact BBC case, and become:

$$s = 2z/h + 1, \quad s_z = 2/h, \quad s_x = s_{xx} = s_{xz} = s_{zz} = s_{xxz} = 0. \tag{II.3.53}$$

Omitting intermediate manipulations, the system of governing equations expressed with the approximated potential reads:

$$\sum_{n=0}^{N_T} \left(a_{n,xx} T_n + \frac{4}{h^2} a_n T_{n,ss} \right) = 0, \qquad -1 \le s \le 1, \tag{II.3.54}$$

$$\sum_{n=0}^{N_T} a_n \left(2n^2 - \frac{\omega^2 h}{g} \right) = 0, \qquad \text{on} \quad s = 1, \tag{II.3.55}$$

$$\sum_{n=0}^{N_T} \left(a_{n,x} + ika_n \right) T_n = 2ika_I F(h,s) e^{ikx_{beg}}, \text{ at } x = x_{beg}, \ -1 \le s \le 1 \tag{II.3.56}$$

$$\sum_{n=0}^{N_T} \left(a_{n,x} - ika_n \right) T_n = 0, \qquad \text{at } x = x_{end}, \ -1 \le s \le 1, \tag{II.3.57}$$

and with one of the BBCs applied on $s = -1$ in the following:

$$\sum_{n=0}^{N_T} (-1)^{n-1} n^2 \left[2 - \frac{4\delta}{3h} \left(n^2 - 1 \right) \right] a_n - \sum_{n=0}^{N_T} (-1)^n \delta_x h a_{n,x} = 0, \quad \text{for model II,} \tag{II.3.58}$$

$$\sum_{n=0}^{N_T} (-1)^{n-1} n^2 \left[2 - \frac{4\delta \left(n^2 - 1 \right)}{3h} + \frac{4\delta^2 \left(n^2 - 1 \right) \left(n^2 - 4 \right)}{15h^2} \right] a_n - \sum_{n=0}^{N_T} (-1)^n \delta_x \left(h - 2\delta n^2 \right) a_{n,x} = 0, \quad \text{for model III,} \tag{II.3.59}$$

where the equality of $\phi_{xx} = -\phi_{zz}$ was used to avoid evaluating second-order spatial derivative of $a_n(x)$. It is clear that the approximated BBC in model III reduces to that in model II when the second-order terms in δ are ignored.

In models I to III, horizontal derivatives are approximated using finite difference schemes applied on centered stencils of customized size with N_{sten} (choosing

from $3, 5, 7, 9$) nodes on a regular grid. By far, the problem has been discretized in the vertical direction using projection on a polynomial basis and in the horizontal direction using a finite difference approach. Eventually, the semi-analytical solution is established efficiently by solving a system of $(N_T + 1) \times \text{npx}$ (complex) linear equations on the $a_n(x_j)$ coefficients, for $j = 1, ..., \text{npx}$ and $n = 0, ..., N_T$. This is currently done using a L-U solver in the code.

3.2.2 Numerical implementation of mild-slope equations (in Premise)

The numerical implementation of the mild-slope equations (models IV-VI) is more straightforward compared to the Whispers3D semi-analytical models (models I-III). Since the elliptic mild-slope equations are simplifications from the full potential linear theory, the Laplace equation no longer needs to be solved. The mild-slope equations are solved by using a code called PREMISE (*Program Resolving the Elliptic MIld Slope Equation*), developed by M. Benoit. It is briefly introduced here.

a/ Numerical discretization and solution of the mild-slope models

We recall the F-P bottom profile of the present study $\tilde{h} = h - \delta$, with δ defined in Eq. (II.3.1). Due to the similarity of the various equations in models IV-VI, a general form of an elliptic equation for the interior nodes of the computational domain can be written as:

$$D(x)\Phi_{xx}(x) + A(x)\Phi_x(x) + B(x)\Phi(x) = 0, \tag{II.3.60}$$

where the coefficients $D(x)$, $A(x)$, $B(x)$ differ from one model to another. The coefficients in model IV (MSE, Eq. (II.3.11)) read:

$$D(x) = 1, \quad A(x) = (CC_g)_x/CC_g, \quad B(x) = k^2. \tag{II.3.61}$$

The coefficients in model V (EMSE, Eq. (II.3.17)) are:

$$D(x) = \left(1 - \frac{g\delta}{\bar{C}\bar{C}_g \cosh^2 \bar{k}h}\right), \quad A(x) = -\frac{g\delta_x}{\bar{C}\bar{C}_g \cosh^2 \bar{k}h}, \quad B(x) = \bar{k}^2. \tag{II.3.62}$$

The coefficients in model VI (MMSE, Eq. (II.3.18)) read:

$$D(x) = 1, \quad A(x) = \frac{(CC_g)_x}{CC_g}, \quad B(x) = k^2 + \frac{gr(\tilde{h})}{CC_g}, \tag{II.3.63}$$

where r is defined in Eq. (II.3.20). The coefficients in models IV and VI are evaluated at the actual bottom elevation $\tilde{h}$, whereas in model V, the coefficients which are evaluated using the constant mean depth h are marked with overbar signs. The nodes at two limits of the computational domain are governed by the

same radiation conditions (Eqs. (II.3.41) and (II.3.42)), as is used in Whispers3D semi-analytical model. Particularly, they are applied at the first two nodes nearest to the lateral boundaries.

The spatial derivatives are approximated using 3-node centered finite difference schemes, which leads to a tridiagonal system of linear equations on the nodal values of Φ. The linear system is complex-valued due to the lateral boundary conditions. It is solved efficiently with the so-called Thomas double-sweep algorithm.

b/ Treatment of bottom slope discontinuity

One particular aspect deserves additional discussion, namely the treatment of nodes where the bed slope is discontinuous (the bottom elevation itself being assumed to remain continuous in all cases considered here). Indeed, it was shown by Porter and Staziker (1995) that the smooth approximations to the free surface elevation obtained by using the long-standing mild-slope equation are not consistent with the continuity of mass flow at locations where the bed slope is discontinuous. In the F-P bathymetry setup, four connecting points between the flat bottom regions and two corrugated regions (at $x = x_1^s, x_1^e, x_2^s$ and x_2^e) exhibit discontinuous bottom gradient (as it is easily seen from the analytical expression Eq. (II.3.1)).

Four options have been implemented and compared in Premise for treating the discontinuity of $\tilde{h}_x$ and $\tilde{h}_{xx}$. They can be applied at any position $x = x_d$ where the bottom slope is discontinuous, this being detected by comparing the left and right first and second derivatives of $\tilde{h}_x$ provided as input data to the code at each node position, e.g. $\tilde{h}_x^-$ and $\tilde{h}_x^+$ for the first derivative (bottom slope):

i). No specific treatment is applied. Starting from the vector of water depth $\tilde{h}$ at nodal positions, the first- and second-order derivatives $\tilde{h}_x$ and $\tilde{h}_{xx}$ are evaluated directly by using 3-point centered finite-difference schemes.

ii). The slope is evaluated as $\tilde{h}_x = (\tilde{h}_x^+ + \tilde{h}_x^-)/2$ at all nodes, resulting in the input value where the slope is continuous (i.e. $\tilde{h}_x^+ = \tilde{h}_x^-$) and an average of the left and right slopes where it is discontinuous (with $\tilde{h}_x^+ = \lim_{x \to x_d^+} \tilde{h}_x(x)$ and $\tilde{h}_x^- = \lim_{x \to x_d^-} \tilde{h}_x(x)$). Where the slope is discontinuous, the second derivative (bottom curvature) is estimated as $\tilde{h}_{xx} = (\tilde{h}_x^+ - \tilde{h}_x^-)/\Delta x$. Otherwise, $\tilde{h}_{xx} = (\tilde{h}_{xx}^+ + \tilde{h}_{xx}^-)/2$ is used.

iii). A local polynomial smoothing is adopted to several nodes on each side of x_d. In the present study, three nodes, i.e.. the discontinuous node of h_x and the previous one and the following one, are affected. A fifth-order polynomial is used to approximate the local bathymetry, whose coefficients are obtained by matching the polynomial with the values of $\tilde{h}$, $\tilde{h}_x$ and $\tilde{h}_{xx}$ of the two ending points of the approximated bottom.

iv). The matching condition proposed by Porter and Staziker (1995) is adopted. This condition, which is referred to as the 'mass-conserving matching condition', ensures the continuity of mass flow at $x = x_d$, thus significantly improving the accuracy of the mild-slope type equations at discontinuity nodes. In this case the mild-slope equation is not written in a discretized form at x_d. Instead, the mass-conserving condition applied at $x = x_d$ requires:

$$\Phi(x_d^-) = \Phi(x_d^+), \tag{II.3.64}$$

$$u_1(x_d)\Phi(x_d)\left[\tilde{h}_x(x_d^+) - \tilde{h}_x(x_d^-)\right] + u_0(x_d)\left[\Phi_x(x_d^+) - \Phi_x(x_d^-)\right] = 0, \tag{II.3.65}$$

where u_0 and u_1 are defined in Eq. (II.3.19) and Eq. (II.3.21), respectively. With this condition, the value of $\tilde{h}_{xx}$ at the discontinuous point of $\tilde{h}_x$ is no longer used.

Note the same matching condition is used in models IV and VI following the recommendation of Porter and Staziker (1995). Currently, this option (iv) is not yet available in model V since additional analysis and tests of its validity are ongoing.

3.3 Convergence and validation tests of numerical models

In this section, we present a series of simulations designed to validate the numerical codes (both Premise and the semi-analytical versions of Whispers3D) and to study the convergence of their results with increasing the spatial resolutions (i.e. decreasing the grid size Δx for both codes, and increasing the value of N_T and N_{sten} for Whispers3D). First, in 3.3.1, the semi-analytical versions of Whispers3D (models I-III) is considered on the F-P resonance case setup. Then, in 3.3.2, the Premise solver for the mild-slope equation models (models IV-VI) is validated by simulating the interaction of waves with a submerged sill of parabolic shape. The convergence tests of the numerical parameters in both solvers have been conducted for F-P bathymetry setup.

3.3.1 Whispers3D semi-analytical models: convergence and validation tests

a/ Description of the simulated case

For the purpose of testing convergence and validation of the models I-III, we simulate the F-P resonance on the basis of the case shown in the figure 6 of Couston et al. (2015). The original setup is: $N_1 = 11$ ripples, $N_2 = 15$ ripples, $\theta_1 = \theta_2 = 0$, $k_b h = 1.64$, $\epsilon = d/h = 0.1$ and resonator length $L_r/L_b = 5.5$ (corresponding to $m = 5$ in Eq. (II.3.30)). The notations of the variables (already defined in Section (3.1)) and the sketch of the bathymetry are recalled in Fig. (II.3.1).

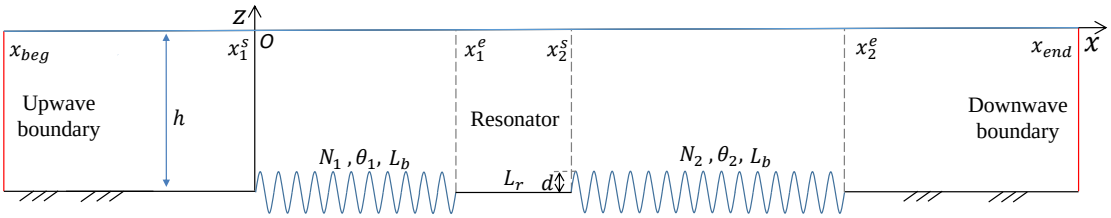

Figure II.3.1: Sketch of the bathymetry setup for F-P resonance.

In practice, we choose $L_b = 0.5$ m for the wavelength of the ripples, giving a theoretical Bragg resonance wavelength $L_B = 2L_b = 1$ m. To ensure the convergence of the simulations, we adopt the same configuration as in Couston et al. (2015), but choose a very challenging $\epsilon = 0.5$ instead of 0.1 as was used in their paper. The tested incident wave-number k varies in the vicinity of the resonance wave-number $k/k_B \in [0.7, 1.3]$ with an interval $\Delta k/k_B = 0.000075$. This corresponds to $8,001$ runs of the case, each of which should take more than $10,000$ wave periods to converge in the time dependent simulations with Whispers3D (i.e. more than 48 h CPU time). However, it takes less than 1 s for each run with the current models I-III using the semi-analytical version of the code.

b/ Convergence test of numerical parameters

In Whispers3D semi-analytical models I-III, the parameters to be tested include the number of terms N_T in the approximation of the velocity potential with Chebyshev polynomials, the stencil size N_{sten} of the finite difference scheme, and the number of nodes in space Δx (npx nodes for the given length of computational domain). The computational domain starts at $x_{beg} = -3$ m (3 m before the first patch of ripples) and ends at $x_{end} = 18.75$ m (3 m after the end of the second patch of ripples). The first patch is $N_1 L_b = 5.5$ m long and the second one $N_2 L_b = 7.5$ m long. Between the two patches, the length of the resonator is 2.75 m. The total length of the computational domain is thus 21.75 m. The list of tested parameters is shown in Table (II.3.1).

The results are shown in Fig. (II.3.2) to (II.3.4) considering first model I. In these figures, the maximum normalized amplitude within the resonator, defined as enhancement factor E^{FP}, is plotted using a logarithmic scale. Four panels are presented: panel (a) shows the overall range of tested incident wave-number; panel (b) considers the local range of incident wave-number near the most pronounced peak of E^{FP}; panel (c) shows the local range near the secondary peak of E^{FP}; panel (d) shows a range where no F-P resonance manifests. It is observed in the first two panels that the results of different choices of parameters make differences. Comparing the last two panels, we see that the results of all tested parameters are superimposed.

In Fig. (II.3.2), choosing $N_{sten} = 5, 7$ or 9 (for a fixed number of nodes npx = 2785 and a fixed value $N_T = 7$) makes nearly no differences even in the vicinity of the F-P resonance. Thus, a stencil size $N_{sten} = 5$ is selected for the sequel. Fig. (II.3.3) shows that, near the two peaks of enhancement factor, the results of $N_T = 5$ differ from the other two curves ($N_T = 7$ and 9). The results of $N_T = 7$ and $N_T = 9$ cannot be distinguished visually for all incident wave-numbers. Thus, the convergence of N_T is achieved for $N_T = 7$. In Fig. (II.3.4), we see that the three choices of npx (or Δx) differ from each other near the two peaks of E^{FP}. In terms of the magnitude of the two peaks of E^{FP} and the corresponding incident wave-numbers, the simulated results with the three values of npx show similar results. For the efficiency of conducting a large number of tests, the discretization corresponding to npx = 2785 is thus chosen.

The same convergence tests were conducted for models III in terms of N_{sten}, N_T and npx. It was observed that the numerical parameters converged to the same values in Whispers3D models with second-order approximated BBC, namely $N_{sten} = 5$, and npx = 2785. The only exception is the N_T parameter in model III. In model III, a second-order term in δ is included which may be more demanding in the representation of potential. In Fig. (II.3.5), it is shown that for $N_T = 5$ the unconverged results distinguish from the converged results not only in the magnitude of two peaks of E^{FP}, but also in the corresponding incident wave-number. More pronounced wave-number downshift takes place for low values of N_T case in model III. The selected value for model I, $N_T = 7$ is not large enough for model III with second-order BBC. In this model, the convergence is achieved for $N_T = 9$. As will be discussed later, the simulations with model II revealed to be somewhat more delicate. We decided to conduct simulations of model II with the same numerical parameters as in model III.

From the convergence tests for three Whispers3D models, it is noticed that, for

Table II.3.1: List of numerical parameters adopted during the convergence tests for N_{sten}, N_T and npx of Whispers3D semi-analytical model

Test	N_T	N_{sten}	npx	Δx (m)	$L_B/\Delta x$
1	7	5	2785	0.0078125	128
2	7	7	2785	0.0078125	128
3	7	9	2785	0.0078125	128
4	5	5	2785	0.0078125	128
5	7	5	2785	0.0078125	128
6	9	5	2785	0.0078125	128
7	7	5	1393	0.015625	64
8	7	5	2785	0.0078125	128
9	7	5	5569	0.00390625	256

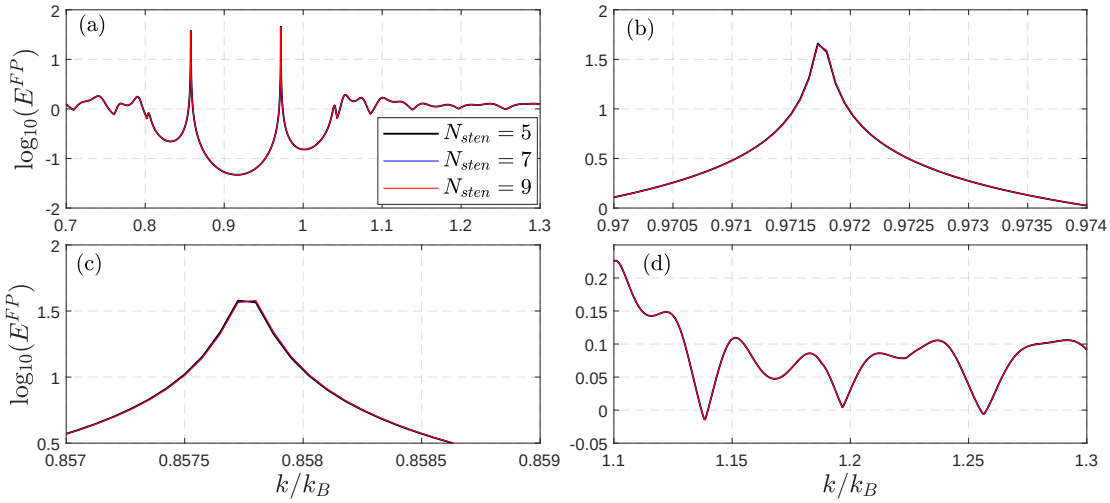

Figure II.3.2: Convergence test of model I with stencil size N_{sten}, with the same parameters $N_T = 7$ and npx = 2785. Panel (a) shows the full tested range of incident wave-number, (b) local range near the first peak of E^{FP}, (c) local range near the second peak of E^{FP}, (d) local range with no resonance.

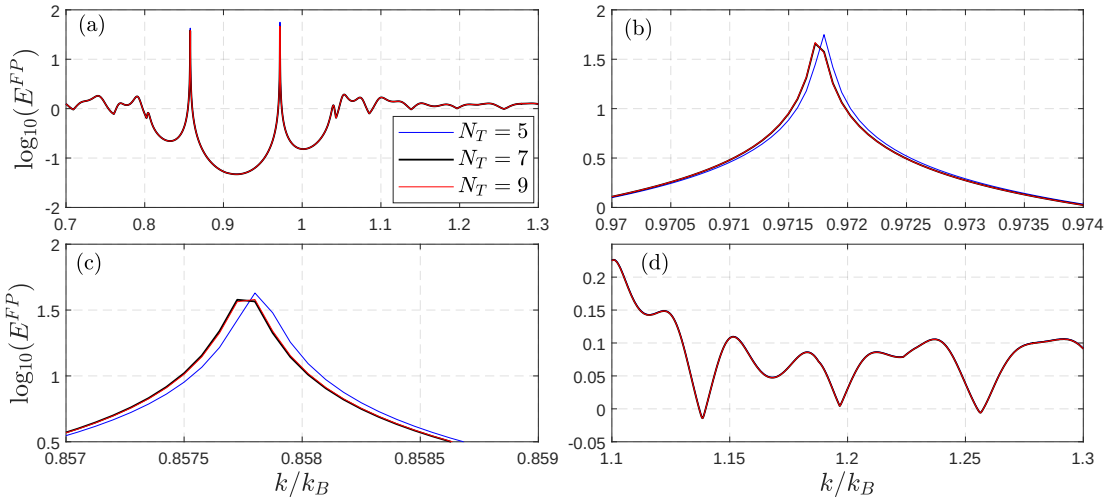

Figure II.3.3: Convergence test of model I with number of Chebyshev polynomial terms N_T for the representation of potential, with the same parameters $N_{sten} = 5$ and npx = 2785. Panel (a) shows the full tested range of incident wave-number, (b) local range near the first peak of E^{FP}, (c) local range near the second peak of E^{FP}, (d) local range with no resonance.

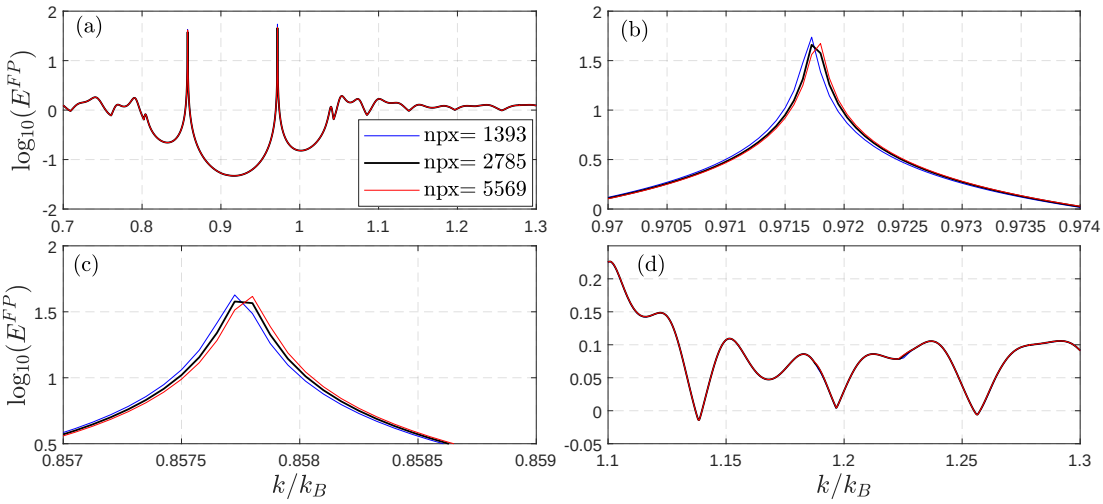

Figure II.3.4: Convergence test of model I with number of nodes in space npx, with the same parameters $N_{sten} = 5$ and $N_T = 7$. Panel (a) shows the full tested range of incident wave-number, (b) local range near the first peak of E^{FP}, (c) local range near the second peak of E^{FP}, (d) local range with no resonance.

the regions of k/k_B away from the resonance, the differences of E^{FP} between different values of numerical parameters are smaller than those near the resonance. Such observations are logical since the resonance is more demanding in the accuracy of the models due to very large amplification of the waves in the resonator. For this reason, the convergence tests should focus on the region near the resonance, which differs from one model to another.

c/ Validation of semi-analytical models by comparing with time-dependent Whispers3D results

As a further demonstration of the validity of Whispers3D semi-analytical models, the simulations of the cases $\epsilon = 0.2$ with varying incident wave-number presented in Zhang and Benoit (2019) are done here with models I and II. We recall that model I corresponds to the time-dependent Whispers3D model 'system A' in Zhang and Benoit (2019), while model II corresponds to the time-dependent Whispers3D model 'system B'. The bottom setup in the PRE paper is similar to what we consider here, except that two additional 3-meter-long relaxation zones are set in the time-dependent simulations on each side of the computational domain shown in Fig. (II.3.1). The calibrated values of numerical parameters $N_{sten} = 5$, $N_T = 7$, npx = 2785 are adopted in the semi-analytical simulations.

In Fig. (II.3.6)(a) the comparison between the time-dependent simulation of Whispers3D and semi-analytical solution with the exact BBC is shown, and in

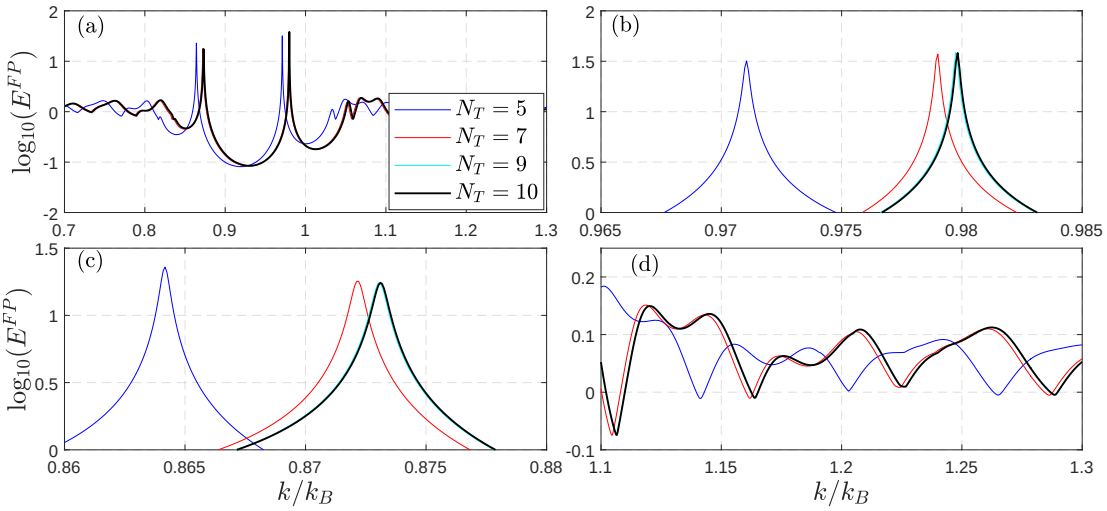

Figure II.3.5: Convergence test of model III with the number of Chebyshev polynomial terms N_T for the representation of potential, with the same parameters $N_{sten} = 5$ and npx = 2785. Panel (a) shows the tested range of incident wave-number, (b) local range near the first peak of E^{FP}, (c) local range near the second peak of E^{FP}, (d) local range with no resonance.

panel (b) the same comparison for the first-order BBC is shown. It can be observed that the enhancement factors E^{FP} within the resonator area of the time-dependent simulations with Whispers3D (so-called system A and system B in Zhang and Benoit (2019)) are well reproduced by the semi-analytical solution of models I and II. This level of agreement of simulations with either the exact BBC in panel (a) or the first-order approximated BBC in panel (b) validates the computations with the semi-analytical model on one hand. Furthermore, on the other hand, it indicates that the results of the previous study in Zhang and Benoit (2019) have reached a converged periodic state. These figures also show the benefits brought by the semi-analytical version of Whispers3D: while a limited number of simulations (about thirty) were done with the time-dependent version of the code in Zhang and Benoit (2019) (each of them taking several hours of CPU time), here no less than 8,001 runs are available within a couple of hours using the semi-analytical version of the code!

3.3.2 Mild-slope models: convergence and validation tests

a/ Description of the validation case: a parabolic hump

In Porter and Staziker (1995), the numerical solution to the MMSE was compared with the full linear solution for both Booij's test problem and a parabolic hump

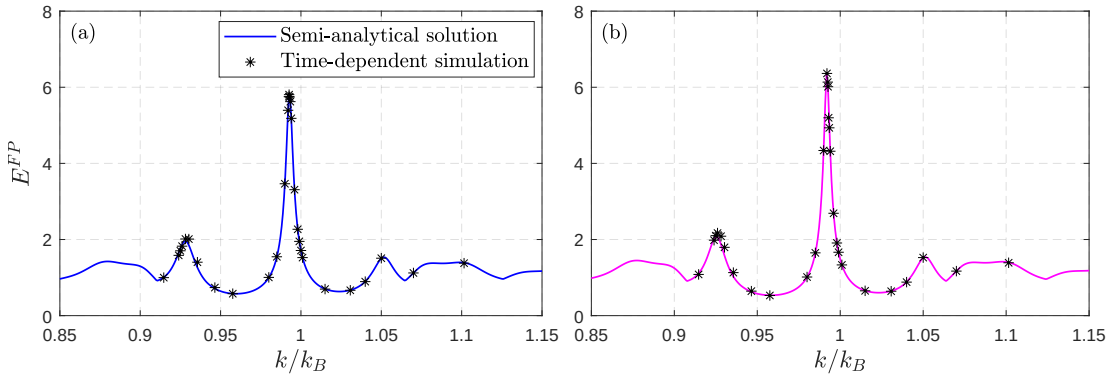

Figure II.3.6: Validation of the semi-analytical model by comparing with time-dependent simulations of the case $\epsilon = 0.2$. Panel (a) shows the comparison between model I (i.e. the semi-analytical solutions of Whispers3D with the exact BBC) and the corresponding time-dependent simulation results of the 'system A' defined in Zhang and Benoit (2019), (b) shows the comparison between model II (i.e. the semi-analytical solutions of Whispers3D with the first-order approximate BBC) and the corresponding time-dependent simulation results of the 'system B' defined in Zhang and Benoit (2019).

test problem. Liu et al. (2012) validated their analytical solution of the MMSE by comparing their results of the parabolic hump case to the simulation results of Porter and Staziker (1995). As the Premise code for numerical models IV-VI has not been reported before, here we examine the validity of Premise code by considering the same parabolic hump topography and comparing our results with those from Porter and Staziker (1995) and Liu et al. (2012).

The water depth function of a symmetric parabolic hump is:

$$h(x) = \begin{cases} h_0, & x < x_0 - \dfrac{L_{hump}}{2}, \\ h_0 + h_{hump}\left[\left(\dfrac{x - x_0}{L_{hump}/2}\right)^2 - 1\right], & x_0 - \dfrac{L_{hump}}{2} \leq x \leq x_0 + \dfrac{L_{hump}}{2}, \\ h_0, & x > x_0 + \dfrac{L_{hump}}{2}, \end{cases} \tag{II.3.66}$$

where h_{hump} is the 'height' of the hump, and L_{hump} denotes the length of the hump, h_0 denotes the water depth of the flat regions, and x_0 is the location where the hump elevation is maximum. The sketch of the tested hump bottom is shown in Fig. (II.3.7). Following Porter and Staziker (1995), a dimensionless parameter $W_s = \omega^2 L_{hump}/g$ is used to normalize the hump length L_{hump} with the deep water wave-number of the incident waves $omega^2/g$. In Porter and Staziker (1995), the hump height is set to $h_{hump} = h_0/2$ and the incident wave angular frequency is

fixed by setting $\omega^2 h_0/g = 1$. k denotes the corresponding incident wave-number in water depth h_0, and L the corresponding wavelength. L_{hump} is varying to show the variation of reflection coefficient C_r against W_s. In Porter and Staziker (1995) and Liu et al. (2012), W_s varies in the range $[0.5, 8]$, which corresponds to, choosing $h_0 = 6$ m, L_{hump} varying from 3 m to 48 m. For that water depth, the incident wavelength (from the dispersion relation of linear waves) is $L \approx 31.42$ m, so that $kh_0 \approx 1.20$.

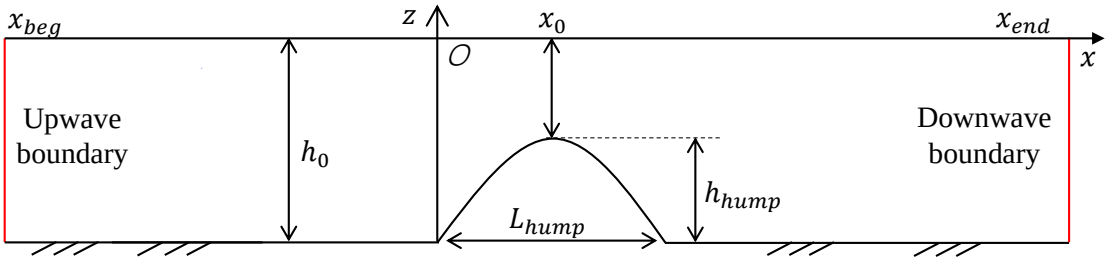

Figure II.3.7: Sketch of a parabolic hump bottom setup.

b/ Validation test of numerical models IV-VI

In Premise, two main numerical parameters or options need to be tested, namely (i) the choice of treatment of the nodes where the derivative h_x is not continuous, and (ii) the spatial resolution of the mesh (Δx) for the evaluation of spatial derivatives using the finite difference scheme. Regarding the former item, four options are currently available for MSE (model IV) and MMSE (model VI) and three for EMSE (model V). The convergence tests of Δx for the parabolic hump bottom case have been conducted and are not shown here: the converged value is $\Delta x = 0.01$ m, which corresponds to $\min(L_{hump})/300$ and approximately $L/3142$.

The reference data of the simulations of the parabolic hump case were digitized from Fig. 3 in Liu et al. (2012) and Fig. 3 in Porter and Staziker (1995), including the results of MSE, MMSE, and full linear simulations. Only the cases with the mass conservation condition were digitized. In Fig. (II.3.8), the simulation results of models IV to VI on the parabolic hump case are shown and compared with the digitized results.

It is observed in Fig. (II.3.8)(a) that the results of model IV (MSE) with options 1, 2 and 3 are superimposed and predict a low value of reflection coefficient C_r (about 0.07 at maximum). Meanwhile, option 4 is in excellent agreement with the calculation of Porter and Staziker (1995) after considering the mass-conserving matching condition. In Fig. (II.3.8)(b), the results of the EMSE (model V) are visually indistinguishable for all three options adopted. The simulation results of MMSE (model VI) with different treatment options of the bottom derivative

discontinuity are shown in Fig. (II.3.8)(c). It is noticed that the results of MMSE with options 1, 2 and 4 are superimposed and again in excellent agreement with the calculation of Porter and Staziker (1995). The simulation with option 3 is however distinct from the three other options. It is anticipated that this is due to the terms proportional to h_{xx} and h_x^2 included in MMSE. Thus, the MMSE model is more sensitive to the local change of bathymetry, especially for the cases with small values of W_s (shorter length of the hump) and associated larger magnitudes of derivatives.

Finally, in Fig. (II.3.8)(d), the comparison between the results of Premise code and the computations of Porter and Staziker (1995) is shown, using option 4 for model IV and VI, and option 1 for model V. The results are very similar for both MSE (model IV) and MMSE (model VI). The simulations of models IV-VI with Premise code are therefore validated.

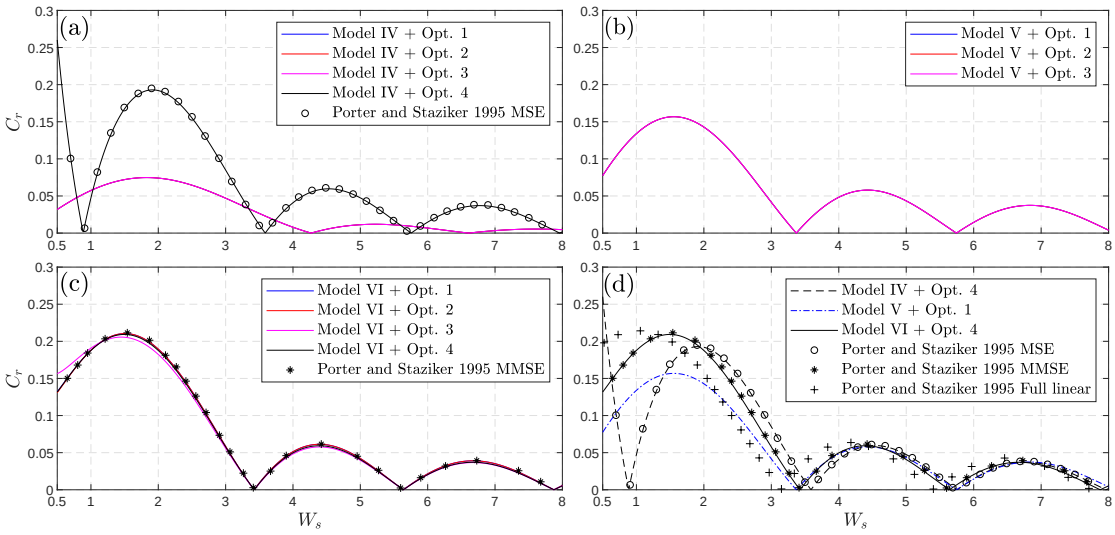

Figure II.3.8: Validation tests of models IV-VI in Premise code with four options of treating discontinuity points of bottom derivative for the parabolic hump bathymetry case. The simulation results of MSE and MMSE models in Porter and Staziker (1995) are digitized and superimposed with the corresponding results of Premise.

c/ Convergence tests of Δx of models IV-VI in F-P resonance case

The models IV-VI computed using Premise code have been validated by the above-mentioned parabolic hump case. Before being used to simulate the F-P resonance case, it is necessary to conduct again convergence tests using the same bathymetry setup (shown in Fig. (II.3.1)) in subsection (3.3.1). Because the F-P resonance case is very sensitive, especially for the cases with large values of ϵ, small differences

could result in significant differences in terms of E^{FP}. In the tested F-P resonance bathymetry, the total length of the computation domain is 21.75 m, the tested relative ripple amplitude is $\epsilon = 0.4$. The incident wave-number is set to $k = 0.997k_B$.

The convergence tests results are shown in Fig. (II.3.9) as a function of npx. In model IV (MSE), the simulation results with options 1-3 converge to the same level for npx larger than about $10,000$. Due to the imposed matching condition, the simulation results converge (relatively slowly) to a different level when using option 4 for npx $> 20,000$. In model V (EMSE), the simulation results with options 1-3 converge to the a certain level which is different from the ones of model IV. For model VI (MMSE), the simulation results with options 1, 2, 4 converge to the same level. A large number of nodes (about 10^6) is however required for MMSE with option 4 to converge. As in the parabolic hump case, using option 3 leads to slightly different results.

Based on these convergence tests, it is decided to use model IV + option 4, model V + option 1, and model VI + option 1 with $\Delta x = 0.001$ m (equivalent to npx $= 21,751$ and $L_B/1000$) for further investigation of the wave-number downshift effect of F-P resonance.

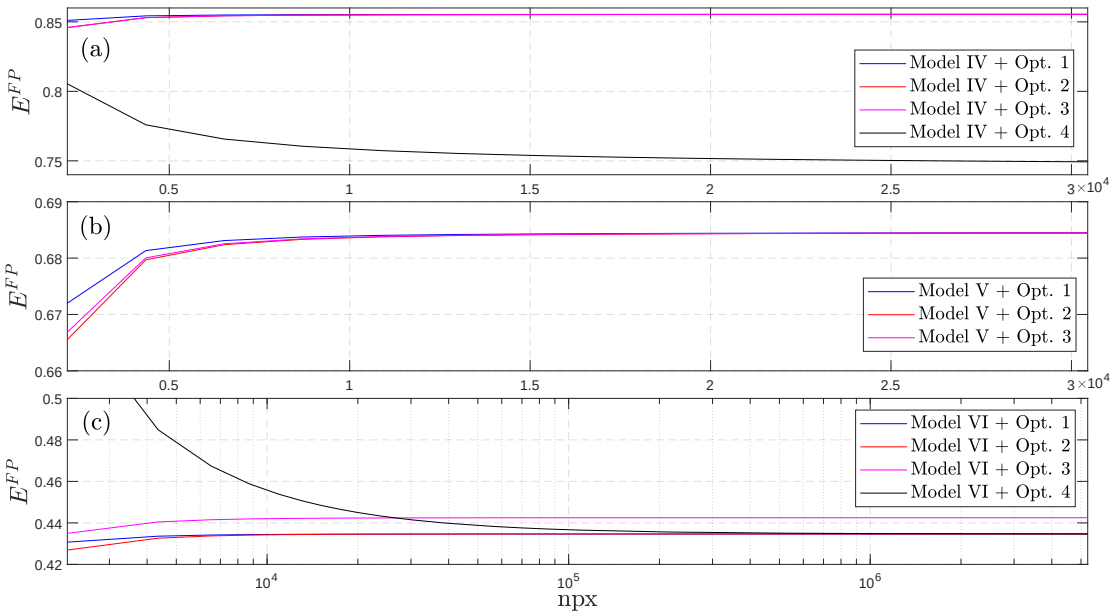

Figure II.3.9: Convergence tests of models IV-VI with npx (Δx) considering four options of treating the discontinuity points of bottom derivative in a F-P resonance bathymetry case. In this case, the incident wave-number is $k = 0.997k_B$.

3.4 Investigation of wave-number downshift in the Fabry-Perot resonance case within seven models

In this section, the F-P resonance is simulated within the seven linear models introduced in Section (3.1). The bottom setup is similar to the one used during the previously presented convergence tests. We set the first patch with $N_1 = 11$ ripples, the second one with $N_2 = 15$ ripples, $\theta_1 = \theta_2 = 0$, $k_b h = 1.64$, resonator length $L_r/L_b = 5.5$, and choose again $L_b = 0.5$ m (corresponding to a theoretical Bragg wavelength $L_B = 1$ m based on ALAS). For the purpose of investigation of wave-number downshift effects for different ripple amplitudes, we consider varying $\epsilon = d/h \in [0.05, 0.5]$ with an interval 0.01. For each value of ϵ, the tested incident wave-number k varies in the vicinity of the resonance wave-number $k/k_B \in [0.7, 1.3]$ with an interval $\Delta k/k_B = 0.00015$, which corresponds to $4,001$ runs. In total, up to $184,046$ runs are thus simulated for each model.

3.4.1 Model VII: ALAS prediction of the F-P resonance case

As a reference, the ALAS (model VII) will be compared with both Whispers3D semi-analytical solutions (models I-III) and mild-slope equations with different approximations (models IV-VI). Model VII is first analyzed before we introduce the results of other more complicated models. It corresponds to the lowest order solution of the problem, with the first-order approximated BBC in terms of δ and keeping only the first-order free surface potential components which lead to resonance. The wave-number is evaluated using the constant mean water depth and does not vary over the corrugated regions (patches of ripples). The results of ALAS are shown in a colormap of Fig. (II.3.10) where the enhancement factor E^{FP} within the resonator is evaluated as a function of ϵ and k/k_B. It is predicted by the ALAS that the resonance conditions is always $k = k_B$ whatever the ripple amplitude ϵ. For a given ϵ, the evolution of E^{FP} is symmetric with respect to k/k_B. It means that the wave-number downshift is not captured in model VII.

The region where significant E^{FP} is achieved for k/k_B close to 1 is called the primary resonance tongue. The secondary resonance tongue refers to the two stripes which start from $k/k_B \approx 0.9$ and ≈ 1.1 for $\epsilon = 0.05$. It is predicted by ALAS that the primary resonance tongue gets narrower as the ripple amplitude increases, and the secondary resonance tongues depart from the primary resonance tongue as ϵ increases. The narrowness of the primary tongue indicates that the F-P resonance condition becomes more and more strict as ϵ increases. The two blue zones beside $k/k_B = 1$ indicate that the wave amplitude within the resonator is close to 0 when no F-P resonance manifests, and the incident waves are nearly fully reflected by the first patch of ripples. It can be noted that slight deviations from the resonance condition for the incident wave-number result in significant differences in terms of E^{FP}. For instance, for $\epsilon = 0.5$, choosing the incident wave-

number $k/k_B = 0.95$ or 1.05 (i.e. a variation of 5% with respect to the resonant wave-number) provokes a strong decrease of E^{FP} from 57.56 at the resonance to about 0.47.

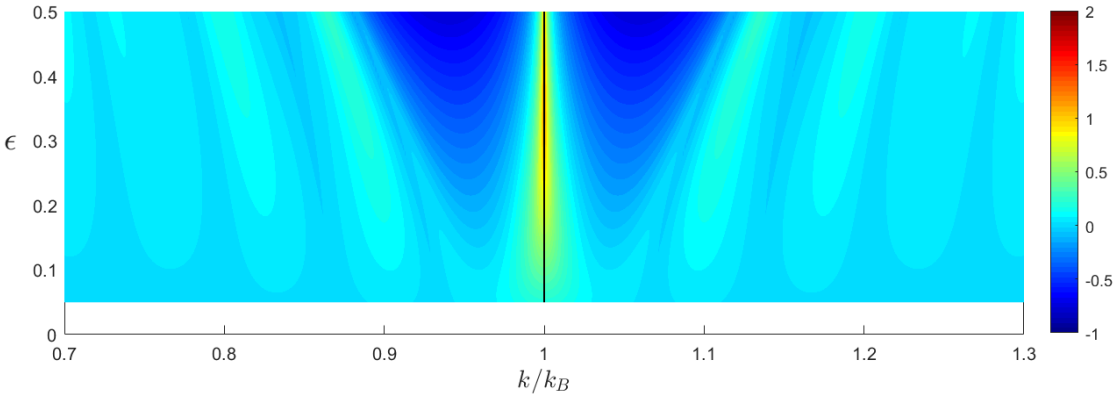

Figure II.3.10: Enhancement factor E^{FP} predicted by the ALAS of the F-P resonance case with varying ϵ and normalized incident wave-number k/k_B. The color scale represents $\log_{10}(\mathrm{E}^{FP})$. The vertical solid line corresponds to $k/k_B = 1$.

The evolution of E^{FP} as a function of ϵ predicted by ALAS is shown in Fig. (II.3.11) when the resonance condition is met (i.e. $k = k_B$). The enhancement factor E^{FP} increases exponentially as ϵ increases. When the bottom is flat $\epsilon = 0$, $E^{FP} = 1$ represents progressive waves. As $\epsilon = 0$ increases to 0.5, the amplification of the incident wave amplitude reaches 57.56! In the following, it will be shown, comparing several models, how different approximations on the BBC affect the F-P resonance condition and the maximum enhancement factor reached.

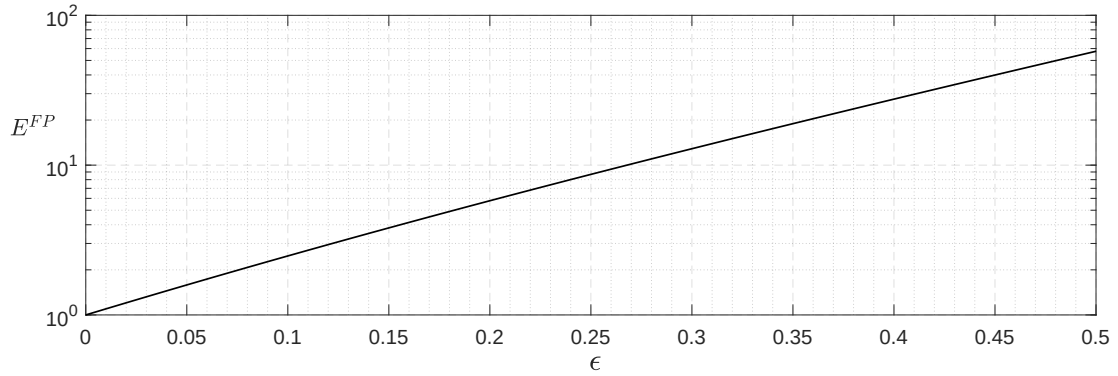

Figure II.3.11: Maximum enhancement factor E^{FP} predicted by the ALAS (model VII) of the F-P resonance case with varying ϵ and $k = k_B$ in logarithmic scale.

3.4.2 Fabry-Perot resonance simulations within models I-III

The F-P resonance cases with the configurations introduced at the beginning of this section have been simulated with Whispers3D semi-analytical code for models I-III. In each model, the numerical parameters (N_T, N_{sten}, Δx) were adopted on the basis of the convergence tests. In Fig. (II.3.12), the colormaps of the enhancement factor E^{FP} within the resonator predicted by models I-III are shown. The prediction of ALAS (model I) is also given in panel Fig. (II.3.12)(a) as reference. In panel Fig. (II.3.12)(b), it is evident that model II fails in describing the F-P resonance when ϵ is relatively large. Visually, poor results appear approximately for $\epsilon > 0.25$. The investigation of the reason for such unsatisfactory results is ongoing work. While testing the numerical parameters for model II, convergence was achieved for $N_T = 9$. Whereas, the convergence was never achieved for npx. For a larger number of nodes (smaller Δx), the results deteriorated. The effects of choosing different N_{sten} is related to the choice of npx. It is suspected that the linear system in model II could become ill-conditioned for larger values of ϵ, the parameters of the solver (which were set identical for all simulations) should probably be tuned. However, we believe that the results of model II for $\epsilon \leq 0.25$ remain reliable since in this range the general pattern of the colormap is similar to that of other models.

Hereafter, model II is temporarily excluded in the further discussion of wave-number downshift for large values of ϵ. In panel Fig. (II.3.12)(c) and (d), it is observed that the semi-analytical solutions are well resolved in models I and III. In these two models, the resonances areas (where significant enhancement factor is achieved) take place for an incident wave-number distinct from the ALAS prediction $k = k_B$. The wave-number downshift takes place. The degree of the downshift increases as the relative ripple amplitude ϵ increases. Furthermore, the degree of the downshift magnitude in model III is slightly more pronounced than that in model II. It indicates that the effects resulting from third- or higher-order BBC play a role. The secondary resonance tongue is clearly asymmetric with respect to $k = k_B$, not only in terms of incident wave-number but also in terms of magnitude of the enhancement factor. Again, the degree of asymmetry of the secondary resonance tongue is more pronounced in model I.

In order to demonstrate the degree of wave-number downshift and the magnitude of E^{FP} in a more precise manner. 401 additional simulations for each value of ϵ have been conducted in the wave-number range $k/k_B \in [X - 0.0025, X + 0.0025]$ in which X denotes the downshifted F-P condition detected in the previous simulations. The discretization of wave-number $\Delta k/k_B$ decreases to 1.25×10^{-5}. In Fig. (II.3.13), the detected resonance wave-numbers corresponding to the maximum values of E^{FP} are shown in panel (a), and the maximum values of enhancement factor E^{FP} are shown in panel (b), both vary as a function ϵ. In panel (a), it is seen that, the downshift decelerates for large ϵ in model III (blue curve). This

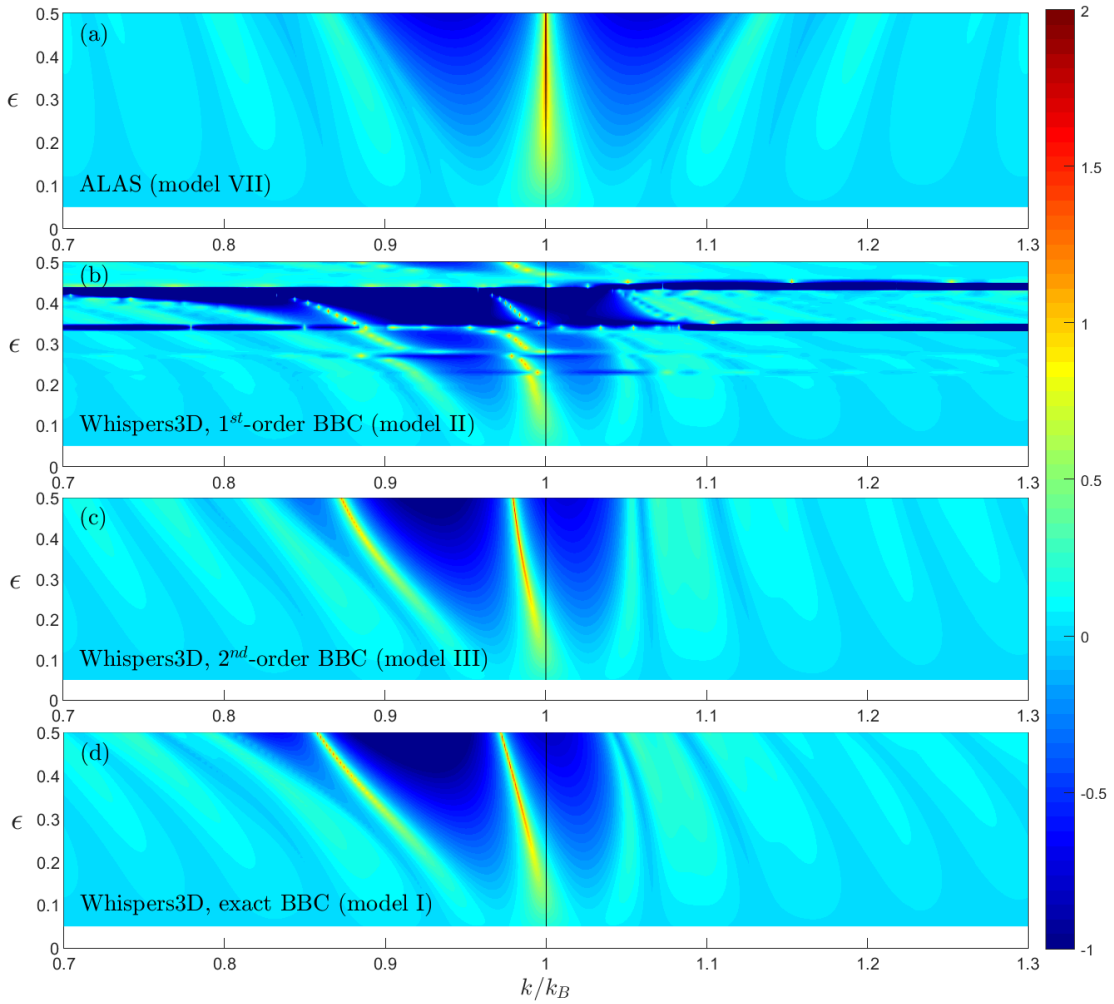

Figure II.3.12: Enhancement factor E^{FP} predicted by models I-III, VII of the F-P resonance case with varying ϵ and normalized incident wave-number k/k_B. The color scale represents $\log_{10}(\mathrm{E}^{FP})$. The vertical solid line corresponds to $k/k_B = 1$.

effect could be related to the higher-order BBC effects which are not included in model III. In panel (b), we note that the prediction of ALAS is in very good agreement with the simulation of model I in which the exact BBC was adopted. For $\epsilon = 0.5$, the enhancement factor in model VII is about 57.56, and in model I 56.3. Meanwhile, model III predicts a lower enhancement value of about 38.51 for $\epsilon = 0.5$. The close match of the maximum values of the enhancement factor between model VII (ALAT) and model I (full linear solution with exact BBC), already noted in Zhang and Benoit (2019), has to be stressed as it was not implied a priori due to several assumptions made while deriving the ALAS solution (and

recalling in addition that the ALAS fails in predicting the wave-number downshift effect).

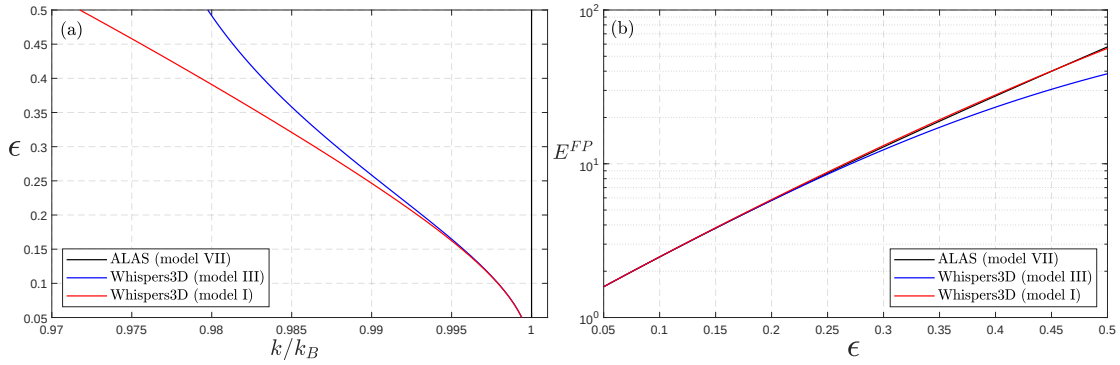

Figure II.3.13: The shifted F-P resonance condition (panel (a)), and the corresponding maximum enhancement factor (panel (b)) predicted by models I, III and VII. In panel (b), the enhancement is shown in logarithmic scale.

3.4.3 Fabry-Perot resonance simulations within models IV-VI

The F-P resonance cases with the same configuration are then simulated within models IV-VI. The colormap of the enhancement factor from the four models are shown in Fig. (II.3.14).

By and large, the wave-number downshift effect can be described by all three mild-slope equations. Even the classical MSE (model IV) shown in Fig. (II.3.14)(b), which is considered not applicable for Bragg resonance case, is able to qualitatively describe the shifted primary and even the sub-resonance tongues. The EMSE and MMSE models show similar results. Compared to model IV, The enhancement factors are smaller for the incident wave number k/k_B lying in the range between the primary and the secondary resonance tongues, i.e. larger blue areas manifest in models V and VI. The shape of the sub-resonance tongues are very similar in models V and VI.

In Fig. (II.3.15), the shifted resonance conditions and the corresponding enhancement factors achieved in such conditions within models IV-VI are shown. The results are compared with ALAS prediction (model VII) too. It is observed in Fig. (II.3.15)(a), the classical MSE with the improvement of mass-conserving matching condition predicts the most pronounced wave-number downshift compared to the other two mild-slope equations. Whereas, in panel (b), the MSE model fails in predicting the magnitude of the enhancement factor E^{FP}. Both models V and VI predict higher E^{FP} than the ALAS. For example, in the case with largest $\epsilon = 0.5$, $E^{FP} = 17.77$ is achieved in model IV (MSE), 57.56 in model VII (ALAS), 70.63 in model VI, and 85.31 in model V.

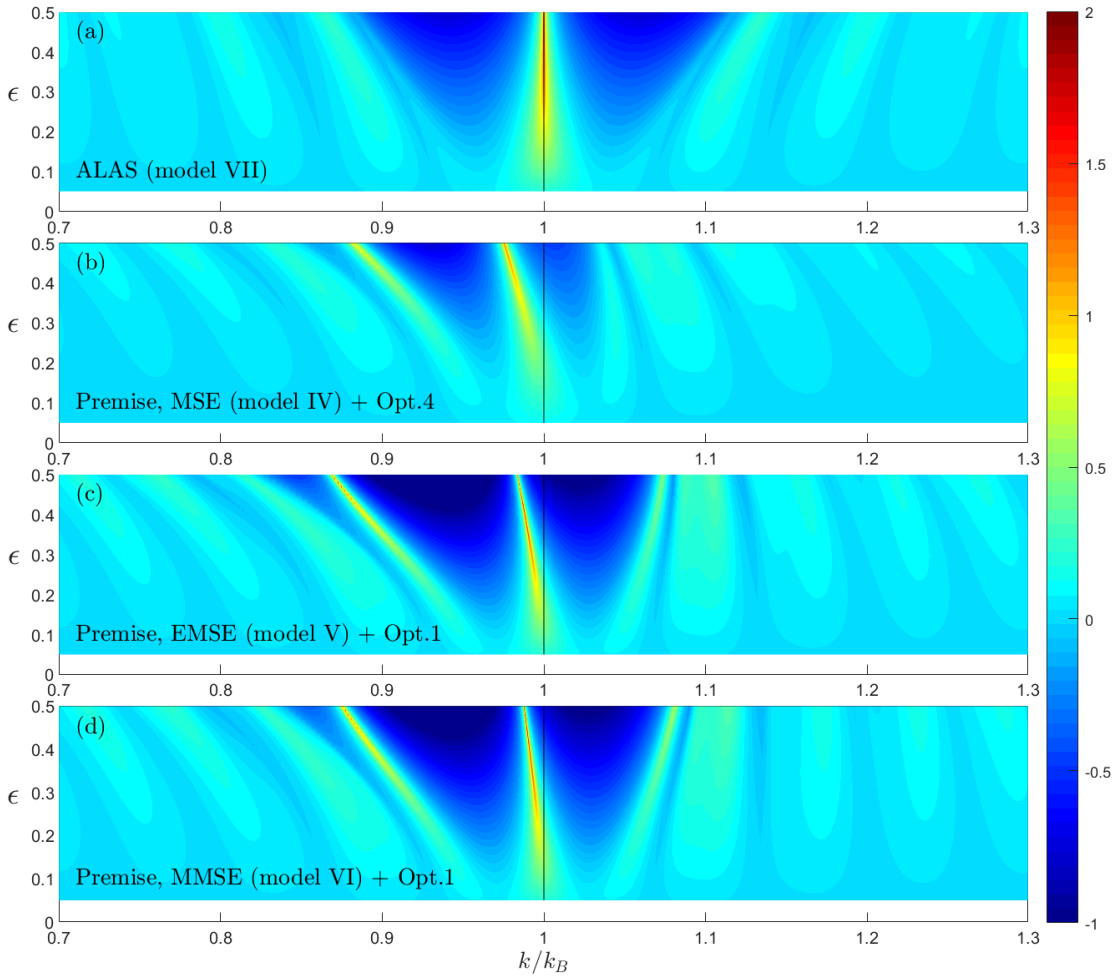

Figure II.3.14: Enhancement factor E^{FP} predicted by models IV-VII of the F-P resonance case with varying ϵ and normalized incident wave-number k/k_B. The color scale represents $\log_{10}(\mathrm{E}^{FP})$. The vertical solid line corresponds to $k/k_B = 1$.

To have a sense of the differences between all the models considered here, the F-P condition and the corresponding E^{FP} of all models I-VII are plotted in Fig. (II.3.16). Taking the results of model I with exact BBC adopted as the benchmark, we observe that model IV predicts the closest F-P resonance condition for large value of ϵ but the worst corresponding enhancement factor for all ϵ considered. In terms of E^{FP}, as already noted, it is the ALAS prediction which agrees surprisingly well the results of model I. As the relative ripple amplitude decreases, the resonance condition tends to $k = k_B$ and E^{FP} tend to 1 for all models.

It has been pointed out by Liu and Yue (1998) that the wave-number downshift

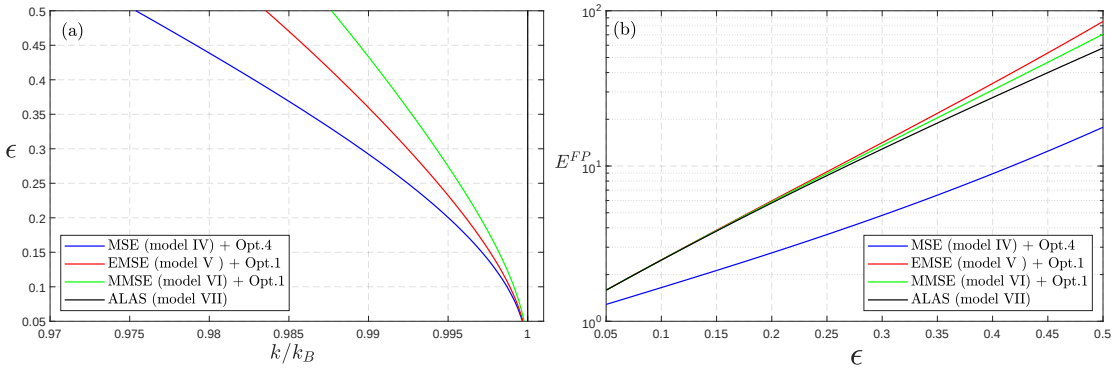

Figure II.3.15: The shifted F-P resonance condition (panel (a)), and the corresponding maximum enhancement factor (panel (b)) predicted by models IV-VII. In panel (b), the enhancement is shown in logarithmic scale.

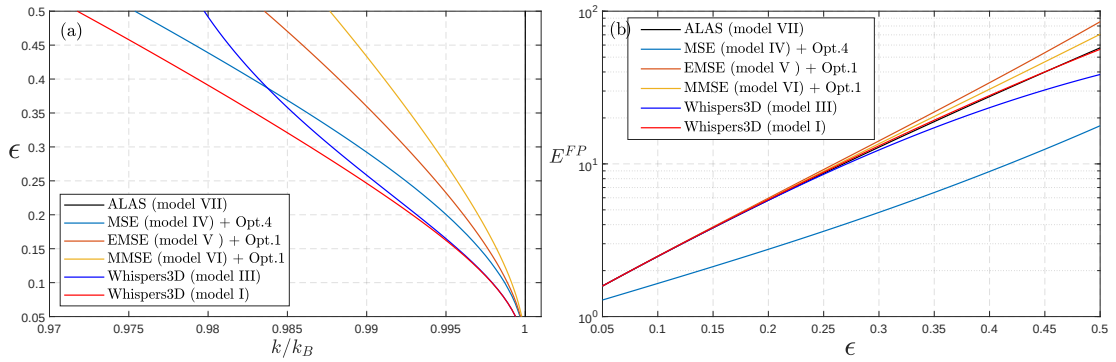

Figure II.3.16: The shifted F-P resonance condition (panel (a)), and the corresponding maximum enhancement factor (panel (b)) predicted by all models I-VII. In panel (b), the enhancement is shown in logarithmic scale.

is related to wave-number varying as a function of local water depth. By using an expansion of the local water depth about the mean water depth level, they showed that averaged wave-number over the corrugated area is larger than the wave-number corresponding to the mean water depth. The differences become more and more significant as ϵ increases. Therefore, a smaller incident wave-number (downshift) is needed to compensate the difference. Models I-VI shown in this part all consider the local wave-number (in model V, it appears in the coefficient proportional to δ). Our results show that, even with the wave-number evaluated considering the local water depth, the degree of downshift is still different among the various models due to different approximations made regarding the BBC.

Chapter 4

Conclusion and outlook

4.1 Summary of findings and conclusions

In this part, we discussed the Bragg scattering problem for water waves in the linear framework. The considered scenario is a variation of the Class I Bragg resonance (some researchers consider it as Class I_2 resonance), the so-called Fabry-Perot resonance. It happens when waves propagate over two patches of ripples on an otherwise flat bottom. It has been recently studied theoretically for water waves by Couston et al. (2015) using an asymptotic method at the lowest order (ALAS). The ALAS predicts that, when the resonance conditions are met, the standing wave amplitudes over the flat region between two patches of ripples (the so-called resonator) increase exponentially with the relative ripple amplitude ϵ. This particular situation of wave-bottom interaction is therefore a possible mechanism explaining the formation of large waves in coastal areas presenting this shape of bottom configuration.

Based on ALAS theoretical analysis, the F-P resonance condition consists of two aspects: the wave-number of bottom ripples being exactly twice than that of the incident wave-number and a particular length of resonator with respect to the incident wavelength. The objective of this part was to investigate the effects of different approximated BBCs and modeling assumptions on the manifestation of the F-P resonance.

The main findings of this part have been reported in a journal paper (Zhang and Benoit, 2019), in which simulations were performed using Whispers3D model with both exact and first-order approximated BBC. Via testing $\epsilon = 0.05$, 0.1, 0.2, and 0.4, it was found that the resonance did not manifest for the theoretical incident Bragg wave-number $k_B = k_b/2$ in the cases with $\epsilon > 0.1$. Instead, the F-P resonance takes place with a slightly smaller incident wave-number. This wave-number downshift, which has been reported by many authors for Class I and II Bragg resonance cases, plays a much more significant role in the F-P setup. This is due to the fact that as ϵ increases, the range of incident wave-numbers prone to

F-P resonance becomes extremely narrow. Slight deviations from the resonance wave-number could result in significant differences in the enhancement achieved within the resonator. The results of Whispers3D with exact BBC (called system A in the above paper) and first-order approximated BBC (system B) showed similar patterns of the evolution of enhancement factor E^{FP}, reflection and transmission coefficients R^{FP} and T^{FP} as the incident wave-number was varying in the primary resonance tongue.

To further demonstrate the wave-number downshift effect in larger ranges of ϵ and k/k_B, more simulations have been conducted in a second step and are shown as supplementary materials in Chapter 3 of this part. First, variations of the full Laplace BVP with exact, first- and second-order BBCs are considered and solved in a semi-analytical manner within the Whispers3D model, drastically improving the efficiency of exploring the wave-number downshift effect in F-P resonance simulations. Furthermore, three models in the mild-slope equation family (MSE, EMSE, MMSE) are also included and compared. In total, seven models (adding the ALAS), labelled as models I-VII, are considered with different approximations made on BBC. In line with our expectations, it is observed that the downshift effect increases with ϵ. The results of models I-VI show different degrees of wave-number downshift in F-P resonance condition. The most pronounced downshift appears in model I in which no approximation is made on BBC. Model II failed in describing the F-P resonance for large ϵ for some numerical reasons. Model IV captured the downshift effect but failed in predicting the correct values of the enhancement factor within the resonator for all ϵ considered here. For small ϵ, models III, V, VI converge to the model I, but the deviations develop as ϵ increases. Our simulations show that with the wave-number evaluated as a function of the local water depth, the degree of downshift is still different due to different approximations made on BBC. This observation indicates that the downshift appears at the first order of BBC, since model II (for small ϵ) and models IV, V captured the downshift. In addition, high-order effects of BBC also play significant role for the manifestation of the F-P resonance.

As an overall take-away message, the manifestation of the F-P resonance in the case of large relative ripple amplitude ϵ (in order to reach large enhancement factors of the standing waves in the resonator) appears to be restricted to a very narrow range of particular conditions, and this range becomes more and more narrow as ϵ increases. As stated in Zhang and Benoit (2019), this extreme narrowness of the resonance range makes the possibility of realizing such resonance for practical coastal applications questionable, or, at least, attainable for only very particular incident wave conditions, all the more so as the required duration to reach maximum amplification of waves in the resonator area was observed to increase roughly exponentially as a function of ϵ. Furthermore, we have also shown that the study of this resonance mechanism requires using accurate mathematical modeling approaches (and accurate numerical implementations as well). Indeed,

approximate models, relying on approximations of the exact BBC and/or specific forms of the solution for the potential (as in the mild slope equation approaches, for instance) were shown to produce solutions which differ from the full linear solution, the magnitude of these differences increasing again with ϵ. This means, for instance, that a practical coastal setup designed to exploit the F-P resonance (for harnessing wave energy as an illustrative purpose) whose design would be based on an approximate model (as the mild slope equation for instance) would probably not meet the expectations in terms of enhancement of wave height in the resonator for large ripple amplitude (or alternatively for incident wave conditions slightly off the target conditions).

4.2 Outlook and perspectives of future work

4.2.1 F-P resonance modeled within linear modeling framework

The simulations and analyses presented in Chapter 3 on the overall comparison of the seven linear modeling approaches need some additional work to be finalized, and possibly proposed for publication. Sticking in the linear framework for surface waves, several aspects deserve additional investigations, in particular:

i). The influence of the treatment of discontinuities of bottom elevation derivatives in all the models requires additional tests and analyses, as it appeared to be quite sensitive for some of the models considered here. The implementation of the matching condition in model V (EMSE model by (Kirby, 1986a)) needs to be realized and validated.

ii). The numerical issue observed with model II for larger values of ϵ needs to be investigated in a deeper manner, understood and resolved.

iii). Additional variants of linear models could also be added, as for example the variants of EMSE and MMSE considered in Chamberlain and Porter (1995) for the study of Bragg resonance.

iv). The possibility to include higher-order modes in the solution of MSE-like models, as done by Porter and Staziker (1995) could also be tested in order to improve the resolving capabilities of models IV-VI on the F-P setup.

v). An analytical solution of the Laplace equation without or with less limitation on the bottom slope would be of interest. In this regard, the Floquet theory could be an option based on the work of Howard and Yu (2007) and Yu and Howard (2010), which do not assume that the bottom corrugations are of infinitesimal amplitude. The sinusoidal corrugated bottom (or other arbitrary periodic bottoms) could be decomposed on a Fourier mode basis following the work of Yu and Howard (2012).

4.2.2 F-P resonance modeled within nonlinear modeling framework

To the limit of my knowledge, the finite-amplitude water wave effects on Bragg resonance are less studied since Bragg scattering is generally considered as a linear-wave phenomenon. Kirby (1986b) considered non-coupling Stokes waves and found that the weak nonlinearity of surface waves has only a secondary effect on Class I Bragg resonance. Hara and Mei (1987) found in their experiments that the free surface nonlinearity could generate infragravity waves for dispersive wave packets. Via fully nonlinear simulations of incident waves with different values of wave steepness, Tang and Huang (2008) showed that the primary resonance tongue of Class I Bragg resonance experiences a significant reduction as wave height increases, probably because some incident wave energy is transferred to the higher harmonics which do not meet resonance condition, thus being only slightly reflected.

Due to the sensitivity of the F-P resonance condition on the incident wave-number for large relative ripple amplitude cases, the high-order dispersion may probably alter the development of the resonance by slightly changing the wave-number. It is anticipated that with the high-order dispersion taken into account, the wave-number within the resonator is more and more affected as the F-P resonance develops and the wave amplitude increases. The F-P resonance condition could be therefore broken, and the two patches of ripples would then tend to reflect nearly all wave energy due to non-resonant wave-bottom interaction. As the wave amplitude decreases in the resonator, the F-P resonance condition could be restored again since the higher-order dispersion effects also decreases.

A natural next step of this work would then be exploring the F-P resonance condition for large ripple amplitude cases with the fully nonlinear version of Whisper3D to elucidate these effects. First steps in this direction have already been undertaken with a couple of nonlinear simulations using Whisper3D (not reported in this manuscript), which have shown the need to implement an accurate and robust generation/absorption technique for incident nonlinear waves of high amplitudes. This work is ongoing and will be reported in the future.

Part III
Breather evolution over sloping bottoms

Dans cette partie, les instabilités des solutions de type "breather" qui apparaissent lorsque les breathers se propagent dans un milieu dissipatif sur une bathymétrie irrégulière sont étudiées. Le train d'ondes de type breather est soumis à des perturbations quand il se propage dans un canal à vagues et donc s'écarte de la trajectoire analytique. Les perturbations comprennent la dissipation visqueuse dans le volume fluide, la variation de la profondeur, les interactions vague-vague non résonantes et le phénomène de déferlement. En raison des instabilités, les breathers se propagent de façon plus complexe de type récurrence Fermi-Pasta-Ulam (FPU). Il a été démontré dans des travaux précédents (see Kimmoun et al., 2016, 2017) que différents ordres de réponses dynamiques des breathers existent en condition de fond plat, avec la dissipation agissant comme la perturbation. La réponse du premier ordre est la récurrence de modulation de type FPU déphasée. Dans la réponse de second ordre, la récurrence se produit accompagnée d'un effet de fission. L'objectif de cette partie du travail est de considérer non seulement la dissipation, mais aussi la variation de fond comme les perturbations des breathers. Nous discutons des effets des différentes propriétés des breathers incidents et des profils bathymétriques sur la réponse dynamique des breathers du fait des instabilités. Dans le chapitre 2, les breathers de type Akhmediev et Peregrine se propagent sur un fond de profil en forme de marche. Dans le chapitre 3, le fond est constitué de deux pentes reliées entre elles. On utilise à la fois un modèle entièrement non-linéaire, mais aussi l'équation de Schrödinger cubique non-linéaire non-conservative avec coefficients variables pour prédire les réponses dynamiques des breathers. Les conclusions sont résumées dans le chapitre 4. L'observation la plus importante de cette partie est que, en raison de la réponse dynamique de second ordre, des vagues scélérates pourraient être provoquées par l'instabilité de modulation dans les zones côtières.

Parmi toutes les choses du monde, il n'en est point de plus molle et de plus faible que l'eau, et cependant, pour briser ce qui est dur et fort, rien ne peut l'emporter sur elle. Pour cela rien ne peut remplacer l'eau. Ce qui est faible triomphe de ce qui est fort; ce qui est mou triomphe de ce qui est dur.

Tao Te King - Le Livre de la voie et de la vertu

Lao Tseu (IVe siècle av. J.-C.)

List of the symbols of Part III

a	carrier wave amplitude
$\mathfrak{a}$	breather parameter
a_{mod}	amplitude of non-exact NLSE solution
A	wave envelope variable in space NLSE formulation
A_{max}	maximum value of positive envelope
A_{min}	minimum value of positive envelope
B	wave envelope variable in time NLSE formulation
c, c_1, c_2, c_3	real-valued constants
CFL	Courant–Friedrichs–Lewy number
C_g	wave group velocity
E	wave energy as a function of space
E_0	initial wave energy
f_c	carrier wave frequency
g	gravity acceleration
h	local water depth
i	imaginary unit, $\sqrt{-1}$
k	local wave-number
L_{deep}	carrier wave-number in deeper region
$L_{shallow}$	carrier wave-number in shallower region
N	number of modulations after fission
R	coefficient of Akhmediev breather
T	canonical time variable of NLSE
T_c	carrier wave period
W	width of wave flume
x_f	breather focusing position
X	canonical time variable of NLSE
α	constant-coefficient NLSE parameter
β	constant-coefficient NLSE parameter
δ	decay rate of wave amplitude
δ_{Dorn}	theoretical dissipation with sidewalls and bottom
δ_{LM}	theoretical dissipation with only sidewalls
ϵ	carrier wave steepness
η	free surface elevation
κ	perturbation wave-number
λ	variable-coefficient NLSE parameter
μ	variable-coefficient NLSE parameter
ν	variable-coefficient NLSE parameter
ν_w	viscosity of water
ν_v	bulk dissipation parameter in Whispers3D
ψ	canonical envelope variable of NLSE
ψ_{AB}	canonical solution of Akhmediev breather
ψ_{KM}	canonical solution of Kuznetsov-Ma breather
ψ_{AP}	canonical solution of Peregrine breather
ω	angular wave frequency
Ω	perturbation angular wave frequency
Ω_{mod}	angular wave frequency of non-exact NLSE solution

Chapter 1

Introduction

Waves in nature are unstable because they always contain perturbations. All these perturbations lead to instabilities along or perpendicular to the wave direction. The most powerful instability is the so-called modulation instability (or Benjamin-Feir instability) (Benjamin and Feir, 1967) that develops in the direction of the carrier waves. In modulational unstable wave trains, the main mode of the carrier wave is associated with side-band perturbations. Eventually, strong temporal compression of envelope profile along with strong wave energy transfer could take place forming a soliton-like wave envelope. The perturbations emerge spontaneously, so waves are of self-modulation characteristics in the unstable regime. Such properties make modulation instability a possible explanation of the formation of freak waves in deep water (Janssen, 2003).

In coastal areas, the bottom effects on the propagation and evolution of waves are nontrivial. As water depth decreases, waves become weakly- or even non-dispersive. The modulation instability cancels and ceases to exist when relative water depth $kh < 1.363$ for unidirectional waves over flat bottom (Zakharov, 1968). For uneven bottom, with decreasing water depth in the direction of wave propagation, the initial envelope soliton could separate into several smaller ones with different values of group velocity and magnitudes. This is the well-known soliton fission law initially introduced by Djordjević and Redekopp (1978), obtained by adopting variable-coefficient non-linear Schrödinger equation. For gradually increasing water depth (Armaroli et al., 2020), on the contrary, the modulation is stabilized resulting in a uniform train of pulses on a background.

In this part, the breathers' propagation and evolution characteristics over sloping bottoms will be studied by means of large-scale experiments and highly accurate numerical models. The breather wave trains are generated in a deeper flat region where modulation instability is included, and then propagate over slopes until shoreline. The major aim is to show that, the formation of large waves in relatively shallow water may be indirectly attributed to the shoaling of offshore modulational unstable wave trains.

1.1 Bibliography survey of the study of modulation instability

The theoretical study of modulation instability for non-linear water waves was conducted almost simultaneously and independently in the 1960s by different researchers (Whitham, 1965; Lighthill, 1967; Benjamin and Feir, 1967; Benjamin, 1967; Zakharov, 1968). A historical review on the theory of modulation instability is available in Zakharov and Ostrovsky (2009), and it is not repeated here. The modulation instability of waves is an ubiquitous phenomenon and has been observed in several physical situations, including water waves (Zakharov, 1968; Segur et al., 2005), electromagnetic waves (Tai et al., 1986; Närhi et al., 2016) and plasma (Galeev et al., 1975; Guo et al., 2016).

The modulation instability could result in a strong compression of wave envelope in space and time. In Fourier spectral domain, the modulation instability originates from the side bands symmetrically located beside the fundamental wave. For the more unstable case, the amplitudes of the side bands increase exponentially in the initial stage of modulation, besides, additional side bands are formed due to the four wave mixing effect. The spectrum broadens from one peak to a triangular cascade form (Chabchoub et al., 2016). If the excited lower side band is of higher wave amplitude compared to the carrier wave, the frequency downshift happens, and the lower side band becomes the new carrier wave. The spreading of carrier wave energy to side bands is reversible in general, and the wave energy will return to the carrier wave after the modulation. This growth-decay circle of an unstable wave train repeats periodically or quasi-periodically in time happens due to complex dynamics of non-ideal input conditions, through the mechanism of *Fermi-Pasta-Ulam* (FPU) recurrence (Akhmediev and Korneev, 1986; Akhmediev and Ankiewicz, 2011). In hydrodynamics, the famous *Non-linear Schrödinger Equation* (NLSE) is a model with third-order in non-linearity and first-order in dispersion. The cubic NLSE describes the evolution of envelope of weakly non-linear (with $\epsilon = ka < 0.1$, k for the carrier wave number, a for the corresponding amplitude) and dispersive waves. It has been used to study the modulation instability in deep water conditions by Zakharov (1968); Chu and Mei (1971) and in uniform arbitrary depth conditions by Hasimoto and Ono (1972); Mei (1992). Even though it is of the lowest order of non-linearity and dispersion, the cubic NLSE describes the four-wave interaction (modulation instability) of water waves with a narrow-banded spectrum reasonably well. One of the most important characteristics of the cubic NLSE is that it is solvable by using *Inverse Scattering Transform* (IST) technique (Zakharov and Shabat, 1972) or by Darboux transform method (Matveev and Salle, 1991). Several analytical exact solutions have been found including non-linear plane wave, solitons, breathers, and rational solutions (Dysthe and Trulsen, 1999; Gaillard, 2011). The breather solutions are a family of exact 'pulsating' solitary waves, including *Akhmediev breathers* (AB) (Akhmediev

et al., 1987), *Kuznetsov-Ma* (KM) breathers (Kuznetsov, 1977; Ma, 1979) and *Akhmediev-Peregrine* (AP) breathers (Peregrine, 1983; Akhmediev et al., 2009a). Especially Peregrine breather (the lowest order of AP breathers) is considered as a prototype of freak waves that appear from nowhere and disappear without a trace (Akhmediev et al., 2009b; Kharif and Pelinovsky, 2003). It has been experimentally confirmed in wave flumes that the maximum amplification of the initial uniform water wave amplitude reaches as much as 3 and even higher (Chabchoub et al., 2011, 2012) for AP breathers. The prediction of cubic NLSE agrees reasonably well, although not perfectly, with the experimental observations.

As an asymptotic theory, the cubic NLSE is limited by the weakly non-linear ($\epsilon < 0.1$) and narrow-banded spectrum assumption. The weakly non-linear assumption is possibly violated during the modulation process even with an initially mild carrier wave amplitude. it has been confirmed in experiments (Lo and Mei, 1985) that the cubic NLSE failed in capturing any asymmetry of non-linear wave packet profile, and it can only describe modulation instability in a short duration as an evolution function. In order to improve the prediction of NLSE for deep water waves, Dysthe (1979) adopted the perturbation method to fourth-order with respect to steepness ϵ. This approach, which is sometimes referred to as modified NLSE (MNLSE), predicts that the wave-induced flow limits the growth of perturbations and that the wave envelope soliton is of asymmetric profile. As is shown by Stiassnie and Shemer (1984), the MNLSE is a particular case of the third-order Zakharov equation, and all the fourth-order terms in MNLSE emerge as a result of the narrow-spectral-width assumption, and none of them is of fourth order in the wave amplitude itself. The MNLSE can predict the maximum amplification of initial large-amplitude wave trains during the modulation process, but the prediction of the most unstable modulational frequency is accurate only for $\epsilon < 0.1$ as indicated in Tulin and Waseda (1999). Trulsen and Dysthe (1996) improved this MNLSE by relaxing the narrow-band requirement $O(\epsilon)$ to a broader regime $O(\epsilon^{1/2})$. Cases with strong mean flow without assuming that wave-induced-flow velocity is equal to the group velocity of fundamental waves can be described using fifth-order NLSE by Slunyaev (2005). The NLSE can be formulated as a conservative Hamiltonian system, for instance, coupled NLSE (Debsarma and Das, 2007) and quartic MNLSE in deep water (Craig et al., 2012; Gramstad and Trulsen, 2011a) or in arbitrary water depth (Gramstad and Trulsen, 2011b). It is difficult to find analytical solutions of higher-order NLSE other than the plane wave solution. The simulations with NLSE type models provide a very good preliminary quantitative description of the evolution of envelope solitons with different bottom conditions. For more accurate quantitative description of modulation instability with larger carrier-wave steepness, Yuen and Lake (1982) suggested adopting the Zakharov equation. Comparisons between fully non-linear potential models and MNLSE in deep water conditions have been reported in Clamond et al. (2006); Slunyaev and Shrira (2013); Adcock and Taylor (2016). It has been shown that

for large-amplitude waves and long-duration simulations, a qualitative agreement between fully non-linear models and NLSE type equations can be achieved for deep water conditions, but they are quantitatively different. So for cases with strong non-linearity and/or tortuous topography it is more appropriate to adopt fully non-linear numerical models.

For ideal initial conditions, NLSE breathers exhibit only one growth-return cycle in the non-periodic (time or space) dimension. However, such ideal signal growth-decay return is hard to achieve and the initial breather focusing followed by a FPU recurrence is generally observed. The complete recurrence of the initial state maybe not reachable due to the effects of frictional dissipation (Kimmoun et al., 2016), non-linear non-resonant wave-wave interaction and breaking wave effects (Iafrati et al., 2014). Besides, when the second- and even higher-order harmonics of the fundamental wave frequency fall within the modulational unstable regime, the breather undergoes decomposition and splits into two sub-pulses, this phenomenon has been demonstrated and observed in optics (Wabnitz and Akhmediev, 2010; Hammani et al., 2011). This phenomenon is defined as higher-order modulation instability by Erkintalo et al. (2011) in optics. Recently for water waves, the fission effect due to the higher-order modulation instability has been confirmed numerically and experimentally by Kimmoun et al. (2017). In their experiments, the collision of two sub-pulses of modulation-induced fission resulted in significant amplification of fundamental waves in the second circle of FPU recurrence. In some cases, the envelope collision even produced higher waves compared to the breather (the first growth-decay circle). Furthermore, in their numerical simulations, the characteristics of higher-order modulation instability have been discussed with the MNLSE, including an additional dissipation term. The inclusion of an additional dissipation term in MNLSE is introduced in Eeltink et al. (2017) to incorporate wind forcing contribution on surface gravity waves. The authors indicated that the effect of dissipation may accelerate the focusing on the second recurrent cycle. This is counter-intuitive since it is generally considered that the frictional dissipation could suppress the modulation instability (Voronovich et al., 2008; Ma et al., 2012).

In coastal areas, the bottom boundary affects the evolution and propagation of solitary waves significantly. The bottom effects on solitary waves have been extensively studied for different types of bottoms, including submerged step, smoothly varying topography, linearly increasing or decreasing slope (Djordjević and Redekopp (1978); Tanaka (1986); Pudjaprasetya et al. (1999); Benilov et al. (2005); Armaroli et al. (2020)). In the work of Djordjević and Redekopp (1978), they discussed the characteristics of the fission of an envelope soliton moving over variable depth by using NLSE with variable coefficients along the direction of wave propagation. Zeng and Trulsen (2012) adopted variable coefficients NLSE to study the change of statistics of irregular waves due to decrease of water depth. They found that a local bathymetric change may provoke non-equilibrium statistics in a region that may extend far beyond the local depth non-uniformity. They antic-

ipate that the probability of freak waves on or near the edge of the continental shelf may exhibit a rather complicated spatial structure for wave fields entering from deep sea. Armaroli et al. (2020) discussed the effect of gradually increasing water depth in the modulation process. They showed that the increasing water depth results in stabilization of wave trains. This is true for not only exact NLSE solutions but also for non-exact initial conditions like waves with harmonic perturbations. It is a consensus that the 2D modulation instability cancels for relative water depth below 1.363. To the best of the author's knowledge, there are only few reports on how breathers generated in deep water evolve as water depth decreases. Benilov et al. (2005) demonstrated asymptotically that as wave packets propagate from deep water to shallow water, they will decrease in amplitude and disperse as approaching the critical relative water depth $kh = 1.363$. Their work was limited by the fact that NLSE fails when water depth is shallower than the threshold. Higher-order NLSE waves were adopted instead in Grimshaw and Annenkov (2011). They showed that, in the framework of Higher-order NLSE, the threshold $kh = 1.363$ is flexible. Wave packets could either penetrate into regions shallower than $kh = 1.363$, or not even reach $kh = 1.363$ depending on the speed of the wave packets. All these previous works focused on whether asymptotic or higher-order NLSE simulation study. No experimental observation is available until now. The main goal of this part is to investigate the evolution of envelope solitons over an uneven bottom. Particular attention is paid to the shallower region where $kh < 1.363$. Before entering the sloping bottom, the envelope solitons are generated in a flat region deeper than $kh > 1.363$ where waves are modulationally unstable. The chosen envelope soliton is AB type solutions of cubic NLSE. The experiments have been conducted in the 'Mid-size Observation Flume' at the Tainan Hydraulics Laboratory (THL) of the National ChengKung University in Taiwan. In order to capture as much as possible the dynamics of envelope soliton evolution in a long basin, including the effects of wave breaking, frictional dissipation, and variable topography, and to compare with the experimental data, the fully non-linear numerical model Whispers3D is adopted. The NLSE with variable coefficients is available and cheap to adopt, and it lies in our interest to examine to what extent the cubic NLSE can describe the instability. The computations will be conducted with cubic NLSE with variable coefficients following the formulation in Zeng and Trulsen (2012) with an additional term to take linear dissipation into account. The formulation of this dissipation term in NLSE with variable coefficients will be introduced in paragraph 1.2.1.b.

1.2 Introduction of the formulation of cubic NLSE and its typical solutions

From a practical point of view, the investigation of NLSE breather solutions is crucial for the study of modulation instability in numerical or experimental basin.

Typically, there are three approaches to trigger unstable side bands in a plane wave background:

(a) Perform monochromatic wave without perturbation in a numerical/physical wave flume for long time evolution. For all numerical or experimental simulations, the unstable side bands will appear naturally after sufficiently long-time evolution due to imperfect environment (for instance the dissipation and the background noise in experiments and due to truncation in numerics). This is referred to as 'un-seeded' experiments;

(b) The modulation can be otherwise imposed in the motion of wave generator, by artificially adding a pair of frequency modes to a sinusoidal (fundamental) wave. The added side band wave-numbers or frequencies should be chosen according to the unstable region diagram, for 2-D cases see Figure 1 in Benjamin and Feir (1967), and for 3-D cases see Figure 5.4 of Kharif and Pelinovsky (2003). This is referred to as 'seeded' experiments;

(c) Start with analytical solutions of cubic NLSE, like Breather solutions, then generate waves based on its Fourier amplitude and phase properties.

In the early pioneering studies like Lake et al. (1977), the method (a) was adopted, then it was indicated in Melville (1982) that the method (b) is of advantages over (a). Method (b) was then widely adopted for example in the experimental study of the two horizontal dimension modulation instability by Toffoli et al. (2013) and also by Hwung et al. (2006) in the THL wave tank. However, this three-wave system represents a truncated spectrum with less degree-of-freedom. As knowledge of instabilities grows, the use of NLSE analytical solutions, namely method (c), is preferred, since the solutions retain higher-frequency modes. It also permits to start at any stage of the modulation process, which greatly releases the constraints on the size of wave flumes. Therefore, in the present study, the modulation instability will be investigated by the use of breather solutions.

1.2.1 Cubic NLSE in arbitrary constant water depth

The NLSE valid for weakly non-linear waves in arbitrary water depth was derived from Eq. (I.2.1) to (I.2.4) by using the method of multiple scales (Hasimoto and Ono, 1972; Mei, 1992). The spatial or temporal evolution of complex wave amplitude function $A(x,t)$ or $B(x,t)$ is described by 'space' or 'time' NLSE, respectively. The formulation of free surface elevation is identical whether $A(x,t)$ or $B(x,t)$ is adopted. The detailed comparison of the 'space NLSE' and 'time NLSE' has been reported in Chabchoub and Grimshaw (2016). In general, the space NLSE is appropriate for the initial-value problem, and the time NLSE is more convenient for wavemaker problem. The expression of free surface elevation formulated with $A(x,t)$ is:

$$\eta = A(x,t)e^{i(kx-\omega t)} + \text{higher harmonics} + \text{c.c.}, \tag{III.1.1}$$

where ω is the carrier wave angular frequency and k its corresponding wave number, c.c. stands for complex conjugate, higher harmonics are omitted due to the assumption of weakly non-linearity.

a/ Conservative formulation

Based on Eq. (III.1.1) the space NLSE is formulated as follows:

$$i\left(\frac{\partial A}{\partial t}+C_g\frac{\partial A}{\partial x}\right)-\alpha\frac{\partial^2 A}{\partial x^2}-\beta|A|^2A=0, \tag{III.1.2}$$

where $C_g=\frac{\mathrm{d}\omega(k)}{\mathrm{d}k}$ is the group velocity in finite water depth, α and β, are the dispersive and non-linear coefficients respectively. The expressions are as follows:

$$\alpha=-\frac{1}{2}\frac{\mathrm{d}^2\omega(k)}{\mathrm{d}k^2}=\frac{\omega h}{2k}\left[\frac{1}{4kh}-\frac{kh}{\sinh^2(2kh)}-\frac{1-2kh\coth(2kh)}{\sinh(2kh)}\right], \tag{III.1.3}$$

$$\beta=\frac{\omega k^2\left(8+\cosh(4kh)-2\tanh^2(kh)\right)}{16\sinh^4(kh)}-\frac{\omega\left(2\omega\cosh^2(kh)+kC_g\right)^2}{2\sinh^2(2kh)\left(gh-C_g^2\right)}. \tag{III.1.4}$$

The Eq. (III.1.2) can be reformulated in the canonical space (X,T) as:

$$i\psi_T+\psi_{XX}\pm2|\psi|^2\psi=0, \tag{III.1.5}$$

by using the following transformation of variables:

$$X=x-C_gt,\quad T=-\alpha t\quad\text{and}\quad\psi(X,T)=\sqrt{\frac{\pm\beta}{2\alpha}}A(X,T). \tag{III.1.6}$$

In the non-dimensional canonical formulation, X is the coordinate in the frame moving with the wave group velocity and T represents the re-scaled time. The sign of the cubic non-linear term is determined by the sign of $\beta/2\alpha$. For water waves, α is positive for any water depth, and β changes sign for $kh=1.363$. When the relative water depth is below 1.363, β is negative so there is a minus sign for the non-linear term in Eq. (III.1.5), denoting the non-focusing NLSE. In such cases, the waves are stable with side bands perturbations. For cases where $kh>1.363$, Eq. (III.1.5) denotes focusing NLSE. In such cases, waves are unstable to side band perturbations.

b/ Non-conservative approximation

In Eq. (III.1.2), the system is conservative. But even for well-controlled experiments in hydrodynamics, the wave energy attenuation in space is inevitable. As

is mentioned in Section (1.1), the dissipation plays a very important role in modulation instability, it is then helpful to consider non-conservative system. A more general formulation of NLSE in Eq. (III.1.2), which takes linear dissipation effect into account, is formulated as:

$$i\left(\frac{\partial A}{\partial t}+C_g\frac{\partial A}{\partial x}\right)-\alpha\frac{\partial^2 A}{\partial x^2}-\beta|A|^2A=i\delta' A. \tag{III.1.7}$$

This is the approximate model used in the study of water waves by Lake et al. (1977). The new term is inserted on the right hand side of Eq. (III.1.7), and $0<\delta'\ll 1$ is a measure of the dissipation rate (here with unit s^{-1}). Given $\delta'=0$, this formulation returns to cubic NLSE. Segur et al. (2005); Ma et al. (2012) showed the sensitivity of modulation instability on the effect of dissipation. Therefore, we understand that the determination of δ' is critical.

It is generally admitted that the wave train energy decreases exponentially along the direction of wave propagation:

$$E(x)=E_0\exp\left(-2\delta x\right). \tag{III.1.8}$$

In the work of Henderson et al. (2015), several theoretical models for the estimation of the dissipation parameter δ (here expressed in m^{-1}) have been compared with measurements. They concluded that different models are useful for different situations, and no universal theoretical formulation is found among all the models they listed. Assuming that the dominant source of dissipation in wave tank experiments is the sidewall and bottom boundary layers, the spatial decay rate δ established by Dorn (1966) is given by:

$$\delta_{Dorn}=\sqrt{\frac{\nu_w}{2\omega}}\left(\frac{2k}{W}\right)\left(\frac{kW+\sinh\left(2kh\right)}{2kh+\sinh\left(2kh\right)}\right), \tag{III.1.9}$$

where $\nu_w=10^{-6}\ \mathrm{m^2s^{-1}}$ is the kinematic viscosity of water at 20°C, W is the flume width. The third part of Eq. (III.1.9) is the water-depth correction mainly resulting from the bottom layer in finite water depth. For deep-water condition, only the two sidewalls affect the spatial decay (Lo and Mei, 1985), so the formulation of the decay rate is simplified as:

$$\delta_{LM}=\sqrt{\frac{\nu_w}{2\omega}}\frac{2k}{W}. \tag{III.1.10}$$

Several experiments indicate that the spatial decay rate is underestimated by Eq. (III.1.9) or Eq. (III.1.10). For example, in the experiments of Segur et al. (2005), $W=0.254$ m, $h=0.2$ m, $f=3.33$ Hz, resulting in $\delta_{Dorn}=0.054\ \mathrm{m}^{-1}$. δ_{Dorn} is approximately half of the measured $\delta=0.11\ \mathrm{m}^{-1}$. In the deep-water experiments of Ma et al. (2012), $W=0.8$ m, $f=1$ Hz, so $\delta_{LM}=\delta_{Dorn}=$

$0.0028\ \mathrm{m}^{-1}$. It is also approximately half of the measured $\delta = 0.0058\ \mathrm{m}^{-1}$ in the case with narrowest spectrum. This observation is also verified in the previous and the present experiments carried out in the THL wave tank. It indicates that the side wall and bottom boundary layers may not be the only source of dissipation. Other terms considered in Henderson et al. (2015), such as air water interface, are not large enough to reach the measured values.

Further more, this is true for flat bottom cases, whereas for variable bottom cases, the dissipation rate δ is supposed to be a function of x as well. The value of δ should be carefully calibrated from case to case.

1.2.2 Cubic NLSE in slowly varying water depth

For variable bottom condition, apart from the weakly non-linear assumption introduced in the derivation of NLSE, it is further assumed that the variation is slow in space, $\mathrm{d}h/\,\mathrm{d}x \sim O(\epsilon^2)$. The NLSE equation with variable coefficients was firstly derived by Djordjević and Redekopp (1978) and re-derived by Zeng and Trulsen (2012), to describe the dynamics of the first harmonic up to cubic order. The dimensional formulation is as follows:

$$i\left(\frac{\partial B}{\partial x}+\frac{1}{C_g}\frac{\partial B}{\partial t}\right)+i\mu\frac{\mathrm{d}(kh)}{\mathrm{d}x}B+\lambda\frac{\partial^2 B}{\partial t^2}+\nu|B|^2B=i\delta\,B, \tag{III.1.11}$$

where the choice of $B(x,t)$ indicates that Eq. (III.1.11) is a time NLSE formulation. The coefficients are all functions of the water depth $h(x)$:

$$\mu=\frac{(1-\sigma^2)(1-kh\,\sigma)}{\sigma+kh(1-\sigma^2)}\ ,\quad \lambda=\frac{1}{2C_g^3}\frac{\mathrm{d}^2\omega(k)}{\mathrm{d}k^2}=\frac{-1}{2C_g\omega}\left[1-\frac{gh}{C_g^2}(1-kh\,\sigma)\left(1-\sigma^2\right)\right], \tag{III.1.12}$$

$$\nu=\frac{-\omega k^2}{16C_g\,\sigma^4}\left[9-10\sigma^2+9\sigma^4-\frac{2C_g^2\,\sigma^2}{gh-C_g^2}\left(4\frac{C_p^2}{C_g^2}+4\frac{C_p}{C_g}(1-\sigma^2)+\frac{gh}{C_g^2}\left(1-\sigma^2\right)^2\right)\right]. \tag{III.1.13}$$

In the expressions of coefficients, $\sigma=\tanh(kh)$, $C_p=\omega/k$ is phase velocity. μ, λ, and ν correspond to shoaling term, dispersion term and non-linear term for variable water depth respectively. The shoaling coefficient μ tends to be 0 as water depth increases. Analog to Eq. (III.1.7), an additional dissipation term is inserted and adapted to time NLSE formulation. For constant water depth case, $\mathrm{d}h/\,\mathrm{d}x=0$, Eq. (III.1.11) becomes time NLSE if the dissipation is ignored.

1.2.3 Typical exact solutions of cubic NLSE

For the non-dimensional solution $\psi(X,T)$ of Eq. (III.1.5), two families of solutions in forms of $c_1\psi(c_1X,c_1^2T)$ and $\psi(X-2c_2T,T)\exp\left[i\left(c_2X-{c_2}^2T+c_3\right)\right]$ can

be found, with c_1, c_2, c_3 being any real parameter. Here we recall three typical solutions of the focusing NLSE in canonical space (X, T), for plain waves: AB, KM breathers, and AP breathers.

a/ Plane wave solutions

The simplest form for solutions of focusing NLSE is a progressive wave moving at group velocity C_g:

$$\psi = \psi_0 \exp\left(2i\psi_0^2 T\right), \tag{III.1.14}$$

where ψ_0 is a measure of wave amplitude. This solution corresponds to second-order Stokes waves when the water depth is infinite. For unstable Stokes waves, the perturbation with wave number $\kappa < 2\psi_0$ will experience exponential growth rate during the modulation. The maixmum exponential growth rate is expected for $\kappa = \sqrt{2}\psi_0$.

b/ Akhmediev breathers

The AB and KM breather solutions are special cases of three-parameter solutions family introduced in Akhmediev et al. (1987). For such cases, the modulation instability process is controlled by a single breather parameter $\mathfrak{a}$, and they can be formulated as follows:

$$\psi_{AB/KM} = \left[1 + \frac{2\left(1-2\mathfrak{a}\right)\cosh\left(2RT\right) + iR\sinh\left(2RT\right)}{\sqrt{2\mathfrak{a}}\cos\left(\Omega X\right) - \cosh\left(2RT\right)}\right]\exp\left(2iT\right), \tag{III.1.15}$$

where the parameters R and Ω are computed from the breather parameter $\mathfrak{a}$:

$$R = \sqrt{8\mathfrak{a}\left(1-2\mathfrak{a}\right)}, \quad \Omega = 2\sqrt{\left(1-2\mathfrak{a}\right)}. \tag{III.1.16}$$

For $\mathfrak{a} > 0.5$, Eq. (III.1.15) represents KM breathers which are periodic in canonical T axis. For $0 < \mathfrak{a} < 0.5$, Eq. (III.1.15) stands for AB which are periodic in canonical X axis. For AB, the parameter R governs the modulation instability growth rate, the maximum growth rate is obtained when $R = 1$, corresponding to $\mathfrak{a} = 0.25$.

c/ Akhmediev-Peregrine breathers

As $\mathfrak{a} \to 0.5$, the period of the wave envelope defined by Eq. (III.1.15) approaches to infinity so that it represents a localized event in both space and time. The limiting case is achieved when $\mathfrak{a} = 0.5$, corresponding to the well-known Peregrine breather (Peregrine, 1983), Eq. (III.1.15) is simplified as:

$$\psi_{AP} = \left(-1 + \frac{4 + 16iT}{1 + 4X^2 + 16T^2}\right)\exp\left(2iT\right). \tag{III.1.17}$$

In this study, the AB solutions are chosen since it allows generating large waves with a prescribed exponential growth rate. It is excellent for the study of the dynamical stabilization of non-linear wave packets and the persistence of large undulatory events.

1.2.4 Stability of NLSE solutions

The main goal of this study is to understand the stability of breather solutions when they evolve over variable bathymetries. It is known from previous studies, that the instabilities could lead to different behaviors such as phase lag recurrence, or fission. It is then crucial to understand the effect of the Akhmediev parameter on the evolution of disturbed solutions.

The study of modulation instability is conducted in general by solving NLSE numerically for an input field of the perturbation form (Hasimoto and Ono, 1972):

$$A(X=0,T) = A_0\left[1 + a_{mod}\cos\left(\Omega_{mod}T\right)\right]. \tag{III.1.18}$$

It has been shown in optics (Dudley et al., 2009; Erkintalo et al., 2011) that when the perturbation amplitude a_{mod} depends on frequency Ω_{mod} with a particular relation, the input field in Eq. (III.1.18) evolves in the same manner as in AB with $\Omega_{mod} = \Omega$ in Eq. (III.1.15). The perturbation amplitude corresponding to Ω_{mod} is:

$$a_{mod} = c\left(1 + \frac{2iR}{\Omega_{mod}^2}\right), \tag{III.1.19}$$

where c is a real coefficient. With such relation, Eq. (III.1.18) represents AB-like, but non-exact solution. Any other form of the perturbation amplitude a_{mod} does not lead to one growth-decay circle of the unstable wave train, but results in multiple growth-decay circles in a FPU recurrence manner.

For non-exact solutions of NLSE, the wave envelope evolution is subject to instabilities. Based on simulations of non-exact initial conditions with conservative deep-water NLSE, the bifurcation diagram, displayed in Fig. (III.1.1), is given to illustrate different orders of the dynamical response for different $\mathfrak{a}$.

In Fig. (III.1.1), left panel shows the change of solution order as function of $\mathfrak{a}$. On the right panels, the examples of envelope evolution in canonical space are shown for different orders. The evolution of exact AB is given on top for reference. Within the framework of conservative deep-water NLSE, it is shown that the non-exact solutions which correspond to AB with different breather parameters $\mathfrak{a}$ evolve as exact AB in the first growth-decay circle. However, different dynamical responses are observed in the second or third circle of recurrence. The so-called 'first-order' solution takes place when $\mathfrak{a} \in [0, 0.375]$, where simple FPU recurrence happens. In the 'second-order', solutions $\mathfrak{a} \in [0.375, 0.444]$, the recurrence is accompanied by fission effect, and in the third hierarchy $\mathfrak{a} \in [0.444, 0.469]$, another envelope bifurcation appears after the first fission.

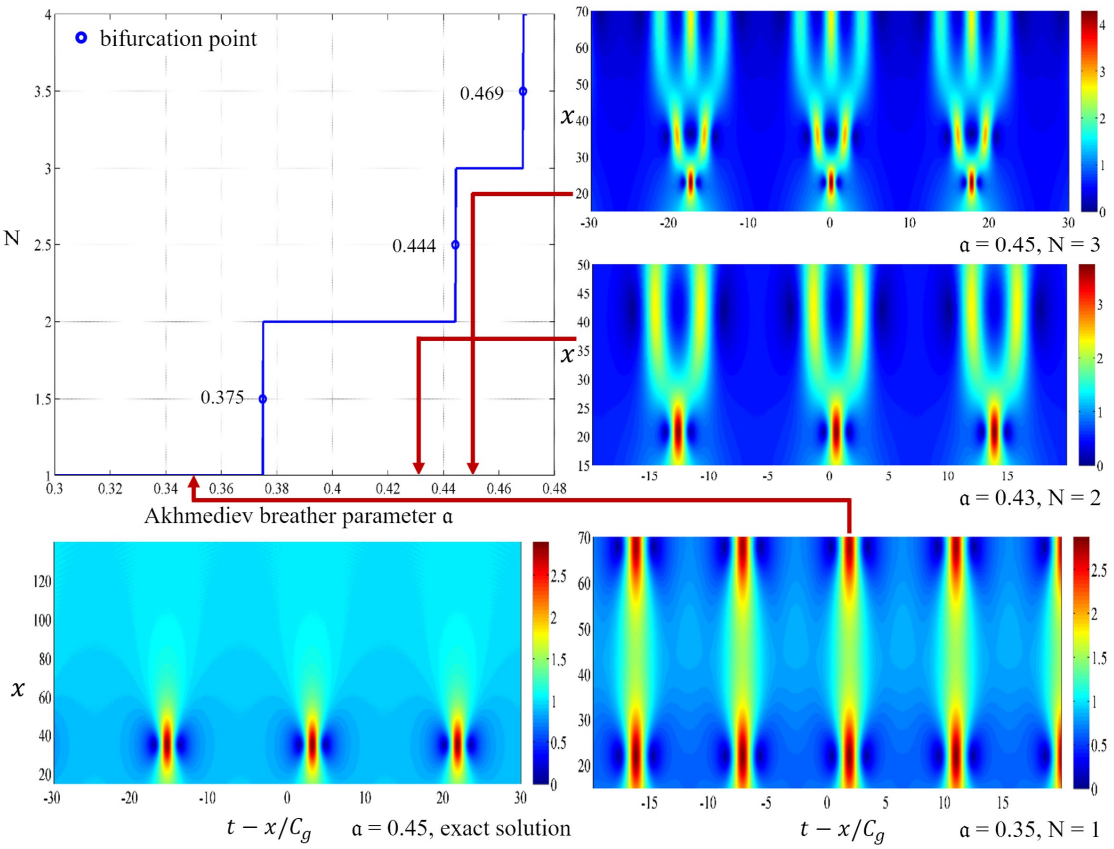

Figure III.1.1: Different orders for the non-exact solution regimes based on different values of $\mathfrak{a}$, the orders are characterized by N, the number of modulations which appear after the fission process. The critical values of $\mathfrak{a}$ are marked, and examples of different order solutions are shown.

We stress that the critical values of $\mathfrak{a}$ for different order transitions should be considered as qualitative rather than quantitative. Fig. (III.1.2) is obtained from conservative deep-water NLSE simulations. In nature, topography, dissipation, and initial wave non-linearities, for example, could alter the dynamical response and play an important role in wave train evolution.

The dissipation effects on the evolution of non-exact NLSE solution given in Eq. (III.1.18) have been discussed in Kimmoun et al. (2017) by means of conservative and non-conservative NLSE simulations. It has been shown that, without dissipation, a collision occurs at the end of the space domain, while this collision is delayed when dissipation is considered. Authors also showed that starting with an exact AB in a non-conservative NLSE, the fission evolution is similar to the one observed with the non-exact solution. It means that dissipation acts as a

perturbation in the exact solution. However, for the evolution of AB case, the dissipation will accelerate the collision of the sub-modulations. The FIG.1 in this work is repeated here to demonstrate the effect of dissipation.

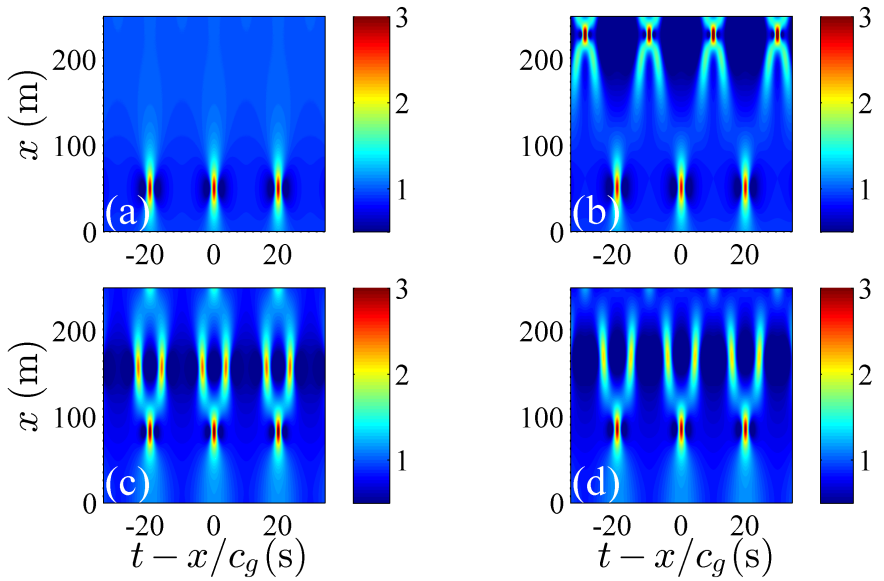

Figure III.1.2: Evolution of exact and non-exact solutions with and without dissipation in deep-water NLSE simulations (Kimmoun et al., 2017). (a): exact AB evolution in conservative system; (b): exact AB evolution in non-conservative system; (c): non-exact AB-like solution evolution in conservative system; (d): non-exact AB-like solution evolution in non-conservative system. The breather parameter $\mathfrak{a} = 0.45$, wave steepness $\epsilon = kA_0 = 0.12$, wave amplitude $A_0 = 0.03$ m at $x = -50$ m, the dissipation rate for non-conservative simulations is $\delta = 3.84 \times 10^{-4}$ m^{-1}.

It is shown in panel (a) that the exact AB solution evolves in a conservative system with one grow-decay circle. When dissipation is added, panel (b) shows that the evolution is accompanied by recurrences, and collisions of different branches of fission are predicted and result in another amplification of wave amplitude. In panel (c), the evolution of non-exact solution given in Eq. (III.1.18) is shown. In this case, Ω_{mod} corresponds to Ω in Eq. (III.1.16) with $\mathfrak{a} = 0.45$, a_{mod} is evaluated based on Ω_{mod} via the above-mentioned relation. It shows similar evolution as the exact solution in the first growth-decay circle, and then fission takes place, corresponding to the second-order solution. In panel (d), the bifurcation of the envelope is affected by the dissipation, and the collision is delayed compared to the case without dissipation.

As mentioned above, effect of the topography on instability regimes is studied. From this starting point, several questions can be expressed:

- Whether the high-order instabilities observed in deep-water persist in the variable bottom cases?
- What is the characteristics of exact AB solutions evolving in a dissipative, spatially varying bathymetry, especially how exact breathers turn into non-exact solutions (due to bottom variation and dissipation) and propagate in shallow water?
- What is the capability of NLSE with variable coefficients in reproducing experimental tests compared with fully non-linear models?
- Could shallow water freak waves explained by the evolution of modulated wave train over uneven bottom which originates from deep water?

Chapter 2

Breather evolution over a prismatic slope connecting two regions of constant depths

When envelope soliton propagates over variable bottoms, in the framework of NLSE, three different dynamic responses are predicted depending on relative water depth. For relatively large water depth, unlike monochromatic waves or shallow-water solitons, the wave packet amplitude counter-intuitively decreases as water depth shoals. For a smaller water depth but still higher than the threshold $kh = 1.363$, the main packet shed 'secondary' solitons, fission is expected. When water depth decreases below the threshold, the wave packet starts to disperse, its envelope becomes wider and smaller. This has been discussed in Benilov et al. (2005) with asymptotic envelope soliton solution of NLSE with variable coefficients. In the present work, the wave packet evolution over uneven bottom is studied experimentally and numerically using exact breather solutions of NLSE.

The experiments have been conducted in the 'Mid-size tank' at the Tainan Hydraulics Laboratory (THL) of the National Cheng-Kung University in Taiwan. The dimensions of this wave tank is 2 m by 2 m in depth and width, and 200 m in length. Such a large facility allows to study the long-term evolution of instabilities. The wave tank is equipped with a piston-type hydraulic wave maker with a maximum frequency of motion of 2.5 Hz. This wave maker is able to absorb waves reflected by the tested bottom profile or the end wall. The facility and the front face of the wave maker are shown in panel (a) and (b) of Fig. (III.2.1). Picture of the wave gauges is displayed in panel (c) of Fig. (III.2.1). 30 to 60 wave capacitance gauges were used for measuring the surface elevation depending on the experimental campaign with sampling frequency of 100 Hz. The same facility and wave gauges were used during all the campaigns described in this dissertation. Then the description will not be repeated hereafter.

The experimental conditions are controlled by five parameters: the carrier wave

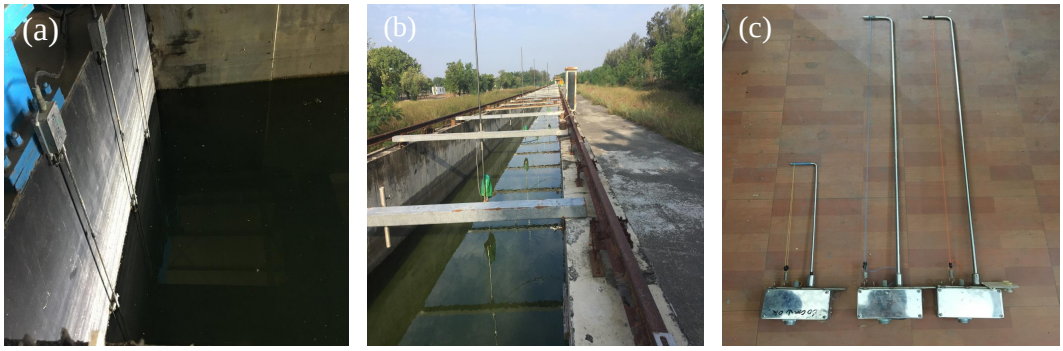

Figure III.2.1: THL facility and equipment used during the experimental campaign (a): active-absorbing piston-type hydraulic wave maker; (b): 'Mid-size tank'; (c): capacitance wave gauges suitable for different water depths.

period T_c, the initial wave steepness at the wave maker ϵ, the dimensional water depth h near the wave maker, the breather parameter $\mathfrak{a}$, and the prescribed focusing point x_f which corresponds to the maximum amplification of envelope amplitude.

In this chapter, we discuss how water waves evolve over the prismatic slope connecting two flat bottoms. As is shown in Fig. (III.2.2), the bottom profile is composed of four parts: (i) starting from the wave-maker (at $x = 0$), a first section of length 35 m with constant water depth corresponding to the deeper part of the domain, (ii) a transition zone with a constant $(1 : 20)$ slope over a distance of 20 m, (iii) a 115 m long shallow water zone with flat bottom, and (iv) a final section of about 10 m in length with the natural bottom of the flume which works as an effective wave absorbing porous media which is made of quarry stones. This wave tank bottom setup is denoted as setup 1. The lateral walls as well as the bottom are constructed of impermeable concrete.

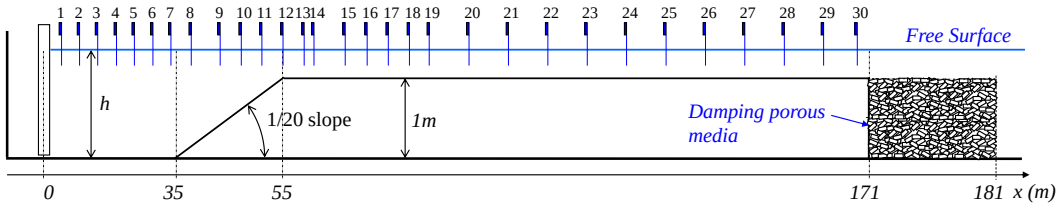

Figure III.2.2: Sketch of the bathymetry setup 1, and the locations of probes

A systematical study has been conducted with 89 tests, covering the $\mathfrak{a} = 0.25, 0.37, 0.5$, $T_c = 0.9, 1.0, 1.1, 1.2$ s, $\epsilon \in [0.09, 0.12]$, water depth $h = 1.2, 1.3$ m

and varying focusing positions x_f locating around the slope. In the following two sections, representative cases will be discussed. The campaign took place from October 2017 to January 2018. I was involved in the measurements of this campaign and the post-processing.

2.1 Case 368: Peregrine breather evolution, one unstable event

Case 368 corresponds to a Peregrine breather. The associated parameters are, $\mathfrak{a} = 0.5$, $\epsilon = 0.11$, $h = 1.3$ m, $T_c = 1.2$ s, and $x_f = 55$ m. For such conditions, the threshold $kh = 1.363$ locates at $x = 52.445$ m, close to the end of the slope $x = 55$ m. The relative water depth changes from deeper region $kh \approx 3.638$ to the shallower flat region $kh \approx 1.065$. The data acquisition lasted for 7 min in allowing the envelope soliton to reach the end of the domain.

2.1.1 Experimental observation

Fig. (III.2.3) shows the evolution of the free surface elevation and its corresponding envelope measured at different positions. Both are normalized by the carrier wave amplitude $a_0 \approx 0.04$ m. The signals are shifted according to the probe positions and the wave group velocity of the carrier wave. It allows to track the focusing event. The envelope is obtained by doing Fourier analysis on sliding windows. The width of the sliding windows is set to $2T_c$ and it is translated $T_c/10$ at each step. Different harmonics are obtained by doing this technique. Then sum up the complex amplitude to the target order of harmonics, we obtain the time evolution of the envelope, up to a specific order. Here the wave envelope is constructed using three harmonics. This method applies for all the envelope computation hereafter, unless specified.

In the left panel of Fig. (III.2.3), it is observed that the amplitude of the modulation is small compared to the amplitude of the wave carrier and then increases up to the focusing point. As the soliton envelope propagates towards the focusing point $x = 55$ m and passes through the bottom slope, the unstable wave packet compresses. Due to the decrease of water depth and the increase of wave amplitudes in the wave packet, the group velocity of waves in the wave packet slows down. The shift of time window x_{Probe}/C_g is slightly overestimated. This explains the position of maximum wave envelope is gradually shifted over the sloping area.

On the right panel of Fig. (III.2.3), the evolution of the wave packet on the second flat bottom region with $kh < 1.363$ is shown. The wave packet broadens as it propagates over the shallower region where waves are modulationally stable. At the same time, the amplitude of its envelope decreases. On each side of the soliton envelope, two instants with minimum values are observed. Their time difference increases during the propagation. To have a more continuous overview,

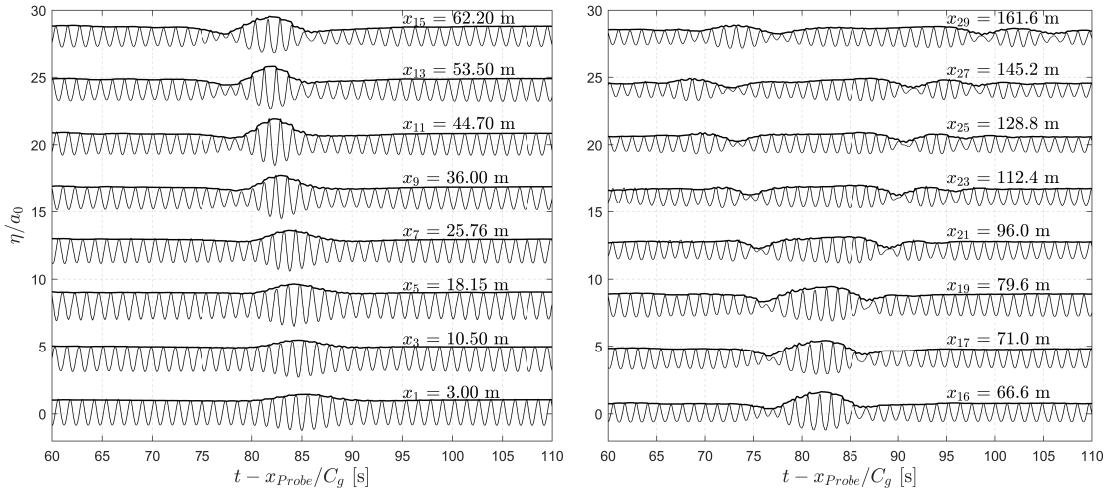

Figure III.2.3: AP case 368: evolution of normalized free surface elevation (solid line) and its envelope (bold solid line) computed via windowed Fourier transform.

a 3D representation of the evolution of the wave envelope in space and in time, is shown in Fig. (III.2.4). The generation and expansion of two modulations in the wave envelope plane is clearly shown, and sub-pulses are observed around $t - x/C_g > 90$ s. These modulations are not observed on the other side around $t - x/C_g < 80$ s.

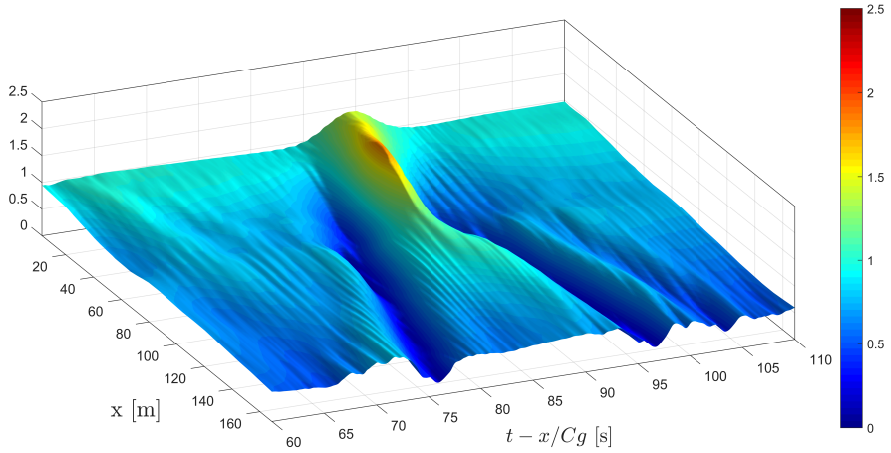

Figure III.2.4: AP case 368: 3D overall view of normalized envelope evolution in space and time. The envelope is normalized by the carrier wave amplitude.

In the panel (a) of Fig. (III.2.5), the spatial evolution of the spectrum is shown.

The frequencies are normalized by the carrier wave frequency f_c. The spectrum broadens as wave packet propagates towards the focusing position: on one hand, the wave energy is gradually transferred to waves with higher frequencies than the carrier frequency; on the other hand, the width of the spectrum part with frequencies lower than the carrier wave frequency is not significantly changed during the modulation. As wave packet reaches the threshold relative water depth 1.363, the four-wave interaction ceases and the higher frequency part of the spectrum stops broadening. Meanwhile, after the slope, a series of low-frequency modes appear. The broadening of spectrum in the shallower region is mainly due to the generation of bound mode harmonics, as the sea state adapts to the new shallow water dynamics.

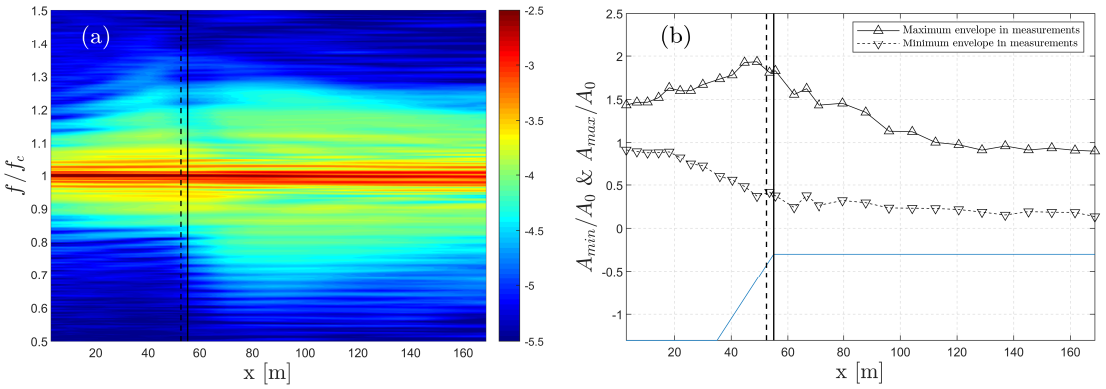

Figure III.2.5: AP case 368: spatial evolution of spectrum and envelope, (a) pseudo color map of the spatial evolution of spectrum in logarithmic scale, wave frequency is normalized by carrier wave frequency f_c, (b) the spatial evolution of the maximum and minimum values of envelope. In both panels, the vertical dashed lines represent the threshold of relative water depth $k_c h = 1.363$, k_c corresponds to carrier frequency f_c, the vertical solid lines represent the focusing position.

In the panel (b) of Fig. (III.2.5), the spatial evolution of the normalized maximum and minimum values of the envelope is shown. They are computed via windowed Fourier analysis. The upper bound of the envelope, A_{max}/A_0 increases as wave packet propagates towards the focusing position. In the meantime, the lower bound of the envelope, A_{min}/A_0 decreases. The increase and decrease stop when the wave packet reaches the relative water depth threshold. For Peregrine breather propagating over deep water, the amplification of carrier wave amplitude is $A_{max}/A_0 = 3$. It is observed that, in case 368 the maximum amplification of $A_{max}/A_0 = 2$ is achieved around the threshold of relative water depth. It is smaller than the expected value in deep water. This is mainly due to two reasons, the wave train is continuously dissipated, and as observed in previous works, the

wave packet amplitude decreases as water depth decreases. In the shallower region, the maximum amplitude of the wave packet continues to decrease and the minimum amplitude holds as constant.

2.1.2 Comparison between fully non-linear model and NLSE with variable coefficients

We recall here the dimensional parameters of the case 368: carrier wave period is $T_c = 1.2$ s, water depth in the deeper region is $h = 1.3$ m, and in shallower region $h = 0.3$ m. The wavelength in the deeper region is $L_{deep} = 2.24$ m, and in the shallower region $L_{shallow} = 1.77$ m. The incident carrier wave amplitude is $a_0 \approx 0.04$ m. The initial wave train at the wavemaker has a maximum envelope amplitude $A_{max} \approx 1.5A_0$.

In the Whispers3D model, $N_T = 7$ is used. The model domain has a regularly spaced grid $\Delta x = 0.07$ m, which corresponds about $L_{deep}/32$ or $L_{shallow}/25$. Waves are generated in a relaxation zone with one wavelength L_{deep} on the left boundary of the domain. The boundary condition is obtained from decomposition of the exact solution at the position of wave maker, instead of the measured signal in the flume. Waves are generated using linear composition for the free surface elevation as well as the velocity potential. Waves are absorbed, on the other side of the numerical basin, in a relatively long relaxation zone with a length of $6L_{deep}$. Waves are generated with the same duration as in experiments, about 5 min. The time step in the model is $\Delta t = T_c/64 = 0.01875$ s. The *Courant–Friedrichs–Lewy* (CFL) number in the current case is $\text{CFL} = L\Delta t/(T\Delta x) = 0.5$ in the deeper region and $\text{CFL} \approx 0.4$ in the shallower region. The NLSE is solved using split-step Fourier method introduced by Taha and Ablowitz (1984).

The inclusion of bulk dissipation in Whispers3D model follows the visco-potential approach of Dias et al. (2008). In such formulation (i.e. Eqs. (I.2.5) to (I.2.6)), the dissipation is applied to the whole bulk of the fluid. In the model of NLSE with variable coefficients, however, the dissipation term δ stands for the exponential attenuation in wave amplitude. The relation between the dissipation rates of Whispers3D and NLSE models is established in Appendix (A.2) within the framework of linear waves.

The value of δ has been measured experimentally via whether harmonic wave tests or the unmodulated part of Peregrine breather tests. In case 368, the measured value is 0.0036 m^{-1}. The dissipation parameter ν_v in Eqs. (I.2.5) and (I.2.6) is calibrated, and the calibrated value is $\nu_v = 1.5 \times 10^{-4}$ m^2/s. It corresponds to $\delta = 0.0034$ m^{-1} considering the shallower water depth. For information, the prediction of Eq. (III.1.9) is $\delta_{Dorn} = 0.0017$ m^{-1} which is about half of 0.0034 m^{-1}. Both are smaller than the measured value of δ because in the flume, the attenuation of wave amplitude in the deeper region is weaker than in shallower region.

In Fig. (III.2.6), the comparison of spatial evolution of the wave envelope is shown. The envelope evolution in measurements shown in panel (a) is well described by the Whispers3D simulation shown in panel (b). In panel (b), as waves propagate towards the focusing position $x = 55$ m, the modulation of the envelope increases in amplitude and is slightly shifted in time axis. After passing through the threshold depth, the modulation (i.e. the envelope soliton) splits into two sub-modulations (i.e. the new smaller envelope solitons with low amplitude). The sub-modulations appear one followed by the other in time due to their different group velocities. In panel (c), where the results for NLSE are displayed, the modulation is symmetric. As the modulation propagates towards the focusing position, there is no shift in the time. It means that the group velocity in NLSE simulation is different from that in measurements and Whispers3D. The abrupt change of slope gradient results in a series of oscillations that propagate with different group velocities.

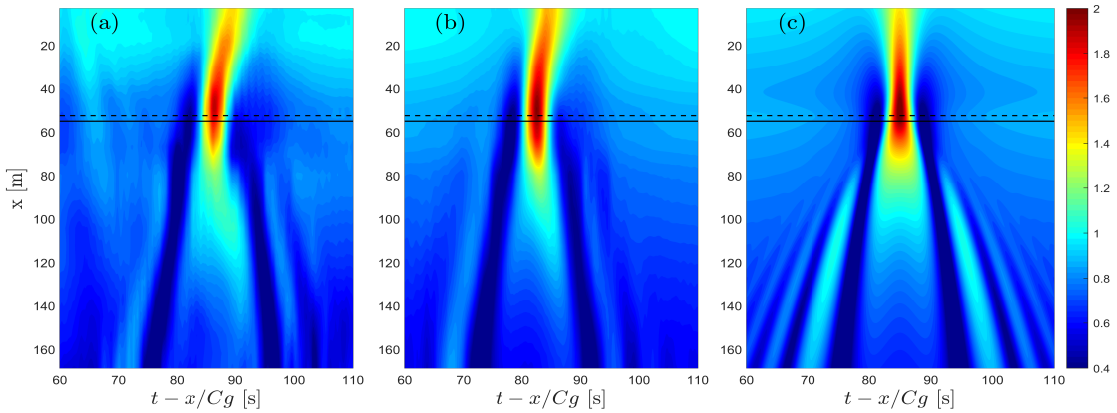

Figure III.2.6: AP case 368: pseudo color view of the normalized envelope evolution in experiments, panel (a), Whispers3D simulation, panel (b), and NLSE simulation, panel (c). In all the panels, the horizontal dashed line represents the threshold of relative water depth $kh = 1.363$, and the horizontal solid line indicates the focusing position.

In Fig. (III.2.7), the spatial evolution of the maximum and minimum of the envelope is shown. In this case, both the NLSE model and Whispers3D model predict well the increase and decrease trend of the modulation. Both maximum and minimum of envelope around the end of the flume is close to the measurements. On one hand, it confirms the measured dissipation rate δ. On the other hand, it also confirms the relation between wave amplitude attenuation rate and bulk dissipation rate derived in Appendix (A.2). The minimum envelope is better described by the Whispers3D model. In NLSE simulation, the minimum envelope reaches 0 and is generally lower than the measurements over the shallower region. The maximum envelope in simulations agrees well with the measurements, except

near the focusing position where the measured values are lower than in simulations. The Whispers3D model gives better results for A_{max} before the focusing point, and for A_{min} after the focusing point, than the NLSE model. This is due to the fact that Whispers3D has better description of higher-order non-linearities, which are absent in cubic NLSE model.

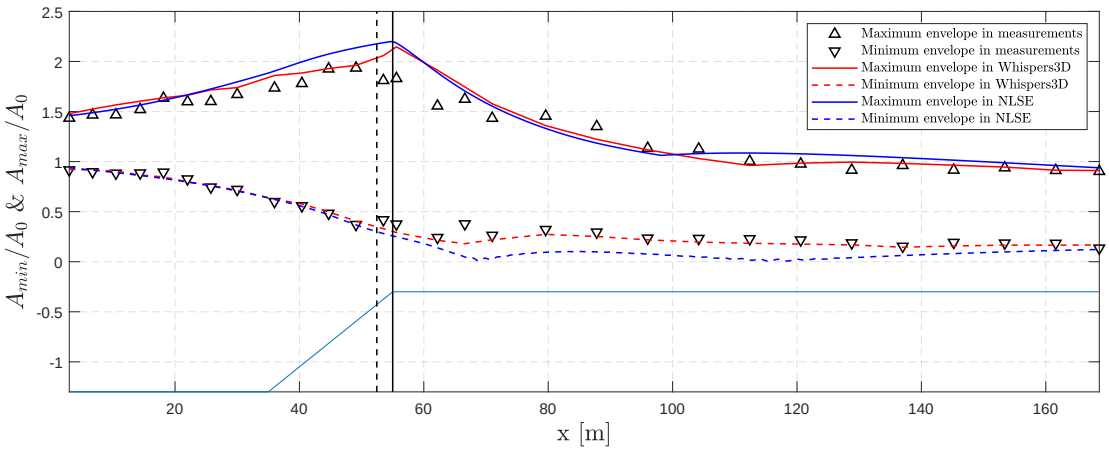

Figure III.2.7: AP case 368: spatial evolution of maximum and minimum envelopes in experiments and simulations with different models. The vertical dashed line represents the threshold of relative water depth $kh = 1.363$, and the vertical solid line represents the focusing position.

In Fig. (III.2.8), the time evolution of the envelope is shown. It is observed that the NLSE model gradually deviate from experiments and Whispers3D simulation. It is known that the NLSE model with variable coefficients is first-order in dispersion, so waves propagate with the linear group velocity of local water depth. The group velocity in measurements is faster than linear group velocity. In the NLSE model results, the envelope is symmetric in time. In the measurements, however, the two modulations with minimum envelope amplitudes are not symmetric. The one that appears earlier in time is of smaller envelope amplitude that the other. This is mainly due to higher-order dispersion effects. A similar asymmetric shape of the envelope was also observed in a flat bottom case in Kimmoun et al. (2017), and with the MNLSE model adopted, this asymmetry of the envelope in time is well captured. It is known that the main difference between the NLSE model and the MNLSE model lies in the capacity of describing wave dispersion. The MNLSE is of second-order dispersion, thus it is closer to experiments and fully dispersive model Whispers3D.

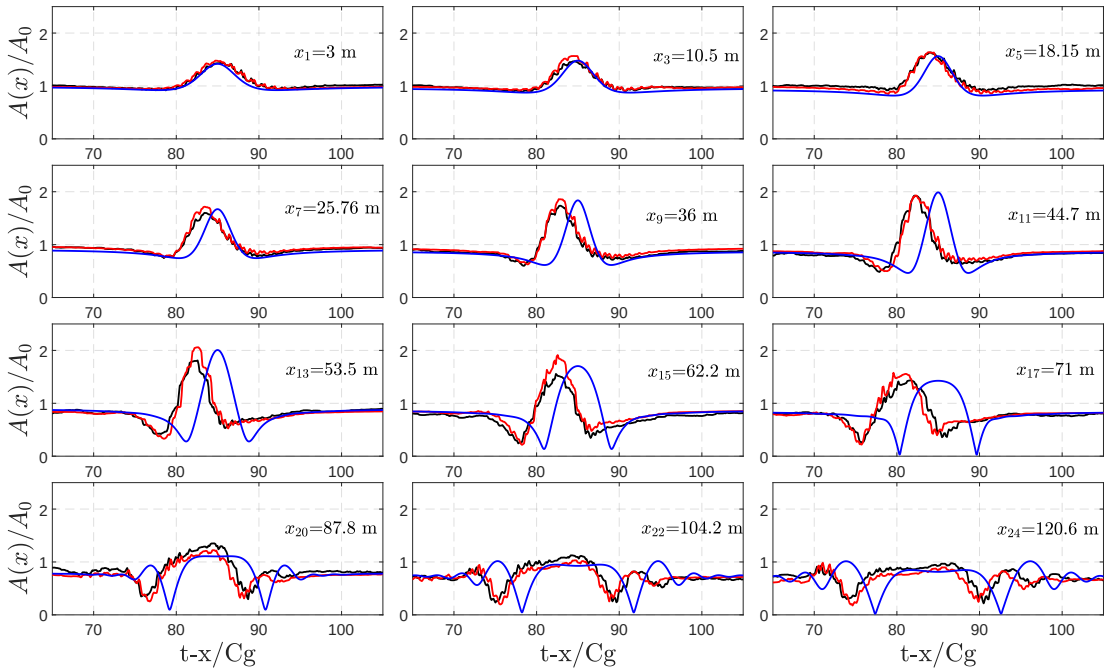

Figure III.2.8: AP case 368: comparison of the time evolution of envelope measured at different positions in experiments and simulations with the different models. Black lines represent measurements, red lines represent the results of Whispers3D simulation results, and blue lines represent the results of NLSE simulation results.

2.2 Case 364: Akhmediev breather evolution, periodic unstable events

In case 364, the breather parameter is $\mathfrak{a} = 0.25$. It corresponds to the largest modulation growth rate for AB. The other parameters are same as in Section (2.1), $\epsilon = 0.11$, $h = 1.3$ m, $T_c = 1.2$ s, and $x_f = 55$ m. Similarly, the threshold $kh = 1.363$ locates at $x = 52.445$ m, close to the end of the slope $x = 55$ m. The relative water depth changes from deeper region $kh \approx 3.638$ to the shallower flat region $kh \approx 1.065$. The Akhmediev breather corresponds to a series of solitons. When a soliton reaches the edge of the slope, a soliton split into multiple solitons due to instabilities. These solitons can be described as oscillations or sub-modulations. In Section (2.1), the experiment showed that one envelope soliton split into two sub-modulations with significantly different group velocities. In this case, it is anticipated that the sub-modulation could appear periodically for each of the envelope solitons. The sub-modulation with larger group velocity could interact with the slower sub-modulation generated previously.

2.2.1 Experimental observation

In Fig. (III.2.9), the evolution of the normalized free surface elevations and their corresponding envelopes measured at different positions are shown. The envelope is also computed via windowed Fourier analysis, and constructed using three harmonics. The modulations of AB appears periodically in time. As the wave packets containing modulations approach to the focusing position $x = 55$ m, the modulations compress as observed in case 368. It is seen that starting from $x = 62.2$ m (probe 15), the envelope solitons gradually decrease in magnitude as they propagate over the shallower region, in the meantime, sub-modulations gradually manifest themselves between the envelope solitons. After some distance (in this case $x = 96$ m), the oscillations that are generated from different solitons overlap with each other resulting in a more complicated pattern in time domain near the end of the flume. This pattern is shown in Fig. (III.2.10), it presents a 3D view of the envelope evolution in space and in time.

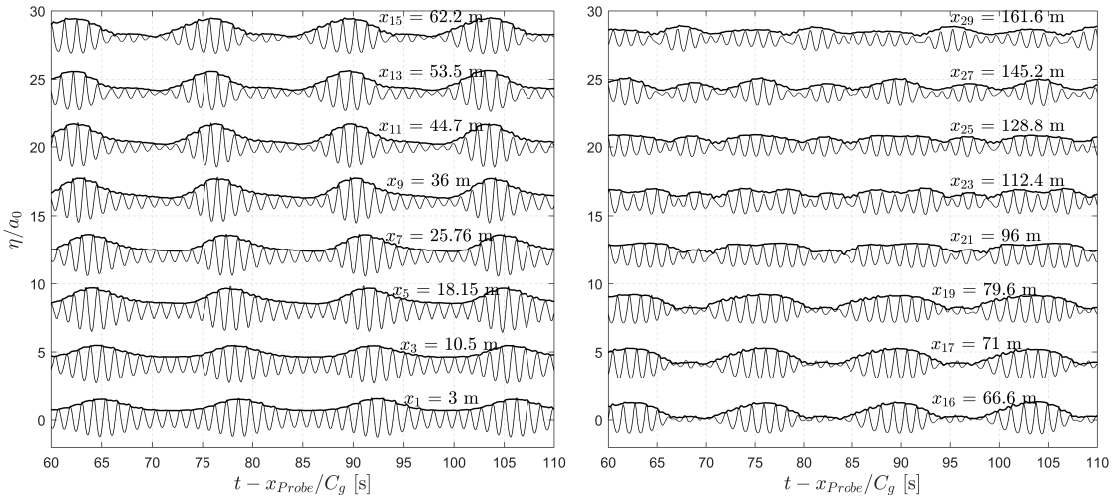

Figure III.2.9: AB case 364: evolution of normalized free surface elevation (solid line) and its corresponding envelope (bold solid line).

In the panel (a) of Fig. (III.2.11), the spatial evolution of the spectrum is shown. In the initial spectrum, the carrier wave frequency at $f/f_c = 1$ is accompanied by a large number of small side bands. Among the side bands, some are of higher energy and remain while wave packet propagates into the shallower region. It is seen that as the wave train propagates over the shallower region, new low-frequency bands appear. This is the differences between the sub- hand super-harmonic sidebands that is not described in NLSE. The carrier wave frequency and the energetic side bands slightly broadens after around $x = 80$ m, and the frequency downshift appears. In the panel (b) of Fig. (III.2.11), the evolution of the maximum and

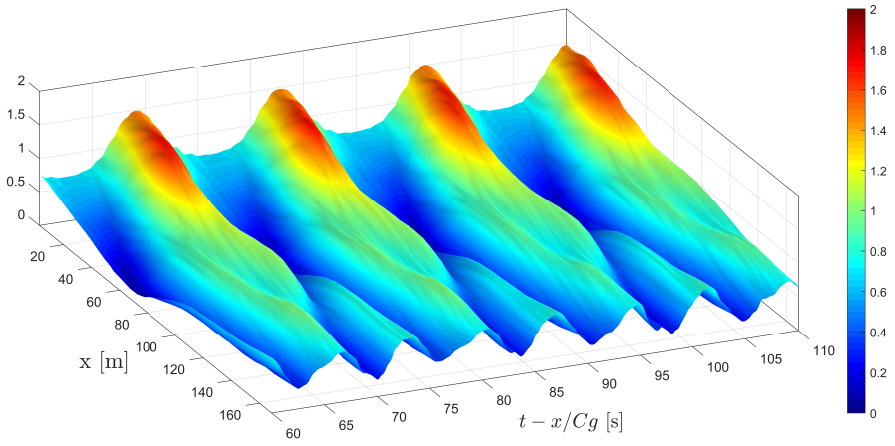

Figure III.2.10: AB case 364: 3D overall view of normalized envelope evolution in space and time. The envelope is normalized by the carrier wave amplitude.

minimum value of envelope is shown. The maximum envelope amplitude at the wave maker boundary is about 1.5 times of A_0. It increases to around $1.7A_0$, near the end of the slope. Then it decreases after entering the shallower region. A bump in the maximum amplitude curve appears near the end of the flume.

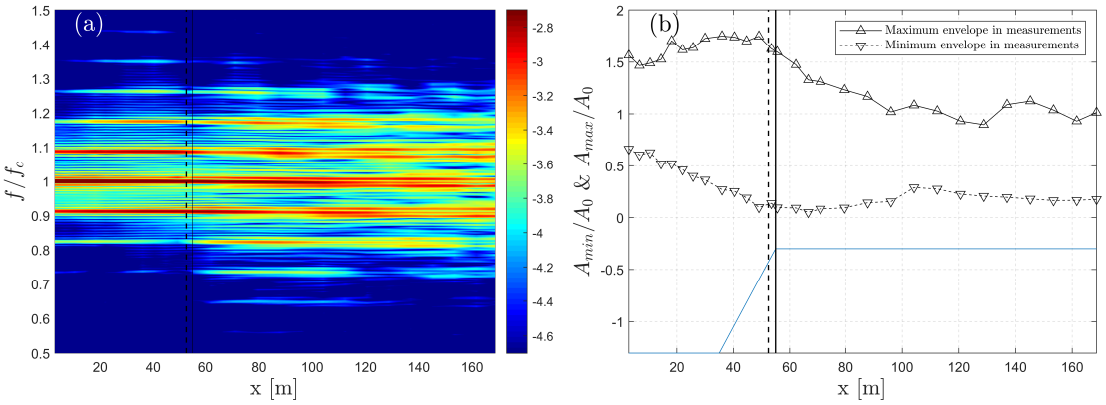

Figure III.2.11: AB case 364: spatial evolution of spectrum and envelope, (a) pseudo color map of the spatial evolution of spectrum in logarithmic scale, wave frequency is normalized by carrier wave frequency f_c, (b) the spatial evolution of the maximum and minimum values of envelope. In both panels, the vertical dashed lines represent the threshold of relative water depth $k_c h = 1.363$, k_c corresponds to carrier frequency f_c, the solid lines represent the focusing position.

2.2.2 Comparison between fully non-linear model and NLSE with variable coefficients

In the numerical simulation with Whispers3D, the chosen N_T, Δx, Δt, bulk dissipation ν_v, and the length of relaxation zones are same as in Section (2.1). The amplitude attenuation dissipation in the NLSE model δ is identical too. In Fig. (III.2.12), the comparison of the normalized wave envelope between the measurements, simulations of Whispers3D and NLSE models are shown. The Whispers3D simulated result in panel (b) is very similar to the measurements in panel (a), including the curly evolution of the initial modulation and the sub-modulation in the middle of two modulations. In panel (b) the modulation around the end of the flume is slightly larger than observed in measurements. Results for NLSE model are displayed in panel (c). The modulation before the end of the slope is not curly. Due to the abrupt change of slope gradient, the instabilities of the AB solution take place in the tests. The instabilities result in a relatively complex pattern of wave envelope. Over the shallower region, the pattern is symmetric and the sub-modulation is more significant than that in the measurements.

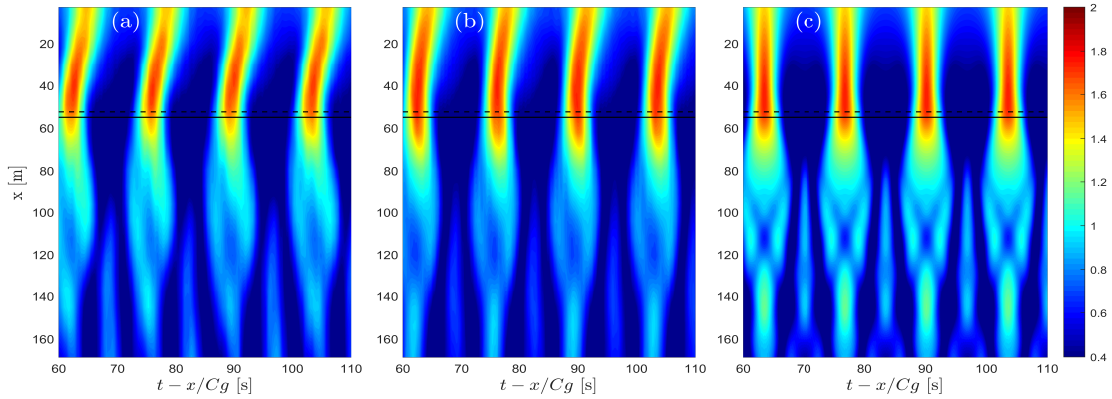

Figure III.2.12: AB case 364: pseudo color view of the normalized envelope evolution in experiments, panel (a), Whispers3D simulation, panel (b), NLSE simulation, panel (c). In all the panels, the horizontal dashed lines represent the threshold of relative water depth $kh = 1.363$, and the horizontal solid lines represent the focusing position.

The spatial evolution of the maximum and the minimum of the envelope is given in Fig. (III.2.13). The agreement of the maximum envelope in simulations with Whispers3D and NLSE models is good until $x \approx 90$ m. Then discrepancies arise. In the experiment, a second local maximum of A_{max} is observed around $x = 140$ m. The Whispers3D model predicts smaller value than the experiment. On the other hand, the NLSE model overestimates the maximum envelope amplitude in the same area. But the re-amplification of A_{max} observed in the experiment, is predicted in both models. For the minimum envelope amplitude evolution in

space, the results of Whispers3D show good agreement with the experimental results along the wave flume.

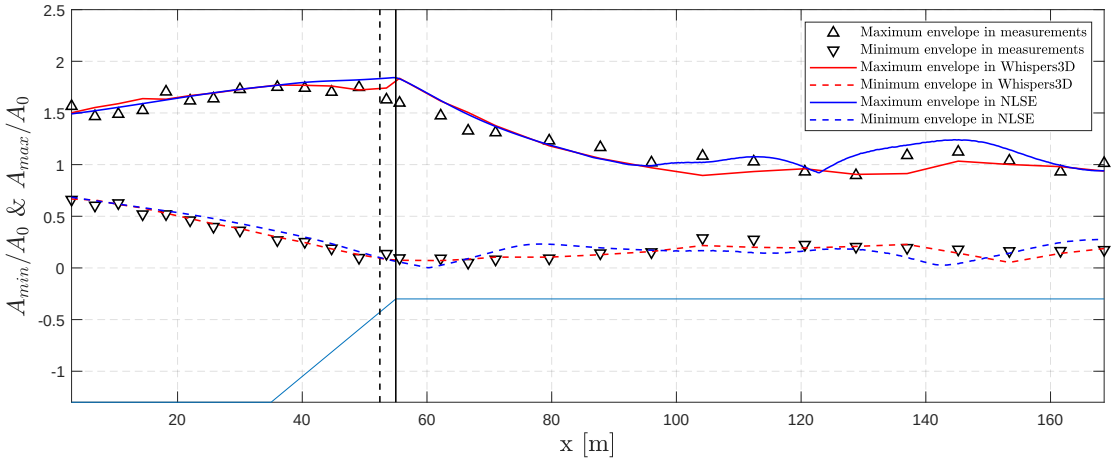

Figure III.2.13: AB case 364: spatial evolution of maximum and minimum envelopes. The vertical dashed line represents the threshold of relative water depth $kh = 1.363$, and the vertical solid line represents the focusing position.

In Fig. (III.2.14), the detailed envelope shape comparison between experiments and simulations with different models is shown. The behavior of NLSE model in the simulation of AB case 364 is similar to that in the AP case 368, two main features are observed. The envelope in NLSE simulations deviates from the measurements gradually. This is due to the dispersion in NLSE is linear. Besides, unlike Whispers3D simulations, the asymmetry of the envelope is not captured in NLSE simulations due to higher-order dispersion. The asymmetry of envelope amplitude in experiments appears in the deeper region and becomes more and more pronounced as the wave train propagates. It indicates an adaptation of the exact solution of AB to the real experimental condition which is dissipative and contains all high-order effects. After entering the shallower region, the modulations decrease gradually in amplitude. In the time domain, the modulation extends and becomes broader due to different group velocity. The amplitude of the sub-modulations increase in amplitude.

2.2.3 Comparison with an additional case 365 with a larger steepness

To show the effect of steepness of the carrier wave, an additional case 365 with the same parameters as in the previous paragraph, with $\mathfrak{a} = 0.25$, $h = 1.3$ m, $T_c = 1.2$ s, and $x_f = 55$ m is considered. The carrier wave steepness is slightly larger with $\epsilon = 0.12$. $\mathfrak{a} = 0.25$ represents the largest instability growth rate. As the wave maker is relatively close to the focusing point (with a distance 55 m),

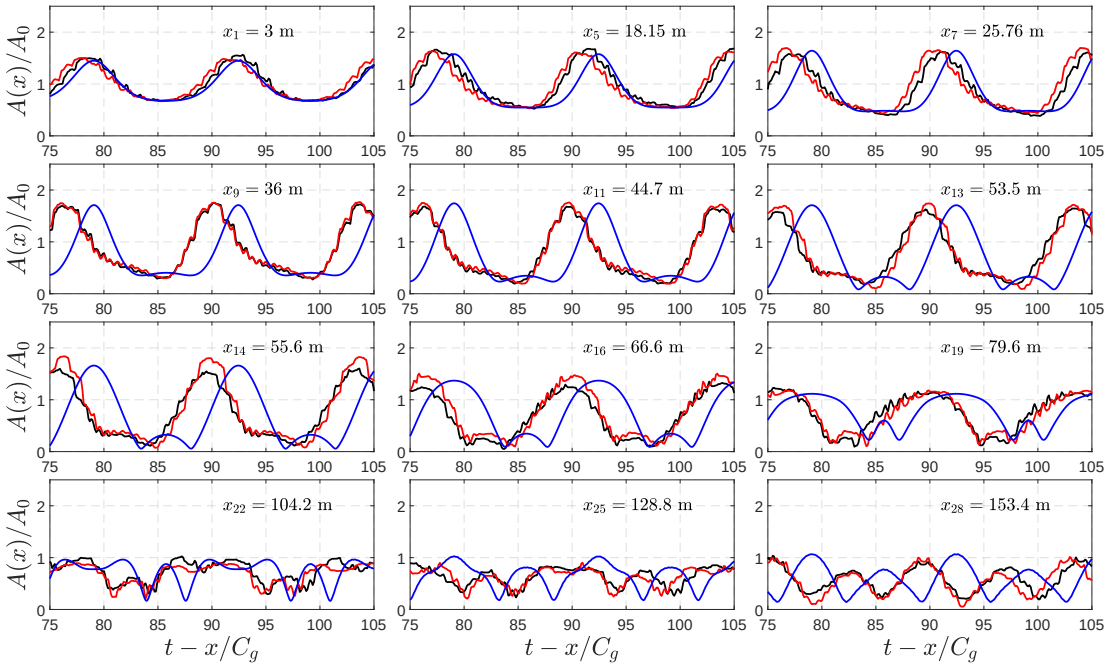

Figure III.2.14: AB case 364: comparison of the time evolution of envelope measured at different positions. Black lines represent measurements, red lines represent Whispers3D simulation results, and blue lines represent NLSE simulation results.

the modulation is already developed. At this boundary, the maximum wave amplification of the modulation is around 1.5 times of the carrier wave amplitude.

In case 365 with slightly larger carrier wave amplitude, the general characteristics of the wave evolution are similar to the case 364. So they will not be repeated here. The main interest here is to compare case 365 with the previous case 364 to find the differences which result from the carrier wave amplitude parameter. In Fig. (III.2.15), the evolution of the maximum and minimum value of normalized envelope is shown. The maximum and minimum values of the normalized envelope A_{max}/A_0 and A_{min}/A_0 in the case 365 with $\epsilon = 0.12$ are smaller than that in the case 364 with $\epsilon = 0.11$. This is due to the fact that the canonical transformation of X is scaled by carrier wave amplitude, for higher steepness, X is longer for the same physical distance. Thus, for the same focusing position x_f, the higher steepness results in a less developed stage of modulation at the wave maker boundary. It is also observed that the re-amplification of A_{max}/A_0 takes place earlier in the case 365. This is anticipated that the instability is stronger and develops faster for the case with larger steepness.

It is seen that, in the previous examples, the normalized amplitude of the perturbation A_{max}/A_0 at the wave maker is a function of the steepness. It is thus

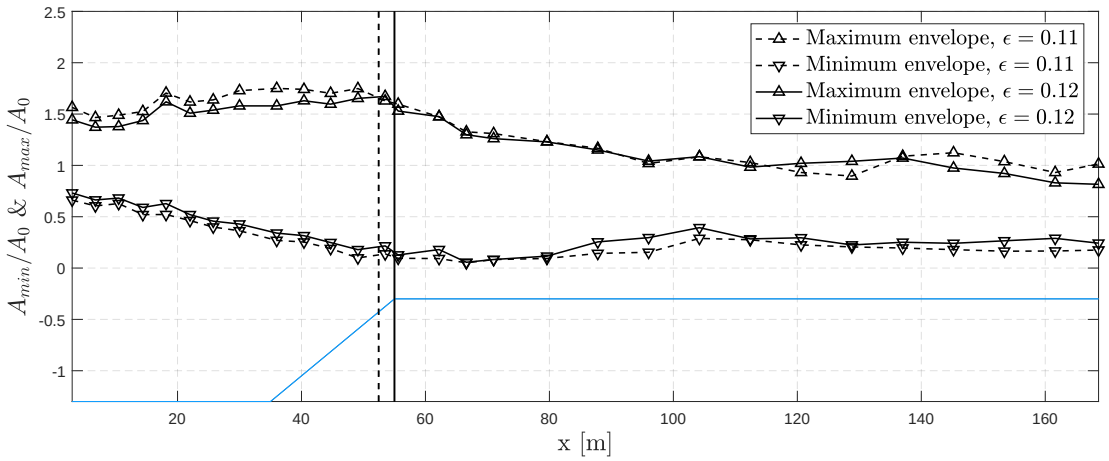

Figure III.2.15: Comparison of maximum and minimum envelope amplitudes evolution in space for AB cases 364 and 365. The vertical dashed line represents the threshold of relative water depth $kh = 1.363$, and the solid line represents the focusing position.

of interest to show the relation of normalized and non-normalized perturbation amplitude with steepness. Here we show their relation within the framework of NLSE. Fig. (III.2.16) shows the maximum and minimum of wave envelope at the wave-maker (55 m before the focusing position) as functions of steepness with other parameters identical as in cases 364 and 365.

In panel (a) of Fig. (III.2.16), the relation between normalized maximum and minimum values of envelope and steepness is shown. It is shown that as the carrier wave steepness increases, the normalized maximum envelope amplitude at the wave maker boundary decreases. This is because, for a larger carrier wave steepness, the wave train modulation is more localized in space. The dimensional amplitude is higher, since A_0 is larger. The limiting case is that when the carrier wave steepness is large enough, 55 m is sufficiently far from the focusing position. The wave train is not modulated yet at $x = 0$ m, so that $A_{max} = A_{min} = A_0$. It is in line with the idea of a rogue (freak) wave 'coming from nowhere' since the perturbations are so small that they are indistinguishable from the carrier waves. For the parameters chosen in the present case, and within the framework of the third-order NLSE model, it is close to such limit for $\epsilon > 0.25$. It should be noticed that such limit is high for weakly non-linear assumption, and with an amplification of 2 considered due to modulation, the steepness will exceed the breaking limit. In panel (b) of Fig. (III.2.16), the relation between dimensional maximum and minimum values of envelope and steepness is shown. It is observed that the dimensional envelope amplitude increases with the carrier steepness. However, around the range $\epsilon \in [0.05, 0.15]$, the increase of the maximum envelope amplitude is not significant. The minimum envelope amplitude, both dimensional and non-dimensional, increase

with ϵ.

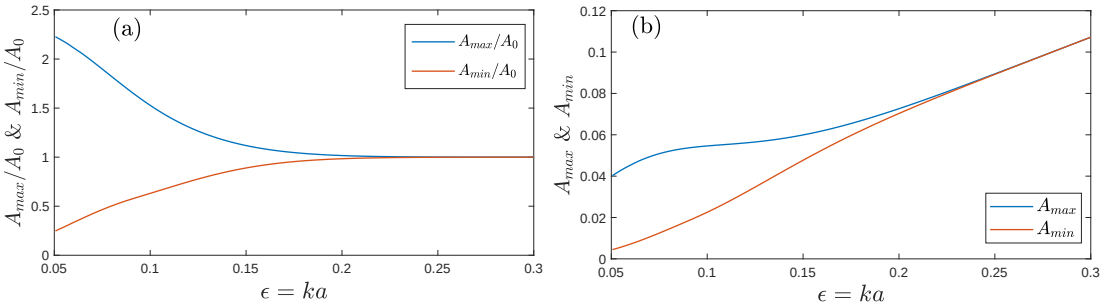

Figure III.2.16: The maximum and minimum values of wave envelope at the wave-maker (55 m before the focusing position) as functions of steepness ϵ with other parameters identical as in cases 364 and 365. In panel (a) the envelope amplitude is normalized by the incident carrier wave amplitude, panel (b) shows the corresponding dimensional envelope amplitude.

As the experimental conditions are identical to previous case 364 except for the steepness, we adopt the same numerical parameters Δx, Δt, N_T, N_{sten} for the simulation of case 365. In Fig. (III.2.17), the envelope evolution in space and time is displayed. The experimental and numerical results of the two cases with different carrier wave steepness are compared. We conclude that the main differences lie in the sub-modulations over the shallower region. Fig. (III.2.17)(a-c) shows that the sub-modulations are of more significant amplitude than the case 364, in Fig. (III.2.17)(d-f). The sub-modulations take place earlier in space. Besides, in the case 365, the NLSE model predicts new bifurcations of the sub-modulations manifest around the end of the flume. In the experimental results in panel (a), the bifurcations are not so clear. In the simulations with Whispers3D in panel (b), the bifurcation is visible.

Here we studied cases where the bottom consists of two flat parts with different water depth. The two flat regions are connected by a slope with a constant gradient. The focusing position locates at the beginning of the shallower region. It is anticipated that small carrier wave steepness, at the wave maker boundary, the modulation is close to maximum modulation which corresponds to the largest amplification of envelope. So the modulation is mild as the wave train propagates towards the focusing position. As waves propagate over the shallower region, the sub-modulation is trivial due to small non-linearity. On the contrary, strong modulation is expected from wave maker to the focusing position while the carrier wave is of large steepness. More complex dynamics is expected around and after the focusing position since the waves are of higher steepness due to amplification. The bound mode non-linear interaction occurs and large amplification may cause breaking events. All these effects result in a more complex pattern as waves prop-

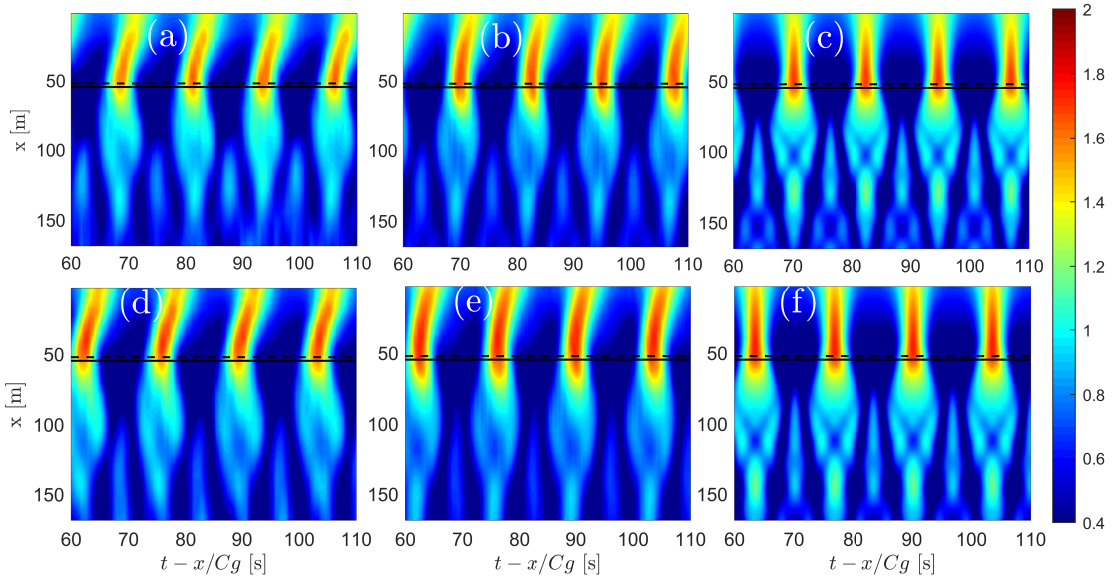

Figure III.2.17: Comparison of experimental and numerical results of the AB cases 364 and 365. In panels (a) to (c), the results correspond to the case 365, and in panels (d) to (f), the results of case 364. Panels (a), (d) correspond to experimental measurements; panels (b), (e) simulations with Whispers3D model; panels (c), (f) simulations with NLSE model.

agate over the shallower flat region after the focusing event. The generation and bifurcation of the sub-modulations are included.

Chapter 3

Breather evolution over two connected bed slopes

In the previous chapter, we have discussed the case where waves propagate in the shallower flat region after an up-slope. It is shown that the abrupt bottom gradient change results in the fission of crest of the modulated wave envelope into two sub-solitons of the envelope over the shallower region. For AB cases, the sub-modulations may overlap with each other, forming a second local amplification of the envelope around the end of the flat region. For larger non-linearity of the incident wave train, the sub-solitons, or sub-modulations appear earlier in space and are of higher amplitudes. However, large steepness conditions under which stronger instability phenomenon would appear are not easy to understand. Because in such non-linear cases, large oscillations take place beside the wave packets. These oscillations come from another unstable mode that develops naturally as the regular wave train becomes very steep. Alternatively, more non-linearity is introduced by setting a mild sloping region after the uphill slope. In the following, the considered bottom is composed of three parts: (i) starting from the wave-maker (at $x = 0$), a section with constant water depth, (ii) a relatively steeper slope with constant gradient, (iii) a long mild slope with a shoreline. The second slope with shoreline works as dissipation zone to absorb incident wave energy. Two bathymetries are tested with different combinations of gradients of two connected slopes. One case is of relatively milder slopes, $1 : 40$ for the first slope and $1 : 200$ for the second. The other is of relatively steeper slopes, $1 : 20$ and $1 : 120$.

In this chapter, we discuss breather evolutions over two different bottom setups. The experimental conditions are still controlled by the five-parameter space $(T_c, \epsilon, h, \mathfrak{a}, x_f)$.

3.1 Akhmediev breather evolution over relatively mild slopes

The bottom profile is shown in Fig. (III.3.1). The considered bottom slope is relatively mild with the first slope being 1/40 and the second 1/200. The first slope starts at $x = 31.175$ m, and the second starts at $x = 51.175$ m. 49 wave gauges are placed in the flume, and their positions are shown in the sketch. As is indicated, probes 1–27 are distributed with equal spacing of 3 m. The probes 27–44 are of a shorter spacing interval of 2 m to get a better description of breather evolution within this area. This wave tank bottom setup is denoted as setup 2. The closest wave gauge to the end of the first slope is probe 17.

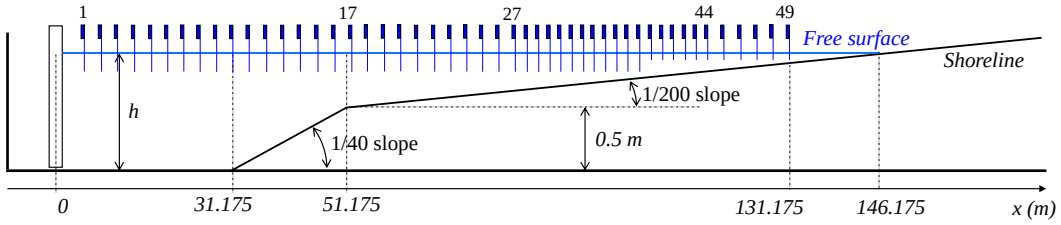

Figure III.3.1: Sketch of the bathymetry setup 2, and the locations of probes

3.1.1 Case 410: experiment and simulation of a weakly non-linear case

During the experimental campaign with bathymetry setup 2, 128 cases were performed for different wave period, wave steepness, Akhmediev parameter and focusing distance. These tests are named case 301 to case 428. Among these cases, regular wave tests were also performed in order to evaluate the dissipation rate. Among all these cases, we have chosen the case 410 because it corresponds to a general behavior observed during this campaign.

In the experimental case 410, the breather parameter is $\mathfrak{a} = 0.35$. The other parameters are $\epsilon = 0.09$, $h = 0.975$ m, $T_c = 1.085$ s, and $x_f = 76.183$ m. The threshold for modulation instability $kh = 1.363$ is located at $x = 76.183$ m, which is the same position as x_f. The relative water depth in the deeper region is $kh \approx 3.339$, it decreases to 0 after the two sloping areas.

In the simulations with Whispers3D model, $N_T = 7$ is used. The numerical step sizes in space is $\Delta x = L_{deep}/32 = 0.0573$ m and time $\Delta t = T_c/64 = 0.00287$ s. The corresponding CFL number is CFL = 0.5 in the deeper region. A 2 meter long relaxation zone is set on the left boundary of the domain for wave generation. As the run-up on shoreline is not our primary target in this study, a flat region is set after kh equals 0.5. In this shallower flat region, a relaxation zone with a length of 10 m is set for wave absorption. The computation domain is now 132.675 m

without the relaxation zones. The dimensional water depth for the shallowest region (for $kh = 0.5$) is as low as 0.068 m. In the simulation with NLSE model, the same shallower flat region is adopted to avoid numerical instabilities. In this case, the bulk dissipation parameter in Whispers3D is $\nu_v = 1 \times 10^{-4}$ m^2/s. The corresponding amplitude decay rate in NLSE is $\delta = 0.0027$ m^{-1}, it is calculated based on the relation of ν_v and δ established in Appendix (A.2).

In Fig. (III.3.2)(a), it is shown that for the experiment case 410, the envelope solitons propagate over two slopes without significant change. The modulations remain significant after the focusing position. The amplitudes of envelope solitons decay mainly due to dissipation.

In Fig. (III.3.2)(b–c), the AB evolution of case 410 is well predicted by both Whispers3D and NLSE models. Even in the modulational stable area with $x >$ 76.183 m, the results of NLSE model with variable coefficients show qualitatively good agreement with measurements. The main differences between the simulations and the experiment appear around the beginning and the end of the flume. At the beginning of the flume $x < 40$ m, probably there were some calibration problems for the wave gauges during the measurements. Around the end of the flume, the differences are not due to reflection, because it is known that a 1/200 slope involves very low wave reflection.

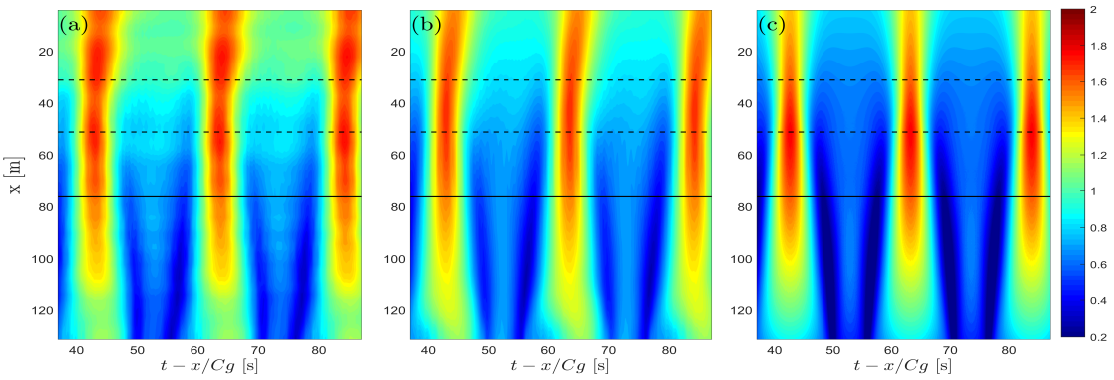

Figure III.3.2: AB case 410: pseudo color view of normalized envelope evolution in experiment, panel (a), Whispers3D simulation, panel (b), and NLSE simulation, panel (c). In all panels, the horizontal solid lines indicate the superimposed location of AB focusing position and the position where the threshold $kh = 1.363$ is achieved. The horizontal dashed lines denote the edges of the first slope.

In Fig. (III.3.3), the maximum and minimum values of the envelope is shown. The spatial variation of the maximum and minimum values of envelope amplitude is mild. The local maximum envelope amplitude is achieved around $x = 40$ m in Whispers3D, and around $x = 52$ m in NLSE. Due to the errors in measurements, it is difficult to determined precisely the real position corresponding to the local

maximum of envelope amplitude. Visually, we consider the maximum locates between 40 m and 60 m. Obviously, the maximum amplification of the wave packet is achieved before the focusing position. This is mainly due to two effects, the dissipation in the flume and the uneven bottom effect. Both of them result in decreased envelope amplitude, but counter-balanced by the increase of envelope amplitude due to modulation. The minimum of the envelope evolution is well captured by the models. Around the end of the flume, $A_{min} \approx 0$ indicates that for a time interval and for a given location, the free surface is not perturbated.

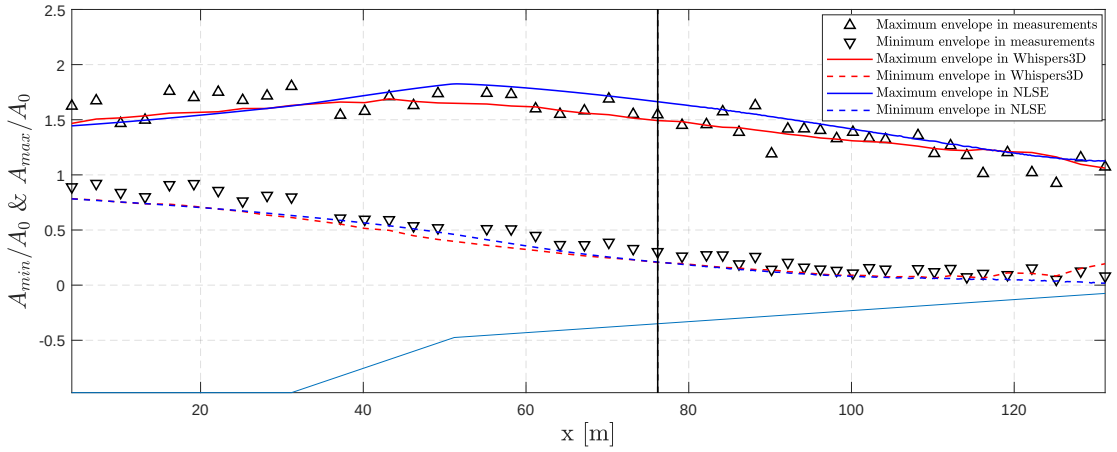

Figure III.3.3: AB case 410: spatial evolution of maximum and minimum envelopes in experiments and simulations with different models. The vertical solid line indicates the superimposed location of AB focusing position and the position where the threshold $kh = 1.363$ is achieved.

In Fig. (III.3.4), the local comparison of envelope profiles in the experiment and simulations is shown. It is observed that the agreement in envelope profile between measurements and Whispers3D simulation is good both in magnitude and in phase. The phase differences of wave packets in NLSE model and Whispers3D is limited. In the experiment, the envelope is nearly symmetric, the asymmetry develops only for shallow water. The most significant asymmetric profile in the measurements is obtained at the last probe. It is well predicted by Whispers3D model.

In Fig. (III.3.5), the spectral evolution for the experiment and the simulation results with different models is compared. As is shown in Fig. (III.3.5)(a), in the measurements the carrier wave frequency and side-band modes within the range $f/f_c \in [0.9, 1.1]$ had limited change as the wave train propagated in the flume. The side-band modes grew asymmetrically over the first steeper slope, namely $x \in [31.175, 51.175]$ m, and around the end of the flume $x > 100$ m. The growth of side-band modes indicates the occurrence of instabilities. The spectral evolution

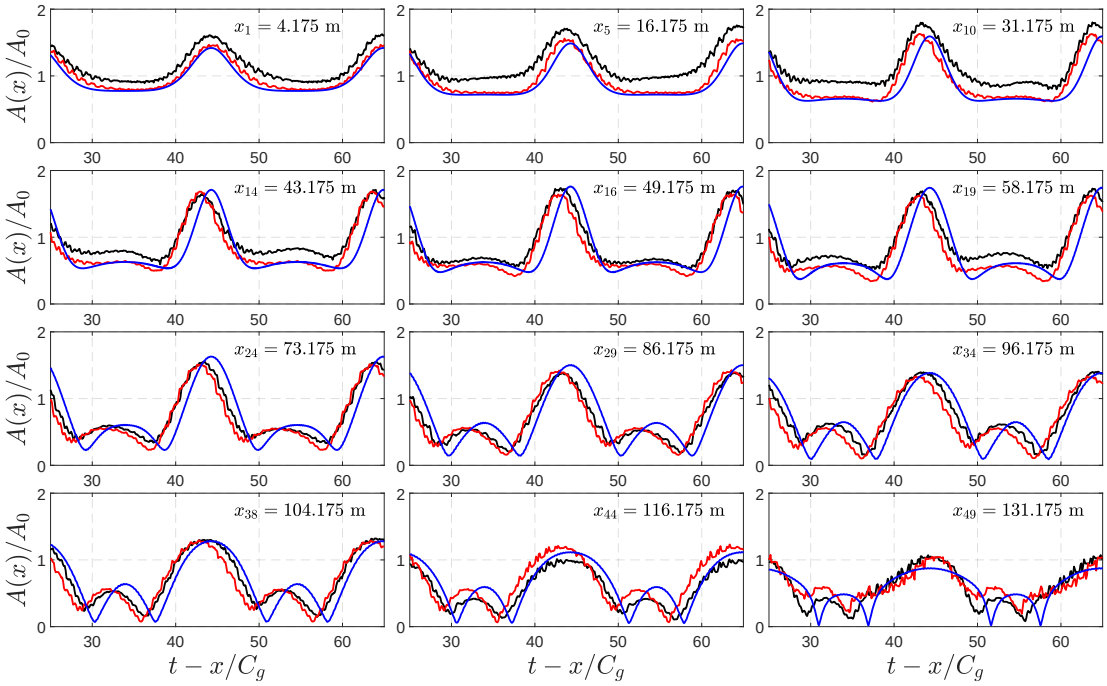

Figure III.3.4: AB case 410: comparison of the time evolution of envelope measured at different positions. Black lines represent measurements, red lines represent Whispers3D simulation results, and blue lines represent NLSE simulation results.

is well predicted by Whispers3D model given in Fig. (III.3.5)(b). Especially the asymmetry of the spectrum is well captured over both the first slope and the end of the flume. The spectral evolution in NLSE model is shown in Fig. (III.3.5)(c). It is, however, symmetric with respect to the carrier wave frequency f_c. The wave energy is more concentrated in the carrier wave, and the side-band modes close to f_c are of less energy compared to the measurements. The growth of side-band modes above the first slope is predicted (though with symmetrical shape). But the growth around the end of the flume is not well predicted. Differences between the measurements and NLSE results arise after $x \approx 60$ m.

3.1.2 Case 415: experiment and simulation of a weakly non-linear case for the largest instability growth rate

In case 415, the non-linearity of the incident wave train and the instability growth rate are increased. In this case, the breather parameter is set to $\mathfrak{a} = 0.25$, and the steepness to $\epsilon = 0.1$. Other parameters are not changed, $h = 0.975$ m, $T_c = 1.085$ s, and $x_f = 76.183$ m. The threshold for modulation instability $kh = 1.363$ locates at $x = 76.183$ m, which is the same position as x_f. The numerical parameters for

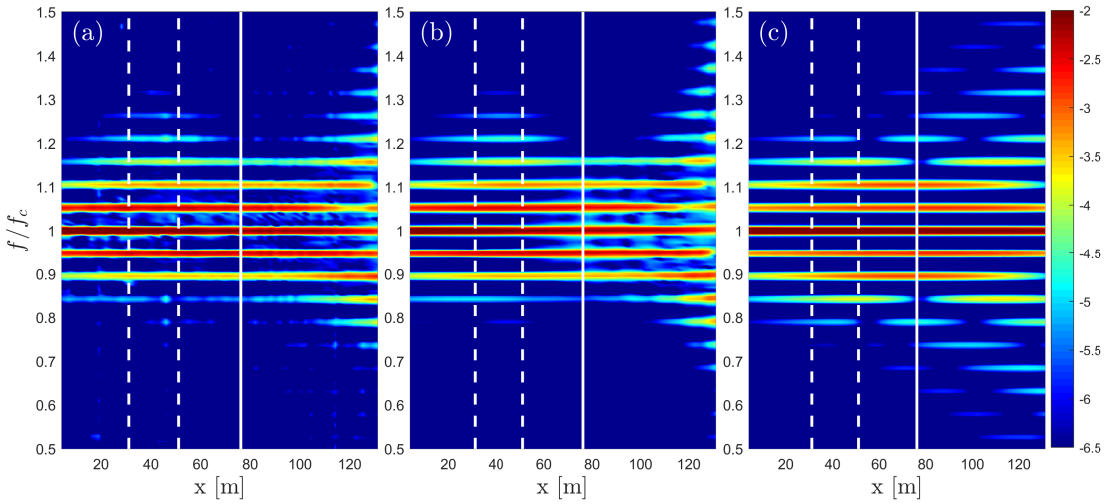

Figure III.3.5: AB case 410: comparison of spatial spectral evolution in measurements panel (a), Whispers3D simulation panel (b), and NLSE simulation panel (c). In all panels, the vertical solid lines indicate the superimposed location of AB focusing position and the position where the threshold $kh = 1.363$ is achieved. The vertical dashed lines denote the two edges of the first slope.

case 415, N_T, N_{sten}, Δx, Δt, ν_v are identical to those in the simulation of case 410 with Whispers3D model. The amplitude decay rate due to dissipation in NLSE is identical as well.

In Fig. (III.3.6)(a), the general evolution of the modulations is similar to case 410. The period of modulations is smaller in case 415 than in case 410 due to a smaller value of $\mathfrak{a}$. The two adjacent modulations get too close to each other so that sub-modulation generation in between is suppressed. The sub-modulations start to manifest around the end of the flume. In Fig. (III.3.6)(b–c), the simulations with both the NLSE and Whispers3D models show good prediction of the AB evolution in bottom setup 2.

In Fig. (III.3.7) are displayed, the spatial evolution of the maximum and minimum values of the envelope amplitude. We confirm that the general agreement between the experiment and simulations with different models is good. The prediction of Whispers3D is better than the NLSE model. In line with case 410, the A_{max} predicted by the NLSE model is higher than Whispers3D as water depth decreases. This is because the amplitude decay rate δ that corresponds to the calibrated ν_v is computed for water depth $h = 0.975$ m. In the simulation with the NLSE model δ is considered as a constant. However, as the water depth decreases, the corresponding δ should be increased due to a stronger dissipation. This could be taken into account by considering spatial variation of δ in NLSE simulations.

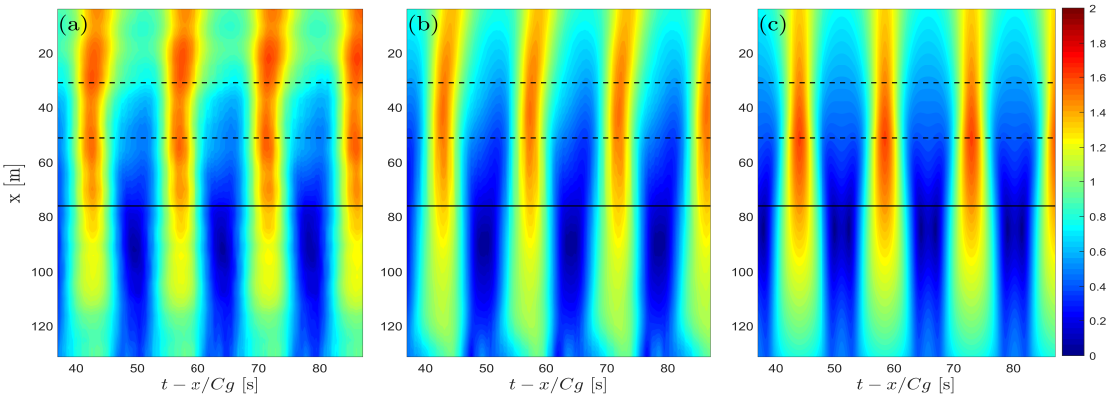

Figure III.3.6: AB case 415: pseudo color view of normalized envelope evolution in experiment panel (a), Whispers3D simulation panel (b), and NLSE simulation panel (c). In all panels, the horizontal solid lines indicate the superimposed location of AB focusing position and the position where the threshold $kh = 1.363$ is achieved. The horizontal dashed lines denote the two edges of the first slope.

However, it is not yet incorporated in the present work. The feature of A_{min} evolution is different from case 410. In case 410, A_{min} approaches to 0 around the end of the flume. For case 415, it decreases to 0 around 92 m and then increases again. In the simulation of case 410 with Whispers3D, such re-increase of A_{min} is also observed near the end of the wave tank. This feature is probably due to the higher carrier wave steepness of the incident wave train.

The time evolution of envelope is compared in Fig. (III.3.8). As the wave train propagate towards the focusing position $x = 76.183$ m, the envelope amplitude of the modulation decreases. In the exact AB solution, the envelope decreases to 0. It is clear at probe 29, the NLSE model predicts the minimum envelope $A_{min} = 0$ twice during one period of modulation. In the current time window, $A_{min} = 0$ takes place around $t - x_{probe}/C_g = 50$ s and 52 s for example. These two time instants are close since $\mathfrak{a} = 0.25$ is small. The results of NLSE model is nearly in phase with the measurements. The magnitudes of the envelopes are well predicted in NLSE model. The measured envelope profile is asymmetric in the upstream region of the flume (see probe 10 to probe 19) and near the end of the flume (see probe 49).

In this section, the bottom effects with relatively mild slopes 1/40 and 1/200 have been studied. It is seen that very limited instabilities of the AB wave trains occurred in the bottom setup 2 for the studied cases. The spatial evolution of the envelope is gentle and the generated sub-modulations are of low amplitude, even though the wave trains propagate in low relative water depth (until $k_c h = 0.5$). This is because the exact AB solutions could adapt to the non-exact solutions

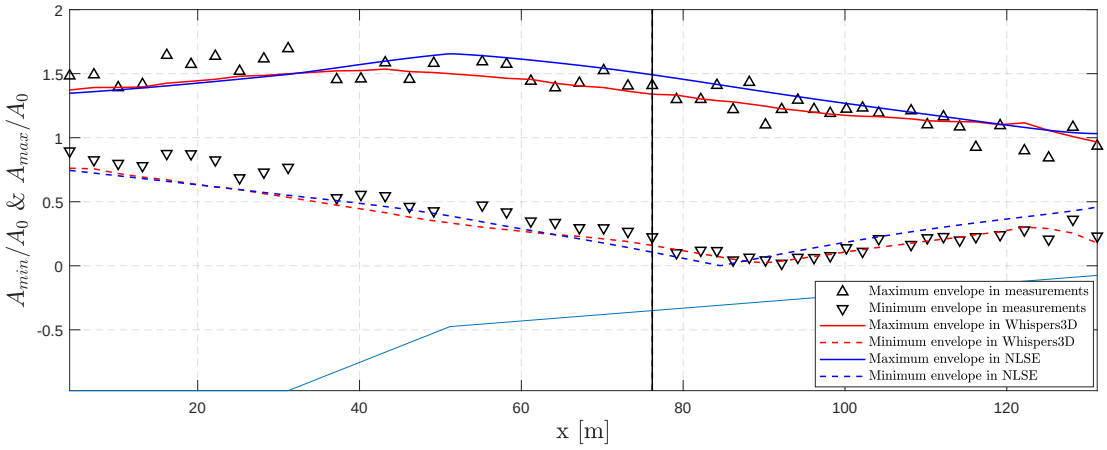

Figure III.3.7: AB case 415: spatial evolution of maximum and minimum envelopes in experiments and simulations with different models. The vertical solid line indicates the superimposed location of AB focusing position and the position where the threshold $kh = 1.363$ is achieved.

which coincides with the experimental condition in a relatively long distance. This hypothesis is supported by the comparison between case 415 and the AB case 364 with the bottom setup 1 in Section (2.2). They share similar non-dimensional parameters: in case 415, $k_c h = 3.34$, $\epsilon = 0.1$ and $\mathfrak{a} = 0.25$; and in case 364, $kh = 3.64$, $\epsilon = 0.11$ and $\mathfrak{a} = 0.25$. The differences are however obvious: in case 364, a particular envelope pattern has been observed; in case 415, the spatial evolution of envelope is mild. It is anticipated that the generation of the sub-modulations in Sections (2.1) and (2.2) is due to more significant depth transition.

3.2 Akhmediev breather evolution over relatively steep slopes

To show more pronounced instabilities as the exact AB solutions adapt to the non-exact solutions which are suitable for the experimental conditions, we consider larger bottom gradients and an incident AB wave train with stronger non-linearity. The bottom profile is shown in Fig. (III.3.1). The first slope is now 1/20 and the second 1/120. The first slope starts at $x = 42.6$ m, the second at $x = 55.6$ m. The water depth decreases by 0.65 m after passing over the steeper slope, and then decreases until 0 m after the second milder slope. As is shown in Fig. (III.3.9), 59 wave gauges are placed in the flume, and their positions are shown in the sketch. This bottom setup is labelled as setup 3.

During this campaign, 60 cases were performed for different wave period, wave

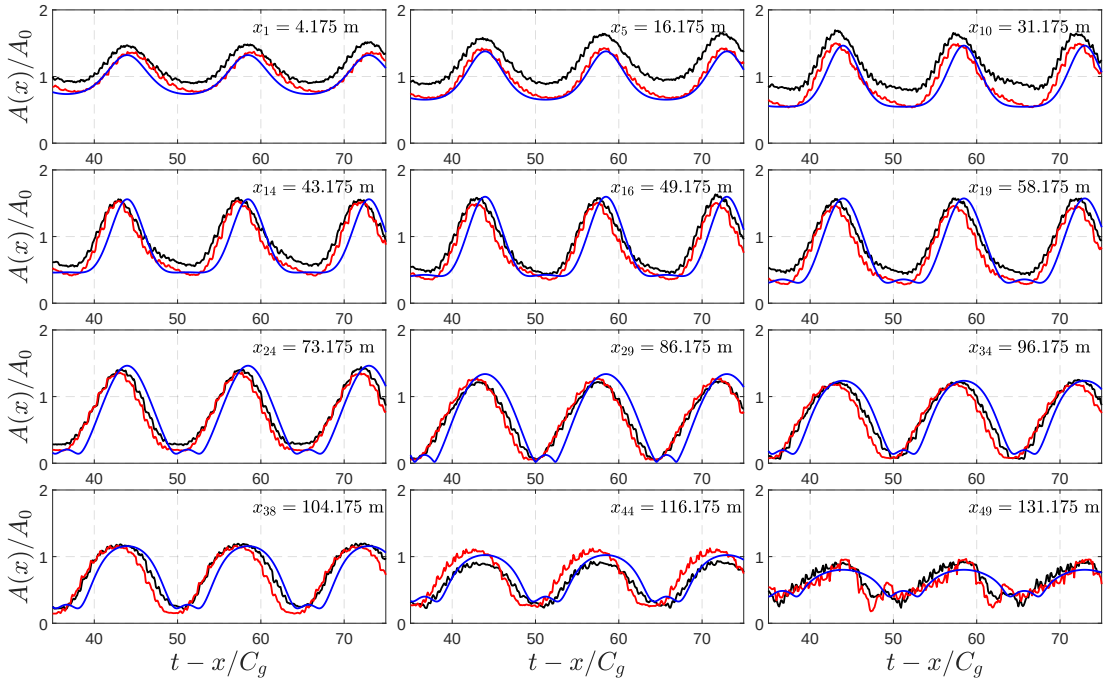

Figure III.3.8: AB case 415: comparison of the time evolution of envelope measured at different positions. Black lines represent measurements, red lines represent Whispers3D simulation results, and blue lines represent NLSE simulation results.

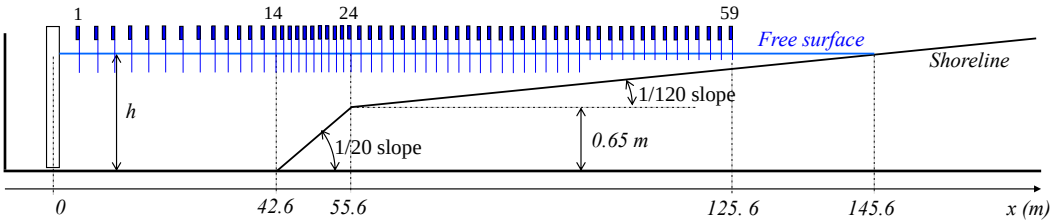

Figure III.3.9: Sketch of the bathymetry setup 3, and the location of probes.

steepness, Akhmediev parameter and focusing distance. These tests are named case 701 to case 760. Among these cases, 8 regular wave trains have been performed to evaluate the dissipation. The main differences from the previous section correspond to higher steepness and focusing points that are located near the edge between the two slopes. The campaign took place from June to August 2019 (I was involved in this campaign).

We show the experimental results of a case with strong non-linearity, case 739. The focusing distance took place before entering the uneven slope. As wave

packets approached the focusing position, the non-linearity of the wave packets was enhanced to a higher level. Due to the enhancement of large carrier wave steepness resulting from shoaling, breaking events were observed around the end of the first slope (i.e. 55.6 m). In this case, the wave parameters are $\mathfrak{a} = 0.46$, $T_c = 0.9$ s, $h = 1.4$ m, $\epsilon = 0.13$. The focusing position is $x_f = 42.6$ m. In the deeper region, $kh \approx 6.956$. The threshold for modulation instability $kh = 1.363$ locates approximately at $x = 116.725$ m.

3.2.1 Case 739: experimental observation

In Fig. (III.3.10)(a), the top view of the envelope evolution in space and time is shown. Due to the choice of a relatively high incident carrier wave steepness, the incident wave train at $x = 0$ m is only mildly modulated, and significant modulation takes place as wave train propagates towards the focusing position $x = 42.6$ m. The incident AB solution focuses at $x_f = 42.6$ m, and the amplitudes of the modulations keep increase until the end of the first slope $x = 52.6$ m. The local maximum value of the wave envelope is achieved before the wave train enters the second slope. As the wave train propagates over the second slope, each modulation splits into two envelope solitons with different group velocities. Two envelope solitons generated due to fission are of different amplitudes, the one with smaller group velocity is of higher amplitude. It would overlap with a sub-modulation (with relatively larger group velocity) generated by the fission of another modulation, and forming an additional enhancement of envelope amplitude. In Fig. (III.3.10)(b), a three-dimensional view is shown. It is noted that around the end of the flume where the relative water depth is low, the collision of two sub-modulations results in considerable high envelope amplitude which is significantly larger than the background wave amplitude.

In Fig. (III.3.11), the evolution of the maximum and minimum values of the envelope amplitude is shown. Two local maximum values should be noted. One is around the end of the first steeper slope $x_{21} = 51.7$ m. After this maximum the value of A_{max} decreases partially due to the breaking events. The other is around the end of the flume $x_{59} = 125.6$ m. They correspond to the amplifications of the carrier wave up to a factor of 2. Especially the second amplification takes place in a relatively shallow, modulationally stable region. It corresponds to the collision of two sub-modulations, which is related to the instability of the AB solution. Such a high amplification meets the criterion of freak waves. **So this case is a piece of experimental evidence that the breather solutions generated upstream could result in freak waves in the shallower region where the modulation instability ceases to exist.**

In Fig. (III.3.12)(a), the spectral evolution is shown. The spectrum broadens as the wave train propagates over the first steeper slope, a similar trend is also observed in Fig. (III.3.5)(a), in case 410 with milder non-linearity and bottom

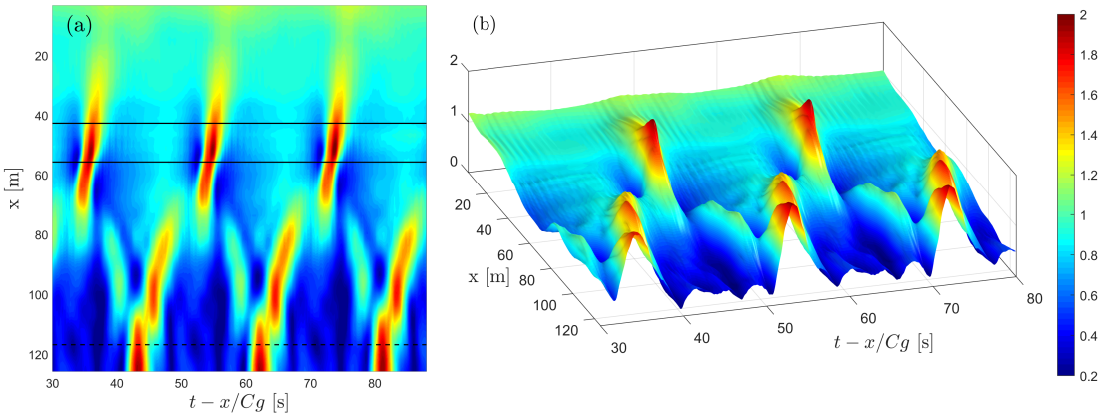

Figure III.3.10: AB case 739: envelope evolution in space and time of the experiment. The envelope is normalized by the carrier wave amplitude, in panel (a) top view, and panel (b) 3D view. In panel (a), the solid lines denote the two edges of the first slope. The dashed line indicates the position where the threshold $kh = 1.363$ is achieved.

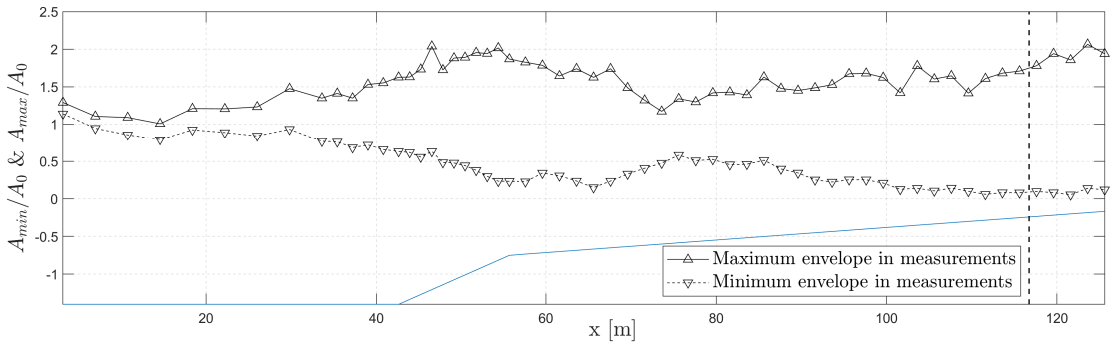

Figure III.3.11: AB case 739: spatial evolution of maximum and minimum envelopes in experiment. The vertical dashed line indicates the position where the threshold $kh = 1.363$ is achieved.

slopes. However, more side-band modes appear and result in broader spectral width in the present case. The growth of side-band modes is asymmetric, with more frequency modes appearing for frequencies higher than f_c. As the wave train propagates over the milder second slope, the spectrum becomes narrower, the energy of the side-band modes with $f/f_c > 1.2$ is transferred back to the main part of the spectrum. The spectral shape becomes nearly symmetric after the connection of two slopes. In Fig. (III.3.5)(b), it is shown that the incident wave spectrum (probe 1) is symmetric with two relatively large side-band modes besides the carrier frequency. As the wave train propagates over the uneven bathymetry, at

probe 21, the spectrum is asymmetric with more side-band modes with frequencies higher than f_c appear. Fewer side-band modes with frequencies lower than f_c take place, but their energy is relatively higher than their counterparts on the higher frequency side of f_c. It is observed that at probe 59, the frequency with the highest energy is $f/f_c \approx 0.9$, a frequency downshift takes place.

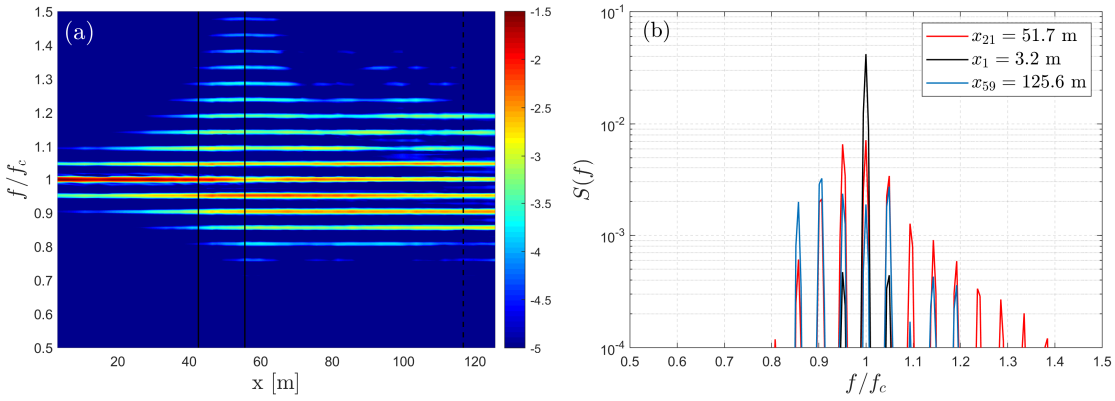

Figure III.3.12: AB case 739: spatial spectral evolution, panel (a) and comparison of spectra measured at different positions panel (b) in experiment. In panel (a), the vertical solid lines indicate the two edges of the first slope. The dashed line indicates the position where the threshold $kh = 1.363$ is achieved.

3.2.2 Case 739: convergence tests of numerical parameters in Whispers3D

It was our target to achieve high non-linearity of the wave train entering the sloping areas. While trying to simulate case 739, particular attention should be paid to the choice of numerical parameters in Whispers3D that are related to the model accuracy. Given the experimental conditions, $k_c h \approx 6.956$ represents the carrier wave is in deep water. And $\epsilon = 0.13$ for the carrier wave, after the enhancement of a factor of 2, the carrier steepness could be as high as 0.26 around $x \approx 52$ m and $x \approx 125$ m. The broad spectral width is observed around the end of the first slope, resulting in a relatively wide range of relative water depth. Especially around the end of the flume, it is challenging to simulate the strong non-linear wave train propagating in shallow water. It brings more complexity since breaking events appeared around the end of the first slope during the experiment. But it is not sure, if we stop the second slope after $k_c h = 0.5$ in simulations, whether waves break or not. The typical choice of numerical parameters, especially $N_T = 7$ and $N_{sten} = 5$ may be too conservative to describe the case 739.

Before going to detailed comments on the comparison of Whispers3D simulation results and measurements, convergence tests of the numerical parameters are

introduced. This is done to justify the reliability of the Whispers3D simulation results for such a challenging experimental condition. The tested parameters include N_T, N_{sten}, and ν_v. The discretization step in space (Δx) and time (Δt) is calibrated just as all the other cases, thus they are omitted here. The choices of $\Delta x = 0.0176$ m and $\Delta t = 0.005$ s balance the accuracy and efficiency of Whispers3D model.

The other numerical parameters used during the convergence tests are not changed. The region from $k_p h = 0.5$ to the shoreline in the experiment flume is replaced by a region with constant depth $k_p h = 0.5$ in simulations. The generation relaxation zone is 3.79 m long corresponding to 3 wavelengths in the deeper region. The damping relaxation zone is 7.58 m long, it corresponds to approximately 6 wavelengths in the deeper region (or equivalently 13 wavelengths for $k_p h = 0.5$). In this case, the approach outlined in Section (3.3) is adopted to model the breaking process. The criterion for determining the starting and the ceasing of the wave breaking process is the angle of wave slope with respect to the x-axis (i.e., η_x). In this case, we choose $\beta_b = 26°$ and $\beta_f = 10°$. The depth-induced breaking effect is modelled by inclusion of an additional dissipative term in Eq. (I.3.9), the dynamic free surface boundary condition. This approach was introduced in Guignard and Grilli (2001). The parameter which characterises the intensity of breaking, $\mu_b = 1.2$ of Eq. (I.3.10) is adopted in the simulations of case 739.

a/ Convergence tests of N_T and N_{sten} parameters

As is observed in previous cases, while the incident AB solution propagates over uneven bottoms, the modulation remains periodic in time. The convergence test is thus carried out by directly comparing the time series of free surface elevation, and focusing on one period of the modulations. The focusing due to the growth of the modulation, where maximum envelope amplitude (thus strongest nonlinearity) takes place, is the most challenging area. The list of tested numerical parameters is given in Table (III.3.1).

Table III.3.1: List of numerical parameters adopted during the convergence test for N_T and N_{sten} of Whispers3D model

Test	N_T	N_{sten}	Δx (m)	$L_{c,deep}/\Delta x$	$L_{c,shallow}/\Delta x$	Δt (s)	$T_c/\Delta x$
1	7	5	0.0351	36	17	0.005	180
2	9	5	0.0351	36	17	0.005	180
3	10	5	0.0351	36	17	0.005	180
4	7	5	0.0176	72	33	0.005	180
5	7	7	0.0176	72	33	0.005	180
6	7	9	0.0176	72	33	0.005	180

In Fig. (III.3.13), the comparison of the time series of surface elevation is shown.

In each panel, the time window is shifted according to the probe positions and local group velocity of the carrier wave. At probe 20, the wave trains including the modulations are superimposed for the three chosen N_{sten}. However, as the wave train propagates over the second slope, differences appear for $N_{sten} = 5$ and $N_{sten} = 7, 9$. For the sub-modulations marked in Fig. (III.3.13) at probe 40, 50 and 52, the results of simulations with $N_{sten} = 7$ and $N_{sten} = 9$ are superimposed. This indicates that the choice of $N_{sten} = 5$ which denotes the five-point finite difference scheme is insufficient for accurately describing case 739, and convergence is achieved for $N_{sten} = 7$.

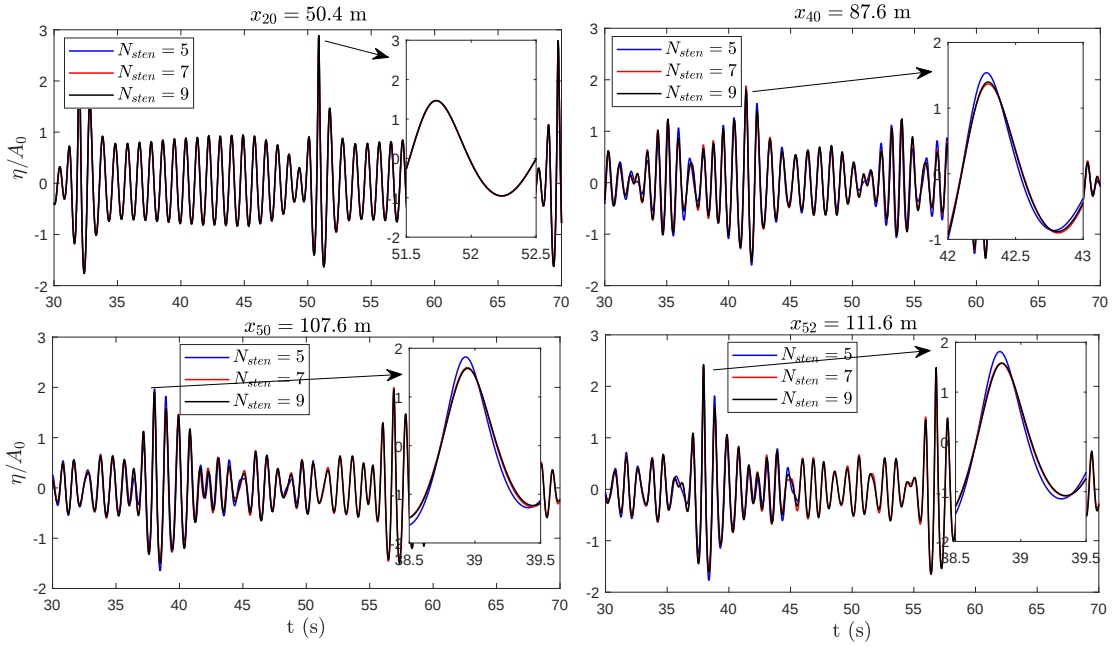

Figure III.3.13: Convergence test of N_{sten}: comparison of free surface elevation.

In Fig. (III.3.14), the convergence test of N_T is shown in the same moving window as in Fig. (III.3.13). Three values of $N_T = 7, 9, 10$ have been tested. It is shown that at the four probe positions, the results of $N_T = 7$ are different from $N_T = 9$ and $N_T = 10$, especially for waves with large amplitude. The differences are mainly due to the different degree of accuracy of the dispersion in Whispers3D model with different N_T. The simulation results with $N_T = 9$ and $N_T = 10$ are of minor differences. So we consider that the convergence is nearly achieved for $N_T = 9$.

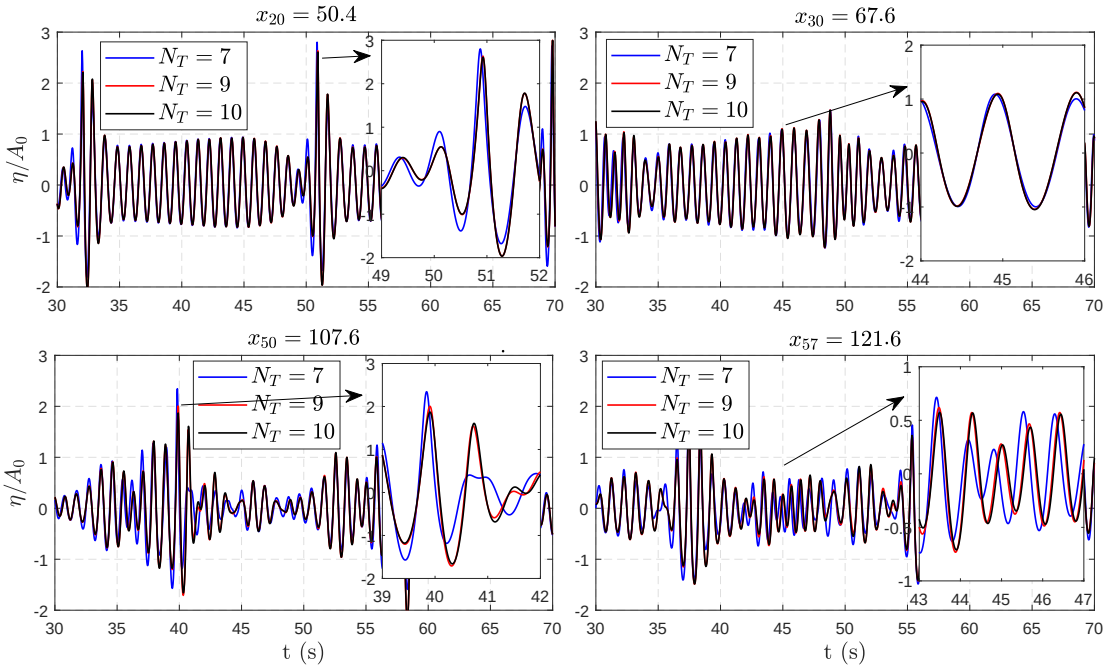

Figure III.3.14: Convergence test of N_T: comparison of free surface elevation

b/ Calibration of bulk dissipation rate ν_v

It has been addressed that the dissipation rate allows to control the complex spatio-temporal arrangement for breather-type solutions in deep water conditions (see Kimmoun et al., 2017). Especially for the cases with a relatively high value of $\mathfrak{a}$, the 'second-order' response of modulations takes place, leading to fission of modulations, as is illustrated in Fig. (III.1.2). The dissipation does not only affect the envelope amplitude decay of AB solutions but also affect the bifurcation of the envelope. Here the sensitivity tests of the dissipation parameter ν_v show the effects of dissipation for AB breathers that propagate over uneven bottom with significant depth transition. The calibration of the dissipation parameter is based on the comparison between measured and simulated envelope evolution, including the qualitative agreement of envelope profile in space and time, and the quantitative comparison of the maximum envelope amplitude A_{max}/A_0.

In Fig. (III.3.15), the spatial evolution of maximum and minimum envelope amplitude is shown. Four values of dissipation parameter ν_v are superimposed with the measured results. It is observed that the effects of dissipation gradually manifest as the wave train propagates towards the end of the flume. By affecting the wave amplitude, the dissipation is directly related to breaking events appearing at the end of the first slope. It is noted that the sudden decrease of A_{max} due

to wave breaking takes place later in the wave tank for larger dissipation rate. And the decrease of A_{max} (intensity of breaking) caused by breaking effect is different, the larger the bulk dissipation, the milder the dissipation due to breaking effects is (comparing the simulation results with $\nu_v = 1.8 \times 10^{-5}$ m^2/s and $\nu_v = 4.0 \times 10^{-5}$ m^2/s). More significant differences happen around the second slope, the re-increase of the A_{max} which is due to collision of the sub-modulations is shifted to the direction of the shore for larger dissipation. For A_{min}, the evolution is similar except for the smallest dissipation rate $\nu_v = 1.8 \times 10^{-5}$ m^2/s.

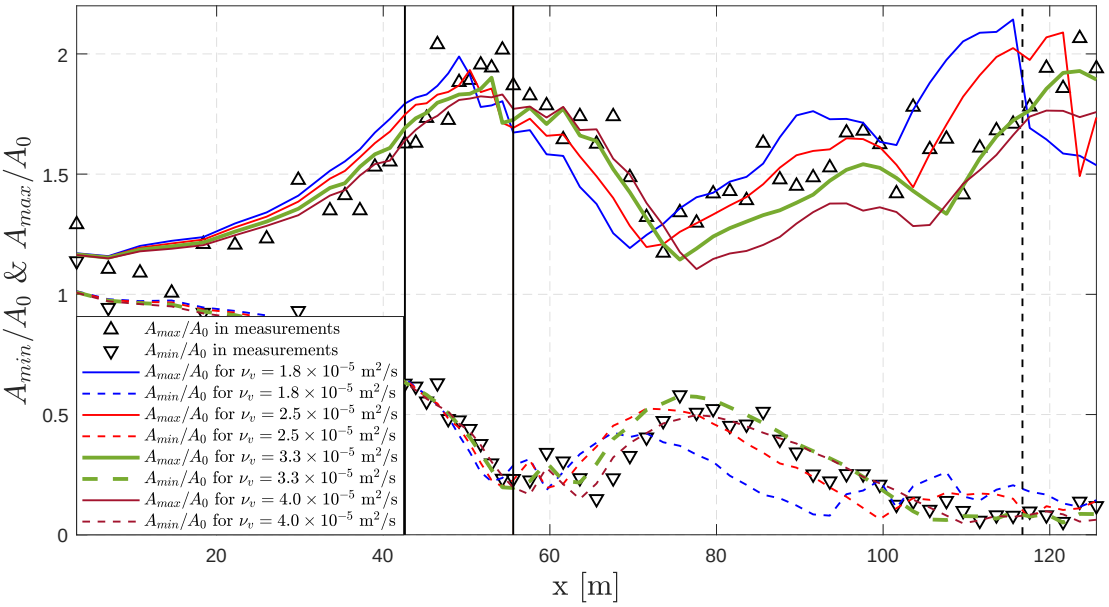

Figure III.3.15: Calibration test of dissipation parameter ν_v: comparison of maximum and minimum envelope amplitudes. The vertical solid lines denote the two edges of the first slope. The vertical dashed line indicates the position where the threshold $kh = 1.363$ is achieved.

In Fig. (III.3.16), the comparison of the envelope evolution in space and time is shown, focused on a short time window. The collision of the sub-modulations takes place around $x = 110$ m in experiment, highlighted by a red arrow. It is noticed that in the simulations with increasing dissipation the distance between the wave maker and the position of collision increases.

Based on the observations listed above, we conclude that the dissipation plays an important role in the AB evolution over the uneven bottom. It affects the wave steepness around the end of the first slope, so different dissipation rates may change the position and intensity of breaking events. It also has non-negligible effects on the wave dispersion by affecting the wave amplitude and wave-number. The group velocities of sub-modulations are thus different. The position where

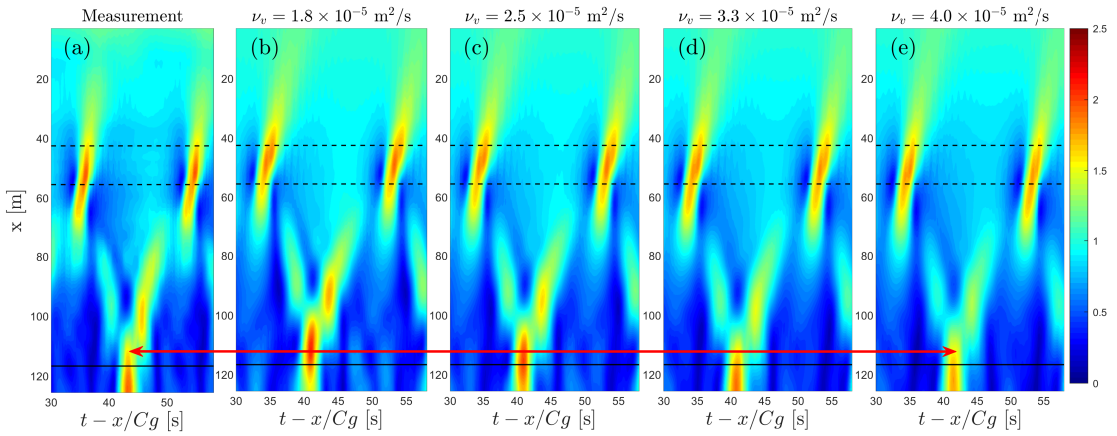

Figure III.3.16: Calibration test of dissipation parameter ν_v: envelope evolution in space and time. In all the panels, the horizontal dashed lines denote the two edges of the first slope. The horizontal solid lines indicate the position where the threshold $kh = 1.363$ is achieved. The horizontal red arrow is a reference line.

the collision of the sub-modulations takes place depends on their group velocities, so different dissipation rates may change the position of collision. The choice of dissipation parameter $\nu_v = 3.3 \times 10^{-5}$ m^2/s results in good agreement for these two aspects: the magnitude of the envelope amplitude, and correct prediction of the position for collision.

3.2.3 Comparison between measurements and simulations with Whispers3D and NLSE models

The numerical parameters for the simulations with Whispers3D is summarized here. The convergence is achieved for $N_{sten} = 7$, $N_T = 10$, and $\Delta x = 0.0176$ m and $\Delta t = 0.005$ s (convergence is not shown). These parameters are chosen to balance the accuracy and efficiency of the simulations. A 3.79 m long generation relaxation zone and a 7.58 m long damping zone are set. The breaking wave detection is based on the geometry of the wave profile. In this study, $\beta_b = 26°$ and $\beta_f = 10°$ represent the onset and end of a breaking wave. The breaking intensity determines the dissipation due to breaking. The associated breaking intensity parameter $\mu_b = 1.2$ is used. Based on the study in the previous paragraph, the bulk dissipation $\nu_v = 3.3 \times 10^{-5}$ m^2/s is chosen. It corresponds to amplitude decay rate $\delta = 0.0023$ m^{-1} for the constant water depth $h = 0.75$ m. This value of h corresponds to the water depth at the end of the first slope.

In Fig. (III.3.17), the comparison between measurements and simulation results of Whispers3D and NLSE models is shown. When parameters are carefully calibrated, Whispers3D predicts well the evolution of wave envelope in space and time.

Very good agreement is achieved not only for modulations and sub-modulations but even the small oscillations of wave envelope between two significant overlapped sub-modulations. The relatively high incident carrier wave steepness results in significant non-linearity of modulation around the end of the first slope which locally violated the weakly non-linear assumption. The NLSE model still provides a qualitatively correct evolution of envelope, apart from the asymmetry profile which has been observed in all above-mentioned NLSE simulations. The fission effect is captured, and the collision takes place nearly in the same position as in the measurements. The main advantage of the NLSE models is the computational time. In the simulations of the shown cases, it takes only a few seconds for NLSE computation, whereas it takes on average 2 days CPU-time for simulating 320 s wave propagation with Whispers3D.

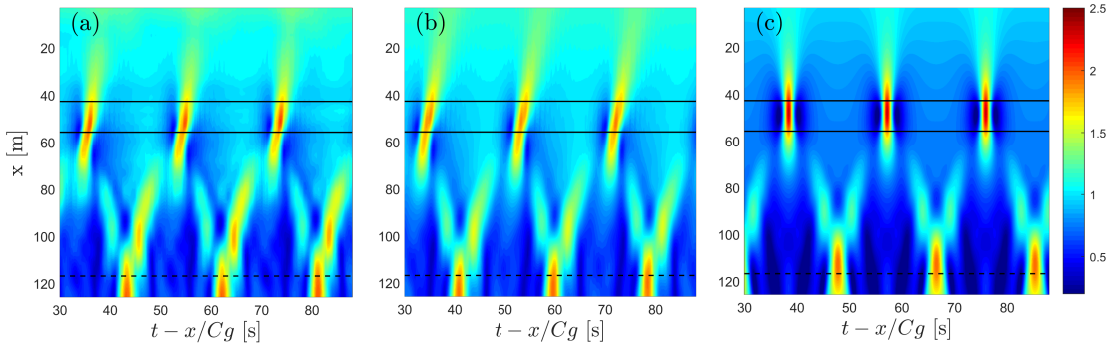

Figure III.3.17: AB case 739: pseudo color view of normalized envelope evolution in experiment panel (a), Whispers3D simulation panel (b), and NLSE simulation panel (c). In all panels, the horizontal dashed lines indicate the position where the threshold $kh = 1.363$ is achieved. The horizontal solid lines denote the two edges of the first slope.

In Fig. (III.3.18), quantitative comparison of the maximum and minimum envelope amplitudes A_{max}/A_0 and A_{min}/A_0 evolution in space is shown. The simulation results of Whispers3D show excellent agreement with measurements. The envelope amplification due to modulation near the end of the first slope, the re-amplification due to collision around the end of the flume, and the local maximum of envelope due to the occurrence of sub-modulations around $x \approx 100$ m are well captured by Whispers3D. In simulation of NLSE however, the amplification rate of A_{max} over the first slope is larger than in measurements. This is due to the fact that NLSE is limited by the weakly non-linear assumption. For such a case with strong nonlinearity, the energy transfer to second or higher harmonics is underestimated by NLSE. Furthermore, the limitation of the envelope due to breaking effects is excluded in NLSE. Due to little energy transferred or dissipated, stronger wave non-linearity results in stronger instabilities and earlier occurrence of the collision

of the sub-modulations in the flume.

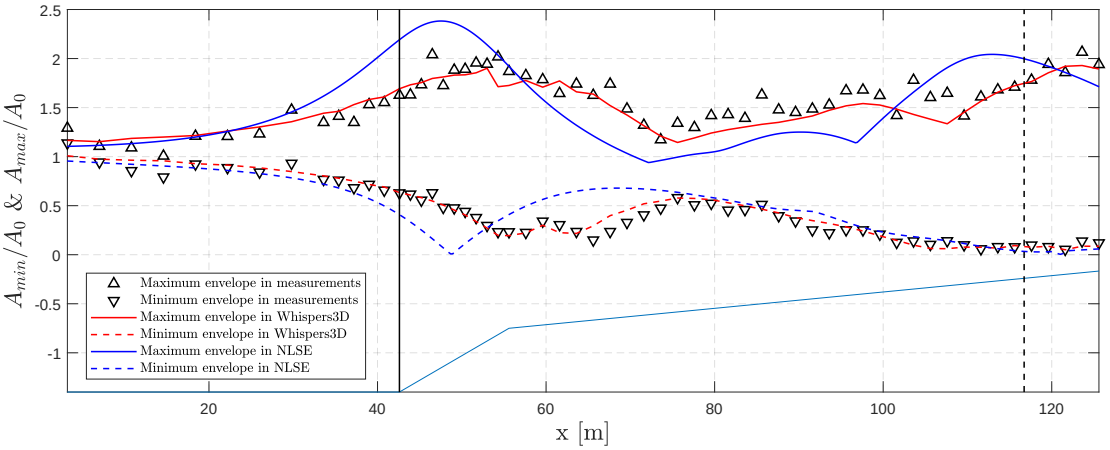

Figure III.3.18: AB case 739: spatial evolution of maximum and minimum envelopes in experiments and simulations with different models. The vertical solid line indicates the focusing position and the vertical dashed line indicates the position where the threshold $kh = 1.363$ is achieved.

In Fig. (III.3.19), the spectral spatial evolution is shown. Again, the spectral evolution is well captured by Whispers3D. In Fig. (III.3.19)(a) and (b), it is seen that the energy decay due to wave breaking around $x \approx 55$ m, mainly take place for the waves with carrier frequency f_c. The energy of the carrier wave in Fig. (III.3.19)(c) shows only gradual decrease in space. The broadening of wave spectra take place around the connection of the first and second slopes in panel (a) and (b). As in previous cases, the spectrum predicted by NLSE is symmetric with wave energy simultaneously transferred to both lower and higher modes of the carrier frequency.

3.2.4 Ongoing numerical investigation of the effects resulting from the bottom slope on the nearshore wave enhancement

It is seen that the behaviour of the AB wave train is evidently different in case 739 from case 410 and 415. As is shown in subsection (3.2.1), there is a second enhancement of the wave amplitude around the end of the flume in case 739. However, only with the three cases shown in this section, it is difficult to conclude which parameter dominates the nearshore wave amplification (collision of the sub-modulations). Since not only the bottom slopes but also the depth variation and the incident wave steepness are changed to achieve higher non-linearity in case 739. Especially the effects resulting from the bottom slopes are hard (at least costly) to investigate experimentally. So the idea is to test numerically, the propagation

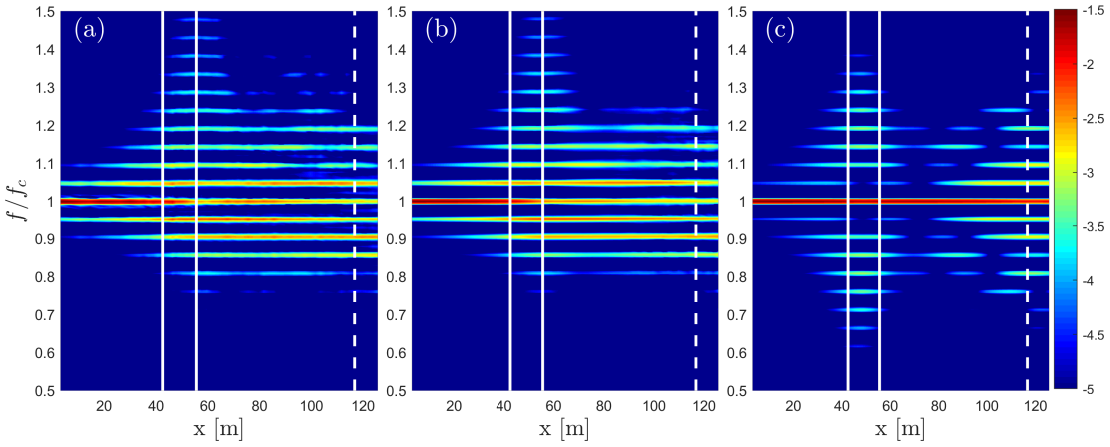

Figure III.3.19: AB case 739: comparison of spatial spectral evolution in measurements panel (a), Whispers3D simulation panel (b), and NLSE simulation panel (c). In all panels, the vertical solid lines indicate the two edges of the first slope. The vertical dashed line indicates the position where the threshold $kh = 1.363$ is achieved.

of the same AB solution as case 739 over different bottom slope combinations.

The incident wave conditions of case 739 are recalled: $\mathfrak{a} = 0.46$, $T_c = 0.9$ s, $\epsilon = 0.13$, and focusing position $x_f = 42.6$ m. The incident wave trains in all new cases are identical to case 739. Three new bottom setups similar to Fig. (III.3.9) but with different combinations of slopes are tested numerically. The water depth near the wave maker is $h = 1.4$ m, and the first slope starts at $x = 42.6$ m in all cases. The tested slopes are shown in Table (III.3.2). In case 739.1, the first steeper slope is changed from $1:20$ in the experiment to $1:40$ for showing the effects of a milder first slope. In case 739.2 and 739.3, the second slope is changed to $1:200$ and $1:80$ respectively to demonstrate the effects of the second slope.

Table III.3.2: List of new bottom slope combinations of case 739

Case	Slope 1	L_{slope1} (m)	Slope 2	L_{slope2} (m)	$x_{kh=1.363}$ (m)
739	1:20	13	1:120	84.42	116.728
739.1	1:40	26	1:120	84.42	129.728
739.2	1:20	13	1:200	140.7	157.48
739.3	1:20	13	1:80	56.28	96.352

The simulations are conducted using Whispers3D model with the calibrated numerical parameters: $N_{sten} = 7$, $N_T = 10$. The discretization in space and time $\Delta x = 0.0176$ m, $\Delta t = 0.005$ s, and viscous dissipation $\nu_v = 3.3 \times 10^{-5}$ m^2/s are adopted. A 3.79 m long generation relaxation zone and a 7.58 m long damping

zone are set. The parameters related to breaking events are $\beta_b = 26°$ and $\beta_f = 10°$ representing the onset and end of a breaking wave, and $\mu_b = 1.2$ for breaking intensity. In the simulations, a shallow-water flat region with $kh = 0.5$ is set in place of the area $kh < 0.5$, since the shoreline run-up is not the target of the present work.

In Fig. (III.3.20), the evolution of the normalized maximum wave envelope A_{max}/A_0 is shown. In case 739.1, the first slope is set with a milder slope. It is observed in Fig. (III.3.20)(a) that, the spatial evolution of two cases is similar until $x = 90$ m. Then differences appear in the sense that in case 739.1 the second local peak of A_{max} appear later in space. It is anticipated that the lag-in-space is partially related to local relative water depth, since in the new case the first slope is 13 m longer than in the original case. In Fig. (III.3.20)(b), the evolution of A_{max}/A_0 is shown with decreasing kh. It allows to compare the envelope evolution under the same local water depth condition. In the flat regions before the first slope ($x = 0$ m to $x = 42.6$ m) and near the end of the computational domain, the relative water depths are $kh = 6.96$ and $kh = 0.5$ respectively. These two regions are represented by the vertical lines at the corresponding water depth in panel (b). The connection point of two slopes is marked by the dot-dashed line. Although the maximum envelope evolution for two cases is similar before $x = 90$ m, the wave train is propagating over different local water depths. The second local peak of A_{max} also appears in case 739.1 but takes place in a deeper region. After the threshold $kh = 1.363$, the maximum envelope rapidly decreases for both two cases. This decrease of A_{max} in the modulational stable area is in line with the asymptotic formulation of Benilov et al. (2005). Since the focusing position $x_f = 42.6$ locates at the beginning of the first slope, the evolution of maximum envelope is dominated by the de-modulation after the focusing. The effects of the first slope gradient are therefore less evident.

In Fig. (III.3.21)(a), the spatial envelope evolution comparison of three choices of the second slope is shown. The collision between the two sub-modulations that results in a second maximum near the shore is also visible for the case 739.2 in which the second slope is 1 : 200. This second local peak does not appear in case 739.3 in which a steeper second slope 1 : 80 is set. This is somewhat unexpected. Because the non-linearity of the wave train is supposed to be enhanced by a steeper second slope and therefore a more significant second peak is expected. In Fig. (III.3.21)(b), the envelope evolution in terms of relative water depth is shown. It is noticed that as the second slope gradient increases, more space is needed to develop the second local peak of A_{max}/A_0. However, as the wave train approaches to the threshold $kh = 1.363$, A_{max} decreases rapidly. So in case 739.3, the wave train achieves the position where the relative water depth is $kh = 1.363$, and the maximum envelope A_{max}/A_0 starts decreasing before the development of the second peak. It indicates that the appearance of a significant second peak of A_{max} is the result of a balance. On one hand, a steep enough second slope is needed

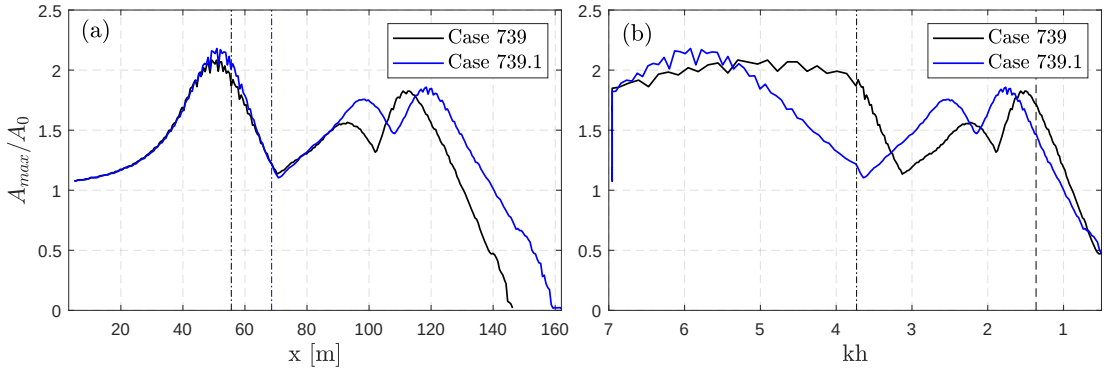

Figure III.3.20: AB case 739: spatial evolution of maximum envelope A_{max} compared with a milder first slope case 739.1. Panel (a) shows the maximum envelope evolution in space, panel (b) shows its evolution as relative water depth decreases. The vertical dot-dashed lines denote the connection between the two slopes, and the dashed line in panel (b) indicates the threshold $kh = 1.363$.

to increase the non-linearity of the wave train. On the other, a milder second slope is also needed to keep enough space before the modulational stable region. In the experiment case 739, it happens to meet this balance. A significant second peak of maximum envelope appears and takes place very close to the modulational stable area.

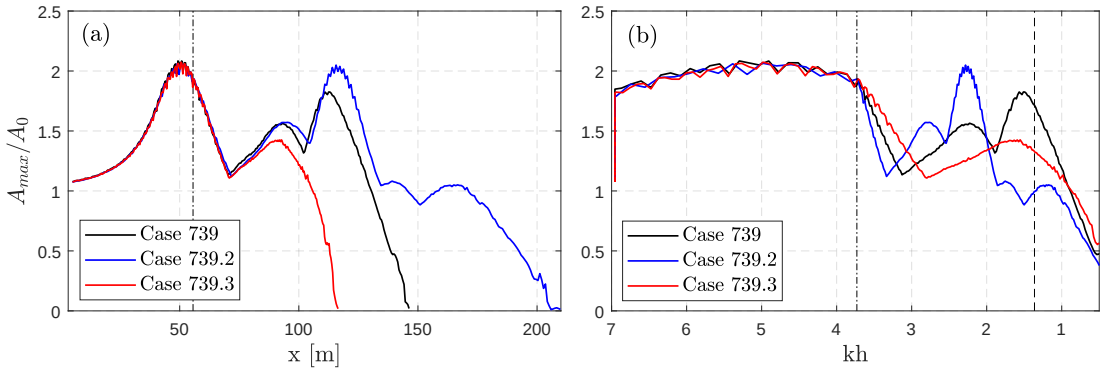

Figure III.3.21: AB case 739: spatial evolution of maximum envelope A_{max} compared with different second slopes in case 739.2 and 739.3. Panel (a) shows the maximum envelope evolution in space, panel (b) shows its evolution as relative water depth decreases. The vertical dot-dashed lines denote the connection between two slopes, and the dashed line in panel (b) indicates the threshold $kh = 1.363$.

Chapter 4

Conclusion and outlook

4.1 Summary of findings and conclusions

It has been shown that, in deep water condition, the instabilities of exact breather solutions may occur when they are performed in experimental wave tanks. Starting with exact breather solutions, different dynamical behaviours of the breather wave train may manifest. These behaviours with different phenomena are considered as 'different orders' dynamical responses. The 'first-order' behavior is the phase-shifted FPU recurrence (see Kimmoun et al., 2016), and the 'second-order' behavior is the collision of the sub-modulations of modulation (see Kimmoun et al., 2017). The occurrence of the instabilities of exact breather solutions and deviation from expected breather trajectories in space and time is possibly due to the 'imperfect experimental condition'. For example, the AB breather is an exact solution of constant-coefficient conservative cubic NLSE for weakly non-linear waves propagating over a flat bottom. Effects which are not included in this equation, like bottom change, dissipation, high-order non-linearity and high-order dispersion and breaking etc., play as disturbances to the exact breather wave train. The instabilities take place while the AB solution adapts to the one that meets the 'real' condition. The dissipation effect is common in all experimental flumes. Its effects on the evolution of exact breather solution have been studied in Kimmoun et al. (2017) within the framework of a non-conservative NLSE model. The effects of uneven bottoms as a source of disturbance on the instabilities of breather solutions are not discussed yet.

This study attempts to contribute to the understanding of the characteristics of breather transformation over slopes and evolution in shallow water. In this part, the exact breather solutions evolving over two kinds of uneven bottom profiles have been investigated experimentally and numerically. The experiments were conducted in a mid-size wave flume in THL. Two different types of bathymetry are considered. One is bottom setup 1 which contains a prismatic slope (1/20) that connects a deep water region on one side and a shallower region on the

other. The other bottom starts with deeper region after which two slopes are set. In the second case, the first slope is steeper to introduce significant instabilities to the wave train, the other slope is milder to decrease the water depth until shoreline. Two different combinations of slopes are considered. The bottom setup 2 is milder, the gradient for the first slope is 1/40, and the second 1/200. The bottom setup 3 is steeper with 1/20 and 1/120 as slopes. Mainly three aspects are considered when choosing the bottom setups: the bottom gradient, the change of gradient between the two areas, and the shoreline (or very shallow water). The frictional dissipation is non-negligible considering the dimension of the wave flume (200 m long). Experiments with regular wave trains have been performed to evaluate the dissipation. Both the uneven bathymetry and the dissipation work as disturbances resulting in instabilities of exact breather solutions. The generated breather wave trains are characterized by a five-parameter space $(T_c, \epsilon, h, \mathfrak{a}, x_f)$. The tested conditions cover a relatively large range in this space. Different levels of incident carrier wave steepness ($\epsilon = 0.09$ to 0.13) were tested in three bottom setups. Both Akhmediev (time-periodic) and Peregrine (non-periodic) breather solutions were included. For Akhmediev breather solutions, different values of $\mathfrak{a}$ were tested from 0.25 to 0.46. The effects of different bottom slope gradient combinations have been investigated with the validated numerical model with well calibrated numerical parameters. By conducting comprehensive analyses of the measured free surface signals, surface envelope computed via windowed Fourier transformation, and spectrum of surface elevation, the following conclusions for the experiments can be drawn:

- As breather solutions propagate over slopes, the envelope solitons are amplified due to modulation and shoaling. In the meantime, the envelope solitons are reduced by dissipation (due to friction and breaking effects) and nonlinear triad wave-wave interaction. The spatial variation of envelope amplitude is a result of the balance of all these phenomena. In general, for cases with low values of ϵ and a long focusing distance x_f, the amplification of envelope takes place in a long-distance such that the dissipation significantly limited the increase. The envelope showed very mild spatial variation. On the contrary, significant spatial variation of the envelope was observed for the wave trains with large values of ϵ. Especially when the focusing takes place around the slope with a larger gradient (1/20 or 1/40 in our cases), the non-linearity of the wave train is further enhanced due to strong shoaling and mild dissipation effects. High incident steepness ϵ not only affects the non-linear behavior (like the breaking effects and higher-order bound modes occurrences) but also the dispersion property (like the wave-number and group velocity) of the wave train. The spectrum of surface elevation underwent broadening near the point with different bottom gradients on each side. A series of side-bands appeared asymmetrically with respect to the carrier wave frequency f_c, with more modes apparent in the range $f > f_c$.

The number of modes appeared in the range $f > f_c$, i.e. the degree of the asymmetry of the spectrum, is a sign of the significance of instabilities. In the cases where sub-modulations are generated, a larger incident steepness results in the earlier occurrence of the sub-modulations in the wave flume.

- The water depth transition and the abrupt change of gradient result in instabilities of the breather solutions. The bathymetry setup 1 is a combination of steep slope (1/20 in bottom setup 1) and significant gradient change (from 1/20 to 0). With this setup, the envelope solitons in both Peregrine and Akhmediev breathers split into two sets of envelope oscillations with different group velocities. In the Akhmediev breather case, these oscillations overlap with the ones generated from another envelope soliton forming a particular envelope pattern in space and time. However, compared to case 364 with bathymetry setup 1, the sub-modulations are smaller in case 415 with bathymetry setup 2. It is anticipated that the differences are due to the relatively mild first slope (1/40) and small gradient change (from 1/40 to 1/200) in bathymetry setup 2. The effects of the second slope have been studied numerically only. It is shown that the second slope also plays an important role for the AB wave train propagation. As the wave train passes the threshold water depth $kh = 1.363$, the maximum envelope decreases rapidly. A steeper second slope increases the non-linearity of the wave train but shortens the distance from the modulational stable region.

- As in deep water case, the 'order' of the dynamical responses of wave trains to disturbances increases as the breather parameter $\mathfrak{a}$. The thresholds for $\mathfrak{a}$ that involve different order behaviors are dependent on many factors such as ϵ, T_c, dissipation rate and slope gradient. For a low value of $\mathfrak{a}$ (0.25 and 0.35 shown in this study), one growth-decay cycle was observed. The phase-shifted FPU recurrence was not observed. The most possible explanations for bathymetry setups 1 and 2 are different. For bathymetry setup 1, strong instabilities were triggered due to the depth transition and gradient change. However, the shallower flat region is of relative water depth lower than the threshold 1.363 such that the modulation focusing can not happen again. For bathymetry setup 2, the instabilities were small because of the mild depth transition, small gradient change and relatively low steepness. For a large value of $\mathfrak{a}$ (0.46 tested), significant incident steepness and relatively steep slopes, a clear 'second-order' behavior of envelope solitons occurred with the generation of sub-solitons. **The generated sub-solitons overlapped with each other resulting in a re-amplification of envelope amplitude around the end of the flume where $kh < 1.363$. The nearshore enhanced waves meet the definition of freak waves.**

- The choice of the carrier wave period T_c and deep water depth h deter-

mines the relative water depth (for a given bathymetry setup). Certainly, the relative water depth also has a non-negligible influence on the wave train evolution. For sufficiently large relative water depth, the breather solution responses to instabilities tend to the deep water case, the bottom effects reduce. For very shallow relative water depth, the wave trains are modulational stable. In the cases with intermediate relative water depth (all cases studied belong to this category), the threshold $kh = 1.363$ is reached over the uneven areas. Before this position, wave envelope evolves due to modulation, the wave train 'breathes' as a result of the resonant four-wave interactions. After this point, the shape of the wave envelope is somewhat 'frozen' and propagate only as energetic wave packets without significant modulation.

In this study, the experiments were also investigated by using two numerical models. One is a fully non-linear dispersive model with dissipation due to friction and breaking events incorporated, Whispers3D. The other is non-conservative third-order NLSE with variable coefficients, which describes waves to third order in non-linearity and first-order in dispersion. Based on the comparison between the results of two models with the measurements, the following remarks of the behavior of two models can be drawn:

- The Whispers3D model shows excellent agreement with measurements for all cases, given the parameters N_T, N_{sten}, Δx and Δt are well-calibrated. Good agreement in both tempo- and spectral-domain between Whispers3D simulation and measurements have been achieved even for the most challenging case 739 which corresponds to high non-linear waves (up to breaking limit) propagating in a wide range of relative water depth. The convergence of this case shows that the influences due to the insufficient value of N_T is more significant than that associated with N_{sten}. High accuracy of dispersion of numerical model is required.

- The adopted NLSE model is of the limited capacity for characterizing high-order wave non-linearity and non-linear dispersion. The dissipation is modelled by a simple linear term which characterizes the decay rate of wave amplitude. However, the simulation results showed very good agreement with experiments for cases with intermediate non-linearity. The instabilities of the breather solutions are quantitatively described by the NLSE model. The limitation of the application of NLSE model mainly comes from its linear dispersion property. The asymmetry of both envelope and spectrum profile is thus not predicted by the NLSE model adopted here. For case 739, the most challenging case with strongest non-linearity, the prediction of NLSE model still qualitatively agrees with measurements.

4.2 Outlook and perspectives of future work

As one of the most important outputs of this part, it has been shown experimentally in case 739 that the breather solutions generated in deep water could result in freak waves hitting the coastal areas. The experimental conditions of case 739 outline a very complicated physics: significant depth variation, relatively steep bottom slopes, strong non-linear incident wave train, and second-order dynamical response of breather wave trains. In this case, it is still not fully clear which parameter or parameters dominate the formation of the freak waves.

In the end of Chapter 3, the ongoing work in this direction is mentioned. Several tests have been conducted to illustrate the effects on the formation of the freak waves resulting from different bathymetries. In the near future, a systematic numerical investigation will be conducted to draw conclusions on which parameters allow to enhance the nearshore wave height. The factors that are going to be tested include:

- The shape of bathymetry. A few combinations of two bottom slopes for the same incident wave train have already been tested. Then the bathymetry effect will be tested by adjusting the relative water depth, the position of focusing due to modulation;
- The period of the envelope, namely the breather parameter $\mathfrak{a}$, which is related to the 'orders' of the dynamical responses of breather solutions;
- The non-linearity of the incident wave train which affects the non-resonant wave-wave interaction on one hand, and affects the envelope variation rate in space due to modulation on the other hand.

Furthermore, the bathymetry setup 3 was inspired by the typical profile of the bathymetry in the north-eastern coast of Taiwan as a simplified bottom profile. This is a position where casualties were reported during typhoons. Therefore, it would be of practical interest to simulate more realistic bottom profiles and local wave conditions based on our first-stage investigations.

Part IV
Irregular waves propagation over sloping bottoms

Pour un état de mer irrégulier, de fortes variations de profondeur induisent des modifications importantes de l'état de mer sur une échelle de longueur relativement courte et l'éloignent de l'état d'équilibre (ou de quasi-équilibre) incident. Dans la zone de profondeur d'eau plus faible, l'état de mer s'adapte progressivement vers un nouvel état d'équilibre. En raison de la dynamique hors équilibre, on s'attend à des statistiques fortement non-gaussiennes et à une intensification de la probabilité d'occurrence des vagues scélérates. L'objectif de cette partie est de mieux comprendre le processus d'adaptation de l'état de mer incident et le comportement non-gaussien. Le chapitre 1 présente les approches déterministes et stochastiques dans l'étude des vagues scélérates, et passe en revue les méthodes d'analyse de données couramment utilisées. Dans le chapitre 2, un cas expérimental représentatif mené au THL et sa simulation correspondante sont examinés en détail. La bathymétrie adoptée est en forme de marche. Les occurrences intensifiées de vagues scélérates sont confirmées dans la région plate à faible profondeur, et les modèles de hauteur de vagues cités ne sont pas capables de décrire les distributions de hauteur de vagues mesurées de manière satisfaisante. Les cas d'expériences et les simulations supplémentaires par rapport au chapitre 2 sont présentés et discutés dans le chapitre 3. L'autre axe de cette partie du travail est basé sur les expériences récentes présentées dans Trulsen et al. (2020). Dans cette campagne, la bathymétrie adoptée est de type barre. Dans le chapitre 4, nous examinons le comportement non-gaussien de l'état de mer du fait des fortes variations de profondeur (shoaling et de-shoaling) en utilisant des simulations entièrement non-linéaires. Les effets du de-shoaling dans l'expérience sont étudiés plus en détail en mettant en place un cas comparatif avec une bathymétrie en forme de marche. Deux groupes de variables de vagues ayant des tendances d'évolution statistique différentes sont identifiés. Nous montrons que les déformations des vagues sur les pentes se produisent indépendamment dans les directions horizontale et verticale. Le de-shoaling modifie le champ d'ondes à l'amont de cette zone et entraîne des oscillations à courte échelle des propriétés spectrales. Les conclusions sont données dans le chapitre 5.

L'eau qui porte le bateau est la même que celle qui le renverse, nous apporte-t-elle une catastrophe ou un bonheur? Cela dépend uniquement de la façon avec laquelle on y fait face.

Xun tseu

Xun Kuang (IIIIe siècle av. J.-C.)

List of the symbols of Part IV

A	local amplitude of wave envelope
Alt^B	atiltness parameter defined in frequency domain
Alt^η	atiltness parameter defined in time domain
b^2	bicoherence
B	bispectrum
BFI	Benjamin-Feir index defined in deep water
B_s	Benjamin-Feir index defined in shallow water
c	constant coefficient of BFI
C	phase velocity
C_g	group velocity of linear theory
C_r	relaxation coefficient function
E_{gr}	wave group energy over corresponding group length
E_I	instantaneous wave energy
E_{SIWEH}	smoothed instantaneous wave energy history
f_n	nth natural mode frequency in a wave flume
f_p	spectral peak frequency
GF	groupness factor defined by SIWEH
h	local water depth
$\bar{H}$	arithmetic mean of wave height
$\mathcal{H}$	Hilbert transform operator
HH	Hilbert-Huang transform operator
$H_{1/3}$	mean wave height of the highest one-third waves
$H_{1/M}$	mean wave height of the highest one-Mth waves
H_{m_0}	characteristic wave height defined in spectral domain
H_s	significant wave height
k_n	nth natural mode wave number in a wave flume
k_p	wave number corresponding to the spectral peak
L_n	nth natural mode wavelength in a wave flume
L_p	wavelength corresponding to the spectral peak
L_{Run}	length of a run of wave group
m_n	nth order moment defined in spectral domain
N_{gr}	group length defined in Hilbert-Huang domain
p	probability density function
P	complementary cumulative distribution function
P_s	power spectrum function
P_v	Cauchy principal value
Q_p	peakedness parameter
S	power spectral density function
$\bar{T}$	arithmetic mean of wave period
$T_{1/3}$	mean wave period of the highest one-third waves
$T_{1/M}$	mean wave period of the highest one-Mth waves
$\bar{T}_{m_{02}}$	mean of wave period defined by m_0 and m_2
$\bar{T}_{m_{04}}$	mean of wave period defined by m_0 and m_4
T_n	nth natural mode period in a wave flume
T_p	spectral peak period
T_{SIWEH}	mean period of smoothed instantaneous wave energy history
U_r	Ursell number
X_n	Fourier coefficient
Z	envelope function

β	biphase
γ	spectral width parameter of JONSWAP spectrum
ε	wave steepness
ζ	orthogonal complement of the free surface elevation
η	free surface elevation
$\bar{\eta}$	arithmetic mean of free surface elevation
Θ	local wave phase of the envelope function
$\kappa^3_{m,n}$	general third order moment of free surface elevation
$\kappa^4_{m,n}$	general fourth order moment of free surface elevation
λ^B_3	skewness defined in frequency domain
λ^η_3	skewness defined in time domain
$\lambda_{m,n}$	general (m+n)th order moment of free surface elevation
μ	relative water depth
ν_{02}	spectral width parameter
ν_{04}	spectral width parameter
Π	nonlinear parameter introduced by Goda
σ	standard deviation of free surface elevation

Chapter 1

Introduction

The modulational instability is one of the most popular mechanisms responsible for the generation of freak waves in deep water conditions, and under certain circumstances, it may also result in large wave occurrences in intermediate and even shallow water conditions. However, researchers have not yet reached a consensus about the applicability of four-wave quasi-resonances in explaining the freak waves in the real world. The major concern lies in the complexity of real sea states since the modulational instability is limited by diverse requirements such as the relative water depth, spectrum width, dissipation, and spreading angle. These factors are hardly fulfilled at the same time as was indicated by Fedele (2016). In coastal areas, the strong depth variations could also result in the formation of freak waves and the non-Gaussian statistics due to non-equilibrium dynamic response of the sea states (Trulsen et al., 2012).

This part is dedicated to the study of high wave formation and its statistical features in irregular sea states induced by strong water depth transition in coastal areas. In the literature, both deterministic and stochastic approaches are adopted to study extreme waves or freak waves. Both of them are of great importance and will be reviewed. Also, the state-of-art of data analysis approaches are reviewed in Chapter 1. This study is on the basis of large-scale experiments in THL and deterministic simulations with fully nonlinear numerical simulations. With such a combination, a step (shoaling) bottom profile is studied. The in-depth analysis of a representative case has been conducted and published in form of a journal paper (Zhang et al., 2019). This paper will be duplicated in Chapter 2. The additional details regarding the complete experimental campaign and validation of the numerical model are given as supplementary materials in Chapter 3. Based on the recent experiments reported in Trulsen et al. (2020), the non-Gaussian sea state behavior and freak wave statistics induced by strong depth variations (including both shoaling and de-shoaling) have been discussed. The results are presented in form of a journal paper (under review), and shown in Chapter 4. In the end, the main findings and conclusions of this part will be summarized in

Chapter 5.

1.1 Bibliography survey of topographic effect on formation of extreme waves

1.1.1 Study of extreme waves with deterministic approach

The geometric, kinematic, and dynamic studies of extreme waves are conducted usually with the deterministic approach. These pieces of information are very useful for diverse practical purposes. For example, it allows offshore/coastal engineers to evaluate the extreme loads on structures and the corresponding structural responses. It also allows naval architects to analysis ship stability, the global and local strength of the vessel, and the vibration of the structural components in the challenging sea conditions. Such studies require precise generations of freak waves at predetermined space-time. In this direction, the dispersive focusing has received much attention. The first linear method was adopted by Longuet-Higgins (1974) to study wave breaking issues. In this method, it is assumed that the free surface waves can be represented by linear superposition of a large number of small wavelets with random phases. The wavelet components are determined from the given spectrum, and they are in phase at the focal position. Tromans et al. (1991) put forward NewWave theory to describe the local displacement of the ocean surface. It contains two parts, one deterministic part describe the extreme wave, the other part is a non-stationary Gaussian process describing the sea state away from the extreme event. Both parts base on the linear assumption in deep water condition (Jonathan and Taylor, 1997), valid in a Gaussian sea. However, it is known that nonlinear waves with bound modes travel faster than predicted by linear dispersion relationship, so the linear assumption may fail when the focusing waves are of large amplitudes and/or when the water depth is intermediate or shallow. Chaplin (1996) adopted successive adjustment to the phases at the wavemaker in order to achieve 0 phase at the focusing point. This procedure partially includes the correction of nonlinear phase shift and phase discrepancies due to other effects. Baldock et al. (1996) studied the nonlinear kinematic and dynamic characteristics of linearly generated focusing waves and compared them with second-order theoretical predictions. Taylor and Williams (2004) reported the second-order effects of large waves in finite water depth by considering NewWave theory as an acceptable model for the linear parts of the measured large waves. Ning et al. (2009) discussed the effect of the nonlinear wave-making method on the transient wave generation. This focusing method has also been systematically investigated in a fully nonlinear numerical wave tank very recently (Wang et al., 2019), the effects resulting from the bandwidth, wave nonlinearity, wave generation method on focal position have been discussed. The NewWave theory has been optimized, by taking second-order correction into consideration, to handle variable water depth

by Whittaker et al. (2016). Recent applications in the studies of run-ups (Whittaker et al., 2017) and wave overtopping of seawalls (Whittaker et al., 2018) with this optimized NewWave theory have shown its applicability to coastal areas. The generated waves will focus at (or near) the prescribed space-time, but besides the focusing event, the free surface is nearly undisturbed. The theory involves the simulation of a single wave rather than a comprehensive sea state.

A more realistic approach is to form an extreme wave in a sea state containing background waves. Cassidy (1999) embed the NewWave into a random wave train while maintaining the random distribution characteristics of phases, known as constrained NewWave theory. Alternatively, Kriebel and Alsina (2000) used a superposition of two wave trains and by tuning the portion of the transient wave energy of the total wave energy, to generate an extreme event in a random sea state with desired statistical characteristics. This method has been tested with uneven (slope or curved) bottom, the bottom effect is not helpful for freak wave formation due to frequency focusing (Cui et al., 2012). Deng et al. (2015) considered a vertical end-wall to investigate the effects of reflected waves on the formation of the extreme waves. For some purposes, particular wave trains need to be generated. For such purposes, Clauss and Steinhagen (2000) proposed an optimization method to reproduce a target extreme wave in a random sea by adopting their *Sequential Quadratic Programming* (SQP) technique. The well-known freak waves like the 'New Year wave' and 'Yura wave' have been reproduced with good agreement (Clauss, 2002). Bennett et al. (2012) compared previous extreme wave generation methods and listed their cons and pros, he suggested that the optimization method (Clauss and Steinhagen, 2000) is more suitable for extreme wave generation compared to NewWave and constrained NewWave theories. Another iterative approach, *Self Correcting Method* (SCM) is provided by Fernández et al. (2014b) by using *Fast Fourier Transform* (FFT) transformation. Based on the similar idea of the work of Chaplin (1996), SCM is capable of handling nonlinear effects that are missing in the linear approaches, and it is also possible to apply this method to uneven bottom cases (Fernández et al., 2014a). More recently, Buldakov et al. (2017) introduced a new iterative approach by adopting harmonic separation technique to generate high waves near breaking limit. Niu et al. (2020) combined second-order wavemaker theory and self correction method using an All-Phase FFT instead of FFT algorithm, to introduce an improved focusing method called *All Phase Correction Method* (APCM). This method shows better agreement with target wave profile and faster convergence of iteration. The effects on the iteration steps required from wave steepness, spectral width, as well as the spectral shape have been discussed.

1.1.2 Study of extreme waves with stochastic approach

In practice, engineers are more interested in the averaged properties to characterize the sea states instead of detailed wave evolution history. The pieces of information regarding averaged wave characteristics like wave amplitude spectrum and wave direction spectrum are needed as input for the whole design-assessment-optimization procedure of coastal structures by using experimental and/or numerical simulations. The stochastic study of waves in coastal areas is of vital importance for marine safety and coastal development. The pioneering work in this direction was given by Longuet-Higgins (1952) for Gaussian sea states and Longuet-Higgins (1963) for non-Gaussian behaviors in weakly nonlinear sea states. In terms of numerical study, the phase-averaged models (like WAM, SWAN, and WaveWatch-III) are adequate considering the balance of accuracy and efficiency, for most engineering purposes. However, for more complicated and local phenomena like the formation of freak waves, the phase-resolved models which require more computational effort are more appropriate.

The bottom effects on wave (and wave groups) nonlinear propagation have been extensively studied for decades. When waves propagate over uneven bottoms, the effects of shoaling, reflection, and refraction are more and more involved as water depth decreases. Due to the energy flux conservation, as water depth decreases, waves become shorter in terms of wavelength and spatially asymmetric in terms of wave profile (Goda, 2000). The presence of the bottom bar could give rise to strong wave-wave nonlinear interactions, resulting in broadened wave spectrum and breaking wave events (depending on the gradient of slope, and incident wave characteristics), see experimental evidence in the work of Beji and Battjes (1993); Ting and Kirby (1994). The statistical characteristics of wave fields over a slope, relevant for freak wave occurrence, have also been studied. Following the statistical study of Longuet-Higgins (1974) for the deep water case, Bitner (1980) reported field measurements of waves propagating over a sloping bottom and derived statistical models to account for non-Gaussian effects of wave height/phase/velocity. Significant differences were observed between real wave measurements and Gaussian model predictions. Recently, it is found that the dynamic response of waves passing over the sloping bottom will result in the non-equilibrium statistics, Zeng and Trulsen (2012) showed numerical evidence in the NLS framework that a significant decrease of skewness and kurtosis due to the depth transition is anticipated. Sergeeva et al. (2011) did simulations with the Korteweg–de Vries (KdV) equation showed that the kurtosis increases as water depth decreases. This process depends on the Ursell number which is the relative importance of nonlinearity and dispersion. Moreover, the probability of the occurrences of extreme waves may be altered due to a nonuniform bottom. The experimental evidence given by Trulsen et al. (2012) showed that the nonuniform bottom enhances the occurrence probability of freak waves and that the statistical parameters reach local maximum

values around the end of the slope. Later on, Gramstad et al. (2013) reported numerical results using a modified Boussinesq model showing that no increase in freak wave occurrence in their sloping bottom case. The opposite results can probably be explained by the different relative water depth in the shallower side. The latest work of Trulsen et al. (2020) indicated a rough threshold of relative water depth around 1.3, over which no significant effect on the kurtosis and freak wave occurrences is anticipated. When the water depth after the slope is lower than this value, significant enhancement of statistical parameters and higher probability of occurrences of freak waves are expected. Their work did not discuss the possible effect of wave steepness, spectral broadness, and slope gradient. Ma et al. (2015) reported an experimental case study on the bottom effect on statistical parameters including skewness, kurtosis, groupiness. The adopted trapezoidal bar allows investigating the evolution of the parameters at leeward. They found that the correlation of freak wave occurrences and the initial spectral width is negligible, but more freak waves are expected with increasing groupiness. Kashima et al. (2014) studied water depth transition from deep to shallow water region related to freak wave occurrences by using experimental tests with different bottom slopes and numerical tests with standard Boussinesq model. Using a proper correction of the nonlinear properties, the adopted Boussinesq model showed good agreement with measurements. Intensified freak wave occurrences have been reported in their study. Based on the same experimental results, Kashima and Mori (2019) reported a practice-oriented study of the uneven bottom effect on the pressure variation on breakwaters. The possibility of relating the change of kurtosis to the 'designed wave pressure' has been discussed therein. However, no matter in the KdV equation or the Boussinesq model, there are limitations on representing wave nonlinear and dispersive properties. The highly nonlinear numerical study of the problem is, to the best of my knowledge, very limited. Viotti and Dias (2014) adopted a fully nonlinear model to study a wide range of relative water depth which exceeds the validation range of KdV and Boussinesq models. A strong transition process connecting two equilibrium states (of the deeper region and the shallower region) has been observed over the slope. Ducrozet and Gouin (2017) reported numerical studies with the HOS model (up to 5^{th}-order). They found that the directionality in a spreading wave field has significant effects on the non-equilibrium statistics and that the extreme wave activity is reduced in a spreading sea. In the next section, different statistical properties that have been adopted to characterize freak waves in the literature will be introduced and used in this work to show the bottom effects on the sea states.

1.2 Bibliography survey of techniques of irregular wave analysis

For short-term statistics, the statistical characteristics are computed from a wave record with a certain duration (normally 15-30 min, or 6-12 h for a storm record). The basic assumption of a random sea state is that the time records can be considered as stationary ergodic stochastic process (Holthuijsen, 2007). The ergodicity means that the statistical characteristics of the ensemble free surface elevation can be represented by one observation with discrete sampling. In this Ph.D. work, the time series recorded by numerical wave gauges as well as real digital wave probes last over 40 min, they will be treated as stationary stochastic processes and the sampling variability is relatively low. In this section, not only the statistical analysis of the free surface elevation, free surface envelope, and individual waves will be introduced, but also the spectral/bispectral analysis in Fourier space will be introduced. Some non-dimensional parameters that are important for characterizing wave conditions are covered too. The idea is to develop a preliminary data processing procedure, as was introduced in Fig. (10.2) of Goda (2000), but with more attention paid for the analysis of extreme waves or freak waves.

It should be stressed that in the present work, the statistical study of extreme waves is different from the one used in the design of maritime structures that adopts the conception of 'return period' basing on long-term observation. The abnormal extreme waves are very local events so that long-term statistics are over simplified for our purpose. And abnormal extreme waves are currently not yet included in the related engineering projects.

1.2.1 Analysis of nonlinear sea states in time domain

a/ Statistical analysis of free surface elevation signal

The raw data one gets from the measuring equipment is the history of oscillation (pressure, voltage, time interval and so on). After calibration, the oscillation signal reflects the free surface elevation variation, η. But the mean level of the free surface elevation is not necessarily located at the mean sea level. The first step is thus to evaluate the mean water level:

$$\bar{\eta} = \langle \eta \rangle \,, \tag{IV.1.1}$$

where the operator $\langle \cdot \rangle$ represents the arithmetic mean, and substrate it from the time series. In an ideal Gaussian sea state, the characteristic of the statistics of surface motion can be fully described by its expected value $\bar{\eta}$ and standard deviation σ:

$$\sigma^2 = \left\langle (\eta - \bar{\eta})^2 \right\rangle . \tag{IV.1.2}$$

However, waves in nature are nonlinear, and sea states deviate from Gaussian. Especially when waves approach coastal areas, the significant deviation of the sea

states from Gaussian states is expected, and waves are of sharper and higher wave crests. Higher-order moments are required to characterize this deviation due to the nonlinear effect. Usually, skewness (3^{rd}-order normalized moment) λ_3^η and kurtosis (4^{th}-order normalized moment) λ_4^η are of interest

$$\lambda_3^\eta = \frac{\left\langle (\eta - \bar{\eta})^3 \right\rangle}{\sigma^3}, \tag{IV.1.3}$$

$$\lambda_4^\eta = \frac{\left\langle (\eta - \bar{\eta})^4 \right\rangle}{\sigma^4}. \tag{IV.1.4}$$

For Gaussian sea states, $\lambda_3^\eta = 0$ and $\lambda_4^\eta = 3$ are expected. The skewness is related to the bound mode harmonics, indicating the asymmetry of the wave profiles. For $\lambda_3^\eta > 0$, the larger skewness the more asymmetry with respect to the mean sea level is expected. It means more pronounced sharp and high crests and flat and shallow troughs. The reverse is true for $\lambda_3^\eta < 0$. The net effect of the 2^{nd}-order bound harmonics on the wave height is 0, so in terms of characterizing freak wave occurrence probability, it is of less interest compared to kurtosis. It is known that the kurtosis consists of two additive contributions, one is quasi-resonance four-wave interactions (the 'dynamic' contribution), the other contribution results from the asymmetries in the shape of the waves (the 'wave-shape' contribution). It is generally believed that kurtosis, especially the dynamic part, is related to the occurrences of abnormal high waves. $\lambda_4^\eta > 3$ indicates an increased probability of occurrence of the largest wave heights (Trulsen et al., 2012), but it is not guaranteed that when $\lambda_4^\eta < 3$, the large waves will not manifest.

The overall vertical asymmetry property of the sea states is characterized by skewness, but waves are also asymmetric in the horizontal direction. This is characterized by the 'atiltness' parameter defined as:

$$Atl^\eta = \frac{\left\langle (\eta_t - \langle \eta_t \rangle)^3 \right\rangle}{\sqrt{\left\langle (\eta_t - \langle \eta_t \rangle)^2 \right\rangle^3}}, \tag{IV.1.5}$$

where η_t denotes the partial derivative of η with respect to time. $Atl^\eta > 0$ means that the waves are leaning forward, and $Atl^\eta < 0$ for backward.

The term 'Gaussian' indicates that waves are linear and uncorrelated among them. It also means that the values of η as a function of time are Gaussian distributed. In the linear approximation, the *Probability Density Function* (PDF) of a time series η with zero-mean is governed by:

$$p(\eta) = \frac{1}{\sigma\sqrt{2\pi}} \exp\left(-\frac{\eta^2}{2\sigma^2}\right). \tag{IV.1.6}$$

The nonlinearity of the measurements can be characterized by comparing the Gaussian distribution (with measured σ) and the histogram of the observed surface elevation. The skewness is related to the asymmetry of the PDF, $\lambda_3^\eta > 0$

indicates that the PDF of η 'leans' towards negative values. The kurtosis is related to the sharpness of the PDF, $\lambda_4^\eta > 3$ indicates that the PDF is higher and narrower compared to the corresponding Gaussian distribution (Goda, 2000). The deviation from Gaussian distribution due to bound modes is incorporated by using an Edgeworth's form of the type-A Gram-Charlier series following the work of, for example, Longuet-Higgins (1963).

b/ Statistical analysis of wave heights

The signal is then treated by wave-by-wave analysis. In time series, a wave is defined as the free surface profile between two successive intersection points where the surface elevation penetrates the still water level and goes downwards or upwards. The corresponding wave period is the time interval between the two successive points. This is the well-known zero-down-crossing or zero-up-crossing method. For Gaussian sea states, they are statistically equivalent which do not influence the evaluation of statistical parameters. However, for highly nonlinear waves, the choice of the zero-crossing method makes differences. Hereafter waves are distinguished by the zero-down-crossing method unless specified.

The identified wave heights are denoted as H_i with corresponding period T_i, they are rearranged in descending order of wave heights. i is the sequential number of the i^{th}-highest wave. The highest wave is $H_{max} = H_1$, with the period $T_{H_{max}}$. Assume there are N waves in total in the time series, the mean wave height is:

$$\bar{H} = \frac{1}{N}\sum_{i=1}^{N} H_i. \tag{IV.1.7}$$

Likewise, the mean wave period is:

$$\bar{T} = \frac{1}{N}\sum_{i=1}^{N} T_i. \tag{IV.1.8}$$

Mean values are rarely used in practice mainly because waves with trivial amplitudes are taken into account. The mean values are different from the intuitively estimated averaged wave height and period, and thus not representative for characterizing the sea states.

The root-mean-square wave height, which is an energy-related quantity, is defined:

$$H_{rms} = \left(\frac{1}{N}\sum_{i=1}^{N}\left(H_i - \bar{H}\right)^2\right)^{1/2}. \tag{IV.1.9}$$

The statistical quantities that are useful of describing the sea states (via wave-by-wave analysis) are the mean height and period of the highest one-mth waves:

$$H_{1/M} = \frac{M}{N}\sum_{i=1}^{M/N} H_i, \quad T_{1/M} = \frac{M}{N}\sum_{i=1}^{M/N} T_i. \tag{IV.1.10}$$

The choices of M can be 3, 10, 100, 250. Among them, the most important measure is $H_{1/3}$, which is considered as the significant wave height, H_s. The significant wave height can alternatively be defined from the wave spectrum, as will be introduced. $H_{1/3}$ is relatively close to the visually estimated wave height, however, this is not true for the 'significant wave period' $T_{1/3}$.

The wave height distribution is of significant importance in this Ph.D. study. For Gaussian sea states in deep water and with narrow spectra, the PDF of wave heights is the Rayleigh distribution as shown by Longuet-Higgins (1952). In this linear theory, the distribution is only governed by one parameter, the variance of the free surface σ:

$$p(H) = \frac{H}{4\sigma^2}\exp\left(-\frac{H^2}{8\sigma^2}\right). \tag{IV.1.11}$$

Even though it is based on strong simplifications, but if one is concerned with the distribution of the majority of the waves, the Rayleigh distribution shows very good performance, even for sea states out of its valid range. This distribution is adopted as a reference, which stands for the expectation of linear behavior.

To emphasize the tail of the wave height distribution, the *complementary cumulative distribution function* (CCDF) in the logarithm coordinate is more straightforward. It is denoted as P and obtained by accumulating the probabilities for the waves that are higher than the considered wave height. Assume that H is a continuous variable, the CCDF of the Rayleigh distribution (also as the reference) is:

$$P(H) = \int_H^{+\infty} p(H)\,\mathrm{d}H = \exp\left(-\frac{H^2}{8\sigma^2}\right). \tag{IV.1.12}$$

According to Forristall (1978) and many other similar reports, if one is concerned with the relatively high waves, then the Rayleigh distribution tends to over predict the heights of the high waves for nearly 10%. To achieve a consistent conclusion, the parameter σ is preferable to be computed from the wave spectrum. This observation has made the present topic more interesting because due to the wave-bottom interaction, the probability of occurrences of high waves is larger than the expectation of Rayleigh distribution.

From the wave-by-wave analysis, the distribution of zero-crossing periods and joint distribution of wave height and period are readily constructed, but they are relatively less concerned for the subject of this study. Thus they are not included here.

c/ Statistical analysis of the envelope of free surface elevation

The envelope of the free surface elevation is considered to have advantages over the wave height as a variable. One important reason is that the envelope is a continuous function of time, and it is, in general, a better-defined quantity compared to the wave height especially for sea states with broad spectra. The zero-crossing method is affected by the sampling frequency, insufficient sampling will result in underestimation of wave heights, whereas excessive sampling ends up in more involvement of noise (too many high-frequency waves). For the envelope distribution, the high sampling frequency is no longer a problem because the envelope is a continuous function of time. And the square of envelope is a direct measure for the potential energy of waves. The envelope Z as a function of t is defined:

$$Z(t) = A\exp(i\Theta) = \eta(t) + i\zeta(t), \tag{IV.1.13}$$

where A and Θ denotes local amplitude and phase correspondingly,

$$A(t) = \sqrt{\eta^2(t) + \zeta^2(t)}, \tag{IV.1.14}$$

$$\Theta(t) = \tan^{-1}\left[\frac{\zeta(t)}{\eta(t)}\right]. \tag{IV.1.15}$$

The orthogonal complement $\zeta(t)$ of the free surface $\eta(t)$ is computed via the Hilbert transform $\mathcal{H}$:

$$\zeta(t) = \mathcal{H}(\eta) = \frac{1}{\pi}P_v\int_{-\infty}^{\infty}\frac{\eta(\tau)}{t-\tau}\,\mathrm{d}\tau, \tag{IV.1.16}$$

P_v denotes the Cauchy principal value. Alternatively, for a relatively short record, the FFT algorithm can be adopted instead to evaluate ζ.

It is shown by Janssen (2014) that for the linear wave motion, the PDF of the envelope is always Rayleigh distributed regardless of the width of the spectrum. Such characteristics make it a good indicator of the nonlinearity of sea states. In the *European Centre for Medium-Range Weather Forecasts* (ECMWF) freak wave warning system, the wave envelope distribution is adopted to assess the most possible maximum wave height (Janssen and Bidlot, 2009). Based on the envelope function, a number of normalized moments are defined:

$$\lambda_{m,n} = \frac{\langle\eta^m\zeta^n\rangle}{\langle\eta^2\rangle^{m/2}\langle\zeta^2\rangle^{n/2}}, \tag{IV.1.17}$$

including the general 3^{rd}-order moments:

$$\kappa^3_{m,n} = \lambda_{m,n}, \quad m+n=3, \tag{IV.1.18}$$

and the general 4^{rd}-order moments:

$$\kappa^4_{m,n} = \lambda_{m,n} + (m-1)(n-1)(-1)^{m/2}, \quad m+n=4. \tag{IV.1.19}$$

These moments are used to characterize the deviation from the normality and also to predict the wave height distribution assuming that the wave height is $H = 2A$ according to Mori and Janssen (2006).

1.2.2 Analysis of nonlinear sea states in frequency domain

In the signal processing toolbox, the Fourier analysis is of fundamental importance and has been applied in diverse branches of physics. The theoretical basis of Fourier analysis is ample and is in-depth reviewed in many monographs like in Papoulis (1977). The rigorous mathematical deducing details fall out of the present study interest. Only the necessary ones are mentioned. Consider the random wave series $\eta(t)$ measured at a fixed position is of zero mean, and it is represented by an infinite number of Fourier series:

$$\eta(t) = \sum_{n=-\infty}^{+\infty} X_n \exp\left(-2i\pi f_n t\right), \tag{IV.1.20}$$

where X_n is the complex Fourier coefficient, and $X_{-n} = X_n^*$, the asterisk indicates complex conjugate, $f_n = 2\pi n/D$ and D is the duration of the signal $\eta(t)$. The evaluation of the Fourier amplitude X_n is:

$$X_n = \lim_{D\to\infty} \frac{1}{D} \int_{-D/2}^{D/2} \eta(t) \exp\left(2i\pi f_n t\right) \mathrm{d}t. \tag{IV.1.21}$$

a/ Fourier spectral analysis

The function which shows the distribution of the averaged wave component amplitude in corresponding frequency band $\mathrm{d}f = 1/D$ along the frequency axis is defined as amplitude spectrum. This analysis is very powerful since it shows in a condensed way the averaged wave amplitude in a small frequency bin. However, it is more common to consider the distribution of averaged variance, the power spectrum $P_s(f)$, defined as:

$$P_s(f) = \frac{1}{2} \left\langle X_n X_n^* \right\rangle, \tag{IV.1.22}$$

and the one-sided power spectral density $S(f)$ is related to $P_s(f)$ by:

$$S(f) = \frac{2}{\mathrm{d}f} P_s(f). \tag{IV.1.23}$$

There are two numerical approaches for the estimation of the power spectrum and its density. One approach is to conduct the Fourier transform of the autocovariance function of the free surface elevation (auto-correlation method). The other is to

carry out FFT to the measured signal directly (periodogram method). The latter approach is much more efficient than the former one.

Here the Welch's averaged periodogram method is adopted. Firstly, the time series is separated into M segments with 50% overlapping rate, and each segment is of $N = 2^{FFT}$ points. Secondly, FFT requires the time series to be periodic in time otherwise the spectral leakage will occur. In most cases, the time series is not periodic, thus a proper window function is required to minimize the leakage, and a corresponding correction factor is used to compensate for the decrease of total energy due to the application of the window. Thirdly, conduct N-points FFT transformation of each segment and take the mean value of M estimates. Fourthly, smooth the obtained spectrum by replacing the evaluated spectral density by the weighted average of the adjacent values. Finally, adjust the estimated spectrum by forcing the consistency of total energy with measurements. A correction factor σ^2/m_0 is multiplied to all estimates of spectral density values, and m_0 is the zeroth spectral moment.

The spectral moments are defined:

$$m_n = \int_0^\infty f^n S(f)\,\mathrm{d}f, \qquad n = 0, 1, 2, ... \tag{IV.1.24}$$

The characterizing properties of irregular sea states are also represented by spectral parameters. The zeroth spectral moment m_0 is a measure of the total energy, and it is equivalent to the variance σ^2 of the surface signal. Replacing the variance with the spectral zeroth moment in Eq. (IV.1.11), the characteristic wave heights are then related to the spectrum.

The significant wave height based on wave spectrum is defined as:

$$H_s = H_{m_0} = 4.004\sqrt{m_0} \approx 4\sqrt{m_0}. \tag{IV.1.25}$$

Hereafter, this definition of significant wave height is adopted unless specified. The averaged wave period is defined as:

$$\bar{T}_{m02} = \sqrt{\frac{m_0}{m_2}}, \tag{IV.1.26}$$

however, this definition is sensitive to the high-frequency range of the spectrum where noise may influence the evaluated mean period significantly. An alternative definition of averaged wave period is:

$$\bar{T}_{m01} = \sqrt{\frac{m_0}{m_1}}. \tag{IV.1.27}$$

The width of the spectrum is defined as:

$$\nu_{04} = \left(1 - \frac{m_2^2}{m_0 m_4}\right)^{1/2}, \tag{IV.1.28}$$

but the estimation of m_4 involves too much noise at high-frequency range. An alternative definition is:

$$\nu_{02} = \left(\frac{m_0 m_2}{m_1^2} - 1 \right)^{1/2}. \tag{IV.1.29}$$

Goda (2000) proposed to use 'peakedness' parameter to describe the spectral shape:

$$Q_p = \frac{2}{m_0^2} \int_0^\infty f S^2(f)\, \mathrm{d}f. \tag{IV.1.30}$$

b/ Fourier bispectral analysis

The Gaussian assumption is not valid for nonlinear waves, and especially not for the highly nonlinear events like extreme waves. The above-mentioned variance spectrum is not able to distinguish the bound mode frequency components resulting from nonlinear wave-wave interaction, and the free wave component. A powerful tool to study the nonlinear process is polyspectral analysis. In particular, the Fourier based bispectral analysis technique has been used to study the triad wave-wave nonlinear interactions and quadratic phase coupling of nonlinear water waves (Hasselmann et al., 1963; Bertin et al., 2018). The bispectrum $B(f_1, f_2)$ is defined as the two dimensional Fourier transformation of the third-order auto-correlation function of the signal. Equivalently, it can also be defined as introduced in Kim and Powers (1979):

$$B(f_1, f_2) = \left\langle X_1 X_2 X_{1+2}^* \right\rangle, \tag{IV.1.31}$$

which is the ensemble average of the triple product of complex Fourier coefficients defined in Eq. (IV.1.21). Two Fourier coefficients of frequencies f_1, f_2 and the conjugate of the Fourier coefficient of sum-frequency $f_1 + f_2$ are adopted. In general, the bispectrum $B(f_1, f_2)$ is complex.

The evaluation of the bispectrum defined in Eq. (IV.1.31) is efficient using the FFT algorithm. The bispectrum is of symmetry properties, $B(f_1, f_2) = B(f_2, f_1) = B^*(-f_1, -f_2) = B(-f_1 - f_2, f_2) = B(f_1, -f_1 - f_2)$. Due to these symmetric properties, only a triangular domain where $f_1, f_2 > 0$, $f_1 > f_2$, and $f_1 + f_2 < F_s/2$ (with F_s as the sampling frequency) of the bispectrum needs to be computed. The averaged wave profile is related to the bispectrum. The bispectrum-defined skewness λ_3^B can be computed as the normalized integral of the real part of the bispectrum according to Hasselmann et al. (1963). The wave profile asymmetry with respect to the vertical axis, the atiltness parameter Atl^B is evaluated from the normalized integral of the imaginary part of the bispectrum

according to Elgar and Guza (1985):

$$\lambda_3^B = \frac{\sum\sum \Re\{B(f_1, f_2)\}}{\sigma^3}, \tag{IV.1.32}$$

$$Atl^B = \frac{\sum\sum \Im\{B(f_1, f_2)\}}{\sigma^3}, \tag{IV.1.33}$$

where $\Re$ and $\Im$ denote the real part and the imaginary parts of the complex number, respectively. The normalized phase of the bispectrum is the so-called biphase $\beta(f_1, f_2)$, defined as:

$$\beta(f_1, f_2) = \arctan\left[\frac{\Re\{B(f_1, f_2)\}}{\Im\{B(f_1, f_2)\}}\right]. \tag{IV.1.34}$$

This definition gives a normalized measure of the phase relationship. The variance of the bispectral estimates could be highly variable depending on the power spectral properties. The commonly used normalization measure of bispectrum is the bicoherence $b^2(f_1, f_2)$, defined as follows:

$$b^2(f_1, f_2) = \frac{|\langle X_1 X_2 X_{1+2}^* \rangle|^2}{\langle |X_1 X_2|^2 \rangle \langle |X_{1+2}^*|^2 \rangle} = \frac{|B(f_1, f_2)|^2}{\langle |X_1 X_2|^2 \rangle \langle |X_{1+2}|^2 \rangle}, \tag{IV.1.35}$$

bounding the real-valued function $b^2(f_1, f_2)$ in $[0, 1]$, if no smoothing or merging applied to the bispectrum.

The bicoherence is a measure of the relative strength of the coupling of the three wave components involved. The biphase is dependent on this parameter, with low bicoherence the biphase is randomly distributed between $-\pi$ and π. The bicoherence $b^2(f_1, f_2)$ does not reveal the direction of the energy transfer among three wave components. The direction is indicated by the sign of $\Im\{B(f_1, f_2)\}$, negative value represents difference interaction, and positive value represents sum interaction.

1.2.3 Analysis of wave grouping characteristics

For this Ph.D. study, and also for many other engineering problems, the knowledge of high wave series is important. The series of successive high waves in which all waves are of heights greater than a certain threshold H_{gr}, is known as a wave group. The groupness of irregular waves is quantified in different ways. A good review of the commonly used parameters and methodologies is given by Medina and Hudspeth (1990). In general, the groupness of irregular sea states is related to the spectral width, the narrower the spectrum is, the stronger grouping characteristics are expected. The peakedness parameter Q_p introduced previously works as a good indicator of groupiness.

a/ Theory of runs of high waves

The preliminary analysis of wave grouping is to consider the definition of wave groups by Goda Yoshimi in the 1970s (Goda, 2000). Following Goda's definition, we consider the zero-crossing wave heights with unsorted order and take the threshold wave height $H_{gr} = H_{1/3}$. The waves whose wave heights successively locate above this reference is called a run of high waves, the number of waves in the run is the run length L_{Run}. The repetition length of high waves is called a total run, and it is defined analogously to the definition of the zero-up-crossing method, which is the number of waves from the first wave in a run to the first wave in the next run. The 'zero' line is the threshold H_{gr}. By this definition, a single high wave can be considered as a wave group, since $L_{Run} = 1$ indicates a wave group consists only one wave, as is shown in Fig. (IV.1.1). In this definition, the key parameter is the number of wave groups with different L_{Run}, and the weighted average of L_{Run}. Kimura (1980) derived the theoretical probability distributions of the run length considering correlated wave heights as a Markov process.

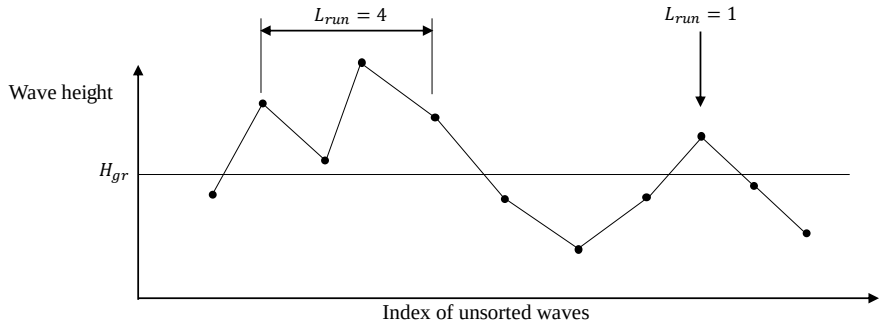

Figure IV.1.1: Sketch of two runs of high waves, one run with $L_{Run} = 4$ and the other with $L_{Run} = 1$, both are wave groups by definition.

b/ Theory of wave energy history

It is known that wave energy is proportional to the variance of wave record and that large waves are of greater energy than that of smaller waves. So the wave groups can be described effectively by the wave energy history. Following the work of Funke and Mansard (1980), the instantaneous wave energy E at the instant t is defined as the convolution of η^2 and a window function W:

$$E_{SIWEH}(t) = \frac{1}{T_p} \int_{-T_p}^{T_p} \eta^2(t+\tau) W(\tau)\, \mathrm{d}\tau, \quad \text{for} \quad T_p \le t \le t_{end} - T_p, \qquad \text{(IV.1.36)}$$

where T_p is the wave period corresponding the spectral peak, t_{end} denotes the end time of wave record, $W(\tau)$ is an arbitrary smoothing function needed to filter out

high frequencies, in the original work of Funke and Mansard (1980), the Bartlett window is chosen:

$$W(\tau) = \begin{cases} 1 - \dfrac{|\tau|}{T_p}, & -T_p/2 \le \tau \le T_p/2, \\ 0 \quad , & \text{elsewhere.} \end{cases} \tag{IV.1.37}$$

It should be noticed that for the two ends of the record, when $t \in [0, T_p]$ and $t \in [t_{end} - T_p, t_{end}]$, the computation formula of the instantaneous wave energy is slightly different:

$$\begin{cases} E_{SIWEH}(t) = \dfrac{2}{T_p + t} \displaystyle\int_{-t}^{T_p} \eta^2(t+\tau) W(\tau)\, \mathrm{d}\tau, & \text{for} \quad 0 \le \tau \le T_p, \\ E_{SIWEH}(t) = \dfrac{2}{T_p + t_{end} - t} \displaystyle\int_{-T_p}^{t_{end}-t} \eta^2(t+\tau) W(\tau)\, \mathrm{d}\tau, & \text{for} \quad t_{end} - T_p \le \tau \le t_{end}. \end{cases} \tag{IV.1.38}$$

$E_{SIWEH}(t)$ is called *Smoothed Instantaneous Wave Energy History* (SIWEH), with which the *Groupness Factor* (GF) is defined and used to quantify the grouping characteristics of a record:

$$GF = \frac{1}{\langle E_{SIWEH} \rangle} \sqrt{\frac{1}{t_{end}} \int_0^{t_{end}} \left[E_{SIWEH}(t) - \langle E_{SIWEH} \rangle \right]^2 \mathrm{d}t}. \tag{IV.1.39}$$

Another parameter based on SIWEH method was introduced by Rye (1982) in his dissertation. It is the mean zero-up-crossing period of $[E_{SIWEH}(t) - \langle E_{SIWEH} \rangle]$, defined as:

$$\bar{T}_{SIWEH} = \frac{1}{T_p} \frac{1}{I} \sum_{i=1}^{I} (T_{SIWEH})_i, \tag{IV.1.40}$$

in which I denotes the total number of zero-up-crossings of the mean level in the SIWEH. This parameter seems to be more propitiate in describing grouping characteristics since it can approximately represent the mean length of the total run of waves with $H_{gr} = H_{rms}$.

In the literature, there is an alternative approach to relate the grouping properties with the fluctuation of local variance. It is called *Local Variance Time Series* (LVTS) method by Thompson and Seelig (1984). But it will not be introduced in detail since LVTS and SIWEH are very similar in essence, and the groupness parameter of LVTS is comparable to GF here.

c/ Theory of wave envelope

What SIWEH method do is to isolate the low-frequency components of the oscillations of η^2, and this is achieved by doing convolution with a smoothing window.

The choice of the low-pass filter makes nontrivial influences, and the spectral leakage range of the proposed Bartlett window in frequency domain is even broader than the rectangular window. This will cause unpredictable effects on the evaluated GF.

Hudspeth and Medina (1989) proposed to use the Hilbert transform to estimate the instantaneous wave energy as a function of $H^2(t)/8$ because it was demonstrated by the same authors that the squared-wave height function $H^2(t)$ is the target function of which the Hilbert transform exactly isolates the low-frequency components of $\eta^2(t)$. It is no longer necessary to specify any filter, and the original signal is not contaminated either.

More recently, Veltcheva and Soares (2016) introduced a new wave group analysis technique by using *Hilbert-Huang Transform* (HHT). The idea of HHT consists of two steps: first, decompose the signal into different modes; then conduct the Hilbert to each of them. The empirical model decomposition procedure will produce a finite number N_{IM} of *Intrinsic Mode Functions* (IMF) $C_j, j = 1, ..., N_{IM}$ and a residual function r_n as:

$$\eta(t) = r_n(t) + \sum_{j=1}^{N_{IM}} C_j(t), \tag{IV.1.41}$$

and the Hilbert to each IMF is:

$$\hat{C}_j(t) = \mathcal{H}(C_j). \tag{IV.1.42}$$

The instantaneous envelope $a_j(t)$, the phase $\Theta_j(t)$ and the corresponding angular frequency $\omega_j(t)$ for the jth-IMF $C_j(t)$ are readily obtained:

$$a_j(t) = \sqrt{\hat{C}_j^2(t) + C_j(t)^2}, \tag{IV.1.43}$$

$$\Theta_j(t) = \tan^{-1}\left[\hat{C}_j(t)/C_j(t)\right], \tag{IV.1.44}$$

$$\omega_j(t) = \partial\Theta_j(t)/\partial t. \tag{IV.1.45}$$

The time-frequency distribution of the squared amplitude is designated as the Hilbert energy spectrum $HH(\omega, t)$. Based on this spectrum, Veltcheva and Soares (2016) defined new group parameters including the new instantaneous energy $E_I(t)$:

$$E_I = \int_0^\infty HH(\omega, t)\,\mathrm{d}\omega. \tag{IV.1.46}$$

The wave groups are identified with a method in analog to the theory of runs, by setting a threshold of wave height or wave energy. The time group length t_{gr} is the time interval between two successive intersections of the $E_I(t)$ and the

chosen level, the group energy E_{gr} is defined for each group by integration over the corresponding time group length t_{gr}:

$$E_{gr} = \int_{t_{gr}} E_I(t)\,\mathrm{d}t. \tag{IV.1.47}$$

The spectral peak frequency in each wave group is denoted as f_{pgr}, and dimensionless number as a measure of group length is defined as:

$$N_{gr} = t_{gr} f_{pgr}. \tag{IV.1.48}$$

1.2.4 Non-dimensional numbers for characterizing wave conditions

In previous analysis techniques, a number of non-dimensional parameters have been introduced in time and frequency domains, and also in groupiness analysis. Herein, some other non-dimensional parameters which are also important for characterizing irregular sea states will be supplemented.

a/ Wave nonlinearity and dispersion characterization

Consider the wave with spectral peak frequency f_p to represent the irregular sea state. The nonlinearity of the sea state is characterized by the steepness:

$$\varepsilon = k_p H_s, \tag{IV.1.49}$$

where k_p is computed by dispersion relationship based on local water depth h and spectral peak frequency f_p. The dispersion parameter is relative water depth, defined as:

$$\mu = k_p h. \tag{IV.1.50}$$

The relative importance of nonlinearity over dispersion is measured by Ursell number, here we use the following definition:

$$Ur = \frac{H_s/L_p}{(h/L_p)^3} = \frac{H_s L_p^2}{h^3}. \tag{IV.1.51}$$

Goda (2000) provided a parameter for measuring wave nonlinearity which is informative for both shallow water and deep water waves:

$$\Pi = (H_s/L_p)\coth^3\mu. \tag{IV.1.52}$$

For deep water waves, it corresponds to steepness, and when water depth gets sufficiently shallow, it reflects the Ursell number.

b/ Benjamin-Feir Index for deep water narrow-banded waves

For the study of the freak wave, assuming that waves are unidirectional in the deep water with the narrow-banded spectrum, Janssen (2003) introduced *Benjamin-Feir Index* (BFI) evaluating the ratio of nonlinearity to frequency dispersion to investigate the importance of quasi-resonant four-wave interaction. The original definition is:

$$\mathrm{BFI} = c\,\frac{k\sqrt{\langle\eta^2\rangle}}{\Delta}, \tag{IV.1.53}$$

where C is a scaling constant, generally $c = \sqrt{2}$ is used, Δ denotes the spectral width which is determined by the half-width at the half-maximum of the spectrum normalized by the peak wave frequency. Note that in Janssen (2003), the authors define $\varepsilon = (k^2\langle\eta^2\rangle)^{1/2}$, whereas in this work, ε denotes k_pH_s. It is also found that the dynamic part of the kurtosis is related to the square BFI parameter. The BFI parameter measures the balance of the nonlinearity and the dispersion, increases as the wave steepness increases or the spectrum width decreases. When the relative water depth is higher than 1.363, the wave train is 'unstable' due to modulational instability, in this case, BFI indicates the relative strength of four-wave interaction. When relative water depth is below the threshold 1.363 the process of nonlinear focusing ceases to exist, so BFI loses its meaning as an indicator of modulational instability.

For regular waves with unstable side-bands, the evaluation of BFI is unique. However, it is not the case for irregular waves. The evaluation of spectral width and peak frequency is not univocally defined, resulting in various BFI computation methods. In the work of Serio et al. (2006); Olagnon and Magnusson (2004), several estimation methods of BFI are compared and so is the variability of the estimates. Here we follow the suggestion of Serio et al. (2006) for computing the spectral peak, spectral width as well as the steepness. The definition of BFI in Eq. (IV.1.53) is replaced by:

$$\mathrm{BFI} = \sqrt{m_0}\hat{k}_pQ_p\sqrt{2\pi}\nu\sqrt{\frac{|\beta|}{\alpha}}, \tag{IV.1.54}$$

where m_0, Q_p are defined already, α, β, ν are the coefficients of cubic NLS equation, $\hat{k}_p$ corresponds to the wave with the frequency $\hat{f}_p$. $\hat{f}_p$ is an estimate of the true peak frequency, involving the use of a weighted integral:

$$\hat{f}_p = \frac{\int_0^\infty fS^4(f)\,\mathrm{d}f}{\int_0^\infty S^4(f)\,\mathrm{d}f}. \tag{IV.1.55}$$

c/ Shallow water extension of Benjamin-Feir Index

In shallow water, it is known that finite-amplitude surface gravity waves generate a current and deviations from the mean surface elevation. This stabilizes the

modulational instability, and as a consequence, the process of nonlinear focusing ceases to exist when $\mu < 1.363$. This shallow water effect due to wave-induced current is studied by Janssen and Onorato (2007), where they adopt the Zakharov equation for intermediate water depth to evaluate the nonlinear source term in the energy balance equation.

In addition, a dimensionless number that measures the balance between nonlinearity and dispersion is introduced in Janssen and Onorato (2007). This parameter, introduced within framework of Zakharov equation, is computed from:

$$B_s^2 = -\frac{C_g^2}{C^2}\frac{gT_{0,0,0,0}}{\omega}\frac{1}{k^2\omega''}\frac{2\langle\eta^2\rangle}{\Delta^2}, \tag{IV.1.56}$$

where the subscript s is used to distinguish from deep water condition, $C = \omega/k$ is the phase velocity. The second derivative of angular frequency is related to α as $\omega'' = -2\alpha$. For any water depth condition, $\alpha > 0$ always holds. $T_{0,0,0,0}$ is a known interaction coefficient with a complicated expression in the general case. Here, only the narrow-band limit of this interaction coefficient is given:

$$\frac{T_{0,0,0,0}}{k^3} = \frac{9\tanh^4(kh) - 10\tanh^2(kh) + 9}{8\tanh^3(kh)} - \frac{1}{kh}\left[\frac{(4C_g - C)^2}{4\left(gh - C_g^2\right)} + 1\right]. \tag{IV.1.57}$$

For more details, it is suggested to refer to the work of Janssen and Onorato (2007).

It is noticed that the first term of Eq. (IV.1.57) is related to the nonlinear dispersion for surface gravity waves, and the second term is due to wave-induced current effects. Two terms cancel each other when $kh = 1.363$, for narrow-band uni-directional waves. With the computation method (IV.1.54) taken into account, we consider the Benjamin–Feir index in the general shallow-water case as:

$$B_s = \mathrm{BFI}\frac{C_g}{C}\sqrt{-\frac{gT_{0,0,0,0}}{k^4\omega\omega''}}, \tag{IV.1.58}$$

where BFI is evaluated following Eq. (IV.1.54) instead of Eq. (IV.1.53). We stress that all the parameters (α, β, $T_{0,0,0,0}$, C_g, etc.) are evaluated using the local values of $\hat{f}_p$. In the deep water limit, $\alpha \to g/(8k\omega)$ and $T_{0,0,0,0} \to k^3$, B_s reduces to BFI.

Apart from the water depth condition, the width of direction spectrum also plays a significant role for the estimation of BFI or B_s of short-crest waves. This is beyond the framework of the present study, thus it is not introduced. For more details and applications in the wave forecast system of the shallow water directional BFI parameter, refer to the unpublished internal report by Janssen and Bidlot (2009) or to the work of Fedele (2015).

Chapter 2

Long-crested irregular wave train evolution over a submerged step bottom profile

The published paper *Statistics of extreme waves in coastal waters: Large scale experiments and advanced numerical simulations*, is shown in this chapter. This paper addresses the formation mechanisms and statistics of extreme waves in the coastal area, by combining two approaches: (i) a series of experiments performed in a large scale facility using unidirectional irregular waves propagating over a variable bottom profile (composed of a 1/20 slope connecting two constant-depth regions), (ii) numerical simulations using two advanced highly nonlinear deterministic wave models. Both the experimental free surface elevation time series and the corresponding numerical results are analyzed using four methods: (i) classical spectral (Fourier) analysis, (ii) bispectral analysis, allowing to gain knowledge on the nonlinear coupling between wave components, (iii) evolution of synthetic parameters characterizing the nonlinearity of the wave field (skewness, kurtosis and asymmetry), and (iv) statistical analysis of distribution of wave heights. Particular attention is paid to the sloping bottom area, and the low-frequency wave dynamics in the flume.

A number of observations have been drawn from the analysis of both the experimental and numerical data. In particular, nonlinear effects are more marked in the area around the end of the slope. Strong second-order nonlinear effects (and also noticeable third-order effects) manifest as waves enter the shallower region. We speculate that the formation of extreme waves is mainly related to these nonlinear effects, which are also responsible for the generation of long waves. Based on the comparison of several existing models for the distribution of wave heights, it appears that the generalized Boccotti's distribution can predict with good confidence the distributions of large wave heights, though it was originally designed for weakly nonlinear deep water waves.

fluids

MDPI

Article

Statistics of Extreme Waves in Coastal Waters: Large Scale Experiments and Advanced Numerical Simulations

Jie Zhang [1,2], Michel Benoit [1,2,*], Olivier Kimmoun [1,2], Amin Chabchoub [3,4] and Hung-Chu Hsu [5]

1 École Centrale Marseille, 13013 Marseille, France; zhang@irphe.univ-mrs.fr (J.Z.); olivier.kimmoun@centrale-marseille.fr (O.K.)
2 Aix Marseille Univ, CNRS, Centrale Marseille, IRPHE UMR 7342, 13013 Marseille, France
3 Centre for Wind, Waves and Water, School of Civil Engineering, The University of Sydney, Sydney, NSW 2006, Australia; amin.chabchoub@sydney.edu.au
4 Marine Studies Institute, The University of Sydney, Sydney, NSW 2006, Australia
5 Department of Marine Environment and Engineering, National Sun Yat-Sen University, Kaohsiung 80424, Taiwan; hchsu@mail.nsysu.edu.tw
* Correspondence: benoit@irphe.univ-mrs.fr

Received: 7 February 2019; Accepted: 20 May 2019; Published: 29 May 2019

Abstract: The formation mechanism of extreme waves in the coastal areas is still an open contemporary problem in fluid mechanics and ocean engineering. Previous studies have shown that the transition of water depth from a deeper to a shallower zone increases the occurrence probability of large waves. Indeed, more efforts are required to improve the understanding of extreme wave statistics variations in such conditions. To achieve this goal, large scale experiments of unidirectional irregular waves propagating over a variable bottom profile considering different transition water depths were performed. The validation of two highly nonlinear numerical models was performed for one representative case. The collected data were examined and interpreted by using spectral or bispectral analysis as well as statistical analysis. The higher probability of occurrence of large waves was confirmed by the statistical distributions built from the measured free surface elevation time series as well as by the local maximum values of skewness and kurtosis around the end of the slope. Strong second-order nonlinear effects were highlighted as waves propagate into the shallower region. A significant amount of wave energy was transmitted to low-frequency modes. Based on the experimental data, we conclude that the formation of extreme waves is mainly related to the second-order effect, which is also responsible for the generation of long waves. It is shown that higher-order nonlinearities are negligible in these sets of experiments. Several existing models for wave height distributions were compared and analysed. It appears that the generalised Boccotti's distribution can predict the exceedance of large wave heights with good confidence.

Keywords: coastal areas; extreme waves; statistical analysis; bispectral analysis; nonlinear wave models

1. Introduction

Extreme wave, also known as freak wave or rogue wave, refers in oceanography to large water wave with crest-to-trough wave height H exceeding twice the significant wave height H_s in the wave field, or with wave crest height η_c higher than $1.25H_s$ [1]. In a Gaussian sea state, wave heights H follow a Rayleigh distribution when the wave field is assumed to be narrow-banded. In such cases, large waves fulfilling the criteria $H/H_s > 2$ are not so unusual, occurring approximately once every 3000 waves. For instance, if the average wave period $T_{ave} = 15$ s, it implies that the observer could

probably encounter one of such waves in 12 h. What makes this particular field of research interesting is the fact that the extreme waves may occur not only in the energetic storm sea state but also in a calm sea state, making these waves outstanding and exceptional compared to the surrounding waves. These extreme waves are supposed to be very rare basing on Rayleigh distribution model, whereas they seem to have a larger occurrence in the real world, as suggested in the following scientific studies and reports [2–5].

The possible mechanisms of the formation of extreme waves are summarised and discussed in recent reviews [6,7]. One of the well-known mechanisms of the generation of freak waves is the so-called Benjamin–Feir (or modulational) instability [8,9], which is frequently studied within the framework of the nonlinear Schrödinger equation (NLS). The NLS equation can describe the evolution of the narrow-banded weakly nonlinear waves [10–13]. More recent reviews show that real sea states are more complex and one needs to consider three-dimensionality [14], dissipation [15–17] and breaking [18] to achieve more accurate modeling of such wave fields. For constant water depth, the modulation instability of unidirectional waves should disappear with the relative water depth $kh < 1.363$ (k denotes the wave number and h is the water depth) [8,19]. However, for the multidirectional sea states, this is no longer the case. The three-dimensionality not only affects the modulation instability but also the statistical parameters [20,21]; the sea states are either focusing or defocusing depending on the spreading angle. Although we are aware of the essential importance of short-crest waves, the topic of this paper is restricted to one horizontal propagation direction case since the uneven bottom effects on freak waves are not fully understood yet in such configuration. Recently, it has been emphasised that the formation of extreme waves is more related to the second/third-order non-resonant or bound harmonic waves than modulation instability, especially in the finite water depth case where the instabilities are further attenuated [22].

The evidence of the link between a water depth transition and a higher probability of the occurrence of extreme waves has been shown both experimentally [23,24], and numerically [25–27]. There are also studies dealing with extreme wave statistics in coastal areas with different shapes of variable bathymetry. Katsardi et al. (2013) [28] conducted experimental tests with unidirectional waves propagating over mild bed slopes (1:100 and 1:250) including breaking zones, and made extensive comparisons of wave height distributions. Nonlinear transformation of irregular waves propagating over sloping bottoms (1:15, 1:30 and 1:45) is discussed using wavelet-based bicoherence in [29]. Ma et al. (2014) [30] studied spatial variations of skewness, kurtosis and groupiness factor for irregular waves over a bar (1:20) in shallow water. The obliquity effects on the statistical parameters are discussed in [21] using 3D simulations with a High-Order Spectral (HOS) model.

In this context, the objectives of the present study were three-fold: (1) studying experimentally the statistical distribution of (extreme) wave heights considering variable bottom coastal conditions in a uni-directional water wave flume; (2) comparing the collected temporal wave profiles and corresponding statistical distributions with the results from two advanced numerical models; and (3) comparing the measured and simulated wave height distributions with a number of existing statistical models. Regarding Objective 1, the spatial evolution of unidirectional irregular sea states due to the presence of a constant bottom gradient was studied in the large scale facility of Tainan Hydraulics Laboratory (THL) in Taiwan. This large facility allowed us to investigate the full life cycle of extreme waves, from the generation to the degeneration. Several cases with different experimental conditions were tested, while one representative case was investigated for the validation of numerical nonlinear models. In addition to the overall evolution of the sea state, particular attention was paid to the sloping bottom zone as well as the two depth transition regions. Regarding Objective 2, two accurate numerical models were adopted to simulate the experiments, both based on the fully nonlinear potential flow theory: a higher-order Boussinesq-type model based on the model in [31] and the highly nonlinear and dispersive model, whispers3D, using a spectral approximation of the potential in the vertical direction [32,33]. As shown below, the corresponding results indicate that the increase of the probability of occurrence of freak waves was clearly observed in experiments and

well captured in the simulations, over a region where the water depth is relatively mildly varying. Both measured and simulated wave profiles were studied by using statistical, spectral and bispectral analysis. Finally, Objective 3 was devoted to the statistical distributions of measured and simulated wave heights comparing with six existing statistical distribution models.

The present article is structured as follows. In Section 2, the experimental set-up and the tested sea state conditions are introduced. The mathematical models and their numerical implementations are presented in Section 3. Several signal processing techniques are adopted to interpret the obtained data: from the measurements as well as the simulations, including spectral analysis (Section 4), bispectral analysis (Section 5), nonlinear wave parameters analysis (Section 6), and statistical analysis of the wave height distribution (Section 7). Conclusively, the main results are summarised in Section 8.

2. Experimental Set-Up and Test Conditions

The experiments were conducted in the 2-D wave flume of THL at Tainan, Taiwan. The flume is 200 m long and 2 m wide. The waves were initially generated in the deeper region with depths of $h = 1.2$ m and 1.3 m. The bathymetry was decomposed into three parts: a 30 m long flat part, a 20 m long part with a constant slope of 1/20 and again a 120 m long flat bottom part. Waves were generated at $x = 0$ m by a piston-type wave-maker, which was also able to absorb part of the wave energy reflected by the uneven bottom or far-field rip-rap mound. The last 30 m part of the flume worked as an effective wave absorber including a deep water area and a mound of stones placed at the end of the flume. Over the flume length, 30 capacitance gauges were used to measure the wave elevation with a sampling frequency of 100 Hz. The locations of the wave gauges are shown in Figure 1.

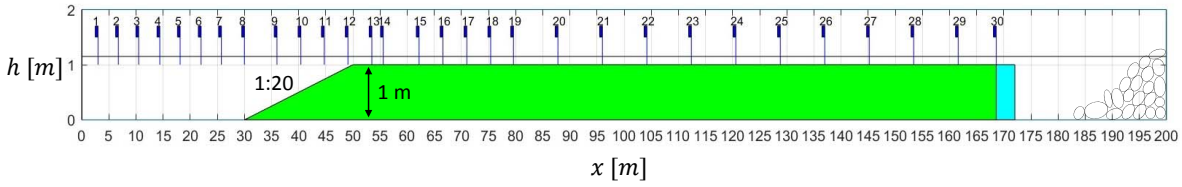

Figure 1. Sketch of the experimental setup, installed at THL.

The first probe, located at $x = 3$ m, was used as a reference for the input signal generated by the wavemaker, and then 7 additional wave probes were used to measure the wave evolution in the deeper area. Probes 9–12 were used to record the wave evolution over the slope. Several probes were distributed in the shallower region to observe the post-dynamics of extreme waves appearing around the end of the bottom slope.

Unidirectional irregular waves were generated using a linear superposition model using random initial phases and amplitudes as determined from a JONSWAP spectrum, given in Equation (1). The experimental condition was controlled by four parameters: water depth h, significant wave height H_s, peak frequency f_p and the peak enhancement factor γ.

$$S(f) = \frac{\alpha g^2}{(2\pi)^4} \frac{1}{f^5} exp\left[-\frac{5}{4}\left(\frac{f_p}{f}\right)^4\right] \gamma^{\exp\left[-(f-f_p)^2/(2\sigma_J^2 f_p^2)\right]}, \quad (1)$$

where g denotes the gravitational acceleration; α denotes the adjustment factor to achieve the target H_s; and σ_J denotes the spectral asymmetric parameter with respect to (w.r.t.) the spectral peak at f_p, with $\sigma_J = 0.07$ when $f < f_p$ and $\sigma_J = 0.09$ when $f > f_p$. The spectrum was discretised using 16,384 = 2^{14} frequency components over the range $[0, 6f_p]$ to generate irregular sea states.

During the experimental campaign, more than 30 cases were tested, which were chosen based on the nonlinearity (wave steepness $k_p H_s$, with k_p being the wave number corresponding to the peak wave period T_p) and the dispersion (w.r.t. the relative water depth $k_p h$) in the deeper and shallower regions. The relative importance of these two effects was measured by the Ursell number $U_r \equiv H_s L_p^2/h^3$.

For each test, the test duration lasted for $1200T_p$. Among all tests, the experimental results of three representative cases shown in Table 1 have already been studied [34].

Table 1. Experimental cases studied in [34].

Case	γ	$h(m)$	$H_s(m)$	$T_p(s)$	Deeper Side			Shallower Side		
					k_ph	k_pH_s	Ur	$k_p'h'$	$k_p'H_s'$	Ur'
1	3.3	1.2	0.05	1.5	2.20	0.092	0.3	0.64	0.166	25.4
2	3.3	1.3	0.10	2.3	1.19	0.092	2.1	0.50	0.197	63.3
3	3.3	1.3	0.10	2.5	1.06	0.082	2.7	0.45	0.185	78.0

(1) Parameters in the shallower side are denoted by $'$; (2) in the shallower region, $h' = h - 1$ m, and $H_s' = H_s\sqrt{C_g/C_g'}$; (3) the group velocity $C_g = \partial\omega/\partial k$, with $\omega = \sqrt{gk\tanh kh}$.

Only Case 2 was selected and simulated in this study for the following reasons: (1) the sea state of Case 1 is almost Gaussian and the number of measured large waves is insufficient to do reliable statistical analysis; (2) in Cases 2 and 3, the relative water depth $k_ph < 1.363$ is verified for the whole bottom profile, which means the effect of modulation instability can be ignored; and (3) Cases 2 and 3 show similar behaviour in both the statistical and spectral analyses. Case 2 is also preferred because fewer wave breaking events happened during the experiment, and they are not accounted for in the two numerical models. Regarding the wave parameters, one difference between the work of Trulsen et al. [23] and the present work is that the nonlinearity of the waves in our case is significantly increased by the shoaling over the slope (note that $k_p'H_s' \approx 0.197$ in our case is larger than $2k_pa_c \approx 0.14$ in the shallower side of Case 1 in [23]) with the dispersion effects, i.e., k_ph and $k_p'h'$ being similar. Regarding the wave tank, our configuration was shorter in the deeper part but longer in the shallower part, also the slope is longer with the normalised length $k_pL_s \approx 18$ (L_s denotes the length of slope) than in [23] where $k_pL_s \approx 8$. Finally, a larger number of wave gauges were set in the flume to follow the wave evolution in space.

3. Numerical Modeling

3.1. General Modeling Approach

The wave problem is formulated in a 2D vertical Cartesian coordinate system (x, z), with x-axis located at the mean free surface level, and z-axis positive upwards. In the framework of potential flow theory, the fluid is assumed to be homogeneous and inviscid and the flow is assumed irrotational so that the wave breaking cannot be directly considered. With the velocity potential $\phi(x, z, t)$ introduced, the nonlinear potential flow problem is:

$$\phi_{xx} + \phi_{zz} = 0, \quad -h(x) \le z \le \eta(x,t), \tag{2}$$

$$\eta_t + \phi_x\eta_x - \phi_z = 0, \quad at\ z = \eta(x,t), \tag{3}$$

$$\phi_t + \frac{1}{2}\left(\phi_x^2 + \phi_z^2\right) + g\eta = 0, \quad at\ z = \eta(x,t), \tag{4}$$

$$h_x\phi_x + \phi_z = 0, \quad at\ z = -h(x), \tag{5}$$

where the subscripts denote partial derivatives (i.e., $\phi_x \equiv \frac{\partial\phi}{\partial x}$).

The free surface boundary conditions (FSBCs) Equations (3) and (4) are expressed as functions of free surface variables $\eta(x,t)$ and $\tilde{\phi}(x,t) \equiv \phi(x, z = \eta, t)$, forming the so-called Zakharov equations:

$$\eta_t = -\tilde{\phi}_x\eta_x + \tilde{w}\left(1 + \eta_x^2\right) + 2\nu\eta_{xx}, \tag{6}$$

$$\tilde{\phi}_t = -g\eta - \frac{1}{2}\phi_x^2 + \frac{1}{2}\tilde{w}^2\left(1 + \eta_x^2\right) - 2\nu\phi_{zz}, \tag{7}$$

where the vertical velocity at the free surface is $\tilde{w}(x,t) \equiv \phi_z(x, z = \eta(x,t), t)$, which is needed to integrate the Zakharov equations in time. Determining $\tilde{w}$ from the free surface variables η and $\tilde{\phi}$ is known as a Dirichlet-to-Neumann (DtN) problem. It should be noticed that the wave flume is large so that the frictional dissipation is significant during the experiments. This is modeled here by adopting two additional viscous terms in Equations (6) and (7), following the work of Dias et al. [35]. The value of ν needs to be calibrated: in our simulations, the value of $\nu = 0.0006$ m^2/s was chosen as it allows reproducing the mean decay rate of wave energy as waves propagate along the wave flume.

3.2. Boussinesq-Type Model

The Boussinesq-type model for the fully nonlinear and dispersive water waves with potential formulations [31] was used to simulate the experiments. In the model, the velocity potential ϕ is expanded around a certain depth $\hat{z}(x)$ in the water column using a power series of the vertical coordinate z:

$$\phi(x,z,t) \approx \sum_{n=0}^{4N_B+1} \frac{1}{n!} (z-\hat{z})^n \hat{\phi}^{(n)}, \tag{8}$$

where N_B is related to the order of the model, and, in our simulations, $N_B = 2$ ws chosen. $\hat{\phi}^{(n)} \equiv \partial^n \phi / \partial z^n|_{z=\hat{z}}$ for $n = 0, 1, 2, 3, ..., \infty$, with $\hat{z}$ is usually fixed at the middle of the water column to optimise the dispersion properties. We define $\hat{w} \equiv \hat{\phi}^{(1)}$ as the vertical velocity at the chosen elevation.

The in-depth study of this model can be found in the literature [31,36,37]. The main steps are briefly recalled here (see [31] for more information). Introducing Equation (8) into the Laplace equation (Equation (2)) and assuming $\hat{z}$ is a function of slow variable δx (with $\delta \ll 1$), the velocity potential ϕ can be formulated as an expression of $\hat{\phi}^{(0)}$ and $\hat{w}$. In the $N_B = 2$ model, the expression of ϕ is truncated at order $O(\delta^2)$ and the higher-order derivatives are up to $4N_B + 1$. The accuracy of the truncation can be significantly improved by adopting the enhancement technique. New expansion variables are obtained by applying the L-operator:

$$\hat{\phi}^{(0)} = L_p(\hat{z}\nabla)\,\hat{\phi}^*, \quad \hat{w} = L_w(\hat{z}\nabla)\,\hat{w}^* \tag{9}$$

where $L_p(\hat{z}\nabla) = L_0 + \nabla\hat{z} \cdot L_1\nabla$ and $L_w(\hat{z}\nabla) = L_0 + \nabla\hat{z} \cdot L_2\nabla$, with $\nabla \equiv \partial/\partial x$ being the horizontal derivative operator. The coefficients of a linear operator $L_0(\hat{z}\nabla)$ are computed to let the high-order derivatives from $2N_B + 2$ to $4N_B + 1$ vanish. The shoaling enhancement operators $L_1(\hat{z}\nabla)$ and $L_2(\hat{z}\nabla)$ are used to optimise the linearised shoaling behaviour of the model. The expressions of these L-operators can be found in [31].

Now, the velocity potential ϕ is expressed as a function of $\hat{\phi}^*$ and $\hat{w}^*$ via Equation (9). The expressions of the potential at the free surface and at the bottom can be derived using the chain rule. With the Dirichlet boundary condition at the free surface $\phi|_{z=\eta} = \tilde{\phi}$ and the bottom boundary condition in Equation (5) expressed in terms of $\hat{\phi}^*$ and $\hat{w}^*$, a linear system is established. The potential ϕ can be obtained from the solutions of the linear system, $\hat{\phi}^*$ and $\hat{w}^*$. Finally, the vertical velocity at the free surface $\tilde{w}$ is computed to advance the model in time.

The numerical solution procedure is based on the finite difference method for the spatial derivative and the explicit fourth-order Runge–Kutta scheme for the time integration. In the horizontal direction, a stencil of seven points is used to apply up to fifth-order derivative operators. In the linearised $N_B = 2$ model, the dispersion relationship is given explicitly by:

$$\frac{C_{N_B}^2}{gh} = \frac{1 + \sum_{n=0}^{2N_B} D_{2n} (kh)^{2n}}{1 + \sum_{n=0}^{2N_B+1} E_{2n} (kh)^{2n}} \tag{10}$$

where C_{N_B} denotes the phase velocity. The coefficients D_{2n} and E_{2n} depend on the expansion level $\hat{z}(x)/h(x)$, and are given by [36] (Equation (25)). To evaluate the dispersion property of this

model, Equation (10) has to be compared to the exact Airy phase velocity in flat bottom condition $C_{Airy}^2/(gh) = \tanh(kh)/(kh)$.

3.3. Whispers3D Model

The modeling approach of whispers3D is presented in previous works [32,33] and summarised hereafter. First, a change of the vertical coordinate from $z \in [-h(x), \eta(x,t)]$ to $s \in [-1,1]$ is applied, mapping the varying domain to a rectangular one:

$$s(x,z,t) = \frac{2z + h(x) - \eta(x,t)}{h(x) + \eta(x,t)} \tag{11}$$

The nonlinear potential system in Equations (2)–(5) can be reformulated using in the new (x,s,t)-space, with $\phi(x,z,t) = \varphi(x,s(x,z,t),t)$. Following Tian and Sato (2008) [38], a spectral approach is used in the vertical to approximate the velocity potential. Using the set of orthogonal Chebyshev polynomials of the first kind, denoted $T_n(s), n = 0,1,...,N_T$, with $s \in [-1,1]$, as an expansion basis, the potential is approximated as:

$$\varphi(x,s(x,z,t),t) \approx \varphi_{N_T}(x,s(x,z,t),t) = \sum_{n=0}^{N_T} a_n(x,t) T_n(s), \tag{12}$$

where the $a_n(x,t)$ coefficients of the T_n terms are now the main unknowns of the problem.

Then, the approximation in Equation (12) of φ is inserted into the governing equations composed of the Laplace equation, a Dirichlet free surface boundary condition (FSBC) with $\varphi_{N_T}|_{s=1} \approx \tilde{\phi}$ and the bottom boundary condition expressed in the (x,s) coordinate system. The so-called Chebyshev-tau method, a variant of the Galerkin method, is used to project the Laplace equation onto the T_n polynomials for $n = 0,1,...,N_T-2$ eliminating the s coordinate and giving a set of N_T-1 equations on the a_n coefficients at each location x. These N_T-1 equations are supplemented with the Dirichlet FSBC and the bottom boundary condition, so that a system of N_T+1 linear equations with N_T+1 unknowns $(a_n, n = 0,...,N_T)$ at each abscissa is formed. The solutions of this linear system are the a_n coefficients, from which the free surface vertical velocity at time t is obtained as:

$$\tilde{w}(x,t) = \frac{2}{h(x) + \eta(x,t)} \sum_{n=1}^{N_T} a_n(x,t) n^2, \tag{13}$$

In the whispers3D model, the first- and second-order horizontal derivatives are approximated using fourth-order finite difference formulas with stencils of five nodes. An explicit third-order Runge–Kutta scheme (SSP-RK3) is used for time marching. The dispersion relation of the linear model in constant water depth was derived analytically by Benoit et al. [39]:

$$\frac{C_{N_T}^2}{gh} = \frac{1 + \sum_{n=1}^{N_T-2} P_n (kh)^{2n}}{1 + \sum_{n=1}^{N_T-1} Q_n (kh)^{2n}}, \tag{14}$$

where the coefficients P_n and Q_n for different values of N_T can be found in Table 1 of [39].

3.4. Simulations of the Experimental Case 2

The whispers3D model solves the fully nonlinear potential flow problem, with no assumptions made regarding the steepness of the surface waves or the bathymetry. In the Boussinesq-type model, with the linear operators applied, the model is "improved" in the dispersion relation accuracy. The rapidly varying bathymetry can be well simulated. The dispersion relations of two models are compared to C_{Airy} in Figure 2 over a wide range of relative water depth kh. It is shown that the relative error varies significantly for different water depths. In intermediate and shallow water,

i.e., $kh \in (0, \pi]$, the relative errors of C_{N_B} and C_{N_T} are small (for instance, below 10^{-5} for $N_T = 7$ or $N_B = 2$). However, the dispersion relation is less accurate for deep water waves in both models. One advantage of the whispers3D model is that the user can adjust the value of N_T easily. In shallow water, a small N_T can improve the efficiency of the model while keeping good accuracy. In deep water, by using large N_T, the model has the possibility to achieve better accuracy for a large value of kh. The dispersion relations of both models are very accurate under the experimental condition ($k_p h \approx 1.2$ for Case 2), thus $N_T = 7$ was chosen in the simulations with whispers3D.

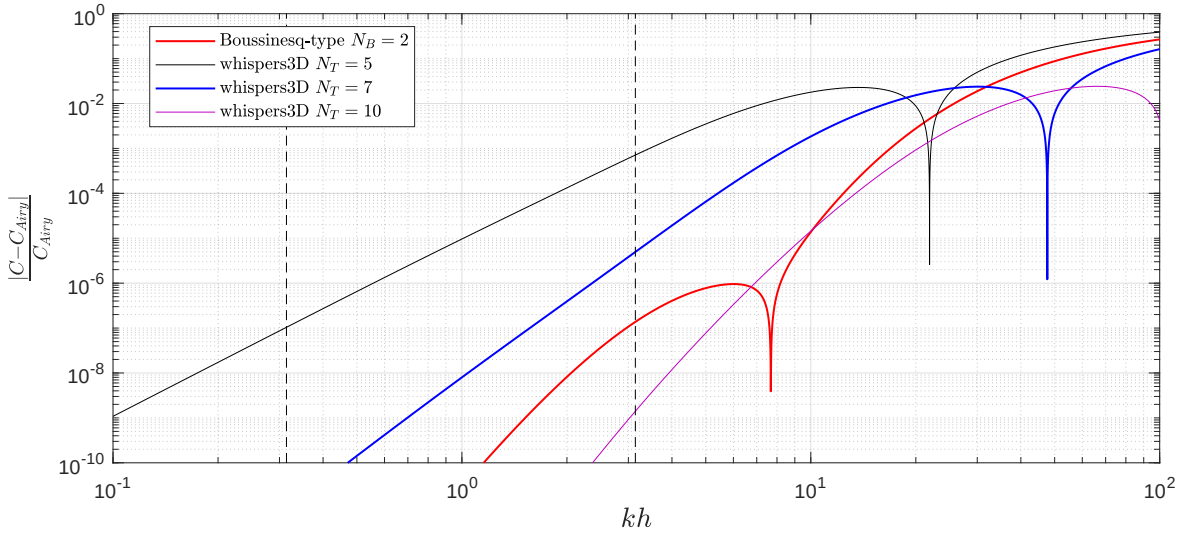

Figure 2. Comparison of the dispersive effects between the Boussinesq-type model ($N_B = 2$) and the whispers3D model (with different choices of N_T) in log-log scale. The two dash lines divide the domain into shallow water region ($kh < \pi/10$), intermediate water depth region, and deep water region ($kh > \pi$).

In the simulations with Boussinesq-type model, the expansion elevation was chosen at $\hat{z} = -0.5h$, the shoaling enhancement factors were chosen to be accurate for $kh \in (0, 30]$; the optimised coefficients are given in Equation (52) of [31]. The chosen time step is $\Delta t \approx 0.016$ s and the horizontal grid size is $\Delta x \approx 0.114$ m, corresponding to the Courant–Friedrichs–Lewy number ($CFL = C\Delta t/\Delta x$, $C = L/T$) is $CFL \approx 0.417$. Waves were generated in a relaxation zone of $3L_p$ long at the left boundary and were absorbed in another of $0.5L_p$ long at the right boundary. This set-up was chosen to achieve a better agreement of the low-frequency domain with the measured data. The measured data at $x = 3$ m were taken as the target spectrum and reconstructed through linear superposition of harmonic incident wave components. In the whispers3D simulation, $N_T = 7$ was used for the approximation of velocity potential. The simulations were made with a time step of $\Delta t = 0.02$ s and a grid size of $\Delta x = 0.05$ m, resulting in $CFL = 1.19$.

In Figure 3, the spatial evolution of the largest wave group observed in the experiment is shown; the simulated results of Boussinesq-type model and whispers3D are also superposed for comparison. Note that the threshold of freak wave is considered locally since the sea state undergoes significant change due to the uneven bottom. For this reason, the free surface elevation in the figure is normalised by the local significant wave height. The origin of the two freak waves in Figure 3h is shown in the energetic wave packet generated around 33 min from the start, where the sea state has already been affected by the reflected long wave. Figure 3a–c shows that the wave form remains quite similar, from the formation of the wave packet until it propagates over the middle of the slope. The simulation results are in good agreement with the measurements in this region. As waves enter the shallower region and propagate within a certain distance, corresponding to the region between Probe 13 (Figure 3g) and Probe 17 (Figure 3f), two waves in the packet are amplified and can be identified as freak waves since their crest elevations exceed 1.25 times of the local H_s. These two freak waves keep their wave profiles

longer in the experiment than in the simulations. On the other hand, both numerical schemes seem to underestimate the group velocity as well as the amplitudes of large waves.

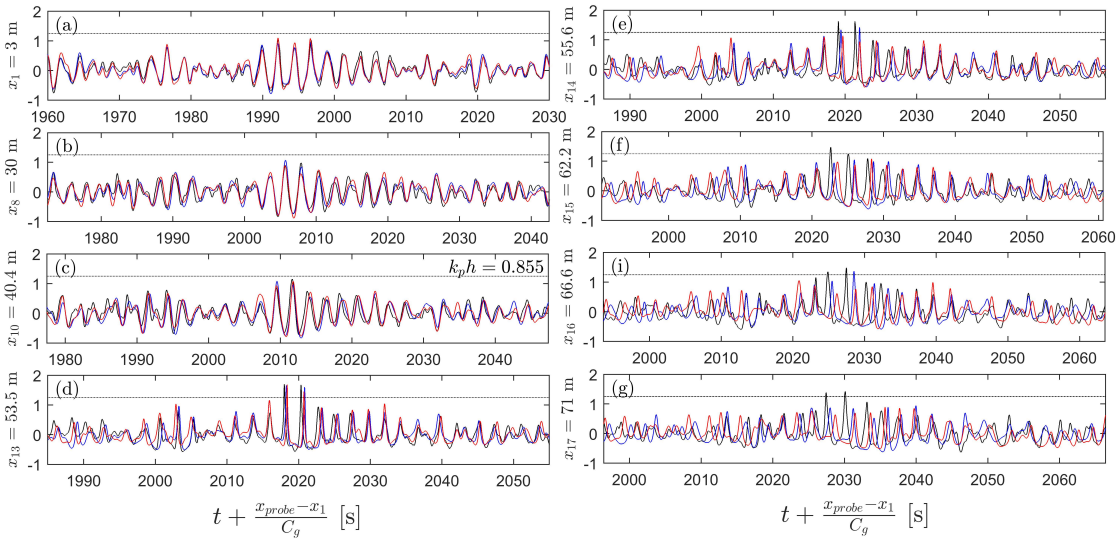

Figure 3. Comparison of the free surface elevation normalised by the local significant wave height at different positions (panel (**a**)–(**g**)) between the simulated results of the Boussinesq-type model (blue lines), whispers3D (red lines) and the measurements (black dot lines). Only the local relative water depth over the uneven region is marked. The threshold of freak wave basing on crest elevation is shown (dash lines).

4. Data Processing: Spectral Analysis

Assuming that the free surface elevation is the sum of a large (infinite) number of statistically independent harmonic waves, each component having a random phase in $[-\pi, \pi]$ and a constant positive amplitude, we operated with a Gaussian sea state and the statistical characteristics can be described through simple Fourier analysis. The spectral analysis was applied to both measured and simulated results. The simulated signals were resampled (by means of interpolation) to have the same sample points. A low-pass filter was applied to the measured signals to exclude the undesired high-frequency band which might be contaminated by the electronic noise of the wave probes. The time window where the analysis was carried out was translated for each wave gauge with the group velocity $C_g(f_p)$, which ensured that all analysed signals recorded at different positions roughly started from the same wave event. The spectra were estimated via Welch's method. The overlapping factor was 50%, with which the signals were separated into a number of segments. First, the Hann window was applied to each segment of signal (approximately 80 s), and then it was Fourier-transformed through 2^{13}-point fast Fourier transform (FFT), resulting in a high spectral resolution $\Delta f = 0.0061$ Hz.

In Figure 4, both the overall spatial evolution of the spectrum and the detailed spectra at four specific positions are shown. It was observed that, as waves propagate over the deeper region, the wave spectra are modulated mainly in the low-frequency range ($f < 0.2$ Hz), and several low-frequency modes are formed before the bottom slope. The low-frequency part is a result of the reflection of unabsorbed long waves and the excitation of the natural modes of the wave flume. The wavemaker and the damping zone only "absorb" a part of the reflected wave energy. Thus, these low-frequency modes increase gradually during the test. Over the bottom slope, second-order effect gets increasingly significant especially around the end of the slope (see the yellow peak at about $2f_p$ in Figure 4a for $x = 53.5$ m and Figure 4b for the corresponding spectrum). After the slope segment, the increase of the second harmonic disappears rapidly. More and more wave energy transfers to the low-frequency part, and, as a result, the spectrum broadens. After some distance, due to the energy transfer the low-frequency peak even exceeds the "original" spectral peak and becomes the "new" highest peak of

the spectrum (see, for instance, Figure 4b, Probe 24). Apart from the nonlinear wave–wave interactions, the evolution of the spectrum is also affected by the friction resulting from the boundaries, which play an important role in the dissipation of wave energy. The frictional dissipation works as a low-pass filter, i.e., the dissipation is stronger for the high frequency waves than for the low-frequency waves.

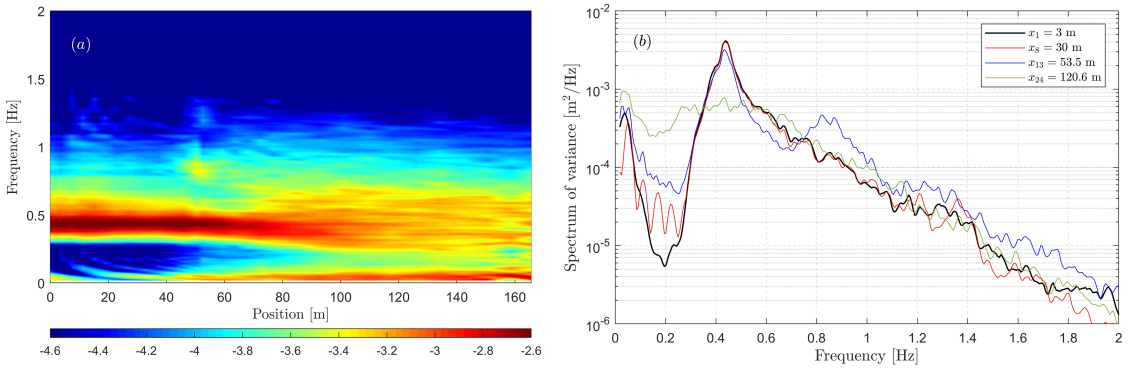

Figure 4. The spectrum of the experimental data shown in different scales: (**a**) the spatial evolution of the spectrum in a log-scale colormap; and (**b**) the spectra of four specific positions.

The spectra simulated with the Boussinesq-type model are shown in Figure 5. The incident wave spectrum shape was well simulated, as waves propagate in the deeper region, the frequencies in the left side of the spectral peak remain in good agreement with the measurements, but differences appear in the higher frequency domain (see Figure 5b). Potentially, some wave–wave interactions occur between the wavemaker and the first probe generating high frequency components. These high-frequency components are considered as free modes in the simulations due to linear wave making, so that they are dissipated rapidly by friction. Around the end of the slope, the second harmonic clearly appears and is more energetic compared to the measured results. The broadening of the spectrum after the slope is well predicted. In total, the Boussinesq-type model provides a good prediction of spectral evolution, despite the slight overestimation of the nonlinear interaction.

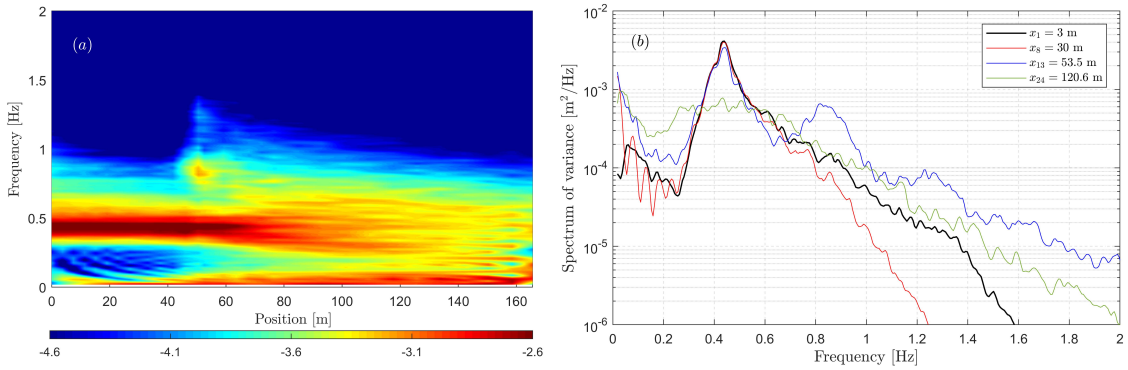

Figure 5. Same plot as Figure 4 for the results of the Boussinesq-type simulation.

The spectra simulated with whispers3D are shown in Figure 6. It is shown that the results of whispers3D are in good agreement with the results of the Boussinesq-type model as well as the measurements. Indeed, this model also overestimates the nonlinear wave–wave interactions around the end of the slope so that second (and also higher) harmonic of the spectral peak receive more energy.

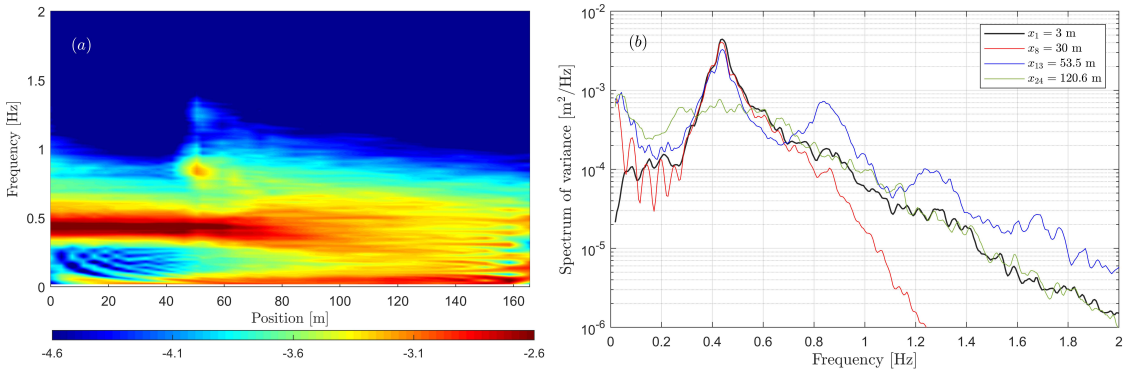

Figure 6. Same plot as Figure 4 for the results of whispers3D simulation.

5. Data Processing: Bispectral Analysis

It is well-known that waves in nature can be strongly nonlinear when they enter in coastal areas. Especially in the case studied here, the nonlinear effects are significant, and a Fourier analysis is insufficient to interpret the data. A powerful tool to study the nonlinear process is the polyspectral analysis, in particular, the Fourier based bispectral analysis technique which has been used to study the triad wave–wave nonlinear interactions and quadratic phase coupling of nonlinear water waves [40,41]. The bispectrum $B(f_2, f_1)$ is defined as the two dimensional Fourier transformation of the third-order auto-correlation function of the signal. Equivalently, it can also be defined as [42]:

$$B(f_1, f_2) = E\left[X_1 X_2 X_{1+2}^*\right], \tag{15}$$

where $E[\cdot]$ is the ensemble average of the triple product of complex Fourier coefficients of two frequencies f_1 and f_2 and their sum $f_1 + f_2$. The asterisk indicates complex conjugate. For time series with zero mean, the Fourier coefficients X_n come from the following decomposition:

$$x(t) = \sum_{n=-\infty}^{+\infty} X_n \exp\left(-2\pi n f_i t\right). \tag{16}$$

This definition is economic regarding the computational effort thanks to the Fast Fourier transform (FFT) algorithm. The bispectrum has symmetry properties, i.e., $B(f_1, f_2) = B(f_2, f_1) = B^*(-f_1, -f_2) = B(-f_1 - f_2, f_2) = B(f_1, -f_1 - f_2)$, which can further simplify the computation.

In the following, the Fourier coefficients X_n were computed in the same way as introduced in Section 4, except that 2^{12}-point FFT was used to get a smoother bispectrum. In Figures 7–9, the imaginary parts of the bispectra are plotted, for both the experimental (upper row) and numerical results (second row for the Boussinesq-type model and lower row for the whispers3D model). The two component frequencies f_1 and f_2 were normalised by the incident peak frequency.

The positive and negative values are represented by the colors in the graphs indicating, respectively, the sum interactions and the difference interactions between the two frequency components. For instance, assume $B(0.1, 1) < 0$, it means that three wave components 0.1 Hz, 1 Hz and 1.1 Hz participate in the nonlinear interaction and the wave energy is transferred from 1.1 Hz to the 0.1 Hz and 1 Hz components. Similarly, if $B(0.1, 1) > 0$, the 1.1 Hz component gain energy from the 0.1 Hz and 1 Hz components.

Figure 7 shows that, in general, the wave–wave interaction between f_p and $2f_p$ is weak in the deeper region. In Figure 7a1, two relatively strong interactions happen around $B(f_p, 0.1f_p)$ (red) and $B(f_p, f_p)$ (blue), which indicates that the wave energy is transferred from both the low-frequency modes around $0.1f_p$ and the second harmonic $2f_p$ to the frequencies around the peak. As waves propagate in the deeper region, in Figure 7b1, it is shown that for the low-frequency domain both sum and difference interactions are present. This pattern indicates that the energy of peak frequency is transferred to both lower and higher frequencies and that the spectrum broadens. This pattern can hardly be seen in the corresponding spectrum due to weak interactions, but as shown below, the spectral broadening is more obvious in the shallower region. In the simulations, this energy transfer is overestimated, resulting in slightly larger long waves. When waves arrive at the end of the deeper region, Figure 7c1 shows that the spot around $B(f_p, 0.1f_p)$ is blue, meaning that the energy transfers mainly from the peak frequency to the low-frequency components and that long waves are generated. In the deeper region, the simulated and measured bispectra are in overall good agreement.

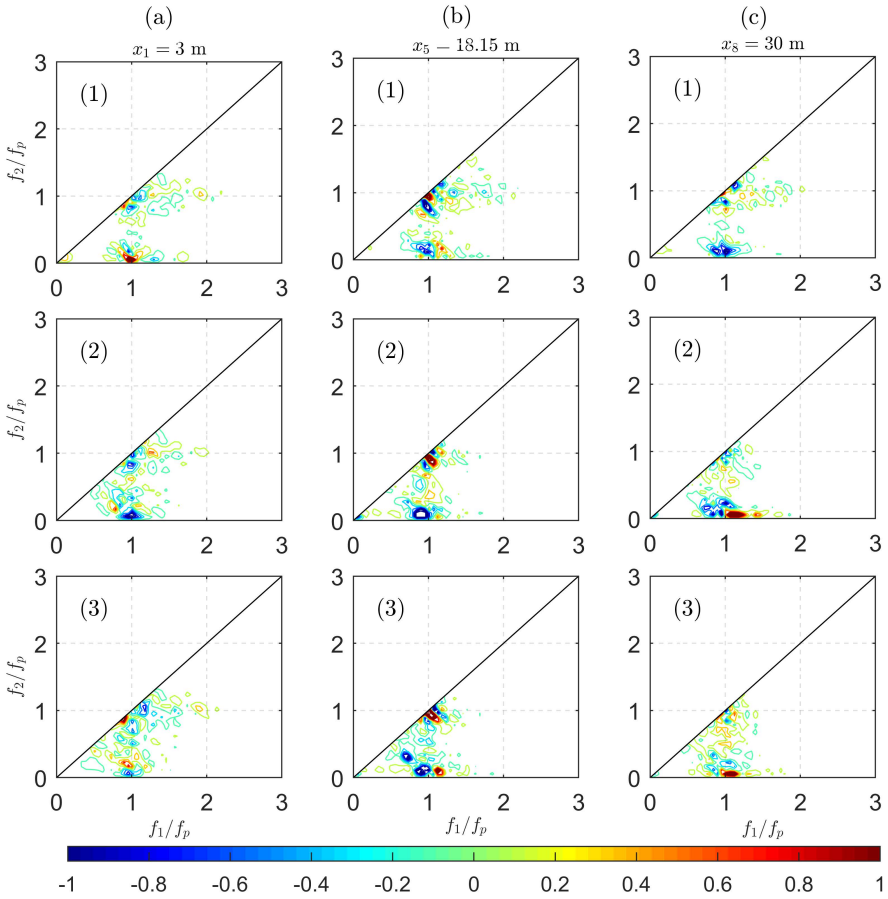

Figure 7. Contour of the imaginary parts of bispectra of Probes 1, 5, and 8 in the deeper region ($k_p h = 1.19$) (corresponding to panels (**a**)–(**c**)). The upper row (panels (**1**)) of graphs presents measured bispectra, while bispectra obtained from numerical results are presented on the second (panels (**2**)) and third rows (panels (**3**)) for the Boussinesq-type and whispers3D models, respectively. All the panels share one colorbar, which is in scale (10^{-8} m^3).

In Figure 8, the bispectra of waves propagating over the sloping bottom area are shown where strong nonlinear effects are expected. In Figure 8d1, it is observed that the nonlinear effect is present but still moderate. In Figure 8e1, the wave–wave interaction is strong, resulting in an increase of the second harmonic $2f_p$ and the low-frequency waves around $0.1f_p$. In Figure 8f1, not only similar characteristics regarding the second harmonic and the long wave generation are seen, but also the wave–wave interactions between f_p and $2f_p$ coupled to $3f_p$ is visible. The long waves are generated from both peak frequency and its

second harmonic $2f_p$ (see the blue spots at $B(f_p, 0.1f_p)$ and $B(2f_p, 0.1f_p)$). In the simulations, the agreement is still good but the intensity (or "magnitude") of nonlinear transfers is slightly overestimated. For instance, the sum interactions of low-frequency modes around $B(f_p, 0.1f_p)$ at all three probes are stronger in the two numerical models than in the experiments. As is shown in Figure 8e2 and e3, the sum interactions at $B(f_p, 2f_p)$ are also a bit stronger in the simulations.

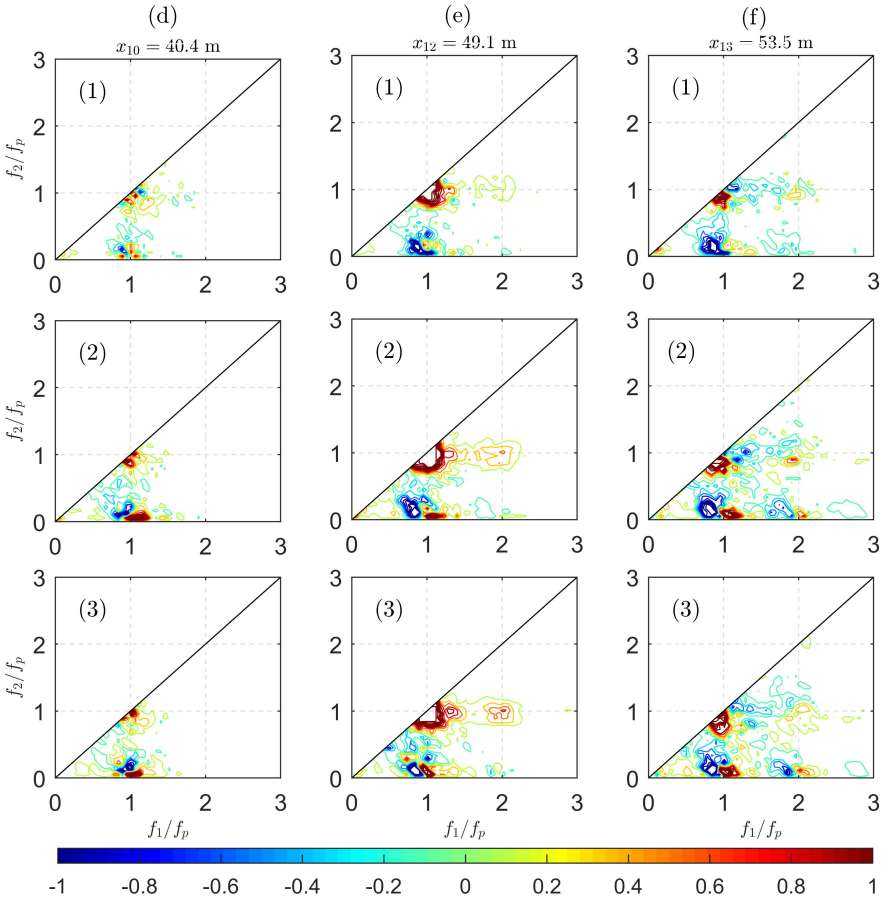

Figure 8. Same plot as Figure 7 for Probes 10, 12, and 13 over the slope (corresponding to panels (**d**)–(**f**)), the corresponding relative water depths are $k_p h = 0.86$, 0.54 and 0.50 respectively.

In Figure 9, three probes are chosen to illustrate the modulation of waves propagating over the shallower region. More wave components participate in the wave–wave interaction, and the contours become more complex. A negative band ranging from $B(0.5f_p, 0.5f_p)$ to $B(0, f_p)$ is observed which indicates the strong energy transfer from the spectral peak to the bands with frequencies lower than the peak. This blue band is clear in Figure 9g1, and disappears in Figure 9i1 because, as the spectral peak keeps losing energy, this energy transfer becomes weaker and weaker. This explains partially the spatial evolution of the spectrum, namely the decrease of the "original" spectral peak, the increase of the low-frequency components (which eventually become new spectral peak) over the shallower region, and the increase of the long wave energy. Another possible reason for this spectral change is the different frictional dissipation rates for different frequencies. The friction dissipates more energy of high-frequency waves while low-frequency wave energy is less dissipated. Finally, a quasi-steady state is reached and the spectral shape keeps almost unchanged, as can be observed for the spectral shape after 100 m in Figure 4a.

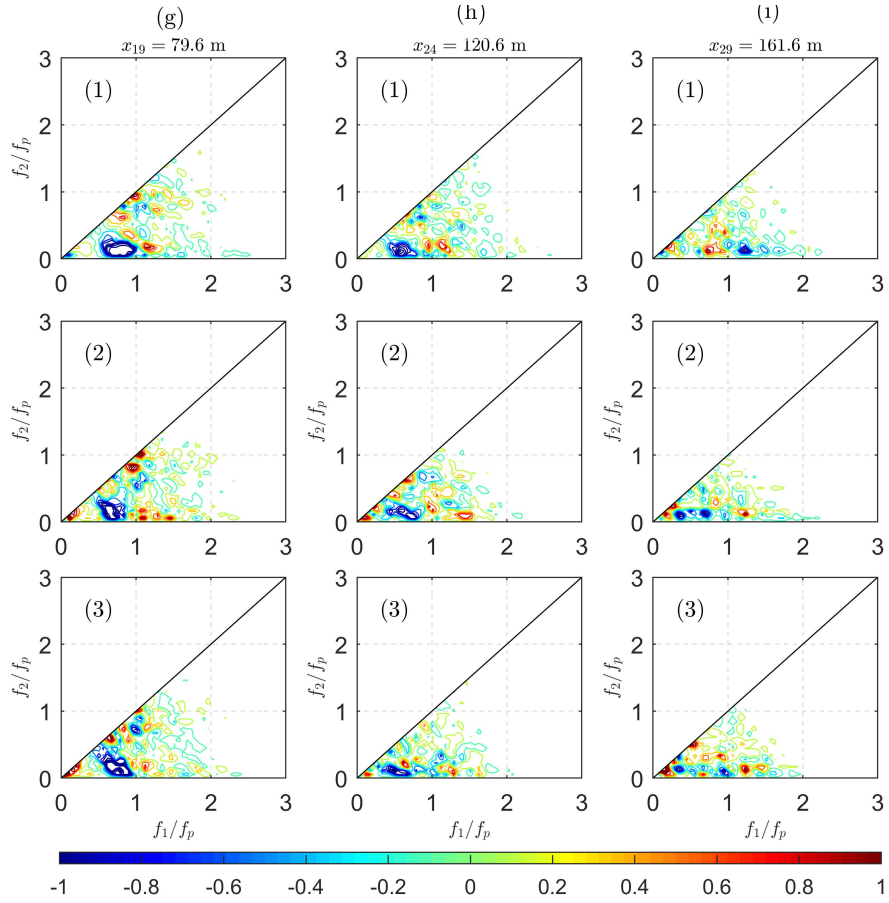

Figure 9. Same plot as Figure 7 for Probes 19, 24, and 29 (corresponding to panels (**g**)–(**i**)) in the shallower region $k_p'h' = 0.50$.

6. Data Processing: Nonlinear Wave Parameters

The free surface elevation is regarded as a stationary stochastic process. In a Gaussian sea state, the characteristic of the statistics of the surface motion can be fully described by its mean $\bar{\eta} = E(\eta)$ and variance $\sigma^2 = E\left((\eta - \bar{\eta})^2\right)$. As waves propagate into coastal areas, the sea states become non-Gaussian and the nonlinearities affect the wave shape, resulting in sharper and higher wave crests. Higher-order moments can be used to characterise nonlinear effects. Usually, skewness (third-order normalised moment) and kurtosis (fourth-order normalised moment) are considered. They can be computed from time series η:

$$Skew_\eta = \lambda_3 = \frac{E\left((\eta - \bar{\eta})^3\right)}{\sigma^3}, \tag{17}$$

$$Kurt_\eta = \lambda_4 = \frac{E\left((\eta - \bar{\eta})^4\right)}{\sigma^4}. \tag{18}$$

The skewness is related to the bound mode harmonics and the asymmetry of the probability density function (PDF) of η, and the kurtosis is related to the sharpness of the PDF [43]. For Gaussian sea states, $\lambda_3 = 0$ and $\lambda_4 = 3$ are expected. For non-Gaussian sea states, $\lambda_3 > 0$ represents asymmetric wave shape (sharper crests and f troughs) and the reverse for $\lambda_3 < 0$. $\lambda_4 > 3$ indicates an increased probability of occurrence of the largest wave heights [23], but it is not guaranteed that, when $\lambda_4 < 3$, the large waves (especially freak waves) will not manifest.

Statistical parameters can also be computed based on the bispectrum. Skewness can be defined as the normalised integral of the real part of the bispectrum [40]; the wave profile asymmetry w.r.t. the vertical axis is related to the normalised integral of the imaginary part of the bispectrum [44]:

$$Skew_{bis} = \frac{\sum\sum \Re\{B(f_1, f_2)\}}{\sigma^3}, \tag{19}$$

$$Asym_{bis} = \frac{\sum\sum \Im\{B(f_1, f_2)\}}{\sigma^4}. \tag{20}$$

In Figure 10, the statistical parameters of the simulations as well as the measured results are shown, and the two different computation methods of the skewness are also compared. It can be seen that the two methods give very similar results; the small differences are probably due to the use of Hann function window (even though a correction factor has already been considered) when computing the Fourier coefficients. It can be seen that both the Boussinesq-type and whispers3D models have good agreement over the two flat bottom regions, but clearly overestimate the maximum skewness (triad wave–wave interaction) around the end of the slope. While the generated waves are almost symmetric w.r.t. the horizontal axis, they become skewed as they propagate over the slope. Around the end of the slope, the wave shape is highly asymmetric w.r.t. the horizontal axis, and the symmetry is not fully recovered in the shallower flat bottom. Regarding the asymmetry parameter, the simulated results agree well with the measured results. As can be seen, this parameter is almost zero except over a short region after the slope which implies that the waves generated are almost symmetric w.r.t. the vertical axis. It is also noted that the presence of the current bottom slope has limited effect on the asymmetry parameter.

In Figure 11, the evolution of the kurtosis is shown. It fluctuates around 3 except for the area around the end of the slope, where a local maximum value is observed. This corresponds to the location of Probe 13. The numerical models predict well the overall evolution of kurtosis along the bottom profile. However, they both overestimate the kurtosis around the end of the slope, and this trend is more marked with whispers3D. This is probably because the breaking events in the experiments, which are not considered in the simulations, limited the maximum wave heights. At the end of the slope, the prediction of whispers3D is more non-Gaussian compared to that of the Boussinesq-type model. According to previous studies (e.g., [23]), the local maximum of kurtosis indicates higher probability of the occurrence of extreme waves. This motivates further investigations of wave height statistics in similar, however, more complicated configurations.

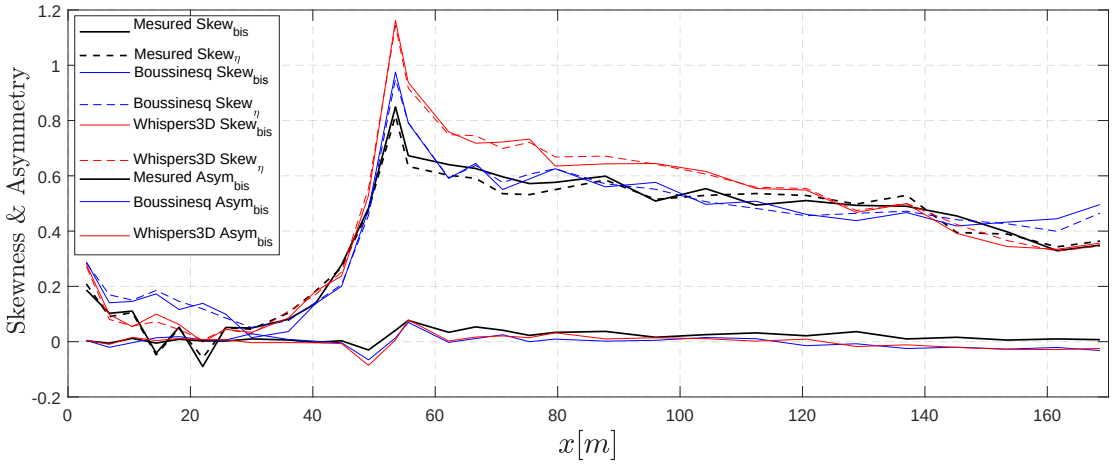

Figure 10. Overall evolution of the nonlinear statistical parameters, skewness and asymmetry, computed from the time series (dash lines) and the bispectrum (solid lines).

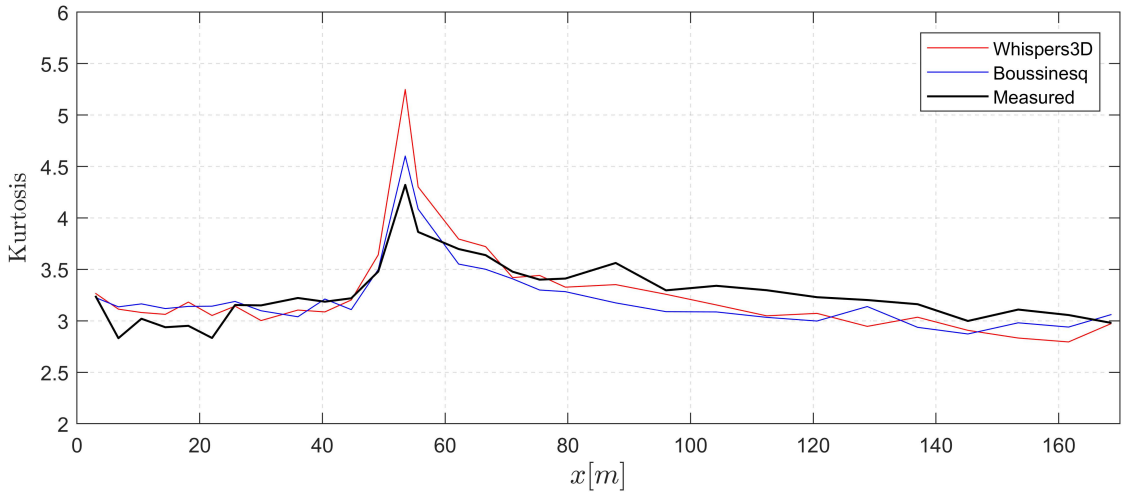

Figure 11. Comparison of the overall evolution of kurtosis between the measured and the simulation results of the two numerical models.

7. Data Processing: Wave Height Distribution

The wave height distribution for the nonlinear shallow water waves has been of interest for oceanographers, as it represents a key input for the design of coastal structures. The understanding of the shallow water wave height distribution is, for the moment, limited not only due to the complexity of coastal hydrodynamics but also due to the complex nearshore environment. The existing distributions are either empirical/semi-empirical or analytical under strong assumptions. For this reason, more experimental data are needed to study the applicability and validity of these models. In the following, some of the most popular distributions are listed and compared with the measurements and the results of the simulations.

7.1. Brief Review of Existing Distribution Models

7.1.1. Rayleigh Distribution

The study of wave height distribution in the early 1950s starts with the work of Longuet-Higgins (1952) [45] for narrow-banded linear deep water waves. The wave heights (H) follow the Rayleigh distribution, whose complementary cumulative distribution function (CCDF) is given by:

$$P_R(H) = \exp\left[-\left(\frac{H}{\sqrt{2}H_s}\right)^2\right]. \tag{21}$$

The wave conditions of the current Case 2 obviously violate the aforementioned assumptions. The Rayleigh distribution is adopted here only for the purpose of comparison. Assume for the signals with zero mean, the relation $H_s \approx 4\sigma$ is fulfilled throughout the domain, then the normalised wave height $H/\sigma = 8$ is the threshold for the freak waves.

7.1.2. Glukhovskiy Distribution and Its Modifications (GV91 and GK96)

As waves propagate into coastal areas, the shoaling effect, as well as the depth-induced wave breaking, are expected, which affect the shape of the distribution. Due to the insufficient understanding of wave breaking and high-order non-Gaussian effects, only empirical or semi-empirical models are available. A more general form of the Rayleigh distribution, namely the Weibull distribution, is used to account for the depth-induced wave breaking in shallow water, as initially proposed by Glukhovskiy [46]:

$$P_G(H) = \exp\left[-A\left(\frac{H}{H^*}\right)^K\right], \tag{22}$$

where A, H^*, and K are the Weibull parameters. which are defined differently in the literature. Van Vledder (1991) [47] (labelled as GV91) modified this model by considering the parameters as:

$$A = \Gamma\left(1/K+1\right)^K, \quad K = \frac{2}{1-H^*/h}, \quad H^* = \frac{H_s}{\sqrt{2}}\frac{\Gamma\left(1/k+1\right)}{\sqrt{\Gamma\left(2/k+1\right)}}, \quad k = \frac{2}{1-\sqrt{8}H_s/\left(4.5636h\right)}, \tag{23}$$

with Γ denoting the gamma function, $\Gamma(x) = \int_0^\infty e^{-t}t^{x-1}\mathrm{d}t$. Klopman (1996) [48] also proposed a modification (labelled as GK96) based on a fit to laboratory data:

$$A = \left[\Gamma\left(\frac{2}{K}+1\right)\right]^{K/2}, \quad K = \frac{2}{1-H^*\beta/h}, \quad H^* = \frac{H_s}{\sqrt{2}}, \quad \beta = 0.7. \tag{24}$$

As input, the local water depth h and the significant wave height H_s are required. Both modified Glukhovskiy's distributions are used and compared hereafter.

7.1.3. Composite Weibull Distribution (CWD)

Another well-known model for wave height distribution in shallow water is the semi-empirical composite Weibull distribution (labelled as CWD here) [49]. In this model, the smaller wave heights are Rayleigh distributed, whereas the larger wave heights follow a Weibull distribution. The distribution requires not only h and H_s but also the bottom slope m. This model also takes wave breaking into consideration:

$$P_{CWD}(H) = \begin{cases} \exp\left[-\left(H/H_1\right)^2\right], & H \le H_{tr} \\ \exp\left[-\left(H/H_2\right)^{3.6}\right], & H \ge H_{tr}, \end{cases} \tag{25}$$

where $H_{tr} = (0.35 + 5.8m)\,h$ denotes the transition wave height between the two distributions, and H_1 and H_2 are scale parameters for wave heights and are given in [49] (see more details in Equation (6) or Table 2 in this reference).

7.1.4. Weibull-Generalised Pareto Distribution (WGP)

More recently, another two-part model, the Weibull-generalised Pareto wave height distribution (labelled as WGP), has been introduced [50]. The parameters, including H_s, local wave number k_L (here the wave number k_p corresponding to the peak frequency f_p is used), and local water depth h are required in this semi-empirical model:

$$P_{WGP}(H) = \begin{cases} \exp\left[-\mu\left(H/H_{tr}\right)^\kappa\right], & 0 \le H \le H_{tr} \\ \exp\left(-\mu\right)\left[1+\frac{\xi}{\alpha}\left(H/H_{tr}-1\right)^{-\frac{1}{\xi}}\right], & H_{tr} \le H \le H_{max}, \end{cases} \tag{26}$$

where

$$H_{tr} = \rho H_s,\ H_{max} = 2\beta\pi\frac{\tanh(k_L h)}{k_L},\ \kappa = \frac{2}{1-\lambda\left(H_s/h\right)^{1.7}},\ \mu = \frac{1}{\kappa\alpha},\ \xi = \frac{\alpha H_{tr}}{H_{tr}-H_{max}}. \tag{27}$$

In this model, except for the required information regarding the waves and bathymetry, four additional parameters are needed to be calibrated: ρ for the transition wave height, α for the scale of Pareto distribution, β for the Miche wave breaking height limit, and λ for the shape of Weibull distribution. According to the results of Wu et al. [50], $\rho = 1$, $\alpha = 0.22$, $\beta \approx 0.15$, and $\lambda = 1$ are used. Unlike CWD, this two-part model is continuous and bounded $(0 \le H \le H_{max})$, and this model has a continuous PDF.

7.1.5. Gram–Charlier Type Model (GBD)

The relationship between the fourth-order moment of free surface elevation and the third-order nonlinearity is studied in [51]. The effects resulting from third-order nonlinearity on the statistics of wave height distribution have been taken into consideration by using Edgeworth's form of a Gram–Charlier series [51–55]; this family of wave height distributions is sometimes referred to as modified Edgeworth Rayleigh distribution (MER). They do not seem to be of specific attraction in describing the statistics of coastal wave heights because the corresponding PDF of MER is not always positive (which is not realistic). In addition, these distributions are derived under the assumption of narrow-banded weakly nonlinear waves in the deep water condition, which is violated in nearshore areas. However, they are attractive in predicting abnormal waves because MER models showed good agreement for the tail of the wave height distribution when compared to some laboratory measurements [54]. Thus, this model is included in the present paper anyways.

A recent model of this family proposed in [55] is a generalised Boccotti distribution (labelled as GBD) in the form of MER, taking third-order nonlinearity and finite spectral width into consideration. Recall the Boccotti's distribution [56]:

$$P_B(H) = c_0 \exp\left(-c_1 \left(\frac{H}{H_s}\right)^2\right), \tag{28}$$

where

$$c_0 = \frac{1+b}{\sqrt{2b\,(1+a)}},\ c_1 = \frac{4}{1+a},\ a = \frac{\left|\int_0^\infty S(\omega)\cos(\omega\tau)\,\mathrm{d}\omega\right|}{\sqrt{m_0}},\ b = \frac{\left|\int_0^\infty \omega^2 S(\omega)\cos(\omega\tau)\,\mathrm{d}\omega\right|}{\sqrt{m_2}}, \tag{29}$$

with $S(\omega)$ denoting the spectral density function, τ corresponding to the time lag of the global minimum of autocorrelation function $R(\tau) = E\left[\eta(t)\eta(t+\tau)\right]$, and m_i denoting the ith-order moment of $S(\omega)$, $m_i = \int_0^\infty \omega^i S(\omega)\mathrm{d}\omega$.

Then, the formulation of GBD is:

$$P_{GBD}(H) = c_0 \exp\left[-c_1 \left(\frac{H}{H_s}\right)^2\right]\left[1 + \frac{\Lambda}{16}c_1^2\left(\frac{H}{H_s}\right)^4 - \frac{\Lambda}{8}c_1\left(\frac{H}{H_s}\right)^2\right], \tag{30}$$

where

$$\Lambda = \Lambda_{04} + \Lambda_{22} + \Lambda_{40},\ \Lambda_{mn} = \frac{E\left[\eta^m \hat{\eta}^n\right]}{\sigma^4} + (-1)^{m/2}\,(m-1)\,(n-1)\,, \tag{31}$$

with $\hat{\eta}$ denoting the Hilbert transform of the free surface elevation η, and $[m, n] = 0$, 2, or 4, but not 3 due to the absence of resonant three-wave interactions. It should be noticed that the CCDF starts with $P_{GBD}(0) \neq 1$, which is not realistic, meaning that this model is not suitable to model the bulk of the distribution, but only its tail for large wave heights.

7.2. Comparative Evaluation of Wave Height Distributions

The wave height distribution at Probe 8 located at the beginning of the slope is first considered and displayed in Figure 12. It can be seen that the Rayleigh distribution predicts well the measured wave height distribution. The agreement between the simulated and the measured data at this position is good, as shown in Figure 12a. In Figure 12b, the other wave height distribution models are similar to the Rayleigh distribution, differences appear only in the prediction of larger waves with $H > 6\sigma$. The measured results show fewer large waves than predicted by the Rayleigh distribution. This can be related to the work of Forristall (1978) [57] showing that the Rayleigh distribution overpredicts the heights of the largest waves in a deep water sea state. From the previous analysis of the nonlinear parameters skewness and kurtosis, the sea state here is quasi-Gaussian and the nonlinear wave–wave interactions are limited for the deeper region. Thus, it is anticipated that the wave heights follow a

Rayleigh distribution. The data show better agreement with the modified Glukhovskiy's methods, GV91 and GK96.

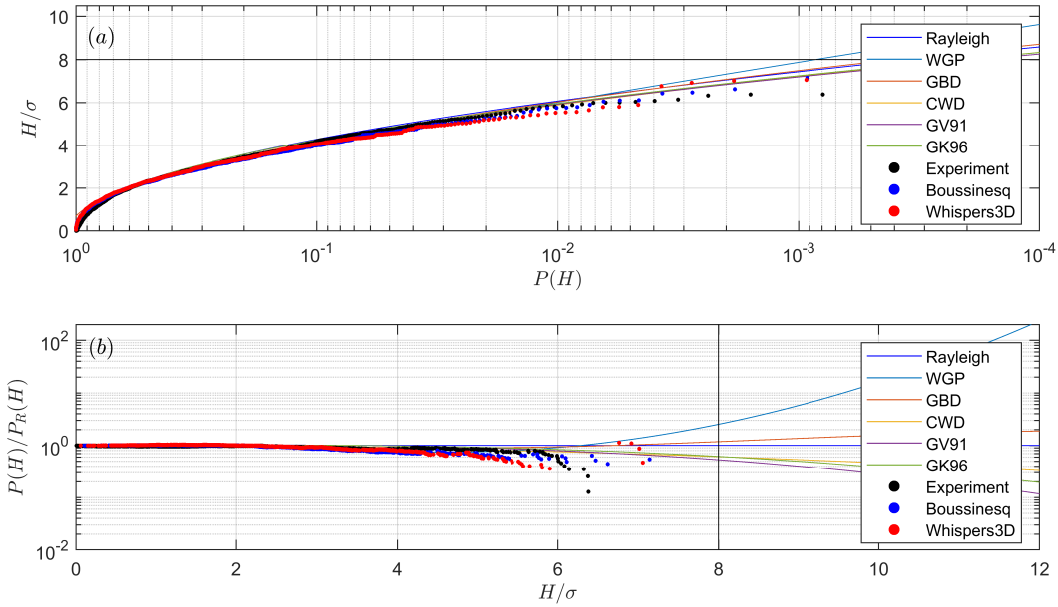

Figure 12. The wave height distributions of measurements, simulations and different models at $x_8 = 30$ m: (**a**) the CCDF as a function of normalised wave height; and (**b**) the deviation from the Rayleigh is shown by the normalised CCDF. The horizontal solid line in (**a**) as well as the vertical solid line in (**b**), both at $H/\sigma = 8$, represent the usual threshold for freak waves.

As waves propagate near the end of the slope, Figure 13 shows a clear increase of the probability of the large waves. The agreement between the measured and simulated results remains good, and the model predictions by CWD and GBD are in better agreement with other models. The two numerical models show similar results. In the Boussinesq-type model, note that one wave fulfils the criteria of freak waves (recalling that $H > 2H_s$ is equivalent to $H > 8\sigma$). However, the corresponding wave height is lower (below the above threshold) in the measured time series. At this position, skewness and kurtosis computed from the measured signal and from the simulated signals are in excellent agreement. The skewness increases approximately to 0.2, whereas the kurtosis is still around 3, indicating that second-order nonlinearity plays a more important role here.

In Figure 14, the wave height distribution after the slope (Probe 13), where the skewness and kurtosis reach their local maximum values, is illustrated. The amount of large waves is larger than the expectation of Rayleigh distribution, and more freak waves appear after the slope. At this location, it is also observed that some sporadic spilling breakers occurred, limiting the number and height of the large waves. It is clearly shown in Figure 14b that all the wave height distribution models except GBD underestimate the probability of wave height for $H > H_s$. The GBD model shows nice agreement for the same wave height range, even though the case studied here lies out of its validity domain. Regarding the simulations, the Boussinesq-type model results agree well with the measurements. The wave heights are overestimated with whispers3D, as are the skewness and kurtosis.

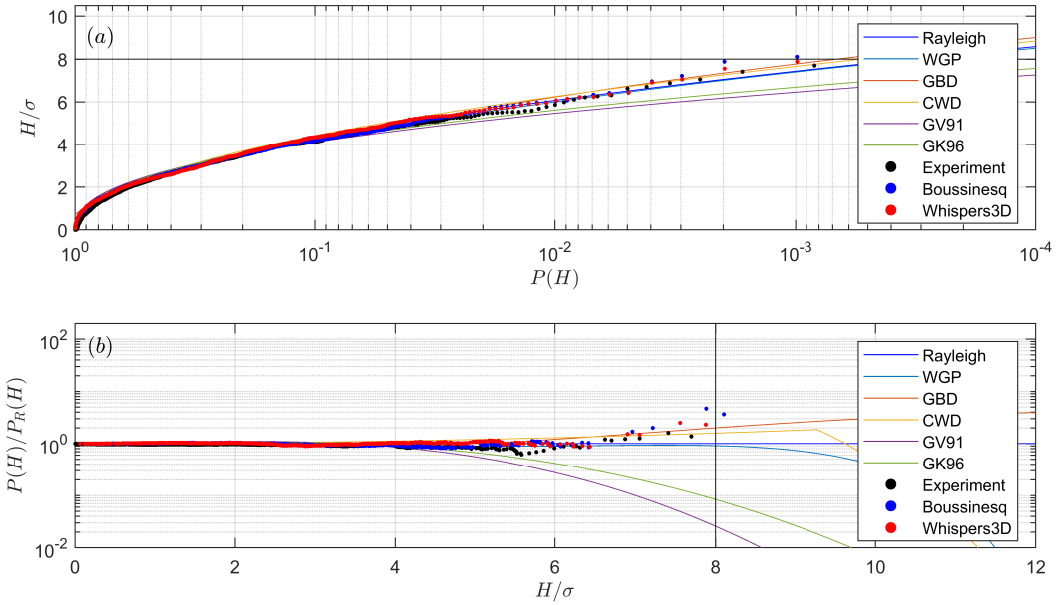

Figure 13. Same plot as Figure 12 at $x_{12} = 49.1$ m.

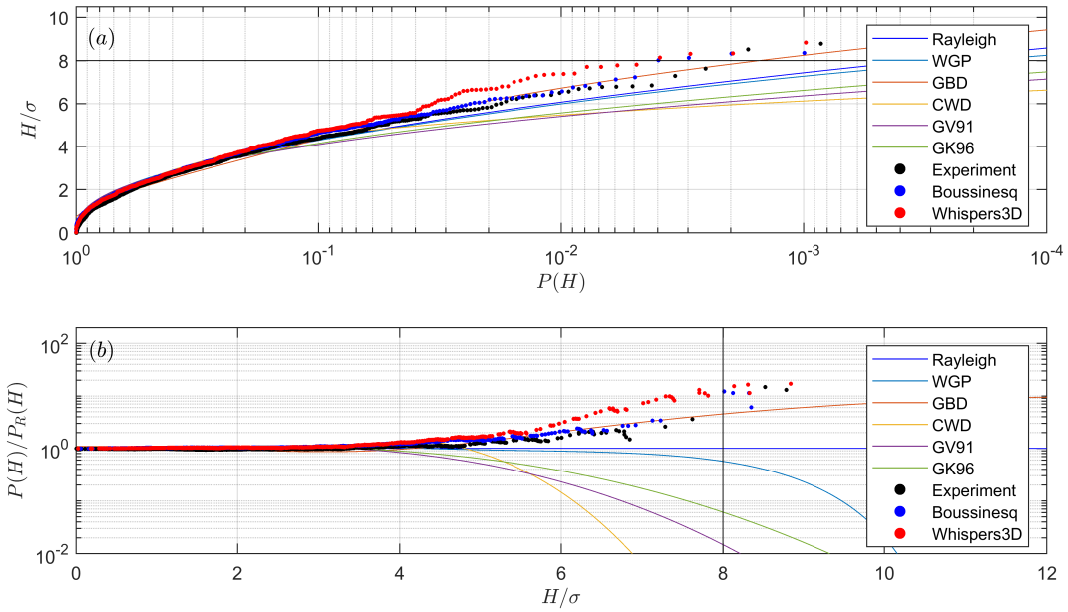

Figure 14. Same plot as Figure 12 at $x_{13} = 53.5$ m.

Then, in Figure 15b, it is shown that the tail of the wave height distribution lowers and the degeneration of the extreme waves starts. This change of wave height distribution is also part of the process of settling down towards a new equilibrium state. However, it was observed in the experiments that some of the generated freak waves will keep their wave form (without breaking) and propagate over a certain distance, even though these waves are quite steep, and propagate in relatively shallow water depth. The prediction of GBD is still good regarding large waves. Other models are lower than the Rayleigh distribution probably because the wave breaking effect is overestimated with these models.

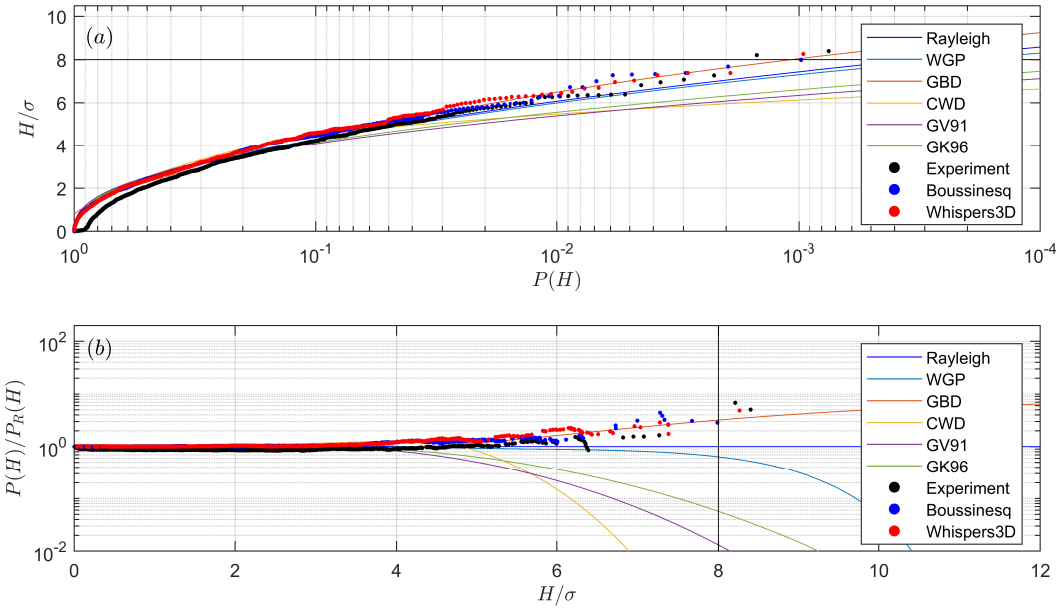

Figure 15. Same plot as Figure 12 at $x_{14} = 55.6$ m.

8. Discussion and Conclusions

To achieve a better understanding of the generation mechanism of extreme waves in coastal areas, large scale experiments at THL and highly accurate numerical simulations with two advanced models were performed. A variable bottom profile was designed to study the effects of a constant bottom slope connecting two flat regions on the occurrence of extreme waves. The experimental conditions were chosen based on two non-dimensional parameters: the wave steepness and the relative water depth. Note that our experimental set-up is different from previous experiments [23,24] regarding the length of slope, the arrangement of the two flat regions, and, most importantly, the nonlinear effects were relatively strong in the experimental cases shown here. Besides, the large scale facility allowed investigating the whole life cycle of the extreme waves. Spectral, bispectral and statistical analyses of the collected data were conducted, through which a more comprehensive understanding of the shoaling process has been drawn.

In line with previous studies [23,25–27], second- and third-order effects appear in the frequency spectrum, and local maximum values of the statistical parameters skewness and kurtosis were observed in the shallower region. It was experimentally observed that the second-order effects rapidly weaken after the end of the slope, as shown Figure 4a. The values of skewness and kurtosis also decrease with the weakening of second-order effect: the skewness decreases to a new level instead of zero due to the asymmetrical wave shape in the shallow water, while the kurtosis decreases back to 3.

The imaginary part of the bispectra was used to demonstrate the phase coupling of wave components and the energy transfer due to nonlinear wave–wave interactions. The nonlinear wave coupling is relatively strong around the end of the slope where mainly second and third harmonics are generated. The generation of third harmonic is small in magnitude, but it can be seen in the variance spectrum. Thus, we speculate that the increase of the occurrence probability of extreme waves is more related to the second-order effects. It was also observed in our experiments that a series of low-frequency waves appear. It is anticipated from the bispectra that long waves are mainly generated by the difference interactions as waves propagate in the flume. The frictional dissipation works as a low-pass filter on the wave spectrum, which has limited effects on these low-frequency modes.

In the deeper region, the sea state is almost Gaussian, and the nonlinear wave–wave interactions are moderate. The wave heights are well described by Rayleigh distribution, except that the latter slightly overpredicts the occurrence probability of the highest waves. The occurrence probability of large waves is significantly increased when waves propagate over the slope. This is due to the

fact that the sea state is transforming from one equilibrium state (in the deeper region) to another (in the shallower region). During this process, some of the largest waves can be identified as freak waves and will propagate for a distance while keeping their wave form. We also emphasise that the process of settling down to the new state takes time and a certain distance (a distance-lag in response to the depth transition), thus the shallower region after the slope is also prone to freak waves due to this lag. This was clearly noticeable in our flume set-up, which contains a long flat shallower region. Since the nonlinearities obviously come into play, nonlinear wave parameters are useful in describing the sea state, especially the kurtosis is related to the occurrence probability of large waves. It was confirmed that strong modifications of the distributions of the largest wave are rather well correlated with larger values of the skewness and kurtosis (see Figures 10 and 11). The Rayleigh distribution is no longer suitable to describe such sea states, thus a number of wave height distribution models were introduced and compared. In the coastal areas with intermediate or shallow water depth, the wave height distribution models are either semi-empirical or analytical with strong assumptions. In this study, not only the modified Glukhovskiy distributions (GV91 and GK96) and two-part distributions such as CWD and WGP were considered, but also another deep water wave height distribution, GBD, was introduced. This distribution is known to have good predictions for extreme waves [54]. As the non-equilibrium statistics appear and fade out over the slope, the probability for large waves increases then decreases in the same manner. It was seen that no distribution model can predict the measured wave height distribution equally well for all probes, but, in the prediction of the occurrence probability of large waves, the generalised Boccotti distribution works reasonably well, although it was originally designed for weakly nonlinear deep water waves. The listed shallow water wave height distribution models underestimate the wave height distribution mainly because they assume waves break during the shoaling process.

The numerical results of the Boussinesq-type model and the whispers3D model agree well with the experimental data. The results are in better agreement in the deeper region than in the shallower region, especially before the reflected long waves reach the probes. In particular, the agreement deteriorates due to the contamination of reflected long waves. A small number of wave breaking events also affect the agreement after the slope. These effects are insignificant at the beginning, but the disagreements accumulate as waves propagate in the flume, and eventually affect the simulated results in a significant way. The agreement is acceptable for the deeper region and the slope area, which is of most interest. Two models show very similar results as they both adopt fully nonlinear FSBC and are capable of accounting for variable bathymetry. We noticed that both models overestimate the nonlinear interactions around the end of the slope. The possible reasons for this are numerous; we anticipate that this is due to the non-equilibrium statistics provoked by the transition of water depth. The small number of wave breaking events may also play a role in constraining the maximum achievable skewness and kurtosis. As a further study, new unidirectional irregular wave experiments in the same facility, but with a new bottom profile containing two constant slopes will be conducted and studied in the future. Finally, it is recalled that wave obliquity and wave directionality were not considered in this study; the effects associated with multidirectional (three-dimensional) sea states are left for future work.

Author Contributions: Definition of the experimental test cases and general methodology, M.B.; experimental campaign and data acquisition, J.Z., H.-C.H., O.K., and M.B.; numerical simulations, J.Z. and M.B.; data processing and interpretation, J.Z.; writing—original draft preparation, J.Z.; and writing—review and editing, O.K., M.B. and A.C.

Funding: Jie Zhang acknowledges funding from China Scholarship Council for his PhD grant (File No. 201604490045).

Acknowledgments: Jie Zhang is grateful to Meng-Syue Li (THL) for his technical support during the experimental campaign, and to Christos E. Papoutsellis for discussions on numerical wave modeling.

Conflicts of Interest: The authors declare no conflict of interest.

Abbreviations

The following abbreviations are used in this manuscript:

HOS	High-Order Spectral
THL	Tainan Hydraulics Laboratory
w.r.t.	with respect to
JONSWAP	Joint North Sea Wave Observation Project
DtN	Dirichlet-to-Neumann problem
FSBC	Free surface boundary condition
CFL	Courant–Friedrichs–Lewy number
FFT	Fast Fourier transform
PDF	Probability density function
CCDF	Complementary cumulative distribution function
GV91	Glukhovskiy's method modified by van Vledder (1991)
GK96	Glukhovskiy's method modified by Klopman (1996)
CWD	Composite Weibull distribution
WPD	Weibull-generalised Pareto distribution
MER	Modified Edgeworth Rayleigh distribution

References

1. Dysthe, K.; Krogstad, H.E.; Müller, P. Oceanic rogue waves. *Annu. Rev. Fluid Mech.* **2008**, *40*, 287–310. [CrossRef]
2. Didenkulova, I.I.; Slunyaev, A.V.; Pelinovsky, E.N.; Kharif, C. Freak waves in 2005. *Nat. Hazards Earth Syst. Sci.* **2006**, *6*, 1007–1015. [CrossRef]
3. Didenkulova, I.; Anderson, C. Freak waves of different types in the coastal zone of the Baltic Sea. *Nat. Hazards Earth Syst. Sci.* **2010**, *10*, 2021–2029. [CrossRef]
4. Nikolkina, I.; Didenkulova, I. Rogue waves in 2006–2010. *Nat. Hazards Earth Syst. Sci.* **2011**, *11*, 2913–2924. [CrossRef]
5. Glejin, J.; Kumar, V.; Nair, T.B.; Singh, J.; Nherakkol, A. Freak waves off Ratnagiri, west coast of India. *Indian J. Mar. Sci.* **2014**, *43*, 1339–1342.
6. Onorato, M.; Residori, S.; Bortolozzo, U.; Montina, A.; Arecchi, F. Rogue waves and their generating mechanisms in different physical contexts. *Phys. Rep.* **2013**, *528*, 47–89. [CrossRef]
7. Adcock, T.A.A.; Taylor, P.H. The physics of anomalous ('rogue') ocean waves. *Rep. Prog. Phys.* **2014**, *77*, 105901. [CrossRef] [PubMed]
8. Benjamin, T.B.; Feir, J.E. The disintegration of wave trains on deep water Part 1. Theory. *J. Fluid Mech.* **1967**, *27*, 417. [CrossRef]
9. Zakharov, V.E. Stability of periodic waves of finite amplitude on the surface of a deep fluid. *J. Appl. Mech. Tech. Phys.* **1968**, *9*, 190–194. [CrossRef]
10. Chabchoub, A.; Hoffmann, N.P.; Akhmediev, N. Rogue Wave Observation in a Water Wave Tank. *Phys. Rev. Lett.* **2011**, *106*, 204502. [CrossRef] [PubMed]
11. Chabchoub, A.; Hoffmann, N.; Onorato, M.; Akhmediev, N. Super rogue waves: Observation of a higher-order breather in water waves. *Phys. Rev. X* **2012**, *2*, 011015. [CrossRef]
12. Chabchoub, A.; Hoffmann, N.; Branger, H.; Kharif, C.; Akhmediev, N. Experiments on wind-perturbed rogue wave hydrodynamics using the Peregrine breather model. *Phys. Fluids* **2013**, *25*, 101704. [CrossRef]
13. Chabchoub, A.; Waseda, T.; Kibler, B.; Akhmediev, N. Experiments on higher-order and degenerate Akhmediev breather-type rogue water waves. *J. Ocean Eng. Mar. Energy* **2017**, *3*, 385–394. [CrossRef]
14. Crawford, D.R.; Lake, B.M.; Saffman, P.G.; Yuen, H.C. Stability of weakly nonlinear deep-water waves in two and three dimensions. *J. Fluid Mech.* **1981**, *105*, 177–191. [CrossRef]
15. Segur, H.; Henderson, D.; Carter, J.; Hammack, J.; Li, C.M.; Pheiff, D.; Socha, K. Stabilizing the Benjamin–Feir instability. *J. Fluid Mech.* **2005**, *539*, 229. [CrossRef]
16. Ma, Y.; Dong, G.; Perlin, M.; Ma, X.; Wang, G. Experimental investigation on the evolution of the modulation instability with dissipation. *J. Fluid Mech.* **2012**, *711*, 101–121. [CrossRef]

17. Henderson, D.M.; Segur, H. The role of dissipation in the evolution of ocean swell. *J. Geophys. Res. Oceans* **2013**, *118*, 5074–5091. [CrossRef]
18. Melville, W.K. The instability and breaking of deep-water waves. *J. Fluid Mech.* **1982**, *115*, 165. [CrossRef]
19. Janssen, P.A.E.M.; Onorato, M. The intermediate water depth limit of the Zakharov equation and consequences for wave prediction. *J. Phys. Oceanogr.* **2007**, *37*, 2389–2400. [CrossRef]
20. Toffoli, A.; Fernandez, L.; Monbaliu, J.; Benoit, M.; Gagnaire-Renou, E.; Lefèvre, J.M.; Cavaleri, L.; Proment, D.; Pakozdi, C.; Stansberg, C.T.; et al. Experimental evidence of the modulation of a plane wave to oblique perturbations and generation of rogue waves in finite water depth. *Phys. Fluids* **2013**, *25*, 091701. [CrossRef]
21. Ducrozet, G.; Gouin, M. Influence of varying bathymetry in rogue wave occurrence within unidirectional and directional sea-states. *J. Ocean Eng. Mar. Energy* **2017**, *3*, 309–324. [CrossRef]
22. Fedele, F.; Brennan, J.; de León, S.P.; Dudley, J.; Dias, F. Real world ocean rogue waves explained without the modulational instability. *Sci. Rep.* **2016**, *6*, 27715. [CrossRef]
23. Trulsen, K.; Zeng, H.; Gramstad, O. Laboratory evidence of freak waves provoked by non-uniform bathymetry. *Phys. Fluids* **2012**, *24*, 097101. [CrossRef]
24. Kashima, H.; Hirayama, K.; Mori, N. Estimation of freak wave occurrence from deep to shallow water regions. *Coast. Eng. Proc.* **2014**, *1*, 34–36. [CrossRef]
25. Zeng, H.; Trulsen, K. Evolution of skewness and kurtosis of weakly nonlinear unidirectional waves over a sloping bottom. *Nat. Hazards Earth Syst. Sci.* **2012**, *12*, 631–638. [CrossRef]
26. Gramstad, O.; Zeng, H.; Trulsen, K.; Pedersen, G.K. Freak waves in weakly nonlinear unidirectional wave trains over a sloping bottom in shallow water. *Phys. Fluids* **2013**, *25*, 122103. [CrossRef]
27. Viotti, C.; Dias, F. Extreme waves induced by strong depth transitions: Fully nonlinear results. *Phys. Fluids* **2014**, *26*, 051705. [CrossRef]
28. Katsardi, V.; de Lutio, L.; Swan, C. An experimental study of large waves in intermediate and shallow water depths. Part I: Wave height and crest height statistics. *Coast. Eng.* **2013**, *73*, 43–57. [CrossRef]
29. Chen, H.; Tang, X.; Gao, J.; Fan, G. Parameterization of geometric characteristics for extreme waves in shallow water. *Ocean Eng.* **2018**, *156*, 61–71. [CrossRef]
30. Ma, Y.; Dong, G.; Ma, X. Experimental study of statistics of random waves propagating over a bar. *Coast. Eng. Proc.* **2014**, *1*, 30. [CrossRef]
31. Bingham, H.B.; Madsen, P.A.; Fuhrman, D.R. Velocity potential formulations of highly accurate Boussinesq-type models. *Coast. Eng.* **2009**, *56*, 467–478. [CrossRef]
32. Yates, M.L.; Benoit, M. Accuracy and efficiency of two numerical methods of solving the potential flow problem for highly nonlinear and dispersive water waves. *Int. J. Numer. Methods Fluids* **2015**, *77*, 616–640. [CrossRef]
33. Raoult, C.; Benoit, M.; Yates, M.L. Validation of a fully nonlinear and dispersive wave model with laboratory non-breaking experiments. *Coast. Eng.* **2016**, *114*, 194–207. [CrossRef]
34. Zhang, J.; Benoit, M.; Kimmoun, O.; Hsu, H.C. Large-scale physical modeling of extreme waves in coastal area. In Proceedings of the Coastlab18, Santander, Spain, 22–26 May 2018.
35. Dias, F.; Dyachenko, A.; Zakharov, V. Theory of weakly damped free-surface flows: A new formulation based on potential flow solutions. *Phys. Lett. A* **2008**, *372*, 1297–1302. [CrossRef]
36. Madsen, P.A.; Fuhrman, D.R.; Wang, B. A Boussinesq-type method for fully nonlinear waves interacting with a rapidly varying bathymetry. *Coast. Eng.* **2006**, *53*, 487–504. [CrossRef]
37. Jamois, E.; Fuhrman, D.R.; Bingham, H.B.; Molin, B. A numerical study of nonlinear wave run-up on a vertical plate. *Coast. Eng.* **2006**, *53*, 929–945. [CrossRef]
38. Tian, Y.; Sato, S. A numerical model on the interaction between nearshore nonlinear waves and strong currents. *Coast. Eng. J.* **2008**, *50*, 369–395. [CrossRef]
39. Benoit, M.; Raoult, C.; Yates, M.L. Analysis of the linear version of a highly dispersive potential water wave model using a spectral approach in the vertical. *Wave Motion* **2017**, *74*, 159–181. [CrossRef]
40. Hasselmann, K.; Munk, W.; MacDonald, G. *Bispectrum of Ocean Waves*; Rosenblatt, M., Ed.; Time Series Analysis; John Wiley: New York, NY, USA, 1963.
41. Bertin, X.; de Bakker, A.; van Dongeren, A.; Coco, G.; André, G.; Ardhuin, F.; Bonneton, P.; Bouchette, F.; Castelle, B.; Crawford, W.C.; et al. Infragravity waves: From driving mechanisms to impacts. *Earth Sci. Rev.* **2018**, *177*, 774–799. [CrossRef]

42. Kim, Y.C.; Powers, E.J. Digital Bispectral Analysis and Its Applications to Nonlinear Wave Interactions. *IEEE Trans. Plasma Sci.* **1979**, *7*, 120–131. [CrossRef]
43. Goda, Y. *Random Seas and Design of Maritime Structures (Advanced Series on Ocean Engineering)*; World Scientific Pub Co Inc.: Singapore, 2010.
44. Elgar, S.; Guza, R.T. Observations of bispectra of shoaling surface gravity waves. *J. Fluid Mech.* **1985**, *161*, 425–448. [CrossRef]
45. Longuet-Higgins, M.S. On the statistical distributions of sea waves. *J. Mar. Res.* **1952**, *11*, 245–265.
46. Glukhovskiy, B.K.H. Investigation of sea wind waves. In Proceedings of the Sea Climatology Conference, Paris, France, 1966; pp 51–71. (In Russian)
47. Van Vledder, G.P. *Modification of the Glukhovskiy Distribution, Report H1203*; Technical Report; WL | Delft Hydraulics: Delft, The Netherlands, 1991.
48. Klopman, G. *Extreme Wave Heights in Shallow Water, Report H2486*; Technical Report; WL | Delft Hydraulics: Delft, The Netherlands, 1996.
49. Battjes, J.A.; Groenendijk, H.W. Wave height distributions on shallow foreshores. *Coast. Eng.* **2000**, *40*, 161–182. [CrossRef]
50. Wu, Y.; Randell, D.; Christou, M.; Ewans, K.; Jonathan, P. On the distribution of wave height in shallow water. *Coast. Eng.* **2016**, *111*, 39–49. [CrossRef]
51. Longuet-Higgins, M.S. The effect of non-linearities on statistical distributions in the theory of sea waves. *J. Fluid Mech.* **1963**, *17*, 459. [CrossRef]
52. Mori, N.; Yasuda, T. A weakly non-gaussian model of wave height distribution for random wave train. *Ocean Eng.* **2002**, *29*, 1219–1231. [CrossRef]
53. Mori, N.; Janssen, P.A.E.M. On kurtosis and occurrence probability of freak waves. *J. Phys. Oceanogr.* **2006**, *36*, 1471–1483. [CrossRef]
54. Tayfun, M.A.; Fedele, F. Wave-height distributions and nonlinear effects. *Ocean Eng.* **2007**, *34*, 1631–1649. [CrossRef]
55. Alkhalidi, M.A.; Tayfun, M.A. Generalized Boccotti distribution for nonlinear wave heights. *Ocean Eng.* **2013**, *74*, 101–106. [CrossRef]
56. Boccotti, P. *Wave Mechanics for Ocean Engineering*; Elsevier Science: Oxford, UK, 2000; Volume 64.
57. Forristall, G.Z. On the statistical distribution of wave heights in a storm. *J. Geophys. Res.* **1978**, *83*, 2353. [CrossRef]

Chapter 3

Supplementary materials: additional experiment and simulation results

3.1 Description of experimental campaign and two additional tests

The transmission of irregular waves over a sloping bottom is a complicated process with the presence of shoaling, nonlinear wave-wave interaction, refraction, reflection, dissipation due to friction, and breaking effects. This experimental campaign in Tainan Hydraulics Laboratory (THL) aimed to investigate the formation of extreme waves in irregular sea states with the presence of sloping bottoms. The facility in THL has been introduced in Part III Chapter 2 for the experimental investigation of modulation instability, and will not be repeated here.

We consider uni-directional long-crested irregular wave trains propagating over a prismatic slope connecting two regions of constant water depths. The bottom slope is fixed, starting at 30 m away from the wave maker and ends at 50 m from the wave maker. The length of the uneven part is 20 m long and depth transition is 1 m (1/20 slope). A large number of tests were conducted with different combinations of parameters to cover a broader range in the four-parameter domain (water depth h, significant wave height H_s, peak frequency f_p, and spectral width γ) which dominates the sea states. The incident wave trains are described by the JONSWAP spectrum with two different spectral widths $\gamma = 3.3$ or 7.0 considered. The examined spectral peak period T_p covers from 1.5 s to 2.7 s. The water depths h range from 1.2 m to 1.4 m, and the significant wave heights H_s vary in $[0.05, 0.12]$ m. The complete list of tested conditions is given in Table (IV.3.1), where non-dimensional parameters including relative water depth μ, steepness ε, and Ursell number Ur computed with the peak period in both the deeper region and the shallower region are shown. The experimental test conditions are con-

trolled by gradually increasing the peak period T_p for different water depth so that the relative water depth μ is gradually decreasing. Then for the same μ, different tests are set with increasing nonlinearity until some minor breaking events appear during tests.

Table IV.3.1: List of all conditions tested during the experimental campaign

Case	h (m)	T_p (s)	H_s (m)	γ	**Deeper region**			**Shallower region**		
					μ	ε	Ur	μ	ε	Ur
1	1.2	1.5	0.05	3.3	2.20	0.092	0.340	0.64	0.166	25.391
2	1.2	1.5	0.08	3.3	2.20	0.147	0.544	0.64	0.265	40.626
3	1.2	1.5	0.09	3.3	2.20	0.165	0.612	0.64	0.298	45.704
4	1.2	1.5	0.10	3.3	2.20	0.183	0.680	0.64	0.331	50.782
5	1.2	1.8	0.11	3.3	1.61	0.148	1.390	0.52	0.329	92.262
6	1.25	1.8	0.08	3.3	1.67	0.107	0.909	0.59	0.207	40.237
7	1.25	1.8	0.10	3.3	1.67	0.133	1.136	0.59	0.259	50.297
8	1.3	2.1	0.12	3.3	1.36	0.125	1.984	0.55	0.250	60.087
9	1.3	2.1	0.12	7.0	1.36	0.125	1.984	0.55	0.251	60.087
10	1.3	2.3	0.10	3.3	1.19	0.092	2.143	0.50	0.197	63.325
11	1.3	2.3	0.10	7.0	1.19	0.092	2.143	0.50	0.197	63.325
12	1.3	2.3	0.11	3.3	1.19	0.101	2.357	0.50	0.216	69.658
13	1.3	2.3	0.11	7.0	1.19	0.101	2.357	0.50	0.216	69.658
14	1.3	2.3	0.12	3.3	1.19	0.110	2.571	0.50	0.236	75.990
15	1.3	2.5	0.10	3.3	1.06	0.082	2.685	0.45	0.185	77.999
16	1.3	2.5	0.12	3.3	1.06	0.098	3.222	0.45	0.222	93.599
17	1.3	2.5	0.12	7.0	1.06	0.098	3.222	0.45	0.222	93.599
18	1.3	2.7	0.09	3.3	0.96	0.067	2.949	0.42	0.157	84.636
19	1.4	1.8	0.12	3.3	1.83	0.157	1.010	0.77	0.234	20.354
20	1.4	2.1	0.12	3.3	1.43	0.123	1.650	0.64	0.210	31.073
21	1.4	2.3	0.12	3.3	1.25	0.106	2.152	0.58	0.196	39.476

[1] In the shallower part, the significant wave heights are amended using the linear shoaling coefficient;

The comparison in the ε-μ space between our experiments and existing experiments conducted by Ma et al. (2014); Trulsen et al. (2012); Kashima et al. (2014) is shown in Fig. (IV.3.1). Our experiments significantly extend the existing database and cover relatively large areas in the ε-μ plane. It is also observed that, in the tested cases, the bottom slope plays an important role in the wave evolution since the steepness and the relative water depth are significantly different in the deeper and shallower regions.

The tested experimental conditions are capable of revealing different trends. Waves in cases 1, 6, 10, 16 are of similar nonlinearity before entering the bottom slope, but with different relative water depths $\mu \in [1.06, 2.2]$. The effects of wave

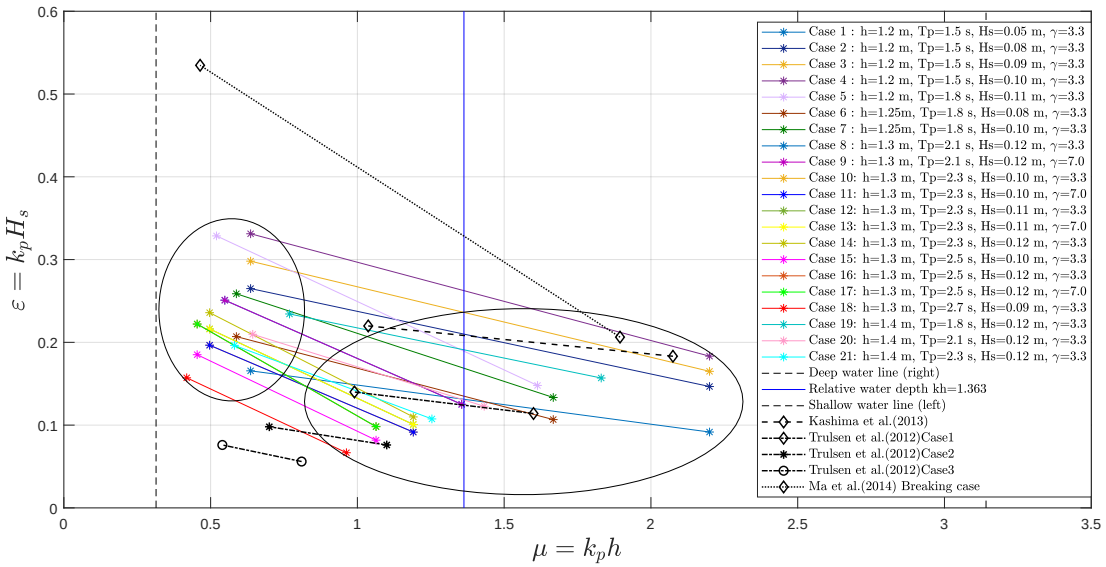

Figure IV.3.1: All tested experimental conditions in ε-μ space are shown in lines of different colors, the experimental conditions adopted in previous studies are shown by the dash, dot, and dash-dot lines. The circles of solid line illustrate the range of this experimental campaign.

nonlinearity are illustrated by comparing the combinations of tests Case 1-5, or Case 10, 12, 14. The effects of the spectral width are shown by considering Case 8-9, Case 10-11, or Case 12-13. By doing the preliminary data processing of all the signals measured at different positions, including the computation of BFI parameter, H_{m_0}, high-order statistical moments skewness λ_3^η, kurtosis λ_4^η and Fourier spectrum and spectral peak frequency f_p, three representative cases have been selected. They are Case 1, 10, 15. They are chosen for different reasons. In Case 1, the relative water depth considerably decreases due to the shoaling from $\mu = 2.2$ to $\mu = 0.64$, while the nonlinearity remains low on both sides of the slope. The sea state is quasi-Gaussian with the lowest value of Ur. In Case 10, the depth variation is less significant compared to Case 1, but the nonlinearity of the sea state is stronger. Case 15 is a comparative case of Case 10 in which the nonlinearity is further increased. The main efforts were dedicated to the study of case 10, and the results are shown in Chapter 3 in the form of a journal paper, the other two cases are shown here as supplemented materials. In Fig. (IV.3.2), the three cases are shown in ε-μ.

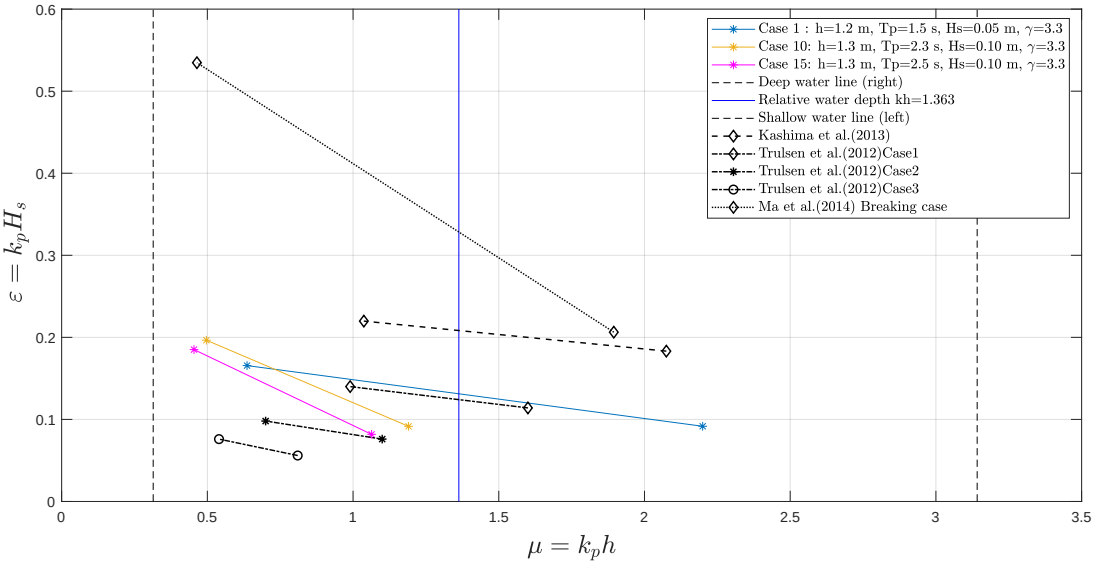

Figure IV.3.2: Three chosen case conditions in ε-μ space are shown in lines of different colors, the experimental conditions adopted in previous studies are shown by the dash, dot, and dash-dot lines.

3.1.1 Case 1: a near Gaussian sea state

In Table (IV.3.1), the experimental condition of Case 1 is given. In this case, the change of relative water depth is significant whereas the wave nonlinearity is mild. The Ursell number, in this case, is the smallest among the three chosen tests. Since the length of the bottom slope remains for all tests, Case 1 is of the fastest transition rate of relative water depth. Furthermore, the shallower region is of relative water depth $\mu = 0.64$ below 1.363, the effect of modulational instability is of secondary importance.

First, the spectral analysis of the recorded time series of all 30 probes is performed. According to the Nyquist–Shannon sampling theorem, the highest distinguishable frequency in our cases is 50 Hz (with sampling frequency being 100 Hz). In the following Fourier analysis, the power density spectra are obtained by using the averaged periodogram procedure introduced in Section 1.2, using 2^{13}-points FFT which results in a spectral resolution $\Delta f = 0.0061$ Hz. The results are shown in Fig. (IV.3.3) and Fig. (IV.3.4). Higher frequencies than 2 Hz in the spectra are of low energy compared to the main part of the spectrum, so they are therefore not shown.

In Fig. (IV.3.3) it is observed that as waves propagate in the flume, the wave energy transfer is very limited. The wave energy is transferred to long waves over the shallower region, but still, trivial compared to the main part in the spectrum.

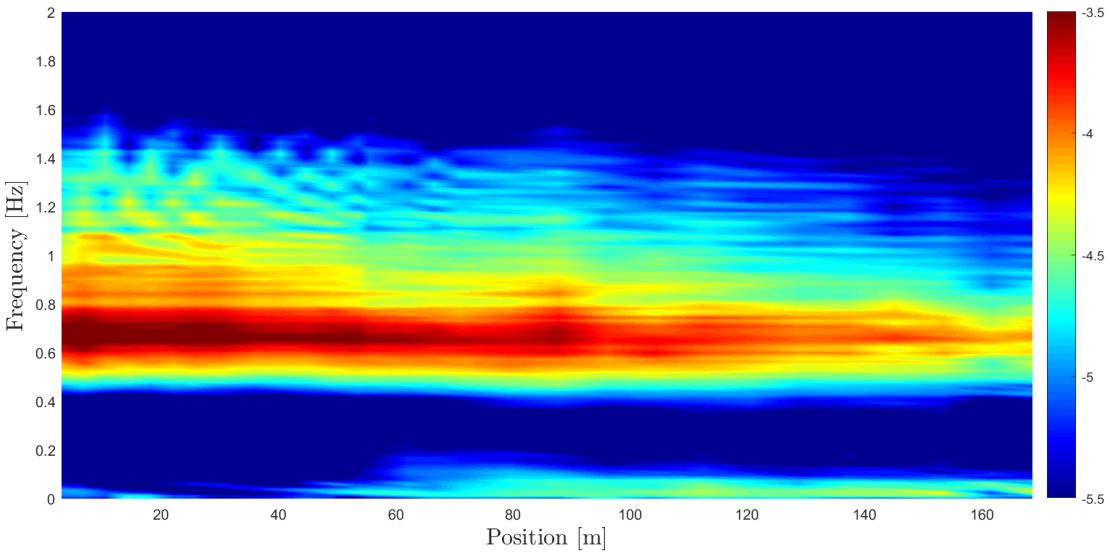

Figure IV.3.3: The spatial evolution of the power density spectrum for Case 1, the spectrum is shown in log-scale colormap, and the colormap limits correspond to the exponential powers.

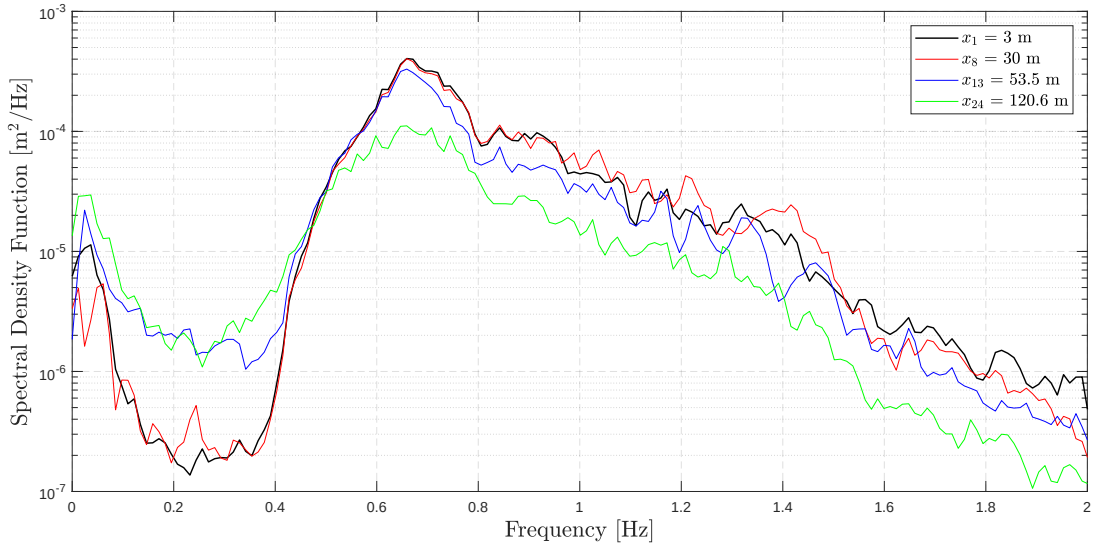

Figure IV.3.4: The power density spectra for Case 1 at four particular positions are shown in detail in the log-scale coordinate, black line for the deeper area close to the wavemaker (probe 1), red line at the toe of the slope (probe 8), blue line for the shallower area 3.5 m after the end of the slope (probe 13), and green line for the shallower part far from the slope (probe 24).

The spectrum keeps its original shape, except for the decrease in magnitude due to continuous attenuation. Visually, there is no obvious excitation of higher harmonics of waves with the spectral peak frequency. The spectral peak, as well as the width of the spectrum, remains similar to the input wave spectrum.

In Fig. (IV.3.4), the detailed spectra of four particular positions are shown. The choice of these positions aims at illustrating the spectral evolution in the deeper region (between Probe 1 and Probe 8), over the bottom slope (between Probe 8 and Probe 13) and in the shallower region (between Probe 13 and Probe 24). Comparing the spectra at Probe 1 and Probe 8, it is observed that there is a minor increase around 1.4 Hz which corresponds the second harmonic of the peak frequency. However, after the slope, this second harmonic loses energy. The spectrum measured at Probe 24 shows that the spectral shape is similar to the input spectrum only slightly broader. The low-frequency in the range $[0, 0.4]$ Hz is of slightly higher (but still small) energy compared to the spectrum measured at Probe 1, no particular low-frequency mode is excited at Probe 13 and 24. The energy of the main part of the spectrum decreases. It is anticipated that the decrease of energy in the main frequency range is due to frictional dissipation. In this case, the sea state is quasi-Gaussian, wave-wave interaction is relatively gentle.

In Fig. (IV.3.5) six parameters are shown, including significant wave height, high-order moments, and spectral width parameter, peak frequency, and B-F index. It is observed that there is no significant enhancement of high-order moments over the depth transition region, λ_3^η and λ_4^η fluctuates around 0 and 3 respectively, as are expected in a Gaussian state. The significant wave height gradually decreases as waves propagate since wave energy is continuously dissipated by the friction. It is indicated by the peakedness parameter Q_p, the spectral shape remains roughly throughout the basin, except that the spectral width is slightly increased as waves propagate over the shallower region (after 60 m). The spectral peak is evaluated following the formula in Eq. (IV.1.55), within the frequency range $[0.2, 2.5]$ Hz. It is clearly shown that the spectral peak was nearly not changed as waves propagated over the flume. In the last panel, the Benjamin-Feir Index with two different evaluation methods is shown. In the area where $kh < 1.363$, both BFI and B_s are manually set negative to stress that the effects of modulation instability are expected to disappear. In such areas, large magnitudes of BFI and B_s denote more pronounced effects from nonlinearity compared to dispersion. Over the bottom slope, both BFI and B_s show a significant magnitude increase. However, since the relative water depth falls below the threshold value of 1.363, the behavior B-F index indicates a more modulationally stable condition. As waves propagate over the shallower region, the value of BFI gradually decreases mainly due to the decrease of wave steepness.

All these observations imply the fact that this case is almost Gaussian, and that the effect of the bottom slope is trivial and negligible in terms of spectral changes.

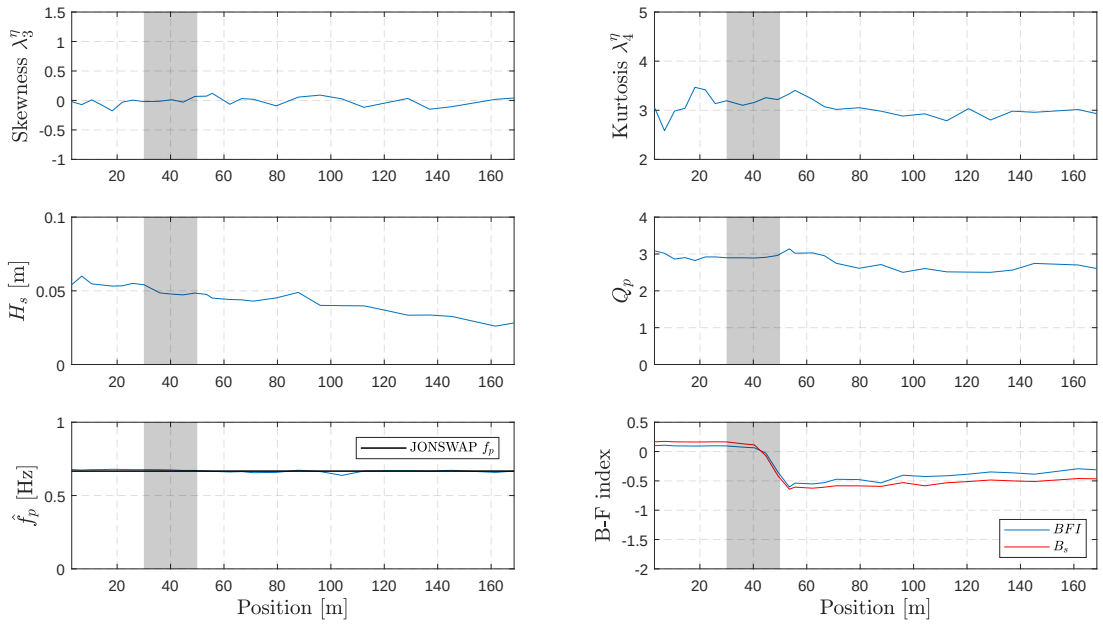

Figure IV.3.5: The spatial evolution of significant wave height H_s, high-order moments skewness λ_3^η and kurtosis λ_4^η and peakedness parameter Q_p, peak frequency $\hat{f}_p$ and B-F index in Case 1, the shading areas denote the depth transition region.

There is also evidence that the non-resonant wave-wave interaction is mild. The wave heights thus follow Rayleigh distribution Eq. (IV.1.11) and the free surface elevation is Gaussian distributed Eq. (IV.1.6). The probability of the occurrence of freak waves is low. But this is only true statistically. In our experiments, we found evidence that the bottom slope can take effect on a very local scale. The evidence is that we found an energetic wave packet which seemed to be 'normal' before the bottom slope, but the wave energy was concentrated to one wave after the slope. The largest wave eventually became an outstanding 'freak' wave.

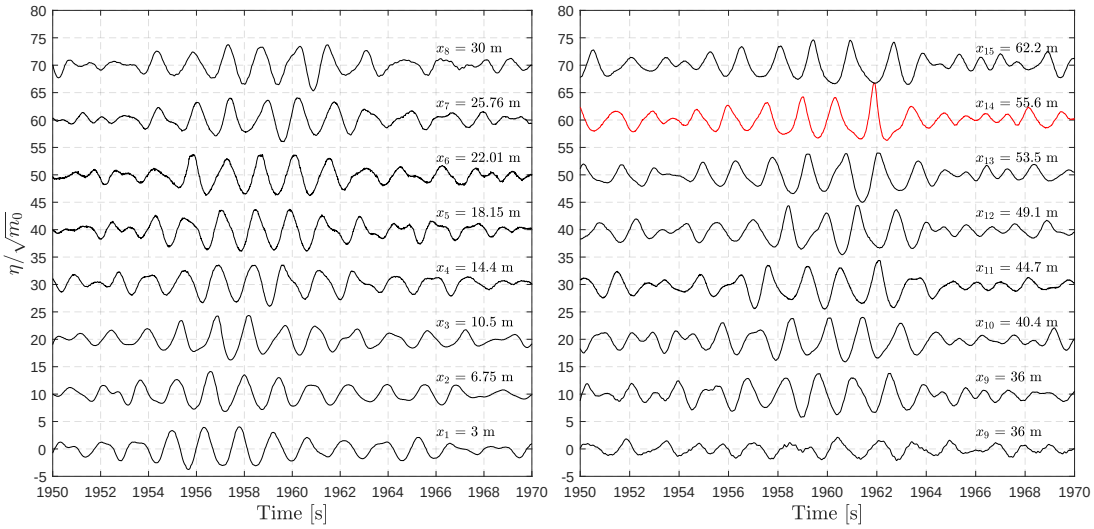

Figure IV.3.6: The evolution of an energetic wave packet in Case 1, the free surface elevation is normalized by local $\sqrt{m_0}$. The signals are shifted in time based on the linear dispersion, and they are shifted in y-axis by 10 for different probes.

As is shown in Fig. (IV.3.6), when waves propagate over the deeper region the energetic wave packet is not outstanding compared to the background, with the largest value of $\eta/\sqrt{m_0} < 8$. But after the slope, this wave packet formed one freak wave with $\eta/\sqrt{m_0} \approx 10.5$, corresponding to $AI \approx 2.6$ at Probe 14 (red signal). Deep troughs are detected at Probe 13 and 15 which are supposed to be the different stages of the freak wave formation. And we conclude that the formation of freak waves is possible even in a modulationally stable quasi-Gaussian sea state.

3.1.2 Case 15: a strongly nonlinear sea state

As indicated by Trulsen et al. (2020), there is a transition relative water depth which should be taken into account. Below a certain threshold, the higher harmonic behavior and the extreme wave statistics are expected. This behavior has been confirmed in Trulsen et al. (2012); Zhang et al. (2019). This threshold is 1.3

in the tests shown in Trulsen et al. (2020). Above this threshold, the sea states are quasi-Gaussian. It is anticipated that no significant increase of skewness and kurtosis after the slope, and that the occurrence probability of high waves is not significantly enhanced (but not impossible). Case 1 is clearly of shallow relative water depth after the slope ($\mu = 0.64$), but with a quasi-Gaussian sea state. No local maxima are observed for skewness and kurtosis. In Case 10 shown in Zhang et al. (2019), and Case 15, which will be introduced below, the relative water depth in the shallower region is slightly lower than in Case 1 ($\mu = 0.5$ and 0.45). Considerable increase of the skewness, kurtosis, and the occurrence probability of freak waves have been reported in Case 10. As a further demonstration of such enhancement, Case 15 is shown. The experimental condition of Case 15 is given in Table (IV.3.1), this case is of slightly stronger nonlinearity (with a few gentle spilling breakers), in relatively shallower water depth compared to Case 10. Case 16 and Case 18 are of shallower relative water depth than Case 15, however, significant spilling breaking effects limited the occurrences of high waves thus they are thus not shown here.

In Fig. (IV.3.7) and Fig. (IV.3.8), the spectra are different from the ones of Case 1. In this case, the spectral evolution is similar to Case 10. It is important to note that after the propagation of waves in the deeper region, a set of modes appear in the low-frequency range $[0, 0.3]$ Hz of the spectrum, whereas they are barely invisible in Case 1. One possible explanation is that the slope reflects more energy before the slope when the relative water depth is small, the reflected waves could resonate with incident waves. The wavemaker can 'absorb' some reflected wave energy so that these modes are not visible near the wavemaker, then and gradually appear as waves leave wavemaker and propagate further. The second-order harmonics are more pronounced at Probe 13, around the end of the slope, it disappears after a short distance in the shallower region. At Probe 13, it is observed two bumps around 1.2 Hz and 1.6 Hz which correspond to the third-order and fourth-order harmonics of the peak frequency 0.4 Hz respectively. However, in log-scale, they represent minor energy level.

It is anticipated that the generation of the low-frequency modes is mainly a result of natural modes instead of non-resonance wave-wave interaction. With the presence of a sloping bottom, the effective flume length should be taken into account since waves are not only reflected by the end wall on the other side of the flume but also by the sloping bottom. The derivation of natural mode in a wave flume with an arbitrary bottom profile with a linear theory is detailed in Appendix A.1. Two additional assumptions are considered in the derivation, one assumption is that natural modes are shallow-water waves in the flume, and the other is that the varying bottom can be discretized with numerous segments. Consider the effective flume length as 50 m, the computed natural modes with this method are listed in Table (IV.3.2). However, it is seen in Fig. (IV.3.7) that the low-frequency modes evolve in space. This is because the slope continuously

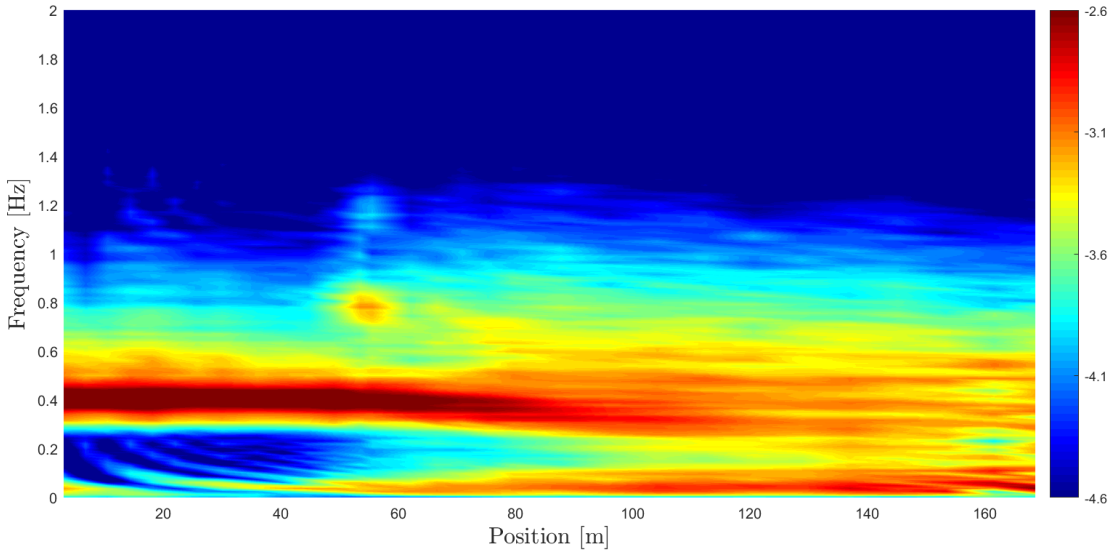

Figure IV.3.7: The spatial evolution of the power density spectrum for Case 15, the spectrum is shown in log-scale colormap, and the limits of the colorbar correspond to the exponential powers.

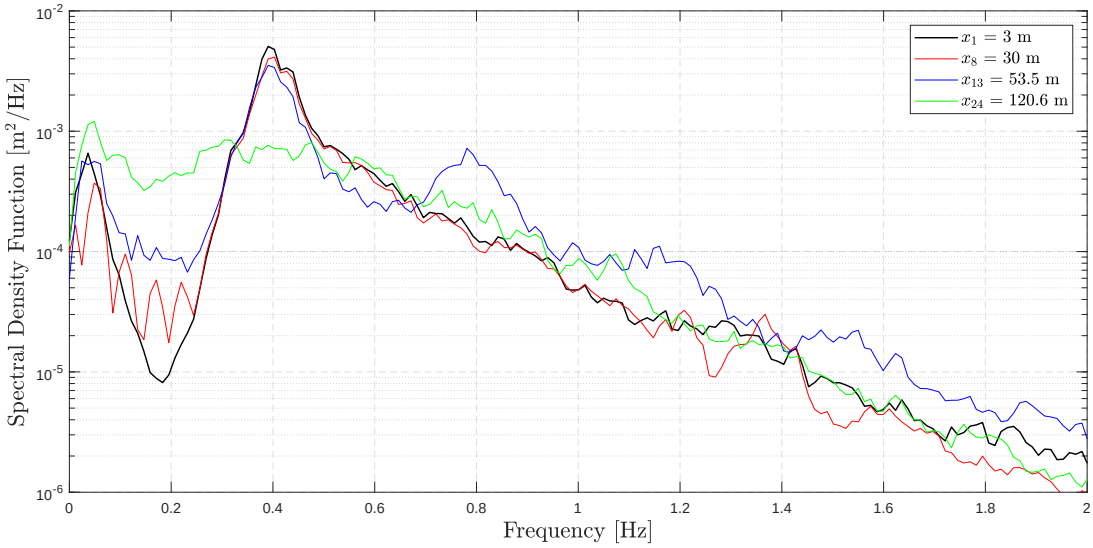

Figure IV.3.8: The power density spectra for Case 15 at four particular positions are shown in detail in the log-scale coordinate, black line for the deeper area close to the wavemaker (probe 1), red line at the toe of the slope (probe 8), blue line for the shallower area 3.5 m after the end of the slope (probe 13), and green line for the shallower part far from the slope (probe 24).

reflects waves so that the effective flume length should be considered as a variable. The content in Table (IV.3.2) is evaluated as a function of x, and the first 5 modes are superimposed in the spatial evolution of wave spectra in Fig. (IV.3.9). The pattern of the evolution of low frequency modes are well predicted by this method.

Table IV.3.2: List of first five resonant frequencies which could be excited in the experiment wave flume

$n-$th mode	f_n (Hz)	T_n (s)	l_n (m)	k_n (rad/m)
1	0.0313	31.934	100.00	0.0628
2	0.0626	15.967	50.00	0.1257
3	0.0939	10.645	33.33	0.1885
4	0.1253	7.984	25.00	0.2513
5	0.1566	6.387	20.00	0.3142
...	...			

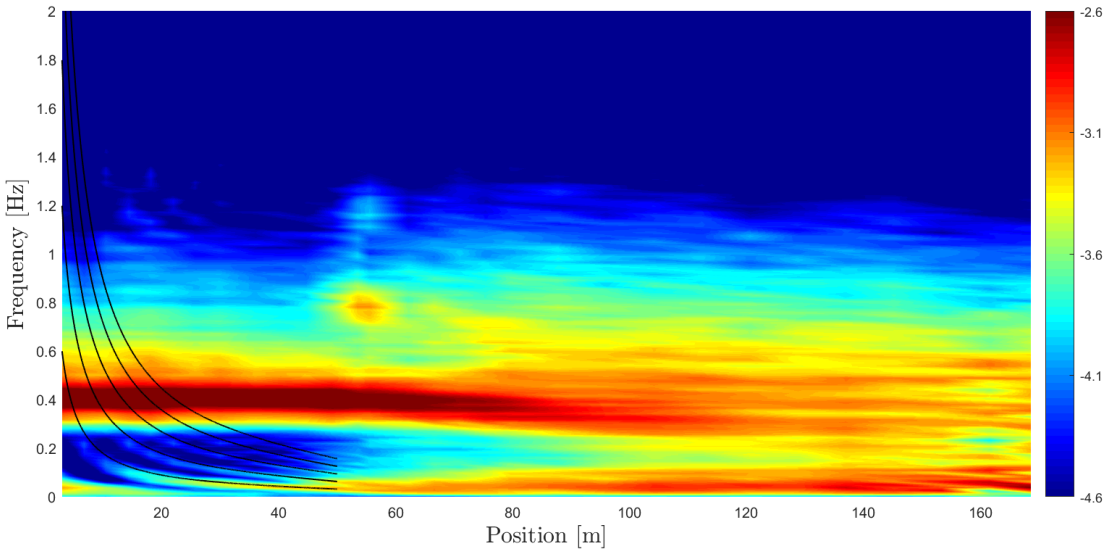

Figure IV.3.9: The spatial evolution of the power density spectrum for Case 15 with first 5 natural modes superimposed.

As for Case 1, six parameters for Case 15 are shown in Fig. (IV.3.10). It is observed that the skewness λ_3^η and kurtosis λ_4^η experienced a significant increase after the sloping area, and local maxima appeared at the beginning of the shallower region. The increase of skewness is mainly caused by the shoaling effect, waves become sharper in crests and flatter in troughs after the slope. The skewness does

not decrease back to the level in the deeper region since waves are of asymmetry profiles in the shallower region. The kurtosis is increased mainly resulting from two sources, one is the dynamic response of the sea state transition from one state (deeper region) to another one (shallower region), and the other is the bound mode nonlinearity. After the slope, λ_4^η decreases significantly indicating that the non-equilibrium dynamic response is the main reason for this local maximum. The evolution of H_s shows the intensity of overall dissipation. It is also noticed that after the sloping area, there is a slight decrease in H_s which is attributed to slightly spilling wave breaking events. In terms of spectral evolution, it is seen that the wave spectrum significantly broadens after the slope, while the spectral peak within $[0.2, 2.5]$ Hz remains around the input peak frequency f_p. However, due to the dissipation of the wave energy of the main spectral area, the spectral peak is replaced by the low-frequency modes outside the range $[0.2, 2.5]$ Hz in the shallower region. In the last panel, there is also a local maximum value for BFI and B_s. Negative values mean that the sea state is modulationally stable, and the local peak represents the nonlinearity effect of the sea state increased significantly. Different definitions of the B-F index show different values, but the trend is similar.

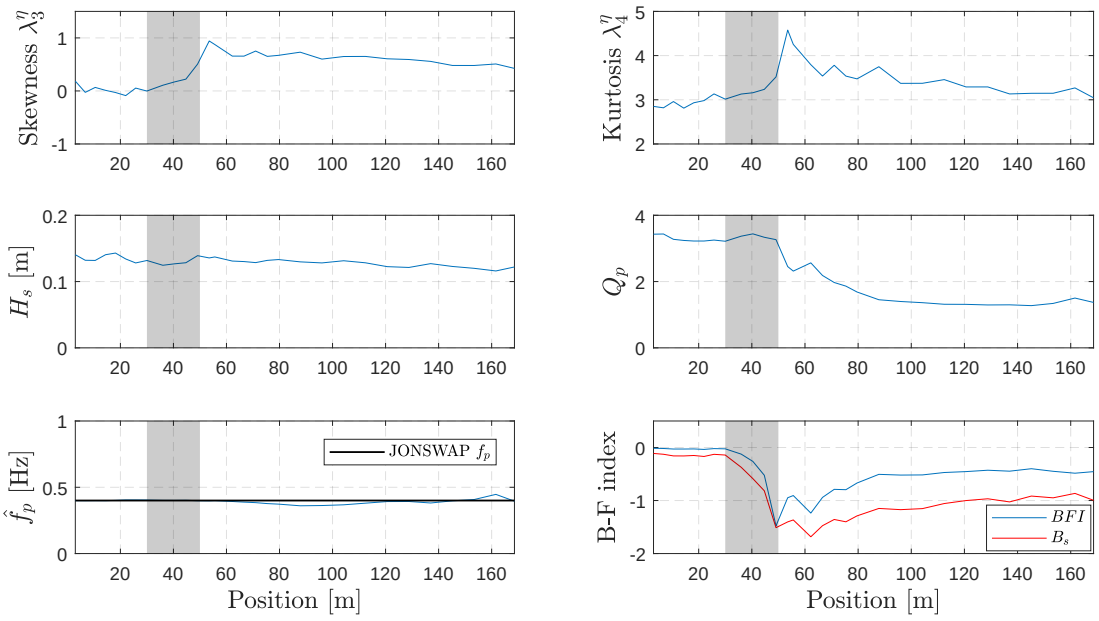

Figure IV.3.10: The spatial evolution in Case 15 of significant wave height H_s, high-order moments skewness λ_3^η and kurtosis λ_4^η and peakedness parameter Q_p, peak frequency $\hat{f}_p$ and B-F index, the shading areas denote the depth transition region.

To conclude, the wave parameters in Case 15 show similar behaviors as they

do in Case 10. Local increases of skewness and kurtosis parameters and significant energy increase of second harmonics in the spectrum are observed shortly after the end of the slope. Such features are not observed in the Case 1 experiments where the sea state is quasi-Gaussian. In Case 1 the relative water depth in the shallower region is $\mu = 0.64$, it is much smaller than the threshold 1.3 observed in Trulsen et al. (2020) but it is close to $\mu = 0.45$ of Case 15. There are two possible explanations for the different sea state dynamic responses in the shallower region between Case 1 and Case 15 (also Case 10). One explanation is that the transition relative water depth in our experiments is between 0.5 and 0.64, such that in Case 10 and Case 15 the relative water depth in the shallower region is below the transition threshold. However, Case 1 is above the threshold and falls in the 'deeper regime'. This is possible because the bottom slope in the current experiments 1/20 is smaller than in Trulsen et al. (2020), 1 : 3.81. The 'deeper regime' might be shallower for milder slopes. The other explanation is that the transition relative water depth is our case is larger than 0.64, so Case 1, 10, 15 are all in the 'shallower regime'. But the non-equilibrium dynamic response of sea states may also result from the nonlinearity of the incident sea state. For cases with low nonlinearity, strong dynamic responses do not manifest. It is difficult to anticipate the transition water depth since in our cases, the relative water depths in the shallower region are in a limited range $\mu = [0.42, 0.72]$.

It is anticipated that both the nonlinearity of the incident sea states, the gradient of the bottom slope also play important roles in the water-depth transition process and affect the transition water depth. In terms of the spectral width, no significant differences have been observed when comparing, for example, Case 10 and 11, Case 12 and 13. The spectral width is of secondary importance in our experimental tests. However, the spectral width may be more important when the shallower region is of larger water depth, where the dispersion effect is more significant. This will be left for future study.

3.2 Additional numerical tests of Case 10 for calibration of model parameters

In the paper presented in Chapter 2, the numerical tests of Case 10 are shown with converged results. The tests of convergence are omitted for brevity. Here they are given as additional materials. The effects of different numerical parameters are shown here, based on which our choices for the numerical parameters are justified.

Various effects play roles in the quality of the agreement between the simulation results and measurements, especially when the measurements are conducted on such a large scale in space (200 m) and long duration in time ($1200T_p$). Differences may result from undesired events in the outdoor flume in THL, like a sudden gust of wind, electronic noise of the wave gauges and insufficient long-wave absorption, etc. Even though in this experimental campaign, the experiments were

conducted at carefully chosen timing, these effects are inevitable and untraceable from the time series. It would be ambitious to seek a perfect overall agreement between simulation results and large-scale long-time measurements in time and space. Small upstream errors will result in considerable disturbances on the waves downstream. For such reasons, we aim at the quantitative agreement with measurements in the deeper region and the beginning of the shallower region. For the shallower region far from the end of the slope (after 100 m), the nonlinear wave propagation in shallow water is outside the subject of the present thesis, the qualitative agreement between simulations and experiments is acceptable.

The convergence tests have been done for the numerical step sizes in space (Δx) and time (Δt), accuracy of numerical models in describing the velocity potential (N_T for Whispers3D and N_B for Boussinesq type model), viscous dissipation parameter ν_v, and the length of relaxation/absorption zones. These tests aim to find the balance between computational cost and optimization of the simulated results.

3.2.1 Dispersion and nonlinear properties of models

For Case 10, $T_p = 2.3$ s, the corresponding wave number is $L_p = 6.86$ m in the deeper region and 3.80 m in the shallower region. The chosen value of $\Delta x = 0.11$ m results in an 8-points description for the third harmonics of waves with peak frequency in the shallower region (frequency $f_{3p} \approx 1.30$ Hz, the corresponding $L_{3p} = 0.89$ m). As is seen in Fig. (IV.3.4) and Fig. (IV.3.8), waves with frequencies higher than 1.2 Hz are of minor energy. The choice of $\Delta x = 0.11$ m is thus adopted in Boussinesq-type model. In the adopted Boussinesq-type model 5^{th} order spatial derivatives are required, so for the sake of numerical stability, $\Delta x = 0.11$ m is used, and $\Delta t = 0.016$ s is chosen for keeping a low value of *Courant–Friedrichs–Lewy* (CFL) number, CFL $= L\Delta t/T\Delta x = 0.42$. In Whispers3D, the spatial derivatives are of second order at most, so we could test smaller Δx, while having a larger Δt for saving time. $\Delta t = 0.02$ s and $\Delta x = 0.05$ m (resulting in CFL $= 1.2$) are chosen.

The values of N_T and N_B are determined based on the relative water depth range $[0.50, 1.19]$ in Case 10. In Fig. (IV.3.11), different choices of N_T (whispers3D) and N_B (Boussinesq-type) have been shown as a function of relative water depth, from which it is seen that for $N_T = 7$ and $N_B = 2$, the relative error of dispersion compared to Airy theory is less than 10^{-8}. They are adequate for describing the dispersive effects in the experiments.

3.2.2 Relaxation zone setting

It is difficult to achieve very good agreement between experiments and simulated results in terms of thelow-frequency range of the spectra. It is anticipated that the quality of the agreement of long waves are partially related to the ability of wave absorption in the numerical basin. One supporting fact is the agreement shown in

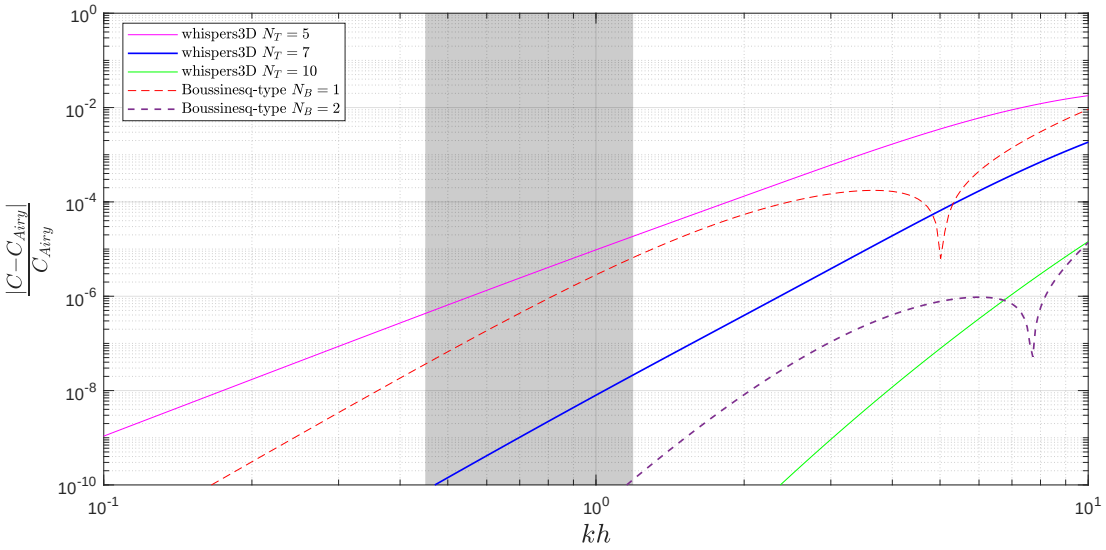

Figure IV.3.11: Comparison of the dispersive properties between the Boussinesq-type model (with $N_B = 1, 2$), the whispers3D model (with $N_T = 5, 7, 10$) and exact Airy solution. The gray area represents the relative water depth region of Case 10.

Fig. (IV.3.9). These long waves are simulated by decreasing the absorption ability in the numerical models. In both whispers3D and the Boussinesq-type models adopted, relaxation zones are set in places of wave making and wave absorbing equipment. This method is adopted to minimize the shock wave effect due to the sudden change of variables. In the relaxation zone $x \in [x^r_{beg}, x^r_{end}]$, the solved surface variables η and $\tilde{\phi}$ are replaced, at each time step, by the imposed target solution η_{tar} and ϕ_{tar}, in the following manner:

$$\begin{cases} \eta(x,t) = [1 - C_r(x)]\,\eta(x,t) + C_r(x)\eta_{tar}(x,t), & x \in [x^r_{beg}, x^r_{end}] \quad \text{(IV.3.1)} \\ \tilde{\phi}(x,t) = [1 - C_r(x)]\,\tilde{\phi}(x,t) + C_r(x)\tilde{\phi}_{tar}(x,t), & x \in [x^r_{beg}, x^r_{end}]. \quad \text{(IV.3.2)} \end{cases}$$

where $C_r(x)$ is the relaxation coefficient as a function of x. If η_{tar}, $\tilde{\phi}_{tar}$ correspond to the measured signal, this relaxation zone corresponds to generation zone and the boundary of the numerical flume is $x_b = x^r_{end}$, if $\eta_{tar} = \tilde{\phi}_{tar} = 0$ then it corresponds to dissipation zone and the boundary of the numerical flume is $x_b = x^r_{beg}$. The expression of the relaxation coefficient $C_r(x)$ is of exponential shape as follows:

$$C_r(x) = \left(1 - \left|\frac{x_b - x}{x^r_{end} - x^r_{beg}}\right|\right)^a, \qquad \text{(IV.3.3)}$$

where a is the exponential power, normally it is suggested to take values larger than 2 according to the length of the relaxation zone.

A short dissipation zone can be adopted to imitate insufficient dissipation on long waves in the wave flume. Since the relaxation zone is implemented in the same manner in two numerical codes, here we take the results of the Boussinesq-type model to illustrate the effect of the length of the relaxation zone. In the present simulations of Case 10, the exponential power $a = 3.5$ in Eq. (IV.3.3) was adopted following the suggestion of Madsen et al. (2003).

The results of the absorption zones with $L_p/2$, L_p, $2L_p$, $3L_p$ in length are tested and compared. The calibration tests for absorption zone length used the first 1500 s of 2760 s measurements in Case 10. The simulated data were resampled with the same sampling frequency (100 Hz) as the experiments. The experimental data with the same duration was adopted to compare with simulation results. The spectral spatial evolution in Case 10 for the first 1500 s is shown in Fig. (IV.3.12). The long-wave modes have been well developed in this duration, and the spectral shape is very similar to the full-time spectral analysis.

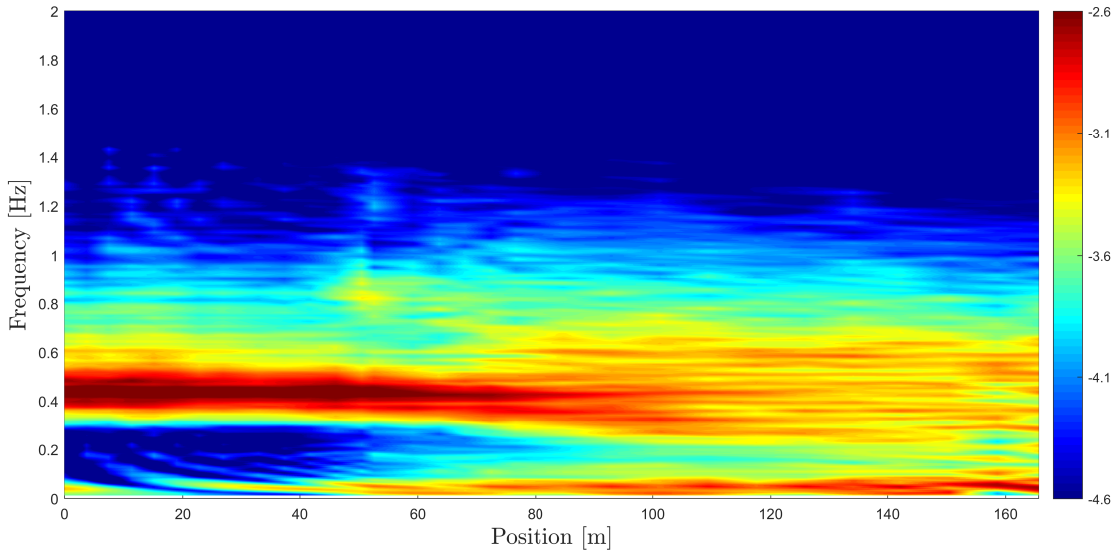

Figure IV.3.12: The spectral spatial evolution of Case 10 for the first 1500 s.

In Fig. (IV.3.13), the different choices of relaxation (absorption) zone lengths are shown. In panel (a) and (b), the dissipation on the low-frequency modes is effective in the Boussinesq-type model, only the lowest frequency around 0.05 Hz accumulates wave energy in the wave flume. Panel (c) and (d) show the better agreement of the emergence of the low-frequency waves as well as their spatial evolution. In panel (d) the major part of the spectrum near the absorption region shows better agreement with the experimental data in Fig. (IV.3.12), whereas, in the other three panels, the wave energy of the major parts of the spectra near the absorption zone is underestimated.

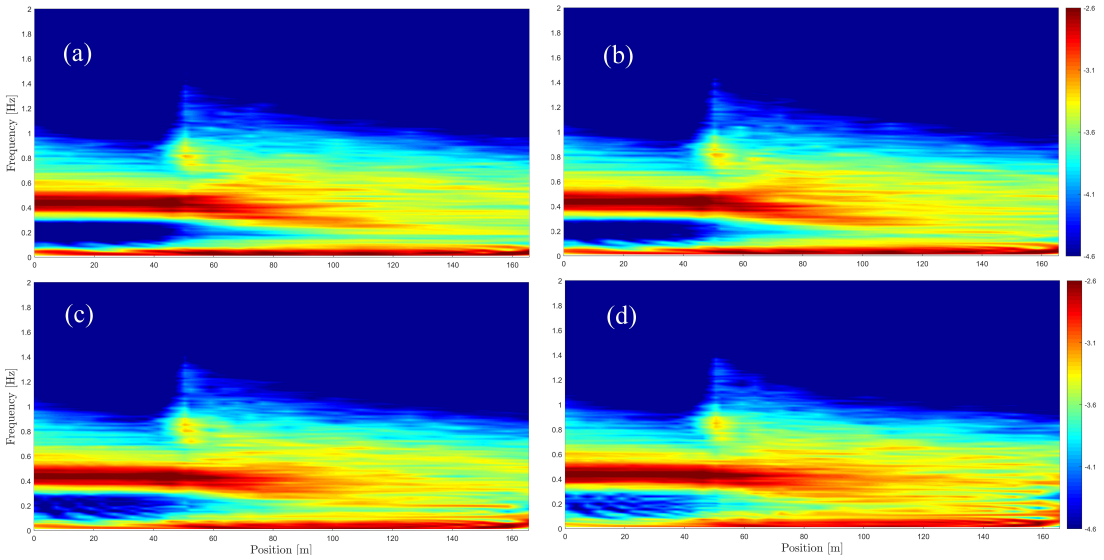

Figure IV.3.13: The spectral spatial evolution of simulations with Boussinesq type model, the absorption zone length is $L_p/2$ in panel (a), L_p in panel (b), $2L_p$ in panel (c), $3L_p$ in panel (d)

The calibration tests of relaxation zone length show the evidence that, the damping of the long waves energy in the experiments was limited. The long waves accumulated wave energy during the experiments. The pattern of the low-frequency range in the experiment is at least qualitatively described by the adopted Boussinesq-type model and also by the Whispers3D model. With the current relaxation zone approach, waves could be properly generated and most of the low-frequency modes could be effectively absorbed. In the experimental cases where the low-frequency waves are of non-negligible energy, a shorter absorption zone can be adopted to model the effects of partial dissipation of long-waves. For Case 10, the absorption zone of one spectral peak wavelength (computed with the deeper water depth) is appropriate to reproduce experimental measurements.

3.2.3 Calibration of overall dissipation

For the simulations of large-scale experiments, it is of the necessity for the inclusion of wave energy attenuation in space. The energy decay is mainly due to the friction effect near the water-wall and water-air interfaces. In both Whispers3D and Boussinesq-type model, the wave energy attenuation is modeled by adding viscous terms in Eqs. (I.2.5) and (I.2.6) in Subsection (2.2). The calibration details of the kinematic viscosity parameter ν_v are given hereafter, and its effects on simulation results are discussed too. The results of the Boussinesq-type model are

shown, the results of Whispers3D show a similar trend.

The tested range of ν_v is $[0.0006, 0.002]$ m^2/s. The agreement between simulated results and measurements is evaluated in terms of two aspects. In the first 100 m near the wavemaker, the agreement in time series is required. However, due to some undesired effects in the open-air flume of THL, small disagreement will evolve and affect the downstream field in a considerable way, so for far-field of the wavemaker, we seek for quantitative agreement of the statistical parameters.

In Fig. (IV.3.14), the comparison between the experimental measurements and the simulated results with different values of the viscosity parameter ν_v is shown. The signals measured at different probes are normalized by the root-mean-square and plotted in two panels. Each of the signals is shifted upward by 10, and backward in time according to the probes positions and the local group velocity. The comparison starts at Probe 12, and previous probes show almost identical results for different values of ν_v because the dissipation is minor for short distance. The effects of dissipation start to show up when waves pass the bottom slope and become more significant as waves propagate over the shallower region. In our case, the simulation results approach to measurements as ν_v decreases. The dissipation affects wave amplitudes and also wave phases (dispersion). In Fig. (IV.3.14), the simulation with $\nu_v = 0.6 * 10^{-3}$ m^2/s shows better agreement in terms of wave profile.

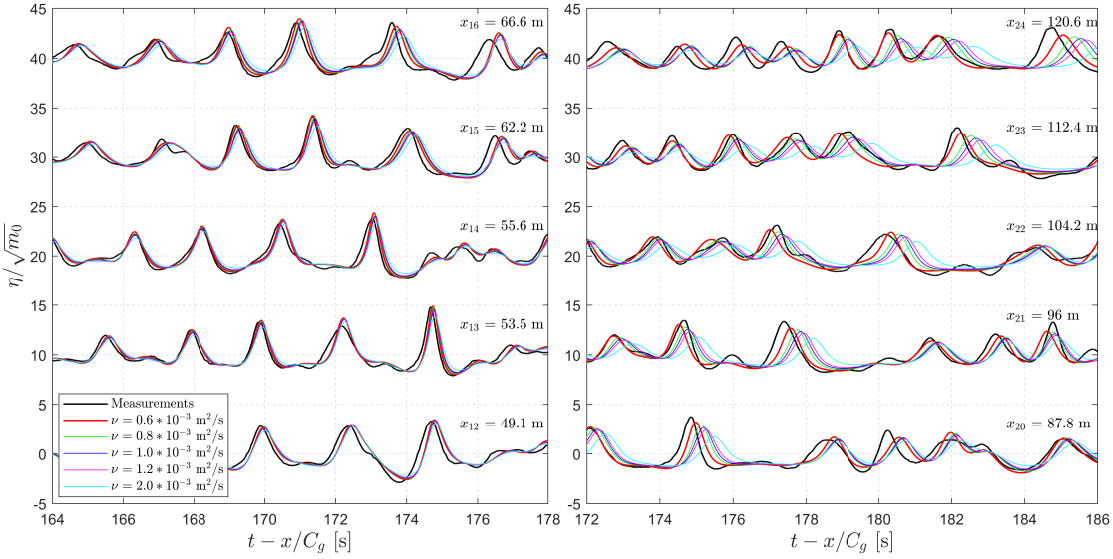

Figure IV.3.14: Wave profile comparison of calibration tests of viscous dissipation parameter ν_v in range $[0.0006, 0.002]$ m^2/s. Black and red lines representing measurements and simulation results with adopted ν_v are bold.

In Fig. (IV.3.15), the statistical parameters of the simulation cases with dif-

ferent ν_v are shown. On the left panels (a), (c), (e) the duration is 500 s, on the other side, panel (b), (d), (f) show the complete simulation (duration 2760 s) taking $\nu_v = 0.6 * 10^{-3}$ m^2/s as the chosen dissipation parameter for Case 10 simulation. The statistical parameters are computed from the wave spectra, including significant wave height H_s, and wave height for particular frequency ranges. The range $[0, 0.2]$ Hz corresponds to the low-frequency infragravity wave part, and $[0.2, 2.5]$ Hz corresponds to the major part of the spectra. It is noticed that the measured wave energy decreases as waves propagate in the wave flume. Especially for the shallower region ($x > 50$ m), since the dissipation rate is related to the local water depth. The significant wave heights H_s decrease in a quasi-linear manner. The simulation results with different ν_v show a similar trend. In panel (a), (c), (e), it is seen that not only the energy decay along the wave flume is quasi-linear but also the viscous dissipation parameter ν_v take effects on the simulated significant wave heights approximately in a linear manner. In panel (b), (d), (f), it is seen that with the chosen value of ν_v, the energy of low-frequency waves is slightly overestimated, but the spatial energy evolution is well predicted. Based on these results, the dissipation was chosen to be $\nu_v = 0.6 * 10^{-3}$ m^2/s.

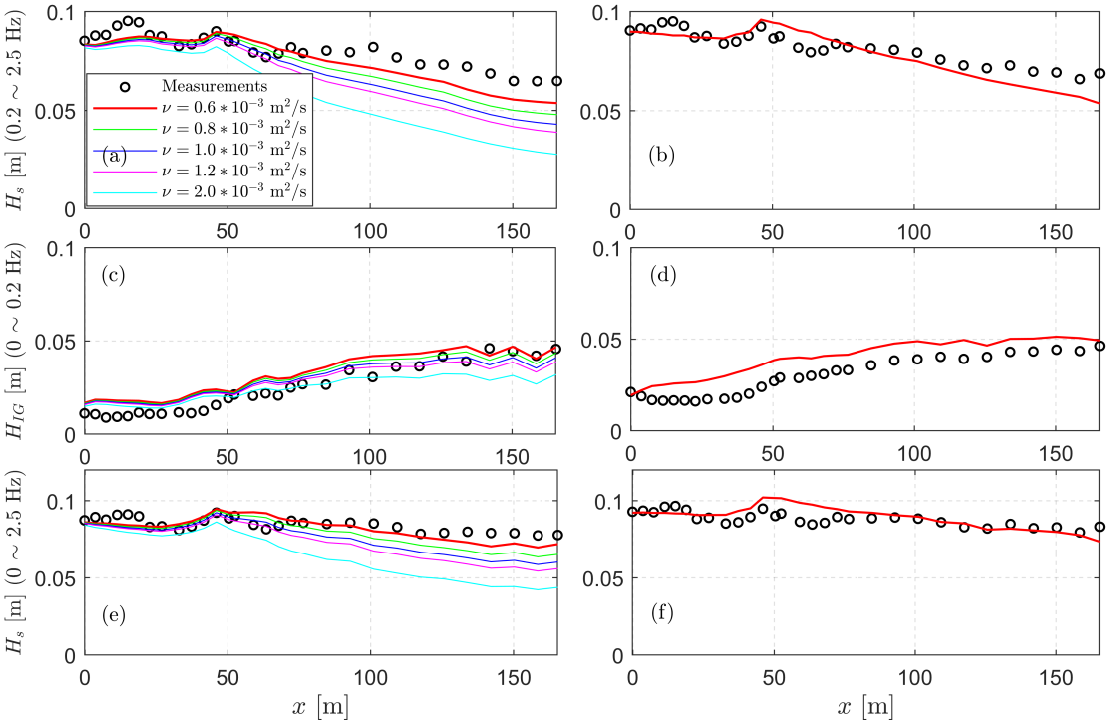

Figure IV.3.15: Wave profile comparison of calibration tests of viscous dissipation parameter ν_v in range $[0.0006, 0.002]$ m^2/s. Black and red lines representing measurements and simulation results with adopted ν_v are bold.

Chapter 4

Long-crested irregular wave train evolution over a submerged bar bottom profile with strong depth transitions (shoaling and de-shoaling)

The paper *Wave-bottom interaction and extreme wave statistics due to shoaling and de-shoaling of irregular long-crested wave trains over steep seabed changes* which is currently under review by Journal of Fluid Mechanics is shown in this Chapter. In this work, we present a numerical investigation using a recently developed fully nonlinear and dispersive model, whispers3D, to investigate the non-equilibrium dynamics and associated statistics of irregular long-crested wave trains propagating over a non-uniform bathymetry which includes both an up-slope (shoaling) and a down-slope (de-shoaling) transition. This work is based on a particular case with strong depth transitions and non-Gaussian behaviour of sea state in a recent experimental campaign, reported recently by Trulsen et al. (2020).

The three main objectives and outcomes of the present study are:

- Demonstrate the capabilities of the proposed numerical modelling approach in representing all the details of the physical mechanisms at play in this situation.

  One particular experiment from Trulsen et al. (2020) is realized in a numerical wave tank, with additional measurements of vertical velocities at the same underwater elevation made in our simulation. The confrontation of measurements and the corresponding simulation results demonstrates the excellent capability of whispers3D for deterministic simulation of irregular non-breaking wave trains of very long duration (equivalent to nearly 5,000

spectral peak periods). This permits a thorough validation of the numerical model as both numerical results and the experimental measurements are analysed in-depth, combining 4 approaches for examining the spatial evolution of the sea state over variable bathymetry: (i) integral sea state parameters (skewness, kurtosis, asymmetry, BFI, etc.), (ii) spectral analysis, (iii) bispectral analysis, (iv) statistical (wave-by-wave) analysis, considering both the distribution of free surface elevation and individual wave heights. To the best of our knowledge a comparison with such a depth of analysis and a level of agreement between experiments and simulations for this type of wave transformation problem has never been reported before.

- Exploit the numerical model to extend the analyses presented in Trulsen et al. (2020).

  This is achieved by considering and analysing the behaviour of other wave characteristics, not measured during the experiments. This allows gaining new insight in the physical processes accompanying wave transformation and a deeper understanding of the physics of wave transformation and the spatial evolution of extreme wave statistics. For instance, we show that the deformations of wave profile take place independently and asynchronously in horizontal and vertical directions, and thus two groups of skewness and kurtosis variables show different statistical features in the transformation process.

- Separate the effects induced by the up-slope and down-slope transitions on wave dynamics and statistics.

  Using the same numerical model, a new comparative case, with the same setup except that the de-shoaling area is replaced with an extended shallower region (i.e. changing from a bar-type to a step-type profile), is investigated to distinguish and assess the effects resulting from de-shoaling. This leads to a clear identification of the effects induced by the down slope transition. Based on a thorough analysis of the results, we find that the de-shoaling affects the up-wave sea state by imposing reflected waves. Besides, the local kurtosis maximum over the down-slope area reported in Trulsen et al. (2020), is proven to result purely from the de-shoaling process.

Wave-bottom interaction and extreme wave statistics due to shoaling and de-shoaling of irregular long-crested wave trains over steep seabed changes

Jie Zhang [1], Michel Benoit†[1]

[1]Aix Marseille Univ, CNRS, Centrale Marseille, Institut de Recherche sur les Phénomènes Hors-Equilibre (IRPHE, UMR 7342), 13013 Marseille, France

(Received xx; revised xx; accepted xx)

The formation of abnormal (extreme) waves in coastal areas can be triggered by wave-seabed interaction, in particular by steep bottom changes. As an incident equilibrium sea-state passes over a submerged step or bar, non-equilibrium dynamics appears locally and forces the sea-state to a new, finite-depth equilibrium along with strong non-Gaussian statistics and intensified occurrence probability of large waves. In this study, the experimental case Run 3 reported by Trulsen et al. [J. Fluid Mech. **882**, R2 (2020)] has been investigated numerically with a fully nonlinear model. Furthermore, as both shoaling and de-shoaling effects exist in the setup with a bar-profile bottom, an additional simulation with a step-profile bottom is performed to isolate the de-shoaling effects. The model is proven excellent by the confrontation of the measurements and simulated results in both time and spectral domains. Strong non-Gaussian behaviour of the sea-state is highlighted after the up-slope transition by combining spectral and bispectral analysis, and characteristic parameters. With a harmonic extraction approach, we show evidence that both second- and third-order effects triggered by the non-equilibrium dynamics significantly enhance the local kurtosis and occurrence of extreme waves. The statistics of kinematics shows the asymmetry of the wave field evolves somewhat independently in horizontal and vertical directions. By comparing the simulations of bar- and step-profile cases, we find the de-shoaling process is responsible for the upstream modulation of nonlinear and dispersive parameters, and the enhancement of kurtosis of both horizontal and vertical velocity and horizontal acceleration over the down-slope area.

Key words:

1. Introduction

In deep-water conditions, abnormal high waves, also called "freak" (or "rogue") waves are frequently explained by the self-modulation property of nonlinear wave trains (Benjamin & Feir 1967; Onorato *et al.* 2005; Toffoli *et al.* 2013). Sudden appearance of these extreme waves can lead to catastrophic consequences (Dysthe *et al.* 2008). As ocean waves propagate toward nearshore areas, they are affected by finite water depth effects and sea bottom variations. The transformation and deformation of sea-states due to non-uniform depth are subject to complex dynamics involving numerous physical processes, including

† Email address for correspondence: benoit@irphe.univ-mrs.fr

shoaling and refraction due to seabed gradients, reflection and diffraction due to islands or seabed irregularities, wave-wave interactions, dissipation due to bottom friction and depth-induced breaking in shallow-water areas (see e.g. Goda 2010).

The propagation of wave trains over strong depth variations is another mechanism for explaining the occurrence of abnormal waves in coastal areas (Kharif & Pelinovsky 2003). In such a situation, the rapid changes of the water depth result in strong modifications to the local wave spectrum, pushing it out of the equilibrium (or near-equilibrium) shape it had offshore. After the depth transition, the sea-state rapidly settles to a new equilibrium compatible with the shallow water depth. The sea-state transition areas could be prone to higher probability of occurrence of extreme waves (see e.g. Trulsen *et al.* 2012; Ma *et al.* 2015; Viotti & Dias 2014; Ducrozet & Gouin 2017). The occurrence probability of these extreme waves can be characterised by statistical parameters of the sea-state, especially kurtosis carrying information on the tail of the statistical distributions of wave crest elevation and wave height (see Janssen 2003; Mori & Janssen 2006). It is thus of interest to investigate the variations of statistical parameters due to rapid depth transitions in coastal areas.

Trulsen *et al.* (2012) reported experiments with long-crested irregular waves propagating over a shoal and showed that local maximum of skewness, kurtosis and an enhanced probability of occurrence of extreme waves could be observed near the end of the slope. Katsardi *et al.* (2013) conducted experimental tests with mild bottom slopes, and concluded that the slope effect can be ignored when the gradient is milder than 1:100. Kashima & Mori (2019) experimentally tested several types of bottom profiles. They suggested that the third-order nonlinearity in the deeper region, where the sea-state is modulationally unstable, provokes aftereffects influencing the downstream sea-state in the shallower region. The amplified extreme waves due to depth changes remain until the surf zone. In the work of Zhang *et al.* (2019), experiments with a sloping bottom were conducted in a large-scale flume, showing similar variation trends of statistical parameters as in Trulsen *et al.* (2012). Strong local triad wave-wave interactions were detected around the end of the slope via Fourier-based bi-spectral analysis. For experiments of uneven bottoms with bar-profile, Ma *et al.* (2015) focused on the parameters including groupiness, skewness, and kurtosis. They found that the appearance of high waves was positively correlated with groupiness. Chen *et al.* (2018) used wavelet-based bi-spectrum to characterise nonlinear triad interactions, showing that nonlinear triad interactions become stronger for steeper slopes.

The local variations of the statistical parameters are related to the significant dynamical responses occurring due to depth changes. Trulsen *et al.* (2020) conducted a series of experiments with a bar-profile bottom with rather steep slopes at both sides. They identified two regimes with different dynamical responses, and showed that the dynamical responses of the sea-states depend on the relative water depth $k_p h$ in the shallower region (where h denotes the water depth and k_p the local peak wave-number). In the so-called "shallower regime" with $k_p h$ being lower than a threshold, significant enhancements of the statistical parameters and the probability of extreme wave occurrence are expected. On the contrary, for waves that enter into a sufficiently deep nearshore zone (the so-called "deeper regime"), the responses of statistical parameters are trivial and do not exhibit large enhancements. The threshold was found to be $k_p h = 1.3$ in their work, but it may vary for different conditions. Trulsen *et al.* (2020) also observed that the local maximum of kurtosis of the horizontal fluid velocity was achieved at a different position from that of the kurtosis of the free surface elevation.

From the modelling viewpoint, Zeng & Trulsen (2012) used the cubic nonlinear Schrödinger equation (NLS) with variable coefficients, to study the influence of variable

bottom profile on the probability of occurrence of extreme waves. In their cases with intermediate water depth and slowly varying bottom, particular patterns of the spatial structure of skewness and kurtosis were identified. Non-equilibrium statistics due to depth transitions may extend beyond the end of the slope. No localised enhancement of statistics over the sloping area was observed, implying the cases considered in Zeng & Trulsen (2012) belong to the "deeper regime". Gramstad *et al.* (2013) used a Boussinesq model with improved linear dispersion properties, while Kashima *et al.* (2014) used a standard Boussinesq model with an artificial correction of nonlinearity to reproduce the experiments of Trulsen *et al.* (2012). Both studies further considered different bottom profiles and observed significant increases of skewness, kurtosis, and probability of occurrence of extreme waves around the end of the sloping bottom areas. Sergeeva *et al.* (2011) studied the dynamical responses of the sea-state over uneven bottom within the framework of the Korteweg-de Vries equation with variable coefficients. They showed that for sea-states with stronger nonlinearity, the dynamical responses are more pronounced. Although these numerical studies insightfully demonstrated the effects of non-equilibrium dynamics due to non-uniform bathymetry, they were inevitably constrained by the limited capability of the approximate models in representing nonlinear and dispersive wave properties over a broad range of relative depth conditions.

Fully nonlinear and dispersive models are therefore of interest in studying the sea-state adaptations due to depth variations. The first study in this path was done by Viotti & Dias (2014) through simulations of the free-surface Euler equations using a spectral method. They showed the non-equilibrium responses in a local region increase for stronger depth variations, resulting in intensified extreme wave occurrence. Ducrozet & Gouin (2017) considered directional sea-states propagating over a sloping bottom with the High-Order Spectral (HOS) method (Dommermuth 2000; Gouin *et al.* 2016), showing the non-negligible influence of the directional spreading on the sea-state dynamics. Zheng *et al.* (2020) adopted a fast multipole boundary element method to simulate the experiments of Trulsen *et al.* (2012), and tested more parameter choices. They discussed the effects of different parameters including wave steepness, relative water depth, and bottom gradient on the length of latency, which is defined as the distance between the end of shoal and the position where skewness and kurtosis reach their maximum. By conducting harmonic extraction with phase-inversion technique, Zheng *et al.* (2020) concluded that the second-order terms are responsible for the local changes of statistical properties. However, with the two-phase technique, the separated 'linear term' is in fact a summation of first-, third-, and higher odd order harmonics. The 'second-order' terms consist of the second-, fourth-, and higher even order harmonics. In their work, no further discussion was made on the possible effects of these ignored harmonics, especially the third harmonic. In the work of Zhang *et al.* (2019), a fully nonlinear and dispersive potential flow code, whispers3D, was adopted and compared with a Boussinesq-type model introduced by Bingham *et al.* (2009). The good agreement with the measurements conducted in a large wave flume demonstrated the high accuracy of whispers3D.

The main objective of the present work is to investigate the non-equilibrium dynamics and associated statistics of irregular long-crested wave trains propagating over non-uniform bathymetry by considering one particular test (Run 3) of the experiments reported in Trulsen *et al.* (2020) (for the sake of brevity, this paper will be referred to as TRJR20, and the chosen case as R3 hereafter). The submerged trapezoidal bar in TRJR20 consists of a rather steep slope at both ends. Our aim is to achieve a better understanding of the non-equilibrium dynamics induced by both shoaling and de-shoaling processes. The effects of the first up-slope transition are discussed on the basis of the in-depth analysis of the original experimental measurements and additional data extracted

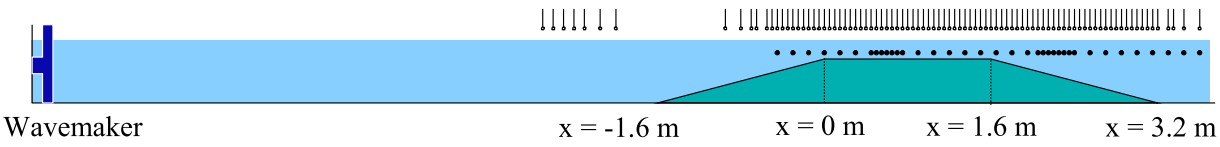

FIGURE 1. Sketch of bottom profile and locations of the wave gauges, adapted from figure 2 of Trulsen *et al.* (2020), and reproduced with permission from Cambridge University Press.

from the simulations. The effects of the de-shoaling area with increasing water depth are analysed by simulating a variation of the R3 case with a step-like profile.

The remainder of this article is laid out as follows. In §2, the configurations of the chosen experimental case of TRJR20 and the numerical modelling approach are recalled. Then in §3, the original R3 case is reproduced with extra information extracted and analysed. In §4, the variation case of R3 with a step-profile is simulated. By comparing with the R3 simulation, the effects of the de-shoaling zone are isolated. In §5, the main findings from this work are summarised, with perspectives for further investigations.

2. Experimental configuration, numerical modelling and analysis methods

2.1. *Experimental setup used by TRJR20*

Details on the description of the experimental facility and tested conditions can be found in the original paper of TRJR20. Here, only their test labelled 'Run 3' is considered, whose data set contains free surface elevation signals measured at 91 locations along the wave flume, and horizontal velocity signals measured at 37 different locations and at an elevation $z_0 = -0.048$ m below the still water level (SWL). The schematic view of the flume is shown in figure 1. It should be noticed that, compared to figure 2 in TRJR20, the origin of the horizontal axis is placed here at the end of the up-slope. We selected this R3 test mainly for two reasons: on the one hand, R3 belongs to the 'shallower regime', with the shoal being shallower than the threshold $k_p h = 1.3$ suggested in TRJR20. The kurtosis of the free surface elevation was enhanced up to 4.2 at the beginning of the shallower flat region in R3, which is the most pronounced amplification among the cases in TRJR20. On the other hand, R3 is the only case with horizontal velocity measurements: this is of interest for a deeper analysis of the wave transformation processes and the validation of orbital velocities computed with the model.

The incident irregular long-crested wave train is generated from a JONSWAP spectrum. The experimental conditions are controlled by four parameters: the water depth h_1 in the deeper flat region, the incident significant wave height $H_{m_0} = 4\sqrt{m_0}$, where m_0 is the zeroth moment of the spectrum, the peak period T_p (or peak frequency f_p) and the peak enhancement factor γ of the JONSWAP spectrum $S(f)$ in the following form:

$$S(f) = \frac{\alpha_J g^2}{(2\pi)^4} \frac{1}{f^5} \exp\left[-\frac{5}{4}\left(\frac{f_p}{f}\right)^4\right] \gamma^{\exp\left[-(f-f_p)^2/\left(2\sigma_J^2 f_p^2\right)\right]}, \tag{2.1}$$

where g denotes the gravitational acceleration, α_J the wave height adjustment factor, and σ_J the spectral asymmetric parameter ($\sigma_J = 0.07$ if $f \leqslant f_p$ and $\sigma_J = 0.09$ if $f > f_p$).

The key parameters of R3 are listed in table 1. The non-dimensional parameters include relative water depth $\mu = k_p h$, steepness $\epsilon = k_p a_c$, and Ursell number $U_r = \epsilon/\mu^3$. The characteristic wave amplitude is $a_c = \sqrt{2}\sigma$, with σ being the standard deviation of the surface elevation: $\sigma^2 = \left\langle (\eta - \langle\eta\rangle)^2 \right\rangle = m_0$, where $\langle\cdot\rangle$ denotes the time-averaging

Run	T_p (s)	γ	Deeper region					Shallower region				
			h_1 (m)	μ_1	H_{m_0} (m)	ϵ_1	Ur_1	h_2 (m)	μ_2	H_{m_0} (m)	ϵ_2	Ur_2
3	1.1	3.3	0.53	1.85	0.025	0.031	0.0049	0.11	0.64	0.025	0.052	0.1918

TABLE 1. Key parameters of the experimental case reported as Run 3 in Trulsen *et al.* (2020).

operator. The non-dimensional numbers are computed and averaged in the first deeper region (marked by subscript 1) and over the shoal crest (marked by subscript 2). Two misprints for μ and Ur in the deeper region were detected in table 1 of TRJR20 and are corrected here. The signals in R3 are recorded over a duration of 90 min (equivalent to about 4,900 waves with period T_p) with a high sampling frequency $f_s = 125$ Hz. No breaking event was reported by TRJR20 during R3 test.

2.2. *Outline of the mathematical and numerical model*

We assume the fluid is inviscid and incompressible, the flow is irrotational and the surface tension is negligible. A two-dimensional Cartesian coordinate system (x, z) is considered. As shown in figure 1, the origin of x-axis along the flume is set at the beginning of the shallower region, and z-axis points upward with $z = 0$ at SWL. The equations governing the fluid motion in a domain with a free surface $z = \eta(x, t)$ and a variable bottom profile $z = -h(x)$ are:

$$\nabla^2\phi = 0 \quad \text{for} \quad -h(x) \leqslant z \leqslant \eta(x,t), \tag{2.2}$$

$$\eta_t + \phi_x\eta_x - \phi_z = 0 \quad \text{on } z = \eta(x,t), \tag{2.3}$$

$$\phi_t + \frac{1}{2}(\nabla\phi)^2 + g\eta = 0 \quad \text{on } z = \eta(x,t), \tag{2.4}$$

$$h_x\phi_x + \phi_z = 0 \quad \text{on } z = -h(x), \tag{2.5}$$

where $\phi(x, z, t)$ denotes the velocity potential, ∇ is the gradient operator ($\nabla\phi \equiv (\phi_x, \phi_z)^T$) and subscripts denote partial derivatives.

The free surface boundary conditions (2.3) and (2.4) are expressed as functions of free surface variables $\eta(x, t)$ and $\tilde{\phi}(x, t) \equiv \phi(x, z = \eta(x, t), t)$, as (Zakharov 1968):

$$\eta_t = -\tilde{\phi}_x\eta_x + \tilde{w}\left(1 + \eta_x^2\right), \tag{2.6}$$

$$\tilde{\phi}_t = -g\eta - \frac{1}{2}\tilde{\phi}_x^2 + \frac{1}{2}\tilde{w}^2\left(1 + \eta_x^2\right), \tag{2.7}$$

where $\tilde{w}(x, t) \equiv \phi_z(x, z = \eta(x, t), t)$ is the vertical component of the velocity at the free surface. To determine the temporal evolution of η and $\tilde{\phi}$, one should evaluate $\tilde{w}$ from $(\eta, \tilde{\phi})$, which is known as the Dirichlet–to–Neumann (DtN) problem. The DtN problem is of fundamental importance for the Zakharov formulation, and various approaches have been discussed (see e.g. Dommermuth 2000; Gouin *et al.* 2016; Madsen *et al.* 2006; Bingham *et al.* 2009; Belibassakis & Athanassoulis 2011; Papoutsellis *et al.* 2018).

In whispers3D, the DtN problem is solved by using a spectral approach in the vertical direction, following Tian & Sato (2008) and Yates & Benoit (2015). This code has been validated for numerous conditions (see Raoult *et al.* 2016; Zhang *et al.* 2019; Simon *et al.* 2019), showing excellent performance for the prediction of wave propagation together with acceptable computational burden. The modelling approach of whispers3D has been presented in Yates & Benoit (2015) and Raoult *et al.* (2016) and is briefly recalled here.

First, a change of vertical coordinate is introduced, with a new vertical variable:

$$s(x,z,t) = \frac{2z + h^-(x,t)}{h^+(x,t)}, \tag{2.8}$$

where $h^{\pm}(x,t) = h(x) \pm \eta(x,t)$. The physical domain in (x,z,t) space with variable bottom and free surface boundaries $z = -h(x)$ and $z = \eta(x,t)$, is mapped into a rectangular domain in (x,s,t) space with two fixed boundaries at $s = \pm 1$.

The nonlinear potential water wave problem (2.2–2.5) is then reformulated in the (x,s,t) space with $\varphi(x,s(x,z,t),t) \equiv \phi(x,z,t)$. Using the set of Chebyshev polynomials of the first kind $T_n(s), n = 0,1,...,N_T$ as an expansion basis for $s \in [-1,1]$, the potential is approximated in the transformed domain as:

$$\varphi(x,s,t) \approx \varphi_{N_T}(x,s,t) = \sum_{n=0}^{N_T} a_n(x,t) T_n(s), \tag{2.9}$$

where the coefficients $a_n(x,t), n = 0,1,...,N_T$, are now the main unknowns.

The approximated potential φ_{N_T} in (2.9) is inserted into the governing equations composed of the Laplace equation, a Dirichlet boundary condition with $\varphi_{N_T}(x, s = 1, t) = \tilde{\phi}(x,t)$ on the free surface, and the bottom boundary condition expressed in the (x,s) domain. This problem is then solved by using the so-called Chebyshev-tau method outlined by Tian & Sato (2008). The spatial derivatives are evaluated using finite difference schemes applied with stencils composed of N_{sten} nodes. The value of N_{sten} is specified by the user to control the order of accuracy. At each time step, the solution of the problem is the set of coefficients $a_n, n = 0,1,...,N_T$ at each abscissa. With these a_n coefficients, the horizontal velocity $u = \phi_x$ and the vertical velocity $w = \phi_z$ can be evaluated as:

$$u(x,z,t) \approx \frac{\partial \varphi_{N_T}}{\partial x} + \frac{\partial \varphi_{N_T}}{\partial s}\frac{\partial s}{\partial x} = \sum_{n=0}^{N_T} a_{n,x} T_n + \frac{h_x^- - s h_x^+}{h^+} \sum_{n=1}^{N_T} a_n T_{n,s}, \tag{2.10}$$

$$w(x,z,t) \approx \frac{\partial \varphi_{N_T}}{\partial s}\frac{\partial s}{\partial z} = \frac{2}{h^+} \sum_{n=1}^{N_T} a_n T_{n,s}. \tag{2.11}$$

At the free surface, $\tilde{w}$ is obtained by taking $s = 1$ in (2.11), and the DtN problem is solved. To march equations (2.6–2.7) in time, an explicit Strong-Stability-Preserving third-order Runge–Kutta (SSP-RK3) scheme (Gottlieb 2005) is used. In whispers3D, no particular assumption is made on the level of dispersion or nonlinearity of the wave train. Furthermore, no extra assumption on the bottom profile is required. The model is thus considered powerful in describing wave dynamics over arbitrary variable bottom profiles. One can balance accuracy and efficiency via a proper choice of the parameters N_T, N_{sten}, and numerical step sizes in space (Δx) and time (Δt). The incident wave train is imposed on the left boundary of the numerical tank and damped on the right boundary using the relaxation zone technique (Bingham & Agnon 2005). Linear wave-making theory is used, which is applicable for the present study as justified in the next subsection.

2.3. *Numerical setup and solution validation*

The effective computational domain, excluding the two relaxation zones, is 6.3 m long, from $x = -2.7$ m to 3.6 m. The generation zone ends at $x = -2.7$ m, i.e. at the position of the first wave probe. The measured signal at this probe was imposed as the incident wave train in the simulations. The relaxation zones are 5.4 m long each, which is roughly

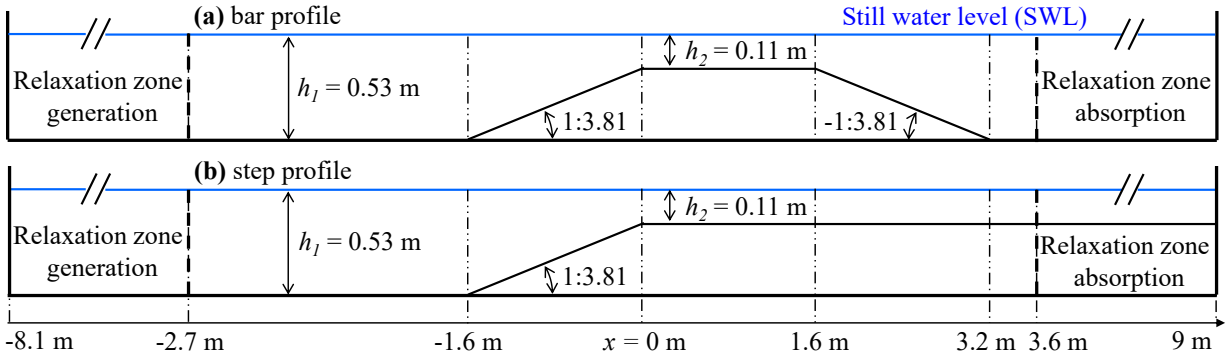

FIGURE 2. Sketch of model setup and bottom profiles adopted in simulations with whispers3D, (*a*) R3-bar profile (identical to the experiment of TRJR20) and (*b*) modified R3-step profile without de-shoaling area.

3 peak wavelengths in the deeper region. In figure 2, the schematic view of the numerical wave tank for the original R3-bar case is shown in panel (a), and its variation for the R3-step case in panel (b).

The simulations lasted 90 min, as in the experiment. After a convergence study on space and time discretizations (not shown here), $\Delta x = 0.01$ m and $\Delta t = 0.01$ s were selected. With this choice, the Courant–Friedrichs–Lewy number, defined as $\mathrm{CFL} = L_p \Delta t/(T_p \Delta x)$, is approximately 1.64 in the deeper region and 0.97 in the shallower region. Similarly, convergence tests showed that $N_T = 7$ and $N_{sten} = 5$ provide high accuracy.

The variance density spectra of both measured and simulated free surface elevation at probe 1 ($x = -2.7$ m) are shown in figure 3, with the target JONSWAP spectrum of R3 experiment superimposed as reference. The spectrum measured at probe 1 ($x = -2.7$ m) is similar to the target spectrum specified to drive the wave-maker (located at $x = -12.38$ m), with no super-harmonic peaks (i.e. at $2f_p$, $3f_p$, etc.) appearing in the spectrum. It indicates that nonlinear wave-wave interactions remained weak for waves propagating from the wave-maker to probe 1. In figure 3(b), wave energy in the low-frequency (LF) range, defined by $f \in [0, 0.5f_p]$, can be observed in the measured spectrum, but the energy level is very low. The generation of LF modes could be related to wave-wave interactions, intrinsic modes of the flume, and reflected waves which are not effectively damped in the experiment. The low energy level of LF modes at probe 1 indicates that the absorption of the wave energy in the experiment was rather effective in the LF range and that the natural modes were not markedly excited. Such observations support the application of linear wave-making theory to simulate the R3 case.

The measured signal at probe 1 was decomposed into 38,588 harmonic components in the range $[0.4f_p, 5f_p]$. By using linear superposition of these components, the driving signals were computed at left end of the domain and at nodes located in the generation zone. The good agreement between the simulated and measured spectra at probe 1, shown in figure 3, confirms the validity of the linear wave generation method. Only some minor differences are observed, i.e. the magnitude of the spectral peak seen in figure 3(a) and the amplitudes of LF modes in figure 3(b). The former is acceptable because the slight overestimation of the simulated spectral density is limited to a very narrow range $[0.95f_p, 1.05f_p]$, but the averaged energy in a slightly broader range $[0.9f_p, 1.1f_p]$ shows similar values for both spectra. The latter differences are of secondary importance since the LF energy in both simulation and experiment is very low compared to the main part of the spectrum.

The submerged bar provokes some reflection of the incident wave train. As no indication of reflection intensity given in TRJR20, a reflection analysis was undertaken here, using

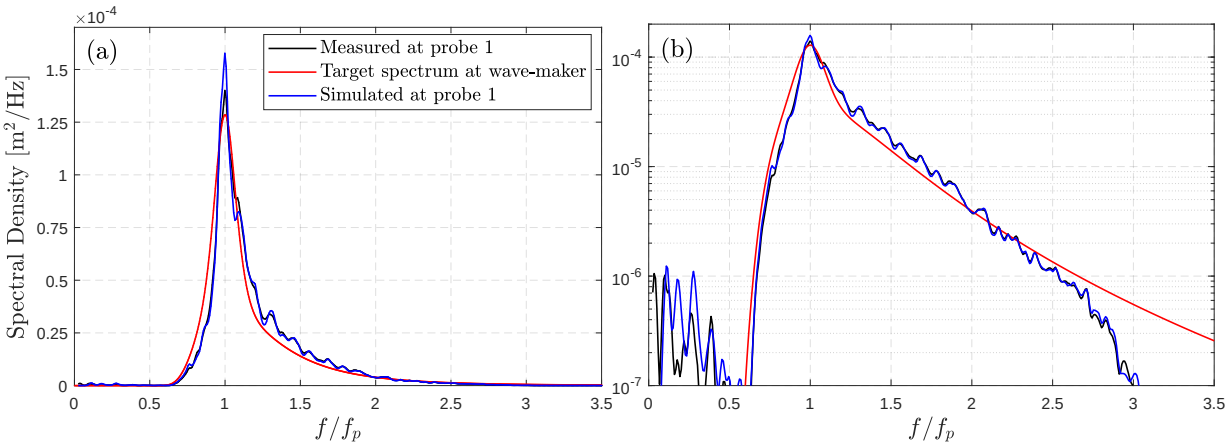

FIGURE 3. Incident variance spectral density of free surface elevation at probe 1 ($x = -2.7$ m) shown in both linear scale (panel a) and logarithmic scale (panel b). As a reference, the target JONSWAP spectrum imposed at the wave-maker ($x = -12.38$ m) in the experiment is superimposed.

an extension of the least square method of Mansard & Funke (1980) applied to the first 7 probes, located before the submerged bar, from $x = -2.7$ m (probe 1) to -2.0 m (probe 7). Note that the spatial arrangement of these probes is not optimal for the reflection analysis: for probes 1-5, the distance between two successive probes is 0.10 m, for probes 5-7, it is 0.15 m. The spectral variations of the reflection coefficient $C_r(f)$ for each frequency component f could nevertheless be assessed for both the experiment and simulation of R3 case. The analysis showed that $C_r(f)$ takes values below 10% in the most energetic range around the peak frequency ($0.75 < f/f_p < 1.5$), with very good correspondence between experiment and simulation. For $f > 1.5f_p$, experimental values of $C_r(f)$ are slightly larger than the ones from the simulation. Below $0.75f_p$, $C_r(f)$ takes larger values, confirming that longer waves are more prone to reflection, but the agreement between experiment and simulation remains quite good. Representative values of the reflection coefficient, defined as $\bar{C}_r = H_{m0,ref}/H_{m0,inc}$ with subscripts 'ref' and 'inc' representing reflected and incident respectively, are 8.9% for the experiment and 6.8% for the simulation. It indicates that the reflection is low (below 10%), in both experiment and simulation.

It should be mentioned that dissipation is not considered in the current simulations. Due to the limited size of the effective computation domain, the differences resulting from dissipation are meant to be of secondary significance. The simulated velocity components are recorded at the same positions as for the horizontal ones in R3 experiment.

To demonstrate qualitatively the high fidelity of the simulation, snapshots of the normalised measured and simulated free surface elevation signals are compared at 16 positions along the wave flume in figure 4. The time window, covering the last 30 s of the run, is shifted according to probe positions and the local group velocity $C_g(f_p) = \mathrm{d}\omega/\mathrm{d}k$. It can be seen that the agreement between the simulation and measurements is excellent all over the domain, even after running nearly 90 min of simulation. Only some minor differences are observed. A small phase shift develops for some waves as they propagate towards the end of the flume: the simulated signal gradually moves ahead of the measurements. This could be explained by the ignored dissipation effect in the simulation: without dissipation, the simulated sea-state is of slightly higher energy, with some waves having slightly larger amplitudes. Due to nonlinear dispersion, the phase and group velocity are larger for waves with higher amplitudes, resulting in this small phase shift with the measurements.

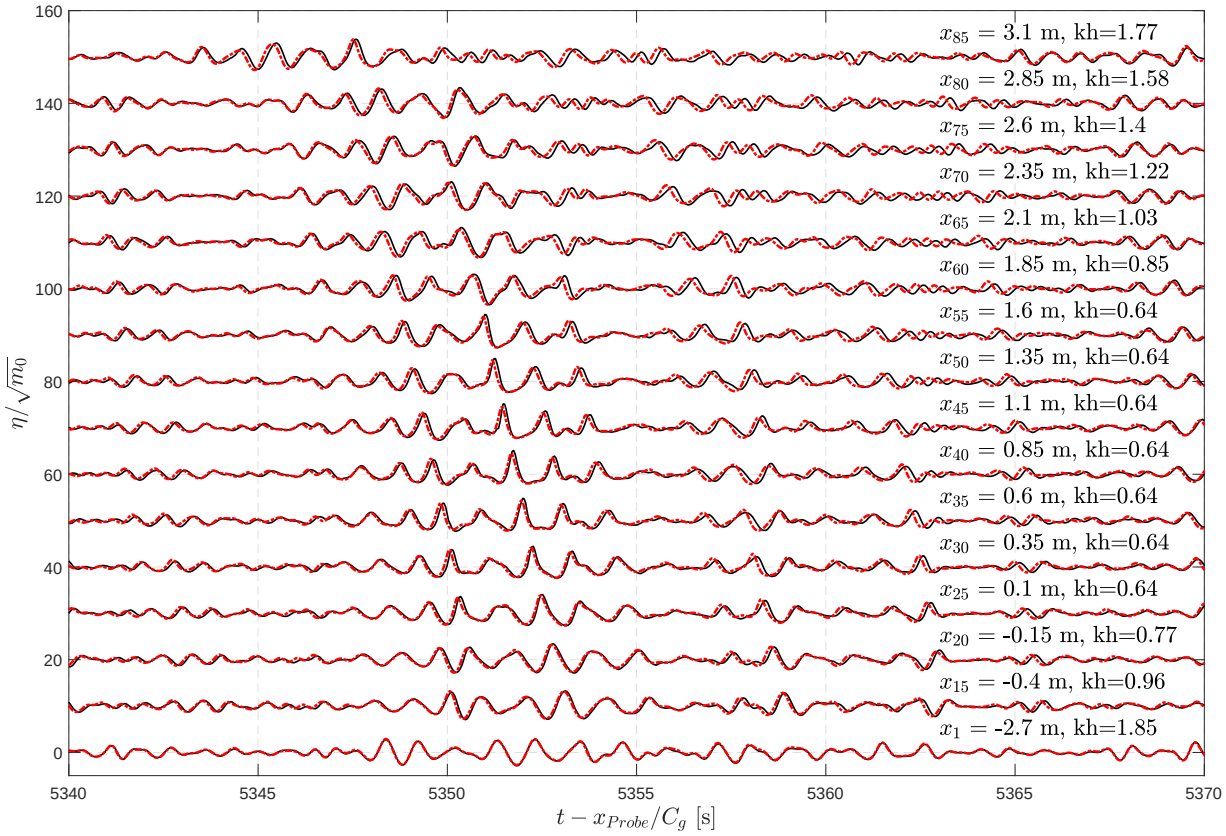

FIGURE 4. Comparison between experimental measurements (black solid lines) and numerical simulation (red dashed lines) of the normalised free surface elevation recorded at 16 positions along the wave flume (probe positions and the corresponding local relative water depths are indicated above each curve). Each of the time series is shifted vertically with an offset of 10 for the sake of clarity.

2.4. *Statistical, spectral and bispectral analysis approaches*

To analyse the wave transformation processes, four conventional analysis approaches are applied: (i) analysis of characteristic wave parameters, (ii) spectral (Fourier) analysis, (iii) bi-spectral (Fourier-based) analysis, and (iv) statistical analysis. Since these analysis techniques are commonly used, the formulations and definitions of notations are reported in appendix A, and we mention below only specific aspects.

Regarding (i), eight non-dimensional parameters are selected to characterise the spatial evolution of the sea-state. The nonlinearity is characterised by the normalised significant wave height $H_{m_0}/H_{m_0,inc}$, steepness parameter $H_{m_0}/\hat{L}_p$ (where $\hat{L}_p$ is the wavelength related to the peak frequency $\hat{f}_p$ evaluated with the method of Young (1995), see (A 3)), skewness λ_3 and kurtosis λ_4 of several kinematic variables (free surface elevation, orbital velocities and accelerations), and the asymmetry parameter computed from bispectrum. The subscript 'inc' denotes the incident wave characteristic given in table 1. The dispersion parameters include the peakedness parameter Q_p, and the normalised local peak frequency $\hat{f}_p/f_{p,inc}$. As a balance of nonlinearity and dispersion, the Benjamin–Feir (B–F) index is considered, with two definitions BFI_{S06} and B_s applicable for different relative depth conditions. The parameter definitions and related formulations are provided in appendix A.1 Regarding (iii), the bispectral analysis includes both bispectrum $B(f_1, f_2)$ and bicoherence $b^2(f_1, f_2)$. The spectral and bi-spectral analysis approaches are described in appendix A.2 Regarding (iv), the statistical distributions of crest-to-trough wave heights H and free surface elevation η are considered to characterise

the deviation of the sea-state from the Gaussianity. The experimental and simulated distributions are compared with the Gaussian distribution for η and the theoretical model of Boccotti (2000) for H. The distributions of η and H are given in appendix A.3.

2.5. *Harmonic separation method*

In addition, a harmonic separation method is adopted here. The idea of group inversion allows decomposing the wave group into fundamental components, and was first adopted by Baldock *et al.* (1996) to study focused wave groups in deep-water. Assuming the time record of, for instance, free surface elevation or wave-induced load on a structure can be approximated by a Stokes-like harmonic series in both frequency and wave steepness, then the higher-order nonlinear contributions to the time record can be separated by using a so-called 'phase-inversion' method. This method requires two tests (either experimental or numerical) using two incident wave trains with identical component amplitudes and frequencies but phases shifted by π. The underlying assumptions of this method are twofold: the existence of a generalised Stokes-type harmonic series expansion in both frequency and wave steepness, and the validity of Stokes's perturbation expansion up to the target order. This method has been applied to study wave-body interactions in uniform water depth (Zang *et al.* 2006, 2010; Fitzgerald *et al.* 2014) and shoaling waves on variable bottom profiles (Borthwick *et al.* 2006; Zheng *et al.* 2020).

The phase-inversion method is however limited by its capacity in distinguishing n-th and $(n+2)$-th order harmonics in a wave group. Especially at higher orders, the overlap between them could occur over a range of frequencies, and it is difficult to separate them accurately with digital filters. In this study, the harmonic separation is achieved with a generalised phase-inversion method recently introduced by Fitzgerald *et al.* (2014), using four phase shifts. The linear primary component and the first three super-harmonics (up to fourth order) can be isolated with linear combinations of four time-histories. The method is here applied to the numerical simulations (as experimental time series are available for a single set of phases). These time-histories come from four whispers3D simulations with the incident signals having the same amplitudes and frequencies but shifted phases, namely 0, $\pi/2$, π, and $3\pi/2$. The linear combinations of time-histories and separated harmonics are as follows:

$$\eta_{1st} = \left(\eta_0 - \eta^H_{\pi/2} - \eta_\pi + \eta^H_{3\pi/2}\right)/4 = \eta^{(1,1)} + \eta^{(3,1)} + \text{h.o.t.}, \tag{2.12}$$

$$\eta_{2nd} = \left(\eta_0 - \eta_{\pi/2} + \eta_\pi - \eta_{3\pi/2}\right)/4 = \eta^{(2,2)} + \eta^{(4,2)} + \text{h.o.t.}, \tag{2.13}$$

$$\eta_{3rd} = \left(\eta_0 + \eta^H_{\pi/2} - \eta_\pi - \eta^H_{3\pi/2}\right)/4 = \eta^{(3,3)} + \text{h.o.t.}, \tag{2.14}$$

$$\eta_{4th} = \left(\eta_0 + \eta_{\pi/2} + \eta_\pi + \eta_{3\pi/2}\right)/4 = \eta^{(2,0)} + \eta^{(4,4)} + \text{h.o.t.}, \tag{2.15}$$

where the subscripts 0, $\pi/2$, π, $3\pi/2$ denote the applied phase shift, the superscript H denotes harmonic conjugate of the signal computed via Hilbert transform. For the separated harmonic components $\eta^{(m,n)}$ on the right-hand-side, the first index m in the superscript denotes the power in amplitude, and the second index n the order of harmonic. The higher-order terms with fifth- and higher-order in amplitudes are omitted and represented by 'h.o.t.'. Note that in (2.15) both the fourth-order harmonic $\eta^{(4,4)}$ and second-order difference harmonic $\eta^{(2,0)}$ appear. As the overlap between these two components is very limited, a simple low-pass filter can be applied to separate them.

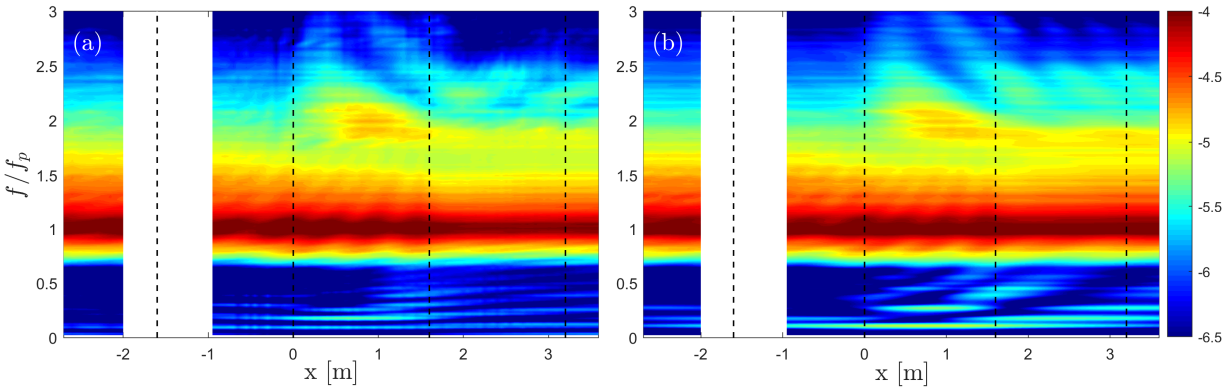

FIGURE 5. Colour maps showing the spatial evolution of variance density spectrum of the free surface elevation of Run 3 calculated from: (a) measurements and (b) simulation results. The vertical dashed lines indicate the limits of the sloping bottom areas, located at $x = -1.6$ m, 0 m, 1.6 m, and 3.2 m.

3. Comparison of simulations and experiments for Run 3 and analysis of wave transformation processes

In this section, a comprehensive comparison between the simulations and measurements of R3 is presented based on the analysis approaches presented in §2.4 (and appendix A) and §2.5. From the simulation results, we extract the same set of data (time-series of η and $u(z_0)$) as recorded during the R3 experiment. Moreover, extra information was gathered, including the vertical velocity and the evolution of phase-shifted incident wave trains. In addition to the comparison of free surface elevation in figure 4, more pieces of evidence are needed to illustrate the capacity of the model to capture the dynamics of waves as they propagate along the wave flume. We also aim at better assessing the non-equilibrium dynamics due to the depth transitions.

3.1. *Spatial evolution of wave spectrum*

The spatial evolution of measured and simulated wave spectra is shown in figure 5. The area with no measurement between probes 7 ($x = -2$ m) and 8 ($x = -0.95$ m) is intentionally left blank. It can be seen that the measured spectrum in figure 5(a) and the simulated one in figure 5(b) are in good agreement. Both show clearly the enhancement of second-order harmonics in the frequency range $[1.5f_p, 2.5f_p]$ over the shallower region. The energy level of the spectral peak at f_p in the measured spectrum is gradually attenuated in space, whereas this level is more or less unchanged in the simulated spectrum. This is speculated to be a consequence of the dissipation which is not considered in our simulation. The dissipation is more effective in the frequency range near the spectral peak than in the high-frequency range. In the LF range $[0, 0.5f_p]$ of both simulated and measured spectra, some long-waves appear, especially after the up-slope area. The long-waves are of slightly higher energy in the simulation as shown in figure 5(b). As discussed in §2.3, the long-waves observed in both panels (a) and (b) of figure 5 are considered to originate from nonlinear wave-wave interactions. It is therefore considered the slight overestimation of the LF energy in figure 5(b) results from stronger nonlinear interaction due to a more energetic spectral peak in the simulation after the up-slope area.

In figure 6, a more detailed comparison of the spectra measured at eight positions is shown to demonstrate the spectral evolution along the wave flume. Figure 6(a) shows the wave train propagates over the deeper region with very limited changes in the main part of the spectrum ($0.5f_p < f < 3f_p$), indicating the nonlinear wave-wave interactions

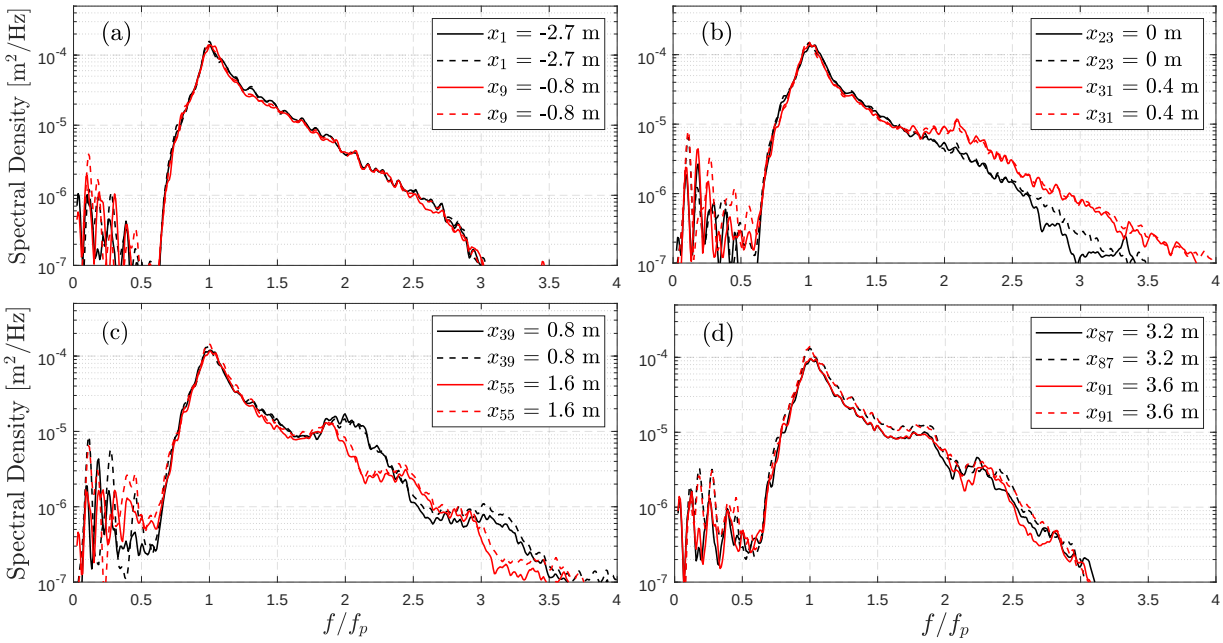

FIGURE 6. Comparison of variance density spectra of surface elevation in different areas: (a) the deeper region till the toe of the up-slope; (b) the beginning of the shallower region; (c) the end of the shallower region; (d) deeper region after de-shoaling. In all the panels, the solid lines represent measurements, and dashed lines are simulation results.

are weak in this range. As the wave train propagates in the shallower region, the waves with frequencies higher than $2f_p$ receive energy in a short distance (figure 6(b)). In figure 6(c), at half-length of the shallower region ($x = 0.8$ m), secondary spectral peaks around $2f_p$ and $3f_p$ manifest. As the wave train approaches the end of the shallower region (from probe 39 to 55), the secondary peaks around $2f_p$ and $3f_p$ are shifted toward lower frequencies. In figure 6(d), the spectrum measured at probe 91 ($x = 3.6$ m) has some similarities with the spectrum measured at probe 1 ($x = -2.7$ m), but the secondary peaks close to $2f_p$ and $3f_p$ do not completely vanish. It indicates the spectral changes resulting from a shoaling area are not fully reversible by setting a symmetrical de-shoaling area due to nonlinear effects. The predictions of whispers3D are seen to be very accurate over a wide frequency range for all spectra shown in figure 6.

3.2. *Evolution of non-dimensional parameters*

In figure 7, the spatial evolution of twelve non-dimensional parameters is shown in eight panels. For all these parameters, the agreement between the experiment and the simulation is excellent. In figure 7(a), the spatial evolution of two normalised significant wave heights corresponding to the components in frequency range $[0, 0.5f_p]$ (LF waves) and $[0.5f_p, 0.5f_s]$ (short waves) are shown. For the short-wave H_{m_0}, small spatial oscillations over the shoal crest can be observed in both experiment and simulation. In the experiment, the H_{m_0} of short waves is attenuated in the shallower flat region (dark grey zone) but almost holds as constants at other locations. The small decrease of H_{m_0} is attributed to the dissipation in the experiment. It is evident that the dissipation is related to the relative water depth, so we speculate that the dissipation in the experiment was mainly induced by friction on the bottom and side-walls. The H_{m_0} for LF waves keeps its low level over all the domain. In figure 7(b), the similar pattern of oscillation of the steepness parameter in the shallower flat region as for H_{m_0} is observed. The increase of the steepness parameter over the up-slope is more pronounced than that of H_{m_0}, since the local peak wavelength is reduced due to shoaling.

In figure 7(c), the evolution of the skewness of the free surface elevation $\lambda_3(\eta)$ and the horizontal velocity $\lambda_3(u(z_0))$ show similar increasing and decreasing trends over the domain. Their maximum and minimum values are achieved roughly at the same positions, both located shortly after the change of bottom gradient (maximum at $x \approx 0.6$ m, and minimum at $x \approx 2.3$ m). The skewness indicates the asymmetry of the probability distribution of the considered variable. For η, a positive skewness indicates waves with sharper crests and flatter troughs, and vice-versa for negative values. According to $\lambda_3(\eta)$, the wave profile is nearly symmetric in the first deeper region and becomes asymmetric with positive skewness over the shallower region. As the wave propagate over the down-slope area, the asymmetry of the wave profile is rapidly inverted. The evolution is similar for the profile of $\lambda_3(u(z_0))$.

In figure 7(d), the values of $\lambda_4(\eta)$ in both experiment and simulation are slightly larger than 3 before the bar. Then, they rapidly increase in the area close to the end of the up-slope, achieving their maxima at the same position as for the skewness. The length of latency is found to be about half of the peak wavelength in the shallower region. Then, $\lambda_4(\eta)$ decreases mildly in a larger area, and eventually goes back to 3 around the end of the domain. No particular change of $\lambda_4(\eta)$ is observed in the de-shoaling area. The evolution trend of $\lambda_4(\eta)$ is well captured by the numerical model, though the maximum value of $\lambda_4(\eta)$ is slightly underestimated by 6%. As was observed in TRJR20, $\lambda_4(u(z_0))$ exhibits a very different behaviour: it does not show any noticeable enhancement over the up-slope area nor over the bar crest, but reaches its maximum value after a short distance in the de-shoaling area. Such behaviour of $\lambda_4(u(z_0))$ is well simulated, including its maximum value.

In figure 7(e), the evolution of the asymmetry parameter is shown. Positive values indicate that, in general, waves are leaning toward the wave-propagation direction, whereas, negative values indicate waves are leaning to the opposite direction. The evolution of asymmetry parameter indicates that the incident waves are almost symmetrical in the horizontal direction for $x < -1$ m. As waves propagate over the bar, the general wave profile leans backward first, and then forward. The most backward-leaning wave profile is achieved in the shallower flat region, and the most forward-leaning profile in the de-shoaling area. We note the largest asymmetry of the sea-state in horizontal direction is achieved before $\lambda_3(\eta)$ takes its maximum and minimum values. This implies the deformations of wave shape in horizontal and vertical directions are largely independent.

Figures 7(f) and 7(g) show that Q_p and $\hat{f}_p$ evolve in an oscillatory manner until the end of the shallower region. After that, the changes of these two parameters are very limited. The evolution of Q_p is remarkably well simulated (figure 7(f)). For $\hat{f}_p$ in figure 7(g), the agreement between the experiment and simulation is also good. The peak frequency is only underestimated, by a few percent at most, in the simulation. By and large, the spectral changes in terms of the spectral width and peak frequency are quite limited.

In figure 7(h), the spatial evolution of the two forms of the B–F index (A 5) and (A 12) is shown in logarithmic scale. In the present case, the threshold $k_p h = 1.363$ for modulation instability is achieved at $x = -0.95$ m and 2.55 m. At these two positions, two forms of the B–F index take 0 because the coefficient $\sqrt{|\beta|/\alpha} = 0$ at this threshold relative water depth (see the expressions of α and β in (A 8) and (A 9)). Between these abscissas, waves are expected to be modulationally stable, both BFI_{S06} and B_s no longer indicate the significance of modulation instability but only characterise the relative importance of nonlinearity and dispersion. Both formulations show significant variations over the up- and down-slopes with similar spatial profiles. The variations of BFI_{S06} and B_s in the modulationally stable area are large compared to those in the unstable area. Such a significant difference is also due to the property of the coefficient $\sqrt{|\beta|/\alpha}$. It monotonically

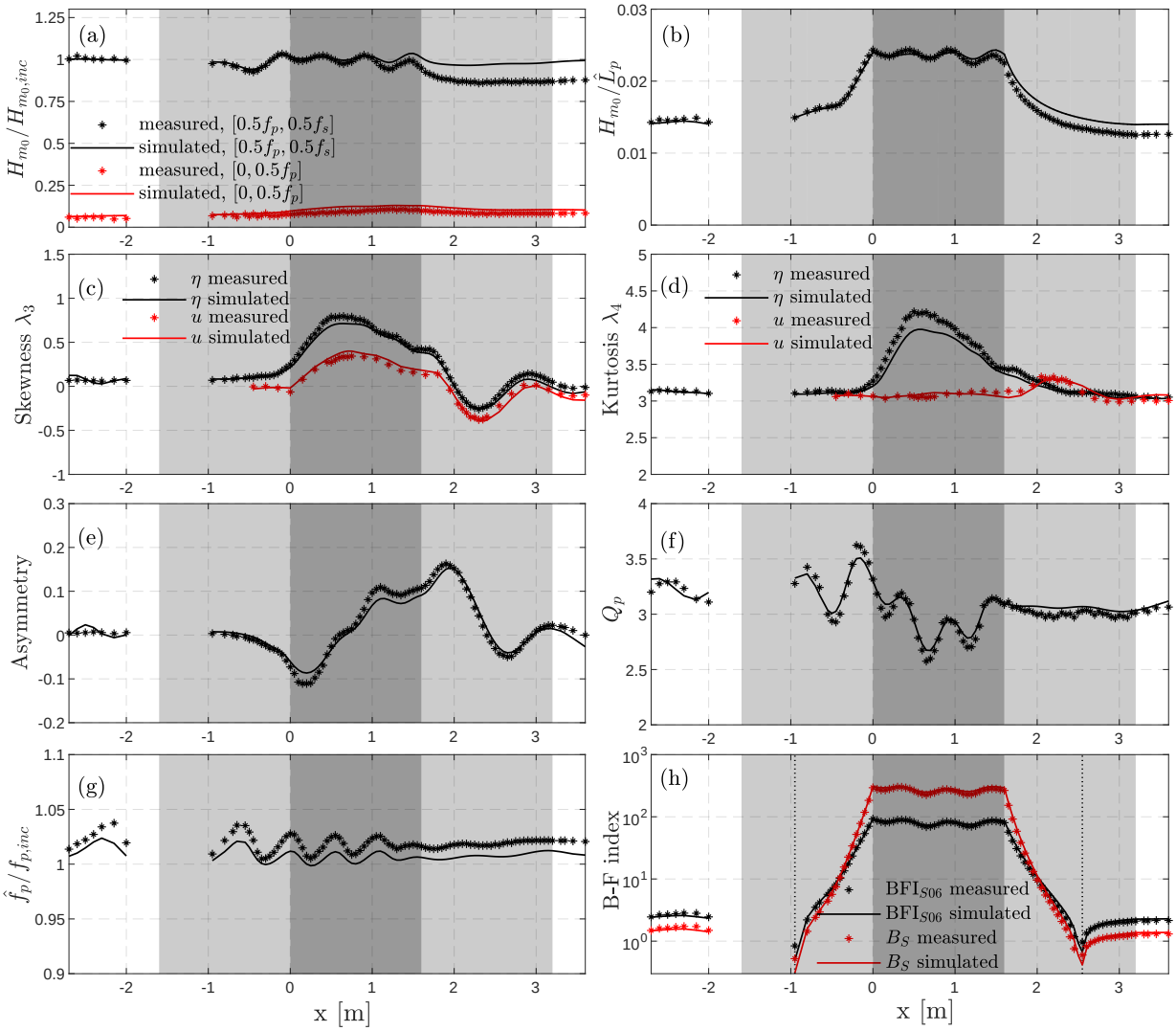

FIGURE 7. Spatial evolution of non-dimensional wave parameters in measurements (∗) and in simulations (solid lines) of R3. The light grey zones indicate the sloping areas and the dark grey zone indicates the shallower flat region. In panel (h), the vertical dash lines denote the positions where the threshold $k_p h = 1.363$ for modulational instability is achieved.

increases from 0 to 1 for $k_p h \geqslant 1.363$, but increases exponentially as $k_p h$ decreases from 1.363 to 0. The magnitude of B_s is higher than that of BFI_{S06} over the shallower region, due to the correction of the wave-induced mean flow. In line with the evolution of H_{m_0} and steepness parameter, the evolution trend changes right after the transition points of bottom gradient for B–F index. It means the change of nonlinearity due to depth variations is more significant than that of the dispersion, and the changes stop immediately when waves enter flat bottom regions.

3.3. *Bispectrum and bicoherence*

Bispectral analysis of η time series allows gaining insight on nonlinear wave coupling between modes. In figures 8 and 9, we show the bicoherence for the relative strength of nonlinear coupling and imaginary part of the bispectrum for the energy transfer direction, in the area from 0.25 m to 1.3 m (over the shallower region). In this area, the skewness and kurtosis vary significantly, with their maximum values achieved at $x \approx 0.6$ m. It indicates the most active nonlinear interaction takes place in this area. Each panel contains the bispectrum from measurements in the lower right triangle and

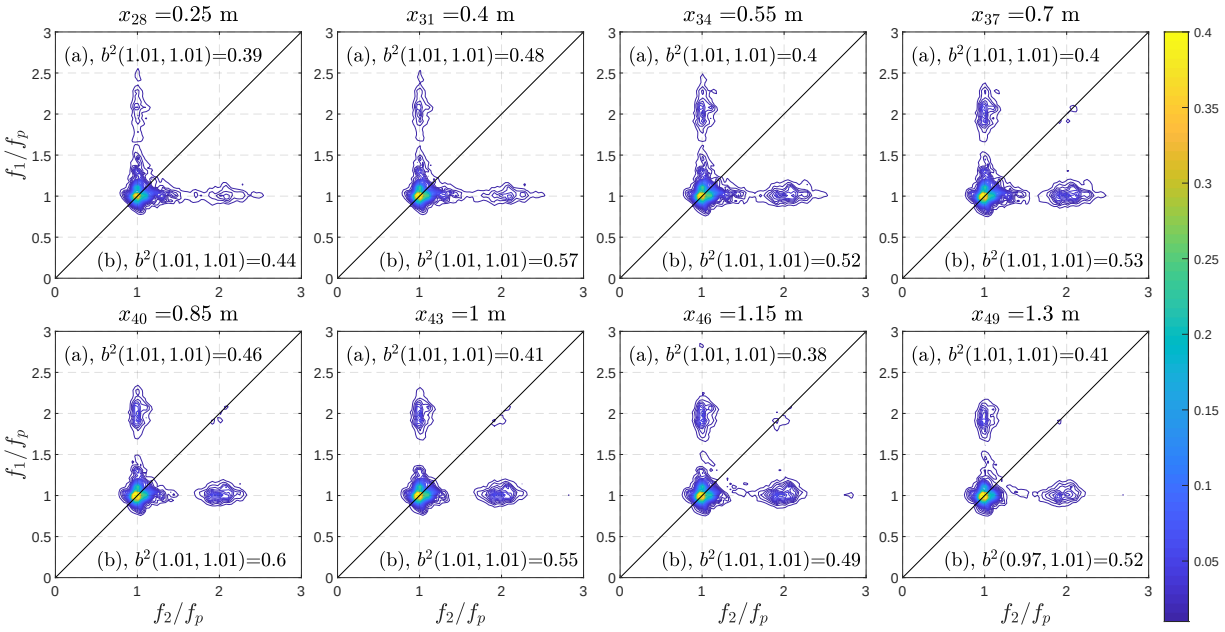

FIGURE 8. Contours of bicoherence over the shallower region at eight probe positions between $x = 0.25$ m (probe 28) and $x = 1.3$ m (probe 49), in (a) simulated results; (b) measurements. The probe numbers and positions are indicated on each panel, together with the corresponding maximum bicoherence values.

the bispectrum from simulation in the upper left triangle (so that the agreement between them can be estimated from the symmetry about the line $f_1 = f_2$).

From the evolution of bicoherence b^2 shown in figure 8, we note the strongest interaction always takes place in the region near the spectral peak. The strongest coupling achieved at $b^2(1.01f_p, 1.01f_p)$ reflects intense energy transfer among $f_1 = 1.01f_p$, $f_2 = 1.01f_p$, and $f_1 + f_2 = 2.02f_p$. This interaction corresponds to the development of the second harmonics around $2f_p$ in the spectrum. A less strong but clearly visible interaction takes place around $b^2(2f_p, f_p)$, which becomes increasingly significant as waves propagate from $x = 0.25$ m to 1.3 m. It corresponds to the development of the third harmonics around $3f_p$. More generally, we notice the non-zero bicoherence in the range between $b^2(f_p, f_p)$ and $b^2(2f_p, f_p)$ from probe 28 to 34, which indicates that the harmonics with frequencies $2f_p \leqslant f \leqslant 3f_p$ are involved in the interactions. This is in agreement with the observations in figure 6(b) where a clear increase is noticed for the whole tail of the spectrum above $2f_p$ at probe 31. After some distance, non-zero values of b^2 appear only around $b^2(f_p, f_p)$ and $b^2(2f_p, f_p)$ resulting in the formation of second and third harmonics. In the simulation, not only the components of the nonlinear interactions but also the levels of bicoherence are well predicted for the listed probes.

In figure 9, the energy transfer direction can be inferred, by considering the imaginary part of the bispectrum. Positive values indicating sum interactions are represented by colours from green to red. Meanwhile, negative values indicating difference interactions are represented by green to blue. It is clearly seen that the sum interactions first take place over the first half of the shallower flat region (from probe 28 to 34), forming the second harmonics around $2f_p$. Close to the centre of the shallower region, at probes 37 and 40, difference interactions appear around (f_p, f_p), indicating energy transfer from second harmonics $2f_p$ back to f_p mode. In this area, both the sum and difference interactions are present. As waves approach the second half of the shallower region (from probe 43 to 49), difference interactions dominate. Besides, difference interactions are present around $\mathrm{Im}\{B(f_p, 0.25f_p)\}$. It indicates energy transfer from the frequency $1.25f_p$ to f_p

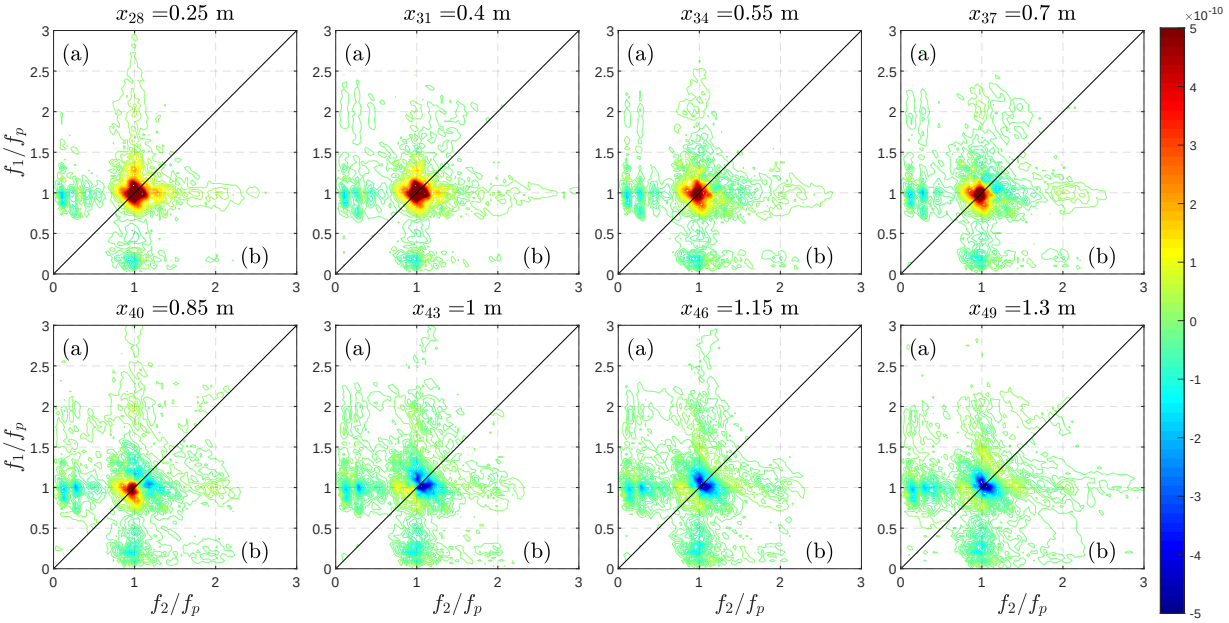

FIGURE 9. Contours of the imaginary part of bispectrum over the shallower region at eight probe positions between $x = 0.25$ m (probe 28) and $x = 1.3$ m (probe 49), in (a) simulated results; (b) measurements. The probe numbers and positions are indicated above each panel.

and $0.25f_p$, thus the generation/enhancement of LF waves with frequency $0.25f_p$. In general, the agreement between simulation and experiment is very good. Only some small differences can be observed in the LF range, which explain the overestimation of LF energy in the simulated spectrum in figure 5(b).

3.4. *Harmonic analysis*

The application of the generalised phase-inversion method outlined by Fitzgerald *et al.* (2014) requires moderate nonlinearity of the sea-state, in order to adopt a Stokes-type harmonic series to represent the time series of η. As wave nonlinearity is significantly enhanced due to shoaling, attention should be paid to the applicability of this approach in the current case. To evaluate the applicability of the harmonic separation technique in the present case, the sea-state is represented by the so-called first-, second-, and third-order harmonics. These characteristic waves are of frequencies f_p, $2f_p$, and $3f_p$ respectively, and their representative wave heights are computed in the same way as for the significant wave height but over different frequency ranges, namely $[0.5f_p, 1.5f_p]$, $[1.5f_p, 2.5f_p]$, and $[2.5f_p, 3.5f_p]$. The representative frequencies and wave heights are computed locally and averaged over the areas with constant depth h_1 and h_2. In figure 10, the representative harmonics are placed in the diagram of Le Méhauté (1976). It is seen the first three harmonics fall in the range of validity of Stokes second-order theory in both flat regions: the harmonic separation method is thus applicable.

After running three additional simulations with $\pi/2$, π and $3\pi/2$ phase shifts for the incident wave train, the contributions of harmonics at different orders η_{1st}, η_{2nd}, η_{3rd}, η_{4th} to the original time record of η can be evaluated from equations (2.12–2.15). The spatial evolution of their spectra is shown in figure 11. It can be seen that the different harmonics have been successfully extracted. The spectrum of the primary components (panel (a)) evolves with nearly no modulation over the domain. Panel (b) indicates the increase of energy around $2f_p$ is mainly due to second-order sum interactions. In panel (c), the third harmonic is seen to be weak except over the bar crest. In panel (d) showing η_{4th}, two components $\eta^{(4,4)}$ and $\eta^{(2,0)}$ should be present according to (2.15). However the

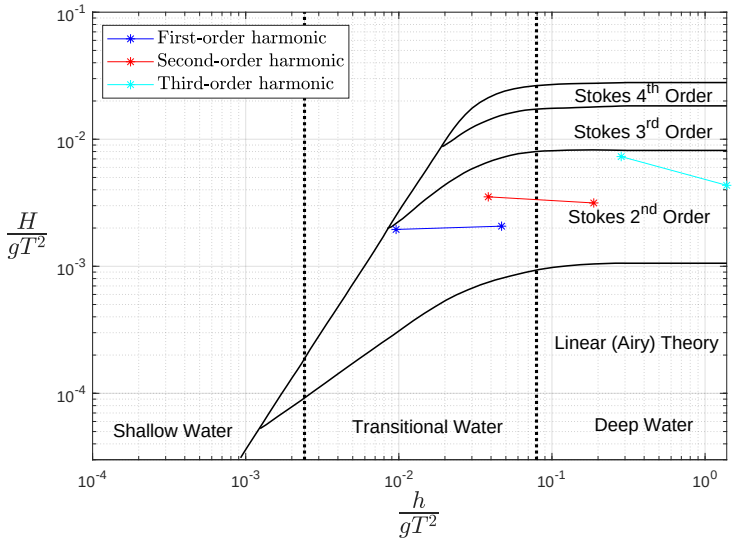

FIGURE 10. Le Méhauté's diagram (Le Méhauté 1976), with the first three representative harmonics of the irregular wave train of R3 added.

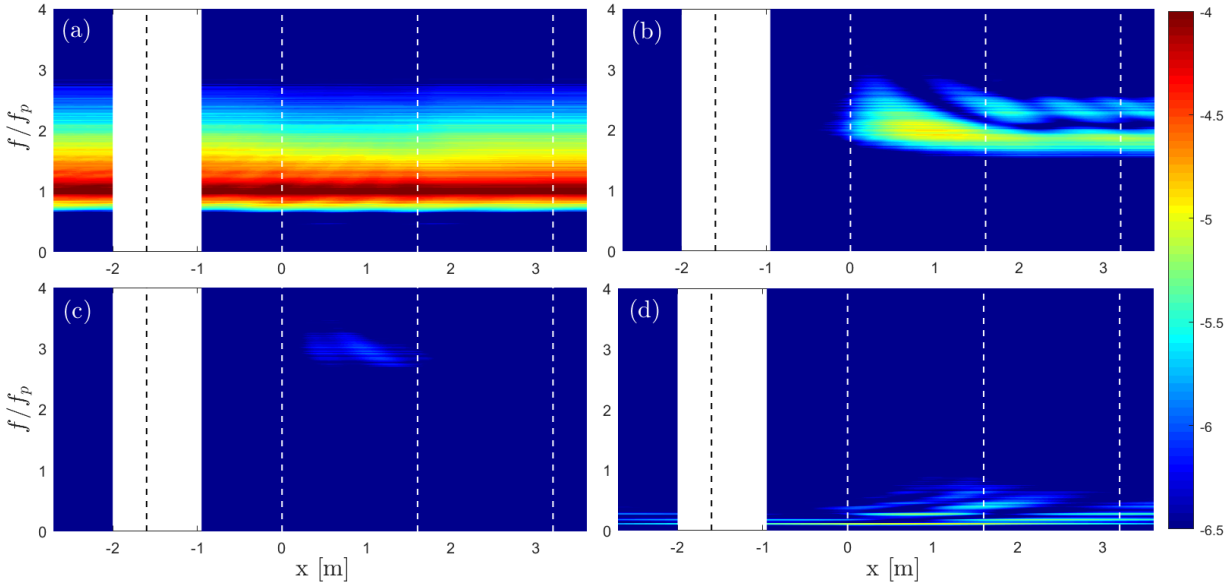

FIGURE 11. Spatial-spectral evolution of extracted harmonics at different orders (in logarithmic scale): (a) the first-order component η_{1st}, (b) the second-order component η_{2nd}, (c) the third-order component η_{3rd} and (d) the fourth-order component η_{4th}. The vertical dashed lines indicate the limits of the sloping bottom areas, located at $x = -1.6$ m, 0 m, 1.6 m, and 3.2 m.

fourth harmonic $\eta^{(4,4)}$ is weaker than the lower bound of the current colour scale, with negligible contribution here. Therefore $\eta_{4th} \approx \eta^{(2,0)}$, showing the role of second-order difference interactions in driving the energy increase of LF waves.

We note that Zheng *et al.* (2020) applied this technique using the phase-inversion approach (i.e. with two time series η and η_π), resulting in the separation of $(\eta_{1st} + \eta_{3rd})$ and $(\eta_{2nd} + \eta_{4th})$, denoted as η_{odd} and η_{even} respectively. Clearly, the two separated components η_{odd} and η_{even} would be subject to some overlap. In the present work, the generalised (four-phase) phase-inversion method permits to isolate the first four harmonics with good quality.

Basing on this decomposition, we analyse the contribution of the four harmonics to the changes of skewness and kurtosis by considering cumulative summations of the separated signals (figure 12). In panel (a), the skewness of the primary component is nearly 0.

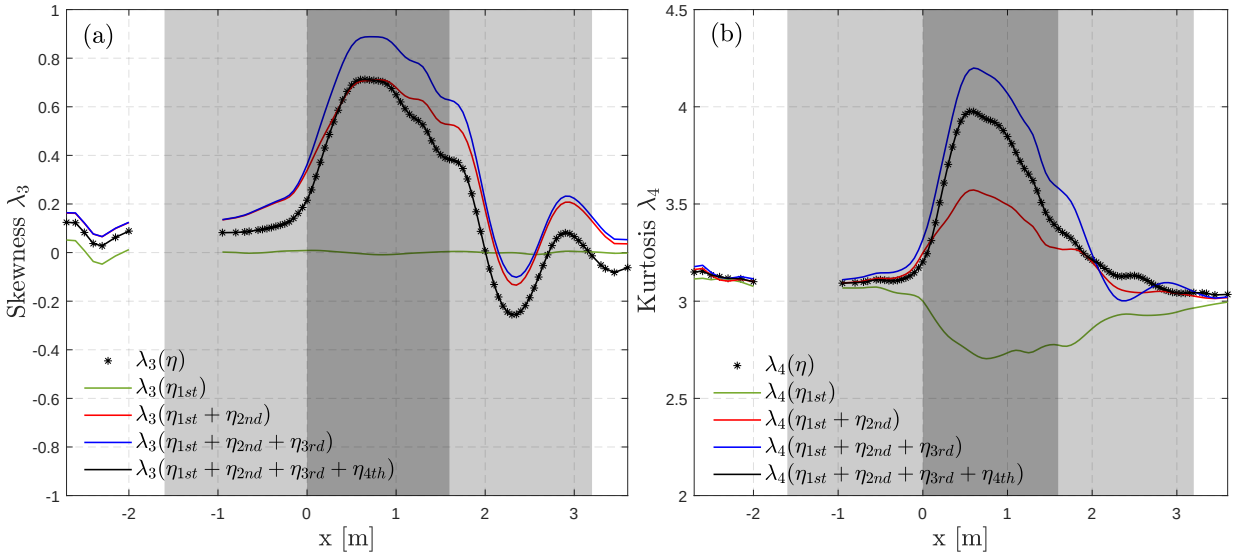

FIGURE 12. Spatial evolution of (a) skewness and (b) kurtosis of the time series of η obtained from the simulation of R3-bar case without phase shift, and different combinations of separated time series (see legend).

By adding the contribution due to second-order sum interaction, $\lambda_3(\eta_{1st}+\eta_{2nd})$ is significantly enhanced, showing very similar variations in space as $\lambda_3(\eta)$. The second harmonic thus dominates the changes of skewness over the entire domain. Although η_{3rd} has little contribution to the spectrum, see figure 11(c), it affects skewness evolution in a non-negligible way. Furthermore, the effects of η_{3rd} appear only in the area where the sea-state is out-of-equilibrium, namely starting shortly after the up-slope and ending shortly after the shallower flat region. We note $\lambda_3(\eta_{1st}+\eta_{2nd}+\eta_{3rd})$ is larger than $\lambda_3(\eta)$, indicating that the LF components due to second-order difference interactions are responsible of a decrease of skewness.

In figure 12(b), it is observed that the kurtosis of the primary component becomes lower than 3 as water depth decreases. The second harmonic component, η_{2nd}, affects the kurtosis over the entire domain, with an evident enhancement over the bar crest. The inclusion of η_{3rd} significantly enhances the kurtosis over the same area as for skewness. Again, the contribution of bound LF waves η_{4th} results in a decrease of kurtosis. Based on these observations, it is anticipated that the changes of skewness and kurtosis due to shoaling are related to both second- and third-order nonlinear interactions in the current case, and the non-equilibrium dynamics is associated with third-order effects, resulting in significant enhancement of kurtosis.

3.5. *Statistical distributions*

In figure 13, the PDFs of η time-series at 6 probes over the bar are shown, with the Gaussian PDF superimposed as a reference. The measured and simulated PDFs show excellent agreement for all the probes shown. In the experiment, the sea-state remains quasi-Gaussian until the end of the up-slope (probe 23). Over the bar crest (from probe 23 to 55), strong deviations from Gaussianity manifest. The positive tail of the distribution is shifted toward higher values of $\eta/\sqrt{m_0}$ indicating that the highest wave crests are noticeably larger in comparison with the Gaussian prediction. Meanwhile, the negative tail is shifted toward lower values, indicating the wave troughs are shallower. Such observations are in agreement with the expectation of positive skewness in this area. Among all the positions shown here, the strongest non-Gaussian behaviour takes place close to the middle of the shallower region (probes 35 to 39), at the length of latency.

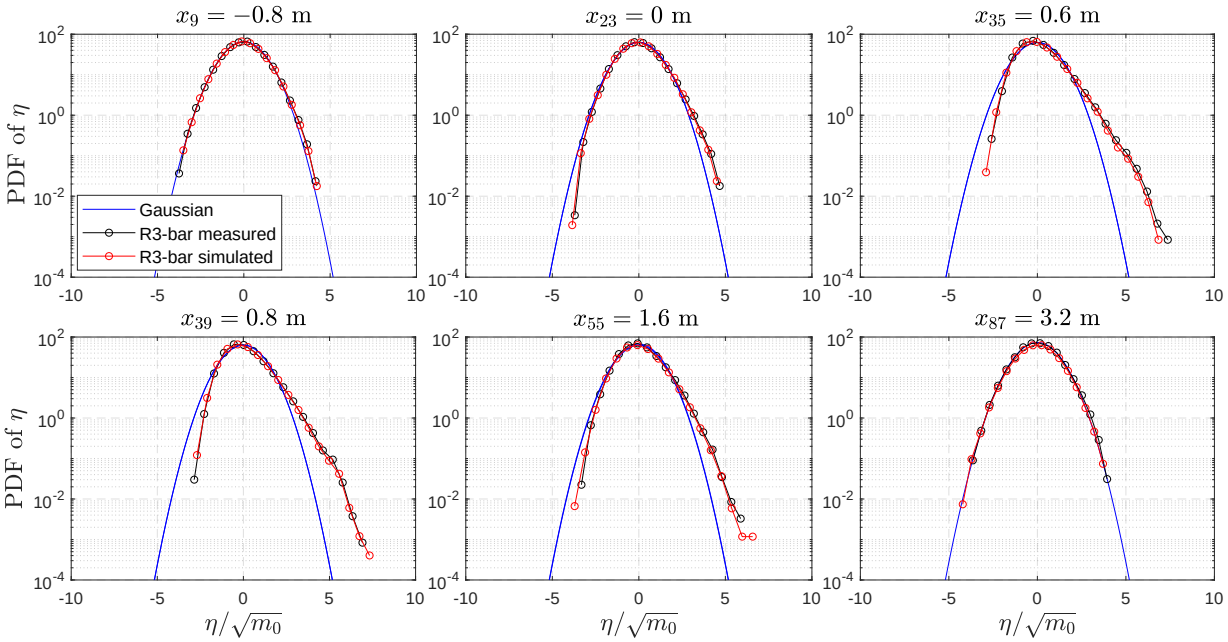

FIGURE 13. Probability density function (PDF) of free surface elevation (η) at 6 probe positions between $x = -0.8$ m (probe 9) and $x = 3.2$ m (probe 87). The probe numbers and positions are indicated above each panel. The Gaussian distribution is superimposed to highlight the nonlinear characteristics of the sea-state.

At the end of the bar crest (probe 55), the deviation of the empirical PDF from the Gaussian one decreases. This is related to the effects of de-shoaling and the weakening of the non-equilibrium dynamics. This is also in agreement with the indication of bispectral analysis, from which we found energy transfer from second harmonic $2f_p$ back to peak frequency f_p, and a decrease of nonlinear interactions. Eventually, at the end of the de-shoaling zone (probe 87), the empirical PDF turns back to Gaussian.

In figure 14, the CCDFs of wave height H are shown at the same positions as in figure 13, with the distribution of Boccotti (2000) superimposed as reference. Again, the agreement between the simulation and measurements is excellent, even in the tail of the distributions. Only few of the largest waves are slightly higher in the simulation at probes 39 and 55. Starting as a quasi-Gaussian process at probes 9, the sea-state undergoes a clear deviation from Gaussianity as waves propagate over the bar crest, with a marked increase of large waves, in particular at probes 35 and 39, and to a lesser extent until the end of this area (probe 55). Over the bar crest, and in particular in the zone 0.5 m $< x <$ 1 m, several "freak waves" can be identified basing on the criterion $H > 2H_{m_0}$. The distribution of Boccotti (2000) predicts that the occurrence probability of waves with $H > 2H_{m_0}$ is lower than 0.01% (the lower limit of the y-axis in figure 14). In agreement with the increase of $\lambda_4(\eta)$ discussed previously (see figure 7(d) or 12(b)), these wave height distributions clearly demonstrate the increase of the occurrence probability of freak waves due to the water depth transition. At the end of the de-shoaling area (probe 87), where the PDF of η is very close to Gaussian in figure 13, the empirical CCDF of H is lower than the theoretical prediction in the high-wave range. We note the CCDF of H at probe 87 is rather close to the distribution observed before the bar crest (probe 9), with a reduction of the occurrence probability of large waves. This is again considered to be an effect of the de-shoaling process.

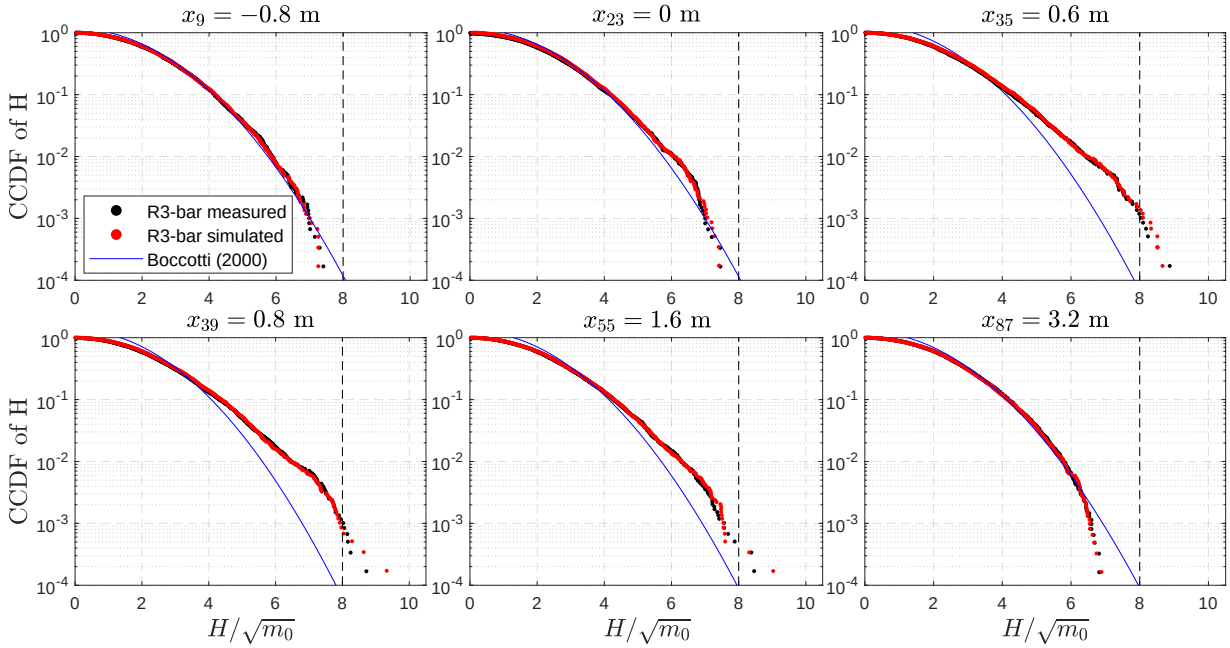

FIGURE 14. Complementary cumulative distribution function (CCDF) of wave height (H) at 6 probe positions between $x = -0.8$ m (probe 9) and $x = 3.2$ m (probe 87). The probe numbers and positions are indicated above each panel. The vertical dashed line in each panel represents the commonly adopted threshold for freak waves: $H = 2H_{m_0}$.

3.6. *Statistics of velocity and acceleration*

In R3 experiment, the horizontal velocity at $z_0 = -0.048$ m has been measured at 37 positions, and studied statistically in TRJR20. In §3.2 we have shown the skewness and kurtosis of $u(z_0)$ simulated with whispers3D are in excellent agreement with the measurements (see figure 7(c-d)). Here, using additional model results, we present a more complete statistical analysis of the kinematic properties, namely the vertical velocity and accelerations in both directions. The local (Eulerian) horizontal and vertical accelerations, denoted as $u_t(z_0)$ and $w_t(z_0)$ respectively, are evaluated as time derivatives of $u(z_0)$ and $w(z_0)$. The computation of derivatives is made with a five-point centred finite difference scheme. In the following, we analyse the spatial evolution of the skewness and kurtosis of 5 variables: $\eta, u(z_0), w(z_0), u_t(z_0), w_t(z_0)$.

In figure 15(a), the evolution of skewness of the 5 kinematic variables is plotted. Two groups of variables can be identified, showing two different spatial evolution patterns. First, we note $\lambda_3(w(z_0))$ and $\lambda_3(u_t(z_0))$ evolve very closely over the whole domain. They both reach two local maximum and one local minimum values, at almost the same positions for both variables (first maximum at $x \approx 0.2$ m, minimum at $x \approx 1.9$ m, second maximum at $x \approx 2.6$ m). In addition, it is noticed that the profile of the asymmetry parameter in figure 7(c) is similar to that of $\lambda_3(w(z_0))$ and $\lambda_3(u_t(z_0))$, despite an opposite sign. In the second group, the spatial profiles of $\lambda_3(\eta)$, $\lambda_3(-w_t(z_0))$ and $\lambda_3(u(z_0))$ present a lot of similarities, though with different magnitudes. The local maximum and minimum values of skewness of these 3 variables are located downstream compared to the ones of $w(z_0)$ and $u_t(z_0)$. The skewness of $w_t(z_0)$ shows the most pronounced variation, with its global maximum achieved around $x = 0.45$ m. The skewness of $u(z_0)$ shows a lower minimum value in the middle of the down-slope area (around $x = 2.3$ m). The spatial profiles of the skewness of these 5 variables and the asymmetry parameter indicate that the adaptation of the sea-state due to depth variations has different impacts on kinematic properties, among which two dominant typical evolution patterns can be identified.

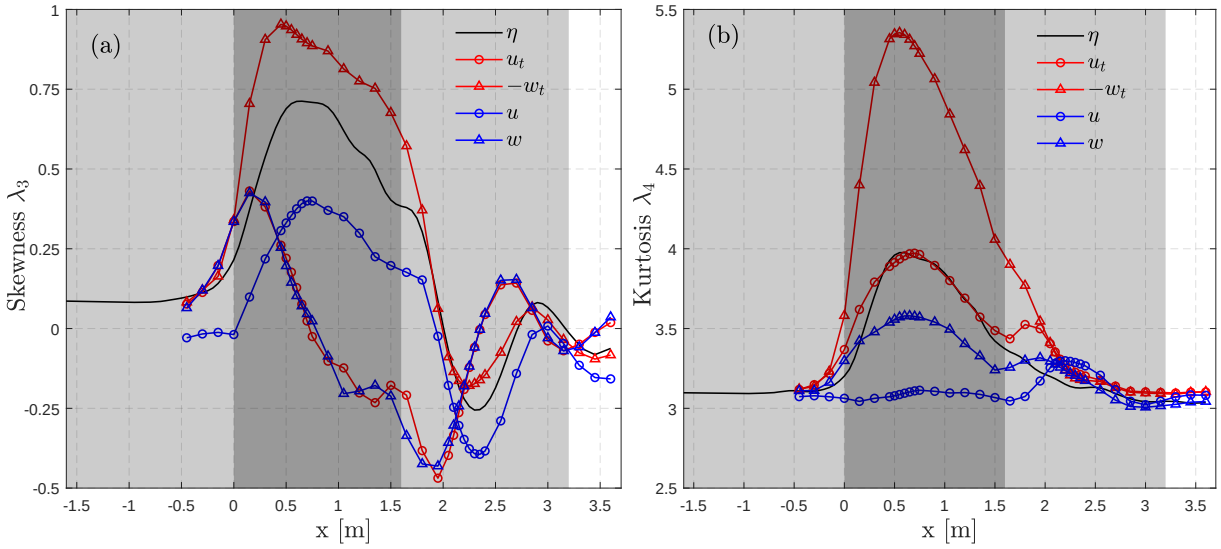

FIGURE 15. Spatial evolution of (a) skewness and (b) kurtosis of five variables obtained from the simulation of R3-bar case: free surface elevation η, horizontal and vertical velocities u, w, horizontal and vertical accelerations u_t, w_t. The velocities and accelerations are computed at the same elevation $z_0 = -0.048$ m.

It is known from linear theory that η, u and $-w_t$ are of the same phase in a linear superposition of progressive harmonic components, while w and u_t are also in phase, but with a phase shift of $\pi/2$ with respect to the variables of the former group. In the nonlinear case, such an expectation is not guaranteed *a priori*. The observations in figures 15(a) indicate that the phase relations among the five variables are somewhat preserved in the present case.

Figure 15(b) shows the kurtosis evolution of the same variables. As was observed in TRJR20, $\lambda_4(u(z_0))$ shows no sign of enhancement over the up-slope or the bar crest, whereas a local maximum is achieved in the down-slope area. This trend is successfully captured in the simulation. However, model results show that $\lambda_4(w(z_0))$, $\lambda_4(u_t(z_0))$ and $\lambda_4(-w_t(z_0))$ (not discussed in TRJR20) are noticeably enhanced over the shallower region, with their maximum values achieved at the same position (about $x = 0.6$ m, corresponding to the length of latency) as for $\lambda_4(\eta)$. Regarding the variables $u_t(z_0)$ and $w(z_0)$, we note that their kurtosis profiles are very similar, as was observed for their skewness profiles in figure 15(a). $\lambda_4(-w_t(z_0))$ shows the most significant enhancement over the bar crest with only one maximum in the domain, as for $\lambda_4(\eta)$. Our results supplement the observations made on $\lambda_4(u(z_0))$ in TRJR20, showing that significant changes of kurtosis of other kinematic properties, namely $w(z_0)$, $u_t(z_0)$ and $-w_t(z_0)$, take place due to depth variations. Furthermore, the kurtosis profiles of these 3 variables are markedly different from the one of $u(z_0)$. All three show a significant increase of kurtosis over the bar crest (implying an increased occurrence probability of their maximum values), in line with the increase of $\lambda_4(\eta)$ in this area.

4. Effects of finite length of the bar crest and de-shoaling

4.1. *Objectives and outline of the simulation with a step-like profile*

In §3, an extensive analysis of the effects induced by wave shoaling in the up-slope area has been performed, together with the effects of the down-slope (de-shoaling). At the up-slope transition, the out-of-equilibrium dynamics of the wave train is associated with the spectral settling from the deeper-water equilibrium state (in depth h_1) to the shallow-

water equilibrium (in depth h_2), and this process takes place over a certain distance after the start of the shallower region. However, this shallower water area is of relatively short length in the R3-bar setup. One may wonder whether the out-of-equilibrium dynamics due to up-slope transition has been fully developed in the shallower region and what is the contribution of the de-shoaling process. The sea-state could enter the de-shoaling area before having reached a new shallow-water equilibrium, it is therefore difficult to conclude which effects govern the sea-state dynamics after the shallower region.

In order to isolate the effects of the two slopes and to better assess the characteristic distance of non-equilibrium dynamics due to the shoaling process, an additional simulation without the de-shoaling area has been conducted with a modified bathymetry profile (R3-step setup in figure 2(b)). The simulation of the new case is conducted with the same numerical parameters as for R3-bar case. In this section, we show the results of this new R3-step case, and compare them with those of R3-bar case. We focus on the spatial evolution of the variance density spectrum (§4.2), non-dimensional parameters (§4.3) and the statistics of the kinematic variables (§4.4).

4.2. *Spatial evolution of wave spectrum*

In figure 16, the spectral evolution in space shows the wave spectra of the two setups exhibit very similar patterns in the area where the bottom profiles are identical ($x < 1.6$ m). After $x = 1.6$ m, the differences in the spectra manifest mainly for two frequency ranges: $f > 1.5f_p$ and $f < 0.5f_p$. In R3-step case, more energy is transferred to components in these two ranges, which is clearly the consequence of stronger nonlinear interactions in the extended shallower region. In figure 16(b) for R3-step case, a second energetic peak around $2f_p$ appears after $x \approx 2.5$ m and lasts until the end of the domain.

In the area from $x = 1.6$ m to 3.6 m, there is a particular spatial evolution of the spectrum for $f > 1.6f_p$, quite different from R3-bar case. It is believed this particular spatial structure in the high-frequency range is due to the simultaneous presence of free and bound components with frequencies being higher harmonics of frequencies close to the spectral peak (typically in the range $[0.8f_p, 1.5f_p]$). This situation is typically encountered when waves propagate over a submerged bar or shoal (Beji & Battjes 1993) or when waves are generated using a wave shape that does not correspond to the stable form of progressive nonlinear waves for the considered depth (Chapalain *et al.* 1992). As it is well-known, if free and bound components at a higher harmonic Nf, with $N = 2, 3, ...$, of the primary frequency f coexist in constant depth, a beating or spatial modulation of the amplitude will manifest. This effect is most apparent here for the second harmonics ($N = 2$) of primary frequencies $f \in [0.8f_p, 1.5f_p]$. The beat length of second harmonics, defined as the distance between two successive maximum values of the spectral amplitude, can be estimated following Massel (1983):

$$L_{beat}(2f) = \frac{2\pi}{k(2f) - 2k(f)}, \tag{4.1}$$

where the wave-numbers $k(f)$ and $k(2f)$ are computed from f and $2f$ using the linear dispersion relation (for depth h_2). Following this idea, the beating length of second harmonics for $f \in [0.8f_p, 1.5f_p]$ have been computed and superimposed in figure 16(b). The estimation of the beating length for $f \in [0.8f_p, 1.5f_p]$ results in a series of curves in the range $[1.6f_p, 3f_p]$ as second harmonics. The distance between two successive curves at a particular frequency corresponds to the beating length. These curves are in good agreement with the spatial modulations of the spectrum in figure 16(b) for $f > 1.6f_p$.

In the R3-bar case (figure 16(a)), this effect is less pronounced due to the variable depth over the down-slope area, but still visible for $f > 2f_p$. It is also noted that for the case of

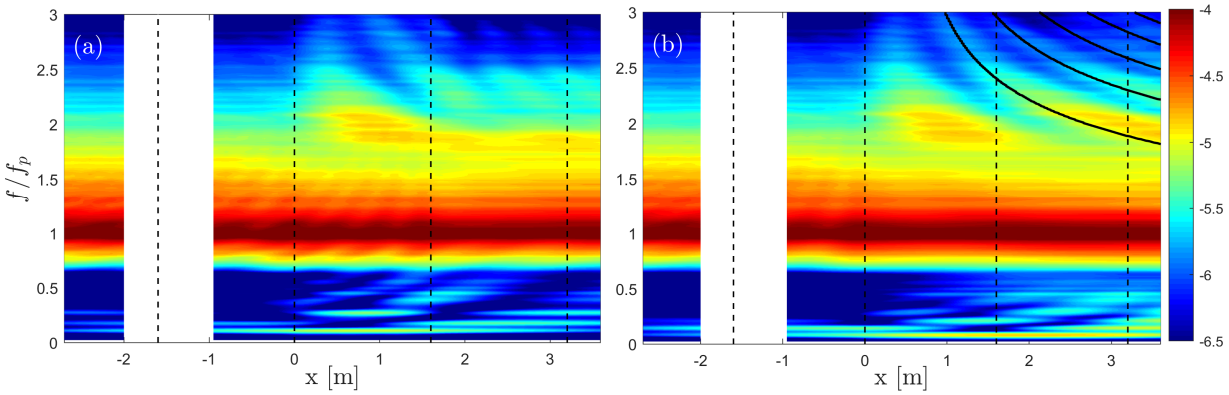

FIGURE 16. Spatial evolution of the variance density spectra in simulations (a) with R3-bar setup, and (b) with R3-step setup. The vertical dashed lines indicate the limits of the sloping bottom areas in R3-bar setup, located at $x = -1.6$ m, 0 m, 1.6 m, and 3.2 m. The solid black curves in panel (b) represent the predicted maximum values of the spectral amplitude, between which the distance in space corresponds to the beating length of the second harmonics of primary frequencies in $[0.8f_p, 1.5f_p]$.

a larger (uniform) depth in (4.1), the beat length would be reduced. This reduction does not appear clearly after the down-slope area in figure 16(a). This is because the area with constant deeper water ($h_1 = 0.53$ m) after $x = 3.2$ m is only 0.4 m long, which is less than the shortest beating length $L_{beat}(3f_p) \approx 0.42$ m in the considered frequency range $[0.8f_p, 1.5f_p]$. However, comparing the spectra of two simulations in the range $x > 1.6$ m and $f/f_p > 2$, some indication of this reduction can be detected in figure 16(a), though the depth is not uniform from $x = 1.6$ m to 3.2 m in the R3-bar case. In summary, the water depth reduction due to the up-slope results in an increase of wave nonlinearity in the shallower area, which manifests in the forms of energy transfer, generation of bound long-waves and increase of the amplitude of the bound super-harmonics of the frequencies near the spectral peak. In addition, as the depth variation is rather abrupt, part of the energy is also transferred to free waves in the same high-frequency range, resulting in the above-described spatial modulation of spectrum magnitude.

In figure 17, the comparison of the spectra in two simulations is shown at four positions after $x = 1.6$ m. At $x = 1.6$ m (figure 17(a)), the main parts of the two spectra are superimposed. As waves propagate in the extended shallower region in R3-step case, differences gradually manifest in figure 17(b-d). In R3-step case, the harmonic peak around $2f_p$ is more pronounced in comparison with R3-bar case, and we notice this peak is gradually shifted from frequencies slightly higher than $2f_p$ to lower frequencies. We also note the spectrum tail in the range $[2.5f_p, 4f_p]$, which is decreased in R3-bar case, is preserved in the R3-step case. This indicates that the de-shoaling process results in a loss of energy of the high-frequency waves. The LF waves receive more energy in R3-step case due to stronger nonlinear interactions in the extended shallower region for $x > 1.6$ m. In R3-bar case, the spectral evolution in figure 17(b-d) is quite limited. It indicates that the spectral adaptation to the shallow-water equilibrium was not fully developed over the 1.6 m long bar crest in R3-bar case, and was balanced by the de-shoaling process.

4.3. *Non-dimensional parameters*

Figure 18 compares the spatial profiles of twelve non-dimensional parameters for R3-bar and R3-step cases. In figure 18(a), the small spatial modulations of $H_{m_0}/H_{m_0,inc}$ calculated in the main frequency range $[0.5f_p, 0.5f_s]$ disappear over the shallower region in R3-step case. It indicates that the de-shoaling process can influence the upstream wave field, possibly via the generation of reflected free waves. Similar trends can be found for

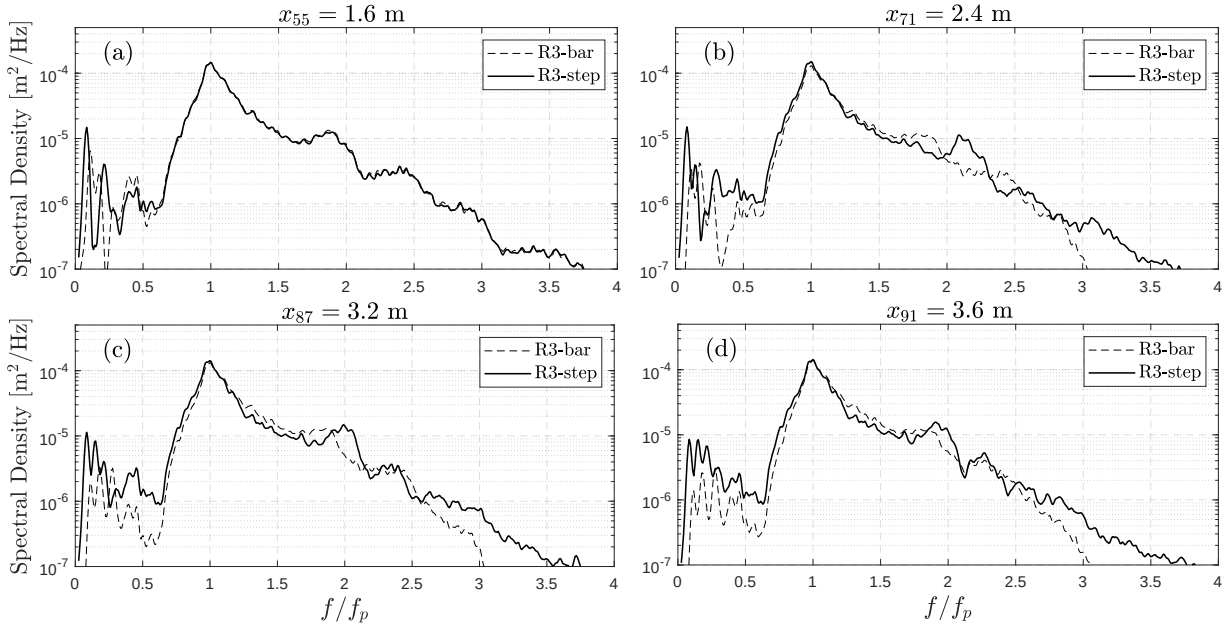

FIGURE 17. Comparison of spectra of the surface elevation at 4 positions from numerical simulations for the R3-step (solid lines) and the R3-bar (dashed lines) cases.

the evolution of steepness parameter, Q_p and $\hat{f}_p/f_p$. In R3-step case, the H_{m_0} of the LF range keeps increasing in the extended shallower region. Due to strong nonlinear interactions in this region, wave energy is continuously transferred toward these sub-harmonic components. In figure 18(b), the decrease of the steepness parameter for $x >$ 1.6 m disappears in R3-step case, because $\hat{L}_p$ remains uniform in the extended shallower region.

In figure 18(c-e), significant discrepancies of skewness, kurtosis and asymmetry parameters from the results of R3-bar case are observed for $x > 1.6$ m. In R3-step case, these parameters are seen to converge toward new constant levels in the extended shallower region, after reaching their maximum/minimum values over the original shallower region. This is an indication that the sea-state is evolving toward a new equilibrium state in the shallower region, since the effects of non-equilibrium dynamics induced by the up-slope gradually decrease in space. In the range $x < 1.6$ m, where both profiles are identical, these statistical parameters are almost superimposed. We thus conclude that the local minimum value of $\lambda_3(\eta)$ and $\lambda_3(u(z_0))$, the local maximum of $\lambda_4(u(z_0))$, and the variations of the asymmetry parameter, observed for $x > 1.6$ m in R3-bar case (see figure 7(c-d)), are caused by de-shoaling effects. This is of interest for interpreting the particular behaviour of $\lambda_4(u(z_0))$ highlighted in figure 7(d): the local maximum of $\lambda_4(u(z_0))$ is not due to the up-slope transition, but to the down-slope one. In R3-step case, $\lambda_4(u(z_0))$ shows nearly no variation over the whole domain, in contrast to $\lambda_4(\eta)$ that experiences strong enhancement in the first part of the shallower region.

Figure 18(f) and 18(g) show the comparison of Q_p and $\hat{f}_p/f_p$, respectively. For these parameters, the differences between the two setups are not restricted to the de-shoaling area but also manifest in the area where the two bottom profiles are identical. The spatial modulations of Q_p and $\hat{f}_p/f_p$ seen in R3-bar case for $x < 1.6$ m become insignificant in R3-step case. As explained above, this indicates that de-shoaling affects not only the wave field in the area after the beginning of the down-slope but also the upstream wave field (reflected waves). Besides this difference, both cases show another modulation of Q_p and $\hat{f}_p/f_p$ before entering the shallower region (i.e. for $x < 0$) attributed to the reflection of incident waves on the up-slope part. In summary, this comparison highlights the fact

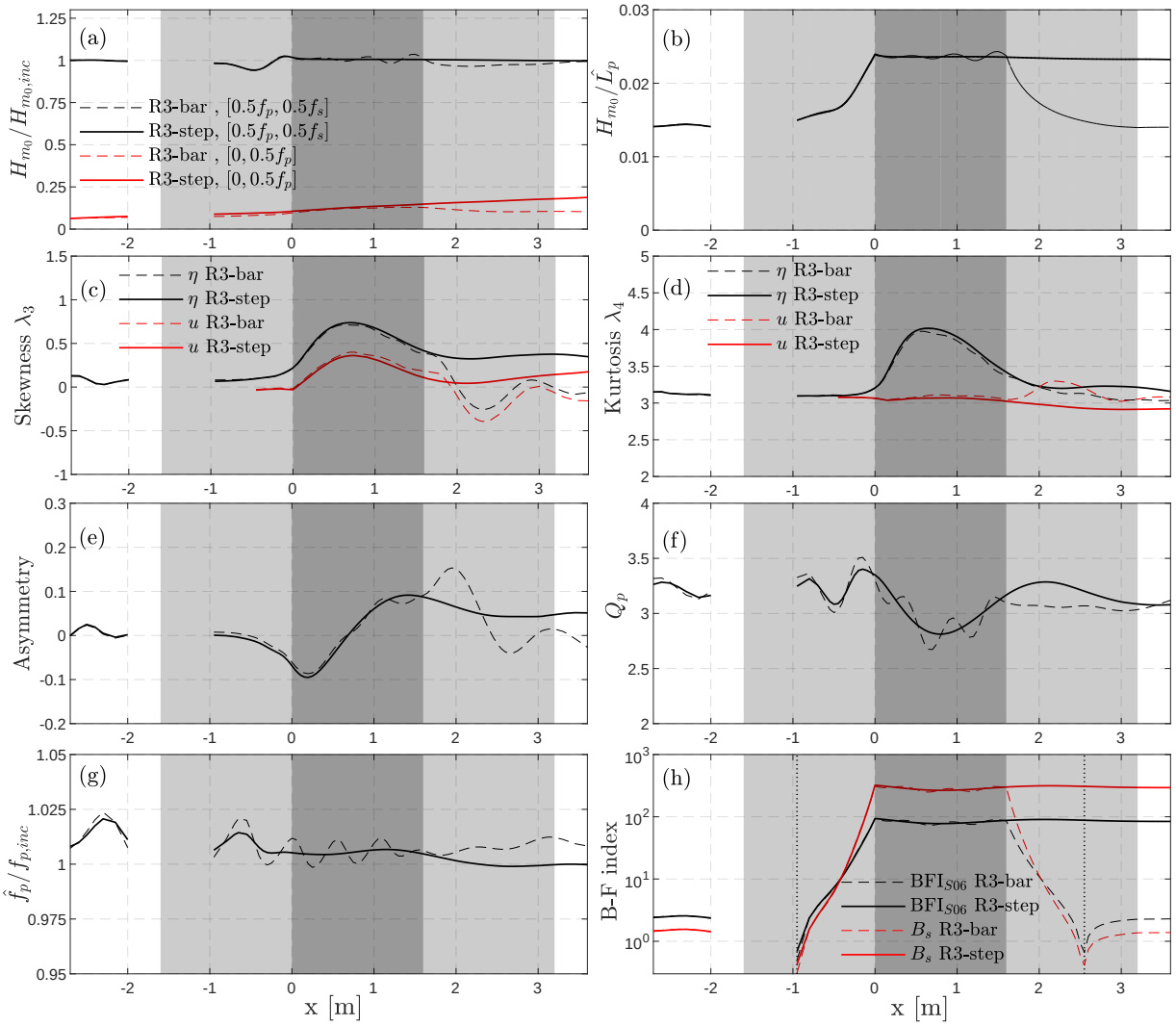

FIGURE 18. Spatial evolution of non-dimensional parameters in simulations of R3 case with de-shoaling area (dashed lines), and without de-shoaling area (solid lines). The light grey zones indicate the sloping areas and the dark grey zone indicates the shallower flat region in the case with the de-shoaling area. In panel (h), the vertical dash lines denote the positions where the threshold $k_p h = 1.363$ for modulational instability is achieved.

that the spatial modulations of Q_p and $\hat{f}_p/f_p$ observed in R3-bar case before $x = 1.6$ m originate from two reflection processes taking place at the up-slope transition (in both cases), and at the down-slope transition (in R3-bar case only).

Figure 18(h) shows the BFI_{S06} and B_s parameters in the R3-step case are almost superimposed with the ones in R3-bar case for $x < 1.6$ m. However, no decrease after $x = 1.6$ m is seen in R3-step case, due to the extended shallower region.

4.4. *Statistics of velocity and acceleration*

Figure 19 compares the spatial profiles of skewness (panel (a)) and kurtosis (panel (b)) of the kinematic properties in the two simulations. In R3-step case, the skewness of all the kinematic properties continue their decreasing or increasing trend over a short distance in the extended shallower region. This is because the non-equilibrium dynamics induced by the up-slope keeps having effects after $x = 1.6$ m. After a short distance in the extended shallower region, the variations of skewness in R3-step case become mild. But it is evident that the steady shallow-water state has not been established yet, even in R3-step case. As an evidence, $\lambda_3(u(z_0))$ keeps its increasing trend until the end of the flume.

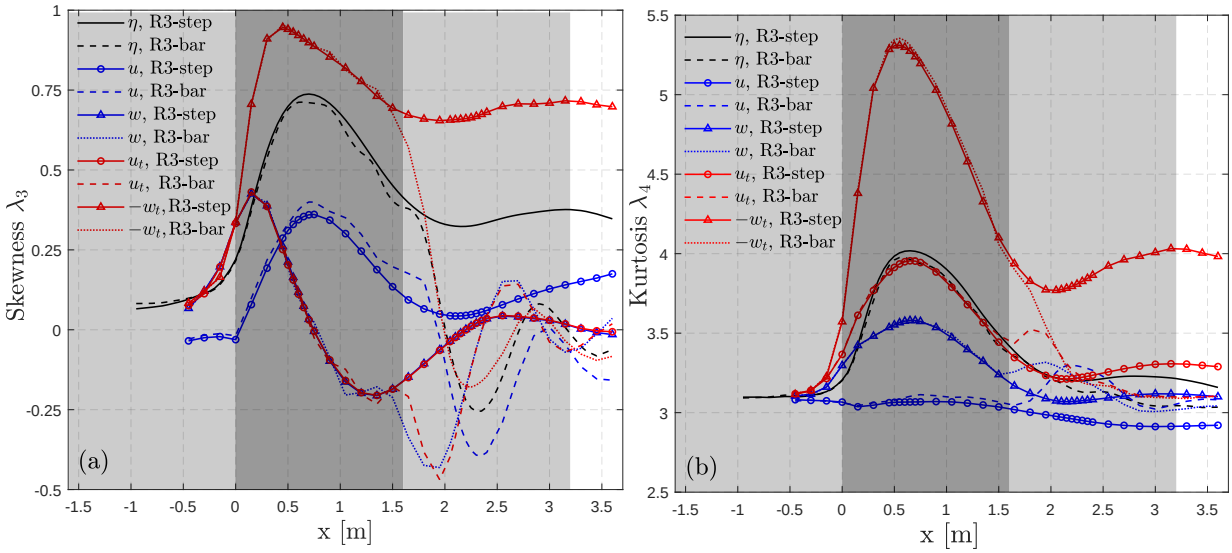

FIGURE 19. Spatial evolution of (a) skewness and (b) kurtosis of five variables η, $u(z_0)$, $w(z_0)$, $u_t(z_0)$ and $-w_t(z_0)$ in both R3-bar and R3-step cases.

Based on the observations in Zhang *et al.* (2019) where a long shallower region was used, we anticipate that the mild modulation of skewness in R3-step case would continue over a longer distance without significant changes if the flume was extended. The skewness differences between the two bottom setups correspond to the de-shoaling effects, and it is clear that the de-shoaling process results in opposite effects to the skewness compared to shoaling. The sharp decrease of skewness after $x = 1.6$ m is mainly due to de-shoaling effects (rather than the decrease of up-slope induced non-equilibrium dynamics). It is also noticed that the de-shoaling process slightly influences $\lambda_3(u(z_0))$ and $\lambda_3(\eta)$ before the down-slope area. Regarding skewness, the most sensitive variable to the change of water depth is w_t.

In line with the observations for skewness, figure 19(b) shows the kurtosis of the five variables continue their decreasing trend over a short distance in the extended shallower region in R3-step case. This is due to the weakening of non-equilibrium dynamics. The differences of kurtosis between R3-step and R3-bar cases again correspond to the de-shoaling effects. Unlike skewness, both shoaling and de-shoaling processes result in enhancement of kurtosis. Since kurtosis involves the mean of an even power of a variable, it does not distinguish, for instance, a deep trough (negative) from a sharp crest (positive) for η. It should be noticed that the effects of de-shoaling process on spatial evolution of kurtosis are different for the five variables. No significant enhancement of $\lambda_4(-w_t(z_0))$ and $\lambda_4(\eta)$ is observed in R3-step case. On the contrary, kurtosis of $u_t(z_0)$, $w(z_0)$, $u(z_0)$ are increased in the extended shallower region of R3-step case. Combined with the behaviour of skewness for these variables in the same region, we know that the increase of kurtosis is due to more negative extreme values (velocity or acceleration in the direction toward bottom). Regarding kurtosis, the most sensitive variable to the depth variation is again $w_t(z_0)$, whereas $\lambda_4(u(z_0))$ shows almost no change over the domain in R3-step case.

5. Discussion and conclusions

Basing on the recent experimental study of TRJR20, we studied the propagation of long-crested irregular waves over variable bottom profiles. With a fully nonlinear and dispersive numerical model, we first studied the case R3 with a submerged trapezoidal bar (R3-bar case) reported in TRJR20. Then, a variation of R3-bar case, with the

down-slope of the bar removed and the shallower flat region extended to the end of the domain, was considered (R3-step case). The main objective was to investigate the spectral adaptation and out-of-equilibrium dynamics of the sea-state due to depth transitions, and the associated statistics of the wave field.

The simulation of the R3-bar case not only validated the numerical model but also permitted extracting more information of the wave field, i.e. vertical velocity and accelerations at the elevation $z_0 = -0.048$ m (below SWL). The sea-state dynamics in R3 case was analysed in-depth by considering the spatial evolution of wave spectrum, bispectrum, eight non-dimensional parameters, distributions of η and H and statistics of kinematics. Additional simulations of the R3-bar case with different initial phases of the incident waves were conducted in order to apply the four-phase harmonic extraction approach, which allows evaluating the contributions of different harmonics in a quantitative manner. The simulation of R3-step case was then conducted, the effects of the de-shoaling process induced by the down-slope could be characterised by comparing with the R3-bar case.

As a first conclusion, the performance of whispers3D model was proven excellent in the deterministic simulation of irregular non-breaking wave train evolution over a long duration (equivalent to nearly $5,000T_p$). In all considered aspects, the comparisons with measurements showed good to outstanding agreement. This includes in particular the statistical distributions of wave heights, where the intensified extreme wave activities were successfully captured by the model. Nevertheless, some minor differences between the simulation and experiment exist. In the simulation, higher levels of significant wave height and steepness parameter after the shallower region, and slightly higher magnitudes of LF modes in the same area were observed. Both bispectrum and harmonic extraction results indicated that the LF modes in the simulation were generated due to second-order difference interaction. It is anticipated for a more energetic sea-state, the nonlinear wave-wave interaction is stronger resulting in more significant energy transfer to both LF modes and higher harmonics of the spectral peak. In the experiment, the wave train was of slightly lower energy after the shallower region than in the simulation due to frictional dissipation effects. The inclusion of dissipation in the model could bring some improvement, at least for the agreement of H_{m_0}.

The sea-state evolution of R3-bar case has been characterised and analysed thoroughly. In addition to the skewness and kurtosis evolution, we have observed a particular spatial modulation for nonlinear parameters (H_{m_0}, $H_{m_0}/\hat{L}_p$), spectral parameters (Q_p, $\hat{f}_p$), and B-F index, completing the analyses reported in TRJR20. The bispectral analysis, and harmonic extraction method permitted to characterise the spectral adaptation in terms of nonlinear interaction. Strong nonlinear coupling was detected, with significant energy transfer among the primary, second harmonics, third harmonics and long-wave components after the shoal. The contributions of these components to the evolution of wave spectrum, skewness and kurtosis have been evaluated by the harmonic extraction technique. Second-order effects were shown to be amplified after the shoaling zone, resulting in the generation of marked second harmonics (due to second-order sum interaction) and long-wave components (due to second-order difference interaction). The former dominated the evolution of $\lambda_3(\eta)$ and resulted in the enhancement of $\lambda_4(\eta)$, whereas the latter resulted in decrease of both parameters. Third harmonics of the primary components were noticeable only over the shallower region, with relatively low levels of energy. Yet their contribution to the kurtosis was evidenced, in particular regarding its maximum value after the length of latency (here equal to about half the local wavelength at peak frequency).

The empirical distributions of η and wave height H showed considerable deviation from Gaussianity (represented by the asymptotic model by Boccotti (2000) for H)

over the shallower region, with several freak waves occurring in the area where $\lambda_4(\eta)$ was close to its maximum. After the down-slope, the deviation from Gaussian models decreased, but the secondary peak close to the second harmonic in the spectrum did not vanish completely. The spectral changes due to a shoaling area are not fully reversible by setting a symmetric de-shoaling area, some wave energy remained in higher-order harmonics. A more complete statistical analysis of the kinematic properties, including free surface elevation, asymmetry parameter, velocities and accelerations components was performed. We found two different trends for the evolution of skewness of these variables, indicating that the deformations of the wave field take place somewhat independently in horizontal and vertical directions. The kurtosis of all the kinematic variables shown but the horizontal velocity (the single one considered in TRJR20) were enhanced, at the same position as $\lambda_4(\eta)$.

The comparison of the R3-bar case with the additional R3-step case allowed to isolate the effects induced by the de-shoaling process. In R3-step case, a particular beating pattern observed for $f > 1.6f_p$ in the range $x > 1.6$ m has been explained by the simultaneous presence of free and bound components in the high-frequency range. It also explains the similar but less pronounced (due to de-shoaling) spectral evolution pattern in R3-bar case. With the R3-step case, it is evident that the small spatial modulations of nonlinear and spectral parameters observed in R3-bar case were due to the de-shoaling process. The de-shoaling process influences the upstream wave field by forcing reflected waves.

In the R3-step case, the statistics of the kinematic variables continued their evolution trends over a short distance in the extended shallower region, then mildly varied until the end of the domain. The shallow-water equilibrium was thus not achieved over the shallower region in R3-bar case, nor is it fully achieved in the R3-step case. The comparison of the skewness and kurtosis in two cases demonstrated that the de-shoaling process affects the skewness of all variables oppositely compared to shoaling. Meanwhile the kurtosis of $u(z_0)$, $w(z_0)$ and $u_t(z_0)$ were enhanced due to de-shoaling.

The knowledge of the "transition water depth" for different dynamic sea-state responses, and the length of latency in the "shallower regime" case are of practical interest, since they are related to whether and in which range should a nearshore structure be protected from depth variation induced freak waves. Next, effort will be made in to improve our knowledge of these properties basing on information about seabed profile and incident spectrum. In complement to experiments, the nonlinear and dispersive whispers3D model will be used for this purpose, based on the accuracy of simulations reported here.

Acknowledgements

Financial support provided by China Scholarship Council (CSC) to fund the Ph.D. research program of J. Zhang (grant No.201604490045) is gratefully acknowledged. We thank K. Trulsen, A. Raustøl, S. Jorde and L.B. Rye for selflessly sharing the experimental data of Run 3 of TRJR20. We also express our gratitude to three anonymous reviewers for their comments and suggestions that helped to improve this article.

Declaration of interests

The authors report no conflict of interest.

Appendix A. Statistical, spectral and bispectral analysis approaches

A.1. *Characteristic non-dimensional parameters*

The skewness λ_3 and kurtosis λ_4 are defined as the third- and fourth-order normalised moments of a time series. The time series in the present work could be the surface elevation, velocity or acceleration in the horizontal or vertical directions. Using the free surface elevation η, their definitions are:

$$\lambda_3(\eta) = \Big\langle (\eta - \langle\eta\rangle)^3 \Big\rangle / \sigma^3, \quad \lambda_4(\eta) = \Big\langle (\eta - \langle\eta\rangle)^4 \Big\rangle / \sigma^4. \tag{A 1}$$

The peakedness parameter Q_p characterising the spectral shape is defined as (see Goda 2010, p. 391):

$$Q_p = \frac{2}{m_0^2} \int_0^\infty f S^2(f)\, \mathrm{d}f. \tag{A 2}$$

Note that narrower the spectrum is, the larger Q_p will be.

The parameter $\hat{f}_p$ is an estimate of the local peak frequency proposed by Young (1995):

$$\hat{f}_p = \left(\int_0^\infty f S^4(f)\, \mathrm{d}f \right) / \left(\int_0^\infty S^4(f)\, \mathrm{d}f \right). \tag{A 3}$$

The corresponding angular frequency is denoted as $\hat{\omega}_p$, the local wave-number and wavelength obtained through the linear dispersion relation are denoted $\hat{k}_p$ and $\hat{L}_p$ respectively.

The B–F index originally introduced in the work of Janssen (2003) plays an important role in understanding the effects of non-resonant four-wave interaction, its formulation reads:

$$\mathrm{BFI}_{J03} = \frac{\hat{k}_p \sqrt{2}\sigma}{\delta / \hat{\omega}_p}, \tag{A 4}$$

where δ denotes the width of the frequency spectrum.

The variation and robustness of B–F index with different parameters estimation approaches have been discussed by Olagnon & Magnusson (2004) and Serio *et al.* (2006). For uni-directional waves in constant water depth h, the threshold of modulation instability is $k_p h = 1.363$. When waves are modulationally unstable with $k_p h > 1.363$, it is suggested to use the formulation given by Serio *et al.* (2006) for single-peaked spectra:

$$\mathrm{BFI}_{S06} = \sqrt{m_0}\hat{k}_p Q_p \sqrt{2\pi}\nu \sqrt{\frac{|\beta|}{\alpha}}, \tag{A 5}$$

where α, β and ν are coefficients of the cubic NLS equation which was derived from equations (2.2–2.5) by using the method of multiple scales (Hasimoto & Ono 1972; Mei 1992):

$$-i\left(\frac{\partial A}{\partial t} + \frac{1}{2}\nu \frac{\omega}{k} \frac{\partial A}{\partial x} \right) + \alpha \frac{\partial^2 A}{\partial x^2} + \beta |A|^2 A = 0, \tag{A 6}$$

where $A(x,t)$ denotes the wave amplitude, i denotes the imaginary unit, ν is the correction to the group velocity for finite depth, α and β are the dispersive and nonlinear coefficients respectively:

$$\nu = \frac{2C_g}{C} = 1 + \frac{2kh}{\sinh(2kh)}, \tag{A 7}$$

$$\alpha = -\frac{1}{2}\frac{\mathrm{d}^2\omega(k)}{\mathrm{d}k^2} = \frac{\omega h}{2k}\left[\frac{1}{4kh} - \frac{kh}{\sinh^2(2kh)} - \frac{1-2kh\coth(2kh)}{\sinh(2kh)}\right], \tag{A 8}$$

$$\beta = \frac{\omega k^2\left(8+\cosh(4kh)-2\tanh^2(kh)\right)}{16\sinh^4(kh)} - \frac{\omega\left(2\omega\cosh^2(kh)+kC_g\right)^2}{2\sinh^2(2kh)\left(gh-C_g^2\right)}. \tag{A 9}$$

For $k_p h < 1.363$, the four-wave interaction vanishes due to the generation of a wave-induced mean flow. Hence, in such cases, waves are stabilised and another form of B–F index is recommended by Janssen & Onorato (2007):

$$B_s^2 = -\mathrm{BFI}_{J03}^2\,\frac{C_g^2}{C^2}\frac{gT_{0,0,0,0}}{k^4\omega}\left(\frac{\mathrm{d}^2\omega}{\mathrm{d}k^2}\right)^{-1}, \tag{A 10}$$

where $C = \omega/k$ is the phase velocity. $T_{0,0,0,0}$ is a known interaction coefficient with a complicated expression in the general case. Here, only its narrow-band limit is given:

$$\frac{T_{0,0,0,0}}{k^3} = \frac{9\tanh^4(kh)-10\tanh^2(kh)+9}{8\tanh^3(kh)} - \frac{1}{kh}\left[\frac{(4C_g-C)^2}{4\left(gh-C_g^2\right)}+1\right]. \tag{A 11}$$

With the computation method (A 5) taken into account, we consider the B–F index in the cases with $k_p h < 1.363$ as:

$$B_s = \mathrm{BFI}_{S06}\,\frac{C_g}{C}\sqrt{\frac{gT_{0,0,0,0}}{2\alpha k^4\omega}}. \tag{A 12}$$

In the deep-water limit, $\alpha \to g/(8k\omega)$ and $T_{0,0,0,0} \to k^3$, B_s reduces to BFI_{S06}. In this study, the coefficients in both two definitions were evaluated using the local peak frequency $\hat{f}_p$.

A.2. *Spectral and bispectral analyses*

The variance density spectrum is obtained by using Welch's method, with 50% overlapping rate of each 2^{14}-point signal segment.

The bispectrum, introduced by Hasselmann *et al.* (1963), characterises the phase-coupling of 3 wave components due to nonlinear interactions. The triad-wave interactions result in wave energy transfer among f_1, f_2, and $f_1 + f_2$. In the present study we follow the definition of bispectrum $B(f_1, f_2)$ in Kim & Powers (1979):

$$B(f_1, f_2) = \left\langle X_1 X_2 X_{1+2}^* \right\rangle, \tag{A 13}$$

which is ensemble average of the triple product of complex Fourier coefficients, X_i denotes the Fourier coefficient of frequency f_i, and the asterisk indicates complex conjugate.

In general, the bispectrum $B(f_1, f_2)$ is a complex quantity. The energy transfer direction is indicated by the sign of $\mathrm{Im}\{B(f_1, f_2)\}$, where $\mathrm{Im}\{\cdot\}$ means taking the imaginary part: negative values mean wave energy is transferred from the component $f_1 + f_2$ to f_1 and f_2 (difference interaction), positive values mean wave energy is transferred from f_1 and f_2 to $f_1 + f_2$ (sum interaction). As a measure of the horizontal asymmetry of the wave profile, the asymmetry parameter can be evaluated following Elgar & Guza (1985):

$$\text{Asymmetry} = \frac{\sum\sum \mathrm{Im}\left\{B\left(f_1, f_2\right)\right\}}{\sigma^3}, \tag{A 14}$$

The commonly used normalisation measure of bispectrum is the bicoherence:

$$b^2(f_1, f_2) = \frac{|B(f_1, f_2)|^2}{\langle |X_1 X_2|^2 \rangle \langle |X_{1+2}|^2 \rangle}. \tag{A 15}$$

The bicoherence $b^2(f_1, f_2)$, bounded in $[0, 1]$, is a measure of the relative strength of the coupling of the three wave components f_1, f_2, and $f_1 + f_2$. For instance, $b^2(f_1, f_2) = 1$ denotes total phase coupling, on the contrary, $b^2(f_1, f_2) = 0$ means the uncorrelated (random) phases.

A.3. *Statistical distributions of surface elevation and wave heights*

The statistical distributions of the free surface elevation and individual wave heights are compared with linear theoretical expectations. Consider the free surface elevation η is the sum of a large number of harmonic waves, each with a constant amplitude and a random phase, then the sea-state is a stationary, Gaussian process. The statistical characteristics are fully described by the variance density spectrum. The high-order moments are then: $\lambda_3(\eta) = 0$ and $\lambda_4(\eta) = 3$. The Gaussian distribution is expressed as (see e.g. Longuet-Higgins 1952):

$$p(\eta) = \frac{1}{\sigma\sqrt{2\pi}} \exp\left(-\frac{\eta^2}{2\sigma^2}\right), \tag{A 16}$$

where p denotes the probability distribution function (PDF). However, it is known that nonlinear finite water effects have great influence on the statistics of the sea-state, causing considerable deviation from the Gaussian model, see the pioneering work of Bitner (1980).

In a Gaussian sea-state with a sufficiently narrow spectrum, the heights of wave crests are Rayleigh distributed. The crest-to-trough wave height could be approximated by twice of the crest height, thus it approximately follows Rayleigh distribution. However, such an assumption is not appropriate for sea-states with finite spectral width, leading to an overestimation of the probability of the high waves (see e.g. Forristall 1978). The wave height distribution models considering spectral width have been studied in, for instance, Naess (1985) and Boccotti (2000). Given that the JONSWAP spectrum with $\gamma = 3.3$ considered in the present study is not sufficiently narrow, the asymptotic model proposed by Boccotti (2000) is chosen as the reference distribution of wave heights:

$$P(H) = \frac{1 + b}{\sqrt{2b\,(1 + a)}} \exp\left(-\frac{H^2}{4\,(1 + a)}\right), \tag{A 17}$$

where $P(H)$ denotes the complementary cumulative distribution function (CCDF), a and b are evaluated as:

$$a = \left| \int_0^\infty S(f) \cos\left(2\pi f \tau^*\right) \mathrm{d}f \right| / m_0, \quad b = \left| \int_0^\infty f^2 S(f) \cos\left(2\pi f \tau^*\right) \mathrm{d}f \right| / m_2, \tag{A 18}$$

with τ^* denoting the time-lag of the global minimum of the autocorrelation function $\rho(\tau) = \langle \eta(t)\eta(t + \tau) \rangle$, and m_2 the second moment of the variance spectrum.

REFERENCES

Baldock, T. E., Swan, C. & Taylor, P. H. 1996 A laboratory study of nonlinear surface waves on water. *Phil. Trans. R. Soc. A.* **354**, 649–676.

Beji, S. & Battjes, J. A. 1993 Experimental investigation of wave propagation over a bar. *Coastal Eng.* **19**, 151–162.

Belibassakis, K. A. & Athanassoulis, G. A. 2011 A coupled-mode system with application

to nonlinear water waves propagating in finite water depth and in variable bathymetry regions. *Coast. Eng.* **58**, 337–350.

Benjamin, T. B. & Feir, J. E. 1967 The disintegration of wave trains on deep water Part 1. Theory. *J. Fluid Mech.* **27**, 417–430.

Bingham, H. B. & Agnon, Y. 2005 A Fourier-Boussinesq method for nonlinear water waves. *Eur. J. Mech. B/Fluids* **24**, 255–274.

Bingham, H. B., Madsen, P. A. & Fuhrman, D. R. 2009 Velocity potential formulations of highly accurate Boussinesq-type models. *Coast. Eng.* **56**, 467–478.

Bitner, E. M. 1980 Non-linear effects of the statistical model of shallow-water wind waves. *Appl. Ocean Res.* **2**, 63–73.

Boccotti, P. 2000 *Wave Mechanics for Ocean Engineering*. Elsevier Science, Oxford.

Borthwick, A. G., Hunt, A. C., Feng, T., Taylor, P. H. & Stansby, P. K. 2006 Flow kinematics of focused wave groups on a plane beach in the U.K. coastal research facility. *Coast. Eng.* **53**, 1033–1044.

Chapalain, G., Cointe, R. & Temperville, A. 1992 Observed and modeled resonantly interacting progressive water-waves. *Coast. Eng.* **16**, 267–300.

Chen, H., Tang, X., Zhang, R. & Gao, J. 2018 Effect of bottom slope on the nonlinear triad interactions in shallow water. *Ocean Dyn.* **68**, 469–483.

Dommermuth, D. 2000 The initialization of nonlinear waves using an adjustment scheme. *Wave Motion* **32**, 307–317.

Ducrozet, G. & Gouin, M. 2017 Influence of varying bathymetry in rogue wave occurrence within unidirectional and directional sea-states. *J. Ocean Eng. Mar. Energy* **3**, 309–324.

Dysthe, K., Krogstad, H. E. & Müller, P. 2008 Oceanic rogue waves. *Annu. Rev. Fluid Mech.* **40**, 287–310.

Elgar, S. & Guza, R. T. 1985 Observations of bispectra of shoaling surface gravity waves. *J. Fluid Mech.* **161**, 425–448.

Fitzgerald, C. J., Taylor, P. H., Taylor, R. E., Grice, J. & Zang, J. 2014 Phase manipulation and the harmonic components of ringing forces on a surface-piercing column. *Proc. R. Soc. A* **470**, 20130847.

Forristall, G. Z. 1978 On the statistical distribution of wave heights in a storm. *J. Geophys. Res.* **83**, 2353.

Goda, Y. 2010 *Random seas and design of maritime structures (3rd edition)*. World Scientific Publishing Company.

Gottlieb, S. 2005 On high order strong stability preserving Runge-Kutta and multi step time discretizations. *J. Sci. Comput.* **25**, 105–128.

Gouin, M., Ducrozet, G. & Ferrant, P. 2016 Development and validation of a non-linear spectral model for water waves over variable depth. *Eur. J. Mech. B. Fluids* **57**, 115–128.

Gramstad, O., Zeng, H., Trulsen, K. & Pedersen, G. K. 2013 Freak waves in weakly nonlinear unidirectional wave trains over a sloping bottom in shallow water. *Phys. Fluids* **25**, 122103.

Hasimoto, H. & Ono, H. 1972 Nonlinear modulation of gravity waves. *J. Phys. Soc. Jpn.* **33**, 805–811.

Hasselmann, K., Munk, W. & MacDonald, G. 1963 *Bispectra of ocean waves. In: M. Rosenblatt Time Series Analysis*. New York: John Wiley.

Janssen, P. A. E. M. 2003 Nonlinear four-wave interactions and freak waves. *J. Phys. Oceanogr.* **33**, 863–884.

Janssen, P. A. E. M. & Onorato, M. 2007 The intermediate water depth limit of the Zakharov equation and consequences for wave prediction. *J. Phys. Oceanogr.* **37**, 2389–2400.

Kashima, H., Hirayama, K. & Mori, N. 2014 Estimation of freak wave occurrence from deep to shallow water regions. *Coast. Eng. Proc.* **1**, 36.

Kashima, H. & Mori, N. 2019 Aftereffect of high-order nonlinearity on extreme wave occurrence from deep to intermediate water. *Coast. Eng.* **153**, 103559.

Katsardi, V., de Lutio, L. & Swan, C. 2013 An experimental study of large waves in intermediate and shallow water depths. Part I: Wave height and crest height statistics. *Coast. Eng.* **73**, 43–57.

Kharif, C. & Pelinovsky, E. 2003 Physical mechanisms of the rogue wave phenomenon. *Eur. J. Mech. B/Fluids* **22**, 603–634.

Kim, Y. C. & Powers, E. J. 1979 Digital bispectral analysis and its applications to nonlinear wave interactions. *IEEE T. Plasma Sci.* **7**, 120–131.

Le Méhauté, B. 1976 *An Introduction to Hydrodynamics and Water Waves*. Springer Berlin Heidelberg.

Longuet-Higgins, M. S. 1952 On the statistical distribution of the height of sea waves. *J. Mar. Res.* **11**, 245–265.

Ma, Y., Ma, X. & Dong, G. 2015 Variations of statistics for random waves propagating over a bar. *J. Mar. Sci. Technol.* **23**, 864–869.

Madsen, P. A., Fuhrman, D. R. & Wang, B. 2006 A Boussinesq-type method for fully nonlinear waves interacting with a rapidly varying bathymetry. *Coast. Eng.* **53**, 487–504.

Mansard, E. P. D. & Funke, E. R. 1980 The measurement of incident and reflected spectra using a least squares method. In *Coastal Engineering 1980*, pp. 154–172.

Massel, S. R. 1983 Harmonic generation by waves propagating over a submerged step. *Coast. Eng.* **7**, 357–380.

Mei, C. C. 1992 *The Applied Dynamics of Ocean Surface Waves*. World Scientific Publishing Company.

Mori, N. & Janssen, P. A. E. M. 2006 On kurtosis and occurrence probability of freak waves. *J. Phys. Oceanogr.* **36**, 1471–1483.

Naess, A. 1985 On the distribution of crest to trough wave heights. *Ocean Eng.* **12**, 221–234.

Olagnon, M. & Magnusson, A. K. 2004 Sensitivity study of sea state parameters in correlation to extreme wave occurrences. In *Proc. 14th Int. Offshore and Polar Engineering Conf. (ISOPE), 23-28 May, Toulon, France*.

Onorato, M., Osborne, A. R. & Serio, M. 2005 Modulational instability and non-Gaussian statistics in experimental random water-wave trains. *Phys. Fluids* **17**, 078101.

Papoutsellis, C. E., Charalampopoulos, A. G. & Athanassoulis, G. A. 2018 Implementation of a fully nonlinear Hamiltonian coupled-mode theory, and application to solitary wave problems over bathymetry. *Eur. J. Mech. B. Fluids* **72**, 199–224.

Raoult, C., Benoit, M. & Yates, M. L. 2016 Validation of a fully nonlinear and dispersive wave model with laboratory non-breaking experiments. *Coast. Eng.* **114**, 194–207.

Sergeeva, A., Pelinovsky, E. & Talipova, T. 2011 Nonlinear random wave field in shallow water: variable Korteweg-de Vries framework. *Nat. Hazards Earth Syst. Sci.* **11**, 323–330.

Serio, M., Onorato, M., Osborne, A. R. & Janssen, P. A. E. M. 2006 On the computation of the Benjamin–Feir index. *Il Nuovo Cimento C* **28**, 893–903.

Simon, B., Papoutsellis, C. E., Benoit, M. & Yates, M. L. 2019 Comparing methods of modeling depth-induced breaking of irregular waves with a fully nonlinear potential flow approach. *J. Ocean Eng. Mar. Energy* **5**, 365–383.

Tian, Y. & Sato, S. 2008 A numerical model on the interaction between nearshore nonlinear waves and strong currents. *Coast. Eng. J.* **50**, 369–395.

Toffoli, A., Fernandez, L., Monbaliu, J., Benoit, M., Gagnaire-Renou, E., Lefèvre, J. M., Cavaleri, L., Proment, D., Pakozdi, C., Stansberg, C. T., Waseda, T. & Onorato, M. 2013 Experimental evidence of the modulation of a plane wave to oblique perturbations and generation of rogue waves in finite water depth. *Phys. Fluids* **25**, 091701.

Trulsen, K., Raustøl, A., Jorde, S. & Rye, L. B. 2020 Extreme wave statistics of long-crested irregular waves over a shoal. *J. Fluid Mech.* **882**, R2.

Trulsen, K., Zeng, H. & Gramstad, O. 2012 Laboratory evidence of freak waves provoked by non-uniform bathymetry. *Phys. Fluids* **24**, 097101.

Viotti, C. & Dias, F. 2014 Extreme waves induced by strong depth transitions: fully nonlinear results. *Phys. Fluids* **26**, 051705.

Yates, M. L. & Benoit, M. 2015 Accuracy and efficiency of two numerical methods of solving the potential flow problem for highly nonlinear and dispersive water waves. *Int. J. Numer. Methods Fluids* **77**, 616–640.

Young, I.R. 1995 The determination of confidence limits associated with estimates of the spectral peak frequency. *Ocean Eng.* **22**, 669–686.

Zakharov, V. E. 1968 Stability of periodic waves of finite amplitude on the surface of a deep fluid. *J. Appl. Mech. Tech. Phys.* **9**, 190–194.

Zang, J., Gibson, R., Taylor, P. H., Taylor, R. Eatock & Swan, C. 2006 Second order

wave diffraction around a fixed ship-shaped body in unidirectional steep waves. *J. Offshore Mech. Arct. Eng.* **128**, 89–99.

Zang, J., Taylor, P. H., Morgan, G., Tello, M., Grice, J. & Orszaghova, J. 2010 Experimental study of non-linear wave impact on offshore wind turbine flundations. In *Coastlab10: 3rd Int. Conf. on the Application of Physical Modelling to Port and Coastal Protection, 28th Sep.–1st Oct., Barcelona, Spain*.

Zeng, H. & Trulsen, K. 2012 Evolution of skewness and kurtosis of weakly nonlinear unidirectional waves over a sloping bottom. *Nat. Hazards Earth Syst. Sci.* **12**, 631–638.

Zhang, J., Benoit, M., Kimmoun, O., Chabchoub, A. & Hsu, H.-C. 2019 Statistics of extreme waves in coastal waters: large scale experiments and advanced numerical simulations. *Fluids* **4**, 99.

Zheng, Y., Lin, Z., Li, Y., Adcock, T. A. A., Li, Y. & van den Bremer, T. S. 2020 Fully nonlinear simulations of unidirectional extreme waves provoked by strong depth transitions: The effect of slope. *Phys. Rev. Fluids* **5**, 064804.

Chapter 5

Conclusion and outlook

5.1 Summary of findings and conclusions

In this part of the Ph.D. thesis, the non-equilibrium characteristics observed when a quasi-steady incident sea state gradually adapts to a new equilibrium after strong depth variations have been studied by large-scale experiments as well as highly accurate numerical simulations. State-of-art data processing techniques related to natural sea-states and freak wave analysis have been broadly reviewed. With these techniques, the temporal and spectral features of the measured (numerically and experimentally) data can be extracted and analyzed. Wave grouping characteristics, as well as effects related to four-wave interaction, can be interpreted in a quantified manner. In this part, two axes of study are considered. One is the experimental and numerical study on the basis of the experimental campaign conducted in THL (Taiwan), in which a step-like bottom profile was adopted. The other is the numerical study based on the experiments reported by Trulsen et al. (2020) in which a bar-like bottom profile was used. In both cases, the spectral and bispectral analysis, statistical wave-by-wave analysis, and integral sea state non-dimensional parameters are adopted to characterize the non-equilibrium dynamic response during the sea-state adaptation process.

In the experimental campaign in the large-scale wave flume in THL, a broad range of experimental conditions has been tested. The relative water depth transition is more pronounced compared to existing experimental tests in similar studies. The sea states are of different degrees of nonlinearity, close to the breaking-limit in some cases. Tested wave spectra are of JONSWAP shape with different values of the peak enhancement factor γ. The relative water depths in the shallower region are lower than 1.363, so modulational instability is expected to be of secondary importance in the shallower region. The complete life-circles of freak waves were tracked in the large-scale flume. The following conclusions are drawn from this study:

- In line with the work of Trulsen et al. (2020), two different trends are ob-

served in our irregular wave experiments conducted in THL. Case 1 is the representative case in which the sea state is quasi-Gaussian before and after the depth transition region. No evident increase of the skewness and kurtosis and no significant wave energy increase of second harmonics after the shoaling step are observed. The other trend is represented by Case 10 (shown in the journal paper by Zhang et al. (2019)) and 15, in which non-negligible energy increase of high-order harmonics and local maxima of λ_3^η, λ_4^η, BFI take place in a short distance after the step. The spectra experience broadening in the shallower region. Wave energy is redistributed over a broad range of frequencies in the spectrum. Several low-frequency modes appear, which can be well predicted by a linear approach outlined in Appendix A.1.

- In our experiments, the relative water depth of the shallower region covers only a limited range $[0.42, 0.77]$, it is difficult to draw conclusive comments on the 'threshold' or 'transition' relative water depth as done in Trulsen et al. (2020). But at least, the Case 1 (and the Case 19 not shown here) in our experimental campaign did not show local maxima of nonlinear parameters. This suggests two possibilities, one is that the 'threshold' depth for different dynamic responses of the sea states over the current $1:20$ slope is between 0.5 (Case 10) and 0.64 (Case 1). The other is that the nonlinearity also plays an important role in determining the dynamic response of water waves propagating over uneven bottoms.

- We stress on the fact that the bottom slope can provoke effects on a very local scale. Even for quasi-Gaussian sea states, like Case 1, the bottom transition could bring the formation of freak waves from an energetic wave packet.

- The numerical simulation study is conducted by using two highly accurate numerical codes, one is a Boussinesq-type model and the other is Whispers3D. Simulations with both codes show good agreement with measurements given the length of relaxation zone, numerical step sizes in space (Δx) and time (Δt), and the parameters N_T (for Whispers3D) and N_B (for Boussinesq-type model) are properly chosen. The agreement is better in the upwave zone near the wavemaker than downwave due to some unexpected perturbations in the outdoor wave flume at THL. The statistical parameters agree well with measurements downstream, thus the models can be used to study the statistical features of freak waves. The conclusion drawn from the detailed comparison between Case 10 simulation results and measurements are given in the conclusion section of the journal paper, and are thus not repeated here.

In the work of Trulsen et al. (2020), long-crested irregular wave trains propagating over a steep ($1:3.81$) step bottom profile have been investigated. The wave-bottom interaction includes both shoaling and de-shoaling processes. With a series of tests with a large range of relative water depth, they found the 'transition'

water depth being 1.3 in their tests. The statistical moments of horizontal velocity are shown to have different evolutions in space compared to that of the free surface elevation. In the numerical study, we adopted Whispers3D to reproduce one of the experimental cases of Trulsen et al. (2020) and extracted additional information from the computed velocity field. Then, the effects of de-shoaling are discussed with a simulation of the same incident wave train propagating over a step bottom profile. A thorough investigation of the sea state adaptation process for both bottom profiles has been conducted by considering various non-dimensional parameters, wave-by-wave statistics, spectral and bispectral analyses. The main findings and conclusions have been reported in a journal paper (submitted), and are thus not repeated here.

5.2 Outlook and perspectives of future work

In this part, the concept of the 'transition' relative water depth has been discussed on the basis of two independent experimental campaigns, one is conducted by our team in the wave flume of THL in Taiwan, and the other by another team in Norway. In our experiments, different parameter combinations in (h, T_p, H_s, γ) space have been considered; however, the range of relative water depth in the shallower region is relatively limited. Meanwhile, the experiments of Trulsen et al. (2020) considered a larger range of shallower region relative water depth but only for intermediate nonlinearity. Both experimental campaigns tested one bathymetry setup (with different slopes).

It remains to be systematically studied whether the transition water depth is influenced by other factors (apart from relative water depth), such as wave nonlinearity, slope gradient, and spectral width. Comparing Cases 1-5 with gradually increasing incident wave amplitudes, the local values of skewness and kurtosis after the slope show a increasing trend. In our experiments, the cases with different γ factor of the JONSWAP spectrum (Case 10 and 11 for example) show very similar results in terms of statistical parameters, indicating that the spectral width plays a secondary role, at least in our tests. As follow-up work, a larger numerical investigation will be conducted with Whispers3D model which has been proven its validity in the simulations of these two experimental campaigns. The purpose is to show whether and how the choices of bottom slope, spectral width, and the nonlinearity of the wave train take effects during the sea state adaptation process over the sloping area.

Part V
Appendices

Une montagne est faite de poignées de terre, un fleuve de nombreux filets d'eau.
Taoïsme, œuvre de Tchouang-tseu
Tchouang tseu (IIIe siècle av. J.-C.)

Appendix A

Derivation details

1.1 The derivation of natural modes in the water flume with arbitrary bottom profile

In experiments, the causes of the formation of long-waves are various, including non-resonant wave-wave interaction and long-wave resonance. As is known that when the length of the basin is an integral multiple of half wavelength, long-wave resonance could take place in the basin. To study the low-frequency waves in experiments, the possible frequencies that may resonate within the flume should be computed. For the arbitrary water depth, within the framework of linear theory, the wavelength (and its corresponding wave-number) is a function of local water depth $h(x)$. The resonance condition in the flume with $\bar{l}_w$ in length, is:

$$l_b = \frac{n\bar{l}_w}{2} = \frac{n\pi}{\bar{k}_w}, \tag{V.A.1}$$

where l_b denotes the length of wave flume, $\bar{l}_w$ denotes the averaged wavelength, and its corresponding wave-number is $\bar{k}_w$.

The averaged wave-number over the wave flume length is defined as:

$$\bar{k}_w = \frac{\int_0^{l_b} k_w(x)\,\mathrm{d}x}{l_b}, \tag{V.A.2}$$

so the resonant condition could be written by replacing $\bar{k}_w$ in Eq. (V.A.1) with Eq. (V.A.2):

$$\int_0^{l_b} k_w(x)\,\mathrm{d}x = n\pi. \tag{V.A.3}$$

Now, consider the following additional assumptions, which generally hold for long waves in the wave flume:

- **Assumption 1** The long waves in the wave flume are of low energy, the wave amplitudes are small compared to their wavelengths (low steepness). The linear wave theory can thus be adopted.
- **Assumption 2** Within the framework of linear theory, the local relative water depth $k_w h$ as a function of x is small all over the basin so that the shallow-water approximation of the linear dispersion relationship could be adopted to estimate local mean angular frequency $\omega_w = k_w\sqrt{gh}$;
- **Assumption 3** The variable bottom could be approximated by a large number of small segments with constant slopes as shown in Figure (V.A.1). The i-th slope segment starts from x_i to x_{i+1} and its length is $l_{b,i} = x_{i+1} - x_i$.

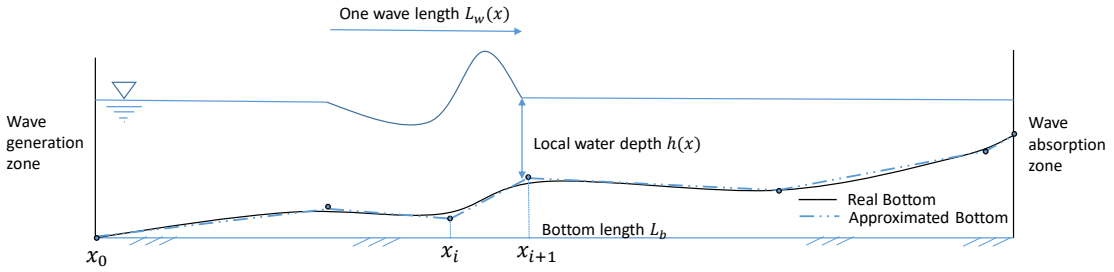

Figure V.A.1: A two dimensional basin with variable bottom.

Applying assumption 2 to the resonant condition given in Eq. (V.A.3), a set of the possible resonant frequencies f_n is obtained:

$$f_n = \frac{\omega_n}{2\pi} = \frac{n\sqrt{g}}{2}\left[\int_0^{l_b} \frac{1}{\sqrt{h(x)}}\,\mathrm{d}x\right]^{-1}, n = 1, 2, 3, \ldots \tag{V.A.4}$$

Using K_n to denote the integral $\int_0^{l_b} 1/\sqrt{h(x)}\,\mathrm{d}x$, the Eq. (V.A.4) is simplified as follows:

$$f_n = n\frac{\sqrt{g}}{2}K_n^{-1}. \tag{V.A.5}$$

Now the assumption 3 is applied here to evaluate K_n in a discrete manner. The real bottom profile is separated into a large number of segments with constant slopes, and the original integration is simplified. The K_n is evaluated as:

$$K_n = \sum_{i=0}^{n-1} \int_{x_i}^{x_{i+1}} \frac{1}{\sqrt{h(x)}}\,\mathrm{d}x, \tag{V.A.6}$$

when the number of segments is large so that $l_{b,i}$ is small enough, the water depth as a function of x is approximated by:

$$h(x) \approx \frac{h(x_{i+1}) - h(x_i)}{l_{b,i}}\,(x - x_i) + h(x_i). \tag{V.A.7}$$

By replacing $h(x)$ in Eq. (V.A.7) into Eq. (V.A.6), the result of the integral could be written as:

$$\begin{aligned} K_n &\approx \sum_{i=0}^{n-1} \frac{2\big(x_{i+1}-x_i\big)}{h(x_{i+1})-h(x_i)}\big[\sqrt{h(x_{i+1}}-\sqrt{h(x_i)}\big] \\ &= \sum_{i=0}^{n-1} \frac{2\big(x_{i+1}-x_i\big)}{\sqrt{h(x_{i+1})}+\sqrt{h(x_i)}} \\ &= \sum_{i=0}^{n-1} \frac{2l_{b,i}}{\sqrt{h(x_{i+1})}+\sqrt{h(x_i)}}. \end{aligned}$$

Now the possible resonant frequencies could be computed by taking the approximated value of K_n, and other properties corresponding to each natural mode are obtained:

$$f_n = n\frac{\sqrt{g}}{2}K_n^{-1} \quad \omega_n = 2\pi f_n, \quad n = 1, 2, 3..., \tag{V.A.8}$$

$$\bar{l}_n = \frac{2l_b}{n} \qquad \bar{k}_n = \frac{2\pi}{\bar{l}_n}, \qquad n = 1, 2, 3.... \tag{V.A.9}$$

This method is valid as long as the shallow water assumption can be considered to hold.

1.2 Relation of different dissipation rates in visco-potential and NLSE models

In NLSE models, the dissipation parameter δ stands for the exponential attenuation rate of wave amplitude. Whereas, the bulk dissipation ν in Whispers3D model following the visco-potential approach of Dias et al. (2008) is applied to the whole computation domain. Here we compute the corresponding amplitude attenuation rate δ for given bulk dissipation rate ν. This computation is performed within the linear framework.

First, recall the two free surface boundary conditions in two-dimensional Euler-Zakharov model applied at $z = \eta(x,t)$, the definition of variables and detailed derivation are given in Section (2):

$$\begin{cases} \eta_t = -\tilde{\phi}_x\eta_x + \tilde{w}\left(1+\eta_x^2\right) + 2\nu\eta_{xx}, & \text{(V.A.10)} \\ \tilde{\phi}_t = -g\eta - \dfrac{1}{2}\tilde{\phi}_x^2 + \dfrac{1}{2}\tilde{w}^2\left(1+\eta_x^2\right) - 2\nu\tilde{\phi}_{zz}. & \text{(V.A.11)} \end{cases}$$

Retaining only the linear terms in the free surface boundary conditions, we get the linearized system of equations on the (linearized) free surface $z = 0$:

$$\begin{cases} \eta_t - \phi_z - 2\nu\eta_{xx} = 0, & \text{(V.A.12)} \\ \tilde{\phi}_t + g\eta + 2\nu\tilde{\phi}_{zz} = 0. & \text{(V.A.13)} \end{cases}$$

Considering uniform water depth, h being constant, the linearized problem with bulk dissipation taken into account becomes:

$$\begin{cases} \phi_{tt} + g\phi_z - 2\nu\left(\phi_{xxt} - \phi_{zzt} + 2\nu\phi_{xxzz}\right) = 0, & z = 0 \quad \text{(V.A.14)} \\ \phi_{xx} + \phi_{zz} = 0, & -h \le z \le 0 \quad \text{(V.A.15)} \\ \phi_z = 0. & z = -h \quad \text{(V.A.16)} \end{cases}$$

We look for harmonic plane wave solution of the system of Eqs. (V.A.14) $\sim$ (V.A.16) of the following form:

$$\phi(x, z, t) = \cosh\left(\kappa(h + z)\right)e^{i\kappa x}e^{-i\omega t}, \tag{V.A.17}$$

where ω denotes angular frequency, $\kappa \equiv a + ib$ is the corresponding complex wave number. The exponential decay of wave amplitude is characterized by the imaginary part of the wave number: $\delta = b$.

Inserting Eq. (V.A.17) into the linearized free surface boundary condition Eq. (V.A.14), the dispersion relation in dissipative medium is obtained:

$$\omega^2\left(1 + 2i\frac{\nu}{\omega}\kappa^2\right)^2 = g\kappa\tanh\left(\kappa h\right). \tag{V.A.18}$$

For given (ω, h, ν), the roots of κ of this dispersion relation can be found. The real part of κ is the wave-number corresponding to ω, and the imaginary part of κ represents the wave amplitude attenuation that corresponds to ν. Especially, when ν is zero, Eq. (V.A.18) reduces to the classical linear wave dispersion relationship. A simple iteration approach can be used to solve Eq. (V.A.18), and will not be detailed here.

Via this approach, the corresponding δ for given ν is obtained. For given δ (from measurements), the corresponding value of ν is found by bisection method.

Appendix B

Publications during the Ph.D. study

2.1 Journal papers

[1] **J. Zhang**, M. Benoit, Effect of finite amplitude of bottom corrugations on Fabry-Perot resonance of water waves, Physical Review E 99 (2019) 053109. doi:10.1103/PhysRevE.99.053109.

[2] **J. Zhang**, M. Benoit, O. Kimmoun, A. Chabchoub, H.-C. Hsu, Statistics of extreme waves in coastal waters: Large scale experiments and advanced numerical simulations, Fluids 4 (2019) 99. doi:10.3390/fluids4020099.

[3] **J. Zhang**, M. Benoit, Wave-bottom interaction and extreme wave statistics due to shoaling and de-shoaling of irregular long-crested wave trains over steep seabed changes, submitted to Journal of Fluid Mechanics.

2.2 Conference papers/abstracts

[1] **J. Zhang**, M. Benoit, Fabry-Perot resonance of coastal water waves: comparison of linear modeling approaches, in Proceedings of 16èmes Journées de l'Hydrodynamique (JH2018), 11, 27-29, November 2018, Marseille, France.

[2] M. Benoit, **J. Zhang**, A numerical study of the importance of nonlinear effects for Fabry-Perot resonance of water waves, in Proceedings of 36th Conference on Coastal Engineering (ICCE), 1 (36), 26, July 30-August 3, 2018, Baltimore, Maryland, USA. doi:10.9753/icce.v36.waves.26.

[3] **J. Zhang**, M. Benoit, O. Kimmoun, H.-C. Hsu, Statistics of extreme waves in coastal waters: large scale experiments and advanced numerical simulations, in

Proceedings of 36th Conference on Coastal Engineering (ICCE), 1 (36), 86, July 30-August 3, 2018, Baltimore, Maryland, USA. doi:10.9753/icce.v36.waves.86.

[4] **J. Zhang**, M. Benoit, O. Kimmoun, H.-C. Hsu, Large-scale physical modeling of extreme waves in coastal area, in the 7th International Conference on the Application of Physical Modelling in Coastal and Port Engineering and Science (Coastlab18), 22-26 May, 2018, Santander, Spain.

Bibliography

T. A. A. Adcock and P. H. Taylor. The physics of anomalous ('rogue') ocean waves. *Reports on Progress in Physics*, 77(10):105901, 2014. doi: 10.1088/0034-4885/77/10/105901.

T. A. A. Adcock and P. H. Taylor. Fast and local non-linear evolution of steep wave-groups on deep water: A comparison of approximate models to fully non-linear simulations. *Physics of Fluids*, 28(1):016601, 2016. doi: 10.1063/1.4938144.

N. Akhmediev and A. Ankiewicz. Modulation instability, Fermi-Pasta-Ulam recurrence, rogue waves, nonlinear phase shift, and exact solutions of the Ablowitz-Ladik equation. *Physical Review E*, 83:046603, 2011. doi: 10.1103/physreve.83.046603.

N. Akhmediev, A. Ankiewicz, and J. M. S. Crespo. Rogue waves and rational solutions of the nonlinear Schrödinger equation. *Physical Review E*, 80(2), 2009a. doi: 10.1103/physreve.80.026601.

N. Akhmediev, A. Ankiewicz, and M. Taki. Waves that appear from nowhere and disappear without a trace. *Physics Letters A*, 373:675–678, 2009b. ISSN 6. doi: 10.1016/j.physleta.2008.12.036.

N. N. Akhmediev and V. I. Korneev. Modulation instability and periodic solutions of the nonlinear Schrödinger equation. *Theoretical and Mathematical Physics*, 69(2):1089–1093, 1986. doi: 10.1007/bf01037866.

N. N. Akhmediev, V. M. Eleonskii, and N. E. Kulagin. Exact first-order solutions of the nonlinear Schrödinger equation. *Theoretical and Mathematical Physics*, 702(2):809–818, 1987. doi: 10.1007/BF01017105.

M. R. Alam, Y. Liu, and D. K. P. Yue. Oblique sub- and super-harmonic Bragg resonance of surface waves by bottom ripples. *Journal of Fluid Mechanics*, 643: 437–447, 2010. doi: 10.1017/s0022112009992850.

D. M. Ambrose, J. L. Bona, and D. P. Nicholls. On ill-posedness of truncated series models for water waves. *Proceedings of the Royal Society A: Mathematical,*

Physical and Engineering Sciences, 470(2166):20130849, 2014. doi: 10.1098/rspa.2013.0849.

T. L. Andersen, M. R. Eldrup, and P. Frigaard. Estimation of incident and reflected components in highly nonlinear regular waves. *Coastal Engineering*, 119:51–64, 2017. doi: 10.1016/j.coastaleng.2016.08.013.

T. L. Andersen, M. R. Eldrup, and M. Clavero. Separation of long-crested nonlinear bichromatic waves into incident and reflected components. *Journal of Marine Science and Engineering*, 7(2):39, 2019. doi: 10.3390/jmse7020039.

F. Ardhuin and R. Magne. Scattering of surface gravity waves by bottom topography with a current. *Journal of Fluid Mechanics*, 576:235–264, 2007. doi: 10.1017/s0022112006004484.

A. Armaroli, A. Gomel, A. Chabchoub, M. Brunetti, and J. Kasparian. Stabilization of uni-directional water-wave trains over an uneven bottom. *arXiv preprint arXiv:2002.12923*, 2020.

G. A. Athanassoulis and K. A. Belibassakis. A consistent coupled-mode theory for the propagation of small-amplitude water waves over variable bathymetry regions. *Journal of Fluid Mechanics*, 389:275–301, 1999. doi: 10.1017/s0022112099004978.

G. A. Athanassoulis and K. A. Belibassakis. New evolution equations for nonlinear water waves in general bathymetry with application to steady travelling solutions in constant, but arbitrary depth. *Discrete and Continuous Dynamical Systems- Series A*, pages 75–84, 2007.

T. E Baldock and D. J. Simmonds. Separation of incident and reflected waves over sloping bathymetry. *Coastal Engineering*, 38(3):167–176, 1999. doi: 10.1016/s0378-3839(99)00046-0.

T. E. Baldock, C. Swan, and P. H. Taylor. A laboratory study of nonlinear surface waves on water. *Philosophical Transactions of the Royal Society of London. Series A: Mathematical, Physical and Engineering Sciences*, 354(1707):649–676, 1996. doi: 10.1098/rsta.1996.0022.

S. Beji and J. A. Battjes. Experimental investigation of wave propagation over a bar. *Coastal Engineering*, 19:151–162, 1993. doi: 10.1016/0378-3839(93)90022-z.

K. A. Belibassakis and G. A. Athanassoulis. A coupled-mode system with application to nonlinear water waves propagating in finite water depth and in variable bathymetry regions. *Coastal Engineering*, 58(4):337–350, 2011. doi: 10.1016/j.coastaleng.2010.11.007.

M. Belzons, V. Rey, and E. Guazzelli. Subharmonic Bragg resonance for surface water waves. *Europhysics Letters*, 16(2):189–194, 1991. doi: 10.1209/0295-5075/16/2/012.

E. S. Benilov, J. D. Flanagan, and C. P. Howlin. Evolution of packets of surface gravity waves over smooth topography. *Journal of Fluid Mechanics*, 533:171–181, 2005. doi: 10.1017/s0022112005004246.

T. B. Benjamin. Instability of periodic wave trains in nonlinear dispersive systems. *Proceedings of the Royal Society of London. Series A. Mathematical and Physical Sciences*, 299(1456):59–76, 1967. doi: 10.1098/rspa.1967.0123.

T. B. Benjamin and J. E. Feir. The disintegration of wave trains on deep water part 1. Theory. *Journal of Fluid Mechanics*, 27(03):417, 1967. doi: 10.1017/s002211206700045x.

S. S. Bennett, D. A. Hudson, and P. Temarel. A comparison of abnormal wave generation techniques for experimental modelling of abnormal wave–vessel interactions. *Ocean Engineering*, 51:34–48, 2012. doi: 10.1016/j.oceaneng.2012.05.007.

M. Benoit, C. Raoult, and M. L. Yates. Analysis of the linear version of a highly dispersive potential water wave model using a spectral approach in the vertical. *Wave Motion*, 74:159–181, 2017. doi: 10.1016/j.wavemoti.2017.07.002.

J. C. W. Berkhoff. Computation of combined refraction-diffraction. *Coastal Engineering Proceedings*, 1(13):23, 1972. doi: 10.9753/icce.v13.23.

J. C. W. Berkhoff. *Mathematical models for simple harmonic linear water waves: Wave diffraction and refraction*. PhD thesis, Delft Hydraulics Laboratory, 1976.

X. Bertin, A. de Bakker, A. van Dongeren, G. Coco, G. André, F. Ardhuin, P. Bonneton, F. Bouchette, B. Castelle, W. C. Crawford, M. Davidson, M. Deen, G. Dodet, T. Guérin, K. I., F. Leckler, R. McCall, H. Muller, M. Olabarrieta, D. Roelvink, G. Ruessink, D. Sous, É. Stutzmann, and M. Tissier. Infragravity waves: From driving mechanisms to impacts. *Earth-Science Reviews*, 177:774–799, 2018. doi: 10.1016/j.earscirev.2018.01.002.

H. B. Bingham, P. A. Madsen, and D. R. Fuhrman. Velocity potential formulations of highly accurate Boussinesq-type models. *Coastal Engineering*, 56(4):467–478, 2009. doi: 10.1016/j.coastaleng.2008.10.012.

E. M. Bitner. Non-linear effects of the statistical model of shallow-water wind waves. *Applied Ocean Research*, 2(2):63–73, 1980. doi: 10.1016/0141-1187(80)90031-0.

N. Booij. A note on the accuracy of the mild-slope equation. *Coastal Engineering*, 7(3):191–203, 1983. doi: 10.1016/0378-3839(83)90017-0.

E. Buldakov, D. Stagonas, and R. Simons. Extreme wave groups in a wave flume: controlled generation and breaking onset. *Coastal Engineering*, 128:75–83, 2017. doi: 10.1016/j.coastaleng.2017.08.003.

M. J. Cassidy. *Non-linear analysis of jack-up structures subjected to random waves*. PhD thesis, University of Oxford, 1999.

L. Cavaleri, F. Barbariol, A. Benetazzo, L. Bertotti, J. R. Bidlot, P. A. E. M. Janssen, and N. Wedi. The Draupner wave: A fresh look and the emerging view. *Journal of Geophysical Research: Oceans*, 121(8):6061–6075, 2016. doi: 10.1002/2016jc011649.

A. Chabchoub and R. Grimshaw. The hydrodynamic nonlinear Schrödinger equation: space and time. *Fluids*, 1(3):23, 2016. doi: 10.3390/fluids1030023.

A. Chabchoub, N. P. Hoffmann, and N. Akhmediev. Rogue wave observation in a water wave tank. *Physical Review Letter*, 106:204502, 2011. doi: 10.1103/PhysRevLett.106.204502.

A. Chabchoub, N. Hoffmann, M. Onorato, and N. Akhmediev. Super rogue waves: observation of a higher-order breather in water waves. *Physical Review X*, 2: 011015, 2012. doi: 10.1103/PhysRevX.2.011015.

A. Chabchoub, M. Onorato, and N. Akhmediev. Hydrodynamic envelope solitons and breathers. In *Rogue and Shock Waves in Nonlinear Dispersive Media*, pages 55–87. Springer International Publishing, 2016. doi: 10.1007/978-3-319-39214-1_3.

P. G. Chamberlain and D. Porter. The modified mild-slope equation. *Journal of Fluid Mechanics*, 291:393–407, 1995. doi: 10.1017/s0022112095002758.

C. N. Chandrasekera and K. F. Cheung. Extended linear refraction-diffraction model. *Journal of Waterway, Port, Coastal, and Ocean Engineering*, 123(5): 280–286, 1997. doi: 10.1061/(asce)0733-950x(1997)123:5(280).

J. R. Chaplin. On frequency-focusing unidirectional waves. In *International Journal of Offshore and Polar Engineering*, volume 6, pages 131–137. International Society of Offshore and Polar Engineers, 1996.

H. Chien, C. C. Kao, and L. Z. H. Chuang. On the characteristics of observed coastal freak waves. *Coastal Engineering Journal*, 44(4):301–319, 2002. doi: 10.1142/s0578563402000561.

V. H. Chu and C. C. Mei. The non-linear evolution of Stokes waves in deep water. *Journal of Fluid mechanics*, 47:337–351, 1971. doi: 10.1017/S0022112071001095.

R. Cienfuegos, E. Barthélemy, and P. Bonneton. Wave-breaking model for Boussinesq-type equations including roller effects in the mass conservation equation. *Journal of Waterway, Port, Coastal, and Ocean Engineering*, 136(1):10–26, 2010. doi: 10.1061/(ASCE)WW.1943-5460.0000022.

D. Clamond, M. Francius, J. Grue, and C. Kharif. Long time interaction of envelope solitons and freak wave formations. *European Journal of Mechanics - B/Fluids*, 25(5):536–553, 2006. doi: 10.1016/j.euromechflu.2006.02.007.

G. F. Clauss. Task-related rogue waves embedded in extreme seas. In *21st International Conference on Offshore Mechanics and Arctic Engineering*, volume 36142, pages 653–665. ASMEDC, 2002. doi: 10.1115/omae2002-28459.

G. F. Clauss and U. Steinhagen. Optimization of transient design waves in random sea. In *Proceedings of the Tenth (2000) International Offshore and Polar Engineering Conference Seattle, USA, May 28-June 2, 2000*, 2000.

L. A. Couston, Q. C. Guo, M. Chamanzar, and M. R. Alam. Fabry-Perot resonance of water waves. *Physical Review E*, 92(4):043015, 2015. doi: 10.1103/physreve.92.043015.

L. A. Couston, M. A. Jalali, and M. R. Alam. Shore protection by oblique seabed bars. *Journal of Fluid Mechanics*, 815:481–510, 2017. doi: 10.1017/jfm.2017.61.

W. Craig and C. Sulem. Numerical simulation of gravity waves. *Journal of Computational Physics*, 108(1):73–83, 1993. doi: 10.1006/jcph.1993.1164.

W. Craig, P. Guyenne, and C. Sulem. Hamiltonian higher-order nonlinear Schrödinger equations for broader-banded waves on deep water. *European Journal of Mechanics B/Fluids*, 32:22–31, 2012. doi: 10.1016/j.euromechflu.2011.09.008.

A. D. D. Craik. The origins of water wave theory. *Annual Review of Fluid Mechanics*, 36(1):1–28, 2004. doi: 10.1146/annurev.fluid.36.050802.122118.

C. Cui, N. Zhang, Y. Yu, and J. Li. Numerical study on the effects of uneven bottom topography on freak waves. *Ocean Engineering*, 54:132–141, 2012. doi: 10.1016/j.oceaneng.2012.06.021.

R. A. Dalrymple and J. T. Kirby. Water waves over ripples. *Journal of Waterway, Port, Coastal, and Ocean Engineering*, 112(2):309–310, 1986.

A. G. Davies. The reflection of wave energy by undulations on the seabed. *Dynamics of Atmospheres and Oceans*, 6(4):207–232, 1982. doi: 10.1016/0377-0265(82)90029-x.

A. G. Davies and A. D. Heathershaw. Surface-wave propagation over sinusoidally varying topography. *Journal of Fluid Mechanics*, 144:419–443, 1984. doi: 10.1017/s0022112084001671.

S. Debsarma and K. P. Das. Fourth-order nonlinear evolution equations for a capillary-gravity wave packet in the presence of another wave packet in deep water. *Physics of Fluids*, 19(9):097101, 2007. doi: 10.1063/1.2772252.

Y. Deng, J. Yang, W. Zhao, L. Xiao, and X. Li. An efficient focusing model of freak wave generation considering wave reflection effects. *Ocean Engineering*, 105:125–135, 2015. doi: 10.1016/j.oceaneng.2015.04.058.

F. Dias, A. I. Dyachenko, and V. E. Zakharov. Theory of weakly damped free-surface flows: A new formulation based on potential flow solutions. *Physics Letters A*, 372(8):1297–1302, 2008. doi: 10.1016/j.physleta.2007.09.027.

I. Didenkulova and C. Anderson. Freak waves of different types in the coastal zone of the Baltic sea. *Natural Hazards and Earth System Science*, 10(9):2021–2029, 2010. doi: 10.5194/nhess-10-2021-2010.

I. Didenkulova and E. Pelinovsky. Rogue waves in nonlinear hyperbolic systems (shallow-water framework). *Nonlinearity*, 24(3):R1–R18, 2011. doi: 10.1088/0951-7715/24/3/r01.

V. D. Djordjević and L. G. Redekopp. On the development of packets of surface gravity waves moving over an uneven bottom. *Journal of Applied Mathematics and Physic*, 29(6):950–962, 1978. doi: 10.1007/bf01590816.

D. G. Dommermuth and D. K. P. Yue. A high-order spectral method for the study of nonlinear gravity waves. *Journal of Fluid Mechanics*, 184:267–288, 1987. doi: 10.1017/s002211208700288x.

W. G. Van Dorn. Boundary dissipation of oscillatory waves. *Journal of Fluid Mechanics*, 24(04):769, 1966. doi: 10.1017/s0022112066000995.

G. Ducrozet and M. Gouin. Influence of varying bathymetry in rogue wave occurrence within unidirectional and directional sea-states. *Journal of Ocean Engineering and Marine Energy*, 3:309–324, 2017. ISSN 2198–6444. doi: 10.1007/s40722-017-0086-6.

J. M. Dudley, G. Genty, F. Dias, B. Kibler, and N. Akhmediev. Modulation instability, Akhmediev breathers and continuous wave supercontinuum generation. *Optics Express*, 17(24):21497, 2009. doi: 10.1364/oe.17.021497.

K. Dysthe, H. E. Krogstad, and P. Müller. Oceanic rogue waves. *Annual Review of Fluid Mechanics*, 40:287–310, 2008. doi: 10.1146/annurev.fluid.40.111406.102203.

K. B. Dysthe. Note on a modification to the nonlinear Schrödinger equation for application to deep water waves. *Proceedings The Royal of Society A: Mathematical, Physical and Engineering Sciences*, 369:105–114, 1979. ISSN 1736. doi: 10.1098/rspa.1979.0154.

K. B. Dysthe and K. Trulsen. Note on breather type solutions of the NLS as models for freak-waves. *Physica Scripta*, T82(1):48, 1999. doi: 10.1238/physica.topical.082a00048.

D. Eeltink, A. Lemoine, H. Branger, O. Kimmoun, C. Kharif, J. D. Carter, A. Chabchoub, M. Brunetti, and J. Kasparian. Spectral up- and downshifting of Akhmediev breathers under wind forcing. *Physics of Fluids*, 29(10):107103, 2017. doi: 10.1063/1.4993972.

R. B. Elandt, L. A. Couston, R. A. Lambert, and M. R. Alam. Bragg resonance of gravity waves and ocean renewable energy. In *Integrated Systems: Innovations and Applications*, pages 211–225. Springer International Publishing, 2015. doi: 10.1007/978-3-319-15898-3_13.

M. R. Eldrup and T. L. Andersen. Estimation of incident and reflected wave trains in highly nonlinear two-dimensional irregular waves. *Journal of Waterway, Port, Coastal, and Ocean Engineering*, 145(1):04018038, 2019. doi: 10.1061/(asce)ww.1943-5460.0000497.

S. Elgar and R. T. Guza. Observations of bispectra of shoaling surface gravity waves. *Journal of Fluid Mechanics*, 161:425–448, 1985. doi: 10.1017/S0022112085003007.

M. Erkintalo, K. Hammani, B. Kibler, C. Finot, N. Akhmediev, J. M. Dudley, and G. Genty. Higher-order modulation instability in nonlinear fiber optics. *Physical Review Letters*, 107(25), 2011. doi: 10.1103/physrevlett.107.253901.

F. Fedele. On the kurtosis of deep-water gravity waves. *Journal of Fluid Mechanics*, 782:25–36, 2015. doi: 10.1017/jfm.2015.538.

F. Fedele. Are rogue waves really unexpected? *Journal of Physical Oceanography*, 46(5):1495–1508, 2016. doi: 10.1175/jpo-d-15-0137.1.

H. Fernández, S. Venkatachalam, S. Schimmels, M. Budzik, and H. Oumeraci. Focused wave generation in laboratory flumes over uneven bottom. In *Proceedings of the Coastal Engineering Conference (2014)*, page 32. Coastal Engineering Research Council, 2014a. doi: 10.9753/icce.v34.waves.32.

H. Fernández, S. Venkatachalam, S. Schimmels, and H. Oumeraci. Extreme wave generation using self correcting method — revisited. *Coastal Engineering*, 93:15–31, 2014b. doi: 10.1016/j.coastaleng.2014.07.003.

C. Fochesato, S. Grilli, and F. Dias. Numerical modeling of extreme rogue waves generated by directional energy focusing. *Wave Motion*, 44(5):395–416, 2007. doi: 10.1016/j.wavemoti.2007.01.003.

G. Z. Forristall. On the statistical distribution of wave heights in a storm. *Journal of Geophysical Research*, 83(C5):2353, 1978. doi: 10.1029/jc083ic05p02353.

P. Frigaard and M. Brorsen. A time-domain method for separating incident and reflected irregular waves. *Coastal Engineering*, 24(3-4):205–215, 1995. doi: 10.1016/0378-3839(94)00035-v.

E. R. Funke and E. P. D. Mansard. On the synthesis of realistic sea states. In *Coastal Engineering Proceedings*, pages 2974–2991. American Society of Civil Engineers, 1980. doi: 10.1061/9780872622647.179.

P. Gaillard. Families of quasi-rational solutions of the NLS and equation and multi-rogue waves. *Journal of Physics A: Mathematical and Theoretical*, 44:435204, 2011. doi: 10.1088/1751-8113/44/43/435204.

A. A. Galeev, R. Z. Sagdeev, I. S. Sigov, V. D. Shapiro, and V. I. Shevchenko. Nonlinear theory for the modulation instability of plasma waves. *Soviet Journal of Plasma Physics*, 1:5–10, 1975.

J. Gemmrich and C. Garrett. Unexpected waves. *Journal of Physical Oceanography*, 38(10):2330–2336, 2008. doi: 10.1175/2008jpo3960.1.

J. Glejin, V. S. Kumar, T. M. B. Nair, J. Singh, and A. Nherakkol. Freak waves off Ratnagiri, west coast of india. *Indian Journal of Marine Sciences*, 43(7): 1339–1342, 2014.

Y. Goda. *Random seas and design of maritime structures (2nd edition)*. World Scientific, 2000. ISBN 981023256X.

Y. Goda and Y. Suzuki. Estimation of incident and reflected waves in random wave experiments. In *Coastal Engineering Proceedings*, pages 828–845, Honolulu, Hawaii, United States, 1976. doi: 10.1017/cbo9781139059107.005.

V. A. Godoi, K. R. Bryan, S. A. Stephens, and R. M. Gorman. Extreme waves in New Zealand waters. *Ocean Modelling*, 117:97–110, 2017. doi: 10.1016/j.ocemod.2017.08.004.

M. Gouin, G. Ducrozet, and P. Ferrant. Development and validation of a non-linear spectral model for water waves over variable depth. *European Journal of Mechanics - B/Fluids*, 57:115–128, 2016. doi: 10.1016/j.euromechflu.2015.12.004.

O. Gramstad and K. Trulsen. Fourth-order coupled nonlinear Schrödinger equations for gravity waves on deep water. *Physics of Fluids*, 23:062102, 2011a. doi: 10.1063/1.3598316.

O. Gramstad and K. Trulsen. Hamiltonian form of the modified nonlinear Schrödinger equation for gravity waves on arbitrary depth. *Journal of Fluid Mechanics*, 670:404–426, 2011b. doi: 10.1017/s0022112010005355.

O. Gramstad, H. Zeng, K. Trulsen, and G. K. Pedersen. Freak waves in weakly nonlinear unidirectional wave trains over a sloping bottom in shallow water. *Physics of Fluids*, 25(12):122103, 2013. doi: 10.1063/1.4847035.

S. T. Grilli, J. Skourup, and I. A. Svendsen. An efficient boundary element method for nonlinear water waves. *Engineering Analysis with Boundary Elements*, 6(2): 97–107, 1989. doi: 10.1016/0955-7997(89)90005-2.

R. H. J. Grimshaw and S. Y. Annenkov. Water wave packets over variable depth. *Studies in Applied Mathematics*, 126(4):409–427, 2011. doi: 10.1111/j.1467-9590.2010.00508.x.

E. Guazzelli, V. Rey, and M. Belzons. Higher-order Bragg reflection of gravity surface waves by periodic beds. *Journal of Fluid Mechanics*, 245(-1):301, 1992. doi: 10.1017/s0022112092000478.

S. Guignard and S. T. Grilli. Modeling of wave shoaling in a 2D-NWT using a spilling breaker model. In *The Eleventh International Offshore and Polar Engineering Conference. International Society of Offshore and Polar Engineers*, 2001.

S. Guo, L. Mei, Y. He, and Y. Li. Modulation instability and ion-acoustic rogue waves in a strongly coupled collisional plasma with nonthermal nonextensive electrons. *Plasma Physics and Controlled Fusion*, 58(2):025014, 2016. doi: 10.1088/0741-3335/58/2/025014.

K. Hammani, B. Wetzel, B. Kibler, J. Fatome, C. Finot, G. Millot, N. Akhmediev, and J. M. Dudley. Spectral dynamics of modulation instability described using Akhmediev breather theory. *Optics Letters*, 36(11):2140, 2011. doi: 10.1364/ol.36.002140.

J. D. Hansom, A. D. Switzer, and J. Pile. Extreme waves. In *Coastal and Marine Hazards, Risks, and Disasters*, pages 307–334. Elsevier, 2015. doi: 10.1016/b978-0-12-396483-0.00011-x.

T. Hara and C. C. Mei. Bragg scattering of surface waves by periodic bars: theory and experiment. *Journal of Fluid Mechanics*, 178:221–241, 1987. doi: 10.1017/s0022112087001198.

H. Hasimoto and H. Ono. Nonlinear modulation of gravity waves. *Journal of the Physical Society of Japan*, 33(3):805–811, 1972. doi: 10.1143/JPSJ.33.805.

K. Hasselmann, W. Munk, and G. MacDonald. *"Bispectrum of ocean waves", in Time Series Analysis. M. Rosenblatt.* John Wiley, New York, 1963. doi: 10.1017/S0022112062000373.

S. Haver. Freak waves: a suggested definition and possible consequences for marine and structures. In *Rogue waves*, pages 23–34, 2004.

D. Henderson, G. K. Rajan, and H. Segur. Dissipation of narrow-banded surface water waves. In *Hamiltonian Partial Differential Equations and Applications*, pages 163–183. Springer New York, 2015. doi: 10.1007/978-1-4939-2950-4_6.

L. H. Holthuijsen. *Waves in Oceanic and Coastal Waters*. Cambridge University Press, 2007. ISBN 0521860288. doi: 10.2277/0521860288.

L. N. Howard and J. Yu. Normal modes of a rectangular tank with corrugated bottom. *Journal of Fluid Mechanics*, 593:209–234, 2007. doi: 10.1017/s0022112007008695.

R. T. Hudspeth and J. R. Medina. Wave group analysis by the Hilbert transform. In *Coastal Engineering 1988*, pages 884–898. American Society of Civil Engineers, 1989. doi: 10.1061/9780872626874.067.

H. Hwung, W. Chiang, and S. Hsiao. Observations on the evolution of wave modulation. *Proceedings of the Royal Society A: Mathematical, Physical and Engineering Sciences*, 463(2077):85–112, 2006. doi: 10.1098/rspa.2006.1759.

A. Iafrati, A. Babanin, and M. Onorato. Modeling of ocean–atmosphere interaction phenomena during the breaking of modulated wave trains. *Journal of Computational Physics*, 271:151–171, 2014. doi: 10.1016/j.jcp.2013.12.045.

P. A. E. M. Janssen. Nonlinear four-wave interactions and freak waves. *Journal of Physical Oceanography*, 33(4):863–884, 2003. doi: 10.1175/1520-0485(2003)33⟨863:nfiafw⟩2.0.co;2.

P. A. E. M. Janssen. On a random time series analysis valid for arbitrary spectral shape. *Journal of Fluid Mechanics*, 759:236–256, 2014. doi: 10.1017/jfm.2014.565.

P. A. E. M. Janssen and J. R. Bidlot. On the extension of the freak wave warning system and its verification. *Not published internal paper of ECMWF*, 2009.

P. A. E. M. Janssen and M. Onorato. The intermediate water depth limit of the Zakharov equation and consequences for wave prediction. *Journal of Physical Oceanography*, 37(10):2389–2400, 2007. doi: 10.1175/jpo3128.1.

P. Jonathan and P. H. Taylor. On irregular, nonlinear waves in a spread sea. *Journal of Offshore Mechanics and Arctic Engineering*, 119(variable.):37–41, 1997. doi: 10.1115/1.2829043.

H. Kashima and N. Mori. Aftereffect of high-order nonlinearity on extreme wave occurrence from deep to intermediate water. *Coastal Engineering*, 153:103559, 2019. doi: 10.1016/j.coastaleng.2019.103559.

H. Kashima, K. Hirayama, and N. Mori. Estimation of freak wave occurrence from deep to shallow water regions. In *Coastal Engineering Proceedings*, volume 1, page 36. Coastal Engineering Research Council, 2014. doi: 10.9753/icce.v34.waves.36.

C. Kharif and E. Pelinovsky. Physical mechanisms of the rogue wave phenomenon. *European Journal of Mechanics - B/Fluids*, 22(6):603–634, 2003. doi: 10.1016/j.euromechflu.2003.09.002.

C. Kharif, E. Pelinovsky, and A. Slunyaev. *Rogue Waves in the Ocean*. Springer Berlin Heidelberg, 2009. ISBN 3540884181.

Y. C. Kim and E. J. Powers. Digital bispectral analysis and its applications to nonlinear wave interactions. *IEEE Transactions on Plasma Science*, 7(2):120–131, 1979. doi: 10.1109/tps.1979.4317207.

O. Kimmoun, H. C. Hsu, H. Branger, M. S. Li, Y. Y. Chen, C. Kharif, M. Onorato, E. J. R. Kelleher, B. Kibler, N. Akhmediev, and A. Chabchoub. Modulation instability and phase-shifted Fermi-Pasta-Ulam recurrence. *Scientific Reports*, 6:28516, 2016. doi: 10.1038/srep28516.

O. Kimmoun, H. C. Hsu, B. Kibler, and A. Chabchoub. Non-conservative higher-order hydrodynamic modulation instability. *Physical Review E*, 96(2):022219, 2017. doi: 10.1103/physreve.96.022219.

A. Kimura. Statistical properties of random wave groups. In *Coastal Engineering Proceedings*, volume 1, pages 2955–2973, 1980. doi: http://dx.doi.org/10.9753/icce.v17.25p.

J. T. Kirby. A general wave equation for waves over rippled beds. *Journal of Fluid Mechanics*, 162:171–186, 1986a. doi: 10.1017/s0022112086001994.

J. T. Kirby. On the gradual reflection of weakly nonlinear Stokes waves in regions with varying topography. *Journal of Fluid Mechanics*, 162:187, 1986b. doi: 10.1017/s0022112086002008.

J. T. Kirby. Current effects on resonant reflection of surface water waves by sand bars. *Journal of Fluid Mechanics*, 186:501–520, 1988. doi: 10.1017/s0022112088000242.

J. T. Kirby and R. A. Dalrymple. A parabolic equation for the combined refraction–diffraction of Stokes waves by mildly varying topography. *Journal of Fluid Mechanics*, 136:453, 1983. doi: 10.1017/s0022112083002232.

D. L. Kriebel and M. V. Alsina. Simulation of extreme waves in a background random sea. In *International Society of Offshore and Polar Engineers*. International Society of Offshore and Polar Engineers, 2000.

E. A. Kuznetsov. Solitons in a parametrically unstable plasma. *Akademiia Nauk SSSR Doklady*, 236:575–577, 1977.

J. Zhang L. Zhang, M. H. Kim and B. L. Edge. Hybrid model for Bragg scattering of water waves by steep multiply-sinusoidal bars. *Journal of Coastal Research*, 15(2):486–495, 1999.

B. M. Lake, H. C. Yuen, H. Rungaldier, and W. E. Ferguson. Nonlinear deep-water waves: theory and experiment. Part 2. evolution of a continuous wave train. *Journal of Fluid Mechanics*, 83(1):49–74, 1977. doi: 10.1017/s0022112077001037.

J. Li, Y. Chen, S. Pan, Y. Pan, J. Fang, and D. M. A. Sowa. Estimation of mean and extreme waves in the East China Seas. *Applied Ocean Research*, 56:35–47, 2016. doi: 10.1016/j.apor.2016.01.005.

M. J. Lighthill. Some special cases treated by the Whitham theory. *Proceedings of the Royal Society A*, 299:28–53, 1967. doi: 10.1098/rspa.1967.0121.

C. Lin and C. Huang. Decomposition of incident and reflected higher harmonic waves using four wave gauges. *Coastal Engineering*, 51(5-6):395–406, 2004. doi: 10.1016/j.coastaleng.2004.04.004.

H. Liu, J. Yang, and P. Lin. An analytic solution to the modified mild-slope equation for wave propagation over one-dimensional piecewise smooth topographies. *Wave Motion*, 49(3):445–460, 2012. doi: 10.1016/j.wavemoti.2012.01.002.

H. Liu, X. Li, and P. Lin. Analytical study of Bragg resonance by singly periodic sinusoidal ripples based on the modified mild-slope equation. *Coastal Engineering*, 150:121–134, 2019. doi: 10.1016/j.coastaleng.2019.04.015.

H. Liu, H. Zeng, and H. Huang. Bragg resonant reflection of surface waves from deep water to shallow water by a finite array of trapezoidal bars. *Applied Ocean Research*, 94:101976, 2020. doi: 10.1016/j.apor.2019.101976.

Y. Liu and S. Li. Resolution of incident and reflected components of nonlinear regular waves. *Coastal Engineering Journal*, 58(3):1650012–1–1650012–21, 2016. doi: 10.1142/s0578563416500121.

Y. Liu and D. K. P. Yue. On generalized Bragg scattering of surface waves by bottom ripples. *Journal of Fluid Mechanics*, 356:297–326, 1998. doi: 10.1017/s0022112097007969.

E. Lo and C. C. Mei. A numerical study of water-wave modulation based on a higher-order nonlinear Schrödinger equation. *Journal of Fluid Mechanics*, 150: 395–416, 1985. doi: 10.1017/s0022112085000180.

M. S. Longuet-Higgins. On the statistical distribution of the heights of sea waves. *Journal of marine research*, 11(3):245–265, 1952.

M. S. Longuet-Higgins. The effect of non-linearities on statistical distributions in the theory of sea waves. *Journal of Fluid Mechanics*, 17(03):459, 1963. doi: 10.1017/s0022112063001452.

M. S. Longuet-Higgins. Breaking waves in deep or shallow water. In *Proc. 10th Conf. on Naval Hydrodynamics*, volume 597, pages 597–605. MIT, 1974.

Y. Ma. The perturbed plane-wave solutions of the cubic Schrödinger equation. *Studies in Applied Mathematics*, 60(1):43–58, 1979. doi: 10.1002/sapm197960143.

Y. Ma, G. Dong, X. Ma, and G. Wang. A new method for separation of 2D incident and reflected waves by the Morlet wavelet transform. *Coastal Engineering*, 57 (6):597–603, 2010. doi: 10.1016/j.coastaleng.2010.01.002.

Y. Ma, G. Dong, and X. Ma. Separation of obliquely incident and reflected irregular waves by the Morlet wavelet transform. *Coastal Engineering*, 58(8):761–766, 2011. doi: 10.1016/j.coastaleng.2011.03.014.

Y. Ma, G. Dong, M. Perlin, X. Ma, and G. Wang. Experimental investigation on the evolution of the modulation instability with dissipation. *Journal of Fluid Mechanics*, 711:101–121, 2012. doi: 10.1017/jfm.2012.372.

Y. Ma, G. Dong, and X. Ma. Experimental study of statistics of random waves propagating over a bar. *Coastal Engineering Proceedings*, 1(34):30, 2014. doi: 10.9753/icce.v34.waves.30.

Y. Ma, X. Ma, and G. Dong. Variations of statistics for random waves propagating over a bar. *Journal of Marine Science and Technology*, 23(6):864–869, 2015. doi: 10.6119/JMST-015-0610-3.

P. A. Madsen, H. B. Bingham, and H. Liu. A new Boussinesq method for fully nonlinear waves from shallow to deep water. *Journal of Fluid Mechanics*, 462: 1–30, 2002. doi: 10.1017/s0022112002008467.

P. A. Madsen, H. B. Bingham, and H. A. Schäffer. Boussinesq-type formulations for fully nonlinear and extremely dispersive water waves: derivation and analysis. *Proceedings of the Royal Society of London. Series A: Mathematical, Physical and Engineering Sciences*, 459(2033):1075–1104, 2003. doi: 10.1098/rspa.2002.1067.

P. A. Madsen, D. R. Fuhrman, and B. Wang. A Boussinesq-type method for fully nonlinear waves interacting with a rapidly varying bathymetry. *Coastal Engineering*, 53(5-6):487–504, 2006. doi: 10.1016/j.coastaleng.2005.11.002.

R. Magne, V. Rey, and F. Ardhuin. Measurement of wave scattering by topography in the presence of currents. *Physics of Fluids*, 17(12):126601, 2005. doi: 10.1063/1.2140283.

E. P. D. Mansard and E. R. Funke. The measurement of incident and reflected spectra using a least squares method. In *Coastal Engineering Proceedings*, pages 154–172. American Society of Civil Engineers, 1980. doi: 10.1061/9780872622647.008.

S. R. Massel. Extended refraction-diffraction equation for surface waves. *Coastal Engineering*, 19(1-2):97–126, 1993. doi: 10.1016/0378-3839(93)90020-9.

V. B. Matveev and M. A. Salle. *Darboux Transformations and Solitons*. Springer Berlin Heidelberg, 1991. doi: 10.1007/978-3-662-00922-2.

J. R. Medina and R. T. Hudspeth. A review of the analyses of ocean wave groups. *Coastal Engineering*, 14(6):515–542, 1990. doi: 10.1016/0378-3839(90)90033-s.

C. C. Mei. Resonant reflection of surface water waves by periodic sandbars. *Journal of Fluid Mechanics*, 152:315–335, 1985. doi: 10.1017/s0022112085000714.

C. C. Mei, T. Hara, and M. Naciri. Note on Bragg scattering of water waves by parallel bars on the seabed. *Journal of Fluid Mechanics*, 186:147–162, 1988. doi: 10.1017/s0022112088000084.

Chiang C Mei. *The Applied Dynamics of Ocean Surface Waves*. WORLD SCIENTIFIC, 1992. doi: 10.1142/0752.

W. K. Melville. The instability and breaking of deep-water waves. *Journal of Fluid Mechanics*, 115:165, 1982. doi: 10.1017/s0022112082000706.

N. Mori and P. A. E. M. Janssen. On kurtosis and occurrence probability of freak waves. *Journal of Physical Oceanography*, 36(7):1471–1483, 2006. doi: 10.1175/jpo2922.1.

M. Närhi, B. Wetzel, C. Billet, S. Toenger, T. Sylvestre, J. Merolla, R. Morandotti, F. Dias, G. Genty, and J. M. Dudley. Real-time measurements of spontaneous breathers and rogue wave events in optical fibre modulation instability. *Nature Communications*, 7(1), 2016. doi: 10.1038/ncomms13675.

I. Nikolkina and I. Didenkulova. Rogue waves in 2006–2010. *Natural hazards and Earth system sciences*, 11(11):2913–2924, 2011. doi: 10.5194/nhess-11-2913-2011.

D. Z. Ning, J. Zang, S. X. Liu, R. E. Taylor, B. Teng, and P. H. Taylor. Free-surface evolution and wave kinematics for nonlinear uni-directional focused wave groups. *Ocean Engineering*, 36:1226–1243, 2009. doi: 10.1016/j.oceaneng.2009.07.011.

X. Niu, X. Ma, Y. Ma, and G. Dong. Controlled extreme wave generation using an improved focusing method. *Applied Ocean Research*, 95:102017, 2020. doi: 10.1016/j.apor.2019.102017.

L. O'Brien, E. Renzi, J. M. Dudley, C. Clancy, and F. Dias. Extreme wave events in Ireland: 2012-2016. *Natural Hazards and Earth System Sciences Discussions*, pages 1–46, 2017. doi: 10.5194/nhess-2017-206.

T. J. O'Hare and A. G. Davies. A comparison of two models for surface-wave propagation over rapidly varying topography. *Applied Ocean Research*, 15(1): 1–11, 1993. doi: 10.1016/0141-1187(93)90028-v.

M. Olagnon and A. K. Magnusson. Sensitivity study of sea state parameters in correlation to extreme wave occurrences. In *International Society of Offshore & Polar Engineering*. International Society of Offshore & Polar Engineering, 2004. ISBN 1-880653-62-1.

M. Onorato, S. Residori, U. Bortolozzo, A. Montina, and F. T. Arecchi. Rogue waves and their generating mechanisms in different physical contexts. *Physics Reports*, 528(2):47–89, 2013. doi: 10.1016/j.physrep.2013.03.001.

A. Papoulis. *Signal Analysis*. Mcgraw-Hill College, 1977. ISBN 0-07-048460-0.

C. Papoutsellis, A. G. Charalampopoulos, and G. A. Athanassoulis. Implementation of a fully nonlinear Hamiltonian Coupled-Mode Theory, and application to solitary wave problems over bathymetry. *European Journal of Mechanics - B/Fluids*, 72:199–224, 2018. doi: 10.1016/j.euromechflu.2018.04.015.

C. E. Papoutsellis, M. L. Yates, B. Simon, and M. Benoit. Modelling of depth-induced wave breaking in a fully nonlinear free-surface potential flow model. *Coastal Engineering*, 154:103579, 2019. doi: 10.1016/j.coastaleng.2019.103579.

J. Peng, A. Tao, Y. Liu, J. Zheng, J. Zhang, and R. Wang. A laboratory study of class III Bragg resonance of gravity surface waves by periodic beds. *Physics of Fluids*, 31(6):067110, 2019. doi: 10.1063/1.5083790.

D. H. Peregrine. Water waves, nonlinear Schrödinger equations and their solutions. *The Journal of the Australian Mathematical Society. Series B. Applied Mathematics*, 25(01):16–43, 1983. doi: 10.1017/s0334270000003891.

D. Porter and D. J. Staziker. Extensions of the mild-slope equation. *Journal of Fluid Mechanics*, 300:367–382, 1995. doi: 10.1017/s0022112095003727.

R. Porter and D. Porter. Interaction of water waves with three-dimensional periodic topography. *Journal of Fluid Mechanics*, 434:301–335, 2001. doi: 10.1017/s0022112001003676.

S. R. Pudjaprasetya, E. Van Groesen, and E. Soewono. The splitting of solitary waves running over a shallower water. *Wave Motion*, 29(4):375–389, 1999. doi: 10.1016/s0165-2125(98)00040-7.

C. Raoult, M. Benoit, and M. L. Yates. Validation of a fully nonlinear and dispersive wave model with laboratory non-breaking experiments. *Coastal Engineering*, 114:194–207, 2016. doi: 10.1016/j.coastaleng.2016.04.003.

V. Rey, E. Guazzelli, and C. C. Mei. Resonant reflection of surface gravity waves by one-dimensional doubly sinusoidal beds. *Physics of Fluids*, 8:1525–1530, 1996. doi: 10.1063/1.868928.

H. Rye. *Ocean wave groups*. PhD thesis, Division of Marine Hydrodynamics, University of Trondeim, Norwegian Institute of Technology, 1982.

H. Segur, D. Henderson, J. Carter, J. Hammack, C. Li, D. Pheiff, and K. Socha. Stabilizing the Benjamin–Feir instability. *Journal of Fluid Mechanics*, 539:229, 2005. doi: 10.1017/s002211200500563x.

A. Sergeeva, E. Pelinovsky, and T. Talipova. Nonlinear random wave field in shallow water: variable Korteweg-de Vries framework. *Natural Hazards and Earth System Science*, 11(2):323–330, 2011. doi: 10.5194/nhess-11-323-2011.

M. Serio, M. Onorato, A. R. Osborne, and P. A. E. M. Janssen. On the computation of the Benjamin-Feir Index. *Il Nuovo Cimento C*, 28(6):893–903, 2006. ISSN 0390-5551. doi: 10.1393/ncc/i2005-10134-1.

B. Simon, C. E. Papoutsellis, M. Benoit, and M. L. Yates. Comparing methods of modeling depth-induced breaking of irregular waves with a fully nonlinear potential flow approach. *Journal of Ocean Engineering and Marine Energy*, 5: 365–383, 2019. doi: 10.1007/s40722-019-00154-7.

A. V. Slunyaev. A high-order nonlinear envelope equation for gravity waves in finite-depth water. *Journal of Experimental and Theoretical Physics*, 101(5): 926–941, 2005. doi: 10.1134/1.2149072.

A. V. Slunyaev and V. I. Shrira. On the highest non-breaking wave in a group: fully nonlinear water wave breathers versus weakly nonlinear theory. *Journal of Fluid Mechanics*, 735:203–248, 2013. doi: 10.1017/jfm.2013.498.

R. Smith and T. Sprinks. Scattering of surface waves by a conical island. *Journal of Fluid Mechanics*, 72(2):373–384, 1975. doi: 10.1017/S0022112075003424.

M. Stiassnie and L. Shemer. On modifications of the Zakharov equation for surface gravity waves. *Journal of Fluid Mechanics*, 143:47–67, 1984. doi: 10.1017/s0022112084001257.

K. D. Suh, C. Lee, and W. S. Park. Time-dependent equations for wave propagation on rapidly varying topography. *Coastal Engineering*, 32(2-3):91–117, 1997. doi: 10.1016/s0378-3839(97)81745-0.

I. A. Svendsen, P. Å. Madsen, and J. B. Hansen. Wave characteristics in the surf zone. In *Coastal Engineering 1978*, pages 520–539. American Society of Civil Engineers, 1978. doi: 10.1061/9780872621909.031.

T. R. Taha and M. J. Ablowitz. Analytical and numerical aspects of certain nonlinear evolution equations. I. analytical. *Journal of Computational Physics*, 55(2):192–202, 1984. doi: 10.1016/0021-9991(84)90002-0.

K. Tai, A. Hasegawa, and A. Tomita. Observation of modulational instability in optical fibers. *Physical Review Letters*, 56(2):135–138, 1986. doi: 10.1103/physrevlett.56.135.

M. Tanaka. The stability of solitary waves. *Physics of Fluids*, 29(3):650, 1986. doi: 10.1063/1.865459.

H. Tang and C. Huang. Bragg reflection in a fully nonlinear numerical wave tank based on boundary integral equation method. *Ocean Engineering*, 35:1800–1810, 2008. doi: 10.1016/j.oceaneng.2008.09.008.

P. H. Taylor and B. A. Williams. Wave statistics for intermediate depth water—NewWaves and symmetry. *Journal of Offshore Mechanics and Arctic Engineering*, 126(1):54–59, 2004. doi: 10.1115/1.1641796.

E. F. Thompson and W. N. Seelig. High wave grouping in shallow water. *Journal of Waterway, Port, Coastal, and Ocean Engineering*, 110(2):139–157, 1984. doi: 10.1061/(asce)0733-950x(1984)110:2(139).

Y. Tian and S. Sato. A numerical model on the interaction between nearshore nonlinear waves and strong currents. *Coastal Engineering Journal*, 50(04):369–395, 2008. doi: 10.1142/s0578563408001879.

F. C. K. Ting and J. T. Kirby. Observation of undertow and turbulence in a laboratory surf zone. *Coastal Engineering*, 24(1-2):51–80, 1994. doi: 10.1016/0378-3839(94)90026-4.

A. Toffoli, L. Fernandez, J. Monbaliu, M. Benoit, E. G. Renou, J. M. Lefèvre, L. Cavaleri, D. Proment, C. Pakozdi, C. T. Stansberg, T. Waseda, and M. Onorato. Experimental evidence of the modulation of a plane wave to oblique perturbations and generation of rogue waves in finite water depth. *Physics of Fluids*, 25(9):091701, 2013. doi: 10.1063/1.4821810.

P. S. Tromans, A. R. Anaturk, and P. Hagemeijer. A new model for the kinematics of large ocean waves-application as a design wave. In *International Society of Offshore and Polar Engineers*, volume III, 1991.

K. Trulsen and K. B. Dysthe. A modified nonlinear Schrödinger equation for broader bandwidth gravity waves on deep water. *Wave Motion*, 24:281–289, 1996. doi: 10.1016/S0165-2125(96)00020-0.

K. Trulsen, H. Zeng, and O. Gramstad. Laboratory evidence of freak waves provoked by non-uniform bathymetry. *Physics of Fluids*, 24(9):097101, 2012. doi: 10.1063/1.4748346.

K. Trulsen, A. Raustøl, S. Jorde, and L. B. Rye. Extreme wave statistics of long-crested irregular waves over a shoal. *Journal of Fluid Mechanics*, 882, 2020. doi: 10.1017/jfm.2019.861.

M. P. Tulin and T. Waseda. Laboratory observations of wave group evolution, including breaking effects. *Journal of Fluid Mechanics*, 378:197–232, 1999. doi: 10.1017/s0022112098003255.

A. Veltcheva and C. G. Soares. Analysis of wave groups by wave envelope-phase and the Hilbert-Huang transform methods. *Applied Ocean Research*, 60:176–184, 2016. doi: 10.1016/j.apor.2016.09.006.

C. Viotti and F. Dias. Extreme waves induced by strong depth transitions: Fully nonlinear results. *Physics of Fluids*, 26(5):051705, 2014. doi: 10.1063/1.4880659.

V. V. Voronovich, V. I. Shrira, and G. Thomas. Can bottom friction suppress 'freak wave' formation? *Journal of Fluid Mechanics*, 604:263–296, 2008. doi: 10.1017/s0022112008001171.

S. Wabnitz and N. Akhmediev. Efficient modulation frequency doubling by induced modulation instability. *Optics Communications*, 283(6):1152–1154, 2010. doi: 10.1016/j.optcom.2009.11.030.

P. Wang, Y. Yao, and M. P. Tulin. An efficient numerical tank for non-linear water waves, based on the multi-subdomain approach with BEM. *International Journal for Numerical Methods in Fluids*, 20(12):1315–1336, 1995. doi: 10.1002/fld.1650201203.

W. Wang, A. Kamath, C. Pakozdi, and H. Bihs. Investigation of focusing wave properties in a numerical wave tank with a fully nonlinear potential flow model. *Journal of Marine Science and Engineering*, 7(10):375, 2019. doi: 10.3390/jmse7100375.

P. D. Weidman, A. Herczynski, J. Yu, and L. N. Howard. Experiments on standing waves in a rectangular tank with a corrugated bed. *Journal of Fluid Mechanics*, 777:122–150, 2015. doi: 10.1017/jfm.2015.318.

B. J. West, K. A. Brueckner, R. S. Janda, D. M. Milder, and R. L. Milton. A new numerical method for surface hydrodynamics. *Journal of Geophysical Research*, 92(C11):11803, 1987. doi: 10.1029/jc092ic11p11803.

G. B. Whitham. A general approach to linear and non-linear dispersive waves using a Lagrangian. *Journal of Fluid Mechanics*, 22(2):273–283, 1965. doi: 10.1017/s0022112065000745.

C. N. Whittaker, A. C. Raby, C. J. Fitzgerald, and P. H. Taylor. The average shape of large waves in the coastal zone. *Coastal Engineering*, 114:253–264, 2016. doi: 10.1016/j.coastaleng.2016.04.009.

C. N. Whittaker, C. J. Fitzgerald, A. C. Raby, P. H. Taylor, J. Orszaghova, and A. G. L. Borthwick. Optimisation of focused wave group runup on a plane beach. *Coastal Engineering*, 121:44–55, 2017. doi: 10.1016/j.coastaleng.2016.12.001.

C. N. Whittaker, C. J. Fitzgerald, A. C. Raby, P. H. Taylor, and A. G. L. Borthwick. Extreme coastal responses using focused wave groups: Overtopping and horizontal forces exerted on an inclined seawall. *Coastal Engineering*, 140:292–305, 2018. doi: 10.1016/j.coastaleng.2018.08.004.

M. L. Yates and M. Benoit. Accuracy and efficiency of two numerical methods of solving the potential flow problem for highly nonlinear and dispersive water waves. *International Journal for Numerical Methods in Fluids*, 77(10):616–640, 2015. doi: 10.1002/fld.3992.

J. Yu and L. N. Howard. On higher order Bragg resonance of water waves by bottom corrugations. *Journal of Fluid Mechanics*, 659:484–504, 2010. doi: 10.1017/s0022112010002582.

J. Yu and L. N. Howard. Exact Floquet theory for waves over arbitrary periodic topographies. *Journal of Fluid Mechanics*, 712:451–470, 2012.

J. Yu and C. C. Mei. Do longshore bars shelter the shore? *Journal of Fluid Mechanics*, 404:251–268, 2000. doi: 10.1017/s0022112099007168.

J. Yu and G. F. Zheng. Exact solutions for wave propagation over a patch of large bottom corrugations. *Journal of Fluid Mechanics*, 713:362–375, 2012. doi: 10.1017/jfm.2012.460.

H. C. Yuen and B. M. Lake. Nonlinear dynamics of deep-water gravity waves. In *Advances in Applied Mechanics*, volume 22, pages 67–229. Elsevier, 1982. doi: 10.1016/s0065-2156(08)70066-8.

V. E. Zakharov. Stability of periodic waves of finite amplitude on the surface of a deep fluid. *Journal of Applied Mechanics and Technical Physics*, 9(2):190–194, 1968. doi: 10.1007/bf00913182.

V. E. Zakharov and L. A. Ostrovsky. Modulation instability: The beginning. *Physica D: Nonlinear Phenomena*, 238(5):540–548, 2009. doi: 10.1016/j.physd.2008.12.002.

V. E. Zakharov and A. B. Shabat. Exact theory of two-dimensional self-focusing and one-dimensional self-modulation of waves in nonlinear media. *Soviet Physics JETP*, 34(1), 1972.

J. A. Zelt and James E. Skjelbreia. Estimating incident and reflected wave fields using an arbitrary number of wave gauges. In *Coastal Engineering Proceedings*, pages 777–789. American Society of Civil Engineers, 1993.

H. Zeng and K. Trulsen. Evolution of skewness and kurtosis of weakly nonlinear unidirectional waves over a sloping bottom. *Natural Hazards and Earth System Science*, 12(3):631–638, 2012. doi: 10.5194/nhess-12-631-2012.

J. Zhang and M. Benoit. Effect of finite amplitude of bottom corrugations on Fabry-Perot resonance of water waves. *Physical Review E*, 99(5):053109, 2019. doi: 10.1103/physreve.99.053109.

Jie Zhang, Michel Benoit, Olivier Kimmoun, Amin Chabchoub, and Hung-Chu Hsu. Statistics of extreme waves in coastal waters: large scale experiments and advanced numerical simulations. *Fluids*, 4(2):99, 2019. doi: 10.3390/fluids4020099.

Interactions vagues-fond marin et mécanismes de formation des vagues scélérates en zone côtière

Résumé: Dans la communauté maritime, le terme de "vague scélérate" est utilisé pour les vagues dont la hauteur dépasse le double de la hauteur significative de l'état de mer considéré, et qui apparaissent plus fréquemment que la prédiction linéaire (i.e. modèle de Rayleigh). Dans les zones côtières, une bathymétrie irrégulière peut également provoquer des vagues extrêmes du fait des interactions entre le fond marin et les vagues. Dans cette thèse, nous nous concentrons sur trois scénarios d'interactions vagues-fond qui peuvent entraîner la formation de vagues extrêmes. Le premier scénario est un phénomène de résonance, connu sous le nom de résonance de Fabry-Pérot, qui peut se développer lorsque des vagues monochromatiques se propagent sur une bathymétrie comportant deux zones d'ondulations sinusoïdales sur un fond par ailleurs plat. Dans le résonateur situé entre les deux zones de rides, une augmentation significative de la hauteur de l'onde incidente peut être obtenue si la condition de résonance est satisfaite. En comparant des simulations numériques avec une condition limite de fond exacte ou approchée et une solution analytique linéaire asymptotique, nous observons un décalage de fréquence de résonance pour la condition de résonance et pour les cas où le rapport entre l'amplitude des ondulations et la profondeur de l'eau est grand. Le second scénario est celui des instabilités des trains de houle modulés en amplitude, appelés communément « breather » qui se propagent sur des fonds irréguliers. Trois types de profils bathymétriques sont étudiées expérimentalement et numériquement avec un modèle entièrement non-linéaire et avec l'équation cubique non-linéaire de Schrödinger. Cette étude a permis de montrer que pour de faibles profondeurs et pour certains paramètres, l'amplitude de la modulation peut atteindre deux fois l'amplitude du train initial. Cette amplification en faible profondeur résulte de mécanismes qui n'existent pas en profondeur constante. Le troisième scénario correspond à des trains de vagues irrégulières unidirectionnelles se propageant sur des profils de fond côtier variables. Lorsqu'un état de mer incident en condition d'équilibre passe sur une barre ou une marche submergée, une dynamique de non-équilibre apparaît et force l'état de mer à un nouvel équilibre compatible avec la profondeur finie, caractérisé par des statistiques fortement non-gaussiennes et une probabilité accrue d'occurrence de vagues extrêmes. La combinaison d'expériences à grande échelle et de simulations complètement non-linéaires permet de mieux comprendre la réponse dynamique du train de vagues. Les données obtenues ont été analysées en profondeur en utilisant une combinaison d'approches spectrales, bispectrales et statistiques.

Mots-clés: vagues côtières extrêmes, vagues scélérates, interactions vagues-fond marin, résonance de Fabry-Pérot, focalisation modulationnelle, vagues non-linéaires.

Wave-seabed interaction and mechanisms of freak wave formation in coastal zones

Abstract: In the maritime community, the term “rogue wave” or “freak wave” is used for waves whose wave height exceeds twice the significant wave height of the background sea state, and that appear more frequently than the linear expectation (i.e. Rayleigh model). In coastal areas, uneven bathymetry could also trigger such high waves due to wave-bottom interactions. In this study, we focus on three scenarios of wave-bottom interactions that may result in the formation of high waves. The first scenario is a resonance phenomenon, known as Fabry-Perot resonance, that may develop when monochromatic waves propagate in a domain with two patches of sinusoidal undulations on an otherwise flat bottom. Within the so-called resonator between the two patches, significant enhancement of incident wave is expected if the resonance condition is met. By comparing numerical simulations with either exact or approximated bottom boundary condition and asymptotic linear analytical solution, we report significant frequency downshift effect of the resonance condition, for cases with large ratios of ripple amplitude to water depth. The second scenario corresponds to the instabilities of amplitude-modulated waves called “breathers” propagating over an uneven bottom. Three kinds of bathymetry profiles are investigated experimentally, and numerically with a fully nonlinear model and the cubic nonlinear Schrödinger equation. Results show that as the instabilities develop, the modulations can split into sub-modulations when waves entered the uneven bottom region. We show experimental evidence that the sub-modulations may overlap with each other forming freak waves nearshore. The third scenario corresponds to irregular long-crested wave trains propagating over uneven coastal bottom profiles. As an incident equilibrium sea state passes over a submerged step or bar, non-equilibrium dynamics appears and forces the sea state to a new, finite-depth equilibrium along with strong non-Gaussian statistics and intensified occurrence probability of large wave events. The combination of large-scale experiments and fully nonlinear simulations allows gaining insight into the dynamical response. The obtained data have been analyzed in-depth using a combination of spectral, bispectral and statistical approaches.

Key words: extreme coastal waves, freak waves, wave-bottom interaction, Fabry-Perot resonance, modulational focusing, nonlinear waves.